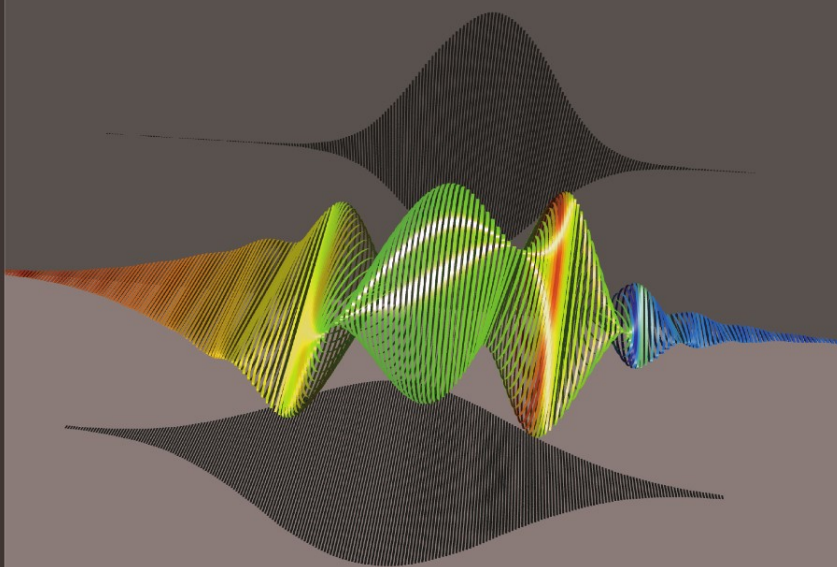# FEMTOSECOND LASER SPECTROSCOPY

Edited by

PETER HANNAFORD

Femtosecond Laser Spectroscopy

Edited by
Peter Hannaford

Femtosecond Laser Spectroscopy

Visit Springer's eBookstore at: http://ebooks.kluweronline.com
and the Springer Global Website Online at: http://www.springeronline.com

Contents

Contributing Authors

Number in parentheses indicates first page of author's contribution.

S. AKTURK (61), School of Physics, Georgia Institute of Technology, Atlanta, Georgia 30332-0430, USA

J. B. ASBURY (167), Department of Chemistry, Stanford University, Stanford, CA 94305, USA

S.N. BAGAYEV (87), Institute of Laser Physics, Siberian Branch, Russian Academy of Sciences, Pr. Lavrentieva, 13/3, 630090 Novosibirsk, Russia

T. BAUMERT (225), Institute of Physics, University of Kassel, Heinrich-Plett-Str. 40, 34132 Kassel, Germany

M. BELLINI (29), Istituto Nazionale di Ottica Applicata (INOA), Largo Fermi 6, 50125, Florence, Italy

T. BRIXNER (225), Physics Department, University of Würzburg, Am Hubland, 97074 Würzburg, Germany

P. CANCIO (109), Istituto Nazionale di Ottica Applicata (INOA), Largo Fermi 6, 50125 Florence, Italy, and European Laboratory for Nonlinear Spectroscopy (LENS), Via Carrara 1, 50019 Sesto Fiorentino FI, Italy

Q. CAO (61), School of Physics, Georgia Institute of Technology, Atlanta, Georgia 30332-0430, USA

B. CHATEL (267), Laboratoire de Collisions, Agrégats et Réactivité (CNRS UMR 5589), IRSAMC, Université Paul Sabatier, 31062 Toulouse CEDEX, France

L.V. DAO (197), Centre for Atom Optics and Ultrafast Spectroscopy, Swinburne University of Technology, PO Box 218, Hawthorn, Victoria 3122, Australia

P. DE NATALE (109), Istituto Nazionale di Ottica Applicata (INOA), Largo Fermi 6, 50125 Florence, Italy, and European Laboratory for Nonlinear Spectroscopy (LENS), Via Carrara 1, 50019 Sesto Fiorentino FI, Italy

V.I. DENISOV (87), Institute of Laser Physics, Siberian Branch, Russian Academy of Sciences, Pr. Lavrentieva, 13/3, 630090 Novosibirsk, Russia

M.D. FAYER (167), Department of Chemistry, Stanford University, Stanford, CA 94305, USA

G. GERBER (225), Physics Department, University of Würzburg, Am Hubland, 97074 Würzburg, Germany

B. GIRARD (267), Laboratoire de Collisions, Agrégats et Réactivité (CNRS UMR 5589), IRSAMC, Université Paul Sabatier, 31062 Toulouse CEDEX, France

X. GU (61), School of Physics, Georgia Institute of Technology, Atlanta, Georgia 30332-0430, USA

P. HANNAFORD (197), Centre for Atom Optics and Ultrafast Spectroscopy, Swinburne University of Technology, PO Box 218, Hawthorn, Victoria 3122, Australia

V.M. KLEMENTYEV (87), Institute of Laser Physics, Siberian Branch, Russian Academy of Sciences, Pr. Lavrentieva, 13/3, 630090 Novosibirsk, Russia

T. KOBAYASHI (133), Department of Physics, University of Tokyo, Hongo 7-3-1, Bunkyo, Tokyo 113-0033, Japan

I.I. KOREL (87), Institute of Laser Physics, Siberian Branch, Russian Academy of Sciences, Pr. Lavrentieva, 13/3, 630090 Novosibirsk, Russia

S.A. KUZNETSOV (87), Institute of Laser Physics, Siberian Branch, Russian Academy of Sciences, Pr. Lavrentieva, 13/3, 630090 Novosibirsk, Russia

C. LINCOLN (197), Centre for Atom Optics and Ultrafast Spectroscopy, Swinburne University of Technology, PO Box 218, Hawthorn, Victoria 3122, Australia

M. LOWE (197), Centre for Atom Optics and Ultrafast Spectroscopy, Swinburne University of Technology, PO Box 218, Hawthorn, Victoria 3122, Australia

D. MAZZOTTI (109), Istituto Nazionale di Ottica Applicata (INOA), Largo Fermi 6, 50125 Florence, Italy, and European Laboratory for Nonlinear Spectroscopy (LENS), Via Carrara 1, 50019 Sesto Fiorentino FI, Italy

M. MERO (305), Department of Physics and Astronomy, University of New Mexico, Albuquerque NM 87131, USA

T. PFEIFER (225), Physics Department, University of Würzburg, Am Hubland, 97074 Würzburg, Germany

V.S. PIVTSOV (87), Institute of Laser Physics, Siberian Branch, Russian Academy of Sciences, Pr. Lavrentieva, 13/3, 630090 Novosibirsk, Russia

W. RUDOLPH (305), Department of Physics and Astronomy, University of New Mexico, Albuquerque NM 87131, USA

A. SHREENATH (61), School of Physics, Georgia Institute of Technology, Atlanta, Georgia 30332-0430, USA

T. STEINEL (167), Department of Chemistry, Stanford University, Stanford, CA 94305, USA

R. TREBINO (61), School of Physics, Georgia Institute of Technology, Atlanta, Georgia 30332-0430, USA

M. WOLLENHAUPT (225), Institute of Physics, University of Kassel, Heinrich-Plett-Str. 40, 34132 Kassel, Germany

J. YE (1), JILA, National Institute of Standards and Technology and University of Colorado, Boulder, Colorado 80309-0440, USA

V.F. ZAKHARYASH (87), Institute of Laser Physics, Siberian Branch, Russian Academy of Sciences, Pr. Lavrentieva, 13/3, 630090 Novosibirsk, Russia

J. ZELLER (305), Department of Physics and Astronomy, University of New Mexico, Albuquerque NM 87131, USA

Foreword

The embryonic development of femtoscience stems from advances made in the generation of ultrashort laser pulses. Beginning with mode-locking of glass lasers in the 1960s, the development of dye lasers brought the pulse width down from picoseconds to femtoseconds. The breakthrough in solid state laser pulse generation provided the current reliable table-top laser systems capable of average power of about 1 watt, and peak power density of easily $10^{12} - 10^{13}$ watts per square centimeter, with pulse widths in the range of four to eight femtoseconds. Pulses with peak power density reaching 10^{20} watts per square centimeter have been achieved in laboratory settings and, more recently, pulses of sub-femtosecond duration have been successfully generated.

As concepts and methodologies have evolved over the past two decades, the realm of ultrafast science has become vast and exciting and has impacted many areas of chemistry, biology and physics, and other fields such as materials science, electrical engineering, and optical communication. In molecular science the explosive growth of this research is for fundamental reasons. In femtochemistry and femtobiology chemical bonds form and break on the femtosecond time scale, and on this scale of time we can freeze the transition states at configurations never before seen. Even for non-reactive physical changes one is observing the most elementary of molecular processes. On a time scale shorter than the vibrational and rotational periods the ensemble behaves coherently as a single-molecule trajectory.

But these developments would not have been possible without the crystallization of some key underlying concepts that were in the beginning shrouded in fog. First was the issue of the "uncertainty principle", which had to be decisively clarified. Second was the question of whether one could

sustain wave-packet motion at the atomic scale of distance. In other words, would the de Broglie wavelength of the atom become sufficiently short to define classical motion – "classical atoms" – and without significant quantum spreading? This too had to be clearly demonstrated and monitored in the course of change, not only for elementary processes in molecular systems, but also during complex biological transformations. And, finally, some questions about the uniqueness and generality of the approach had to be addressed. For example, why not deduce the information from high-resolution frequency-domain methods and then Fourier transform to obtain the dynamics? It is surely now clear that transient species cannot be isolated this way, and that there is no substitute for direct "real time" observations that fully exploit the intrinsic coherence of atomic and molecular motions.

Theory has enjoyed a similar explosion in areas dealing with *ab initio* electronic structures, molecular dynamics, and nonlinear spectroscopies. There has been progress in calculating potential energy surfaces of reactive systems, especially in their ground state. On excited-state surfaces it is now feasible to map out regions of the surface where transition states and conical intersections are important for the outcome of change. For dynamics, new methods have been devised for direct viewing of the motion by formulating the time-dependent picture, rather than solving the time-independent Schrödinger equation and subsequently constructing a temporal picture. Analytical theory has been advanced, using time-ordered density matrices, to enable the design of multidimensional spectroscopy, the analogue of 2-D (and higher) NMR spectroscopy. That the coupling between theory and experiment is profound is evident in many of the chapters in this volume.

Other areas of studies are highlighted in this volume. The making of femtosecond combs for precision metrology and spectroscopy, and the advances in nonlinear and multidimensional optical techniques are two examples of such frontiers. The ability to count optical oscillations of more than 10^{15} cycles per second can potentially provide all-optical atomic clocks with a new limit of precision. Similarly, the ability to generate sub-femtosecond pulses pushes the limit and resolution toward new studies of electron dynamics. Besides these advances in precision (optical cycles) and pulse duration (pulse width) there are those concerned with the phase. Beginning in 1980, the phase of an optical pulse has been experimentally under control and pulses of well-defined phases (π, $\pi/2$, etc) have been generated and utilized in, among other applications, the control of emission from molecules. But only recently could composite phases be prescribed with a feedback algorithm to control the outcome of a reactive channel, as shown in this volume. Coherent control is a frontier field stimulating research in both theory and experiment.

Edited by Peter Hannaford this volume is a welcomed edition to the field as it brings together the latest in some areas of developments with an impressive mix of new methodologies and applications. The use of femtosecond combs for precision measurements is well covered and coherent control is presented with demonstrations for atomic, molecular and electronic processes. Nonlinear optical methods, including novel geometries of photon and vibrational echoes, are described for the investigation of molecular systems, in particular dye molecules, hydrogen-bonded networks, semiconductor quantum dots, and biomolecules. Measurements of ultrashort pulses, time-resolved reflection and transmission methods, and real-time spectroscopy with sub-5-femtosecond visible pulses provide the means for exploring new regimes and resolutions.

This book in the series on *Progress in Lasers* gives an exposé of some current and exciting research areas in the technology of pulse generation and in the applications of femtoscience.

Ahmed Zewail
California Institute of Technology
Pasadena, California
May 2004

Preface

When I was first approached to edit a volume on *Femtosecond Laser Spectroscopy* in 2000, I did not anticipate that the field was about to explode, with the announcement of a series of remarkable new developments and advances. This volume describes these recent developments in eleven chapters written by leading international researchers in the field. It includes sections on:

- Femtosecond optical frequency combs, which are currently revolutionising ultrahigh precision spectroscopy and optical frequency metrology;
- Soft X-ray femtosecond laser sources, which promise to have important applications in biomedical imaging;
- Attosecond laser sources, which will provide the next generation of sources to study ultrafast phenomena such as electron dynamics;
- Novel methods for measuring and characterizing ultrashort laser pulses and ultrashort pulses of light;
- Coherent control of atomic, molecular and electron dynamics with tailored femtosecond laser pulses;
- Real-time Spectroscopy of molecular vibrations with sub-5-fs pulses; and
- Multidimensional femtosecond coherent spectroscopies for studying molecular and electron dynamics.

Indeed, it is gratifying to see that with the recent advent of attosecond laser sources the title of this volume may soon be rendered obsolete.

I would like to thank each of the contributors for their cooperation in preparing this volume, and Ahmed Zewail for writing the Foreword. I appreciate the amount of work that goes into writing chapters of this type when the authors are heavily burdened with other demands on their time. I

Peter Hannaford
Swinburne University of Technology
Melbourne, June 2004

Chapter 1

PHASE CONTROLLED FEMTOSECOND LASERS FOR SENSITIVE, PRECISE, AND WIDE BANDWIDTH NONLINEAR SPECTROSCOPY

Jun Ye

JILA, National Institute of Standards and Technology and University of Colorado
Boulder, Colorado 80309-0440, USA
Ye@jila.colorado.edu

Abstract: Recent progress in precision control of pulse repetition rate and carrier-envelope phase of ultrafast lasers has established a strong connection between optical frequency metrology and ultrafast science. A wide range of applications has ensued, including measurement of absolute optical frequencies, precision laser spectroscopy, optical atomic clocks, and optical frequency synthesis in the frequency-domain, along with pulse timing stabilization, coherent synthesis of optical pulses, and phase-sensitive extreme nonlinear optics in the time-domain. In this chapter we discuss the impact of the femtosecond optical frequency comb to atomic and molecular spectroscopy. Measurements performed in the frequency-domain provide a global picture of atomic and molecular structure at high precision while providing radio-frequency clock signals derived from optical standards. Time-domain analysis and experiments give us new possibilities for nonlinear optical spectroscopy and sensitive detections with real-time information.

Key words: Phase control, femtosecond lasers, optical comb, precision frequency metrology, nonlinear spectroscopy.

1.   INTRODUCTION TO FEMTOSECOND OPTICAL FREQUENCY COMB

Precise phase control of femtosecond lasers has become increasingly important as novel applications utilizing the femtosecond laser-based optical

comb are developed that require greater levels of precision and higher degrees of coherence and control [1]. Improved stability is beneficial for both frequency-domain applications, where the relative phase or "chirp" between comb components is unimportant (e.g., optical frequency metrology), and, perhaps more importantly, time-domain applications where the pulse shape and/or duration are vital, such as in nonlinear optical interactions [2]. For both types of applications, minimizing jitter in the pulse train and noise in the carrier-envelope phase is often critical to achieve the desired level of precision and coherence. Phase-stabilized mode-locked femtosecond lasers have played a key role in recent advances in optical frequency measurement [3-5], carrier-envelope phase stabilization [2, 6, 7], all-optical atomic clocks [8, 9], optical frequency synthesizers [10], coherent pulse synthesis [11], and broadband, phase-coherent spectral generation [12].

   Mode-locked lasers generate short optical pulses by establishing a fixed phase relationship between all of the lasing longitudinal modes. To understand the connection between the time-domain and frequency-domain descriptions of a mode-locked laser and the pulse train that it emits, a key concept is the carrier-envelope phase. This is based on the decomposition of the pulses into an envelope function, $\hat{E}(t)$, that is superimposed on a continuous carrier wave with frequency ω_c, so that the electric field of the pulse is written as $E(t) = \hat{E}(t)e^{i\omega_c t}$. The carrier-envelope phase, ϕ_{CE}, is the phase shift between the peak of the envelope and the closest peak of the carrier wave. In any dispersive material, the difference between group and phase velocities will cause ϕ_{CE} to evolve. This group-phase velocity mismatch inside a laser cavity produces a pulse-to-pulse phase shift accumulated over one round-trip as $\Delta\phi_{CE}$.

   When ϕ_{CE} is constant, the spectrum of a femtosecond optical comb corresponds to identical pulses emitted by the mode-locked laser. For a single pulse, the spectrum is the Fourier transform of its envelope function and is centered at the optical frequency of its carrier. Generally, for any pulse shape, the frequency width of the spectrum will be inversely proportional to the temporal width of the envelope. For a train of identical pulses, separated by a fixed interval, the spectrum can easily be obtained by a Fourier series expansion, yielding a comb of regularly spaced frequencies, where the comb spacing is inversely proportional to time interval between successive pulses, i.e., the inverse of the repetition rate f_{rep} of the laser. The Fourier relationship between time and frequency resolution guarantees that any spectrometer with sufficient spectral resolution to distinguish the individual comb lines cannot have enough temporal resolution to separate successive pulses. Therefore, the successive pulses interfere with each other inside the spectrometer and the comb spectrum occurs because there are certain discrete frequencies at which the interference is constructive. Using

the result from Fourier analysis that a shift in time corresponds to a linear phase change with frequency, we can readily see that the constructive interference occurs at $n f_{rep}$, where n is an integer.

When ϕ_{CE} is evolving with time, such that from pulse to pulse (with a time separation of $T = 1/f_{rep}$) there is a phase shift of $\Delta\phi_{CE}$, then in the spectral domain a rigid shift will occur for the frequencies at which the pulses add constructively. This shift is easily determined as $(1/2\pi)\,\Delta\phi_{CE}\,/T$. Thus the optical frequencies, ν_n, of the comb lines can be written as $\nu_n = n f_{rep} + f_0$ where n is a large integer of order 10^6 that indexes the comb line, and f_0 is the comb offset due to pulse-to-pulse phase shift, $f_0 = (1/2\pi)f_{rep}\,\Delta\phi_{CE}$. The relationship between time- and frequency-domain pictures is summarized in Fig. 1-1. The pulse-to-pulse change in the phase for the train of pulses emitted by a mode-locked laser can be expressed in terms of the average phase (v_p) and group (v_g) velocities inside the cavity. Specifically, $\Delta\phi_{CE} = (1/v_g - 1/v_p)\,l_c\omega_c$, where l_c is the round-trip length of the laser cavity and ω_c is the "carrier" frequency.
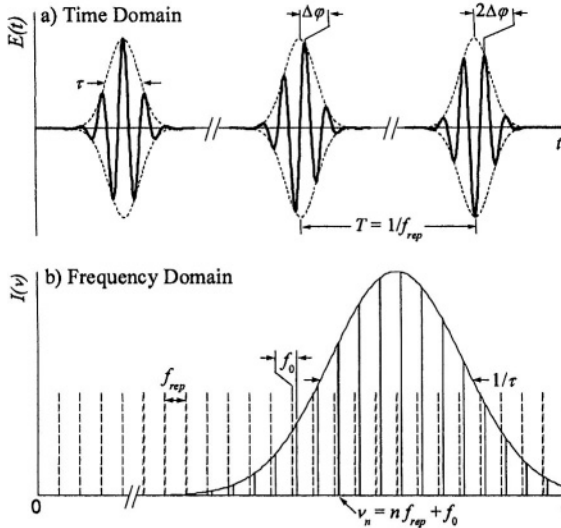
Figure 1-1. Summary of the time-frequency correspondence for a pulse train with evolving carrier-envelope phase.

Armed with the understanding of the frequency spectrum of a mode-locked laser, we now turn to the question of measuring the absolute frequencies of comb lines. For a frequency measurement to be absolute, it must be referenced to the hyperfine transition of ^{133}Cs that defines the second. From the relations listed above we see that determining the absolute optical frequencies of the femtosecond comb requires two radio frequency (RF) measurements, that of f_{rep} and f_0. Measurement of f_{rep} is straightforward;

we simply detect the pulse train's repetition rate (from tens of MHz to several GHz) with a fast photodiode. On the other hand, measurement of f_0 is more involved as the pulse-to-pulse carrier envelope phase shift requires interferometric measurement, whether it is carried out in the time-domain [13] or frequency-domain [14]. When the optical spectrum spans an octave in frequency, i.e., the highest frequencies are a factor of two larger than the lowest frequencies in the spectrum, measurement of f_0 is greatly simplified. If we use a second harmonic crystal to frequency double a comb line, with index *n,* from the low frequency portion of the spectrum, it will have approximately the same frequency as the comb line on the high frequency side of the spectrum with index 2*n*. Measuring the heterodyne beat between these two families of optical comb lines yields a difference frequency by $2\nu_n - \nu_{2n} = 2\left(nf_{rep} + f_0\right) - \left(2nf_{rep} + f_0\right) = f_0$, which is just the offset frequency. Thus, an octave-spanning spectrum enables a direct measurement of f_0 [6]. Note that an octave-spanning spectrum is not required; it just represents the simplest approach. We designate this scheme, shown in Fig. 1-2(a), as "self-referencing" since it uses only the output of the mode-locked laser. Self-referencing is not the only means of determining the absolute optical frequencies given an octave-spanning spectrum. For example, the absolute optical frequency of a CW laser can be determined if its frequency lies close to comb line *n* in the low frequency portion of the femtosecond comb spectrum.   Then the second harmonic of the CW laser will be positioned close to the comb line 2*n*. Measurement of the heterodyne beat between the CW laser frequency, ν_s, and the comb line *n* gives $f_{beat1} = \nu_s - \left(nf_{rep} + f_0\right)$ and between the second harmonic of the CW laser and comb line 2*n* gives $f_{beat2} = 2\nu_s - \left(2nf_{rep} + f_0\right)$. Mixing the beats with appropriate weighting factors gives $f_{beat2} - 2f_{beat1} = 2\nu_s - \left(2nf_{rep} + f_0\right) - \left(2\nu_s - 2\left(nf_{rep} + f_0\right)\right) = f_0$, which represents the second detection scheme shown in Fig. 1-2(b) [9].

An octave-bandwidth optical comb is not straight-forward to produce. A Fourier-transform limited pulse with a full width at half maximum (FWHM) bandwidth of an octave centered at 800 nm would only be a single optical cycle in duration. Such short pulses have not been achieved. Fortunately, neither a transform-limited pulse nor a FWHM of an octave is actually needed.   The pulse width is unimportant as the measurement and control techniques are purely frequency domain approaches. Experimentally, it has been found that even if the power at the octave spanning points is 40 dB below the peak, it is still possible to observe strong f-to-2f heterodyne beats. Still, the necessary comb bandwidth is larger than that from a typical sub-10-fs mode-locked Ti:sapphire laser. One approach to produce this sufficient spectral bandwidth is based on self-phase modulation directly inside the Ti:Sapphire crystal itself [15] or inside an additional glass plate located inside the laser cavity with secondary coincident time and space foci [16].

These techniques require carefully designed mirrors and laser cavities. Additional spectral bandwidth can also be obtained by minor changes in the cavity configuration of a high repetition rate laser, although it has not yet yielded sufficient intensity at the octave points for the observation of f-to-2f beats [17]. Another widely adopted approach is to generate the extra comb bandwidth using microstructure fibers that have zero group velocity dispersion (GVD) within the emission spectrum of a Ti:sapphire laser [18]. The large index contrast for waveguiding inside microstructure fibers has two consequences: first, the ability to generate a zero in the GVD at visible or near-infrared wavelengths and, secondly, the possibility of using a much smaller core size. This allows broadband continuum generation with only 10^{-9} J pulse energies.
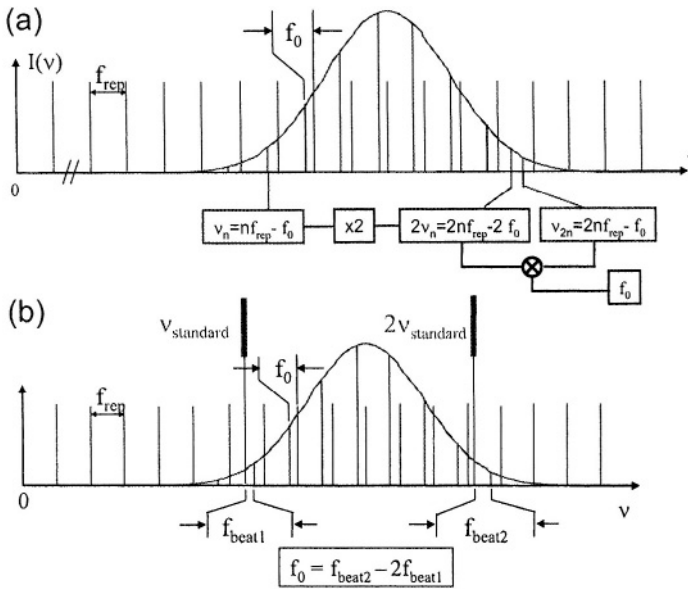
Figure 1-2. Two equivalent schemes for measurement of f_0 using an octave-spanning optical frequency comb. In the self-referencing approach, shown in (a), frequency doubling and comparison are accomplished with the comb itself. In the second approach, shown in (b), the fundamental frequency ($v_{standard}$) and its second harmonic of a CW optical standard are used to determine f_0 . These two basic schemes are employed for absolute optical frequency measurement and implementation of optical atomic clocks.

For the purpose of using a femtosecond optical comb for absolute optical frequency measurements, it is straight-forward to establish the frequency values of all of the comb components. The comb's frequency spacing (f_{rep}) can be phase locked with high precision via detection of higher harmonics of f_{rep} relative to an RF standard. The value of f_0 is determined and controlled

using schemes shown in Fig. 1-2. Control of f_0 requires a servo transducer acting differentially on the intracavity group and phase delays. One common method for adjusting f_0 is to swivel the end mirror in the arm of the laser cavity that contains the prism sequence [19]. An alternative method of controlling f_0 is via modulation of the pump power, with likely contributions from the nonlinear phase, spectral shifts, and the intensity dependence in the group velocity [20]. It is worth noting that a scheme implemented by Telle et al. [21] allows the frequency comb to be free running (without any active stabilization) while making highly precise measurement or connection for an optical frequency interval located within the comb bandwidth.

   The dramatic simplification of a complex optical frequency chain to that of a single mode-locked laser has greatly facilitated optical frequency measurement. Another important aspect of this new technology is its high degree of reliability and precision and lack of systematic errors.   For example, recent tests have shown that the repetition rate of a mode locked laser equals the mode spacing of the corresponding comb to within the measurement uncertainty of 10^{-16}. The uniformity of the comb mode spacing has also been verified to a level below 10^{-17}, even after spectral broadening in a fiber [3, 4]. Comparison between two separate fs comb systems, both linked to a common reference source (microwave or optical), allows one to examine the intrinsic accuracy of a femtosecond-comb-based frequency measurement system, currently at a level of a few parts in 10^{16} with no measurable systematic effects [22]. Direct comparisons of absolute optical frequency measurements between the femtosecond comb technique and the traditional harmonic frequency chain approach have also produced assuring mutual confirmations at the 10^{-12} to 10^{-14} level [5, 23].

   As the measurement precision for optical frequencies continues to advance, the stability limitation imposed by available RF standards used for fs comb stabilization becomes an important issue [23, 24]. Instead of operating a fs comb using RF references, it appears to be advantageous to operate the comb by stabilizing it to an optical frequency standard. The fs comb in turn produces optically derived stable clock signals in the RF domain, leading to a so-called "optical atomic clock" [8, 9, 25]. Recent experimental demonstrations support the concept that, in the future, the most stable and accurate frequency standards will be based on optical transitions [26, 27]. Stepping down the stability level by one or two orders of magnitude, portable optical frequency standards that offer compact, simple, and less expensive system configurations have also shown competitive performance with (in)stability near 10^{-14} at 1 to 10 s averaging time [28].

   To realize an optical atomic clock, an optical comb needs to be stabilized to a pre-selected optical frequency source at a precision level that exceeds the optical standard itself. f_0 can be extracted in a straight-forward manner

using either schemes shown in Fig. 1-2. f_0 is then stabilized with respect to either f_{rep} or an auxiliary stable RF source. It is worth noting that stabilization of f_0 at a few mHz is more than adequate, as it yields fractional frequency noise of $< 10^{-17}$ for an optical carrier. A heterodyne beat between one of the comb components and the optical standard (ν_s) yields information about fluctuations in f_{rep}. For the particular case shown in Fig. 1-2(b), $f_{beat2} - f_{beat1} = 2\nu_s - (2nf_{rep} + f_0) - (\nu_s - (nf_{rep} + f_0)) = \nu_s - nf_{rep}$, producing a direct link between the frequencies ν_s and f_{rep}. After appropriate processing, this error signal is used to stabilize the phase of f_{rep} coherently to ν_s, thereby producing an output clock signal in the RF domain derived from ν_s.

Besides the capability of deriving RF signals from an optical frequency standard, a fs comb can, of course, also be used to transfer the stability of optical standards across vast frequency gaps to other optical spectral regions. Easy access to the resolution and stability offered by optical standards will greatly facilitate the application of frequency metrology to precise spectroscopic investigations. For spectroscopy applications, we indeed often desire a single-frequency and reasonably powered optical carrier wave that can be tuned to any desired optical spectral feature of interest. Realization of such an optical frequency synthesizer (analogous to its RF counterpart) will add a tremendously useful tool for modern spectroscopy experiments. Ideally, one would realize a high precision optical frequency synthesizer based on a stable fs comb linked to an optical frequency standard. One could foresee an array of diode lasers, each covering a successive tuning range of ~ 10 to 20 nanometers that would collectively cover most of the visible spectrum. Each diode laser frequency would be controlled by the stabilized optical comb, and therefore be directly related to the absolute time/frequency standard in a phase coherent fashion, while the setting of the optical frequency would be accomplished via computer control.

In our preliminary implementation of such an optical frequency synthesizer [10], the fs comb system is referenced by an I_2-based optical frequency standard at 532 nm. A CW diode laser, as well as a CW Ti:sapphire laser, is used to tune through targeted spectral regions (for example, Rb D1 and D2 lines at 795 and 780 nm for the diode laser and I_2 hyperfine transitions in the region of 490 - 520 nm) with desired frequency step sizes, while maintaining absolute reference to the stabilized optical comb. A self-adaptive search algorithm first tunes the CW laser to a specified wavelength region with the aid of a wavelength measurement device (100 MHz resolution). A heterodyne beat signal between the laser's frequency and that of a corresponding comb line is then detected and processed. For fine-tuning, an RF source provides a tunable frequency offset for the optical beat. Once the laser frequency tuning exceeds f_{rep}, we reset the RF offset frequency back to the original value to start the process over again.

The laser frequency can thus be tuned smoothly in an "inch-worm" manner along the comb structure. We have demonstrated two fundamental aspects of an optical frequency synthesizer; namely continuous, precise tuning of the optical frequency as well as arbitrary frequency setting on demand. The entire search process takes about a minute.

2.   PRECISION ATOMIC SPECTROSCOPY – STRUCTURE AND DYNAMICS

The first example of spectroscopic application of a precisely stabilized femtosecond comb centers on investigation of a two-photon transition in laser cooled Rb atoms. Phase coherence among the successive pulses interacting with a cold atomic sample brings immediately to mind the approach of Ramsey interference for precision atomic spectroscopy. However, the difference here is that the bandwidth associated with the femtosecond pulse is so broad that one is enabled to explore the structure of a large number of atomic states all at once, along with the possibility of studying coherent accumulation in a multi-level system [29]. It is thus possible to simultaneously explore the global structure and dynamics of an atomic system. The multi-pulse interference in the time domain gives an interesting variation and generalization of the two-pulse based temporal coherent control of the excited-state wave-packet.

From the frequency domain perspective, it is also straight-forward to appreciate the fact that the spectroscopic resolution and precision will not be compromised by the use of ultrafast pulses since they are associated with a phase-stabilized, wide-bandwidth femtosecond comb. Phase coherence among various transition pathways through different intermediate states produces multi-path quantum interference effects on the resonantly enhanced two-photon transition probability in the cold Rb atoms. The two-photon transition spectrum can be analyzed in terms of the pulse repetition rate (f_{rep}) and the carrier-envelope offset frequency (f_0) [30]. Both can be stabilized to high precision. With a set of measurements taken at a few different, but predetermined, combinations of f_{rep} and f_0, one can essentially derive all relevant atomic energy level positions in absolute terms.

Doppler-free two-photon spectroscopy is carried out usually with two equal-frequency cw laser beams propagating in opposite directions. The two-photon transition rate can be resonantly enhanced via the intermediate states with two different laser frequencies [31] or accelerated atomic beams [32], with a small residual Doppler effect. High-resolution two-photon spectroscopy using pulsed light has also been demonstrated [33], with the recent extension to cold atoms [34]. The unique feature of the present work

is that the wide bandwidth optical comb allows all relevant intermediate states to resonantly participate in the two-photon excitation process, permitting the phase coherence among different comb components to induce a stronger transition rate through quantum interference. Following the initial proposal and the subsequent theoretical investigations, we are exploring experimentally this novel, high-resolution spectroscopy using a femtosecond laser [35].
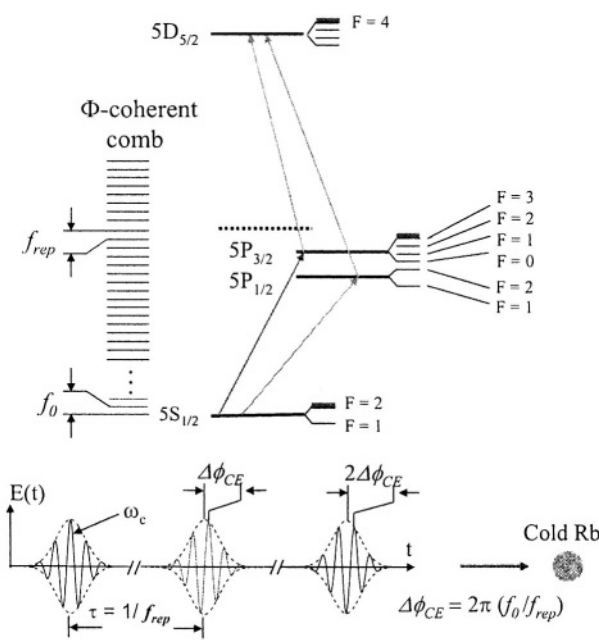
Figure 1-3. Top: Schematic of the relevant energy levels of the [87]Rb atom and the frequency-domain perspective of the atom-light interaction. Bottom: Time-domain picture showing a sequence of mode-locked pulses, with the relevant interaction parameters in f_{rep} and $\Delta\phi_{CE}$.

Figure 1-3 shows the relevant [87]Rb energy levels involved in the two-photon transition from the ground state $5S_{1/2}$ to the excited state $5D_{3/2}$. The dipole-allowed intermediate states, $5P_{3/2}$ and $5P_{1/2}$, are located ~ 2 nm and 17 nm below the virtual level, respectively. Also shown is a regularly spaced comb of optical frequencies around 800 nm. The experimental bandwidth of the comb is ~ 50 nm, emitted from a 10 fs, 100 MHz repetition-rate mode-locked Ti:sapphire laser. Adjustment of f_{rep} and f_0 allows the comb components to line up with corresponding hyperfine states of $5P_{3/2}$ and $5P_{1/2}$ to resonantly enhance the two-photon transition. This dependence of the multi-path quantum interference on f_{rep} and f_0 leads to simultaneous stabilization of both quantities, and thereby the entire comb. The frequency-

domain analysis is complemented by the time-domain multi-pulse Ramsey interference picture, as illustrated in Fig. 1-3, where the relevant quantities for interaction are $\tau = 1/f_{rep}$ and $\Delta\phi_{CE}$. Both the frequency-domain and the time-domain analyses produce the same result on the two-photon transition spectra when one assumes a static distribution among the relevant atomic states. However, to follow the time evolution of the system, it is necessary to explore the interaction dynamics from one pulse to the next, taking into account both the atomic coherence and the optical coherence. The general Liouville equation for the density-matrix components of the atomic states, along with phenomenological decay terms, are used to derive a set of Bloch equations describing the evolution of all relevant levels associated with the ground, the excited, and the intermediate states.
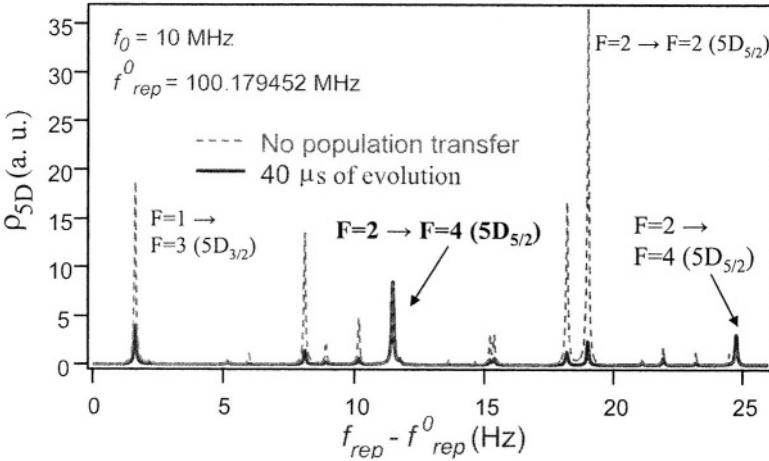
Figure 1-4. Density-matrix calculation of the excited state population due to the two-photon transition induced in ⁸⁷Rb by the phase-coherent fs pulse train. The nominal values of f_{rep} and f_0 are indicated. The spectrum given by the dashed line corresponds to the case with a static population while the spectrum given by solid line shows dynamic evolution after 4000 pulses.

Figure 1-4 illustrates the calculated population of the 5D states due to the two-photon transition, showing clear evidence of population transfer when the number of interacting pulses increases. Not surprisingly, the most dominant transition pathway when a large number of pulses is involved is $5S_{1/2}$ (F=2) $\rightarrow$ $5P_{3/2}$ (F=3) $\rightarrow$ $5D_{5/2}$ (F=4), which represents a so-called closed transition. The horizontal axis represents a scanning of f_{rep} from its nominal value indicated in the figure. The actual optical frequency for the two-photon transition is near 385 THz, which represents a harmonic order of 3.85×10^6 of f_{rep}. Therefore, a change in f_{rep} by ~ 26 Hz implies a repeat in

the optical comb spectrum near the two-photon transition region, and hence a repeat in the two-photon spectra.

Figure 1-5 shows experimental two-photon spectra resonantly enhanced by the intermediate states. We clearly confirm the predicted effect of population transfer by the pulse sequence when we compare the two spectra obtained under the influence of 1,200 and 250,000 pulses, respectively. Basically, the only transition pathway survived at the limit of a large number of pulses is $5S_{1/2}$ (F=2) $\rightarrow$ $5P_{3/2}$ (F=3) $\rightarrow$ $5D_{5/2}$ (F=4). It is interesting to note that we have also observed the pure two-photon transition pathway (energies of the two photons are degenerate) that is not resonantly enhanced by the intermediate states. The signal is indicated in Fig. 1-5 by a small peak (around 19 Hz) in the 2.5 ms evolution curve represented by diamonds, which repeats every 13 Hz in the scan of the f_{rep} value. This observation is consistent with the fact that a pure two-photon transition would repeat its signal every time the pulse spectrum is shifted by half of the repetition frequency. More recent work has pushed the spectroscopy resolution to the limit of the natural linewidth of 660 kHz associated with the D-state lifetime, owing to the use of ultracold atoms and careful control of photon momentum transfer. The work on this simple two-photon transition dynamics thus provides a solid link between the time-domain picture of carrier-envelope phase and the frequency-domain picture of f_{rep} and f_0. One practical consequence of these results is that we can now control both degrees of freedom for the femtosecond comb directly by a transition in cold atoms.
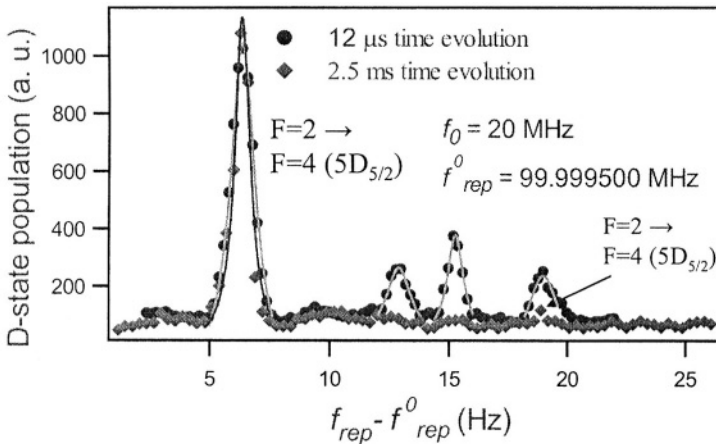
Figure 1-5. Experimental observation of resonantly enhanced two-photon transition in cold [87]Rb atoms with a clear influence by the pulse sequence on the atomic state dynamics.

3.   MOLECULAR SPECTROSCOPY AIDED BY FEMTOSECOND OPTICAL FREQUENCY COMB

Before we study examples of molecular spectroscopy aided by the technology of the precision frequency comb, we would like to discuss briefly the implications of the frequency-domain control of the femtosecond laser to the time-domain experiments. Prior to the development of femtosecond comb technology, mode-locked lasers were used almost exclusively for time-domain experiments. Although the femtosecond comb technology has primarily impacted on the frequency-domain applications described earlier, it is having an impact on time-domain experiments and promises to bring about just as dramatic advances in the time-domain as it has in optical frequency metrology and optical clocks. Indeed, it is fascinating to blur the boundary between traditional CW precision spectroscopy and ultrafast phenomena. The time-domain applications put stringent requirements on the carrier-envelope phase coherence. Stabilization of the "absolute" carrier-envelope phase at a level of tens of milliradians has been demonstrated and this phase coherence is maintained over an experimental period exceeding many minutes [36], paving the groundwork for synthesizing electric fields with known amplitude and phase at optical frequencies. Working with two independent femtosecond lasers operating at different wavelength regions, we have synchronized the relative timing between the two pulse trains at the femtosecond level [37], and also phase locked the two carrier frequencies, thus establishing phase coherence between the two lasers. By coherently stitching optical bandwidths together, a "synthesized" pulse has been generated [11]. With the same pair of Ti:sapphire mode-locked lasers, we have demonstrated widely tunable femtosecond pulse generation in the mid- and far-IR using difference-frequency-generation [38]. The flexibility of this new experimental approach is evidenced by the capability of rapid and programmable switching and modulation of the wavelength and amplitude of the generated IR pulses. A fully developed capability of producing phase-coherent visible and IR pulses over a broad spectral bandwidth, coupled with arbitrary control in amplitude and pulse shape, represents the ultimate instrumentation for coherent control of molecular systems. A pulse train with good carrier-envelope phase coherence is also very promising for experiments that are sensitive to ϕ_{CE}, i.e., the "absolute" pulse phase [2]. This can be manifested in "extreme" nonlinear optics experiments, or coherent control.

The capability to precisely control pulse timing and the pulse-carrier phase allows one to manipulate pulses using novel techniques and achieve unprecedented levels of flexibility and precision, as will be demonstrated in the work on time resolved spectroscopy of molecules. For example, the

simultaneous control of timing jitter and carrier-envelope phase can be used to phase coherently superpose a collection of successive pulses from a mode-locked laser. By stabilizing the two degrees of freedom of a pulse train to an optical cavity acting as a coherent delay, constructive interference of sequential pulses will be built up until a cavity dump is enabled to switch out the "amplified" pulse [39]. Such a passive pulse "amplifier", along with the synchronization technique we developed for pulse synthesis, has made a strong impact on the field of nonlinear-optics based spectroscopy and imaging of bio-molecular systems, showing significant improvements in experimental sensitivity and spatial resolution [40, 41]. With the enhanced detection sensitivity comes the capability of tracking real time biological dynamics. An ultrafast laser locked to a high stability cavity is also expected to demonstrate extremely low pulse jitter and carrier-envelope phase noise, which will be particularly attractive for time-domain experiments. In addition, we are exploring the use of pulse-cavity interactions to obtain a high sensitivity in intracavity spectroscopy (linear and non-linear) with a wide spectral coverage, as well as to enhance nonlinear interaction strengths for high efficiency nonlinear optical experiments.

With these new sets of tools in hand, it is appropriate to revisit the topics of precision molecular spectroscopy. It is also interesting to explore spectroscopy in a more broad sense. For example, one can now carry out precision spectroscopy using ultrafast lasers. On the other hand, coherent control of molecular motion can be performed in the spirit of precision measurement. The capability of absolute optical frequency measurements in the visible and IR spectral regions adds a new meaning to the term of precision molecular spectroscopy. Understanding of molecular structure and dynamics often involves detailed spectral analysis over a broad wavelength range. Such a task can now be accomplished with a desired level of accuracy uniformly across all relevant spectral windows, allowing precise investigations of minute changes in the molecular structure over a large dynamic range. For example, absolute frequency measurement of vibration overtone transitions and other related resonances (such as hyperfine splitting) reveals precise information about the molecular potential energy surface and relevant perturbation effects. We have pursued such a study in iodine molecules, performing high-resolution and high-precision measurement of hyperfine interactions of the first excited electronic state (B) of I_2 over an extensive range of vibrational and rotational quantum numbers towards the dissociation limit [42]. Experimental data demonstrate systematic variations in the hyperfine parameters that confirm calculations based on *ab initio* molecular potential energy curves and electronic wave functions derived from a separated-atomic basis set. We have accurately determined the state-dependent quantitative changes of hyperfine

interactions caused by perturbations from other electronic states and identified the respective perturbing states. Our work in I_2 near the dissociation limit is also motivated by the desire to improve cell-based portable optical frequency standards [43]. Indeed, I_2-stabilized lasers have already demonstrated high stability (< 5×10^{-14} at 1 s averaging time) and have served well for optical atomic clocks [9].

4. I_2 HYPERFINE INTERACTIONS, OPTICAL FREQUENCY STANDARDS AND CLOCKS

The hyperfine structure of I_2 rovibrational levels includes four contributions: nuclear electric quadrupole *(eqQ)*, spin-rotation (*C*), tensorial spin-spin (*d*), and scalar spin-spin (δ) interactions. Agreement between experiment and theory using the four-term effective hyperfine Hamiltonian is at the kilohertz level for a few selected transitions. For the first excited electronic state *B* with the $^2P_{3/2} + {}^2P_{1/2}$ dissociation limit, our goal is to perform a systematic high-precision investigation of hyperfine interactions over an extensive range of rovibrational quantum numbers coupled with a large range of internuclear separations. Such a study has allowed us to understand the rovibrational dependence of the hyperfine interactions (as well as the dependence on internuclear distance) based on *ab initio* molecular potential energy curves and the associated electronic wave functions. Careful analysis of various perturbation effects leads to precise determination of molecular structure over a large dynamic range.

Prior studies have concentrated on a few isolated rovibrational levels for the high vibrational levels $v' = 40$ to 82 in the *B* state [44-46]. For vibrational levels below $v' = 43$, only functional forms on the state-dependent variations of the hyperfine interactions have been investigated from empirical data [47]. Combining absolute optical frequency metrology with high-resolution and broad wavelength-coverage laser spectroscopy, we have measured ~ 80 rovibrational transitions with the upper vibrational levels (from $v' = 42$ up to $v' = 70$) stretching from a closely bonded molecular basis to a separated-atomic basis appropriate for the $^2P_{3/2} + {}^2P_{1/2}$ dissociation limit, providing kHz-level line accuracies for most hyperfine components. The study is performed in the wavelength region of 530 to 498 nm. Measurements performed on a large set of rovibrational quantum numbers provide systematic information on state-dependent variations in the hyperfine interactions caused by perturbation from other nearby states. Figure 1-6 shows a simple schematic of the ground and the first excited electronic states of I_2 and their relevant dissociation limits. The lower panel in Fig. 1-6 shows a clear trend of linewidth narrowing with decreasing

transition wavelength. However, this tendency is complicated by variations in linewidths among different rotational or hyperfine components when the transitions approach the pre-dissociation region. The initial linewidth narrowing at shorter wavelength may indicate among other interesting effects that the Franck-Condon factor in the transition probability is reduced when the excited state reaches a higher vibration level. As the excited state approaches the dissociation threshold, the limit on lifetime imposed by predissociation and other effects will need to be taken into consideration.
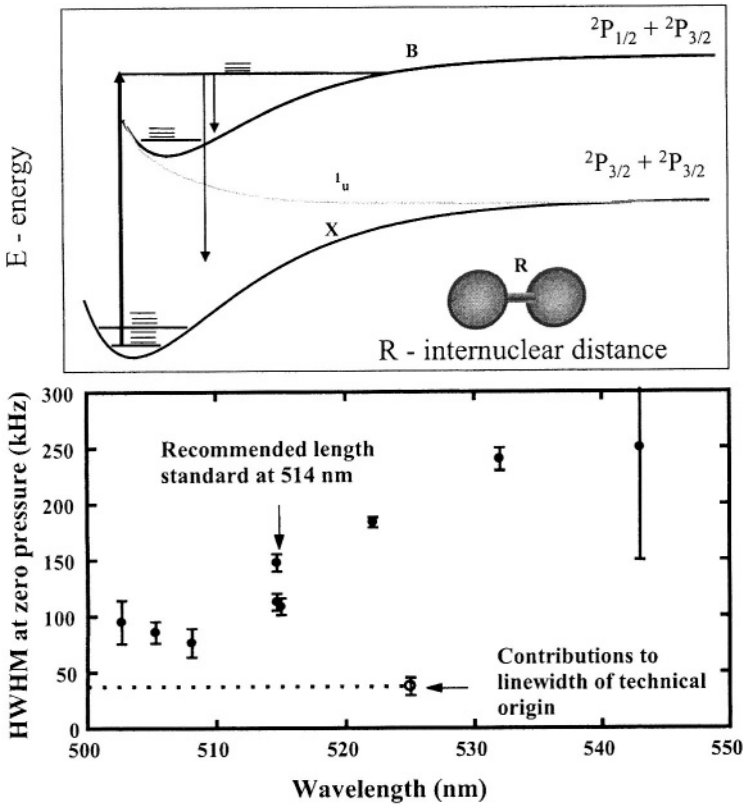
Figure 1-6. The ground state and the first excited state of I_2 with their associated dissociation limit. The lower panel shows a narrowing trend of the transition linewidth when the excited state approaches the dissociation limit.

Figure 1-7 illustrates the systematic rovibrational dependences for all four hyperfine parameters. Each solid line is a fit of the experimental data for rotational dependence belonging to a single vibrational level (v'). In general, all hyperfine parameters have a monotonic dependence on both rotational and vibrational quantum numbers except for the levels in the

vicinity of $v' = 57$ to 59. However, the v-dependence of eqQ_B reverses its trend after $v' = 60$. For the sake of figure clarity, the eqQ_B data for $v' > 60$ are not shown. Another important observation is that for levels of $v' = 57 - 59$ all hyperfine parameters except for C_B bear abnormal J-dependences due to perturbations from a 1_g state through accidental rotational resonances.

Combining data from this work and the literature [47], investigations of the hyperfine spectra now cover the majority of the vibrational levels ($3 \leq v \leq 82$) in the B state. Therefore, it is now possible and useful to explore the global trend of these hyperfine parameters in the B state. Suppressing the rotational dependence, hyperfine parameters as functions of pure vibrational energy $E(v')$ are found to increase rapidly when molecules approach the dissociation limit, which is a result of the increasingly strong perturbations from other high-lying electronic states sharing the same dissociation limit with the B state. While the variation of C_B is smooth over the whole range, eqQ_B, d_B, and δ_B all have local irregularities at three positions: $v' = 5$ where the $B'':1_u$ state crosses nearby, around $v' = 57$ to 59 (see discussions above), and from $v' = 76$ to 78, due to the same 1_g state [44, 46].

To examine these hyperfine parameters in terms of internuclear separation R, the vibrational average of the hyperfine parameters is removed by inverting the expression $O(v',J') = \langle v'_{J'} | O(R) | v'_{J'} \rangle$, where $O(v',J')$ denotes one of the four hyperfine parameters. Figure 1-7 plots eqQ_B, C_B, d_B, and δ_B against R-centroid evaluated from $\langle v'_{J'} | R | v'_{J'} \rangle$ (with $| v'_{J'} \rangle$ properly normalized), along with the corresponding residual errors of the interpolation. In Fig. 1-8(a), (b), (c), and (d), the solid lines are calculated from $\langle v'_{J'} | O(R) | v'_{J'} \rangle$ and the symbols are the experimental data. Consistent with C_B's smooth variation, the interpolation function $C_B(R)$ has small residual errors (within ±0.03, relative) for the entire range from $v' = 3$ to 70. On the contrary, the large residual errors in the interpolation of eqQ_B, d_B, and δ_B for $v' \geq 56$ reflect their abnormal variations observed around $v' = 57$ and 59, restricting a reliable interpolation only to levels of $v' < 56$. In the region of $R < 5$ Å, valuable information can be readily extracted from eqQ_B to assist the investigation of I_2's electronic structure. Unlike the other three hyperfine parameters whose major parts originate from perturbations at nearly all possible values of R, a significant part of eqQ_B is due to the interaction between the nuclear quadrupole moment Q and the local electric field gradient $q(R)$ generated by the surrounding charge distribution of a largely B state character. Thus, for $R < 5$ Å, where perturbations from other electronic states are negligible, the vibration-removed interpolation function $eqQ_B(R)$, coupled with *a priori* information on $q(R)$, can be used to determine the I_2 nuclear quadrupole moment or serve as a benchmark for molecular *ab initio* calculations of the electronic structure at various values of R.
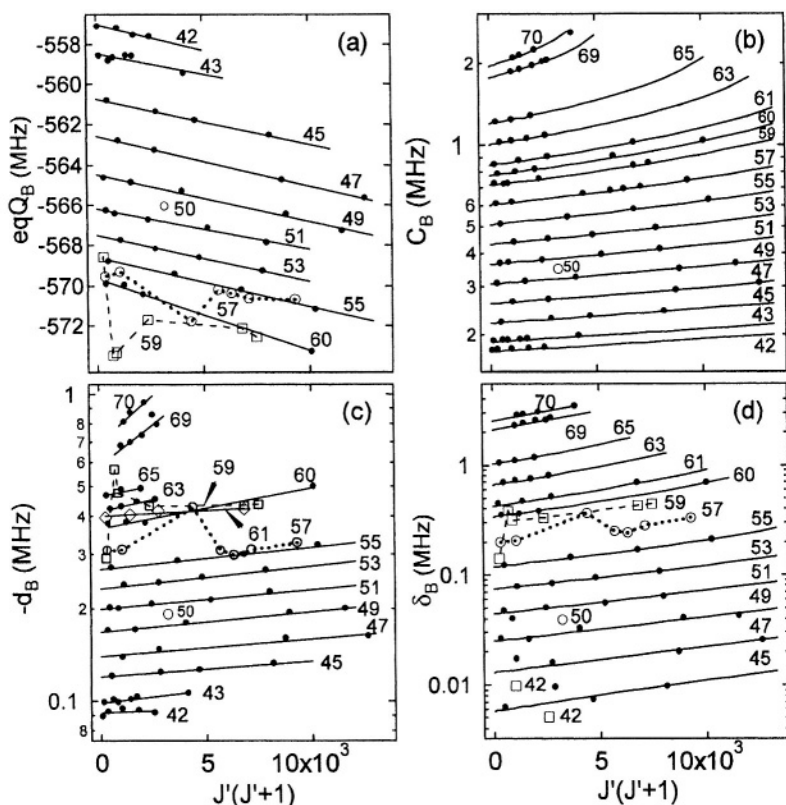
Figure 1-7. Rovibrational dependence of the *B* state hyperfine parameters (a) eqQ_B , (b) C_B, (c) d_B , and (d) δ_B . Note (b), (c), and (d) are semilog plots and the vertical scale of (c) has been inverted. Each solid line is a fit for *J*-dependence for each vibrational level (*v'* indicated in the figure). Experimental data in squares and open circles show abnormal variations of eqQ_B, d_B , and δ_B around *v'* = 57 and 59.

Precision measurements on *B-X* hyperfine spectra provide an alternative and yet effective way to investigate the potential energy curves *(PECs)* sharing the same dissociation limit with the *B* state as well as the associated electronic wave functions. To demonstrate this, we perform calculations of eqQ_B, C_B, d_B, and δ_B based on the available *PECs* and electronic wave functions derived from a separated-atomic basis set. For both vibrational and rotational dependences, the *ab initio* calculation results agree very well with the experimental data for *v'* $\geq$ 42 (*R*-centroid $\geq$ 3.9 Å). In short, we have extended the range of separated-atomic basis calculations from levels near the dissociation limit to low vibrational levels (*v'* = 5) and have found very

good agreement with the experimental data on both vibrational and rotational dependences.
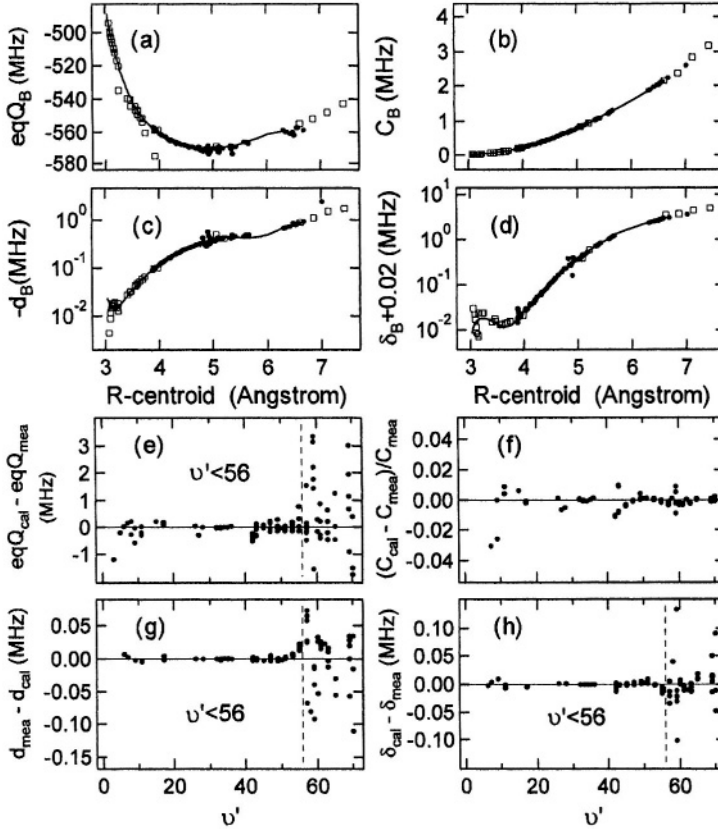
Figure 1-8. (a) eqQ_B, (b) C_B, (c) d_B, and (d) δ_B versus *R*-centroid. Solid lines are calculated from $\langle v'_{J'} | O(R) | v'_{J'} \rangle$. Symbols are experimental data (dots: this work, squares: literature). (e) - (h) show residual errors of the interpolation.

Besides these interesting studies in hyperfine structure, the narrow-linewidth I_2 transitions in this wavelength range also provide excellent cell-based optical frequency references for laser stabilization. Frequency-doubled Nd:YAG/^{127}I$_2$ at 532 nm has proved to be one of the best portable optical frequency standards with compact size, reliability, and high stability ($< 5 \times 10^{-14}$ at 1 s). To reach a better frequency stability, it is useful to explore I_2 transitions at wavelengths below 532 nm, where the natural linewidths decrease at a faster rate than the line strengths. We have measured the systematic variation of the I_2 transition linewidths within the range of 532 - 498 nm, with the linewidth decreasing by nearly 6 times when the wavelength is changed from 532 nm to near the dissociation limit [43]. The

high *S/N* results indicate that I_2 transitions in the wavelength range 532 - 501 nm hold great promise for future development of optical frequency standards, especially with the advent of all solid state Yb:YAG lasers. One exciting candidate is the 514.67 nm standard [48], with a projected stability $< 10^{-14}$ at 1 s.

5.   EXTENSION OF PHASE-COHERENT FS COMBS TO THE MID-IR SPECTRAL REGION

Being able to combine the characteristics of two or more pulsed lasers working at different wavelengths certainly provides a more flexible approach to coherent control. The capability of synchronizing the repetition rates and phase-locking the carrier frequencies of two mode-locked lasers opens many applications. It may be particularly important in the generation of tunable femtosecond sources in other previously unreachable spectral regions. Figure 1-9 shows the cross-correlation measurement of the two stabilized mode-locked Ti:sapphire lasers using both sum (SFG) and difference frequency generation (DFG). The DFG signal produced by a GaSe crystal can be tuned from 6 micron and onto any longer wavelength regions with a high repetition rate (the same as that of the original laser) and a reasonable average power (tens of microwatts). Arbitrary amplitude waveform generation and rapid wavelength switching in these nonlinear signals are simple to implement. The ultimate goal of this work is to make an optical waveform synthesizer that can create an arbitrary optical pulse on demand and use the novel source to study and control molecular motion. For frequency metrology and precision molecular spectroscopy in the IR region, we note that the difference frequency generation approach produces an absolute-frequency calibrated IR comb when the two Ti:sapphire lasers are synchronized and share a common offset frequency f_0.

One of the important spectral regions is 1.5 μm, where compact, reliable, and efficient mode-locked lasers exist and there is rich information on molecular spectroscopy. Frequency reference grids in this spectral window could also find applications in dense wavelength division multiplexed (DWDM) systems, photonic samplers in high-speed A/D conversion, and distribution of optical frequency standards over optical fiber networks. The synchronization and phase-locking approach for Ti:sapphire lasers can be extended to cover mode-locked lasers at 1.5 μm. We have indeed achieved tight synchronization and coherent phase locking between the repetition rates and the optical carriers, respectively, for the 1.5 μm mode-locked laser sources and a Ti:sapphire-based fs frequency comb, which is used as the clockwork for an optical atomic clock.
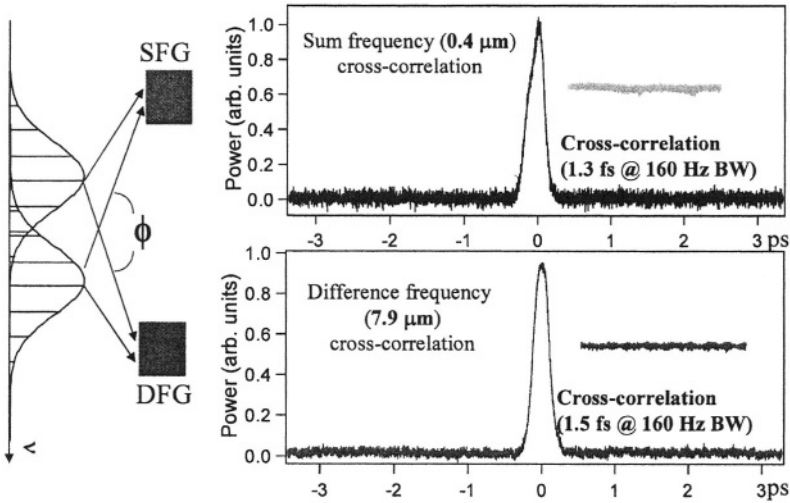
Figure 1-9. Simultaneous sum and difference frequency generations from two stabilized femtosecond lasers. Also shown are the amplitude fluctuations at the half-power point due to the relative timing jitter between the two parent lasers.

A phase-coherent link between mode-locked lasers requires two distinct conditions to be met, as shown in Fig. 1-10(a). The comb spacing of the 1.5 μm source ($f_{rep,1550}$) must be stabilized to the optical clock's fs comb spacing ($f_{rep,775}$). Second, the combs' offset frequencies ($f_{0,775}$ and $f_{0,1550}$) must be phase locked together. This latter step requires spectral overlap between the two combs. The wide bandwidth optical frequency comb generated by the mode-locked fs Ti:sapphire laser is phase locked to a highly stable, iodine-based optical frequency standard. The optical comb of the 1.5 μm source is frequency doubled and compared against the Ti:sapphire comb at a mutually accessible spectral region to generate a heterodyne beat between the two combs.

Under simultaneous control of synchronization and phase locking, Fig. 1-10 (b) shows frequency-counting records of the heterodyne beat signal between the 1.5 μm laser and the Ti:sapphire laser. At 1 s gate time, the rms fluctuation (σ_{rms}) of the heterodyne beat ($2 \times f_{0,1550} - f_{0,775}$) is reduced to 3.2 mHz, in sharp contrast to the 1.5 MHz rms fluctuation when $f_{0,1550}$ is not stabilized. By monitoring the beat error signal produced by the digital phase detector we ensure that no cycles have slipped for the phase-locked loop over this measurement period. Allan deviation of the stabilized beat frequency record is shown in Fig. 1-10(c), determined with respect to the 1.5 μm optical carrier frequency [49].
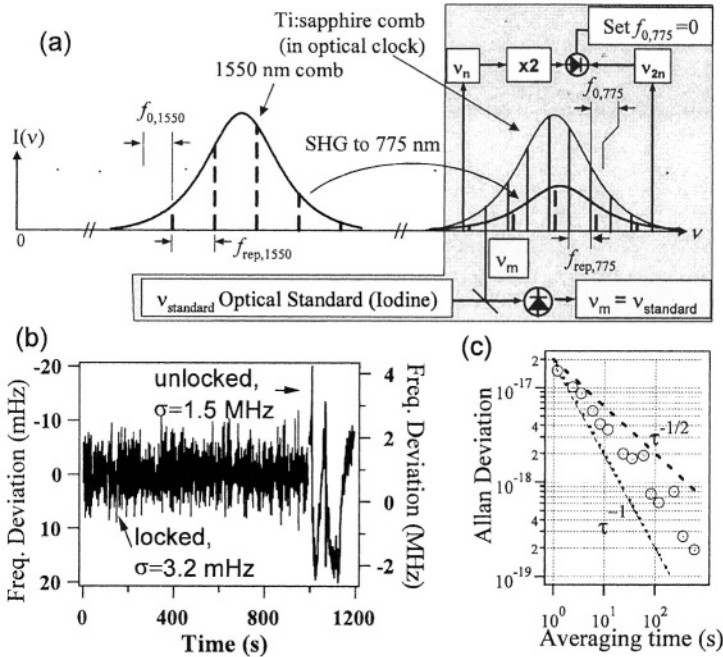
Figure 1-10. (a) Schematic diagram of simultaneous synchronization and phase locking between a 1.5 μm mode-locked laser diode and a 775 nm mode-locked Ti:sapphire laser. The shaded area shows the implementation of an optical clock based on a Ti:sapphire fs comb phase-stabilized to an iodine standard. The laser diode's repetition frequency is 8 times that of the Ti:sapphire (not as shown in the figure). (b) The heterodyne beat recorded by a frequency counter at 1 s gate time, under no phase locking (short trace, with respect to the right vertical axis) and phase locking (long trace, with respect to the left vertical axis). (c) The Allan deviation associated with the phase-locked signal.

6.   FEMTOSECOND LASERS AND EXTERNAL OPTICAL CAVITIES

The combination of ultra-short pulses and optical cavities will open doors for a variety of exciting experiments. This requires the understanding of the intricate pulse-cavity interactions and the subsequent development of techniques to efficiently couple the ultra-short pulses into a high finesse optical cavity and coherently store them in the cavity. An immediate impact is on precision stabilization of ultrafast lasers [50]. Similar to the state-of-art stabilization of CW lasers, a cavity-stabilized ultrafast laser is expected to demonstrate superior short-term stability of both the pulse repetition

frequency and the carrier-envelope phase. The improved stability is beneficial in particular for time-domain applications where the signal processing bandwidth is necessarily large. Another attractive application lies in broadband and ultrasensitive spectroscopy. The use of high finesse cavities has played a decisive role for enhancing sensitivity and precision in atomic and molecular spectroscopy. We expect a dramatic advancement in the efficiency of intracavity spectroscopy by exploiting the application of ultra-short pulses. In other words, a high detection sensitivity is achievable uniformly across the broad spectrum of the pulse. Applying cavity-stabilization techniques to femtosecond lasers, the comb structure of the probe laser can be precisely matched to the resonance modes of an empty cavity, allowing an efficient energy coupling for a spectroscopic probe. Molecular samples located inside the high finesse cavity will have a strong impact on the dispersive properties of the cavity. In fact it is this dispersion-related cavity-pulling effect that will aid our sensitive detection process when we analyze the light transmitted through the cavity. Preliminary data on spectrally resolved, time-domain ring down measurement for intracavity loss over the entire femtosecond laser bandwidth are already quite promising.

To develop sources for ultrafast nonlinear spectroscopy, a properly designed, dispersion-compensated cavity housing a nonlinear crystal will provide efficient nonlinear optical frequency conversion of ultrashort optical pulses over spectral regions where no active gain medium exists. Furthermore, by simultaneously locking two independent mode-locked lasers to the same optical cavity, efficient sum and/or difference frequency generation can be produced over a large range of wavelengths. Under a similar motivation, a passive cavity can be used to explore coherent superposition of ultra-short pulses, with cavity stabilization providing the means to phase coherently superpose a collection of successive pulses from a mode-locked laser. The coherently enhanced pulse stored in the cavity can be switched out using a cavity-dumping element (such as a Bragg cell), resulting in a single phase-coherent amplified pulse. The use of a passive cavity also offers the unique ability to effectively amplify pulses at spectral regions where no suitable gain medium exists, such as for the infrared pulses from difference-frequency mixing or the UV light from harmonic generation. Unlike actively dumped laser systems, the pulse energy is not limited by the saturation of a gain medium or a saturable absorber needed for mode-locking. Instead, the linear response of the passive cavity allows the pulse energy to build up inside the cavity until limited by cavity loss and/or dispersive pulse spreading. Therefore, storage and amplification of ultra-short pulses in the femtosecond regime requires precise control of the reflected spectral phase of the resonator mirrors as well as the optical loss of

the resonator. While the reflected group delay of the mirrors only changes the effective length of the resonator, the group delay dispersion (GDD) and higher-order derivatives of the group delay with respect to frequency affect the pulse shape. The net cavity GDD over the bandwidth of the pulse needs to be minimized in order to maintain the shape of the resonant pulse and allow for the coherent addition of energy from subsequent pulses. Figure 1-11 illustrates the evolution of a 50 fs pulse inside a cavity with a finesse of 3,140 under the conditions of zero cavity dispersion (dashed curve) and finite dispersion (solid curve). Three representative pulses at different stages of amplification are also shown to illustrate the pulse buildup process. Although the 50 fs pulse is stretched by the dispersive cavity, it is not severely distorted due to its coupling with the incident pulse train. If the incident pulses become too short, the cavity finesse too high, or the laser repetition frequency deviates significantly from the cavity free-spectral-range (FSR) frequency, the intra-cavity pulse may quickly pull apart into several pulses, and the meaning of a single pulse width would be lost.
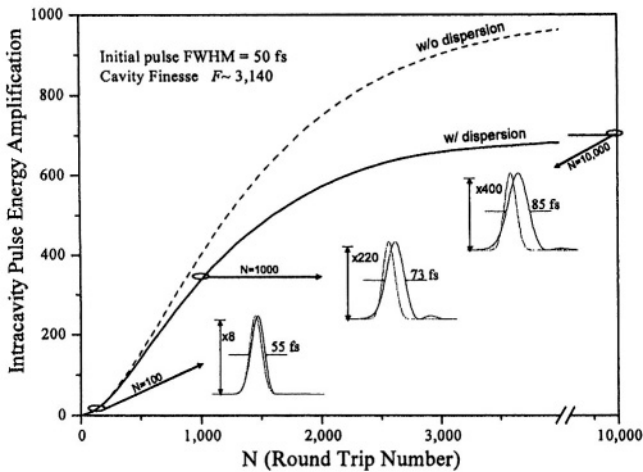
Figure 1-11. Coherent evolution of a 50 fs pulse inside the cavity. Dashed line indicates the ideal case of a dispersion-free cavity perfectly matched with the incident pulse train, while the solid line shows the effect of cavity dispersion in limiting the amount of energy coupled into the cavity.

We have applied the coherent pulse-stacking technique to both picosecond and femtosecond pulses. Initial studies have already demonstrated amplification of picosecond pulses of greater than 30 times at repetition rates of 253 kHz, yielding pulse energies greater than 150 nJ [41]. With significant room left for optimization of the cavity finesse (current value of ~ 350, limited by the cavity input-coupling mirror), we expect that

amplifications greater than a hundred times are feasible, bringing pulse energies into the µJ range. While the use of picosecond pulses allows us to separate out complications arising from intra-cavity dispersion, for sub-100 femtosecond pulses, dispersive phase shifts in the cavity mirrors become an important topic. Preliminary results in enhancing low individual pulse energies for sub-50 fs pulses illustrate the importance of GDD control. The external enhancement cavity incorporated specially designed negative GDD low-loss mirrors to simultaneously compensate for the Bragg cell's 3 mm of fused silica and provide a high finesse. The input-coupling mirror transmission was ~ 0.8%, with a measured cavity finesse of 440. An intracavity energy buildup of ~ 130 is expected, leading to single pulse amplifications of approximately 52 for the current set-up given the 40% dumping efficiency of our Bragg cell. The negative GDD mirrors were designed to only partially compensate for the total cavity dispersion. The remaining cavity GDD was estimated at + 20 to + 30 fs^2. Controlling the intracavity pressure allows fine-tuning of the net cavity GDD to zero. Experimental results are in good agreement with independent numerical calculations. The input pulses of 47 fs duration are experimentally enhanced by a factor of ~ 120 inside the passive cavity, with the output pulses broadened only to ~ 49 fs.

An important application of these advanced pulse control technologies is in the field of nonlinear-optics based spectroscopy and nanoscale imaging. For example, using two tightly synchronized picosecond lasers, we are able to achieve significant improvements in experimental sensitivity and spatial resolutions for coherent anti-Stokes Raman scattering (CARS) microscopy [40]. Vibrational imaging based on CARS spectroscopy is a powerful method for acquisition of chemically selective maps of biological samples [51, 52]. In CARS microscopy, pulsed pump and Stokes beams are focused tightly to a single focal spot in the sample to achieve a high spatial resolution. The third-order nonlinear interaction produces a signal photon that is blue-shifted (anti-Stokes signal) with respect to the incident beams. Strong CARS signals are obtained whenever the frequency difference between the pump and Stokes coincides with a Raman-active vibrational mode, which gives rise to the molecule-specific vibrational contrast in the image. Recent studies and technological improvements have demonstrated the exciting capability of CARS microscopy to attain high-resolution vibrational images of unstained living cells.

Practical applications of the CARS microscopy technique require pulsed light sources: optimized peak powers help boost the nonlinear signal. Pulses with temporal widths of 1-2 picoseconds (ps) should be used to match to the vibration bandwidths in order to optimize the CARS signal, with minimized non-resonant background and compromising spectral resolution. An

important technical challenge is to achieve tight synchronization between two mode-locked lasers that produce the frequency difference that matches the vibrational resonance. Another important consideration is that while the repetition rate of the pulse train needs to be low enough to avoid thermal damage to the cell due to a high average power, the peak power of the pulses needs to be reasonably high to aid the nonlinear signal strength. A schematic set-up combining CARS spectroscopy and pulse manipulation is shown in Fig. 1-12. The technologies of pulse synchronization and coherent pulse stacking therefore become ideal tools for carrying out this task of spectroscopy plus microscopy.
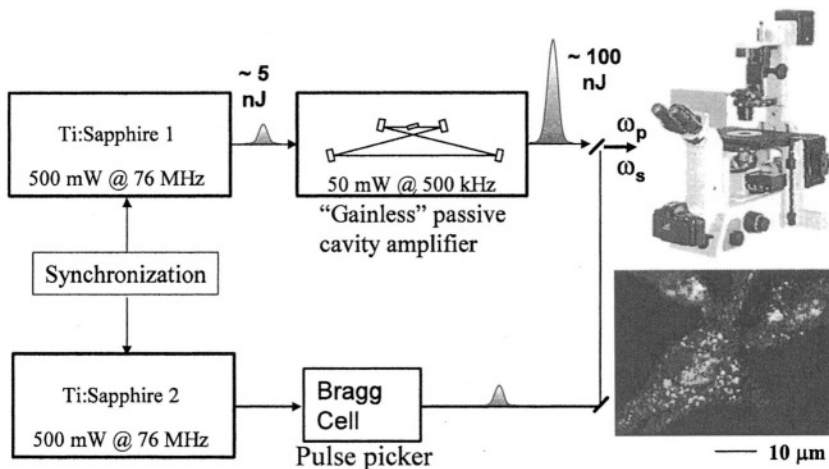
Figure 1-12. Schematic set-up for coherent anti-Stokes Raman scattering (CARS) microscopy on living cells using two separate picosecond mode-locked lasers. The two lasers are tightly synchronized to minimize detection noise while the pump laser is enhanced in its peak power by a passive optical cavity. High *S/N* image of distribution of lipids in a live unstained fibroblast cell is achieved via resonant detection of C-H vibration frequency.

Acknowledgments

References

1. S. T. Cundiff and J. Ye, *Rev. Mod. Phys.* **75**, 325 (2003).
2. A. Baltuska, T. Udem, M. Uiberacker, M. Hentschel, E. Goulielmakis, C. Gohle, R. Holzwarth, V. S. Yakoviev, A. Scrinzi, T. W. Hänsch and F. Krausz, *Nature* **421**, 611 (2003).
3. T. Udem, J. Reichert, R. Holzwarth and T. W. Hänsch, *Opt. Lett.* **24**, 881 (1999).
4. T. Udem, J. Reichert, R. Holzwarth and T. W. Hänsch, *Phys. Rev. Lett.* **82**, 3568 (1999).
5. J. Ye, T. H. Yoon, J. L. Hall, A. A. Madej, J. E. Bernard, K. J. Siemsen, L. Marmet, J.-M. Chartier and A. Chartier, *Phys. Rev. Lett.* **85**, 3797 (2000).
6. D. J. Jones, S. A. Diddams, J. K. Ranka, A. Stentz, R. S. Windeler, J. L. Hall and S. T. Cundiff, *Science* **288**, 635 (2000).
7. A. Apolonski, A. Poppe, G. Tempea, C. Spielmann, T. Udem, R. Holzwarth, T. W. Hänsch and F. Krausz, *Phys. Rev. Lett.* **85**, 740 (2000).
8. S. A. Diddams, T. Udem, J. C. Bergquist, E. A. Curtis, R. E. Drullinger, L. Hollberg, W. M. Itano, W. D. Lee, C. W. Oates, K. R. Vogel and D. J. Wineland, *Science* **293**, 825 (2001).
9. J. Ye, L. S. Ma and J. L. Hall, *Phys. Rev. Lett.* **87**, 270801 (2001).
10. J. D. Jost, J. L. Hall and J. Ye, *Optics Express* **10**, 515 (2002).
11. R. K. Shelton, L. S. Ma, H. C. Kapteyn, M. M. Murnane, J. L. Hall and J. Ye, *Science* **293**, 1286 (2001).
12. A. Baltuska, T. Fuji and T. Kobayashi, *Phys. Rev. Lett.* **88**, 133901 (2002).
13. L. Xu, C. Spielmann, A. Poppe, T. Brabec, F. Krausz and T. W. Hänsch, *Opt. Lett.* **21**, 2008 (1996).
14. H. R. Telle, G. Steinmeyer, A. E. Dunlop, J. Stenger, D. H. Sutter and U. Keller, *Appl. Phys.* B **69**, 327 (1999).
15. T. M. Fortier, D. J. Jones and S. T. Cundiff, *Opt. Lett.* **28**, 2198 (2003).
16. R. Ell, U. Morgner, F. X. Kärtner, J. G. Fujimoto, E. P. Ippen, V. Scheuer, G. Angelow, T. Tschudi, M. J. Lederer, A. Boiko and B. Luther-Davies, *Opt. Lett.* **26**, 373 (2001).
17. A. Bartels and H. Kurz, in *XIII International Conference on Ultrafast Phenomena*, edited by M. M. Murnane, N. F. Scherer, D. J. D. Miller and A. M. Weiner (OSA, Vancouver, BC, 2002), Vol. 72, p. 173.
18. J. K. Ranka, R. S. Windeler and A. J. Stentz, *Opt. Lett.* **25**, 25 (2000).
19. J. Reichert, R. Holzwarth, T. Udem and T. W. Hänsch, *Opt. Commun.* **172**, 59 (1999).
20. K. W. Holman, R. J. Jones, A. Marian, S. T. Cundiff and J. Ye, *Opt. Lett.* **28**, 851 (2003).
21. H. R. Telle, B. Lipphardt and J. Stenger, *Appl. Phys.* B **74**, 1 (2002).
22. S. A. Diddams, L. Hollberg, L. S. Ma and L. Robertsson, *Opt. Lett.* **27**, 58 (2002).
23. M. Niering, R. Holzwarth, J. Reichert, P. Pokasov, T. Udem, M. Weitz, T. W. Hänsch, P. Lemonde, G. Santarelli, M. Abgrall, P. Laurent, C. Salomon and A. Clairon, *Phys. Rev. Lett.* **84**, 5496 (2000).
24. J. Ye, J. L. Hall and S. A. Diddams, *Opt. Lett.* **25**, 1675 (2000).
25. G. Wilpers, T. Binnewies, C. Degenhardt, U. Sterr, J. Helmcke and F. Riehle, *Phys. Rev. Lett.* **89**, 230801 (2002).
26. R. J. Rafac, B. C. Young, J. A. Beall, W. M. Itano, D. J. Wineland and J. C. Bergquist, *Phys. Rev. Lett.* **85**, 2462 (2000).
27. L. Hollberg, C. W. Oates, E. A. Curtis, E. N. Ivanov, S. A. Diddams, T. Udem, H. G. Robinson, J. C. Bergquist, R. J. Rafac, W. M. Itano, R. E. Drullinger and D. J. Wineland, *IEEE J. Quantum Electron.* **37**, 1502 (2001).

28. J. Ye, L. Robertsson, S. Picard, L. S. Ma and J. L. Hall, *IEEE Trans. Instrum. Meas.* **48**, 544 (1999).
29. D. Felinto, C. A. C. Bosco, L. H. Acioli and S. S. Vianna, *Phys. Rev.* A **6406** (2001).
30. T. H. Yoon, A. Marian, J. L. Hall and J. Ye, *Phys. Rev.* A **63**, 011402 (2000).
31. J. E. Bjorkholm and P. F. Liao, *Phys. Rev. Lett.* **33**, 128 (1974).
32. O. Poulsen and N. I. Winstrup, *Phys. Rev. Lett.* **47**, 1522 (1981).
33. R. Teets, J. Eckstein and T. W. Hänsch, *Phys. Rev. Lett.* **38**, 760 (1977).
34. M. J. Snadden, A. S. Bell, E. Riis and A. I. Ferguson, *Opt. Commun.* **125**, 70 (1996).
35. A. Marian, X. Xu and J. Ye, *Bulletin Am. Phys. Soc.* **48**, 136 (2003).
36. T. M. Fortier, D. J. Jones, J. Ye, S. T. Cundiff and R. S. Windeler, *Opt. Lett.* **27**, 1436 (2002).
37. R. K. Shelton, S. M. Foreman, L. S. Ma, J. L. Hall, H. C. Kapteyn, M. M. Murnane, M. Notcutt and J. Ye, *Opt. Lett.* **27**, 312 (2002).
38. S. M. Foreman, D. J. Jones and J. Ye, *Opt. Lett.* **28**, 370 (2003).
39. R. J. Jones and J. Ye, *Opt. Lett.* **27**, 1848 (2002).
40. E. O. Potma, D. J. Jones, J. X. Cheng, X. S. Xie and J. Ye, *Opt. Lett.* **27**, 1168 (2002).
41. E. O. Potma, C. Evans, X. S. Xie, R. J. Jones and J. Ye, *Opt. Lett.* **28**, 1835 (2003).
42. L. S. Chen and J. Ye, *Chem. Phys. Lett.* **381**, 777 (2003).
43 W. Y. Cheng, L. S. Chen, T. H. Yoon, J. L. Hall and J. Ye, *Opt. Lett.* **27**, 571 (2002).
44. J. Vigué, M. Broyer and J. C. Lehmann, *Phys. Rev. Lett.* **42**, 883 (1979).
45. C. J. Bordé, G. Camy, B. Decomps and J.-P. Descoubes, *J. Physique* **42**, 1393 (1981).
46. J. P. Pique, F. Hartmann, S. Churassy and R. Bacis, *J. Physique* **47**, 1917 (1986).
47. B. Bodermann, H. Knockel and E. Tiemann, *Eur. Phys. J.* D **19**, 31 (2002).
48. R. J. Jones, W. Y. Cheng, K. W. Holman, L.-S. Chen, J. L. Hall and J. Ye, *Appl. Phys.* B **74**, 597 (2002).
49. K. W. Holman, D. J. Jones, J. Ye and E. P. Ippen, *Opt. Lett.* **28**, 2405 (2003).
50. R. J. Jones and J. C. Diels, *Phys. Rev. Lett.* **86**, 3288 (2001).
51. A. Volkmer, J. X. Cheng and X. S. Xie, *Phys. Rev. Lett.* **87**, 023901 (2001).
52. L. D. Book, J. X. Cheng, A. Volkmer and X. S. Xie, *Biophysical Journal* **80**, 171A (2001).

Chapter 2

SUPERCONTINUUM AND
HIGH-ORDER HARMONICS

"Extreme" Coherent Sources for Atomic Spectroscopy and Attophysics

Marco Bellini*

Istituto Nazionale di Ottica Applicata (*INOA*)
Largo Fermi 6, 50125 Florence, Italy
bellini@inoa.it

Abstract   Simple experiments, set up to investigate how the coherence properties of short and intense laser pulses are transferred to radiation generated in extremely nonlinear interactions with matter, have given access to a wealth of new information and have allowed unexpected advances in several different fields. Here, we review some of these experiments and discuss their implications for the development of new methods in ultra-high spectral and temporal resolution studies of matter.

1.   INTRODUCTION

Ultrashort laser pulses are an invaluable tool to study ultrafast atomic and molecular events on a femtosecond timescale. The advent of mode-locking techniques has allowed the generation of pulses whose duration comprises just a few oscillations of the optical field, while the development of chirped-pulse-amplification methods has opened the way to ultra-intense laser pulses, which are capable of driving extremely nonlinear phenomena in matter. As a matter of fact, the latest major developments in the field of laser physics are a direct

*Also at European Laboratory for Nonlinear Spectroscopy (LENS) and Istituto Nazionale per la Fisica della Materia (INFM), Florence, Italy.

outcome of the parallel evolution of both techniques, and have recently led to the generation of intense few-cycle pulses and to the first glimpses on a new scientific era – attophysics.

These latest achievements, however, wouldn not have been possible without a number of important new discoveries, which have helped to clarify the scientific background and have provided new essential tools for the development of the final techniques. The generation of attosecond pulses, in particular, relies both on a complete understanding of well-developed methods for the production of high-order laser harmonics and on the availability of few-cycle intense laser pulses with an accurately controlled absolute phase.

In this chapter, I will focus on studies performed in our laboratory on the radiation produced in the extreme ultraviolet (XUV) by the process of high-order harmonic (HOH) generation and on the white-light supercontinuum (SC) obtained when intense laser pulses impinge on transparent materials. I will show that, using simple experimental ideas to investigate the coherence properties of these two different kinds of "extreme" light sources, we were able to obtain interesting and unexpected results in fields that could initially appear to be almost completely unrelated, like strong-field atomic physics and high-precision optical metrology. Finally, I will merge these two apparently distant subjects in order to give just a quick glimpse on how these experiments played a fundamental role in the race toward the breaking of the femtosecond barrier and the development of attophysics.

2.   HIGH-RESOLUTION SPECTROSCOPY WITH ULTRASHORT PULSES

Exploiting the extremely high peak intensities characteristic of ultrashort laser pulses to excite multiphoton processes or to drive highly nonlinear phenomena (and generate new wavelengths, for example), while maintaining the high resolution characteristic of CW sources to investigate very narrow spectral structures of atoms or molecules, is one of the forbidden dreams of the laser experimentalist. Unfortunately, the two conditions of ultrashort pulse duration and high spectral resolution normally appear in striking contrast, since short pulses invariably correspond to broad spectral bandwidths that limit the frequency resolution to the inverse of the pulse duration (see Fig. 2.1 a). However, if pairs of time-delayed and phase-locked pulses (like those generated by splitting a single laser pulse by means of a Michelson interferometer) are used, a simple Fourier transformation shows that the corresponding spectrum maintains the broad bell-shaped envelope, but also acquires a sinusoidal modulation with a spectral period given by the inverse of the temporal separation τ between

the two pulses (see Fig. 2.1 b). In the ideal case, where the two time-delayed pulses with electric fields $E_1(t)$ and $E_2(t+\tau)$ are perfectly phase-locked, their combined spectrum is easily found to be

$$I_t(\omega,\tau) = I_1(\omega) + I_2(\omega) + 2\sqrt{I_1(\omega)I_2(\omega)}\cos(\omega\tau), \qquad (2.1)$$

which reduces to

$$I_t(\omega,\tau) = 2I(\omega)(1 + \cos(\omega\tau)) \qquad (2.2)$$

in the case of equal pulse intensities $I(\omega) = I_1(\omega) = I_2(\omega)$.

It is this $1/\tau$ fringe period that now sets the instrumental resolution and allows one, in principle, to investigate very fine spectral features if a long time delay τ is available[1].

The idea of using a pair of phase-locked pulses in order to achieve better spectral resolution can also be extended by the use of longer sequences of equally time-delayed and phase-locked pulses. The spectrum that one obtains in this case still exhibits the broad bandwidth related to the short pulse duration, but is now modulated in a sharper and sharper fashion as longer pulse sequences are used (see Fig. 2.1 c). In the case of N equally spaced (by a delay τ) and phase-locked pulses, the textbook solution for the corresponding spectrum is given by the expression

$$I(\omega,\tau) = I_0(\omega)\left(\frac{\sin N\omega\tau/2}{\sin \omega\tau/2}\right)^2 \qquad (2.3)$$

and the spectral interference pattern is the well-known array of intense and sharp interference maxima at $\omega_n = n\frac{2\pi}{\tau}$, with some small residual modulations in between. In the ideal limit of an infinite train of phase-locked and equally-spaced pulses of duration τ_p, the resulting spectrum essentially consists of a "comb" of infinitely sharp lines, equally separated by a frequency spacing corresponding to the inverse of the inter-pulse period and extended over a frequency range inversely proportional to τ_p. The advantages of such a peculiar spectral distri-

---

[1]The first demonstration of high-resolution spectroscopy of multiphoton atomic transitions with ultrashort pulses dates back to 1996, when we showed that it was indeed possible to measure line splittings (the hyperfine separation of the $8S_{\frac{1}{2}}$ state in cesium in that case) in a two-photon transition with a spectral resolution much better than that given by the single-pulse spectral width [1]. This is the same principle of Fourier Transform Spectroscopy that normally uses broad-bandwidth CW sources to perform medium-to-high resolution studies in the medium- and far-infrared. One of the advantages of employing this technique with short pulses is that one can now use their high peak intensities to move to different spectral regions or to investigate new transitions involving two or more photons [2].
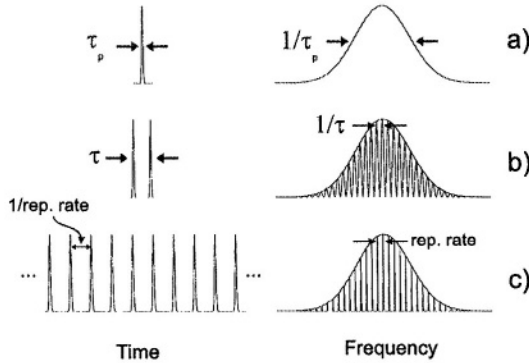
Figure 2.1. A single laser pulse has a frequency bandwidth which scales with the inverse of its duration τ_p (a). If one uses a pair of phase-locked pulses, delayed by a time τ, the resulting spectrum maintains the broad envelope of width $1/\tau_p$ but with a sinusoidal modulation of spectral period $1/\tau$ (b). This width sets the new instrumental resolution. If one uses an infinite sequence of pulses, locked in phase and equally delayed in time by the interval τ, the spectrum breaks up in a "comb" of very narrow lines (the "teeth") equally spaced by a frequency interval $1/\tau$ (c).

bution are evident: this spectral comb can be used as a precise ruler to measure unknown frequency intervals in a relatively simple way. By locking two laser lines to two different "teeth" of the comb, and by counting the integer number of interposed teeth, one can immediately obtain the unknown frequency gap, if the separation between the teeth is well known. A mode-locked laser is a natural way for generating such an ideally infinite sequence of time-delayed pulses with a well-defined phase relationship [3]. Its spectrum (given by the set of equally-spaced longitudinal modes of the cavity) is a broad comb of frequencies with a mode separation equal to the measurable and controllable pulse repetition rate (see Fig. 2.1 c). The largest frequency gap that can be bridged with such a comb is determined by the inverse of the pulse duration τ_p (if the pulse is Fourier transform-limited), but it can be widely extended if nonlinear interactions are used to broaden the spectrum.

In any case, one of the essential requirements for these novel spectroscopic techniques to work is that the phase coherence between the pulses in the sequence is accurately preserved. The experiments described below were mainly aimed to check this coherence preservation in the particular highly-nonlinear processes of HOH and SC generation, but their results went far beyond the initial scope. Besides demonstrating phase coherence in both cases and achieving high-resolution with a Ramsey-type XUV spectroscopy, we clarified the microscopic processes of high-order harmonic generation and established the

basis for the invention of the femtosecond frequency combs, the two essential ingredients for the generation of attosecond pulses.

3.   HIGH-ORDER HARMONICS

3.1   Basic Principles

Pulses with frequencies which are odd-order harmonics of the fundamental laser frequency can be generated by the interaction of short and intense laser pulses with the atoms of a supersonic gas jet. The most impressive characteristic of HOH is the existence of a *plateau* in the emitted spectrum [4, 5]. At variance with the usual exponential decay of the conversion efficiency for increasing harmonic orders (as found with the perturbative treatment of non-linearities in a medium), the HOH spectrum only presents such an exponential decay for the first few harmonics, being quickly replaced by a region of almost constant efficiency (the *plateau*), which may comprise many successive orders. Depending on the wavelength, duration and peak intensity of the pulses, and on the ionization potential of the atoms, very high orders can be efficiently generated at wavelengths down to the XUV or to the soft X-ray regions. The maximum extension of the *plateau* is defined by the so-called *cut-off* energy, which is normally found to follow a rather simple law:

$$E_{cut-off} \approx I_P + 3.2\,U_P, \qquad (2.4)$$

where I_P is the ionization potential of the gas, and $U_P \propto I\lambda^2$ (with I and λ the peak intensity and wavelength of the driving laser, respectively) is the so-called ponderomotive energy (see Ref. [6] for a recent review).

3.2   Phase Coherence in Harmonic Generation

Although harmonic sources are extremely appealing due to the lack of other easily accessible alternatives in these spectral regions, the extremely broad bandwidth associated with their short pulse duration seems to prevent their use for spectroscopy. In fact, even if some low-to-medium-order harmonics can be generated with pump pulses in the nanosecond and picosecond range [7–9], allowing one to keep a good spectral resolution for selected applications, higher-order harmonics can only be created at intensities above 10^{13} W/cm^2 by ultrashort laser pulses. A 100 fs pulse is already characterized by a spectral width in the THz range.

A way to overcome this limit is with the application of the two-pulse technique, described above, to the harmonic radiation, by splitting and delaying the

XUV pulses by means of a Michelson interferometer before sending them to the samples under study. Unfortunately, the use of this technique with HOH pulses is far from straightforward, mainly because good interferometers cannot be built to work in the XUV due to the lack of suitable optics. One can think of solving this problem by moving the interferometer in the path of the laser beam, in order to create two phase-locked and time-delayed pump pulses that would then generate equally phase-related XUV pulses, but the question at this point concerns the preservation of the phase lock in the generated pulses: if the process of HOH generation were an incoherent one, no phase relationship could be preserved between the XUV pulses, and such a scheme for spectroscopy with harmonics would be useless.

A simple way to test the mutual phase coherence between the harmonic pulses produced by phase-locked pump pulses is to generate them in two separate spatial regions and look for interference fringes in the far field: the existence of a stable interference pattern would show that the two secondary sources have preserved a memory of the phases of their parent pulses[2]. A first experiment concerning HOH was carried out in Lund, where harmonics were generated by focusing 30 ps laser pulses into an argon gas jet [11]. After the focusing lens, the laser pulses were split and given a slight fixed displacement (both in space and time) thanks to the walk-off in a birefringent plate, and a common polarization component was selected before entering the interaction region. Harmonics were then generated in two different positions in the gas jet and we looked for interference fringes in the far field, after spectral dispersion produced by a grating. Nice, stable and highly-contrasted fringes were unexpectedly observed, indicating that the generation process was not as phase-destructive as initially thought, and demonstrating that harmonic generation could become a suitable source for XUV interferometry [12] and high-resolution two-pulse spectroscopy.

A second experiment was later performed at LENS using a Michelson interferometer to split and delay the laser pulses (only about 100 fs long, in this case) so that their temporal and spatial separation in the focus could be carefully adjusted and controlled [13]. Very clear interference fringes were again observed on the Micro-Channel-Plate detector placed beyond the exit slit of the vacuum monochromator, and the temporal coherence of the harmonics could be determined by observing the decay of the fringe visibility as a function of the

---

[2]A preliminary experiment with the third harmonic generated in air gave very interesting and encouraging indications [10], although it was not possible to directly extrapolate the results to higher orders and the general thought was that, in such a case, the generation process would have completely messed up the phases of the harmonic pulses, destroying any interference.

inter-pulse delay. Almost transform-limited XUV pulses with coherence times of the order of the expected duration of the harmonics themselves (about 40 fs) were generated, showing that not only was the phase not scrambled in the process, but also that a negligible frequency chirp was imparted to the secondary pulses.

While doing this, we also discovered some new and unexpected features: the presence of two clearly distinct spatial regions in the pattern of harmonic emission, with drastically different coherence properties (see Fig. 2.2). There was an inner region with the long coherence times described above and a diffuse outer halo, containing more than half of the total emitted flux, with an extremely short temporal coherence, of the order of just a few femtoseconds.

3.3   Some Insight into the Microscopic Generation Process

We unexpectedly found that this was one of the most direct proofs of the validity of the theoretical models currently used to describe the microscopic physical mechanisms involved in the process of HOH generation. According to the standard picture of the HOH generation process [14], during every half optical cycle of the laser pulse electrons undergo tunnel ionization through the potential barrier formed by the atomic potential and by the electric field potential of the laser; after being accelerated in the ionization continuum by the field, they may come back to the ion core and finally recombine to emit harmonic photons that release the accumulated kinetic and ionization energy. Single-atom models also predict that harmonics are emitted with an intensity-dependent phase, proportional to the amount of time spent in the continuum by the generating electrons.

Simple calculations show that the highest harmonic orders (in the so-called *cutoff*) can only derive from electrons which have been released at a well defined time in each half optical cycle of the laser. On the other hand, it is equally easy to see that lower-order harmonics (in the *plateau*) essentially come from two different classes of electrons which are emitted at different moments, spend different amounts of time in the continuum following different trajectories, but nevertheless come back to the ion with the same correct kinetic energy to generate that given harmonic (see Fig. 2.2). For these harmonics, the "short" trajectory imposes a phase that does not vary much with the laser intensity, whereas the phase corresponding to the "long" trajectory varies rapidly with the laser intensity. Such a "long" electronic trajectory gives rise to strongly divergent angular emission because the rapid spatial variation of the phase with the focused laser intensity leads to a strong curvature of the phase front. This radiation also has a very short coherence time, since the harmonic pulse is
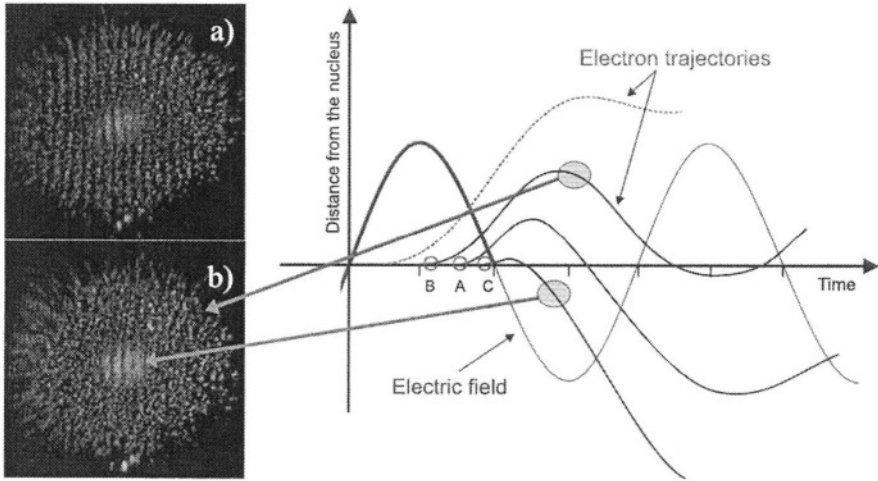
Figure 2.2. Snapshots of the interference fringes produced by the 15th harmonic generated in argon. In a), taken at a delay of 0 fs, fringes appear all over the image with a good visibility, while they disappear in the outer region of b), taken at a delay of 15 fs. The diffuse halo surrounding the central bright spot has a much shorter coherence time than the inner region. On the right we show a schematic representation of the possible classic electronic trajectories leading to the emission of such harmonic photons every half laser optical cycle. Electrons which are ionized while the field amplitude grows are driven away from the ion and never recombine to generate harmonics (dashed curve). Electrons escaping with a decreasing field leave the ion, oscillate in the continuum and come back with additional kinetic energy that can be converted into photon energy (solid curves). The maximum return energy (corresponding to the highest harmonic orders generated) is carried by electrons ionized in **A**. A given lower harmonic (like the one on the left) can be generated by electrons released either in **B** or in **C**, since both trajectories correspond to the same final return velocity (same angle of intersection with the horizontal axis). Electrons "born" in **B** suffer a stronger intensity-dependent phase modulation since they spend a much longer time in the continuum.

strongly chirped due to the rapid temporal variation of the phase during the pulse. By contrast, the phase variation corresponding to the "short" trajectory is much less important: the emitted radiation has a long coherence time and is much more collimated (for a more detailed discussion see Ref. [15]). If one is somehow able to select just one of these electron trajectories, (for example, just using harmonics in the cut-off region, where XUV photons can only be generated by one electron trajectory corresponding to the maximum return kinetic energy), then HOH radiation will be essentially composed of a train of sub-femtosecond XUV pulses, emitted every half optical cycle of the driving laser pulse.

3.4   Collinear, Phase-Coherent, Harmonic Pulses

The experiments described above demonstrated that the process of HOH generation does not scramble the phase of the XUV radiation and that two phase-locked pump pulses can indeed produce two phase-locked harmonic pulses. In those experiments, however, the two harmonic pulses were generated in two spatially separated zones while, to generate the modulated spectrum described in Eq. 2.2, the pulses need to be collinear. This also means that the two time-delayed laser pulses have to interact with the same atoms to produce harmonics and that the second pulse of the pair may generate harmonics in a less efficient way or with significant phase disturbances due to the presence of free electrons. As a result, the possibility of using the produced harmonic pulses for some Fourier or Ramsey-type spectroscopy would be seriously compromised.

In order to check the phase lock in a collinear case, a new experiment was carried out in two different configurations [16]: in the first one, we selected a narrow wavelength interval and observed the temporal interference fringes as the time delay between the harmonic pulses was scanned; in the second, we observed the spectra corresponding to pairs of harmonic pulses at different time delays to confirm our results also from the spectral point of view, in a way similar to the experiments by Salières et al. [17].

The temporally integrated signal $I(\omega_s, \tau)$ observable at the exit slit of a spectrometer centred at ω_s as a function of the delay τ can be obtained by considering the harmonic field as the sum of two identical and temporally separated pulses. If $F(\omega - \omega_s)$ is the transmission function of the monochromator filter, which we assume to be symmetric and much narrower than the single-pulse spectrum $I_0(\omega)$, we obtain

$$I(\omega_s, \tau) \propto |I_0(\omega_s)\,(1 + \tilde{F}(\tau)\cos(\omega_s\tau)), \qquad (2.5)$$

where $\tilde{F}(\tau)$ is the Fourier transform of $F(\omega)$, normalized to have $\tilde{F}(0) = 1$, and corresponds to the contrast of the resulting interference fringes. Measuring the fringe visibility as a function of the delay thus simply yields the Fourier transform of the filter transmission function. Expression 2.5 shows that two short time-delayed pulses that would not normally interfere due to their temporal separation may be forced to overlap again as a result of the broadening of their temporal profile introduced by the spectral filtering. The width of the spectral filter sets the maximum time delay for the existence of interference fringes[3]. In the case of identical harmonic pulses, there should be no degradation of the fringe contrast other than that caused by the limited spectral resolution of the monochromator and given by Eq. 2.5. If, on the other hand, one of the two harmonic pulses is degraded, for example, by passing through a partially depleted medium, then the fringe contrast should show a much faster decay with the time delay. The same effect is obtained not only in the case of a simple intensity imbalance, but also in the case of a phase disturbance of one of the two pulses.

The experimental set-up was similar to that of the previous experiment, and harmonics were observed downstream of the exit slit of the monochromator by means of a phosphor screen and a photomultiplier, while scanning either the time delay between the pulses or the monochromator wavelength. Figure 2.3 shows the fifth and seventh harmonic signals obtained by scanning the time delay on a small scale in the region of well-separated laser pulses. The stretching of the duration of the harmonic pulses due to the spectral filtering of the monochromator is evident, as these pulses keep interfering even for such large temporal separations. The same figure also presents the modulated two-pulse spectra corresponding to the same harmonics. According to expectations, the spectra exhibit the broad envelope of the single pulse, with a superposed sinusoidal modulation showing fringes with a period

$$\delta\lambda = \lambda^2/c\tau. \tag{2.6}$$

Our measurements were in good agreement with the simple expression 2.5, which only takes into account the finite spectral resolution of the monochromator, and is connected with the fact that, when the fringe period approaches such a value, the observed contrast starts to decrease due to the blurring of adjacent minima and maxima that finally washes out the whole interference pattern. It

---

[3]Note that, in the absence of such a filtering effect, interference fringes would only last for delays up to the coherence time of the pulses, of the order of a few tens of femtoseconds.
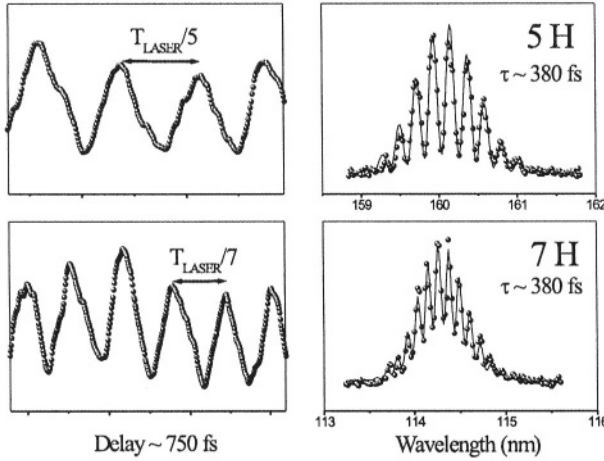
Figure 2.3. Two-pulse time-integrated intensity versus time delay for the fifth and the seventh harmonics at $\tau \approx 750$ fs (left column). Plots on the right show the two-pulse spectra of these harmonics at a fixed delay. The solid lines are fits to expression 2.5.

was thus demonstrated that no degradation of the fringe contrast was present due to the generation process itself (at least for medium-order harmonics and laser intensities up to 1.5×10^{14} W/cm^2) and that it was indeed possible to generate collinear pairs of phase-locked XUV radiation pulses. By replacing the filtering action of the monochromator with the narrow resonance of an atomic system, this technique may then allow the study of its spectral characteristics with an unprecedented resolution for this wavelength region.

3.5 Ramsey Spectroscopy with High-Order Harmonics

Ramsey-type spectroscopy with ultrashort laser pulses [18–20, 1]has been applied to bound state spectroscopy with optical sources in single-photon as well as in multi-photon and multi-step transitions [21, 2, 22, 23]. In its simplest scheme, one can consider the sinusoidally modulated two-pulse spectrum depicted in Fig. 2.1 b and imagine that a narrow atomic transition is placed somewhere under the broad spectral envelope. If the delay between the incoming pulses is varied, the fringe pattern moves and the transition will shift in and out of resonance in a sinusoidal fashion. Of course, when the delay gets so long that the period of the spectral fringes becomes comparable or smaller than the transition linewidth, then the contrast of the excitation modulation will tend to decay. From a different point of view, one can consider the first short pulse as inducing a coherence in the two-level system and creating a dynamical

polarization of the medium. The induced polarization oscillates at the transition frequency with a decaying amplitude during the dephasing time. The second pulse, depending on its phase with respect to the polarization oscillation, can enhance or destroy the residual system excitation. As a result, any excitation-related observable exhibits interference fringes when varying the delay between the two pulses. In more complex excitation schemes, involving more than two interacting states, the modulation of the fringe pattern and the appearance of beat notes can give information on the energy separation of nearby levels and on their lifetimes.

High-order harmonics are ideal candidates to study the spectral characteristics of high-lying excited states with one-photon transitions. With the experiments described above we had verified the possibility of producing collinear phase-locked harmonic pulse pairs so that the next step was to use them to perform high-resolution spectroscopy in the XUV. For the first test of Ramsey-type spectroscopy with HOH, a pair of krypton autoionizing states, resonant with the ninth harmonic of our Ti:sapphire laser, were chosen [24]. As schematically shown in the inset of Fig. 2.4, two phase-locked ninth-harmonic pulses at about 88 nm simultaneously excited the $4p^5(^2P_{1/2})6d'$ and $4p^5(^2P_{1/2})8s'$ states, separated by about 29 meV, well below the 90 meV of the single-pulse spectral width. The quantum interference of the states was expected to manifest itself as a fringe pattern in the electron signal versus the delay between the pulses, with a fringe spacing given by the atomic transition period [25], in this case about 0.29 fs. The modulation of the fringe contrast on the scale of the state lifetime, amounting to tens or hundreds of fs, should have reflected the decay and the possible beating of the autoionizing states.

The experimental set-up is sketched in Fig. 2.4 and was basically the same as used for the previous tests on phase coherence, but the exit slit of the monochromator was here replaced by a second pulsed gas jet of kripton atoms. An electron-energy and ion-mass time-of-flight spectrometer (TOF) was used to analyze the ionization products while scanning the inter-pulse time delay with a stepper-motor-controlled translation stage or with a piezoelectric crystal moving one arm of the interferometer. The electrons produced by the photoionization of krypton atoms left the interaction region and were analyzed by the TOF spectrometer, while the spectrally unresolved field of the selected harmonic was observed downstream from the interaction region by a phosphor/photomultiplier pair, whose signal gave a pulse-by-pulse monitor of the harmonic intensity. The interference fringes in the electron signal as the delay was smoothly varied around 110 fs are shown in Fig. 2.5. As the two states had an energy separation below the TOF electron-energy resolution, both continua
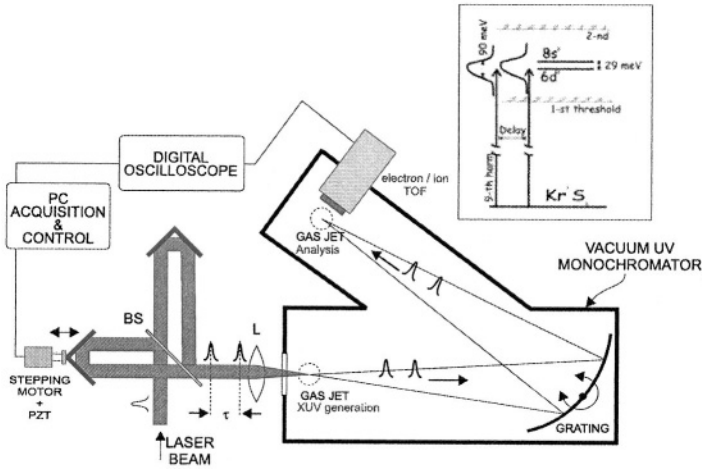
Figure 2.4. Experimental set-up and scheme of the interaction (inset), showing the involved autoionizing levels of the krypton atom: the ninth harmonic, generated by focusing the phase-locked pulse pair in the xenon jet, is selected by the monochromator grating and crosses the krypton jet in the interaction chamber. The electrons ejected in the one-photon ionization process are energy-analyzed by a TOF spectrometer

contributed to the observed ionization signal. The modulation was clearly visible above the statistical fluctuations, and had the expected period of about 290 attoseconds. The simultaneous detection of the transmitted harmonic intensity
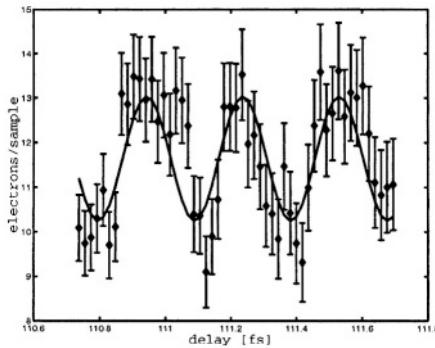
Figure 2.5. Detail of the fringe pattern around the 110 fs delay. The fringe spacing corresponds to the 0.29 fs period of the atomic transition.

did not show any modulation, thus verifying the absence of residual optical interferences between the harmonic pulses. The fringe contrast as a function of the pulse delay was compared with the theoretical curve obtained from the

state energies, widths, ionization constants, and the Fano parameters reported in the synchrotron measurements of Ref. [26]. Being in a perturbative regime, no coupling was taken into account between the two states, which thus evolve independently following two-state dynamics in the Fano approach. The theoretical ionization probabilities for the two states were then simply summed to give the total ionization signal. The energy difference between the two states was expected to give rise to a beating with a period of about 140 fs and our experimental data indeed showed such modulation in fairly good agreement with the calculated curve.

The clear signature of quantum interferences were the proof that a Ramsey-type approach in the XUV is possible. Such a spectroscopic tool, based on relatively simple table-top equipment, might thus become an attractive alternative to synchrotron radiation sources for selected applications. Furthermore, the use of more elaborate pulse sequences, or even the extension toward phase-locked harmonic pulse trains, might soon lead to the extension of the domain of precision spectroscopy and metrology (see the frequency-comb technique in Chapters 4 and 5 of this volume) to the short-wavelength region.

4.   SUPERCONTINUUM

4.1   Basic Principles

Since the first observations in the late 1960s [27], the phenomenon of supercontinuum generation, i.e., the extreme spectral broadening resulting in the generation of white light when ultrashort and powerful laser pulses propagate in a transparent medium, has been demonstrated in a variety of materials, including solids, liquids [28], and gases [29, 30]. Its broadband and ultrashort characteristics make it a unique light source [31, 32] for applications, and it is now routinely used for femtosecond time-resolved spectroscopy [30, 33], in optical pulse compression for the generation of ultrashort pulses [34, 35], or as a seed pulse of optical parametric amplifiers [36–38].

Supercontinuum (SC) generation results from a complex interplay of self-phase-modulation [27, 28, 39], self-focusing [29, 40], and several other nonlinear optical effects. The collapse of the beam profile due to self-focusing is one of the main ingredients for the generation of the continuum when the power of the pump pulse reaches a critical threshold. Experiments have indeed shown that the threshold for SC generation corresponds to the calculated critical value for self-focusing [29, 30, 40, 41]. It has been demonstrated that when intense ultrashort laser pulses are focused in transparent media, they tend to break up into a number of intense filaments [42–44], and that, due to the competition

between focusing by the Kerr effect and defocusing by free electrons (created in multiphoton or avalanche ionization), the diameter of these filaments and the peak laser intensity inside them tends to remain constant against increasing input pulse energies [45].

The combined action of the highly nonlinear phenomena involved in the generation of SC might lead one to conclude that even small perturbations in the conditions of interaction with the medium can strongly affect the amplitude and phase properties of the white-light pulses. In particular, one may expect that small intensity variations in the pump pulses or small inhomogeneities in the materials may lead to dramatic phase and intensity fluctuations in the generated supercontinua.

4.2 Phase Preservation in the Supercontinuum Generation Process

After the experiments on the coherence of high-order harmonics, we decided to use the same simple experimental apparatus to test the mutual phase coherence of the light pulses generated in this different kind of extremely nonlinear process. We just replaced the system for harmonic generation with a plain 2 mm thick plate of calcium fluoride (CaF_2) after the misaligned Michelson interferometer, so that the two phase-locked laser pulses could independently produce two white-light pulses. After the interaction zone and after the two diverging continua had propagated in air for some distance, they were finally overlapped on a screen where we hoped to observe interference fringes.

The results of this simple experiment were once again quite unexpected: when the two pump pulses were properly balanced in intensity and adjusted for zero relative delay, the two white-light continua that had been separately generated showed the surprisingly clear and stable white interference fringes depicted in Fig. 2.6, indicating that we were dealing with highly phase-correlated secondary sources[4] [46].

In order not to damage the medium, the pulse energy was limited to about 1 μJ, and the generation of a white-light continuum was normally observed to proceed through the creation of a single light filament with an estimated peak intensity of the order of 10^{12-13} W/cm^2. Higher energies involved the

---

[4]Note that there is a substantial difference between this and a simple Young's or Michelson's type experiment: in such cases two spatial portions of the same beam, or two time-delayed replicas of the same pulse, are recombined to give interference. In our experiments on HOH and SC, on the contrary, the interference fringes appear because of the spatio-temporal superposition of two secondary light pulses independently generated in two separate positions of the medium. For the complex and apparently unpredictable characteristics of the generation processes at play, one could expect such pulses to be highly unrelated.
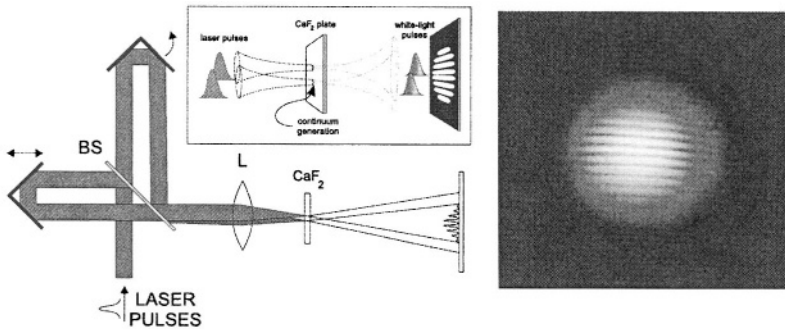
Figure 2.6. Scheme of the experiment for the observation of white-light interference fringes. The two pump pulses are generated by the same laser system and by the same Michelson interferometer described above. Two independent SC pulses are generated in the material and then propagate and overlap on a screen. A snap-shot of the observed interference pattern is also shown, taken with an exposure time of about 2 seconds and with a laser repetition rate of 1 kHz. The very good visibility of the fringes indicates that the phase lock is not only preserved on a shot-to-shot basis, but that a constant phase relationship is maintained over at least thousands of shots.

breakup of the pulse into multiple filaments, giving rise to highly structured patterns as a result of the spatial interference among the different, and mutually coherent, white-light sources thus produced. Although visually interesting, we tried to avoid this effect, and all the measurements were performed in the single-filament regime. In general, any transparent material available in the laboratory (from quartz and glass plates to water cells and Plexiglas windows) was able to produce nicely interfering white light at various degrees of efficiency.

4.3   Collinear, Phase-Coherent, Supercontinuum Pulses

The previous experiment, dealing with the mutual coherence of SC pulses generated with amplified laser systems in bulk media, demonstrated that spatially separated white-light sources could exhibit high-visibility spatial interference fringes [46–48]. However, no indication had been given about the possibility of generating collinear phase-locked continua in a bulk medium. Although this is the fundamental process at the base of the recent and successful technique of frequency comb generation in photonic fibers with mode-locked lasers (see Sect. 6), the equivalent mechanism in bulk media has to take place at much higher intensities and the nonlinear processes involved are therefore far less smooth and controllable. In the previous case of spatially separated sources, the pump laser pulses did not interfere in the medium and each pulse generated white light independently from the other. In the collinear case, a sub-

stantial optical interference can take place between the laser pulses for delays shorter than the pump coherence time and the high intensities reached at the interference maxima may damage the material and prevent stable and efficient generation. Even in the case of delays longer than the temporal coherence of the pump pulses, the second pulse of the white-light pair has to be generated in a region which has already strongly interacted with the first one, and one might expect a degradation of the mutual coherence of the two supercontinua.

The next step was then to set up an experiment to investigate the coherence properties of time-delayed and phase-locked collinear SC pulses [49]. By mounting one of the interferometer mirrors on a PZT-controlled tilt stage, one could accurately split and recombine the 30 fs laser pulses to make them propagate collinearly and produce clear spectral interferences when time-delayed. A lens focused the pulses in glass windows with thickness ranging between 0.5 and 5 mm and the spectra of the produced white light were observed after a re-collimating lens by means of a spectrometer, based on a 2048-pixel photodiode array and with a spectral coverage extending from 520 to about 1180 nm. In the ideal case, where the two time-delayed white-light pulses are perfectly phase-locked, their combined spectrum is easily found from Eq. 2.2 and is expected to show a clear sinusoidal modulation of high visibility, with a period depending on the inter-pulse delay and on the wavelength (see Eq. 2.6). Our objective was then to verify that, when the two white-light pulses were generated by two time-delayed, phase-locked laser pulses with reasonably equal efficiencies, such a modulated spectrum would indeed appear and extend over all the visible and near-IR regions. Figure 2.7 shows the appearance of
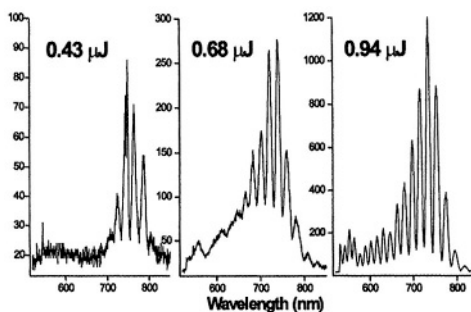
Figure 2.7. Appearance of white-light spectral interference fringes on the visible side of the laser spectrum in a 1 mm thick glass plate. In the sequence of spectra measured at different single-pulse energies, one can observe the birth of a single supercontinuum pulse and the appearance of the second, phase-locked pulse, which produces a clear sinusoidal modulation in the spectrum.

the white-light continuum on the short-wavelength side of the modulated laser

spectrum: at low power, no SC was present, but when the pulse energy was increased, visible components started to appear without visible modulations. Only when the pulse energy was increased close to 1 μJ, clear spectral interferences appeared. This is simply explained by the presence of a threshold behavior connected with the modifications in the spatial profile of the pulses due to self-focusing, combined with a slight imbalance in the peak intensity of the two pump pulses. While at low power neither pulse had suffered sufficient self-phase-modulation to significantly broaden its spectrum, at intermediate values one of the two had reached the critical power for self-trapping and the intensity in the so-formed filament had given rise to the new spectral components in the visible region. Only when the second pulse reached the same threshold, a comparable amount of white light was suddenly coherently generated, allowing the corresponding spectral components of the two pulses to interfere. By recording the evolution of the different spectral components of the SC in the single-pulse and single-filament regime as a function of the laser pulse energy we indeed found a general behavior similar to the one shown in Fig. 2.8 for the region around 550 nm. Experimental values in the 5-10 MW range for the threshold power of supercontinuum formation agree well with the calculated critical power for the onset of self-focusing and indicate the close connection between the two phenomena. As long as the pulse energy was not increased
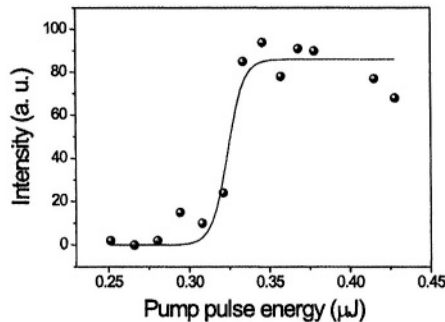
Figure 2.8. Behavior of the SC intensity variation as a function of the incoming laser pulse energy for a wavelength of about 550 nm. Filled circles are experimental data while the solid line is a fit with an hyperbolic tangent function.

too much above this single-filament threshold, to a level such that both pulses were able to independently generate stable white light, the resulting spectrum was always characterized by very stable interference fringes of high contrast extending through all the visible and up to about 1.1 μm. The pulse peak intensity in the focus under these conditions was estimated to range between 1 and

5 times 10^{12} W/cm^2 depending on the medium thickness, with a waist radius of about 15 μm.

By changing the delay τ between the pump pulses it was possible to vary the period of the spectral fringes. Two examples of the spectra, in the visible and in the near-IR region, corresponding to different time delays between the pulses, are shown in Fig. 2.9. The fringe period measured in the region around
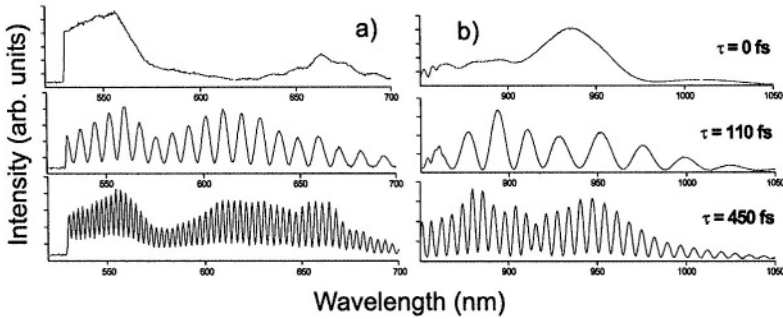
Figure 2.9. Visible a) and near-IR b) portions of the two-pulse SC spectrum displaying sinusoidal modulations of different period as a function of the time delay between the pump pulses.

900 nm is also shown in Fig. 2.10 as a function of the delay. The expected behavior (see Eq. 2.6) with the inverse of the time separation between the pump pulses is well reproduced by the experimental data. Increasing the time
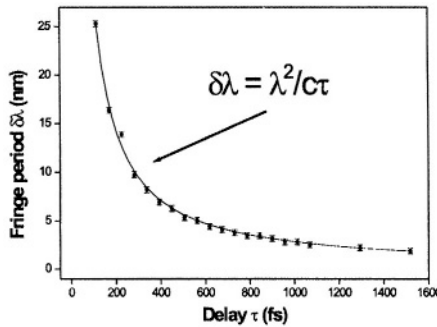
Figure 2.10. Fringe period as a function of the time delay τ between two laser pulses. Filled circles represent data points while the solid curve is a fit to the expected $1/\tau$ behavior.

delay normally reduces the fringe visibility due to the finite resolution of the spectrometer. However, other sources of contrast degradation may result from a difference in the conversion efficiency of the two laser pulses or the loss of mutual coherence between the two supercontinua. If the first pulse somehow

degrades the medium after its passage, then the second pulse generates much
less intense white light and the fringe contrast $V(r)$ decreases as

$$V(r) = \frac{2\sqrt{r}}{1+r},\tag{2.7}$$

where $r = I_1(\omega)/I_2(\omega)$ is the ratio of the two SC intensities. Even without
any intensity imbalance between the two white-light pulses, the passage of the
first pulse might perturb the phase evolution of the second and contribute to a
decrease of the fringe contrast. In order to discriminate between these sources
of contrast decay, we studied the behavior of the fringe visibility as a function
of the relative pulse delay for different spectral components. In particular, we
determined the decay curves for two regions of the white-light spectrum above
and below the laser wavelength, and compared them with the visibility curve
for the modulated laser spectrum obtained without interaction with the medium.
Once again, we were able to show that the fringe contrast nicely followed the
decay curve as expected in the case of purely resolution-limited visibility, and
that SC generation does not spoil the phase coherence of the laser pulses.

Finally, we tested the effects of pulse energy imbalance on the generation
and the phase coherence of the white light. As one could expect from Fig. 2.8,
we found that, above the threshold and close to the balanced condition, SC
can stand as much as 30% of pump intensity imbalance without substantially
degrading the fringe contrast (see Fig. 2.11). On the contrary, the change in
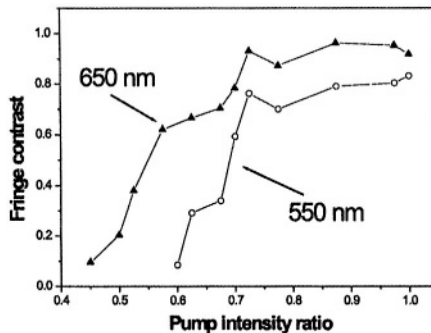
Figure 2.11.   Fringe contrast as a function of the pump pulse energy imbalance for two spectral
regions of the SC: triangles correspond to 650 nm and circles to 550 nm. Solid lines connecting
the experimental points are just a guide for the eye.

the intensity of one beam produced noticeable effects in the position of the
fringes. A pulse peak intensity increase ΔI of about 3×10^{12} W/cm^2 in the

focus caused a shift of about 6 fringes in the spectral interference pattern around 600 nm. This fringe shift could be compensated by increasing the path length of the other pulse, consistent with the effects of a positive nonlinear refraction index n_2. One could easily verify that this fringe shift is compatible with the one calculated from

$$\Delta\varphi = \frac{2\pi}{\lambda} n_2 \Delta I L \tag{2.8}$$

for the propagation in a medium of thickness $L \approx 5$ mm and nonlinear refractive index $n_2 \approx 10^{-16}$ cm^2/W in the case of a similar intensity variation.

4.4   Multiple-Beam Interference from an Array of Supercontinuum Sources: a Spatial Comb

As a further step to test the mutual coherence of SC, we realized the spatial-domain counterpart of the frequency-comb configuration, by generating a linear array of equally spaced SC sources in a bulk material and studying their far-field interferences[5] [50].

The usual Michelson interferometer was used in a slightly different configuration: by properly adjusting the angle of one of its folding mirrors, it was possible to change the angle between the outgoing laser pulses and produce straight interference fringes of variable period in the zone of beam crossing. A cylindrical lens was then placed after the interferometer in order to focus the outgoing pulses along a direction orthogonal to the plane containing the laser beams. In such a configuration the straight interference fringes were compressed down to between 10 and 20 microns in one dimension, while the spacing and the width of the spots in the other dimension could be simply adjusted by changing the relative angle between the two beams. Glass and quartz plates of different thickness (ranging from 2 to 10 mm) were placed in the focus position, and the regions of high intensity corresponding to the maxima of the interference fringe pattern could become the sources for SC emission. The laser pulse energy was varied in order to reach the threshold for white light generation from several consecutive interference maxima. Even at the highest intensities available with our laser system, SC generation from the different sources in the array always proceeded through the formation of a single filament, and multiple filamentation from a single source was never observed. After the interaction region, the SC pulses propagated towards a screen where they formed complex interference patterns. The fringe system was studied by scanning a photomul-

---

[5]Note that multiple Supercontinuum sources require an even more stringent relative-phase stability in order to produce a stable and clear interference pattern.

tiplier, apertured by a pinhole, along a direction perpendicular to the fringes by means of a computer-controlled translation stage, while colored filters were placed in front of the detector to select different spectral regions in the visible continuum. In order to study the near-field region inside the transparent material, the source area was also imaged on a distant screen and magnified (by a factor of about 40) by means of a lens. The interaction geometry is illustrated
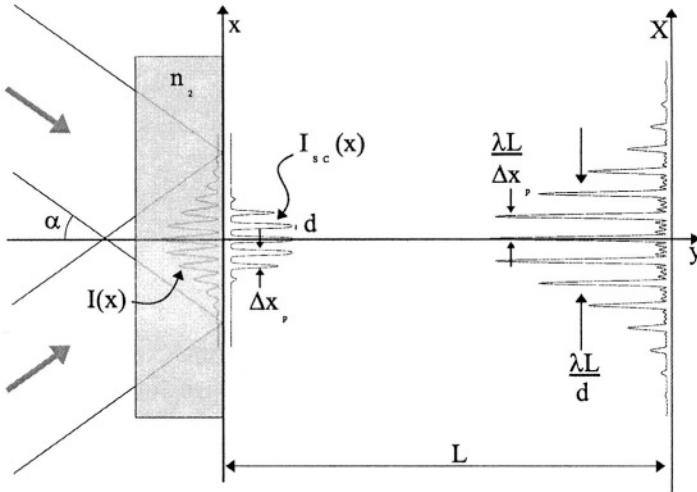
Figure 2.12. Sketch of the experimental set-up illustrating the geometry of the interaction. Two laser pulses intersect at an angle 2α and form an interference pattern on the x plane inside the material. The maxima of this interference pattern become the sources for supercontinuum radiation which propagates to a screen placed at a distance L.

in Fig. 2.12: the two laser beams intersect with an angle 2α and we assume that the delay between the two arms of the interferometer is adjusted so that the pulses cross the plane $x = 0$ at the same time. In this case, the different positions along the x axis simply map different relative delays τ between the arrival time of the two pulses as

$$\tau(x) = 2\frac{x}{c}\sin(\alpha). \qquad (2.9)$$

If the coherence time of the laser pulses is τ_c (we assume that we are dealing with Fourier-transform-limited Gaussian pulses, with a pulse duration $\tau_c \approx 30$ fs and peak intensity I) then one can expect to observe an interference fringe

pattern of good visibility for a spatial extension of about

$$\Delta x_c \simeq \frac{c\tau_c}{2\sin(\alpha)} \qquad (2.10)$$

and with a fringe period of

$$\Delta x_p = \frac{\lambda}{2\sin(\alpha)}. \qquad (2.11)$$

So, by varying the angle α it is easily possible to change the dimensions of the source area and the fringe spacing in a wide interval (note that, in all cases, the total number of fringes in the array is constant, independent of the angle between the beam directions, and of the order of 10-20). Neglecting the spatial distribution of the pump intensity and considering a simple interference of two plane waves, the two-pulse pump intensity distribution $I(x)$ in the $y = 0$ plane can be simply found. In this case

$$I(\tau) = 2I(1 + V(\tau)\cos(\omega\tau)), \qquad (2.12)$$

where the fringe visibility $V(\tau)$ is given by

$$V(\tau) = e^{-(\frac{\tau}{\tau_c})^2 \ln 2} \qquad (2.13)$$

and one can make use of Eq. 2.9 to convert the time delays into a transverse spatial position.

In order to simulate the process of white-light generation in the case of our multiple-source arrangement, we modeled the SC intensity dependence on the pump intensity with a hyperbolic tangent function, according to the behavior observed in Fig. 2.8[6]. Clearly, also the number N of SC sources (and, consequently, the spatial extension of the array) is a directly controllable parameter, via the control of the pump pulse energy. High laser power allows generation from many spatially-separated sources, while a lower power limits the production of white light to only a few central interference maxima. By varying the pump pulse energy, the number of SC sources was changed from 3-4 to as many as 40 when the full laser power allowed self-focusing also for interference maxima in the extreme wings of the pattern. Figure 2.13 shows

---

[6]Note that the introduction of an hyperbolic tangent function with a characteristic threshold and saturation behavior has an evident connection with the onset of beam self-focusing and with the sudden intensity clamping due to the formation of a filament in the medium.
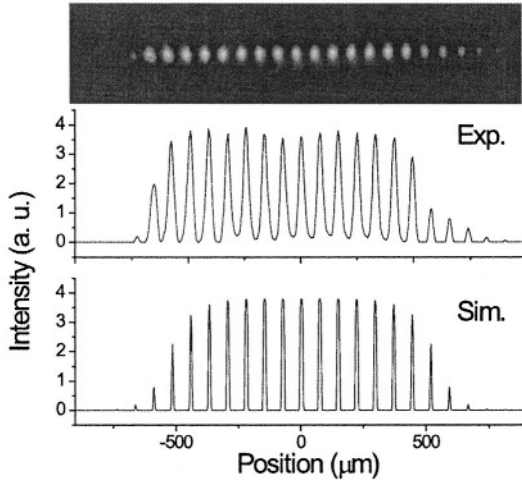
Figure 2.13. Experimental CCD image of the SC array source region. Also shown are the profiles obtained by an horizontal cut across the image (middle plot) and the simulated SC intensity distribution from Eqs. 2.12 and 2.13 (bottom plot). An array of about 15 white-light sources of almost constant intensity was produced in this case: the extension of the array was measured to be about 1 mm, with an inter-source spacing of 75 μm.

a near-field image, taken with a CCD camera, of the interaction region, where many equally-spaced sources of white light were clearly visible. An horizontal cut of this figure indicated that the central part of the pump interference pattern produced SC secondary sources of almost constant intensity despite the Gaussian profile of $I(x)$. The use of the hyperbolic tangent function to cut the low-intensity pump regions and to saturate the interference maxima made it possible to reproduce the intensity distribution of the white-light sources in a very reasonable way.

In order to evaluate the mutual phase coherence among the white-light sources, we studied the far-field interference patterns produced by the array on a screen placed at a distance L. As indicated in Eq. 2.3, a linear array of N phase-locked, infinitesimal sources equally spaced by a distance Δx_p should produce an array of intense sharp peaks spaced by $\frac{\lambda L}{\Delta x_p}$, with $N - 2$ smaller (by a factor of approximately N^2) peaks interposed (see Fig. 2.12 for reference). Figure 2.14 a shows the experimental profile of the interference pattern produced by the array of white-light sources as seen by a scanning detector in the far-field. The expected structure described by Eq. 2.3 is evident, with a clear array of strong interference maxima with smaller peaks interposed at regular distances. In this particular case, the laser pulse energy had been adjusted so
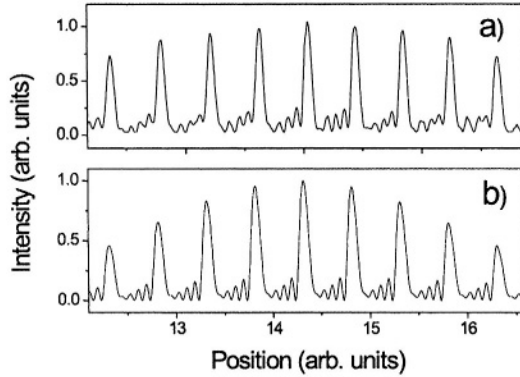
Figure 2.14. a) Experimental profile of the multiple-SC-beam interference pattern detected by scanning a photomultiplier in the far-field. Only the green part of the spectrum is selected by means of colored filters. b) Calculation of the far-field interference pattern generated by an array of phase-locked SC sources under the same conditions as a). A relative phase, proportional to the laser intensity in the different filaments, is introduced in order to reproduce the experimental behavior of the secondary peaks.

that only 6 to 8 interference maxima reached the threshold intensity for SC generation and we could infer that the white-light sources were filaments with a diameter of the order of $10\ \mu m$ or less. Although the intensity distribution among the secondary maxima was not as regular as expected from the ideal case, it was nevertheless clear that only a smooth and slowly varying phase had to be present across the array of SC sources. By using the calculated intensity distribution in the source area and the expression 2.8 for the induced nonlinear phase, we could simply estimate the phase distribution $\Delta\varphi(x)$ in the array, and find that a propagation distance of a few mm was sufficient to establish phase shifts of tens of radians between the central peaks and the outer ones. A simulated far-field pattern, obtained by Fast Fourier Transformation of the calculated source intensity-phase distributions, is shown in Fig. 2.14 b for the situation corresponding to the experimental results of Fig. 2.14 a. The qualitative agreement with the experimental data is evident.

Also, in this case, we found that all the multiple-beam interference patterns were extremely stable in time, indicating that the phase distribution was essentially the same from shot to shot, with little perturbation due to laser intensity fluctuations.

5. PHASE PRESERVATION IN CHIRPED-PULSE AMPLIFICATION

One further test concerning the phase preservation of ultrashort radiation involved the process of chirped-pulse amplification, normally used to boost the energy of the pulses coming from a mode-locked laser [51]. Here the idea was to compare, in an interferometric (i.e., phase-sensitive) way, a single pulse from a laser oscillator with its replica having undergone the process of amplification, to determine if their phases had been significantly scrambled or not[7]. By placing a beamsplitter before the pulse stretcher of the laser amplifier, both the oscillator pulses and their amplified versions were emitted from the system and made to interfere, after the delay in the multipass amplifier had been exactly compensated by an external delay line. Temporal interferences between a single amplified pulse and its twin in the oscillator train (at 80 MHz repetition rate) were observed as periodic modulations of their combined signal while finely scanning the optical delay line. Measurements were performed for different numbers of passes in the amplifier and for varying gain factors, up to full amplification and re-compression of 0.6 mJ pulses.
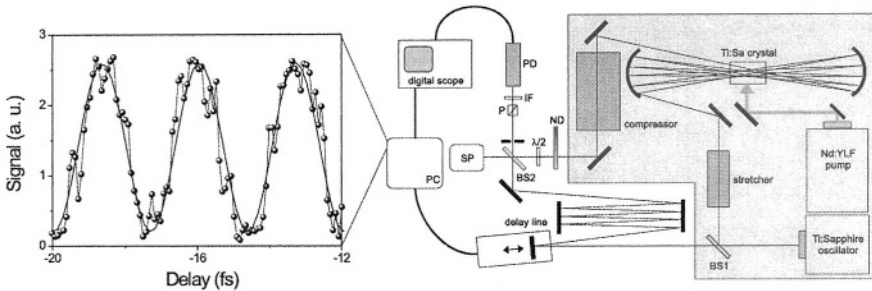
Figure 2.15. Experimental set-up. The shaded area delineates the amplified laser source. ND: variable neutral density filter; P: cube polarizer; $\lambda/2$: half-wave plate; IF: narrow-band interference filter; PD: fast photodiode; SP: spectrometer; BS1 and BS2: 50% beam splitters; PC: personal computer. Also shown is the interference signal (filled circles) obtained while scanning the delay between the original laser pulse and its amplified replica. The solid line is a fit to a sine function.

In order to single out the possible deleterious effects of amplification from those coming from other unavoidable instabilities in the system on the phase co-

---

[7]Possible causes of dephasing include cross-phase modulations due to a pulse-to-pulse jitter of the pump energy or self-phase modulations due to shot-to-shot variations in the intensity of the amplified pulse itself or, finally, beam-pointing instabilities in the stretcher/compressor stages of the amplifier.

herence of the CPA pulses, we compared all the measurements of the oscillator-amplifier first-order cross-correlations with the same signals obtained with the amplification turned off. Figure 2.15 shows the experimental set-up and a portion of the cross-correlation signal obtained after nine passes in the amplifier. Clear and stable interference fringes demonstrated that the effect of amplification was reproducible and could in principle be controlled. Even in the case of full amplification and re-compression, the measured r.m.s. phase jitter between the two pulses was about 0.4 rad and did not change, within the accuracy of the measurement procedure, while switching on and off the pump laser (thus indicating that its main cause was environmental noise and not amplification). A prudential assumption of 0.1 rad as the upper limit for the total r.m.s. amplification-induced phase jitter was thus established and allowed one to conclude that the CPA process can substantially preserve the phase fingerprints of the original pulses.

6.   FREQUENCY COMBS, ABSOLUTE PHASE CONTROL, AND ATTOSECOND PULSES

Besides their interest for a better understanding of the basic mechanisms and for the applications of these novel "extreme" sources, the experiments on the coherence properties in HOH and SC generation and CPA were fundamental starting points for the successive developments in the field of optical metrology and attophysics.

The measurements on the phase coherence of HOH had demonstrated that just a few main electronic trajectories are responsible for the XUV emission and that, by properly selecting the experimental conditions, it is possible to select only one of such trajectories and thus emit a single XUV attosecond pulse for each half-cycle of the pump laser. If an intense laser pulse with a duration of just a few optical cycles (i.e., less than about 5 fs for a visible/near-IR pulse) is used to generate harmonics, and its intensity is selected such that cut-off photons can be generated only close to the peak of the pulse envelope, then the emitted radiation will consist of at most one or two attosecond-duration bunches of XUV photons. However, the emission pattern will normally not be repetitive from one laser shot to another, making the diagnostics and the use of such isolated attosecond pulses almost impossible, because, when dealing with few-cycle laser pulses, another parameter (normally forgotten for pulses of longer duration) comes into play and becomes crucial. This parameter is the so-called carrier-envelope-offset phase φ_{CEO}, and its variation in mode-locked laser pulses is connected with the fact that the phase velocity and group velocity inside the laser cavity are different. The absolute phase of the carrier

field oscillation thus normally slips by $\Delta\varphi_{CEO}$ with respect to the envelope from one pulse to the next one in a mode-locked train. In order to generate single attosecond pulses in a stable and reproducible way, one needs to start from identical and phase-customizable few-cycle pump pulses, and the only possibility to achieve this is by controlling and stabilizing φ_{CEO}.

This is where our activity on the supercontinuum came into play: by demonstrating the phase preservation in the process of SC generation, we had also shown that it was in principle possible to build a white-light frequency comb using a mode-locked laser to produce a train of phase-locked SC pulses after the interaction with a nonlinear medium. The results of our experiments and the introduction of a new kind of special optical fiber[8] [52]contributed to make such devices a reality and to revolutionize the whole field of optical metrology and spectroscopy [53–56]. Femtosecond frequency combs are now replacing old-style frequency chains wherever a precise measurement of an optical frequency is required because, with the realization of combs so wide as to extend over more than one optical octave, this technique now constitutes a solid self-referencing method, allowing the measurement of absolute optical frequencies with extreme accuracy in a single step from the microwave frequency standard [56]. Indeed, the frequency of the nth mode of the comb is simply given by

$$f_n = nf_r + f_0, \tag{2.14}$$

where f_r is the easily measured and controlled laser repetition rate, and f_0 is the so-called *offset frequency,* which can be measured by beating the blue side of an octave-spanning comb with the red side of its frequency-doubled version. The interesting part is that f_0 is simply related to $\Delta\varphi_{CEO}$ by

$$f_0 = \frac{\Delta\varphi_{CEO}\, f_r}{2\pi} \tag{2.15}$$

i.e., f_0 is just a measure of the slip rate of φ_{CEO}. It is evident that, by setting f_0 to zero or appropriately stabilizing it by some feedback loop, it becomes possible to control the absolute phase of the laser field and to generate a sequence of truly identical pulses. Finally, the demonstration that the phase characteristics

---

[8]"Photonic crystal fibers" or "holey fibers", essentially consisting of a very small silica core surrounded by a regular structure of "holes". They have the interesting characteristic of supporting the propagation of highly spatio-temporally confined visible pulses over long distances. This allows high nonlinearities to build up along the fiber and can give rise to SC generation already from nanoJoule-level pump pulses of a mode-locked laser.

of low-energy pulses from a mode-locked laser can be preserved in the process of chirped-pulse amplification [51], has now paved the way for the routine production of few-cycle, high-intensity, and phase-controlled, pulses.

Such pulses have already proved capable of generating reproducible single attosecond pulses for extremely high temporal resolution studies [57], but the availability of phase-controlled intense pulses will also have strong implications for a whole range of new phenomena in high-intensity laser-matter interactions, where the absolute phase of the field plays a fundamental role to trace [58]and steer [57, 59–61]the electronic dynamics in unprecedented ways.

7.   CONCLUSIONS

We have reported some recent experiments aimed to demonstrate and characterize the coherence properties of two kinds of "extreme" radiation sources: high-order laser harmonics and supercontinuum. Besides allowing the first applications of XUV interferometry and Ramsey spectroscopy, the studies on HOH generation have shed light on the basic mechanisms involving the role of electronic trajectories in the production of high-energy photons. On the other hand, experiments on the phase coherence in SC generation started the adventure of femtosecond frequency combs that, besides their fundamental role in precision spectroscopy and metrology, are now allowing the control of the absolute phase of few-cycle pulses. These two fields are now converging in a new, exciting direction – the generation and application of the shortest pulses ever created.

Acknowledgments

References

1. M. Bellini, A. Bartoli and T. W. Hänsch, *Opt. Lett.* **22**, 540 (1997).

2. V. Blanchet, C. Nicole, M. A. Bouchene and B. Girard, *Phys. Rev. Lett.* **78**, 2716 (1997).

3. J. N. Eckstein, A. I. Ferguson and T. W. Hänsch, *Phys. Rev. Lett.* **40,** 847 (1978).

4. M. Ferray, A. L'Huillier, X. F. Li, L. A. Lompré, G. Mainfray and C. Manus, *J. Phys. B* **21**, L31 (1988).

5. A. McPherson, G. Gibson, H. Jara, U. Johann, T. S. Luk, I. McIntyre, K. Boyer and C. K. Rhodes, *J. Opt. Soc. Am. B* **4**, 595 (1987).

6. P. Saliéres, A. L'Huillier, P. Antoine and M. Lewenstein, *Adv. At. Mol. Opt. Phys.* **41**, 83 (1999).

7. C. Lyngå, F. Ossler, T. Metz and J. Larsson, *Appl. Phys. B* **72**, 913 (2001).

8. K. S. E. Eikema, W. Ubachs, W. Vassen and W. Hogervorst, *Phys. Rev. A* **55**, 1866 (1997).

9. F. Brandi, D. Neshev and W. Ubachs, *Phys. Rev. Lett.* **91**, 163901 (2003).

10. M. Bellini and T. W. Hänsch, *Appl. Phys. B* **65**, 677 (1997).

11. R. Zerne, C. Altucci, M. Bellini, M. B. Gaarde, T. W. Hänsch, A. L'Huillier, C. Lyngå and C. G. Wahlström, *Phys. Rev. Lett.* **79**, 1006 (1997).

12. D. Descamps, C. Lyngå, J. Norin, A. L'Huillier, C.-G. Wahlström, J.-F. Hergott, H. Merdji, P. Saliéres, M. Bellini and T. W. Hänsch, *Opt. Lett.* **25**, 135 (2000).

13. M. Bellini, C. Lyngå, A. Tozzi, M. B. Gaarde, T. W. Hänsch, A. L'Huillier and C.-G. Wahlström, *Phys. Rev. Lett.* **81**, 297 (1998).

14. P. B. Corkum, *Phys. Rev. Lett.* **71**, 1994 (1993).

15. C. Lyngå, M. B. Gaarde, C. Delfin, M. Bellini, T. W. Hänsch, A. L'Huillier and C.-G. Wahlström, *Phys. Rev. A* **60**, 4823 (1999).

16. M. Bellini, C. Cavalieri, C. Corsi and M. Materazzi, *Opt. Lett.* **26**, 1010 (2001).

17. P. Saliéres, P. L. Le Deroff, T. Auguste, P. Monot, P. D'Oliveira, D. Campo, J. F. Hergott, H. Merdji and B. Carré, *Phys. Rev. Lett.* **83**, 5483 (1999).

18. M. M. Salour, *Rev. Mod. Phys.* **50**, 667 (1978).

19. J. T. Fourkas, W. L. Wilson, G. Wakerle, A. D. Frost and M. D. Fayer, *J. Opt. Soc. Am.* **6**, 1905 (1989).

20. R. R. Jones, D. W. Schumaker, T. F. Gallagher and P. H. Bucksbaum, *J. Phys. B* **28**, L405 (1995).

21. R. Van Leeuwen, M. L. Bajema and R. R. Jones, *Phys. Rev. Lett.* **82**, 2852 (1999).

22. M. A. Bouchene, V. Blanchet, C. Nicole, N. Melikechi, B. Girard, H. Ruppe, S. Rutz, E. Schreiber and L. Wöste, *Eur. Phys. J. D* **2**, 131 (1998).

23. M. A. Bouchene, C. Nicole and B. Girard, *Opt. Commun.* **181**, 327 (2000).

24. S. Cavalieri, R. Eramo, M. Materazzi, C. Corsi and M. Bellini, *Phys. Rev. Lett.* **89**, 133002 (2002).

25. S. Cavalieri and R. Eramo. *Phys. Rev. A* **58**, R4263 (1998),

26. J. Z. Wu, S. B. Whitfield, C. D. Denise Caldwell, M. O. Krause, P. Van Der Meulen and A. Fahlman, *Phys. Rev. A* **42**, 1350 (1990).

27. R. R. Alfano and S. L. Shapiro, *Phys. Rev. Lett.* **24**, 584 (1970).

28. R. L. Fork, C. V. Shank, C. Hirlimann and R. Yen, *Opt. Lett.* **8**, 1 (1983).

29. P. B. Corkum, C. Rolland and T. Srinivasan-Rao, *Phys. Rev. Lett.* **57**, 2268 (1986).

30. F. A. Ilkov, L. Sh. Ilkova and S. L. Chin, *Opt. Lett.* **18**, 681 (1993).

31. R. R. Alfano. *The Supercontinuum Laser Source,* Springer-Verlag, New York, 1989.

32. "Special Issue on Supercontinuum", *Appl. Phys. B* **77** (2003).

33. S. A. Kovalenko, A. L. Dobryakov, J. Ruthmann and N. P. Ernsting, *Phys. Rev. A* **59**, 2369 (1999).

34. R. L. Fork, C. H. Brito Cruz, P. C. Becker and C. V. Shank, *Opt. Lett.* **12,** 483 (1987).

35. E. T. J. Nibbering, O. Dühr and G. Korn, *Opt. Lett.* **22,** 1335 (1997).

36. V. V. Yakovlev, B. Kohler and K. R. Wilson, *Opt. Lett.* **19,** 2000 (1994).

37. M. K. Reed, M. K. Steiner-Shepard and D. K. Negus, *Opt. Lett.* **19,** 1885 (1994).

38. K. R. Wilson and V. V. Yakovlev, *J. Opt. Soc. Am B* **14,**444 (1997).

39. G. Y. Yang and Y. R. Shen, *Opt. Lett.* **9**, 510 (1984).

40. W. L. Smith, P. Liu and N. Bloembergen, *Phys. Rev. A* **15**, 2396 (1977).

41. J. Ranka, R. W. Schirmer and A. Gaeta, *Phys. Rev. Lett.* **77**, 3783 (1996).

42. A. Brodeur, F. A. Ilkov and S. L. Chin, *Opt. Commun.* **129,** 193 (1996).

43. A. Brodeur and S. L. Chin, *Phys. Rev. Lett.* **80**, 4406 (1998).

44. A. Brodeur and S. L. Chin, *J. Opt. Soc. Am. B* **16,** 637 (1999).

45. W. Liu, S. Petit, A. Becker, N. Aközbek, C. M. Bowden and S. L. Chin, *Opt. Commun.* **202**, 189 (2002).

46. M. Bellini and T. W. Hänsch, *Opt. Lett.* **25**, 1049 (2000).

47. W. Watanabe, Y. Masuda, H. Arimoto and K. Itoh, *Opt. Rev.* **6,** 167 (1999).

48. W. Watanabe and K. Itoh, *Jpn. J. Appl. Phys.* **40,** 592 (2001).

49. C. Corsi, A. Tortora and M. Bellini, *Appl. Phys. B* **77,** 285 (2003).

50. C. Corsi, A. Tortora and M. Bellini, *Appl. Phys. B* **78**, 299 (2004).

51. C. Corsi and M. Bellini, *Appl. Phys. B* **78**, 31 (2003).

52. J. K. Ranka, R. S. Windeler and A. J. Stentz, *Opt. Lett.* **25**, 25 (2000).

53. S. A. Diddams, D. J. Jones, J. Ye, S. T. Cundiff, J. L. Hall, J. K. Ranka, R. S. Windeler, R. Holzwarth, T. Udem and T. W. Hänsch, *Phys. Rev. Lett.* **84,** 5102 (2000).

54. J. Reichert, M. Niering, R. Holzwarth, M. Weitz, Th. Udem and T. W. Hänsch, *Phys. Rev. Lett.* **84**, 3232 (2000).

55. M. Niering, R. Holzwarth, J. Reichert, P. Pokasov, Th. Udem, M. Weitz, T. W. Hänsch, P. Lemonde, G. Santarelli, M. Abgrall, P. Laurent, C. Salomon and A. Clairon, *Phys. Rev. Lett.* **84**, 5496 (2000).

56. D. J. Jones, S. A. Diddams, J. K. Ranka, A. Stentz, R. S. Windeler, J. L. Hall and S. T. Cundiff, *Science* **288**, 635 (2000).

57. A. Baltuška, Th. Udem, M. Uiberacker, M. Hentschel, E. Goulielmakis, Ch. Gohle, R. Holzwarth, V. S. Yakovlev, A. Scrinzi, T. W. Hänsch and F. Krausz, *Nature* **421**, 611 (2003).

58. M. Hentschel, R. Kienberger, Ch. Spielmann, G. A. Reider, N. Milosevic, T. Brabec, P. Corkum, U. Heinzmann, M. Drescher and F. Krausz, *Nature* **414,** 509 (2001).

59. T. Brabec and F. Krausz, *Rev. Mod. Phys.* **72**, 545 (1999).

60. G. G. Paulus, F. Grasbon, H. Walther, P. Villoresi, M. Nisoli, S. Stragira, E. Priori and S. D. Silvestri, *Nature* **414,** 182 (2001).

61. D. B. Milosevic, G. G. Paulus and W. Becker, *Phys. Rev. Lett.* **89,** 153001 (2002).

Chapter 3

THE MEASUREMENT OF ULTRASHORT LIGHT – SIMPLE DEVICES, COMPLEX PULSES

Xun Gu, Selcuk Akturk, Aparna Shreenath, Qiang Cao, and Rick Trebino
School of Physics, Georgia Institute of Technology
Atlanta, Georgia 30332-0430, USA

Abstract: Recent developments have extended the state of the art of ultrashort-light-pulse measurement using Frequency-Resolved-Optical-Gating (FROG) considerably. FROG devices for measuring the intensity and phase of ultrashort laser pulses have become so simple that essentially no alignment is required. In addition, such devices not only operate single shot, but they also yield the two most important spatio-temporal distortions, spatial chirp and pulse-front tilt. With other FROG variations, it is now possible to measure more general ultrashort *light* pulses (i.e., pulses much more complex than common laser pulses), with time-bandwidth products as large as several thousand and as weak as a few hundred photons, and despite other difficulties such as random absolute phase and poor spatial coherence.

Key words: Ultrashort, ultrafast, and diagnostic.

1.   INTRODUCTION

Since its introduction a decade ago, Frequency-Resolved Optical Gating (FROG) has become an effective and versatile way to measure ultrashort laser pulses, whether a 20 fs UV pulse or an oddly shaped IR pulse from a free-electron laser [1]. Indeed, FROG has measured the intensity and phase of ~ 4 fs pulses [2] and variations on it are now measuring attosecond pulses.

But now that we have achieved the ability to measure such ephemeral events reliably it is important, especially for spectroscopic applications, to go beyond the measurement of mere ultrashort *laser* pulses whose intensity and phase are well-behaved in space, time, and frequency and which have

fairly high intensity. It is important to be able to measure ultrashort *light* pulses whose intensity and phase are *not* well-behaved in space, time, and frequency and which often are not very intense. It is important to be able to measure such pulses as ultrabroadband continuum light pulses emerging from micro-structure optical fiber and weak luminescence from molecules important in biology and human physiology – light pulses whose measurement will lead to new technologies or teach us important things about life, not just how well our laser is aligned. And it is important to do so with a simple device, not one so complex that it could easily introduce the same distortions it hopes to measure. In short, the goal is not a complex device that can only measure simple pulses but a simple device that can measure complex pulses.

We have recently made significant progress in all of these areas. It is now possible to measure ultrashort light pulses whose time-bandwidth product exceeds 1000 [3], pulses with as little as a few hundred photons (and simultaneously with poor spatial coherence and random absolute phase) [4], and pulses with spatio-temporal distortions like spatial chirp and pulse-front tilt [5, 6]. It is also possible to measure pulses in a train in which each is different [3]. And it is possible to do so quite easily.

Of course, measuring ultrashort *laser* pulses remains easier than measuring ultrashort *light* pulses, but, recently, measuring ultrashort laser pulses became *extremely* easy. The new variation on FROG, called GRENOUILLE [7], has no sensitive alignment knobs, only a few elements, and a cost, weight, and size considerably less than previously available devices (including now obsolete autocorrelators). GRENOUILLE yields traces identical to those in FROG, and hence yields the full pulse intensity and phase for arbitrary pulses using the same commercially available computer algorithm. It can do so for as little as a single laser pulse, and, because it uses a *thick* nonlinear crystal (unlike other pulse-measurement methods, which require extremely thin crystals, yielding very few signal photons), it is also very sensitive – more sensitive than autocorrelators. GRENOUILLE also measures the spatio-temporal distortions, spatial chirp and pulse-front tilt [5, 6], without the need for modifications in its apparatus. GRENOUILLE can also be arranged so that it measures the beam spatial profile, as well, so that it can accurately be said that GRENOUILLE measures essentially every quantity of interest about an ultrashort laser pulse. GRENOUILLE is already in use in over one hundred labs all over the world, and it is rapidly becoming the standard for ultrashort laser pulse measurement.

In this chapter, we review these developments, which are quite general and so should have many applications in a wide range of fields, especially ultrafast spectroscopy.

2.   FROG AND CROSS-CORRELATION FROG

FROG involves time-gating the pulse with itself and measuring the spectrum versus the delay between the two pulses [1]. When a well-characterized reference pulse is available, Cross-correlation FROG (XFROG) takes advantage of this and gates the unknown pulse with this reference pulse [8]. The general expression for both FROG and XFROG traces is

$$I_{XFROG}(\omega,\tau) = \left| \int_{-\infty}^{\infty} E_{sig}(t,\tau)\exp(-i\omega t)\,dt \right|^2 , \qquad (3.1)$$

where the signal field, $E_{sig}(t, \tau)$, is a combined function of time and delay, usually of the form $E_{sig}(t, \tau) = E(t)\,E_{gate}(t - \tau)$. In FROG, the gate function, $E_{gate}(t)$, is the unknown input pulse, $E(t)$, that we are trying to measure. In XFROG, $E_{gate}(t)$ can be any known function (i.e., pulse) acting as the reference pulse. In general, $E_{sig}(t, \tau)$ can be any function of time and delay that contains enough information to determine the pulse.
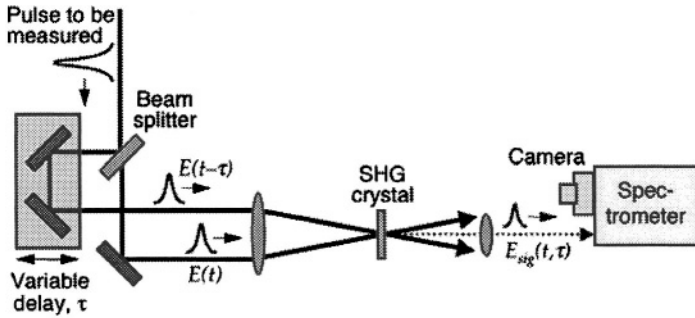
Figure 3-1. Schematic of a FROG (frequency-resolved autocorrelation) apparatus. A pulse is split into two, and one pulse gates the other in a nonlinear-optical medium (here a second-harmonic generation crystal). The second harmonic pulse spectrum is then measured vs. delay. XFROG involves an independent, previously measured gate pulse.

Like autocorrelation, which FROG replaces, these techniques use optical nonlinearities to perform the gating; e.g., second-harmonic generation (SHG) for FROG (Fig. 3-1) and the related process, sum-frequency generation (SFG), for XFROG. These processes allow the creation of a signal pulse whose field is proportional to the product of two input pulse fields.

The FROG and XFROG traces are spectrograms of the pulse (although the FROG trace might better be called the "auto-spectrogram" of the pulse)

and, as a result, are generally very intuitive displays of the pulse. It is easy to show that retrieving the intensity and phase from the FROG or XFROG trace is equivalent to a well-known solved problem, two-dimensional phase retrieval. We have thus used modified phase-retrieval routines, which have proved very robust and fast for retrieving pulses from traces. Indeed, FROG and XFROG yield the pulse intensity and phase vs. time or frequency, with only a few "trivial" ambiguities. This is a great improvement over autocorrelation, which yields at best a rough measure of the pulse length and little or no information about the actual pulse shape and phase.

3. DITHERED-CRYSTAL XFROG FOR MEASURING ULTRACOMPLEX SUPERCONTINUUM PULSES

Arguably, the most complex ultrashort pulse ever generated is ultrabroadband supercontinuum, which can now be generated easily in recently developed microstructure and tapered optical fiber, using only nJ input pulses from a Ti:Sapphire oscillator [9]. Many applications of the supercontinuum require good knowledge of the light, especially its phase. In an effort to characterize the intensity and phase of this extremely complicated pulse, FROG, particularly Cross-correlation FROG (XFROG), is so far the only technique that has been able to successfully measure this pulse [3, 10]. Not only does XFROG deliver an experimental trace that allows the retrieval of the intensity and phase of the pulse in both the time and frequency domains (and even more, as will be clear below), but the XFROG trace itself, which is a spectrogram of the pulse, also proves to be a very intuitive tool for the study of the generation and propagation of the supercontinuum. Many individual processes important in supercontinuum generation, such as soliton generation and fission, can be much more easily identified and studied by observing the XFROG trace than by considering the temporal or spectral intensity and phase.

Our XFROG apparatus is shown in Fig. 3-2. The main challenge in attempting to use XFROG (or any other potential method) to measure the supercontinuum is obtaining sufficient bandwidth in the SFG crystal. This typically requires using an extremely thin crystal, in this case a sub-five-micron crystal, which is not practical and which would generate so few SFG photons that the measurement would not be possible were it to be used. Instead we angle-dither a considerably thicker (1 mm) crystal [11] to solve this problem. Because the crystal angle determines the frequencies that are phase-matched in the SFG process, varying this angle in the course of the measurement allows us to obtain as broad a range of phase-matched frequencies as desired.
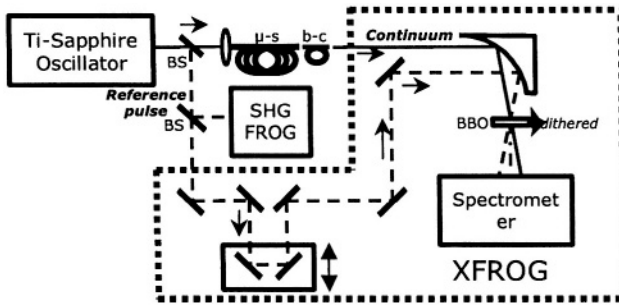
Figure 3-2. Schematic diagram of our multi-shot XFROG measurement apparatus. BS: beam-splitter; **μ-s:** microstructure fiber; b-c: butt-coupling fiber.

We performed the first XFROG measurement of the microstructure-fiber supercontinuum on supercontinuum pulses generated in a 16 cm long microstructure fiber with an effective core diameter of ~ 1.7 microns. In the measurement, we performed SFG between the supercontinuum and the 800 nm Ti:Sapphire pump pulse as the nonlinear gating process. In order to phase-match all the wavelengths in the supercontinuum, the nonlinear crystal (BBO) was rapidly dithered during the measurement with a range of angles corresponding to the entire supercontinuum bandwidth. We measured an experimental trace that was parabolic in shape, in agreement with the known group-velocity dispersion of the microstructure fiber (Fig. 3-3). We found that the supercontinuum pulses had a time-bandwidth product of ~ 4000, by far the most complicated pulses ever characterized. Despite the general agreement between the measured and retrieved traces, the results from the intensity and phase retrieval were somewhat unexpected: the retrieved trace contained an array of fine structure not present in the measured trace, and the retrieved spectrum also contained ~ 1 nm scale fine structure, contrary to the smooth spectrum previous experiments had shown. However, we then performed single-shot spectrum measurements (using a spectrometer), which confirmed our findings, that is, the ~ 1 nm scale fine features do exist in the supercontinuum spectrum, but only on a single-shot basis, as wild shot-to-shot fluctuations wash them out completely in multi-shot measurements in spectrometers. These fine spectral features agreed with theoretical calculations very well.

The reason the XFROG retrieval helped us recover the unstable fine spectral features lies in the intrinsic information redundancy of FROG traces. Indeed, any FROG trace is a two-dimensional temporal-spectral representation of a complex field, and the two axes are two sides of one coin. The same information is present in both axes. In our case, the unstable fine spectral features also correspond to slow temporal modulations, which are

detectable in a multi-shot measurement. Although the experimental XFROG trace that we measured lacked the fine spectral features because our measurement was made on a multi-shot basis, the long temporal features in the traces, however, were sufficient to assist the retrieval algorithm to find a result with fine spectral features. Such a trace is closest to the measured trace, among all possible solutions. This is a big advantage of FROG: lost frequency resolution is recoverable from the FROG measurement via redundant temporal information.
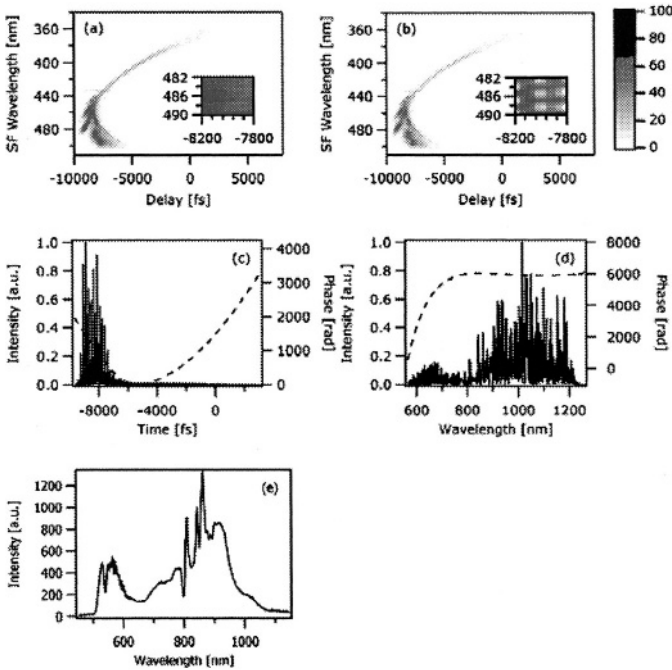
Figure 3.3. XFROG measurement of the 16 cm long microstructure-fiber continuum with an 800 nm, 30 fs pre-characterized reference pulse: (a) measured trace, (b) retrieved trace, (c) retrieved temporal intensity (solid) and phase (dash), (d) retrieved spectral intensity (solid) and phase (dash), and (e) independently measured spectrum. The XFROG error was 0.012. The insets in plots (a) and (b) are higher-resolution sections in the traces. Traces are 8096 × 8096 in size. SF: sum frequency.

The newly revealed fine spectral structure and shot-to-shot instability of the supercontinuum pulses will inevitably present profound and often undesirable implications to the application of this light. For the many researchers who use this continuum, a very important question to ask is how we can create a cleaner supercontinuum that is free of or less plagued with these problems.

These results have been instrumental in helping us understand the underlying spectral broadening mechanisms and in confirming recent advances in numerical simulations of supercontinuum generation in the microstructure fiber. Simulations using the extended nonlinear Schrödinger equation (NLSE) model have matched experiments amazingly well [12, 13]. Although most microstructure-fiber supercontinuum experiments use 10 – 100 cm of fiber, simulations have revealed that most of the spectral broadening occurs in the first few mm of fiber. Further propagation, which still slowly broadens the spectrum through less significant nonlinear processes, such as Raman self-frequency shift, yields only increasingly unstable and fine spectral structure due to the interference of multiple solitons in the continuum spectrum.
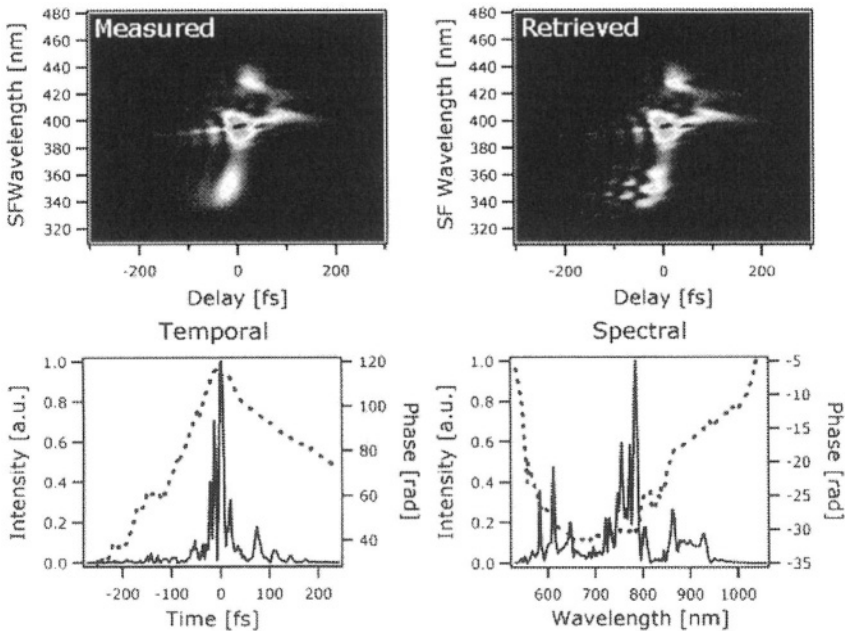
Figure 3-3. XFROG measurement and retrieved pulse for the 8 mm long microstructure-fiber continuum with an 800 nm 40 fs pre-characterized reference pulse: (a) measured trace, (b) retrieved trace, (c) retrieved temporal intensity (solid) and phase (dashed), (d) retrieved spectral intensity (solid) and phase (dashed).

This observation suggests that use of a short (< 1 cm) length of microstructure fiber would still yield supercontinuum generation, and the resulting continuum will still be broad, but short, more stable, and with less fine spectral structure. To test this hypothesis, we generated a supercontinuum in an 8 mm long microstructure fiber with 40 fs Ti:Sapphire oscillator pulses and performed similar XFROG measurements of it [10].

We see from Fig. 3-4 that the retrieved trace is in good agreement with the measured one, reproducing all the major features. The additional structure that appears in the retrieved trace can be attributed to shot-to-shot instability of spectral fine structure in the continuum spectrum as discussed in detail above. The retrieved continuum intensity and phase vs. time and frequency are shown in the bottom panels of Fig. 3-4. The most obvious feature in this figure is that the continuum from the 8 mm long fiber is significantly shorter than the picosecond continuum generated in the 16 cm long fiber and, indeed, consists of series of sub-pulses that are shorter than the input 40 fs pulse. At the same time, the short-fiber continuum has less complex temporal and spectral features than the continuum pulses measured from longer fibers previously. The spectral phase of the short fiber continuum varies only in the range of 25 rad, which is relatively flat compared with the spectral phase of the long-fiber continuum, which is dominated by cubic phase spanning over 1000π rad.

In view of the complexity of the continuum, we made an independent measurement of the continuum spectrum using a spectrometer and averaged over $\sim 10^7$ pulses. We found excellent agreement between the retrieved spectrum and that independently measured using the spectrometer (not shown). Slight discrepancies were also due to fluctuations in the spectrum from shot to shot in the continuum, which smear out the spectrometer-measured, but not the FROG-measured, spectrum.

In conclusion, XFROG has been the only method to successfully measure the intensity and phase of the microstructure-fiber continuum, arguably the world's most complicated pulse (time bandwidth product ~ 4000 from a 16 cm fiber). These measurements have revealed unstable nm-scale features in the continuum spectrum. Measurements performed on the continuum generated from an 8 mm fiber show that a short fiber generates more stable and less complicated pulses.

4. OPA XFROG FOR MEASURING ULTRAWEAK FLUORESCENCE

Whereas measuring continuum is challenging due to its extreme complexity and instability, continuum is nonetheless a relatively intense (nJ), spatially coherent beam. Unfortunately, this cannot be said of ultrashort fluorescence from scientifically interesting "non-fluorescent" bio-luminescent molecules. Most biologically important excitations decay rapidly and yield extremely weak luminescence, since the biological use must compete with fluorescence. Such pulses are also spatially incoherent, and they have random absolute phase. While their measurement would yield

important insight into the dynamics of many biological processes [14-17], their measurement proves even more challenging.

Indeed, interferometric methods, such as spectral interferometry, which are well-known for their high sensitivity, prove inadequate for such measurements due to both the light's spatial incoherence and random absolute phase.

In this section we present a non-interferometric technique capable of measuring trains of few-photon spatially incoherent light pulses with random absolute phase [18]. This technique is a variation on the XFROG method and hence involves spectrally resolving a time-gated pulse and measuring its spectrum as a function of delay to yield an XFROG trace or a spectrogram of the pulse. The nonlinear process used in this technique, however, is optical parametric amplification (OPA) or difference frequency generation (DFG), which involves not only time-gating the pulse to be measured, but also *amplifying* it in the process. The weak pulses are amplified by up to ~ 10^5 by an intense, bluer, shorter, synchronized gate pulse and then spectrally resolved to generate an OPA XFROG trace. We then use a modified FROG retrieval algorithm to retrieve the intensity and phase of the ultraweak pulse measured from the OPA XFROG trace.

In addition to the above complexities, ultrafast fluorescence is also broadband. We use a noncollinear OPA (NOPA) geometry in order to phase-match the broad bandwidth while scanning the delay and generating the OPA XFROG trace. Group velocity mismatch (GVM) becomes an important issue in time-gating such broadband pulses with the much shorter gate pulse [19-24]. But GVM can be minimized in the OPA XFROG measurement by using the NOPA geometry as well. A suitable crossing angle can be chosen so that the GVM is minimized while simultaneously maximizing the phase-matched bandwidth. This allows the use of thicker OPA crystals to improve the gain.

We first discuss the basic theory behind OPA XFROG. We then demonstrate OPA XFROG measurements of trains of pulses as weak as 50 aJ, that is, having ~ 150 photons per pulse. These pulses have average powers of 50 fW. Finally, we also demonstrate NOPA XFROG for pulses having large bandwidths of ~ 100 nm.

In both OPA and DFG, a strong bluer "pump" pulse is coincident in time in a nonlinear optical crystal with another pulse (which, in the OPA literature, is usually called the "signal" pulse, but we will avoid this terminology as it conflicts with our use of the term "signal," and call it "unknown pulse" instead). If the pump pulse is strong, it exponentially amplifies both the unknown pulse (OPA) and also noise photons at the same frequency (usually referred to as the optical parametric generation, or OPG, process), and simultaneously generating difference-frequency (often called

the "idler") photons [25, 26]. Either the OPA or the DFG pulse can be spectrally resolved to generate an XFROG trace.

From the coupled-wave OPA equations, the electric field of the OPA XFROG signal from the crystal has the form

$$E_{sig}^{OPA}(t,\tau) = E(t) f_{gate}^{OPA}(t-\tau), \qquad (3.2)$$

where, as before, $E(t)$ is the unknown input pulse and we have assumed that the pump pulse intensity remains unaffected by the process, which should be valid when the pulse to be measured is weak and we only need to amplify it enough to measure it. The OPA gate function is given by

$$f_{gate}^{OPA}(t-\tau) = \cosh\left(g\left|E_{ref}(t-\tau)\right|z\right). \qquad (3.3)$$

where the gain parameter, g, is given by the expression

$$g = \frac{4\pi d_{eff}}{\sqrt{n_{OPA}\lambda_{OPA}}\sqrt{n_{DFG}\lambda_{DFG}}} \qquad (3.4)$$

Thus, the unknown pulse undergoes exponential gain during OPA. And very importantly, *the gating and gain processes do not alter the pulse phase.*

It must be pointed out that in OPA XFROG, unlike other FROG methods, the input pulse is present as a background, even at large delays in the OPA XFROG trace. The equation and the corresponding XFROG algorithm take this into account while retrieving the intensity and phase of the pulse. For high gain, this background becomes negligible.

In the case of DFG XFROG, the idler is spectrally resolved to yield the DFG XFROG trace. Although it has been known that DFG can be used to measure fairly weak pulses [27], the method has never been demonstrated for cases with gain. Including the effect of gain the DFG electric field is given by

$$E_{sig}^{DFG}(t,\tau) = E(t) f_{gate}^{DFG}(t-\tau)^{*}. \qquad (3.5)$$

The unknown input pulse here is the same as in the case of OPA. The gate function now has the form

$$f_{gate}^{DFG}(t-\tau) = \exp\left(i\phi_{ref}(t-\tau)\right)\sinh\left(g\left|E_{ref}(t-\tau)\right|z\right), \quad (3.6)$$

where $\phi_{ref}(t - \tau)$ is the phase of the reference pulse. If the reference pulse is weak, the net gain is small and the above expression reduces to the form $f_{gate}^{DFG}(t-\tau) = E_{ref}(t-\tau)$.

The unknown pulse can thus be easily retrieved from the measured trace using the iterative XFROG algorithm, modified for the appropriate gate pulse. For high gains, the reference-gate pulse experiences gain-shortening in time, a desirable effect. GVM between the gate pulse (commonly referred to as the pump pulse for the OPA process) and the unknown pulse can distort measurement of phase by affecting the gain experienced by the unknown pulse. Thus the interaction length between the pump and unknown pulse during parametric amplification is limited by GVM. The larger the GVM, the shorter the interaction length will be. Therefore, in order to obtain gain over the entire bandwidth, it is necessary to choose a crystal whose length is of the order of, but less than, the interaction length.
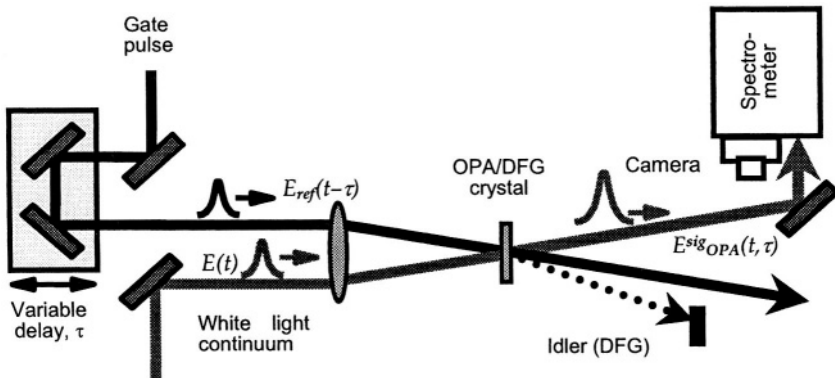
Figure 3.5. Schematic of experimental apparatus for OPA XFROG.

It is also possible to eliminate GVM in OPA XFROG by crossing the pump and unknown pulse at a crossing angle, which can be calculated for specific wavelengths using a public domain computer program "GVM" within nonlinear optics software SNLO [28]. The non-collinear geometry is particularly useful in working with broadband pulses, since it is possible to choose an optimal crossing angle that will minimize the GVM over the entire bandwidth range, while simultaneously allowing the entire bandwidth to be phase-matched.

Our experimental set-up for OPA/DFG XFROG is shown in Fig. 3-5. In our experiments, the output from a femtosecond KM Labs Ti:Sapphire (Ti:S) oscillator was amplified by a kilohertz repetition rate Quantronix 4800 series

Ti:Sapphire regenerative amplifier (RGA). The amplified 800 nm pulse was first characterized using a commercially available Swamp Optics GRENOUILLE. The pulse was then split into two. One pulse generated a white-light continuum (with poor spatial coherence) in a 2 mm thick sapphire plate, which was then spectrally filtered using a band-pass filter to yield a narrow spectrum. This pulse was attenuated using neutral density filters to act as the weak unknown pulse.
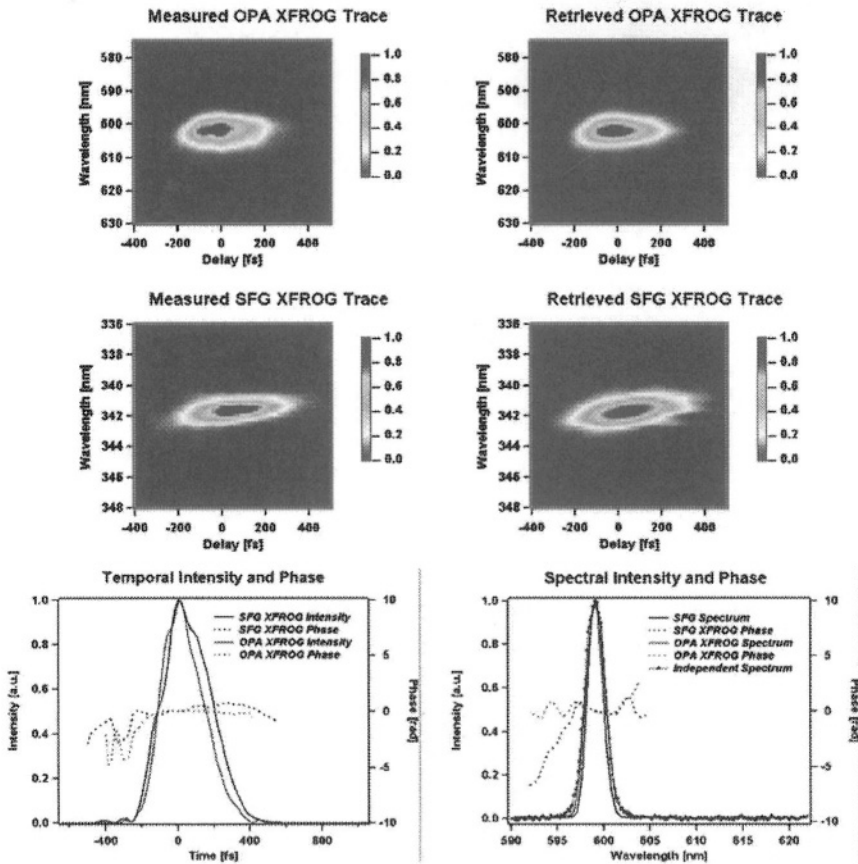
Fig. 3-6. The measured and retrieved traces and retrieved intensity and phase vs. time and the spectrum and spectral phase vs. wavelength of a spectrally filtered continuum from a sapphire plate. The retrieved intensity and phase from the OPA XFROG measurement of 80 fJ pulses agrees well with the retrieved intensity and phase of unattenuated continuum of 80 pJ using the established technique, SFG XFROG.

The other pulse was frequency-doubled using a 1 mm thick Type I BBO crystal and passed through a variable delay line to act as the gate (pump)

pulse for the OPA process. The two pulses were focused at a ~ 3° crossing angle using a 75 mm spherical mirror into a 1 mm BBO Type I crystal. The resulting OPA signal was spectrally resolved and imaged onto a CCD camera integrated over a few seconds.
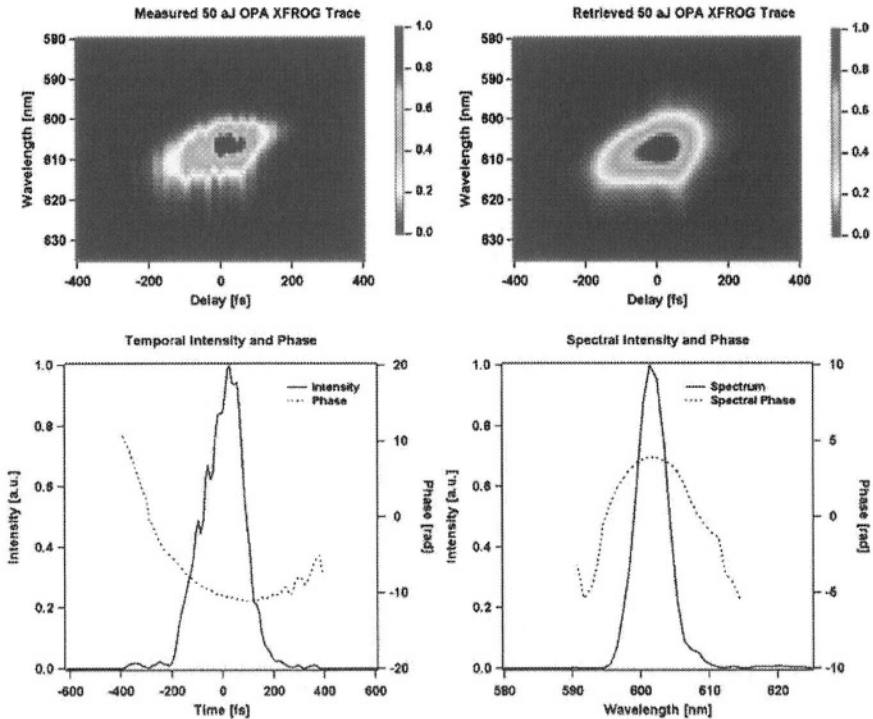
Fig. 3-7. OPA XFROG measurement of a 50 aJ attenuated and filtered continuum generated using a sapphire plate.

In the first case, we attenuated the filtered white light continuum to 80 fJ and measured its OPA XFROG trace. The pulse in this case experienced an average gain of about cosh(5.75) ~ 150. Its intensity and phase retrieved using the OPA XFROG algorithm are shown in Fig. 3-6. A comparison of the intensity and phase of the same pulse, unattenuated at 80 pJ, is also shown. This was made using the less sensitive, but well established, technique of SFG XFROG. Both techniques yielded identical pulses and the independently measured spectrum of the filtered white light matched well with the OPA XFROG retrieved spectrum. This established OPA XFROG as a legitimate pulse measurement technique which could measure pulses ~ 10^3 weaker than those measured by SFG XFROG.

Next, we pushed the technique much harder by attenuating the filtered white light continuum down to 50 aJ and retrieved its intensity and phase using the OPA XFROG technique. Figure 3-7 shows the measured traces

with their intensity and phase retrieved for an average gain of $G \sim 10^5$. The OPA signal was only about 5 times more intense than the background caused by OPG in the nonlinear crystal. This background is likely to be the lower limit on how weak the unknown pulse can be and still be measured accurately using the OPA XFROG technique. Despite this, OPA XFROG is the most sensitive ultrashort-pulse measurement technique, capable of measuring pulse trains with an average power of tens of fW, considerably better that interferometric techniques such as spectral interferometry, which have been demonstrated in measuring high-repetition-rate trains of pulses with zJ $(10^{-21}$ J) of energy, but with average powers of hundreds of fW.
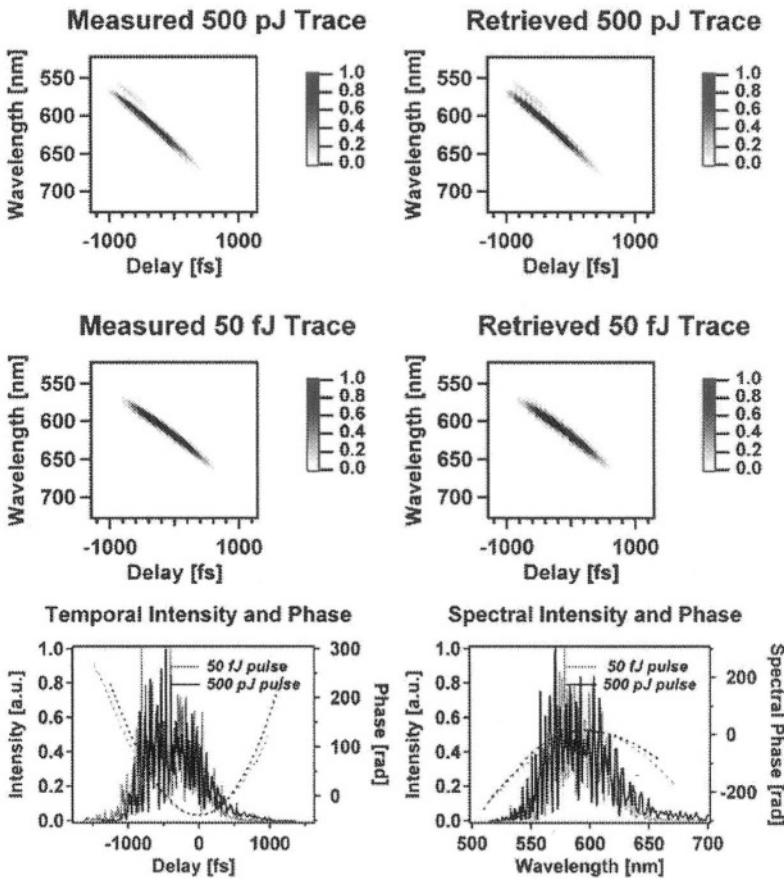
Figure 3-8. OPA XFROG measurements of broadband white light continuum for cases of low gain in a 500 pJ strong pulse and high gain in a 50 fJ weak pulse.

Finally, using a NOPA geometry, we crossed the pump pulse and white light continuum at an angle of ~ 6.5° (internal in the crystal), chosen in order to minimize GVM. Using band-pass filters again we spectrally filtered the white light continuum, this time to a bandwidth of ~ 100 nm. We performed OPA XFROG measurements for two cases, as shown in Fig. 3-8. For the first OPA XFROG trace, the energy of the pulse was measured to be 500 pJ. The gain experienced in this instance was ~ 50, which we considered the low gain condition. This pulse was then attenuated by four orders of magnitude to 50 fJ and its OPA XFROG trace measured again. This condition had a higher gain of ~1000. The intensity and phase from the two cases compared well, showing that higher gain did not distort the spectral phase during the OPA XFROG measurement process.

The Group Delay Mismatch (GDM) between the various frequencies of the unknown pulse and the pump pulse was calculated to be ~ 100 fs over the nearly 60 nm spectral envelope FWHM of a 860 fs long pulse. A thinner crystal would further reduce the GDM, but requiring a compromise on the gain that can be achieved. This sets a limitation on how weak a pulse can be measured. In this demonstration, we used a 2 mm thick Type I OPA crystal which was able to measure 50 fJ weak broadband pulses. Geometrical smearing effects in both the longitudinal and transverse directions were calculated to be 56 fs and 34 fs, respectively, for the non-collinear geometry.

As an aside, it must be pointed out that the structure in the white light continuum is real and is the nature of white light continuum generated by nonlinear optical processes. This structure would not be observed in spectral measurements using spectrometers for reasons we discussed earlier. Another reason is that the white light continuum from the sapphire plate in these experiments was collected from multiple filaments in the spatially incoherent bulk-generated continuum, in order to duplicate the poor spatial behavior of broadband fluorescence. So the spatial incoherence would also wash out the structure. Our OPA XFROG measurements retrieved a typical spectrum of the broadband continuum structure. The observed robust behavior of the XFROG algorithm that we see here has also been demonstrated in other broadband continuum measurements [3].

The experiments discussed above have all been performed using the OPA XFROG geometry. DFG XFROG should yield similar results with the same gain. Thus OPA/DFG XFROG promises to be a powerful new technique which opens up the field of pulse measurement to ultrafast and ultraweak, complex and broadband, arbitrary light pulses.

5.   EXTREMELY SIMPLE FROG DEVICE

While the above methods can measure very complex light pulses, they do not involve complex devices. However, if the pulse to be measured is a fairly simple laser pulse, then we might expect the device to be very simple. In

fact, we recently showed that it is possible to create a SHG FROG device for measuring ultrashort laser pulses that consists entirely of only four or five optical elements, and it is so simple that, once set up, it never requires realignment.
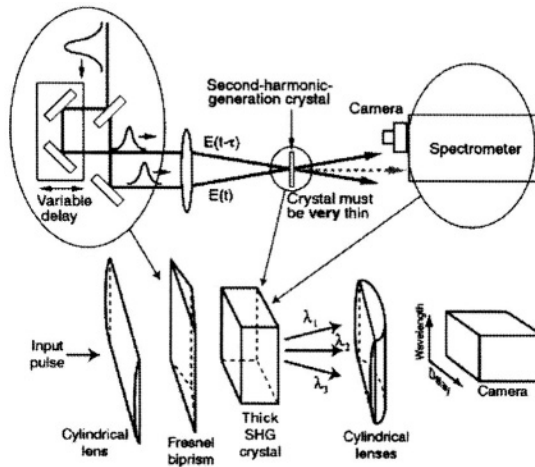
Figure 3-9. FROG device (top) and the much simpler GRENOUILLE (bottom), which involves replacing the more complex components with simpler ones.

We call this simple variation GRENOUILLE (GRating-Eliminated No-nonsense Observation of Ultrafast Laser-Light E-fields) [7]. GRENOUILLE involves two innovations (see Fig. 3-9). First, a Fresnel biprism replaces the beam splitter and delay line in a FROG, and, second, a thick crystal replaces the thin crystal and spectrometer in a FROG, yielding a very simple device.
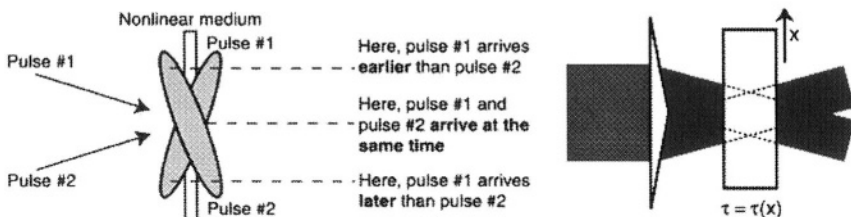
Figure 3-10. Single-shot FROG measurements involve crossing large beams at a large angle, so that the relative delay between the two beams varies transversely across the crystal (left). This can be accomplished more easily and without the need for alignment using a prism with a large apex angle (right).

   Specifically, when a Fresnel biprism (a prism with an apex angle close to 180°) is illuminated with a wide beam, it splits the beam into two and crosses these beamlets at an angle as in conventional single-shot autocorrelator and FROG beam geometries, in which the relative beam delay is mapped onto the horizontal position at the crystal (see Fig. 3-10). But, better than conventional single-shot geometries, the beams here are *automatically aligned* in space and in time, a significant simplification. Then, as in standard single-shot geometries, the crystal is imaged onto a CCD camera, where the signal is detected vs. position (i.e., delay) in the horizontal direction.
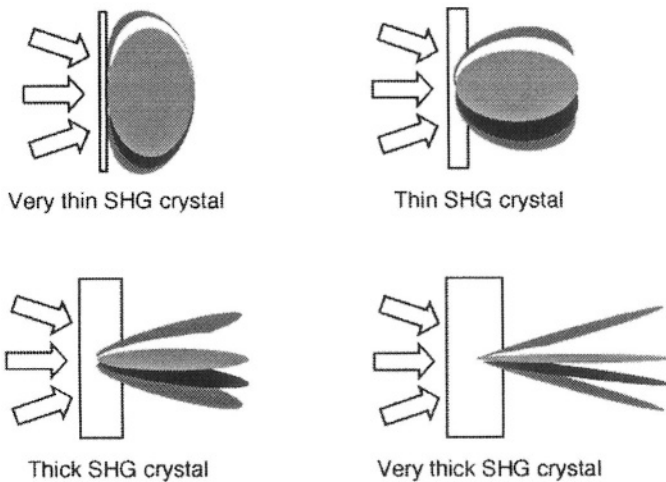
Figure 3-11. Polar plots of SHG efficiency vs. output angle for various colors of a broadband beam impinging on a SHG crystal. Different shades of grey indicate different colors. Note that, for a thin crystal (upper left), the SHG efficiency varies slowly with angle for all colors, leading to a large phase-matching bandwidth for a given angle. As the crystal thickness increases, the polar plots become narrower, leading to very small phase-matching bandwidths. The thinnest crystal shown here would be required for all pulse-measurement techniques. GRENOUILLE, however, uses a thick crystal (lower right) to spectrally resolve the autocorrelation signal, yielding a FROG trace – without the need for a spectrometer.

   FROG also involves spectrally resolving the pulse after it has been time-gated by itself. GRENOUILLE (see Fig. 3-11) combines both of these operations in a single *thick* SHG crystal. As usual, the SHG crystal performs the self-gating process: the two pulses cross in the crystal with variable delay. But, in addition, the thick crystal has a very small phase-matching bandwidth, so the phase-matched wavelength produced by it varies with angle. Thus, the thick crystal also acts as a *spectrometer*. The first

cylindrical lens must focus the beam into the thick crystal tightly enough to yield a range of crystal incidence (and hence exit) angles large enough to include the entire spectrum of the pulse. After the crystal, a cylindrical lens then maps the crystal exit angle on to position at the camera, with wavelength a near-linear function of (vertical) position.

The resulting signal at the camera will be an SHG FROG trace with delay running horizontally and wavelength running vertically (see Fig. 3-12).
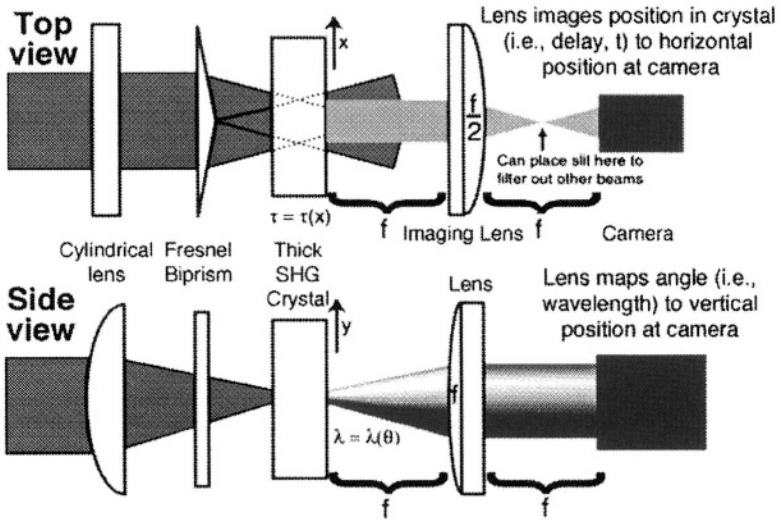
Figure 3-12. Top and side views of GRENOUILLE.

The key issue in GRENOUILLE is the crystal thickness. Ordinarily, achieving sufficient phase-matching bandwidth requires *minimizing* the group-velocity mismatch, GVM: the fundamental and the second harmonic must overlap for the entire SHG crystal length, L. This condition is: $GVM \cdot L \ll \tau_p$, where τ_p is the pulse length, $GVM \equiv 1/v_g(\lambda_0/2) - 1/v_g(\lambda_0)$, $v_g(\lambda)$ is the group velocity at wavelength λ, and λ_0 is the fundamental wavelength. For GRENOUILLE, however, the opposite is true; the phase-matching bandwidth must be *much less than* that of the pulse:

$$GVM \cdot L \gg \tau_p, \tag{3.7}$$

which ensures that the fundamental and the second harmonic *cease* to overlap well before exiting the crystal, which then acts as a frequency filter.

On the other hand, the crystal must not be too thick, or group-velocity *dispersion* (GVD) will cause the pulse to spread in time, distorting it:

$$GVD \cdot L \ << \ \tau_c, \tag{3.8}$$

where $GVD \equiv 1/v_g(\lambda_0 - \delta\lambda/2) - 1/v_g(\lambda_0 + \delta\lambda/2)$, $\delta\lambda$ is the pulse bandwidth, and τ_c is the pulse coherence time ($\sim$ the reciprocal bandwidth, $1/\Delta\nu$), a measure of the smallest temporal feature of the pulse. Since GVD < GVM, this condition is ordinarily already satisfied by the usual GVM condition. But here it will not necessarily be satisfied, so it must be considered.

Combining these two constraints, we have

$$GVD \ (\tau_p / \tau_c) \ << \ \tau_p / L \ << \ GVM. \tag{3.9}$$

There exists a crystal length L that satisfies these conditions simultaneously if

$$GVM / GVD \ >> \ TBP, \tag{3.10}$$

where we have taken advantage of the fact that τ_p/τ_c is the time-bandwidth product (TBP) of the pulse. Equation 3.10 is the fundamental equation of GRENOUILLE.

For a near-transform-limited pulse (TBP $\sim$ 1), this condition is easily met because GVM >> GVD for all but near-single-cycle pulses. Consider typical near-transform-limited (i.e., $\tau_p \sim \tau_c$) Ti:Sapphire oscillator pulses of $\sim$ 100 fs duration, where $\lambda_0 \sim 800$ nm and $\delta\lambda \sim 10$ nm. Also, consider a 5 mm BBO crystal – about 30 times thicker than is ordinarily appropriate. In this case, Eq. 3.9 is satisfied: 20 fs/cm << 100 fs/0.5 cm = 200 fs/cm << 2000 fs/cm. Note that, for GVD considerations, shorter pulses require a thinner, less dispersive crystal, but shorter pulses also generally have broader spectra, so the same crystal will provide sufficient spectral resolution. For a given crystal, simply focusing near its front face yields an effectively shorter crystal, allowing a change of lens or a more expanded beam to "tune" the device for shorter, broader-band pulses. Less dispersive crystals, such as KDP, minimize GVD, providing enough temporal resolution to accurately measure pulses as short as 50 fs. Measurements of somewhat complex $\sim$ 100 fs pulses are shown in Fig. 3-13. Conversely, more dispersive crystals, such as $LiIO_3$, maximize GVM, allowing for sufficient spectral resolution to measure pulses as narrowband as 4.5 nm ($\sim$ 200 fs transform-limited pulse length at 800 nm). Still longer or shorter pulses are also measurable, but with less accuracy (although the FROG algorithm can incorporate these effects and extend GRENOUILLE's range). Also, note that the temporal-blurring effect found in thick nonlinear media [5] is not found in the SHG geometry.
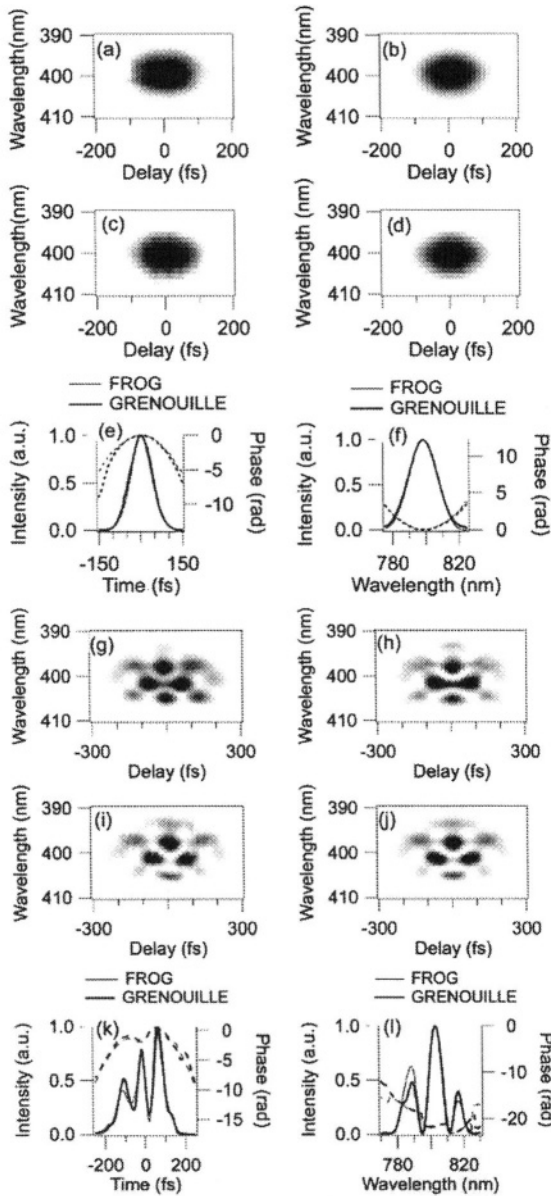
Figure 3-13. GRENOUILLE (and, for comparison, FROG) measurements of a pulse. (a) Measured GRENOUILLE trace. (b) Measured FROG trace. (c) Retrieved GRENOUILLE trace. (d) Retrieved FROG trace. (e), (f) Measured intensity and phase vs. time and frequency for the above traces. (g)-(l) Analogous traces and retrieved intensities and phases for a more complex pulse. Note the good agreement among the measured and retrieved spectrograms.

The main factor limiting GRENOUILLE's accurate measurement of shorter pulses is material-induced dispersion in the transmissive optics, including the necessarily thick crystal. Since shorter pulses have broader spectra, material dispersion is more significant and problematic. Another factor is that, for GRENOUILLE to work properly, the entire pulse spectrum must be phase-matched for some beam angle, requiring a large range of angles in the nonlinear crystal. This can be accomplished using a tighter focus, but then the resulting shorter confocal parameter of the beam reduces the effective crystal length that can be used, reducing spectral resolution.

Fortunately, these problems can be solved by designing a tighter focused, nearly-all-reflective GRENOUILLE, which can measure 800 nm laser pulses as short as 20 fs [29]. We convert almost all the transmissive components to reflective ones, except the Fresnel biprism (~1.3 mm of fused silica). This eliminates most of the material dispersion that would be introduced by the device. Moreover, the "thick" crystal required to spectrally resolve (using phase-matching) a 20 fs pulse is also thinner: only 1.5 mm. This not only allows us to eliminate dispersion induced by the crystal, but also allows us to focus tighter (this yields a shorter beam confocal parameter, decreasing the effective nonlinear interaction length), covering the spectra of short pulses. This is important because the device must be able to measure pulses with bandwidths of ~ 50 nm, that is, the device should have ~ 100 nm of bandwidth itself. The short interaction length in the crystal reduces the device spectral resolution, but fortunately, due to their broadband nature, shorter pulses require less spectral resolution. With these improvements, a GRENOUILLE can be made that is as simple and as elegant as the previously reported device (Fig. 3-14), but which is capable of accurately measuring much shorter pulses: 20 fs or shorter.

To test the reliability of our short-pulse GRENOUILLE, we used a KM Labs Ti: Sapphire oscillator operating with ~ 60 nm (FWHM) of bandwidth, and we used an external prism pulse compressor to compress the pulse as much as possible. We measured the output pulse with conventional multi-shot FROG and with our GRENOUILLE. We then used the Femtosoft FROG code to retrieve the intensity and phase for both measurements. Figure 3-15 shows measured and retrieved traces as well as the retrieved intensity and phase for multi-shot FROG and GRENOUILLE measurements, all in excellent agreement with each other. The pulse that GRENOUILLE retrieved in these measurements is 19.7 fs FWHM. This is the shortest pulse ever measured with GRENOUILLE to the best of our knowledge.

This device can also measure longer pulses as well without modification. Its spectral resolution of a few nm (the precise values depend on the pulse wavelength) makes it capable of measuring pulses as long as ~ 200 fs.
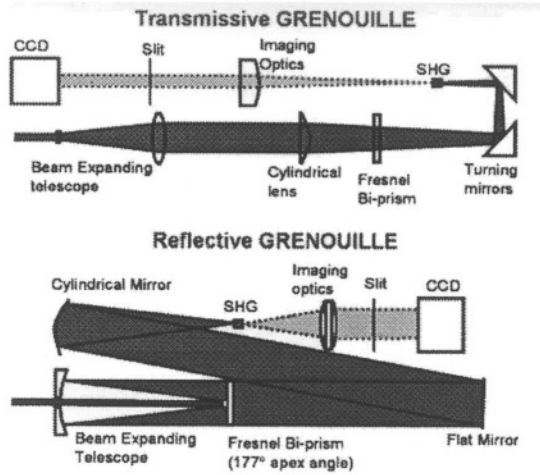
Figure 3-14. Compact GRENOUILLE geometries. Transmissive design for measuring pulses as short as 50 fs (top) and reflective GRENOUILLE design for measuring ~ 20 fs pulses. In the reflective design, the primary mirror of the Cassegrain telescope is conveniently cemented to the back of the Fresnel biprism (the only transmissive optic).
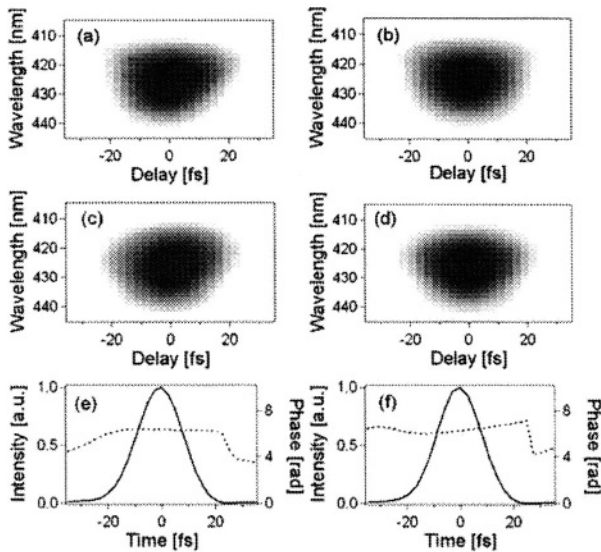
Figure 3-15. Comparisons of short-pulse GRENOUILLE and multi-shot FROG measurements. (a) Measured GRENOUILLE trace. (b) Measured multi-shot FROG trace. (c) Retrieved GRENOUILLE trace. (d) Retrieved multi-shot FROG trace. (e) Retrieved intensity and phase vs. time for GRENOUILLE measurements (temporal pulse width 19.73 fs FWHM). (f) Retrieved intensity and phase vs. time for multi-shot FROG measurements (temporal pulse width 19.41 fs FWHM).

   Because ultrashort laser pulses are routinely dispersed, stretched, and (hopefully) compressed, it is common for them to contain spatio-temporal distortions, especially spatial chirp (in which the average wavelength of the pulse varies spatially across the beam) and pulse-front tilt (in which the pulse intensity fronts are not perpendicular to the propagation vector). Unfortunately, convenient measures of these distortions have not been available. Fortunately, we have recently shown that GRENOUILLE and some other single-shot SHG FROG devices automatically measure both of these spatio-temporal distortions [5, 6]. And they do so without requiring a single alteration in the set-up.
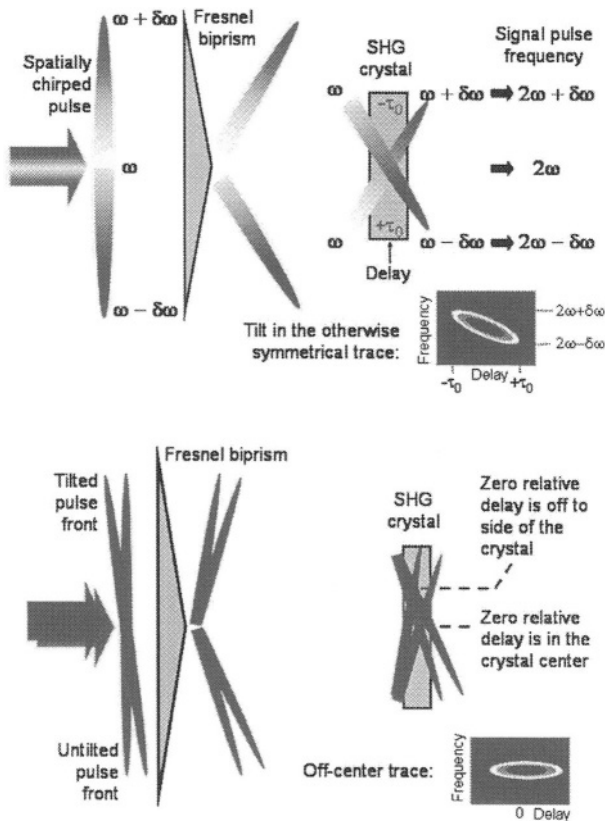
Figure 3-16. Spatial chirp tilts (shears) the trace (above), and pulse-front tilt translates the trace (below) in GRENOUILLE measurements. This allows GRENOUILLE to measure these distortions easily and without modification to the apparatus.

    Specifically, spatial chirp introduces a shear in the SHG FROG trace, and
pulse-front tilt displaces the trace along the delay axis. Indeed, the single-
shot FROG or GRENOUILLE trace shear is approximately *twice* the spatial
chirp when plotted vs. frequency and *one half* when plotted versus
wavelength (Fig. 3-17). Pulse-front tilt measurement involves simply
measuring the GRENOUILLE trace displacement (Fig. 3-16). These trace
distortions can then be removed and the pulse retrieved using the usual
algorithm, and the spatio-temporal distortions can be included in the
resulting pulse intensity and phase.
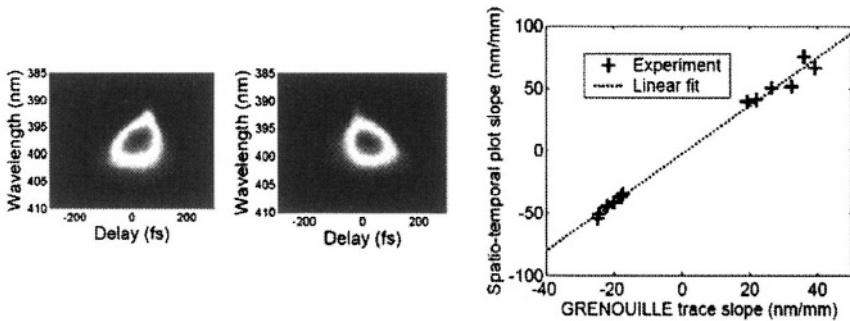
Figure 3-17. Experimental GRENOUILLE traces (left) for pulses with positive and negative
spatial chirp. The tilt in GRENOUILLE traces reveals the magnitude and sign of spatial chirp.
Right: Slopes of GRENOUILLE traces and corresponding spectrum vs. position slopes for
various amounts of spatial chirp.

    We have also made independent measurements of spatial chirp by
measuring spatio-spectral plots (i.e., spatially resolved spectra), obtained by
sending the beam through a carefully aligned imaging spectrometer
(ordinary spectrometers are not usually good diagnostics for spatial chirp
due to aberrations in them that mimic the effect) and spatially resolving the
output on a 2D camera, which yields a tilted image (spectrum versus
position) in the presence of spatial-chirp. We find very good agreement
between this measurement of spatial chirp and that from GRENOUILLE
measurements (Fig. 3-17).

    To vary the pulse-front tilt of a pulse, we placed the last prism of a pulse
compressor on a rotary stage. By rotating the stage we were able to align and
misalign the compressor, obtaining positive, zero, or negative pulse-front tilt.
Figure 3-18 shows theoretical and experimental values of pulse-front tilt in
our experiments (right) and some experimental GRENOUILLE traces for
different amounts of pulse-front tilt (left). We find very good agreement
between theoretical values of pulse-front tilt and that from GRENOUILLE
measurements.
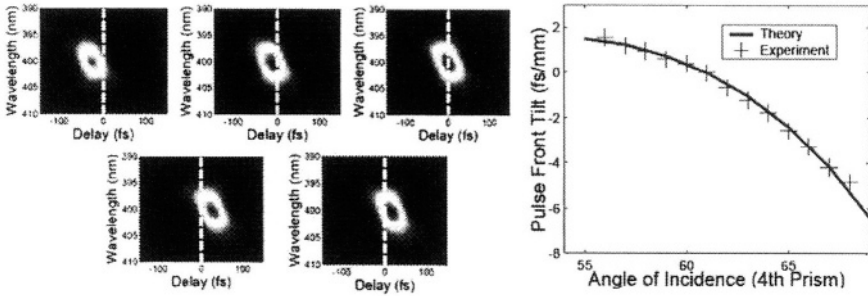
Figure 3-18. Measured GRENOUILLE traces for pulses with very negative, slightly negative, zero, slightly positive, and very positive pulse-front tilt (note that spatial chirp is also present in all these traces). The horizontal trace displacement is proportional to the pulse-front tilt (left). Theoretically predicted pulse-front tilt and the experimentally measured pulse-front tilt using GRENOUILLE (right).

It is important to note that GRENOUILLE not only measures the magnitudes of these two spatio-temporal distortions, but it also measures their sign. GRENOUILLE can also measure all odd orders of the spatial chirp, although this additional power is not yet of great interest.

The ability to measure spatio-temporal distortions easily is already proving useful: we have found that most commercial ultrafast amplifiers emit beams with both spatial chirp and pulse-front tilt. And we have found that pulse-front tilt is present, not only in beams with angular dispersion (as is commonly believed), but also in beams with both spatial and temporal chirp.

6. CONCLUSIONS

In short, GRENOUILLE provides not only the pulse intensity and phase vs. time and frequency, but also the otherwise difficult-to-measure spatio-temporal distortions, spatial chirp and pulse-front tilt. Indeed, we have found that GRENOUILLE is the most sensitive measure of pulse-front tilt available. It can also be set up to yield the pulse spatial profile, providing essentially every quantity ever desired about an ultrashort pulse in a very simple, compact package. Other FROG variations, XFROG and OPA XFROG, can measure extremely complex light pulses with as little as ~ 100 photons. In addition, these latter methods can measure these pulses despite such additional complexities as poor spatial coherence, random absolute phase, and massive shot-to-shot jitter. We look forward to their application to the study of exotic new phenomena.

Acknowledgments

References

1. R. Trebino, *Frequency-Resolved Optical Gating: The Measurement of Ultrashort Laser Pulses* (Kluwer Academic Publishers, Boston, 2002).
2. A. Baltuska, M. S. Pshenichnikov and D. Wiersma, *Opt. Lett.* **23**, 147 (1998).
3. X. Gu, L. Xu, M. Kimmel, E. Zeek, P. O'Shea, A. P. Shreenath, R. Trebino and R. S. Windeler, *Opt. Lett.* **27**, 1174 (2002).
4. J. Zhang, A. P. Shreenath, M. Kimmel, E. Zeek, R. Trebino and S. Link, *Opt. Expr.* **11,** 601 (2003).
5. S. Akturk, M. Kimmel, P. O'Shea and R. Trebino, *Opt. Expr.* **11,** 68 (2003).
6. S. Akturk, M. Kimmel, P. O'Shea and R. Trebino, *Opt. Expr.* **11,** 491 (2003).
7. P. O'Shea, M. Kimmel, X. Gu and R. Trebino, *Opt. Lett.* **26**, 932 (2001).
8. S. Linden, H. Giessen and J. Kuhl, *Phys. Status Solidi B* **206,** 119 (1998).
9. J. K. Ranka, R. S. Windeler and A. J. Stentz, *Opt. Lett.* **25**, 25 (1999).
10. Q. Cao, X. Gu, E. Zeek, M. Kimmel, R. Trebino, J. Dudley and R. S. Windeler, *Appl. Phys. B* **77,** 239 (2003).
11. P. O'Shea, X. Gu, M. Kimmel and R. Trebino, *Opt. Expr.* **7,** 342 (2000).
12. A. L. Gaeta, *Opt. Lett.* **27,** 924 (2002).
13. J. Dudley, X. Gu, X. Lin, M. Kimmel, E. Zeek, P. O'Shea, R. Trebino, S. Coen and R. S. Windeler, *Opt. Expr.* **10,** (2002).
14. S. Haacke, S. Schenkl, S. Vinzani and M. Chergui, *Biopolymers* **67,** 306 (2002).
15. N. Hampp, *Chemical Reviews* **100,** 1755 (2000).
16. T. Kobayashi, T. Saito and H. Ohtani, *Nature* **414,** 531 (2001).
17. S. Schenkl, E. Portuondo, G. Zgrablic, M. Chergui, S. Haacke, N. Friedman and M. Sheves, *Chem. Phys. Chem.* **4,** 5020 (2002).
18. J. Y. Zhang, A. P. Shreenath, M. Kimmel, E. Zeek, R. Trebino and S. Link, *Optics Expr.* **11,** 601(2003).
19. G. Cerullo and S. De Silvestri, *Rev. Sci. Instr.* **74,** 1 (2003).
20. A. V. Smith, *Opt. Lett.* **26,** 719 (2001).
21. A. Andreoni, M. Bondani and M. A. C. Potenza, *Opt. Commun.* **154,** 376 (1998).
22. R. Danielius, A. Piskarskas, A. Stabinis, G. P. Banfi, P. Ditrapani and R. Righini, *J. Opt. Soc. Am. B* **10,** 2222 (1993).
23. C. Radzewicz, Y. B. Band, G. W. Pearson and J. S. Krasinski, *Opt. Commun.* **117,** 295 (1995).
24. P. Ditrapani, A. Andreoni, G. P. Banfi, C. Solcia, R. Danielius, A. Piskarskas, P. Foggi, M. Monguzzi and C. Sozzi, *Phys. Rev. A* **51,** 3164 (1995).
25. R. W. Boyd, *Nonlinear Optics* (Second Ed., Academic Press, 2002).
26. R. L. Sutherland, *Handbook of Nonlinear Optics* (Marcel Dekker, Inc, 1996).
27. S. Linden, J. Kuhl and H. Giessen, *Opt. Lett.* **24,** 569 (1999).
28. A. V. Smith, *Proc. SPIE* **3928,** 62 (2000).
29. S. Akturk, M. Kimmel, P. O'Shea and R. Trebino, *Opt. Lett., in press* (2004).

Chapter 4

FEMTOSECOND COMBS FOR PRECISION METROLOGY

S.N. Bagayev, V.I. Denisov, V.M. Klementyev, I.I. Korel, S.A. Kuznetsov, V.S. Pivtsov and V.F. Zakharyash
Institute of Laser Physics, Siberian Branch, Russian Academy of Sciences
Pr. Lavrentieva, 13/3, 630090 Novosibirsk, Russia

Abstract   A new stage of development of optical clocks and synthesizers is possible with the use of highly stable femtosecond lasers. Using femtosecond lasers and special optical fibres, a highly stable frequency comb covering the frequency interval up to several hundreds of THz with a spacing from 100 MHz to 1 GHz has been developed. Experimental schemes for the femtosecond optical clock based on the $He-Ne/CH_4$ and $Nd:YAG/I_2$ frequency standards are presented. The possibility of using tapered fibres for optical clocks and synthesizers is investigated. It is shown that, depending on their influence on the frequency characteristics of the spectral components of the transmitted radiation, tapered fibres can be used in femtosecond optical clocks and synthesizers.

Key words: Femtosecond laser, supercontinuum, femtosecond comb, optical frequency stabilization, optical clock, optical synthesizer, microstructure optical fibre, tapered optical fibre.

1.   INTRODUCTION

In recent times, it has become evident that high-precision metrological measurements in the optical region of the spectrum, especially in navigation and communication systems and in precision measurements of physical quantities (in particular, the fundamental constants), are more and more in demand. During development of a laser frequency standard, one should allow for its use in different spectral regions, that is, the possibility of transmission of the frequency characteristics of a highly stable signal for

high-precision measurements in the above-mentioned problems. But most applications of frequency standards are in the microwave region. Thus, the use of optical frequency standards requires the transfer of the frequency characteristics from the optical to the microwave region, i.e., an optical clock is necessary. An optical clock consists of an optical frequency standard and a frequency division system from the optical to the microwave region. Earlier, frequency division systems were complicated and cumbersome devices consisting of a specially selected and phase-synchronized chain of lasers in the near-infrared, far-infrared, and submillimeter regions, microwave generators, and fast frequency mixers [1]. Frequency synthesizers of similar construction require the presence of a frequency train at the output. The idea of using a continuous laser of ultrashort pulses for optical frequency standards and for laser spectroscopy with superhigh resolution was first proposed more than 20 years ago [2-4]. In Ref. 3, this idea was realized experimentally with the use of a continuous dye laser of picosecond pulses with synchronous pumping. The real breakthrough, however, took place only in recent years as a result of the rapid development of femtosecond lasers [5] and the appearance of special optical (microstructure and tapered) fibres for the broadening of their spectrum [6-8]. The new stage of development of optical clocks and synthesizers is associated only with the use of highly stable femtosecond lasers. The use of femtosecond lasers is related to its radiation spectrum. This spectrum is a comb with equidistant modes. Stabilizing the femtosecond comb with the help of a frequency standard, we obtain a set of stable optical and intermode frequencies in the radio-frequency region. Thus, with the use of femtosecond lasers frequency division to the radio-frequency range can take place in one cascade.

The femtosecond comb used in metrology can be simplified if the spectral width of the comb is greater than an octave, i.e., the maximum frequency of the comb is greater than two times the minimum frequency [9]. But even for the smallest pulse duration (5 fs at a wavelength of $0.8 \ \mu m$) this spectral width is not achieved. Thus, the problem of obtaining considerable spectral broadening whilst maintaining highly precise equidistant modes remains. The most popular method of spectral broadening uses special optical fibres; namely, microstructure (holey) and tapered fibres. Microstructure fibres are single-mode fibres with a set of periodic air pipes in the cladding, each a few microns in diameter. The manufacture of such fibres was first reported in Ref. 6. An advantage of microstructure fibres is the possibility of obtaining single transverse mode radiation propagation over a very wide spectral range, for instance, covering the radiation spectrum of a Ti:Sapphire laser. Experimentally, the possibility of using microstructure fibres for supercontinuum (SC) generation by a continuous femtosecond Ti:Sapphire laser pulse train was first demonstrated for laser

powers less than 10 nJ in Ref. 9. Supercontinuum generation with controlled parameters would be an ideal tool for precision metrology. Thus, a highly stable frequency comb covering the frequency interval up to several hundreds of THz with a spacing from 100 MHz to 1 GHz has been developed. This makes it possible to cover large frequency intervals in synthesis systems and to simplify their structure considerably [10, 11].

Recently, SC generation from the ultraviolet (UV) to the infrared (IR) range was demonstrated by the propagation of a femtosecond Ti:Sapphire pulse train through a tapered fibre [8]. The advantages of tapered fibres over microstructure fibres are their cheapness and the possibility of changing their parameters over a wide range. Furthermore, the propagation in tapered fibres can be described by a relatively simple numerical analysis. A more detailed description is presented in Sect. 3, which is devoted to the broadening process of the spectrum of the femtosecond pulses in tapered fibres.

For precision measurements of absolute optical frequencies and frequency intervals in the optical region, there are several techniques that use the femtosecond comb [12]. All of these techniques are based on the stabilization of the spectral components of the femtosecond comb by their phase locking to a highly stable reference laser standard. Thus, any frequency within the range of the existing frequency comb can be determined by a simple measurement of the beat frequency between this frequency and the nearest mode of the comb.

2. THE USE OF A FEMTOSECOND COMB FOR THE CREATION OF AN OPTICAL CLOCK

The first experiment on the use of a mode-locked laser for absolute optical frequency measurements referenced directly to a microwave clock was performed at MPQ (Germany) [13]. This experiment measured simultaneously the frequency of a CH_4-stabilized He-Ne laser and the 1S – 2S interval in hydrogen. The corresponding frequency interval, with a width of 44 THz, was divided down to the radio-frequency region using a mode-locked laser. Later, the same group compared the results of this chain with an octave-spanning comb [14]. The octave interval method using spectral broadening in a microstructure fibre, however, turned out in the meantime to be the simplest method. This method was used to measure the absolute frequencies of several other atomic, ionic, or molecular reference transitions, such as iodine [15], rubidium (two-photon transition) [15], calcium [16, 17], ytterbium ions [18, 19], mercury ions [17], and strontium ions [19]. Relative uncertainties as small as 1×10^{-14} were achieved [17, 18].

Recently, numerous experiments on the investigation of microstructure fibres and the creation of an optical clock on the basis of a broadened

femtosecond comb and frequency synthesizers have been carried out. The experimental investigations [20] have shown that femtosecond lasers have an equidistance of intermode intervals not worse than 3×10^{-17}. This means that without allowing for other extraneous effects, the precision of frequency measurements can reach the level of 3×10^{-17}.
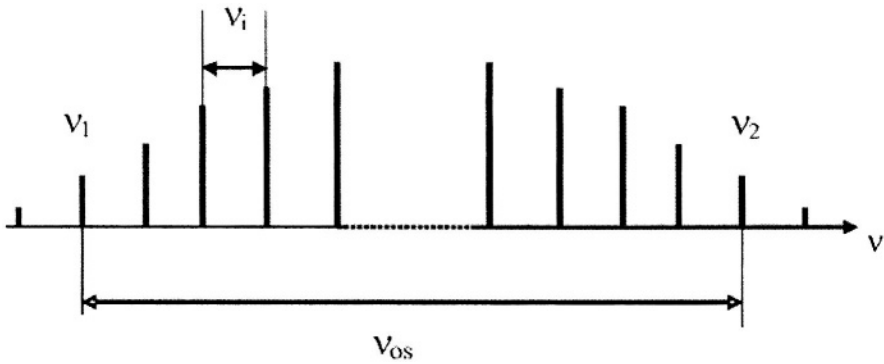
Figure 4.1. Physical principle of the femtosecond optical clock.

There are several schemes for constructing a femtosecond optical clock. As a rule, the frequency (or harmonic) of the optical standard (OS) must be in the generation range of the femtosecond laser. Special optical microstructure or tapered fibres are used to broaden this range. Schemes for the IR and UV regions of the spectrum are much more complex. We propose a scheme that is free from these limitations (Fig. 4-1) [21]. If the equality $v_2 - v_1 = v_{OS}$ is satisfied with the help of phase-locking, the frequency difference $v_2 - v_1$ will be phase-locked to the frequency of the optical standard. Thus, the frequency difference $v_2 - v_1$ and all other intermode frequencies will have the same frequency characteristics (such as linewidth and stability) as those of the optical standard. Notice that in this scheme only the intermode interval of the femtosecond laser is stabilized. If the clock is used for absolute frequency measurements, the absolute frequency of components of the femtosecond laser must also be stabilized by phase-locking to the frequency standard. Our experimental system (Fig. 4-2) [22] includes a Ti:Sapphire laser as a frequency comb generator and a He-Ne/CH$_4$ laser as a frequency standard. Thus, in our case the radiation wavelength of the frequency standard is equal to $3.39 \ \mu m$ and, therefore, the generation of frequency combs as wide as 88.5 THz (around 200 nm) is necessary. This problem was solved by passing the Ti:Sapphire laser pulses through special fibres: microstructure optical fibres and tapered fibres.
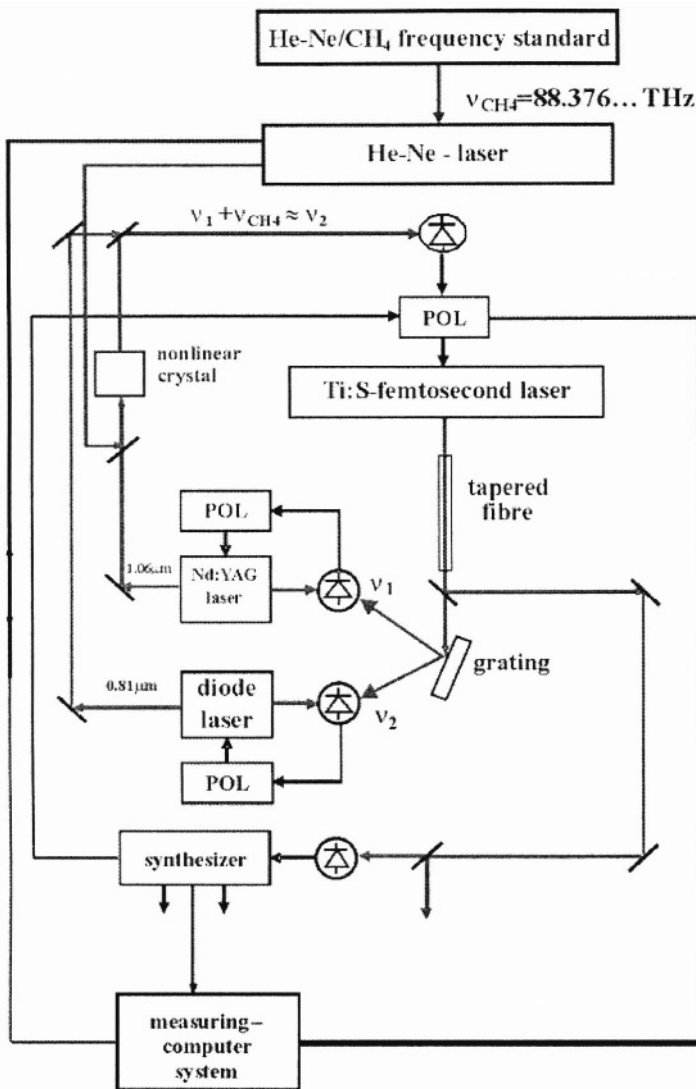
Figure 4-2. Femtosecond optical clock based on a He-Ne/CH$_4$ standard. POL: phase offset lock system.

The output power of our He-Ne/CH$_4$ laser is ~ 1 mW, which is not sufficient for frequency conversion. For this purpose, a He-Ne laser with a power of 15 mW is used. The frequency of this laser is phase locked to the frequency of the He-Ne/CH$_4$ standard. The parameters of the femtosecond Ti:Sapphire laser are as follows: output power 400 mW, pulse duration 40 fs, FWHM of spectrum ~ 20 nm (~ 10 THz), and pulse repetition frequency

(intermode interval) 100 MHz. The necessary spectral width was obtained by passing the Ti:Sapphire radiation through a tapered or microstructure fibre. The fibres were manufactured at the University of Bath (United Kingdom). A tapered fibre manufactured from Corning SMF-28, a standard tele-communications fibre with a core diameter of ~ 9 μm, was used. The cut-off wavelength is about 1250 nm. The radiation spectrum broadened by the fibre must cover the range from 1.064 μm to 0.81 μm. A spectral width much greater than this range is undesirable, because in this case the power of the required spectral components is reduced. In the present case, however, the power of each mode is $\sim 10^{-7}$ W.

In practice, it is impossible to use such power levels for the summation or subtraction of frequencies. To overcome this problem, the frequencies of the Nd:YAG laser ($\lambda = 1.064$ μm, power ~ 100 mW) and the diode laser ($\nu = 0.81$ μm, power ~ 10 mW) were phase locked to specific modes of the Ti:Sapphire laser. Thus, these lasers served as power amplifiers of the Ti:Sapphire laser modes. The tuning range of the Nd:YAG laser with diode pumping is up to 300 GHz, and the tuning range of the diode laser up to 150 THz (30 nm).

The frequencies of the Nd:YAG and He-Ne lasers were combined in a AgGaS$_2$ nonlinear crystal. The sum frequency power obtained was ~ 1 mW. The beat signal between the sum frequency and the diode laser frequency was transferred to a phase offset lock system (POL), and the error signal from the POL was transferred to the PZT driver of the Ti:Sapphire laser to control the intermode interval. As a result, the intermode interval of the Ti:Sapphire laser was stabilized to the frequency of the He-Ne/CH$_4$ standard. Thus, the frequency characteristics of the He-Ne/CH$_4$ standard are transferred from the optical domain to the radio-frequency domain in one step. The scheme is self-contained, i.e., it does not require the introduction of external reference frequencies. As the intermode frequency is in the radio-frequency domain, it can be measured with an accuracy of 10^{-14} - 10^{-15} with respect to another frequency standard (say, a H-maser).

The above set-up can be simplified by the use of a femtosecond Ti:Sapphire laser with a Nd:YAG/I$_2$ frequency standard. Since the Nd:YAG/I$_2$ frequency corresponds to the fibre-broadened spectrum, it is sufficient to make use of a typical scheme (Fig. 4-3). The Nd:YAG/I$_2$ frequency standard was developed at the Institute of Laser Physics [23]. It radiates simultaneously fundamental and doubled frequencies, which are supplied to individual photodiodes. The corresponding spectral components of the Ti:Sapphire laser radiation passed through the fibre are also supplied to the same photodiodes. The beat frequencies from the photodiodes are sent to the POL, from which error signals are supplied to the control elements of the Ti:Sapphire laser. As a result, both the intermode interval and the absolute frequency of the spectral components of the femtosecond

Ti:Sapphire laser are stabilized. The parameters of the He-Ne/CH$_4$ and Nd:YAG/I$_2$ frequency standards are approximately the same. The scheme with Nd:YAG/I$_2$ is, however, much simpler.
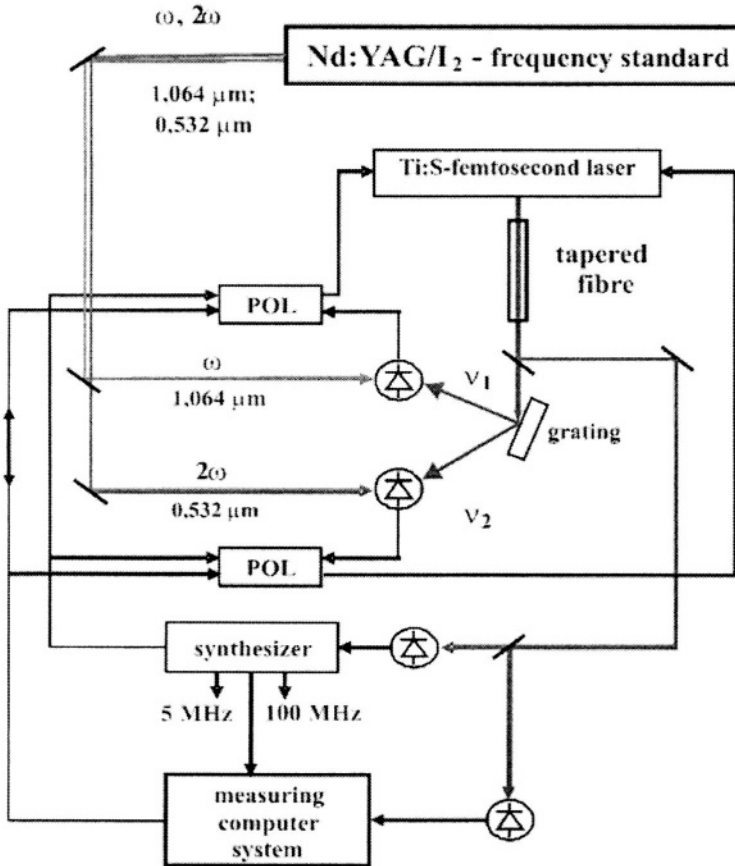
Figure 4-3. Femtosecond optical clock based on a Nd:YAG/I$_2$ standard.

Presently, besides Ti:Sapphire lasers, various femtosecond lasers, such as Nd-media ($\lambda \sim 1.06$ μm), Yb-media ($\lambda = 1.03 - 1.05$ μm), Cr:Forsterite ($\lambda \sim 1.25$ μm), Cr^{4+}:YAG and Er-media ($\lambda \sim 1.5$ μm) lasers, have also been thoroughly investigated. These are lasers that have already been used for SC generation. Thus, the lasers mentioned can be used to create femtosecond optical clocks and synthesizers. The only insufficiently investigated element in the schemes described is the fibre for the broadening of the femtosecond laser spectrum. An essential shortcoming of microstructure fibres is the complexity of the numerical calculation of the spectral broadening in such

fibres in a specific experiment, since it is necessary to take into account nonlinear optical processes with imprecisely known parameters. Tapered fibres make possible the theoretical calculation of the spectral broadening depending on the power of the femtosecond laser and the parameters of the fibre itself. However, although there is some experience with using microstructure fibres for such schemes, the possibility of using tapered fibres for optical clocks and synthesizers has not yet been studied.

3.   SPECTRAL BROADENING OF FEMTOSECOND PULSES IN TAPERED FIBRES

Let us describe in more detail the process of spectral broadening of femtosecond pulses in tapered fibres. Tapered fibres are produced from ordinary telecommunication fibres. The structure of such fibres is shown in Fig. 4-4. It can be seen in the figure that fibres of this type consist of an untapered fibre, a conical transition zone, and a narrow central part, that is the waist. During stretching, the decrease in the diameters of the cladding and the core are proportional. It is just in the waist that the spectral broadening of the femtosecond laser pulses takes place. It is shown below that the effectiveness of this broadening is determined mainly by the ratio of the nonlinear length to the effective fibre (waist) length and by the dispersion profile in the spectral region close to the central frequency of the incident laser radiation.
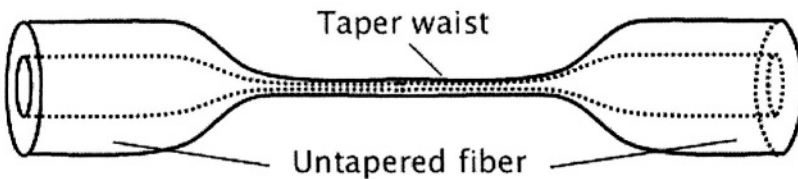
Figure 4.4. Tapered fibre structure.

The nonlinear length depends on the radiation intensity and the effective nonlinear area associated with the fibre parameters. The dispersion profile of a certain fibre can be found by using the characteristic equation for the fundamental mode [24] and the Sellmeier equation [25]. Some examples of

dispersion profiles obtained for different fibre waist diameters are shown in Fig. 4-5. It can be seen in the figure that, for typical wavelength values of the Ti:Sapphire laser of 800 – 850 nm, the waist diameter can be chosen to satisfy the desired requirements of dispersion, for the central wavelength to be in the regions of normal, anomalous, or zero dispersion. Since the waist creation process can be controlled rather easily, the achievement of the desired waist diameter and length is usually not difficult. Thus, the fibre parameters can be varied over a wide range and tuned to the external radiation, which means that the spectral characteristics can be controlled.
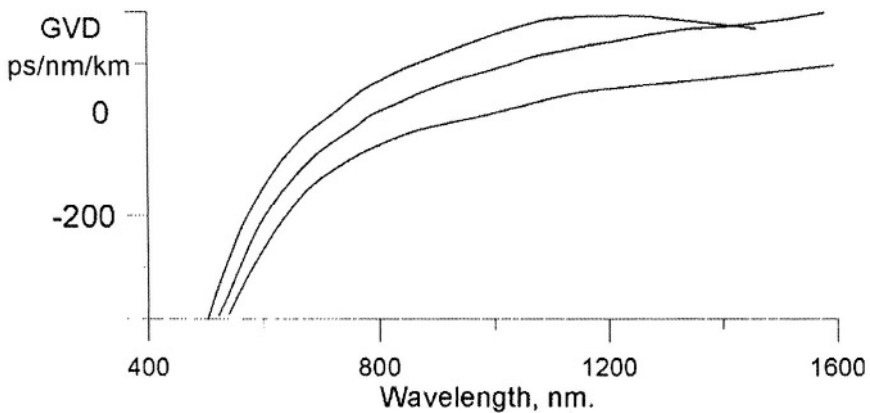
Figure 4-5. Dispersion profiles for taper waist diameters of 2, 2.5 and **3 μm** (left to right). Positive values correspond to anomalous dispersion.

The geometry itself of tapered fibres determines the relative simplicity of the numerical model that describes the pulse propagation and hence the spectrum formation and broadening. In contrast to microstructure fibres with a complex structure and complex profiles of spatial dispersion, a tapered fibre can be considered as a rod with a single step of the refractive index. This is possible since spectral broadening takes place in the taper waist and the influence of the non-tapered fibre zone or the transition zone can usually be neglected due to the low efficiency of nonlinear effects at the small-scale length. In this respect, the description of tapered fibres is similar to that of classical models of cylindrical fibres with a step-like refractive index profile.

The main factor which causes the spectral broadening of ultrashort pulses in tapered fibres is self-phase modulation (SPM). This nonlinear effect is due to the nonlinear phase growth during pulse propagation in the fibre [26]:

$$\phi_{NL}(z, T) = |S(0, T)|^2 \, \frac{z}{L_{NL}} \tag{4.1}$$

where L_{NL} is the nonlinear length, z is the waist length, and $S(0, T)$ is the initial pulse shape. Since the nonlinear phase depends on the pulse shape, its time derivative at a fixed pulse point can be considered as the detuning between the instantaneous and central frequencies. It is clear from the above relation that the broadening is greater for a long fibre waist and small waist diameters, since the nonlinear length depends on the effective nonlinear area. Besides, it can be expected that the broadening will increase with increasing peak power and decreasing pulse duration, because in the first case the nonlinear length becomes smaller and in the second case the input pulse spectrum is broader.

Some papers [8, 27, 28] are devoted to the problem of generation of the SC in tapered fibres. In these papers the main factors that affect the spectral broadening and its envelope shape are studied. An experimental investigation of the spectral characteristics of broadened Ti:Sapphire laser radiation versus the parameters of the fibre waist and external radiation was performed in Ref. 27. These papers present spectra for various waist diameters $(1 - 3 \text{ } \mu\text{m})$ and lengths. The peak powers, central wavelengths, and pulse duration were varied. In general, most of the data confirm the dependences mentioned above. Nevertheless, there are some interesting results which require further detailed discussion. An interesting experimental result is the absence of essential spectral broadening in the fibre when the central wavelength is in the region of normal dispersion. The authors explain SC generation in their fibres as a soliton induced process. Thus, in the experiment with laser radiation tuned to the normal dispersion region, the soliton regime is not realized and, hence, the SC generation does not occur.

The soliton mode in fibres is possible in the anomalous dispersion region, where the solutions of the nonlinear Schrödinger equation (NLSE) [29], which describes pulse propagation in fibres, have some peculiarities due to the combined action of nonlinear effects (SPM, shock wave formation, stimulated Raman scattering (SRS), or their combination), and group velocity dispersion (GVD). Thus, anomalous dispersion causes the generation of solitons, that is, spatially independent or periodic NLSE solutions [29]. Another important effect connected with anomalous dispersion is the modulation instability [30], which has similar causes but is beyond the scope of this paper.

Earlier, soliton induced SC generation was mainly associated with microstructure fibres, where under certain conditions (anomalous dispersion, relatively low intensities, etc.) the possibility of SC generation was

demonstrated both theoretically and experimentally [31]. This regime presupposes the formation of fundamental solitons shifted to the red region and non-soliton radiation shifted to the blue region. In this case, spectral broadening proved to be much greater than it could be under the influence of only nonlinear effects, such as SPM or SRS. In contrast to this case, the radiation intensity in the taper waist is usually very high and hence SPM must effectively broaden the spectrum. Another important feature is that in most cases the dispersion length of tapered fibres is greater than the waist length, and this complicates considerably the soliton formation process.

There is, however, some indirect evidence in favor of the assumption about possible soliton formation in tapered fibres. In Ref. 31 it was shown, for example, that spectral broadening increases for higher values of anomalous dispersion of group velocities; that is, the spectral broadening of "red" pulses is greater than that of "blue" pulses. This fact can be treated as soliton splitting SC generation, since the probability of formation of spatially stable NLSE solutions increases as one moves deeper into the anomalous dispersion region. On the other hand, the mentioned case of the absence of SC generation is rather atypical, while there are some examples [28] of essentially spectral broadening in the normal dispersion region. In any case, soliton splitting in tapered fibres remains an interesting and scantily explored (both experimental and theoretical) problem.

So far, we were discussing the spectral broadening of a single pulse. In a typical experiment involving SC generation in a fibre, the external radiation is a sequence of pulses, whose spectrum, generally speaking, may not coincide with the spectrum of a single pulse. Actually, the main difference between the single pulse spectrum and the pulse train spectrum is the presence of a frequency comb, which is the main characteristic of most SC applications.

A numerical description of the pulse train spectrum after propagation in a fibre can be made by taking the Fourier transform of the time series representing the output radiation. In general, the spectrum of the train of ultrashort pulses can be expressed as a product of a discrete spectrum (i.e., the frequency comb) typical for periodic processes and a continuous spectrum (the envelope) related to the spectrum of a single pulse if there are no fluctuations in the pulse train:

$$S(\omega) = F_P(\omega)F_D(\omega) , \tag{4.2}$$

where $F_P(\omega)$ is the continuous spectrum (the spectrum of a single pulse), and $F_D(\omega)$ is the discrete spectrum (the so-called femtosecond comb).

It should be mentioned that in this approach we assume that the pulse train is perfect, which means the equality of all parameters of pulses within

the train, i.e., the shapes, phases, amplitudes, and inter-pulse intervals for all pulses in the train are the same. Any fluctuations lead to differences both in the shapes of the frequency comb spectral components and the spectral envelopes. A statistical analysis of the spectra of the pulse process has been studied rather thoroughly [32]. However, the complexity of the nonlinearities in the fibre makes it practically impossible to use these methods directly for precise solutions. Below, we assume that a pulse train is a perfect temporal sequence with equal pulses. This is the case when the envelope of the spectrum of the output pulse train can be calculated by an ordinary nonlinear Schrödinger equation [26]:

$$\frac{\partial U}{\partial z} = \hat{D}U + \frac{i}{L_{NL}}\left[|U|^2\,U + \frac{2i}{\omega_0 T_p}\frac{\partial}{\partial \tau}\left(|U|^2\,U\right) - \frac{T_R}{\tau}U\frac{\partial}{\partial \tau}|U|^2\right]. \quad (4.3)$$

Here D is the differential dispersion operator:

$$\hat{D} = \sum_{m=2}^{N}\frac{i^{m+1}}{m!}\frac{\beta_m}{T_p^m}\frac{\partial^m}{\partial \tau^m}$$

$$(4.4)$$

where β_m is the group velocity dispersion (GVD) of the m-th order; $L_{NL} = (\gamma P_0)^{-1}$ is the nonlinear length; γ is a parameter of nonlinearity related to the effective mode area; P_0 is the peak power; ω_0 is the central frequency; τ_R is a parameter related to the slope of the stimulated Raman scattering gain line; and T_P is the pulse duration.

Thus, the NLSE takes into account the influence of GVD, SPM, the shock wave, and SRS. All of these effects essentially affect the pulse propagation in tapered fibres. The necessity of allowing for high-order GVD is caused by some peculiarities of the propagation of ultrashort pulses in fibres, and also by the fact that the central wavelength is often close to the dispersion wavelength (zero dispersion point).

Numerical NLSE solutions are usually obtained by using SSFM (split-step Fourier method) [33]. Independent allowance for nonlinear and dispersion effects in a small spatial step l satisfying the inequality $l < L_{NL} < L_D$ ($L_D = T_0^2/|\beta_2|$ is the dispersion length) is a characteristic feature of this method. This makes it possible to reduce the computations considerably.

The numerical results are compared with the experimental spectra in Fig. 4-6. It can be seen that the spectral broadening ratio is determined by the peak power. This fact is quite understandable, since SC generation in tapered fibres, in contrast to microstructure fibres with soliton induced

spectral broadening, is mainly due to SPM, i.e., the nonlinear phase growth proportional to the peak power.
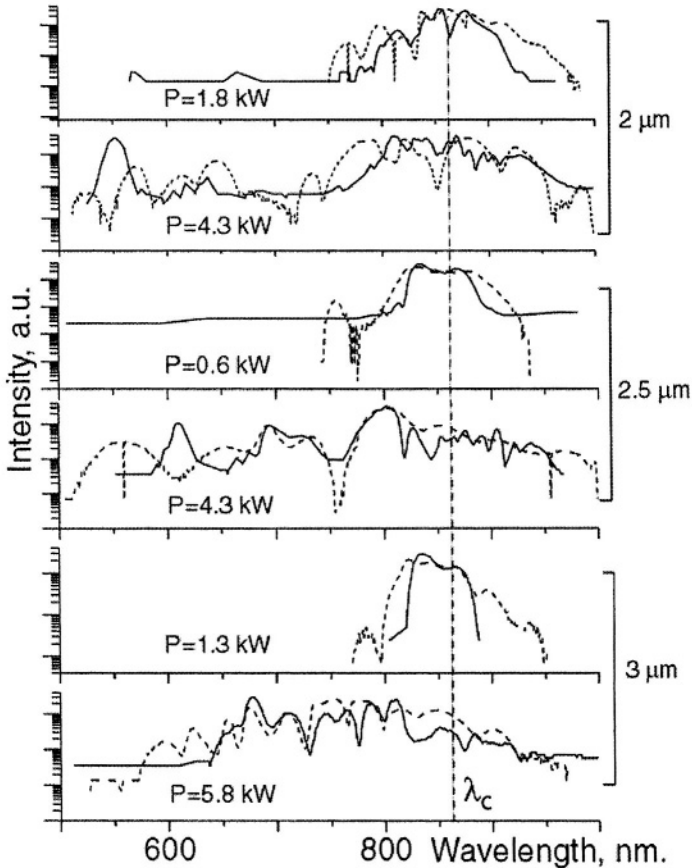
Figure 4-6. Comparison of experimental measurements and numerical calculations of the spectral envelope obtained for taper waist diameters of 2, 2.5 and 3 μm and different peak powers. The solid line corresponds to the experimental results and the dashed line to numerical calculations. Hyperbolic cosecant pulses, duration: 160 fs, waist length: 6 cm.

Under the experimental conditions, $L_{NL}/L_{WAIST} \approx 10^2$ ($L_{NL} = 0.4 - 0.8$ mm for various intensities). This ratio can be approximately interpreted as a SPM coefficient of spectral broadening. At the same time, the dispersion length does not depend on the pulse intensity and, for a fixed waist diameter, the pumping wavelength and the pulse duration remain within about $20 - 30$ cm.

Since $L_{NL}/L_D \ll 1$, nonlinear effects dominate over dispersion. This is why in our experiments soliton splitting is unlikely. It should be noted that for SPM that leads to spectral broadening, minimum GVD is an important condition for the maximum spectral width, since otherwise GVD causes an increase in the pulse duration, thereby narrowing the spectrum. Nevertheless, the numerical investigation has shown that the dispersion terms in the NLSE are very essential even for the spectrum envelope shape.

Self-phase modulation gives symmetric spectral shapes for typical pulse temporal profiles (Gaussian and super-Gaussian shapes, and the hyperbolic cosecant) used in the numerical modeling, while most of the experimental spectra are asymmetric. This means that although SPM is the main SC generation effect, a detailed description of the spectrum requires allowance for other nonlinear and dispersion effects. In many cases, experimental spectra have a complex structure with multiple peaks and dips. Since precise numerical solution makes it possible to predict the amplitude at a desired spectral point, it is a very important task for spectral control.

The basic reasons for spectral asymmetry in tapered fibres are self-induced Raman scattering, wavefront shaping (shock wave formation), and temporal asymmetry of the initial pulse and dispersion profile.

Since the dispersion profile itself is nonlinear and asymmetric with respect to the central wavelength (see Fig. 4-5), it causes asymmetry in the spectral evolution of the pulse. In the numerical simulation, asymmetry appears as different values of high-order terms of the dispersion operator (4.4) calculated in the frequency domain in the step-split Fourier method. The wavefront steepening (shock wave formation) causes some extra broadening on the trailing edge of the pulse [34]. As a result, the blue part of the spectrum becomes broader than the red part. But, simultaneously with this extra broadening, the steepening leads to an increased influence of the dispersion effects. Thus, in a sense, we have a counteraction of the shock wave formation and dispersion effects. Depending on the dispersion profile of the fibre, the extra broadening can be visible or suppressed by the influence of dispersion.

Raman self-scattering [35] can be explained using a SRS model in which blue components of the pulse spectrum are considered as a pumping for red components. It should be noted that for femtosecond pulses this mechanism begins its action at the very onset of propagation, since the spectral width of the incident pulse (20 THz according to experimental conditions) exceeds the frequency of the Raman shift (about 13 THz in silica). The effectiveness of this mechanism is caused by the high power densities in the waist.

Figure 4-7 shows that Raman self-scattering strongly affects the spectral envelope. This result was obtained by using a simple numerical model of pulse propagation in the absence of any other nonlinear and dispersion effects. In this model, the spectrum is considered as a frequency comb.

Therefore, the evolution of the pulse spectrum can be described as the SRS interaction of individual spectral components:

$$\frac{dI_R}{dz} = g_R I_R I_B .$$

(4.5)

Here, g_R is the Raman coefficient, and I_R and I_B are the Stokes component and the pumping intensity, i.e., they are neighboring spectral components in our model.
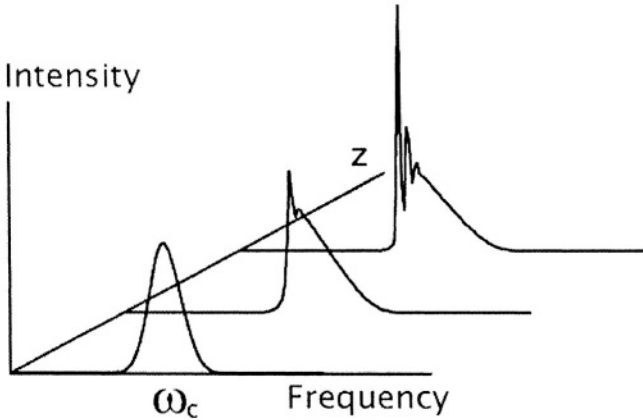
Figure 4-7. Evolution of the spectrum envelope in the tapered waist due to Raman self-scattering. Peak power: 10 kW, waist length: 6 cm. Self-phase modulation, shock wave, and dispersion are not taken into account.

A peculiarity of the SRS of ultrashort pulses in the SC generation mode is that Raman scattering strongly affects the spectrum shape at the very beginning of the evolution, when the pulse spectrum is narrow and the intensities of the spectral components are high. If the broadening is more or less uniform, the efficiency of SRS decreases. In some cases, the SRS term in the NLSE leads to the formation of so-called Raman solitons [36] in microstructure fibres.

Undoubtedly, one of the most important factors that affect the spectral envelope is the initial pulse shape. A strong relation between the pulse shape and its evolution is obvious from the NLSE, since all of its terms directly depend on the time derivative. Varying the pulse shape, one can obtain fundamentally different spectra. Thus, the Gaussian pulse after SPM-caused spectral broadening has a multi-peak spectral structure with maxima at the

periphery, while sharp shapes, such as the supergaussian or hyperbolic cosecant, have a central maximum and some small peaks on both sides. Therefore, the arbitrary asymmetric pulse can have an even more complicated spectrum envelope after propagation in a fibre.

Thus, the main mechanisms of formation of the spectral envelope of femtosecond laser radiation for the broadening process in tapered fibres have been determined. By varying the input radiation and fibre parameters one can obtain a desired shape of the envelope of the broadened spectrum, which is of great importance for practical applications.

Another important characteristic for the applications of tapered fibres is the noise amplification level affecting the stability of radiation frequency components.

4. FREQUENCY STABILITY OF FEMTOSECOND COMB BY PASSAGE OF FEMTOSECOND PULSES THROUGH A TAPERED FIBRE

To study the stability of the comb as a result of propagation of the femtosecond pulses through a tapered fibre, the following technique was developed [28]. By using frequency synthesis, intermode beats were transferred to the low frequency region. Then, the beats were precisely measured at a selected frequency of about 200 Hz. It should be noted that the final aim in the development of methods and techniques of precise measurement is the measurement of absolute optical frequencies with a high accuracy (of up to $10^{-15} - 10^{-16}$) by using a femtosecond optical clock.

The results of these measurements were obtained by comparing the intermode frequency with the frequency of the H-standard, as described below. The scheme of the experimental set-up is presented in Fig. 4-8. The set-up consists of a H-standard on the one hand and a femtosecond laser on the other hand. The intermode frequency of the laser is stabilized by phase-locking (PL) to the H-standard. The set-up itself may be divided into the following two channels: channel 1 ("synthesis and filtration from H-standard") and channel 2 ("synthesis from the Ti:Sapphire laser"). Channel 1 transfers the frequency properties (spectral characteristics) of the H-standard to a frequency of 20 MHz (F_3). In the same way, channel 2 using a frequency synthesizer transforms the intermode frequency f_m to a frequency of 20 MHz ± 200 Hz (F_3^*). The signal being measured is obtained at the output of mixer M2 and is determined as the frequency difference between the mixed F_3 and F_3^*. The comparison system is constructed so that the frequency F_3 phase-locked to the H-standard always has the properties given by the standard. The signal passing through channel 2 from the laser (i.e.,

from photodiode PD1) contains all frequency fluctuations. These are intrinsic fluctuations of the Ti:Sapphire laser and the fluctuations acquired in the tapered fibre. The output power and the optical spectra of the Ti:Sapphire laser were monitored by a power meter and by a multichannel spectrum analyzer, respectively. The spectrum broadened by the fibre was observed and recorded by a multichannel spectrometer.
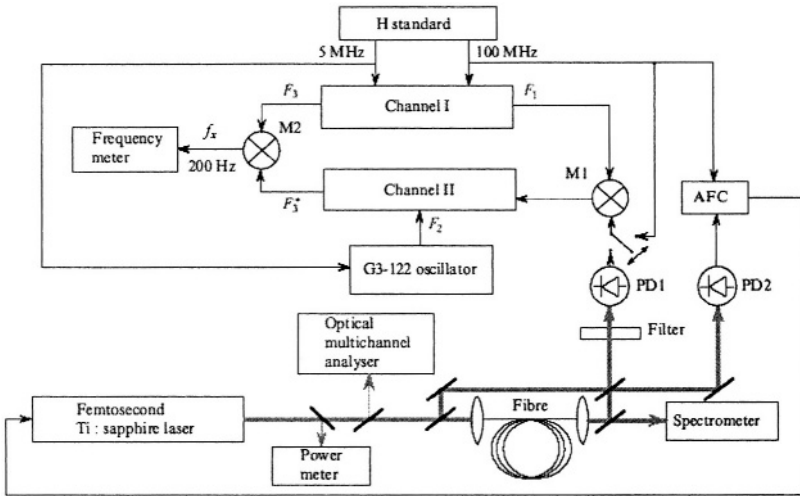
Figure 4-8. Principal scheme of the experimental set-up. AFC: automatic frequency control; M1, M2: mixers; PD1, PD2: photodiodes.

There is an important possibility for this comparator to check its own performance on its own time scale. For this, a frequency of 100 MHz from the H-standard has to be sent to the input of mixer M1. Using thermo-stabilized (up to ~ 0.1 °C) quartz oscillators and resonant amplifiers in both channels, the noise of the comparison system is greatly filtered out. The formula for the intermode frequency synthesis is as follows:

$$f_m = F_1 - F_2 + F_3^*/10 = F_1 - F_2 + F_3/10 \pm f_x/10, \qquad (4.6)$$

where $F_1 = 99.5$ MHz, $F_3^* = F_3 \pm f_x$, $f_x \approx 200 \pm \delta f_x$ (Hz), and δf_x includes the frequency fluctuation f_m. Therefore, the relative accuracy of evaluation of f_m is

$$\delta f_m/f_m = \delta f_x/10 f_m, \qquad (4.7)$$

since δF_1, δF_2 and $\delta F_3 \ll \delta f_x$.

Specifically, the experiments consisted of measurements of $\delta f_m/f_m$ at various averaging times at the input and output of the tapered fibre. First, the intrinsic frequency noise of the system was studied by substituting f_m for the signal at a frequency of 100 MHz from the H-standard (i.e., by using its own time scale). Thus, at the output of mixer M3 a signal of frequency $f_x^* = 200 \pm \delta f_x$ (Hz) appeared (here f_x^* corresponds to the signal from the H-standard). The following results for various averaging times were obtained: 3.1×10^{-12} in 10 s, 3.4×10^{-13} in 10^2 s, 3.12×10^{-14} in 10^3 s, and 3×10^{-15} in 10^4 s. Hence, the set-up allows one to perform intermode frequency measurements with a relative accuracy of $10^{-14} - 10^{-15}$ in an averaging time from 10^3 s to 10^4 s.
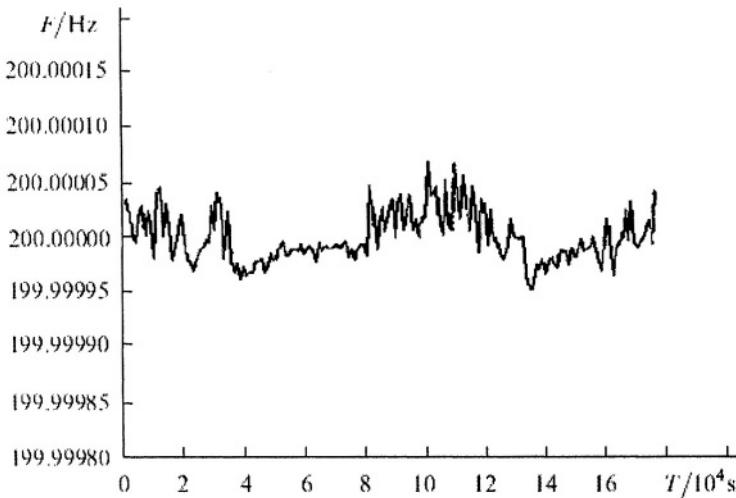
Figure 4-9. Frequency stability of the measuring system versus time during 24 hours (the averaging time is 1000 s).

Investigations of the stability dependence of the measuring system on the time during a day have been carried out. The results are presented in Fig. 4-9. One can see that the mean of the frequency being measured depends on the averaging time and varies within the daily interval only in the case of a long averaging time. For the same averaging time, daytime amplitude fluctuations are one order of magnitude greater than at night. These fluctuations are suppressed owing to a specific design of the system.

It is very important to know whether the intermode frequency stability is still maintained after the passage of a highly stable femtosecond pulse train through a fibre system. In recent publications, investigations of the

intermode frequency stability of a highly stable femtosecond laser (similar to the one described in Ref. 37) have been carried out. Series of measurements at various averaging times were performed at the input and output of a tapered fibre. The results are presented in Fig. 4-10. From the results presented one can see that the stability of f_m is worse than the stability that could be provided by the measuring system. Also, the stability of f_m after the passage of a pulse train through the fibre has greatly changed. For a short averaging time, the stability decreases by more than a factor of two. As the averaging time increases the stability of f_m improves and, in 1000 s, almost reaches the original value measured at the input of the tapered fibre.
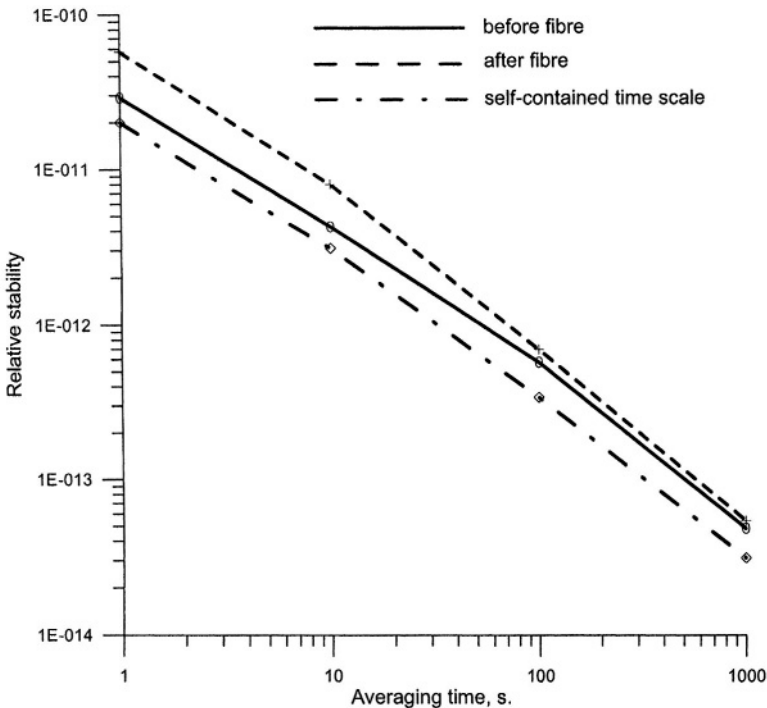
Figure 4-10. Intermode frequency stability.

Next, a possible dependence of the stability of f_m on the region of the broadened spectra was studied. For this, by using color filters, the entire broadened spectrum was divided into two parts for stability measurements at the output of the fibre in different spectral regions. The results are presented in Table 4-1. In the same table, the results obtained at the input of the fibre are also given. From the table, one can see that the propagation of femtosecond pulses in the fibre causes additional noise. The noise increases

asymmetrically: the noise in the long wavelength region exceeds that in the short wavelength region.

Table 4-1. Stability measurements at the output of the fibre in different spectral regions.

Experimental Conditions	Number of Measurements	Root-mean-square deviation (Hz) for an averaging time 100 s
In front of a fibre	98	5.74×10^{-5}
Behind a fibre $\lambda = 400 - 650$ nm	92	6.94×10^{-5}
Behind a fibre $\lambda = 700 - 1000$ nm	83	8.46×10^{-5}

Low frequency (1 Hz – 10 Hz) instability of the broadened spectrum envelope was investigated. Angular fluctuations of the input radiation are the reasons for the spectrum envelope instability if the untapered part of the fiber (Fig. 4-4) is multimode. Therefore, microstructure fibres are used now. Work to correct this situation is currently under way, since tapered fibres have a rather simple manufacturing technology and are cheaper than microstructure fibres.

5.   CONCLUSIONS

The new stage of development of optical clocks and synthesizers is possible only with the use of highly stable femtosecond lasers. Using femtosecond lasers and special optical fibres, a highly stable frequency comb covering the frequency interval up to several hundreds of THz with a spacing from 100 MHz to 1 GHz has been developed. This makes it possible to cover large frequency intervals in synthesis systems and to simplify their structures considerably. A principle for the construction of femtosecond optical clocks has been proposed. This has made it possible to simplify considerably the general scheme of the clock and expand its area of application. Experimental schemes for the femtosecond optical clock based on $He\text{-}Ne/CH_4$ and $Nd{:}YAG/I_2$ frequency standards have been presented. The possibility of using tapered fibres for optical clocks and synthesizers has been investigated. The main mechanisms of formation of the envelope of the femtosecond laser radiation spectrum broadened by a tapered fibre have been established. The results of theoretical calculations are in qualitative agreement with the experimental measurements. By varying the parameters

of the injected radiation and the tapered fibre, one can obtain at will the required shape of the broadened spectrum envelope, which is important for practical applications. The influence of a tapered fibre on the stability of the spectral components of a propagating continuous sequence of femtosecond pulses from a Ti:Sapphire laser has been investigated. At small times (10 s), the intermode frequency stability decreases by a factor of two. As the averaging time increases, the stability improves, and at an averaging time of 1000 s it practically coincides with the stability at the tapered fibre input. Thus, it has been shown that, depending on their degree of influence on the frequency characteristics of the spectral components of propagating radiation, tapered fibres can be used in femtosecond optical clocks and synthesizers.

Acknowledgments

References

1. V.P. Chebotayev, V.G. Goldort, V.M. Klementyev, M.V. Nikitin, B.A. Timchenko and V.F. Zakhariash, *Appl. Phys. B* **29**, 63 (1982).
2. Ye.V. Baklanov and V.P. Chebotaev, *Appl. Phys.* **12**, 97 (1977).
3. J.N. Eckstein, A.I. Ferguson and T.W. Hänsch, *Phys. Rev. Lett.* **40**, 847 (1978).
4. S.N. Bagayev, V.P. Chebotayev, V.M. Klementyev and O.I. Pyltsin, *Proc. 10th Int. Conf. on Laser Spectroscopy,* Font-Romeu, France, June 17-21, p. 91 (1991).
5. T. Brabec and F. Krausz, *Rev. Mod. Phys.* **72**, 545 (2000); J.L. Hall and J. Ye, *Optics and Photonics News,* February, p. 44 (2001).
6. J.C. Knight, T.A. Birks, P.St.J. Russell and D.M. Atkin, *Opt. Lett.* **21**, 1547 (1996).
7. J.C. Knight, J. Broeng, T.A. Birks and P.St.J. Russell, *Science* **282**, 1476 (1998); P.St.J. Russell, *Laser Focus World,* September, p. 77 (2002); A.M. Zheltikov, *Physics-Uspekhi* **170**, 1203 (2000).
8. T.A. Birks, W.J. Wadsworth and P.St.J. Russell, *Opt. Lett.* **25**, 1415 (2000).
9. J.K. Ranka, R.S. Windeler and A.J. Stentz, *Opt. Lett.* **25**, 25 (2000).
10. S.A. Diddams, D.J. Jones, J. Ye, S.T. Cundiff, J.L. Hall, J.K. Ranka, R.S. Windeler, R. Holzwarth, T. Udem and T.W. Hänsch, *Phys. Rev. Lett.* **84**, 5102 (2000).
11. D.J. Jones, S.A. Diddams, J.K. Ranka, A. Stentz, R.S. Windeler, J.L. Hall, and S.T. Cundi, *Science* **288**, 635 (2000).
12. H.R. Telle, G. Steinmeyer, A.E. Dunlop, J. Stenger, D.H. Sutter and U. Keller, *Appl. Phys. B* **69**, 327 (1999); J. Reichert, R. Holzwarth, Th. Udem, and T.W. Hänsch, *Opt. Commun.,* **172**, 59 (1999); D.J. Jones, S.A. Diddams, J.K. Ranka, A. Stentz, R.S. Windeler, J.L. Hall, and S.T. Cundi, *Science,* **288**, 635 (2000); R. Holzwarth, M.

Zimmermann, Th. Udem, and T.W. Hänsch, *IEEE J. Quantum Electron.* **37**, 1493 (2001).

13. J. Reichert, M. Niering, R. Holzwarth and M. Weitz, Th. Udem and T.W. Hänsch, *Phys. Rev. Lett.* **84**, 3232 (2000).

14. R. Holzwarth, Th. Udem, T.W. Hänsch, J.C. Knight, W.J. Wadsworth and P.St.J. Russell, *Phys. Rev. Lett,* **85**, 2264 (2000).

15. S.A. Diddams, D.J. Jones, J. Ye, S.T. Cundiff and J.L. Hall, *Phys. Rev. Lett.* **84**, 5102 (2000).

16. J. Stenger, T. Binnewies, G. Wilpers, F. Riehle, H.R. Telle, J.K. Ranka, R.S. Windeler and A.J. Stentz, *Phys. Rev.* A **63**, 021802(R) (2001).

17. Th. Udem, A.A. Diddams, K.R. Vogel, C.W. Oates, E.A. Curtis, W.D. Lee, W.M. Itano, R.E. Drullinger, J.C. Bergquist and L. Hollberg, *Phys. Rev. Lett.* **86**, 4996 (2001).

18. J. Stenger, Chr. Tamm, N. Haverkamp, S. Weyers and H.R. Telle, *Opt. Lett.* **26**, 1589 (2001).

19. S.N. Lea, et al., *Proc. 6th Symp. on Frequency Standards and Metrology,* Singapore (2002).

20. Th. Udem, J. Reichert, R. Holzwarth and T.W. Hänsch, *Opt. Lett.* **24**, 881 (1999).

21. S.N. Bagayev, S.V. Chepurov, V.M. Klementyev, S.A. Kuznetsov, V.S. Pivtsov, V.V. Pokasov and V.F. Zakharyash, *Appl. Phys. B* **70**, 375 (2000); S.N. Bagayev, S.V. Chepurov, V.M. Klementyev, D.B. Kolker, S.A Kuznetsov, Yu.A. Matyugin, V.S. Pivtsov, M.N. Skvortsov and V.F. Zakharyash, *Quantum Electronics* **31**, 383 (2001).

22. S.N. Bagayev, A.K. Dmitriyev, S.V. Chepurov, A.S. Dychkov, V.M. Klementyev, D.B. Kolker, S.A. Kuznetsov, Yu.A. Matyugin, M.V. Okhapkin, V.S. Pivtsov, M.N. Skvortsov, V.F. Zakharyash, T.A. Birks, W.J. Wadsworth and P.St.J. Russell, *Laser Physics* **11***, 1270 (2001).

23. M.V. Okhapkin, M.N. Skvortsov, A.M. Belkin, N.L. Kvashnin and S.N. Bagayev, *Opt. Commun.* **203**, 359 (2002).

24. A.W. Snyder and J.D. Love, *Optical Waveguide Theory* (Chapman and Hall, London, 1983) p. 253.

25. D. Marcuse, *Light Transmission Optics* (van Nostrand Reinhold, New York, 1982) p.12.

26. G.P. Agrawal, *Nonlinear Fibre Optics* (Boston, Academic, 1989).

27. S.M. Kobtsev, S.V. Kukarin and N.V. Fateev, *Quantum Electronics* **32**, 11 (2002); J. Teipel, K. Franke, D. Turke, F. Warken, D. Meiser, M. Leuschner and H. Giessen, *Appl. Phys. B* **77**, 245 (2003).

28. S.N. Bagayev, V.I. Denisov, V.F. Zakharyash, V.M. Klementyev, I.I. Korel, S.A. Kuznetsov, V.S. Pivtsov and S.V. Chepurov, *Quantum Electronics* **33**, 883 (2003).

29. A. Hasegawa and F. Tappert, *Appl. Phys. Lett.,* **23**, 142 (1973); R.K. Dodd et al., *Solitons and Nonlinear Wave Equations* (Academic, New York, 1982).

30. T. Taniuiti and H. Washimi, *Phys. Rev. Lett.* **21**, 209 (1968); A. Hasegawa, *Opt. Lett.* **9**, 288 (1984).

31. J. Hermann et al., *Phys. Rev. Lett.* **88**, 17 (2002).

32. D. Eliyahu, R.A. Salvatore and A. Yariv, *J. Opt. Soc. Am. B* **13**, 7 (1996); I.G. Fuss, *IEEE J. Quantum Electron.* **30**, 2707 (1994).

33. R.A. Fisher and W.K. Bischel, *Appl. Phys. Lett.* **23**, 661 (1973).

34. N. Tzoar and M. Jain, *Phys. Rev. A* **23**, 1266 (1981).

35. E.M. Dianov et al., *JETP Letters* **41**, 242 (1985).

36. B.R. Washburn, S.E. Ralph and R.S. Windeler, *Optics Express* **10**, 575 (2002).

37. S.N.Bagayev, V.F.Zakharyash, V.M.Klementyev, V.S.Pivtsov and S.V.Chepurov, *Quantum Electron.* **27**, 317 (1997).

Chapter 5

INFRARED PRECISION SPECTROSCOPY USING FEMTOSECOND-LASER-BASED OPTICAL FREQUENCY-COMB SYNTHESIZERS

P. De Natale, P. Cancio and D. Mazzotti
Istituto Nazionale di Ottica Applicata (INOA)
Largo Fermi 6, 50125 Florence, Italy and
European Laboratory for Nonlinear Spectroscopy (LENS)
Via Carrara 1, 50019 Sesto Fiorentino FI, Italy
denatale@inoa.it, pcp@inoa.it, mazzotti@inoa.it

Abstract   Femtosecond-laser-based optical frequency comb synthesizers (OFSs) can play a fundamental role in precision spectroscopy and laser frequency control in the infrared (IR), as has happened in the visible and near-IR regions of the spectrum. Increasing demand for precise frequency measurements in the IR has resulted in a number of ideas for IR frequency synthesis (IFS) with visible combs. IR frequency synthesis and measurement require narrow linewidth, well-controlled and often widely tunable laser sources as well as high-accuracy frequency references. In this paper we review the state of the art of IR metrology following the advent of the OFS. In particular, we describe our system which uses a non-linear difference-frequency-generated (DFG) IR source combined with an OFS to develop a widely tunable IR laser source with very narrow linewidth and with a frequency directly traceable to the Cs primary standard. The frequencies of saturated absorption spectra belonging to the intense molecular ro-vibrational transitions in this region can be measured with our OFS-referenced DFG source. An unprecedented dense grid of secondary frequency standards can be created with this DFG-OFS combination.

Keywords: Kerr-lens mode-locked femtosecond Ti:sapphire laser, optical frequency-comb synthesizer, microstructure fiber, difference-frequency generation, mid-IR frequency metrology, high-resolution molecular spectroscopy.

1.   EVOLUTION OF METROLOGICAL SOURCES IN THE IR: FROM SYNTHESIZED FREQUENCY CHAINS TO FS-OPTICAL FREQUENCY COMBS

Since 1967, when the frequency of the HCN laser at 0.891 THz was measured in terms of the Cs primary standard [1], until the end of the last century, infrared metrology has been evolving in terms of infrared frequency synthesis (IFS). This technique has been used by metrologists to generate intermediate frequencies in order to control and measure very stable IR oscillators against the microwave reference, by building complicated frequency chains [2]. In the 1970s, IFS-based measurements of the $78~\mu m$ and $28~\mu m$ water vapor laser [3] and approximately 100 lines in various branches of the CO_2 laser around $9~\mu m$ and $10~\mu m$ [4] were the intermediate oscillators used to measure, for the first time, the absolute frequency of the most popular IR standard: the $3.39~\mu m$ He-Ne laser locked to the $F_2^{(2)}$ component of the transition $\nu_3, P(7)$ of CH_4 [4]. The present value of the speed of light [5] and the modern definition of the *meter* SI unit [6] arose from this type of measurement. Their use as IR standards, as a bridge between microwave and visible frequencies, did not stop the quest toward more accurate references. In fact, in the 1980s, the accuracy of frequencies at $9\text{--}10~\mu m$ for the CO_2 laser and at $3.39~\mu m$ for the $CH_4/He\text{-}Ne$ laser were improved [7, 8], or $10~\mu m$ standards with new molecular absorbers were realized, e.g., the OsO_4/CO_2 [9] and the SF_6 molecular beam/CO_2 [10].

For IR precision spectroscopy, these metrological oscillators have played the role of secondary frequency standards for heterodyne molecular spectroscopy. The frequencies of more than 35 000 molecular transitions in the wavelength range between 2.3 and $20.6~\mu m$ were measured using this technique [11]. Similar heterodyne spectroscopy on molecular rotational transitions in the far-IR between 200 and $2\,600~\mu m$ [12] was performed by down-conversion of CO_2 laser differences in a metal-insulator-metal (MIM) diode [13, 14]. These measurements, together with other data coming from Fourier-Transform IR molecular spectroscopy, provide, at present, a precise calibration frequency atlas for high-resolution molecular spectroscopy in the IR [12].

Apart from the complexity, the large dimensions, the high cost and the considerable effort required to build and operate IFS chains, another significant drawback is that they are designed to measure just one IR/optical frequency or to satisfy a specific spectroscopic application. A new approach was required by the metrological and spectroscopic community to vastly simplify IR/optical frequency measurements. The idea was to create a precise ruler in the frequency domain, made of an equally spaced series of calibrated frequency spikes, thus called "optical frequency comb" (OFC). Such an OFC can be generated by looking in the frequency domain at the Fourier-transformed spectrum of a time-domain repetitive short laser pulse envelope. In the 1990s, a strong effort was

made to apply this idea by the group of Ohtsu and co-workers in the region of the near-IR with the so-called Fabry-Perot electro-optic (FPEO) OFC [15, 16]. In their set-up, the pulse envelope train was generated by very efficient external phase modulation of a narrow-linewidth stabilized continuous-wave (CW) laser whose frequency was known. OFCs with an operation range up to 50 THz around $1.55\ \mu m$ were developed by expanding the conventional FPEO-OFC by self-phase-modulation in a fiber [17]. They were used not only for metrology and precision spectroscopy applications [18] but also, and particularly in this spectral region, for communication applications [19]. In other spectral regions, such as the visible or mid-IR, where efficient FPEO modulation is technically difficult to achieve, we had to wait until the end of the last century to see the first visible OFC based on a mode-locked fs laser [20, 21]. This system, based on the pioneering work in the 1970s [22], consists of an OFC that covers the large (several THz) emission band of an optically-pumped mode-locked fs Ti:sapphire laser around 800 nm. By broadening up to an octave the emitted spectrum from these sources with self-phase-modulation and four-wave mixing in photonic fibers [23] or by constructing mode-locked laser sources with ultra-short pulses [24], a compact and reliable all-solid-state optical frequency synthesizer (OFS) has been developed that can basically measure any optical frequency against the Cs primary standard [25]. With the advent of this device, not only metrological institutes but also small-scale spectroscopic laboratories, can measure or synthesize any optical frequency with extreme precision. In fact, in the last six years, visible OFSs have been used for high-precision spectroscopy of simple atoms such as H [26] or He [27] that are relevant for the determination of fundamental physical constants. Moreover, clock oscillators based on visible transitions of atomic ions (Hg^+ [28], Yb^+ [29] and In^+ [30]) or neutral atoms (Ca [28, 31], Rb [32] and Sr [33]), measured with high precision using the OFS, can now be proposed for a new definition of the *second*.

Although experimental efforts have recently allowed the development of OFSs operating up to $2.3\ \mu m$ using mode-locked fs fiber lasers, at present other methods must be used to extend the OFS spectral coverage to longer wavelengths. A possible approach that has been pursued in our group is to use the visible OFS in combination with frequency down-conversion optical techniques in nonlinear crystals to transfer the visible comb to mid-IR frequencies. This approach has analogies with the work by Evenson and co-workers, who, about twenty years ago, transferred the CO_2 metrological references at 9–$10\ \mu m$ to the far-IR [13].

2.   MOLECULAR TRANSITIONS FOR IR FREQUENCY METROLOGY

A large number of strong, dipole-allowed molecular transitions, because of their fundamental ro-vibrational band structure, fall in the mid-IR region [34]. Their absolute frequency can be precisely measured using high-resolution spectroscopy techniques, e.g., IFS heterodyne spectroscopy [11], as we described in Sect. 1. As a consequence, a natural comb (with not equally spaced teeth) of absolute frequency standards in that wavelength region can be built. The usefulness of such a grid obviously depends on the spectral density of the molecular transitions and on their frequency accuracy and precision. Regarding the former requirement, in Ref. [12] frequencies of more than 35 000 transitions of OCS, CO, CO_2, OsO_4, SF_6, HF, N_2O, SO_2, CS_2 and NO molecules are reported in the wavelength range between 2.3 and 20.6 μm. Graphically, we show this density in the spectral range 3.1–5 μm in Fig. 5.1: in the upper graph, the linestrengths[1] of the most intense ro-vibrational transitions of a few simple molecules (CO, N_2O, CO_2, CH_4, OCS) are plotted. For the latter requirement, the precision of spectroscopic transition frequency measurements is proportional to the ratio of the signal-to-noise (*S/N*) ratio of the recording to the transition linewidth. Apart from *S/N,* which is characteristic of each spectroscopic technique used, measuring narrower transitions is the key to improve the precision by, sometimes, orders of magnitude. In fact, for the measurements reported in [12], the relative precision ranges between 2×10^{-12} and 2×10^{-7}, depending whether the recordings are sub-Doppler or Doppler-limited, respectively. Thus, sub-Doppler spectroscopy is required to obtain a very precise natural IR comb, since very narrow natural linewidths can be potentially achieved in molecular transitions: the natural linewidth of CO_2 transitions around 4.25 μm, for example, is about 200 Hz. Unfortunately, some broadening effects, namely transit-time broadening, collisional broadening, laser linewidth and power broadening, prevent the achievement of the natural-linewidth limit of sub-Doppler spectroscopy. Although some techniques can be implemented to minimize these effects, e.g., spectroscopy with slow molecules and long absorption paths [8, 36] or Ramsey interference spectroscopy with molecular beams [10], frequency measurements of IR molecular transitions using saturation spectroscopy can achieve relative precisions of about 10^{-10} or even better. The final uncertainty also depends on systematic effects, that can vary in nature: from the accuracy of the frequency reference chosen to link the molecular transition frequency to the primary standard to uncontrolled line-shifts and/or line-asymmetries. An accurate measurement and/or control of systematic effects is needed to create a grid of secondary frequency standards.

---

[1] Data and units from the HITRAN database

In the lower graph of Fig. 5.1 we have plotted the squared dipole moments of the same molecular transitions as shown in the upper graph. This graph gives a quantitative indication of the intensity necessary to saturate these transitions, since the saturation intensity is proportional to the squared dipole moment. We note that transitions belonging to the same ro-vibrational band have almost the same saturation intensity, whereas they have different absorbances (i.e., differ-
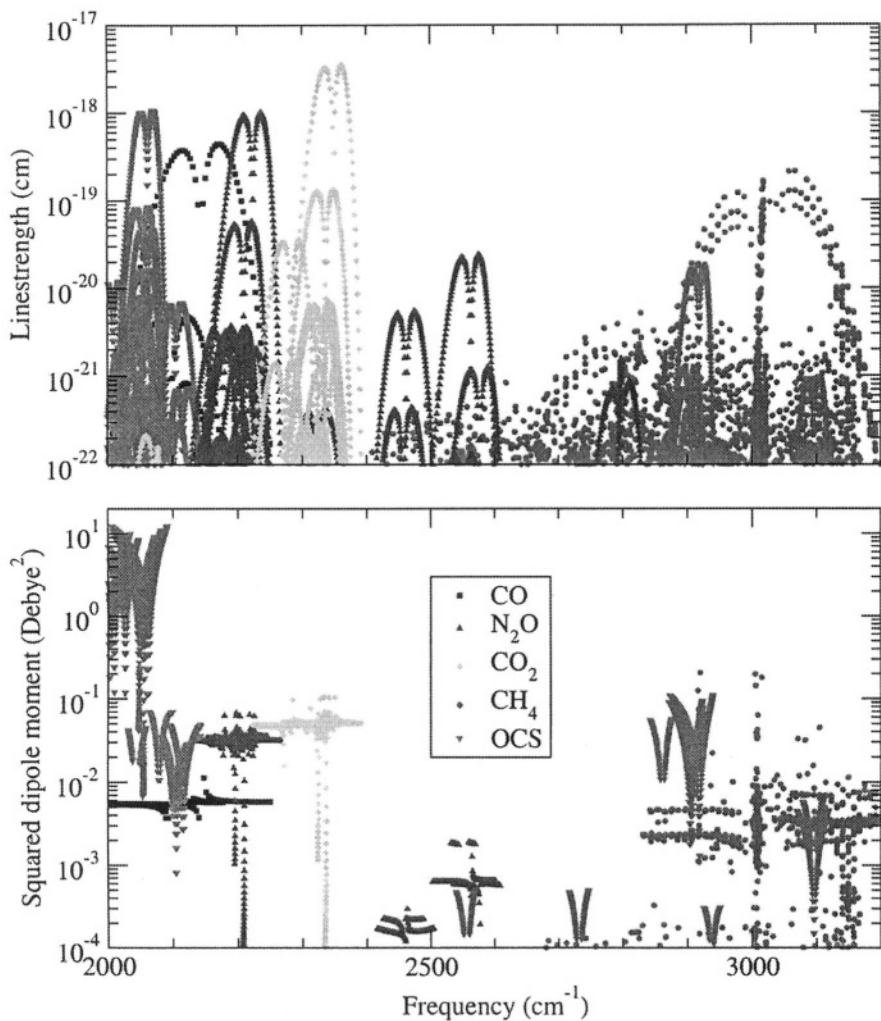
Figure 5.1. Infrared spectra of five common molecular species at 296 K temperature (Picture from [35]).

ent linestrengths), due to different energy-level populations. Since observing saturated transitions in the same ro-vibrational band with similar *S/N* requires at least the same absorbance level, the number of absorbing molecules (i.e., pressure) must be increased, or spectroscopic techniques with longer absorption paths must be used.
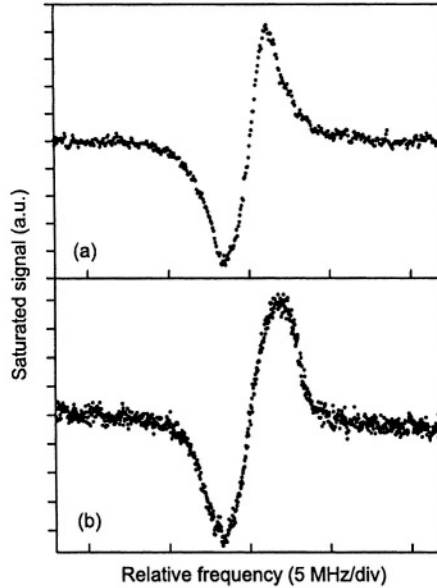
Figure 5.2. First-derivative saturated absorption spectra of some ro-vibrational transitions of the ν_3 band of CO_2 around 4.25 μm. (a) R(14) transition (linestrength $S = 3.5 \times 10^{-18}$ cm, $\nu = 2\,360.109$ cm^{-1}) recorded with a cell, absorption path-length $l = 1$ mm, pressure $P = 6.7$ Pa, beam-waist $w = 35$ μm, *S/N* = 78, full width at half maximum (FWHM) $\Gamma = 2.7$ MHz. (b) R(58) transition ($S = 3.1 \times 10^{-20}$ cm, $\nu = 2\,384.189$ cm^{-1}) recorded with a FP cavity, $l = 40$ m, $P = 0.4$ Pa, $w = 280$ μm, *S/N* = 30, $\Gamma = 3.3$ MHz (Pictures from [38]).

During the last three years, our group has performed sub-Doppler saturated-absorption spectroscopy of CO_2 around 4.25 μm [37–41] by using low-power IR radiation generated by frequency difference in periodically-poled (PP) crystals, as we describe in Sect. 3. Although the first Lamb-dip spectra of the strongest ro-vibrational line (R14) of the ν_3 band of CO_2 were recorded in a cell [38], Lamb dips with similar or better *S/N* were measured for weaker lines when the IR radiation was coupled to a Fabry-Perot (FP) cavity to enhance the absorption path length [40, 41]. In Fig. 5.2, we show two first-derivative saturated absorption spectra of the R(14) and R(58) lines recorded in a cell and in a FP cavity, respectively. Although their linestrengths differ by more than two orders of magnitude, a comparable *S/N* was observed for the weaker line

R(58). Similar results were obtained for transitions such as R(76) or R(82), whose linestrengths differ by more than four orders of magnitude with respect to R(14). Another important improvement coming from the use of a FP cavity is the intensity enhancement of the IR radiation interacting with molecules. As a consequence, saturation spectroscopy can be performed with low-power laser sources or, for a given laser power, higher saturation intensities can be achieved. Moreover, a reduction of the transit-time broadening is expected since a larger beam-waist can be used to obtain the same saturation intensity.

3.   IR COHERENT SOURCES

In this section we give an overview of the state of the art of coherent light sources in the IR for precision molecular spectroscopy. In this field, novel sources, still under development, could contribute by allowing the development of next generation photonic devices, as described in Sect. 3.2. An example of such a new photonic device, combining a DFG spectrometer and a visible OFS, is given in Sect. 4.2.

3.1   Present Coherent Sources

Tunable coherent sources are generally based on one or a combination of three mechanisms: a wide enough gain curve, tuning of the gain curve by external parameters, e.g., temperature, or frequency mixing in appropriate nonlinear materials [42].

At longer wavelengths, from 9–10 μm up to several hundred μm, molecular lasers relying on ro-vibrational transitions for the stimulated emission have been operated at high gas pressures, to overcome the Doppler limit on the gain width for each line. At gas pressures of several bar, where Lorentzian-shaped profiles dominate, typical separations of several tens of GHz between adjacent lines in CO_2 lasers have been bridged and a continuous emission profile has been obtained. Similar configurations have been used with other molecular lasers.

On the other side of the IR spectrum and for a limited time, color-center lasers were the infrared counterpart of dye lasers in the visible region. Based on wide gain curves due to added imperfections in the lattice of alkali halide crystals, further broadened by phonon interaction, they are able to emit CW radiation in the 1–3 μm wavelength range. Typical linewidths for these sources are a few hundred kHz and the best performances go down to few tens of kHz [43]. The difficult operation and maintenance of color-center lasers, together with their cost, has probably caused the disappearance of such sources from most laboratories.

A very important role has been played, as IR tunable sources, by semiconductor diode lasers. Cryogenically-cooled devices have been used at longer wavelengths, up to a few tens of μm, but the broad linewidth, the often multi-

mode emission and the low powers (generally less than 1 mW) have limited their range of application. The technology of room-temperature operated devices, on the other hand, has greatly improved in the last fifteen years, mainly driven by the telecommunication market. The result is that, nowadays, a very wide range of products, encompassing the visible up to about 2 μm is available. As is well known, the main advantages of these lasers are the compactness, the relatively low cost and wide availability, the high-quality standard, the wide range of available configurations and the very wide continuous tunability. These motivations have made semiconductor diode lasers wide-spread in any IR spectroscopic application, from sensing applications in field work [44] to cutting-edge measurements for frequency metrology [28].

Beyond 2 μm wavelength, semiconductors more recently have been engineered to generate relatively high power (up to about 100 mW) in single mode from the so-called "quantum-cascade lasers" [45]. CW operation of these lasers, generally cryogenically cooled, has been demonstrated in the 2–85 μm range. They have found application for high-resolution spectroscopy [46, 47], although their availability is still very limited and the need for cryostats does not favor their use. More demanding spectroscopic applications require a narrow laser linewidth that, for quantum-cascade lasers, is basically determined by the noise of the power supply that has, at the same time, to provide currents in the few ampere range. To date, there have been few demonstrations of sub-Doppler recordings with quantum-cascade lasers [48]. The possibility to "tailor" the semiconductor structure to obtain emission at the desired wavelength is paving the way to simultaneous multi-wavelength emission [49].

In parallel with diode lasers, a major development has been experienced in recent years by IR-emitting solid-state lasers. Apart from classical Nd:YAG lasers at 1 064 nm, now delivering up to several watts with a linewidth at the kHz level, other combinations of active and host materials, e.g., Tm:Ho:YAG, have allowed single-mode tunable emission even beyond 2 μm wavelength, with powers up to 100 mW [50].

A similar development has been experienced by fiber lasers and amplifiers, that have also benefited from much improved pumping diodes [51]. As for semiconductor lasers, the very rapid improvement of fiber-based sources has been driven by telecommunication applications. While frequency tunability in fiber lasers is mostly obtained by compressing and stretching the fiber, generally using piezo-electric actuators, optical injection is used for tuning fiber amplifiers [52]. Particularly interesting for infrared high-resolution spectroscopy could be fiber lasers based on stimulated Raman scattering, for a potentially wide tunability range [53].

Beyond the 2 μm wavelength region, mostly nonlinear frequency mixing techniques can provide tunable radiation. Nonlinear frequency mixing originates from the interaction of sufficiently high intensity electromagnetic fields

with transparent dielectric media which, along given directions that depend on the crystal structure and chemical composition, allow electrons to be moved sufficiently far from their rest orbitals. This peculiar material property is expressed in terms of the polarization **P** which, when expanded as a Taylor series, gives rise to nonlinear terms:

$$\mathbf{P} = \epsilon_0 (\chi^{(1)} \mathbf{E} + \chi^{(2)} \mathbf{EE} + \chi^{(3)} \mathbf{EEE} + \ldots), \qquad (5.1)$$

where the susceptibility tensors $\chi^{(i)}$, of rank $i + 1$, only depend on the dielectric and **E** is the electric field. Most IR tunable sources rely for frequency generation on the second order $\chi^{(2)}$ term, which can give rise to the strongest nonlinear effects in materials with the required symmetry. In particular, the two $\chi^{(2)}$ driven processes that are relevant to IR generation are parametric and difference frequency down-conversion. A breakthrough for IR sources based on nonlinear processes has resulted from the introduction in the last decade of periodically-poled (PP)-crystals that have, at the same time, significantly increased the conversion efficiency, widened the possible frequency combinations to the whole transparency range of each specific PP-crystal, and made less critical the achievement of phase-matching conditions, when compared to more traditional birefringent phase matching [54].

The development of CW optical parametric oscillators (OPO) has benefited strongly from PP-crystal technology, which makes it possible to build devices with a much lower oscillation threshold, thus requiring a pump power that is orders of magnitude lower than before. Hence, very compact all-solid-state devices can be built that are able, using a single pumping source, to deliver powers up to several hundred mW. Operation of OPOs up to about $4.5 \ \mu$m has been obtained, mainly using $KTiOPO_4$ (KTP) and $LiNbO_3$ PP-crystals, and their application to high-resolution spectroscopy has been demonstrated [55, 56]. However, the full application potential, in terms of high power and wide tunability, of these devices seems to be not yet fully exploited, probably due to the complicated set-ups required and to the difficult control of the instantaneous emitted wavelength.

Sources operating up to about $5 \ \mu$m, based on difference-frequency generation (DFG) processes, make use of basically the same materials used for OPOs and the enhanced efficiency afforded by PP-crystals has allowed single-pass operation with generation of powers exceeding 1 mW [57, 58]. The intrinsic simplicity of IR frequency control of DFG set-ups routinely allows sub-Doppler molecular spectroscopy, when narrow linewidth and low-noise pumping sources are used. Indeed, high-resolution sub-Doppler spectroscopy of CO_2 around $4.25 \ \mu$m was performed with a DFG-based IR source [59, 38, 40, 41]. This source uses a 150 mW diode laser at 850 nm and a 800 mW Nd:YAG laser at 1 064 nm as pump and signal lasers mixed in a 40 mm-long $LiNbO_3$ PP-crystal. Under these conditions, up to $12 \ \mu$W of radiation at $4.25 \ \mu$m was generated with

a quantum-limited intensity noise in a 5 kHz bandwidth [59]. The linewidth of the generated IR is a few hundred kHz, limited by the pump diode laser. Indeed, this laser is mounted in a master/slave configuration to reduce its linewidth from several MHz to about 500 kHz. These spectroscopic and intensity-noise characteristics of our source, even with the low power generated, allowed us to perform very sensitive spectroscopy [60, 61] and to observe saturated-absorption spectra of CO_2 transitions [38, 40], as we have explained in Sect. 2. Recently, the IR generated power of this DFG source has been boosted up to $170 \ \mu W$ by amplifying up to 5 W the Nd:YAG laser with a Yb fiber amplifier [41]. With this power, saturated transitions of other molecules with higher saturation intensity, or of less abundant isotopes can be observed: in Ref. [41], saturation spectroscopy of $^{16}OC^{17}O$ in natural abundance has been performed.

Beyond the transparency range of $LiNbO_3$ and $RbTiOAsO_4$ (RTA), other non-PP birefringent materials have been used, such as $AgGaS_2$, $AgGaSe_2$ and GaSe, to generate IR radiation at wavelengths up to $20 \ \mu m$ [62]. The combination of powerful and narrow linewidth fiber-based sources and nonlinear generation seems to be very promising also for remote sensing and *in situ* applications [63].

For more than twenty years the longer wavelength spectral range, up to millimeter waves, has been the domain of another class of mixers, namely MIM and metal-semiconductor (Schottky) diodes [13]. The very low conversion efficiency of these mixers only allows CW generation with powers up to a few μW. However, their extremely wide bandwidth, especially for the MIM diode that can be operated from RF to visible frequencies, allows interrogation of molecular and atomic transitions over a very wide tunability range. As an example, the tunable far-IR spectrometer, when pumped by metrological-grade CO_2 lasers, has been used to generate radiation in the $1 \ mm - 50 \ \mu m$ spectral range, and high-resolution atomic and molecular spectroscopic studies in this interval could be performed [12]. To date, though other solid state mixers have been tested for the far-IR region [64], the MIM diode still represents the mixer (also working as emitter) with the widest bandwidth. Coherent radiation generation in MIM diodes, using gas lasers, has been extended to about 8 THz [65], whereas mixing using semiconductor sources has given encouraging results [66].

3.2   Future IR Sources and Materials

The present trend indicates that, in the near future, gas lasers will be more and more superseded by solid-state sources including, in this category, semiconductor and fiber-based systems. Furthermore, efficient spectral coverage of wide spectral intervals, like the IR region, will increasingly require sources based on frequency generation by nonlinear mixing processes. New doping ions and crystalline hosts are under development as active IR laser materials

in solid-state lasers [67], while polycrystalline ceramic materials will increasingly allow manufacture of very high-power laser sources [68]. Powers higher than 250 W have already been obtained by Yb-doped fiber lasers [69], and wavelengths up to about $2\ \mu$m are emitted by Tm-doped fiber lasers with 14 W power and 215 nm tuning range [70]. However, if a narrow linewidth is peculiar to lasing in doped crystals, fiber-based lasers operating around $2\ \mu$m still require significant improvements to become useful tools for precision spectroscopy. Semiconductor diode lasers are more and more reliable, powerful and low-noise pumping sources for these laser systems. On the other hand, quantum-cascade lasers should increasingly assume a leading role for IR precision spectroscopy, though the present need of temperature tuning around low temperatures[2] for wavelength-tunable, CW operation may represent a serious limitation for sub-Doppler spectroscopy. Indeed, a fluctuation as low as 10 mK in the cryostat servo-controlled temperature may result in a laser frequency jitter of 10 MHz[3], which should be compared with typical molecular sub-Doppler linewidths of less than 1 MHz. Room temperature operation and pulsed regime have been tested for these lasers, which have proved to be useful for Doppler-limited spectroscopy [47]. Synthesized frequencies, generated by nonlinear parametric processes or difference-frequency down-conversion, are increasingly benefiting from improved nonlinear materials and processes as well as from better optoelectronic devices. Micro-machining of nonlinear crystals in order to fabricate "photonic bandgap" materials, seems promising for building new photonic devices [71]. This new class of components relies on the periodicity of the refractive index to create a "bandgap" for photons (in analogy with what happens for electrons confined in semiconductors) which experience a periodic ionic potential in semiconductor lattices. Following this analogy, a very strict periodicity in photonic materials and a high contrast of refractive index are needed to allow the creation of 1-D, 2-D or 3-D band-gaps. Engineering of semiconductor materials can provide very high $\chi^{(2)}$ values and a wavelength transparency range up to about $20\ \mu$m [72]. Semiconductors are therefore very promising for IR sources based on nonlinear generation, also for the possibility they offer of integration with diode laser pumping sources. They could help to obtain continuous spectral coverage of the so-called molecular "fingerprint" region, that conventionally extends from 3 to $15\ \mu$m, using very compact and rugged coherent sources.

---

[2] Typical values are close to 77 K

[3] Assuming a frequency tuning of 1 GHz/K

4.   EXTENDING VISIBLE/NEAR-IR FS COMBS TO THE MID-IR

4.1   Visible/Near-IR Combs

Currently, as explained in Sect. 1, visible OFSs are based on mode-locked fs Ti:sapphire lasers. In the late 1980s Ti:sapphire was a newly discovered solid-state laser material that had the necessary broad gain bandwidth to support fs pulses [73]. In fact, just a few years later self-starting passive mode locking was first discovered [74, 75] and then explained [76, 77]. Mode-locked lasers generate short optical pulses by establishing a fixed phase relationship between all of the lasing longitudinal modes [78]. Mode locking requires a mechanism that results in higher net gain for short pulses compared to CW operation. This can be achieved either by means of an active element or passively by means of a saturable absorber (real or effective). Passive mode locking yields the shortest pulses because, up to a limit, the self-adjusting mechanism becomes more effective as the pulse shortens [79]. Effective saturable absorption typically utilizes the nonlinear index of refraction of some material together with spatial effects or interference to produce higher net gain for shorter pulses. Currently, the generation of ultrashort optical pulses is dominated by the Kerr-lens mode-locked Ti:sapphire laser because of its excellent performance and relative simplicity [80]. Since Kerr-lens mode locking produces a non-resonant saturable absorber, it is inherently broad-band and thus capable of generating ultrashort pulses, down to 5 fs [81–83], which corresponds to less than two cycles of the laser light. As lasing in Ti:sapphire occurs in a wide band of longitudinal modes, compensation of the group velocity dispersion (GVD) is required to obtain short fs pulses. GVD was first achieved by a pair of intracavity prisms [84]; then it was greatly improved by the optimization of the intracavity dispersion [85] and by the invention of "chirped" mirrors [86, 87], recently upgraded to doubly chirped mirrors [81, 82].

Starting from the time evolution of a mode-locked laser emitting a periodic train of short pulses, it can be shown [22, 88] that the corresponding optical spectrum has the form of an OFC with equally spaced teeth, whose frequencies can be written as

$$\nu_n = n\nu_r + \nu_0, \qquad (5.2)$$

where n is an integer number, ν_r is the repetition rate of the pulse train and ν_0 is the carrier-envelope offset frequency. ν_0 is the frequency offset with respect to the absolute zero frequency due to the carrier/envelope phase shift $\Delta\phi_0$. The pulse-to-pulse phase change $\Delta\phi_0$ in the pulse train emitted by a mode-locked laser occurs because the phase and group velocities inside the cavity are different, due to dispersion in all optical elements.

Determining the absolute optical frequencies of comb teeth requires that both ν_r and ν_0 are measured and/or controlled, relative to the Cs primary standard

at 9 192 631 770 Hz. Measurement of ν_r is straightforward: since ν_r typically ranges from tens of MHz to a few GHz, one simply must detect the pulse train with a fast photodiode. However, measurement of ν_0 is not so simple: a photodiode is not sensitive to phase, but only to intensity. If the OFS spectrum spans at least an octave in frequency, an interferometric measurement of ν_0 is possible. If the "red" portion of the comb spectrum is frequency doubled by a nonlinear crystal and the second-harmonic-generated (SHG) radiation $(2\nu_n)$ is allowed to beat with the corresponding direct "green" portion of the comb spectrum (ν_{2n}), the heterodyne frequency difference (from Eq. 5.2) is just the ν_0 frequency. This method is designated as self-referencing, since it only relies on the output of the mode-locked laser. A self-referenced OFS is the simplest and most elegant way to measure and control ν_0, but it is not strictly required [89]. Electronic servo loops are used to actively stabilize the measured ν_r and ν_0 frequencies to a Cs-referenced RF synthesized signal. The laser cavity length is varied using a piezo-mounted mirror to stabilize ν_r. In the first optical combs, in order to stabilize ν_0, the end mirror was swiveled in the arm of the laser cavity that contains the prism sequence [90]. At present, amplitude modulation of the pump laser [91–95] is the most commonly used method. Finally, when the comb spectrum is used as a frequency ruler to measure the absolute frequency of an unknown CW laser, also the integer order n of the nearest comb tooth has to be determined. To do this, a preliminary coarse measurement of the CW laser frequency by use of a wavelength-meter with an uncertainty better than $\nu_r/2$ is required.

Obtaining a self-referenced OFS is not a straight-forward task. Although octave-spanning teeth generation is not strictly required[4], mode-locked Ti:sapphire lasers with the shortest pulse duration developed so far [83, 24] do not provide the octave-spanning condition[5], limited by the gain bandwidth of the Ti:sapphire material. Additional frequencies must be generated for this purpose. At present, this is accomplished by using optical fibers, external to the laser cavity. In these fibers, mainly self-phase modulation [53] and nonlinear optical effects (four-wave mixing) are responsible for the OFS spectral broadening. The amount of broadening that can be obtained in ordinary optical fibers is limited, primarily because the temporal spreading of the pulse, due to the group velocity dispersion, reduces the peak intensity. Using a low-repetition-rate laser to raise the pulse energy, an octave-spanning spectrum has been obtained with an ordinary fiber [91]. The discovery [98] that air-silica microstructure (photonic) fibers have zero GVD within the emission spectrum of a Ti:sapphire laser eliminated

---

[4]Experimentally, it has been found that even if the power at the octave-spanning points is 40 dB below the peak, it is still possible to observe strong f-to-$2f$ heterodyne beats

[5]These sources can be used as self-referenced combs [96, 97], but in this case the $2f$-to-$3f$ beat is used to control the ν_0 frequency

this difficulty and led to rapid progress in the field of fs OFCs by allowing continuum generation with only nJ pulse energies [23]. The zero GVD in these fibers is due to their large index of refraction contrast, which implies also the possibility of using a much smaller core size. This largely increases the light intensity in the core, thereby enhancing nonlinear effects. As simpler alternatives to microstructure fibers, tapered silica fibers [99, 100] and highly nonlinear fibers made of Ge-doped silica [101] have achieved an octave-spanning spectral broadening.

Currently, laser frequencies corresponding to wavelengths up to 1100 nm can be measured by fs-Ti:sapphire-laser-based OFSs broadened in photonic fibers. Indeed, we have recently reported a frequency measurement at 1 083 nm by using an OFS of this type [27]. In our OFS, the photonic fiber was specially designed to produce sufficient intensity for measurements at these limiting frequencies. Another mode-locked fs source must be used for longer wavelengths. Recently, a strong effort was made in this sense combining mode-locked fs fiber lasers with photonic fibers [101–106]. With these systems, the spectral coverage of fs-laser-based OFSs combined with broadening fibers allows operation in the near-UV/near-IR region (350–2 300 nm).

4.2   Bridging the Gap with Difference Frequency Generation and Optical Parametric Oscillators

Frequency down- and up-conversion techniques have long been used whenever appropriate frequency references were not available within the tuning range of the coherent source in use. This approach was particularly important when stable references were available in very limited number, due to the fortuitous coincidence of appropriate atomic or molecular transitions and laser sources. Frequency chains themselves, discussed in Sect. 1, are examples of such setups, though much more complicated, always using as reference the Cs primary standard. As we have also discussed in previous sections, these nonlinear frequency conversion techniques have been replaced by the OFS in the visible-near IR range of the spectrum. However, IR coverage of OFCs is limited mainly by fiber losses and by the emitted bandwidth of presently used fs lasers. Regularly spaced spikes can then represent ideal "harbors" that can always be used for locking any other source at visible/near-IR wavelengths. It is therefore quite natural to think of nonlinear optical frequency down-converters, such as DFG and OPOs, for transferring OFC-based metrology to the intermediate IR range. Indeed, both devices rely on three input/output frequencies, two of which can be in principle locked to an OFS, the third being thereby determined. Until now, DFG sources have proved to be better suited for very precise sub-Doppler spectroscopy, mainly due to the deterministic link between the two input frequencies and the frequency of the generated radiation. Further combination

with an OFS, with additional servo loops for phase locks, requires the simplest possible configuration that, again, favors the use of DFG over OPOs.

In the following we briefly describe the operation principles of our DFG-OFS combined system [107, 108] with a view to the potential of such a device for IR frequency metrology. In Fig. 5.3 we graphically show the set-up of our experimental apparatus. The IR laser is a DFG-based source which uses a 850 nm diode laser and a 1 064 nm Nd:YAG laser as the pump and signal lasers of the DFG process as described in Sect. 3. Our OFS is a commercial prototype[6] that uses a 30 fs and 1 GHz repetition rate mode-locked Ti:sapphire laser as the comb source. The system is self-referenced with a spectral coverage from 500 to 1100 nm. The offset and repetition-rate frequencies are controlled and traceable to the Cs primary standard by locking to a very stable GPS-disciplined 10 MHz quartz oscillator. To transfer the OFS metrology to the IR, both pump and signal DFG lasers are phase-locked to the closest corresponding teeth of the OFS. A hybrid digital/analog electronics is used for locking the two DFG lasers to the comb. Therefore, the frequency of the IR radiation is automatically determined by the OFS repetition frequency, the comb mode numbers for the pump/signal frequencies ν_p and ν_s, and the RF beat note between the pump/signal lasers and these comb modes. We note that the first important advantage of the DFG-OFS combination is that the IR frequency does not depend on the OFS offset frequency parameter, which simplifies the system operation and makes it suitable even with OFSs that are not self-referenced. The comb oscillator stability, which is $< 3 \times 10^{-13}$ for a time scale $1 \text{ s} < \tau < 30 \text{ s}$ given by the quartz oscillator stability, determines the ultimate precision of the IR frequency, when robust phase locks of the pump/signal lasers are achieved. Moreover, the idler IR frequency accuracy of 1×10^{-13} is directly traceable to the Cs primary standard via the GPS system.

Another important feature of the DFG-OFS system is a drastic reduction of the idler radiation linewidth due to the fact that the OFS is actually used as a broad-band mixer to maintain the phase relationship between pump and signal DFG lasers. The idler linewidth can be narrowed to a limit mainly depending on the linewidth of the comb tooth closest to the pump frequency, Γ_c, and on the quality of the phase-locked loops. Ideally, with perfect phase-locked loops, this limit is given by $(1 - \nu_s/\nu_p)\Gamma_c \approx 0.2\Gamma_c$ due to the phase-noise difference between the comb teeth at 1 064 and 850 nm, respectively. In our case Γ_c is about 100–200 kHz mainly due to the phase-noise of the standard 1 GHz frequency, chosen as OFS repetition rate reference, and to the 3.5×10^5 teeth that separate it from the pump frequency. Indeed, the idler linewidth of about 500 kHz is narrowed with the DFG-OFS system to a maximum value of about 20–40 kHz. Narrower linewidths can be achieved by a drastic reduction of

---

[6]MenloSystems model FC8003

the tooth order if an OFS reference closer to the pump and signal frequencies is chosen. As a consequence, the best set-up for maximum idler linewidth reduction should include a visible or near-IR frequency standard to which the OFS can be locked [109, 28].
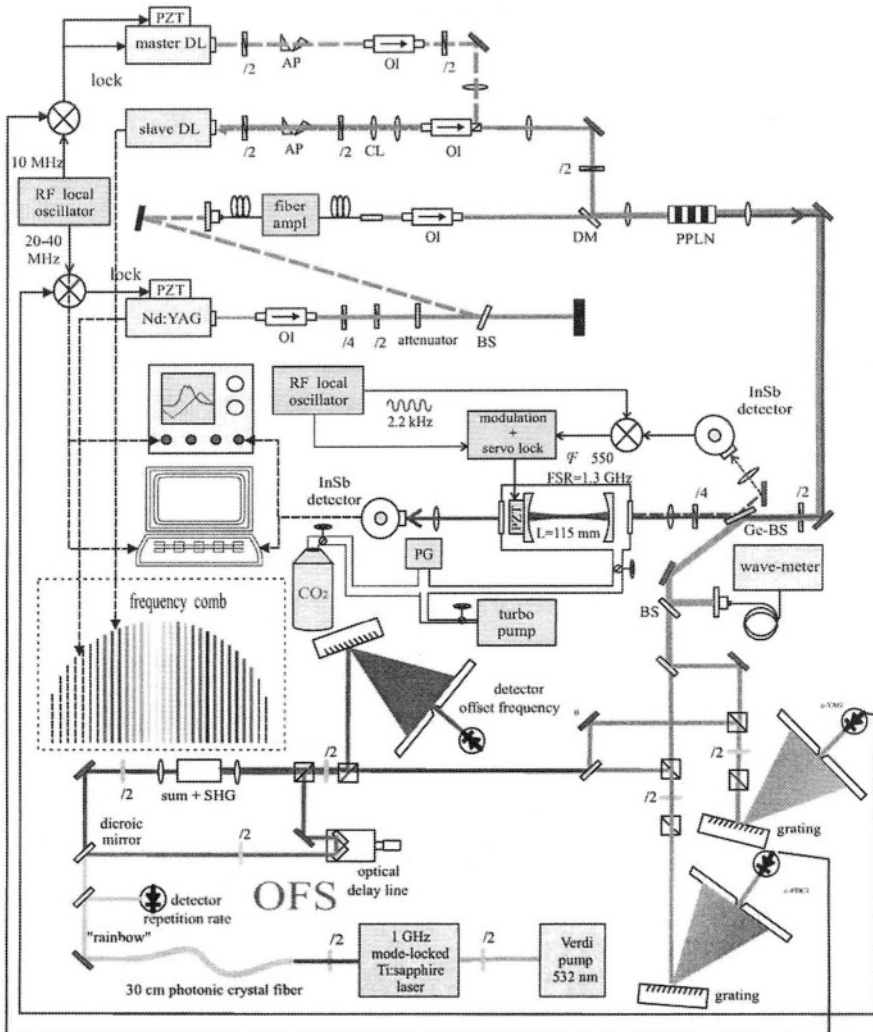
Figure 5.3. Schematic of our DFG-OFS set-up [108]. Legend: PZT = piezo-electric actuator, AP = anamorphic prisms, OI = optical isolator, DL = diode laser, CL = cylindrical lens, DM = dichroic mirror, PPLN = periodically-poled $LiNbO_3$ crystal, BS = beam splitter, FSR = free spectral range, $\lambda/2$, $\lambda/4$ = half-, quarter-wave plates, PG = pressure gauge.

   With such a system, sub-Doppler IR spectroscopy can be performed by using a simple vacuum-tight cell filled with the gas of interest or by using high-finesse FP cavities to enhance the sensitivity, as described in Sect. 2. The drawbacks of a set-up that includes an enhancement cavity are partly due to the added operating complication, especially to the lock between the cavity resonance and the input DFG laser that makes the frequency scan. Moreover, added amplitude noise on the recorded spectrum, mainly depending on the lock quality and on the cavity fringe steepness, must be expected (see Fig. 5.2). The recording in Fig. 5.4 shows a first-derivative lineshape of the CO_2 R(56) ro-vibrational transition recorded with the DFG-OFS system and a FP cavity filled with 0.5 Pa of CO_2.

   This transition is slightly more intense than the R(58) line shown in the bottom part of Fig. 5.2. Since the R(58) transition was recorded using the same DFG source and FP cavity, a direct comparison between these two figures can be made. The frequency scale of this spectrum is absolute, with a precision and an accuracy that are comparable to the values given in the DFG-OFS system described above. Indeed, when a proper fit function is chosen, the absolute frequency of the transition can be measured. The achievable precision depends on the *S/N* and linewidth of the observed signal, whereas the final accuracy depends not only on the idler frequency accuracy, but also on systematic effects that can shift the recorded line center frequency. Among them, subtle effects can be observed, enhanced by the cavity, that can induce line asymmetries.

Figure 5.4. First-derivative saturated-absorption spectra of R(56) ro-vibrational transitions of the ν_3 band of CO_2 at $2\,383.359$ cm^{-1} (linestrength $S = 4.7 \times 10^{-20}$ cm) recorded with the DFG-OFS system and a FP cavity. Path length $l = 40$ m, pressure $P = 0.5$ Pa, beam waist $w = 280\ \mu$m, *S/N* $= 360$, FWHM $\Gamma = 0.7$ MHz.

The *S/N* ratio may be limited by the detection technique, the detector noise-equivalent power, the preamplifier electronics, optical fringing and frequency fluctuation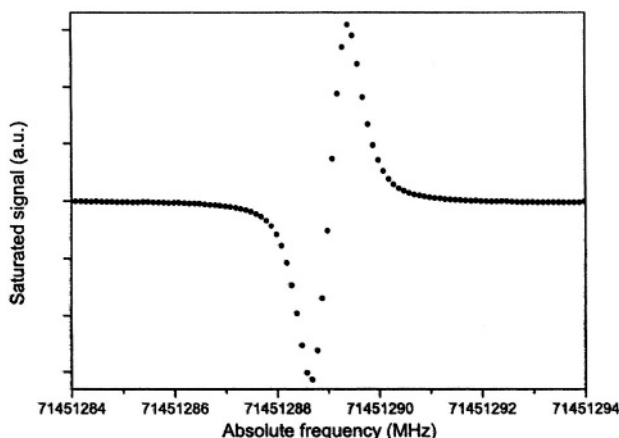s of the IR source with respect to the cavity transmission peak (that acts as frequency to amplitude fluctuation converter). As reported in Ref. [41], these frequency fluctuations were the dominant noise source in our system. Locking the pump and signal lasers to the OFS, the *S/N* was improved by almost 10 times, as can be seen by comparing the recordings of Fig. 5.2 and Fig. 5.4.

It is of special interest to determine the minimum molecular linewidth that can be observed with such a DFG-OFS system, including a Fabry-Perot enhancement cavity. Indeed, the precision of the frequency measurements is inversely proportional to the actual linewidth and, of course, the resolution of the system directly depends on the limiting linewidth. The molecular linewidth is determined by several contributions : natural lifetime (Γ_n), pressure broadening (Γ_p), transit-time broadening (Γ_{tt}) and residual IR source width (Γ_{IR}). For IR molecular transitions, similar to that in Fig. 5.4, Γ_n is about 200 Hz (FWHM), generally negligible with respect to the other contributions. $\Gamma_p = \gamma P_T$ is about 30 kHz, assuming a pressure-broadening coefficient $\gamma \approx 45$ kHz/Pa [110, 61]; $\Gamma_{tt} = 1/(\pi w_0)\sqrt{2k_B T/M}$ is about 380 kHz, where the beam waist at the cavity center is $w_0 = 280\ \mu$m; Γ_{IR} is reduced to $0.2\Gamma_c < 50$ kHz, as indicated above. Power broadening gives just an overall multiplicative correction $\sqrt{1 + I/I_s}$ to the total width, i.e., about 40% increase for $I/I_s \approx 1$. Also, a modulation broadening of about 30% must be included when a modulation index close to unity is chosen [44]. These values give a total linewidth of about 0.8 MHz, which is in agreement with the linewidth measurement for the transition in Fig 5.4. For such a recording, a five-fold linewidth reduction was noticed, with respect to a recording taken with the DFG alone, without locking the lasers to the OFS (see Fig. 5.2 and Fig. 5.4). Further narrowing of the IR idler radiation, e.g., by locking the OFS to a visible standard, could allow one to build a new accurate grid of frequency references in the IR, with an unprecedented spectral coverage and accuracy [35].

5.   CONCLUSIONS AND PERSPECTIVES FOR IR COMBS

Two different worlds that have evolved independently have come together to make possible the present revolution of frequency metrology. The technology of very broad-band, fs pulsed laser sources (OFSs), never considered as metrological tools in the past, has merged with optical standards based on ultrastable, highly monochromatic CW oscillators. A crucial "ingredient" of OFSs is non-linear optics. It enters through Kerr-lens mode locking of the fs laser cavity and through one of the most recent achievements, the "photonic crystal fiber",

which allows the actual spectrum to be spread from the visible blue/green to the near-IR. Again nonlinear optics, by frequency down-conversion in nonlinear crystals, may contribute to extend OFS frequency metrology to the very wide and largely "unexplored" IR region, though full of important molecular "signatures". A further simplification of OFSs is expected to come from all-fiber systems, which should prove especially useful for telecommunication applications. Until new fiber materials for low-loss IR propagation become available, nonlinear frequency down-conversion will be necessary to extend OFS-based metrology to the IR. However, on a medium term timescale, the richness of ro-vibrational transitions, which characterizes the "fingerprint" region, could directly provide a new set of standards. Proper solution to three challenging aspects needs to be found, anyway. The first is related to the capability to saturate a large enough number of transitions. The second requires the recording of linewidths close to the natural linewidth in order to allow precise line center determination. The third, and probably most elusive, aspect is related to systematic effects, which can seriously degrade the final accuracy and reproducibility in frequency determination, if not rigorously taken into account.

As is typical of many important innovations, the number of papers in this field is steeply increasing, new ideas are emerging, and our short account of the "state of the art" is likely to become obsolete quite soon. From this "melting pot" of novel technologies we expect that new, unpredictable effects will come to light, answering many questions and paving the way for new ones.

Acknowledgments

References

1. L. O. Hocker, A. Javan, R. Ramachandra, L. Frenkel and T. Sullivan, *Appl. Phys. Lett.* **10**, 147 (1967).

2. J. S. Wells, K. M. Evenson, G. W. Day and D. Halford, *Proc. IEEE* **60**, 621 (1972).

3. K. M. Evenson, J. S. Wells, L. M. Matarrese and L. B. Elwell, *Appl. Phys. Lett.* **16**, 159 (1970).

4. K. M. Evenson, J. S. Wells, F. R. Petersen, B. L. Danielson and G. W. Day, *Appl. Phys. Lett.* **22**, 192 (1973).

5. K. M. Evenson et al., *Phys. Rev. Lett.* **29**, 1346 (1972).

6. *Metrologia* **19**, 163 (1984).

7.   A. Clairon, B. Dahmani and J. Rutman, *IEEE Trans. Instrum. Meas.* **29**, 268 (1980).

8.   S. N. Bagayev, A. E. Baklanov, V. P. Chebotayev and A. S. Dychkov, *Appl. Phys. B* **48**, 31 (1989).

9.   O. Acef, *IEEE Trans. Instrum. Meas.* **46**, 162 (1994).

10. L. F. Constantin, R. J. Butcher, A. Amy-Klein, C. J. Bordé and C. Chardonnet, *J. Phys. IV Pr.* **10–Pr8**, 199 (2000).

11. A. G. Maki and J. S. Wells, *J. Res. NIST* **97**, 409 (1992).

12. G. Guelachvili et al., *Pure Appl. Chem.* **68**, 193 (1996), and refs. therein.

13. K. M. Evenson, D. A. Jennings and F. R. Petersen, *Appl. Phys. Lett.* **44**, 576 (1984).

14. P. De Natale, M. Bellini, W. Goetz, M. Prevedelli and M. Inguscio, *Phys. Rev. A* **48**, 3757 (1993).

15. M. Kourogi, K. Nakagawa and M. Ohtsu, *IEEE J. Quantum Electron.* **29**, 2693 (1993).

16. M. Kourogi, B. Widiyatmoko, and M. Ohtsu, *IEEE Photonics Technol. Lett.* **8**, 560 (1996).

17. K. Imai, M. Kourogi and M. Ohtsu, *IEEE J. Quantum Electron.* **34**, 54 (1998).

18. C. Ishibashi et al., *Opt. Commun.* **19**, 1777 (1994).

19. T. Morioka, S. Kawanishi, K. Mori and M. Saruwatari, *Electron. Lett.* **30**, 790 (1994).

20. T. Udem, J. Reichert, R. Holzwarth and T. W. Hänsch, *Opt. Lett.* **24**, 881 (1999).

21. T. Udem, J. Reichert, R. Holzwarth and T. W. Hänsch, *Phys. Rev. Lett.* **82**, 3568 (1999).

22. J. N. Eckstein, A. I. Ferguson and T. W. Hänsch, *Phys. Rev. Lett.* **40**, 847 (1978).

23. S. A. Diddams et al., *Phys. Rev. Lett.* **84**, 5102 (2000).

24. A. Bartels and H. Kurz, *Opt. Lett.* **27**, 1839 (2002).

25. T. Udem, R. Holzwarth and T. W. Hänsch, *Nature* **416**, 233 (2002), and refs. therein.

26. M. Niering et al., *Phys. Rev. Lett.* **84**, 5496 (2000).

27. P. Cancio et al., *Phys. Rev. Lett.* **92**, 023001 (2004).

28. T. Udem et al., *Phys. Rev. Lett.* **86**, 4996 (2001).

29. J. Stenger, C. Tamm, N. Haverkamp, S. Weyers and H. R. Telle, *Opt. Lett.* **26**,1589 (2001).

30. J. von Zanthier et al., *Opt. Lett.* **25**, 1729 (2000).

31. J. Stenger et al., *Phys. Rev. A* **63**, 021802 (2001).

32. D. J. Jones et al., *Science* **288**, 635 (2000).

33. G. Ferrari et al., *Phys. Rev. Lett.* **91**, 243002 (2003).

34. G. Herzberg, *Molecular Spectra and Molecular Structure Vols. I, II, II,* Krieger Publishing Company, 2nd edition, 1992.

35. S. Borri, P. Cancio, G. Giusfredi, D. Mazzotti and P. De Natale, in *International Conference on Lasers, Applications, and Technologies: Advanced Lasers and Systems,* volume 5137 of *SPIE Proceedings,* page 339, SPIE, 2003.

36. S. N. Bagayev et al., *Appl. Phys.* **10**, 231 (1976).

37. P. De Natale, G. Giusfredi, P. Cancio, D. Mazzotti and M. Inguscio, in *Laser Spectroscopy – Proceedings of the XIV International Conference (ICOLS99),* page 13, Singapore, 1999, World Scientific Publishing.

38. D. Mazzotti et al., *Opt. Lett.* **25**, 350 (2000).

39. G. Giusfredi, D. Mazzotti, P. Cancio and P. De Natale, *Phys. Rev. Lett.* **87**, 113901 (2001).

40. D. Mazzotti, S. Borri, P. Cancio, G. Giusfredi and P. De Natale, *Opt. Lett.* **27**, 1256 (2002).

41. S. Borri et al., *Appl. Phys. B* **76***, 473 (2003).

42. W. Demtröder, *Laser Spectroscopy,* Advanced Texts in Physics, Springer–Verlag, Berlin, 3nd edition, 2003.

43. C. Breant, T. Baer, D. Nesbitt and J. L. Hall, in *Laser Spectroscopy – Proceedings of the VI International Conference (ICOLS83),* page 138, Springer–Verlag, 1983.

44. L. Gianfrani, M. Gabrysch, C. Corsi and P. De Natale, *Appl. Optics* **36**, 9481 (1997).

45. J. Faist et al., *Science* **264**, 553 (1994).

46. G. Gagliardi et al., *Eur. Phys. J. D* **19**, 327 (2002).

47. C. Roller et al., *Opt. Lett.* **28**, 2052 (2003).

48. J. T. Remillard et al., *Opt. Express* **7**, 243 (2000).

49. A. Tredicucci et al., *Nature* **396**, 350 (1998).

50. M. Marano, P. Laporta, A. Sapia and P. De Natale, *Opt. Lett.* **25**, 1702 (2000).

51. R. Paschotta et al., *Opt. Commun.* **136**, 243 (1997).

52. P. Cancio, P. Zeppini, P. De Natale, S. Taccheo and P. Laporta, *Appl. Phys. B* **70**, 763 (2000).

53. G. P. Agrawal, editor, *Nonlinear Fiber Optics,* Academic Press, 3rd edition, 2001.

54. M. M. Fejer, G. A. Magel, D. H. Jundt and R. L. Byer, *IEEE J. Quantum Electron.* **28**, 2631 (1992).

55. E. V. Kovalchuk et al., *Opt. Lett.* **26**, 1430 (2001).

56. U. Stroßner et al., *J. Opt. Soc. Am. B* **19**, 1419 (2002).

57. D. Richter, A. Fried, B. P. Wert, J. G. Walega and F. K. Tittel, *Appl. Phys. B* **75**, 281 (2002).

58. P. Maddaloni, G. Gagliardi and P. De Natale, to be published, 2004.

59. D. Mazzotti et al., *Appl. Phys. B* **70**, 747 (2000).

60. D. Mazzotti, P. Cancio, G. Giusfredi, M. Inguscio and P. De Natale, *Phys. Rev. Lett.* **86**, 1919 (2001).

61. D. Mazzotti, G. Giusfredi, P. Cancio and P. De Natale, *Opt. Lasers Eng.* **37**, 143 (2002).

62. J.-J. Zondy, *Opt. Commun.* **119**, 320 (1995).

63. M. Erdelyi, D. Richter and F. K. Tittel, *Appl. Phys. B* **75**, 289 (2002).

64. E. R. Brown, K. A. McIntosh, K. B. Nichols and C. L. Dennis, *Appl. Phys. Lett.* **66**, 285 (1995).

65. H. Odashima, M. Tachikawa, L. R. Zink and K. M. Evenson, *Opt. Lett.* **22**, 822 (1997).

66. G. Gagliardi et al., *Opt. Lett.* **27**, 521 (2002).

67. G. Galzerano, M. Marano, S. Taccheo and P. Laporta, *Opt. Lett.* **28**, 248 (2003).

68. J. Lu et al., *Opt. Lett.* **27**, 1120 (2002).

69. J. Nilsson et al., in *Advances in Fiber Lasers,* volume 4974 of *SPIE Proceedings, page* 50, SPIE, 2003.

70. W. A. Clarkson et al., in *XIV International Symposium on Gas Flow, Chemical Lasers, and High-Power Lasers,* volume 5120 of *SPIE Proceedings,* page 482, SPIE, 2003.

71. V. Berger, volume 531 of *Lecture Notes in Physics, page* 366, Springer–Verlag, Heidelberg, 1999.

72. V. G. Dmitriev, G. G. Gurzadyan and D. N. Nikogosyan, volume 64 of *Springer Series in Optical Sciences,* Springer–Verlag, Berlin, 1997.

73. P. F. Moulton, *J. Opt. Soc. Am. B* **3**, 125 (1986).

74. D. K. Negus, L. Spinelli, N. Goldblatt and G. Feugnet, in *Advanced Solid-State Lasers,* volume 10 of *OSA Proceedings,* page 120, Washington, DC, 1991, Optical Society of America.

75. D. E. Spence, P. N. Kean and W. Sibbett, *Opt. Lett.* **16**, 42 (1991).

76. U. Keller, *Opt. Lett.* **16**, 1022 (1991).

77. F. Salin, J. Squier and M. Piché, *Opt. Lett.* **16**, 1674 (1991).

78. J.-C. Diels and W. Rudolph, *Ultrashort Laser Pulse Phenomena: Fundamentals, Techniques, and Applications on the Femtosecond Timescale,* Academic Press, Dan Diego, 1996.

79. E. P. Ippen, *Appl. Phys. B* **58,** 159 (1994).

80. V. Magni, G. Cerullo, S. De Silvestri and A. Monguzzi, *J. Opt. Soc. Am. B* **12,** 476 (1995).

81. U. Morgner et al., *Opt. Lett.* **24,** 411 (1999).

82. D. H. Sutter et al., *Opt. Lett.* **24,** 631 (1999).

83. R. Ell et al., *Opt. Lett.* **26,** 373 (2001).

84. R. L. Fork, O. E. Martinez and J. P. Gordon, *Opt. Lett.* **9**, 150 (1984).

85. M. T. Asaki et al., *Opt. Lett.* **18,** 977 (1993).

86. R. Szipocs, K. Ferencz, C. Spielmann and F. Krausz, *Opt. Lett.* **19,** 201 (1994).

87. L. Xu, C. Spielmann, F. Krausz and R. Szipocs, *Opt. Lett.* **21**, 1259 (1996).

88. S. T. Cundiff, *J. Phys. D* **35,** R43 (2002).

89. H. R. Telle et al., *Appl. Phys. B* **69,** 327 (1999).

90. J. Reichert, R. Holzwarth, T. Udem and T. W. Hänsch, *Opt. Commun.* **172,** 59 (1999).

91. A. Apolonski et al., *Phys. Rev. Lett.* **85**, 740 (2000).

92. A. Poppe et al., *Appl. Phys. B* **72,** 977 (2001).

93. L. Xu et al., *Opt. Lett.* **21,** 2008 (1996).

94. F. W. Helbing, G. Steinmeyer, J. Stenger, H. R. Telle and U. Keller, *Appl. Phys. B* **74,** S35 (2002).

95. K. W. Holman, R. J. Jones, A. Marian, S. T. Cundiff and J. Ye, *Opt. Lett.* **28,** 851 (2003).

96. U. Morgner et al., *Phys. Rev. Lett.* **86,** 5462 (2001).

97. T. M. Ramond, S. A. Diddams, L. W. Hollberg and A. Bartels, *Opt. Lett.* **27,** 1842 (2002).

98. J. K. Ranka, R. S. Windeler and A. J. Stentz, *Opt. Lett.* **25**, 25 (2000).

99. T. A. Birks, W. J. Wadsworth and P. S. Russell, *Opt. Lett.* **25**, 1415 (2000).

100. W. J. Wadsworth et al., *J. Opt. Soc. Am. B* **19,** 2148 (2002).

101. J. W. Nicholson et al., *Opt. Lett.* **28,** 643 (2003).

102. J. Rauschenberger, T. M. Fortier, D. J. Jones, J. Ye and S. T. Cundiff, *Opt. Express* **10,**1404 (2002).

103. A. Apolonski et al., *J. Opt. Soc. Am. B* **19,** 2165 (2002).

104. F. L. Hong et al., *Opt. Lett.* **28,** 1516 (2003).

105. I. Thomann et al., *Opt. Lett.* **28**, 1368 (2003).

106. H. Hundertmark et al., *Opt. Express* **11,** 3196 (2003).

107. P. De Natale et al., in *Laser Spectroscopy– Proceedings of the XVI International Conference (ICOLS03),* page 63, Singapore, 2004, World Scientific Publishing.

108. D. Mazzotti, P. Cancio, M. Prevedelli, G. Giusfredi and P. De Natale, to be published, 2004.

109. S. A. Diddams et al., *Science* **293,** 825 (2001).

110. Harvard–Smithsonian Center for Astrophysics, 2004, http://www.hitran.com.

Chapter 6

REAL-TIME SPECTROSCOPY OF MOLECULAR VIBRATIONS WITH SUB-5-FS VISIBLE PULSES

Takayoshi Kobayashi
Department of Physics, University of Tokyo
Hongo 7-3-1, Bunkyo, Tokyo 113-0033, Japan
kobayashi@phys.s.u-tokyo.ac.jp

Abstract: In this review article, research on ultrafast processes in a molecular aggregate system is described to show the usefulness of sub-5-fs real-time spectroscopy in studies of vibrational dynamic processes in molecules. We focus here on the J-aggregates of porphyrin, which have Frenkel excitons as elementary excitations, but the method can be applied to many other molecular systems including dyes, charge-transfer complexes, polymers, biomolecules, and organo-metallic compounds. Using such short pulses, many interesting phenomena can be discovered. Dynamic intensity borrowing is one such phenomena clarifying the mechanism of the dynamic mixing of the electronic states via molecular vibration. Photo-excitation of J-aggregate systems using extremely broadband visible–near-IR pulses with sub-5-fs duration was performed. By the vibronic coupling mechanism, a coherent molecular vibration is expected to be observed in real-time pump-probe spectra at various probe wavelengths. The vibration has a frequency of $244 \, \mathrm{cm^{-1}}$ corresponding to an oscillation period of 135 ± 4 fs. This vibration was analyzed to obtain the time-frequency two-dimensional difference transmission spectrum. An analysis of the phase and amplitude of the oscillation has revealed that both the negative (bleaching and photo-induced emission) and positive (photo-induced absorption) signals are modulated synchronously. This experimental result is well explained in terms of a transition dipole moment modulated by dynamic intensity borrowing from an intense B-transition (or Soret transition) to a weak Q-transition through vibronic interaction. The wave packet observed in the present study can be classified as a Herzberg-Teller type, which is a different mechanism from the frequently studied Franck-Condon type.

Key Words: Real-time spectroscopy, molecular vibration, group-delay dispersion, wave-packet, J-aggregate, Herzberg-Teller, Franck-Condon.

1.   INTRODUCTION

The recent development of ultrashort pulse lasers has enabled us to utilize extremely short pulses in the sub-5-fs time regime [1-6] and has brought about femtosecond real-time spectroscopy. In the fields of molecular physics and solid-state physics, this has revealed a wealth of information about vibrational dynamics and vibrational coherence in molecular and condensed matter systems. Wave packets are prepared as a simultaneous excitation of many levels in the vibrational manifold by an ultrashort laser pulse with spectral width larger than the vibrational frequencies. The wave packets are observed by several techniques such as time-resolved absorption and fluorescence spectroscopies. Various improvements have been made in short pulse generation to achieve high time resolution and a pulse duration short enough to excite high-frequency vibrational modes. Non-collinearly phase-matched optical parametric conversion, especially, has been attracting great interest as a novel method for ultrashort pulse generation in the visible and near-infrared (NIR) spectral regions with extremely short duration and/or frequency tenability [1-6]. Non-collinear optical parametric amplifiers (NOPAs) based on this scheme have been exploited to generate sub-5-fs pulses in the visible–near-infrared by our group.[6] Such an ultrashort laser pulse can be applied to the study of the electron-vibration interaction in molecular systems or the exciton-phonon interaction in translation-symmetric systems containing excitons such as single crystals or J-aggregates through the observation of the vibrational wave packet.

Since the first observation of molecular vibrations in the condensed phase by Rosker et al. [7], coherent nuclear motions on a femtosecond time-scale have been observed in a few dye molecules [8, 9], in polymers [10, 11], and in biological substances [12-14]. Concerning exciton systems, our group has also reported coherent molecular vibration in polydiacetylene [11] and a metal-halogen complex [15] which shows large lattice relaxation energy because of its quasi-one-dimensionality and charge-transfer properties. On the other hand, in the case of J-aggregates with an exciton system, which couples weakly with the molecular vibration, few investigations have been performed [13, 14] and the origin of the oscillations is not fully understood. The phase of the oscillations of the signal due to molecular vibrations, especially, has hardly been investigated at all. The phase information cannot be obtained from conventional time-resolved vibrational spectroscopy such as time-resolved (coherent or incoherent spontaneous) Raman scattering and time-resolved infrared absorption spectroscopies. Information about the dynamic processes of vibrational modes together with their phases is expected to provide a most important clue for understanding the chemical reaction and geometrical relaxations expected to take place universally in

many molecules resulting from different electronic distributions between the ground and excited electronic states. They will offer a type of real-time configurational change of the molecules in the excited and intermediate states. Even transition-state molecular structures can be revealed in certain cases.

In the present review article, a molecular vibrational mode excited in J-aggregates by visible-NIR short pulses through very strong vibronic coupling among many vibrational modes is described to show the usefulness of such a short pulse laser. The method is of course useful for molecular systems with more modes coupled strongly to the electronic transition corresponding to the spectrum of the short pulse. In such cases it is more interesting and useful sometimes to obtain multidimensional potential curves from the data analysis of the probe spectrum dependence of the phases of these molecular vibrations.

The reason for studying molecular J-aggregates using our record shortest optical pulse is as follows. Molecular J-aggregates have attracted much attention because of several characteristic features of their spectroscopic properties [16-18]. Among the properties super-radiant luminescence with much shorter lifetime is one of the most typical features. This is due to motional or exchange narrowing which also results in another very characteristic feature of sharp absorption and fluorescence peaks. The effect is also the cause of the weak vibronic coupling and it is therefore interesting to study the impulsive excitation of molecular vibration. Inter-molecular interaction between transition dipole moments results in the coherent delocalization of excitons over an aggregate [19]. Previously, we proposed that the aggregate has a hierarchical structure which is described by a *macroaggregate* composed of many *mesoaggregates* as a sub-system [19]. The attractive forces inducing aggregation in the latter and former are due to the van der Waals interaction (transition dipole-transition dipole ($\mu_{tr} - \mu_{tr}$)) and the static dipole-static dipole ($\mu_{st} - \mu_{st}$) interaction. The transition dipole-transition dipole interaction is more sensitive to thermal fluctuations, because it is an off-diagonal interaction sensitive to the phase of the relevant electronic state. The static dipole is a diagonal element and is not affected by the phase disturbance of the wave functions. The mesoaggregates then have a large static dipole moment accumulated by aggregation, and further aggregation of mesoaggregates forms a macroaggregate, since the former is not disturbed much by thermal fluctuations. It is very important to carefully characterize the above hierarchical structure in order to discuss the experimental results obtained by the coherent interaction with a coherent laser pulse. Hereafter, "J-aggregate" is used in place of "mesoaggregate".

The excitonic transition in J-aggregates is characterized by sharp absorption and emission bands, called the J-band, for which transition

energies are lower than those of monomers by twice the dipole-dipole interaction energy (represented as *J*) [16-23] minus the dispersion energy (van der Waals energy). Among many J-aggregates composed of aromatic or macrocyclic compounds, tetraphenylporphine tetrasulfonic (TPPS) J-aggregates are of special interest since they are considered to be model substances for aggregates of the light-harvesting antenna chlorophyll with a storage-ring configuration in photosynthesis. Since the first reports on the formation of J-aggregates independently by Fleischer et al. [20] and Pasternack et al. [21], a number of investigations have been performed using linear and nonlinear electronic spectroscopies which have elucidated the spectroscopic properties characteristic of the excitonic transition in porphyrin J-aggregates [16-23]. The absorption spectrum of TPPS aggregates shows a relatively weak band in the visible region and a relatively strong peak in the near-ultraviolet, denoted as the Q-band and the B-band, respectively. The latter is sometimes called the blue band or Soret band, which is named after a scientist who studied the spectroscopy of the molecule extensively. The two transitions allow the formation of a two-band Frenkel exciton system. It is especially noted that the stationary fluorescence of J-aggregates shows a small Stokes shift (~ 20 meV). Although several studies have been made of exciton-phonon coupling [24-26], only a few investigations related to the coherent molecular vibration coupled to the exciton in J-aggregates have been reported [27] in the real-time domain. This is because the excitons interact only weakly with vibrations and very high time resolution is required for direct measurement of intra-molecular vibrations including the phases of various modes and any change of the frequencies of the vibrational modes. Recent progress on ultrashort laser pulses has enabled us to investigate directly the coherent molecular vibration induced by the electronic transition through electron-vibration coupling. Since real-time wave-packet motions in dye molecules and bacteriorhodopsin were utilized to explain the vibrational features observed in the pump-probe signal traces by Shank and coworkers [28-30], various materials in the condensed phase, including the chlorophyll J-aggregates [27], have been studied by real-time pump-probe spectroscopy [22, 31-39]. During the last five years, we have developed a novel optical parametric amplifier (OPA) which can generate sub-5-fs pulses with the spectrum extending from the visible to the NIR [1, 5, 6].

In the present study, we apply both single-channel and multi-channel sub-5-fs real-time spectroscopy to molecular J-aggregates in order to shed light on the exciton-vibration coupling in the one-dimensional Frenkel-exciton system, which shows a small exciton-vibration interaction manifested by a negligibly small Stokes shift between the absorption peak and the fluorescence peak. Porphyrin J-aggregate was used as one of the

model substances for the Frenkel exciton system. In spite of the weak exciton-vibration coupling revealed in the stationary absorption spectrum in the ground state, coherent molecular vibration could be clearly observed in the time dependence of the induced absorption change. The experimental results are well explained by a new model: modulation of the Q-band-transition dipole moment oscillator strength by transfer of the intense allowed B (Soret)-band to the weak forbidden Q-band through vibronic interaction. We call this new mechanism of modulation of the transition probability "dynamic intensity borrowing" (DIB) [22]. The direct observation of the transient oscillation and clear spectral dependence of the amplitude and phase enable us to elucidate the interaction between the exciton and the molecular vibration in more detail.

2. EXPERIMENTAL

2.1 Sample

Tetraphenylporphine tetrasulfonic acid (TPPS: Tokyo Kasei) and polyvinylalcohol (PVA: Kanto Chemical) were used without further purification. The sample preparation of a unidirectional oriented film has been described elsewhere [22, 23].

2.2 Stationary Absorption and Raman Spectra

Figure 6-1 shows the stationary absorption spectrum of the J-aggregates and the laser spectrum. The absorption spectrum of the J-aggregates is characterized by two main bands, the B-band (S_2-exciton state: $\hbar\omega_{max} = 2.53\,\text{eV}$) and the Q-band ($S_1$-exciton state: $\hbar\omega_{max} = 1.75\,\text{eV}$). In the following we shall focus on these two bands (quasi-two-band Frenkel-exciton system [22, 24]). Figure 6-2 shows the stationary resonance Raman spectrum of the sample excited at 488 nm (2.541 eV) by an Ar laser. This excitation wavelength is in resonance with the B-band (2.53 eV). Two distinct peaks are observed at 244 and $316\,\text{cm}^{-1}$. Ohno et al. [25] and Akins et al. [26, 27] attributed the two bands at $241\,\text{cm}^{-1}$ and $317\,\text{cm}^{-1}$ to out-of-plane ruffling and doming modes, respectively [26, 27].

These two bands are drastically enhanced, by a factor of more than 30, with respect to the corresponding two bands of the diacid monomer at 233 and $310\,\text{cm}^{-1}$. The same enhancement effect of the Raman scattering intensity is also observed for $TCPPH_4^{2+}$ (tetraphenylporphine tetracarboxyl acid) aggregates [26] at 236 and $314\,\text{cm}^{-1}$ and for CuTOOPP ((5,10,15,20-

tetrakis [4-(1-octyloxy) phenyl] porphinato) copper-(II)) aggregates [27] at
386 cm^{-1}. Therefore, the enhancement is most likely to be due to the change
of the vibronic coupling strength by aggregate formation. Thus, the two
molecular vibrations are not in-plane vibration but out-of-plane modes,
which are expected to affect the van der Waals dipolar interaction between
adjacent porphinato-macrocycles induced by the changes in the distance
between the transition dipoles and in the magnitude of the coupled transition
dipoles. Figures 6-3 (a) and (b) show the structures of a porphyrin molecule
and a J-aggregate, respectively. Figure 6-3 (c) shows the structural diagram
of the ruffling motion of the porphyrin molecule.
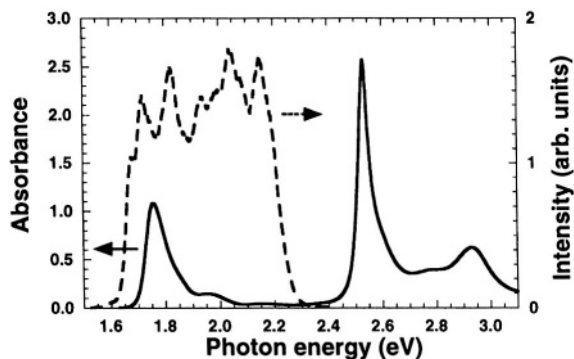

Figure 6-1. Stationary absorption spectrum of the TPPS J-aggregates (solid line) and the laser
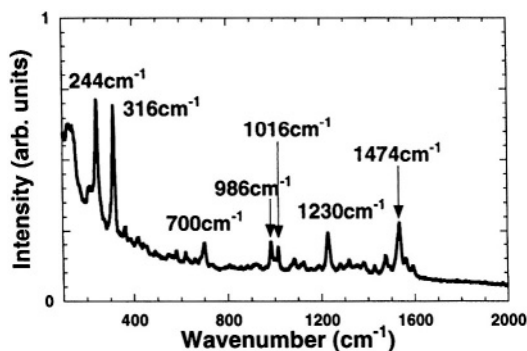spectrum (dashed line).

Figure 6-2. Resonance Raman spectrum of TPPS J-aggregates. The excitation wavelength is
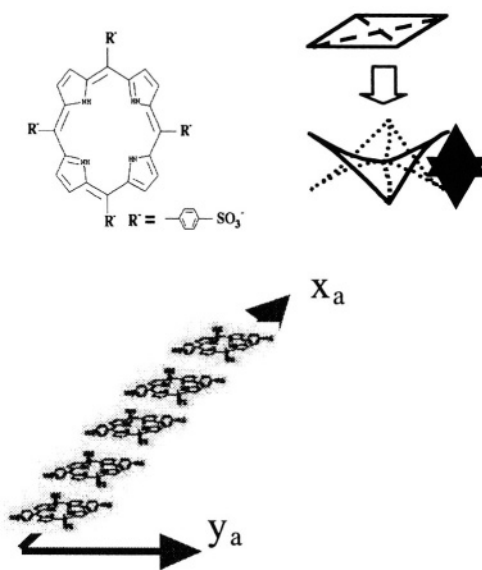488 nm.

Figure 6-3. Top: Structures of a porphyrin molecule (left) and a J-aggregate (right). The *x*-axis corresponds to the stacking direction. The porphyrin molecules make an angle θ with the *x*-axis. Bottom: Structural diagram of the ruffling motion of the porphyrin molecule.

2.3   Sub-5-fs Real-time Pump-Probe Apparatus

The experimental set-up of the sub-5-fs time-resolved pump-probe system is based on lock-in detection, and is shown in Fig. 6-4. The optical parametric amplifier is in the non-collinear geometry between the pump pulse and seed pulse created by the supercontinuum generation process in a 2 mm thick sapphire plate by tightly focussing a small fraction (a few percent or less) of the regenerative amplified Ti:sapphire laser output. A spatial mode pattern is most essential to obtain a stable and spatially reproducible continuum without the formation of multi-filaments in the sapphire plate. The non-collinear optical parametric amplifier (NOPA) also has two sets of chirped mirrors (CMs) to compensate for the group delay (GD) between the signal and the idler before and after the NOPA due to group-velocity dispersion (GVD). The first set before the NOPA is a pair of CMs to pre-compensate the chirp for the seed to overlap with the pump inside the nonlinear crystal. The seed pulse is reflected once at the surface of each CM. The second set is also composed of two CMs and the seed is reflected four times at each CM to minimize the amplified signal to be used

for both the pump and probe in real-time spectroscopy. The phase change spectra of CMs inevitably have oscillatory structure due to the effects of interference. In order to avoid this residual spectral feature, the pairs are selected so they have opposite phase structures to compensate each other. The details are described in the following paragraph. Moreover, the pulse front of the pump is tilted using a prism and lens-pair, which form an inverted Galilean telescope to adjust the tilting angle.
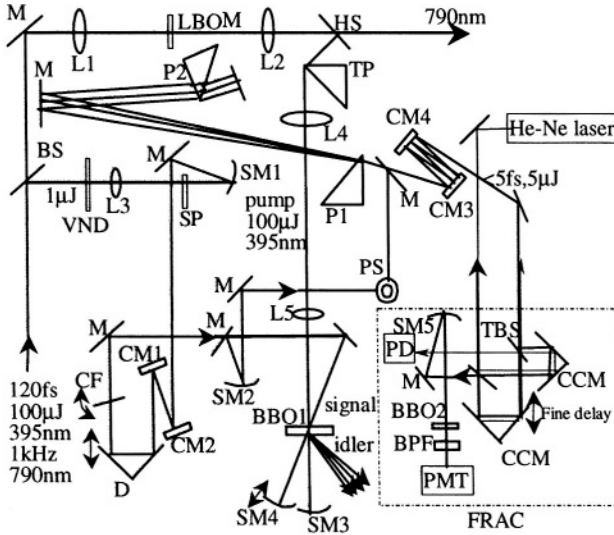

Figure 6-4. Schematic of the visible sub-5-fs pulse generator: L, lens; M, mirror; CYM, cylindrical mirror; BS, beam splitter; HS, harmonic separator; TP, prism for pulse-front tilting; L_1, L_2, lenses for the telescope; CMs, chirped mirrors; SMs spherical mirrors (γ = 100 mm); VND, variable neutral-density filter; SP, sapphire plate; WSM, spherical mirrors (γ = 120 mm); CF, cut-off filter; D, optical delay line; PS, periscope; P_1, P_2, 45° fused silica prisms; CCMs, corner-cube mirrors; FRAC, frequency-resolved autocorrelator, PD, photodiode; TBS, thin beam splitter; BPF, band-pass filter. A grating-prism pair compressor is also used for the chirped mirror-prism compressor.

Group-delay dispersion (GDD) compensation of the amplified pulses originating from the femtosecond continuum generation in the sapphire plate is performed using a pair of ultra-broadband-chirped mirrors (UBCMs) by taking into account the higher-order dispersion of the whole system including a 45° fused-silica prism pair, air along the optical path, and a beam splitter. By global optimization across the whole spectral range, the best compression is obtained in the case of a 1 m slant length and a 6.0 mm insertion length of the prism pair at 650 nm and eight reflections in four round trips between the two UBCMs in the pair, as shown in Fig. 6-4.
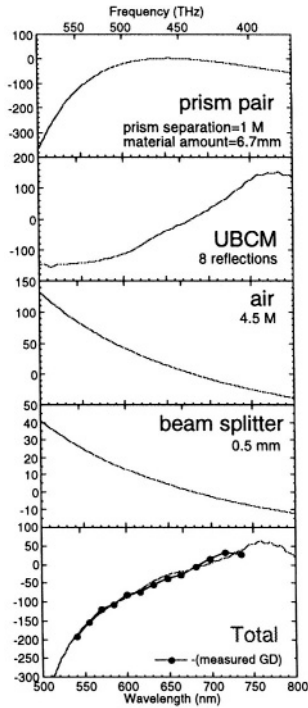
Figure 6-5. Group-delay property of the compressor. Top to bottom: GDs of the prism pair, the UBCM pair with four round-trips, air with a 4.5 m path length, the beam splitter in the FRAC, and the total compressor. Also shown at the bottom is the measured GD of the signal (full circles) with the sign reversed.

To obtain full-bandwidth amplification, the compressor is divided into two sections before and after the BBO crystal, namely, the pre-compressor and the main compressor. The pre-compressor comprises one UBCM pair in a single round-trip configuration, and the main compressor has another pair in a three round-trip configuration and other elements. Insertion of the UBCM pair before the crystal reduces the seed chirp to a GD difference of about 10 fs between 530 and 770 nm, and the inequality $\Delta T + \Delta T_{BBO} < \tau_p/2 = (GVM_{p\text{-}s})_{max}$ is fulfilled, where $(GVM_{p\text{-}s})_{max}$ is the maximum group-velocity mismatch between pump and signal. By tailoring the conditions and parameters as described above, full-bandwidth amplification by the double-path amplifier is achieved. As reflected in the measured chirp properties of the signal and idler, effects such as a self-phase modulation or cascaded second-order process seem to be weak enough under the experimental conditions. Thus, reduction of the initial chirp effect does not significantly change the net pulse parameters including the overall chirp property.

The pulse energy in about **7 μJ** just after the BBO crystal, and after the main compressor with about 70% throughput it becomes about **5 μJ**. The highest throughput of about 80% is obtained by using properly selected UBCMs: only reflection on the surfaces of the prisms causes loss. The group delay property of the compressor is shown in Fig. 6.5.
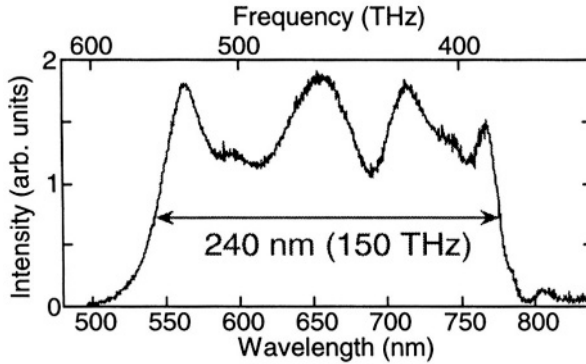

Figure 6-6. Spectrum of the signal pulses under full bandwidth operation.

The spectrum of the signal is shown in Fig. 6-6. The spectral shape depends on the positions of the delay lines, which are fixed to maximize the bandwidth. The FWHM is as large as 240 nm corresponding to 150 THz. If the pulse is Fourier-transform limited (FTL), then the FWHM of the pulse is calculated to be 4.4 fs. This bandwidth is slightly narrower than that reported in Ref. 6. The cut-off filter of the seed effectively suppresses the amplification around 790 nm, where the chirp exhibits a large nonlinearity. The collimated seed-pump beam interaction also avoids spectral broadening of the signal caused by the beam divergence [6], which is accompanied by an undesirable spatial chirp. Careful attention to both of these details is essential to obtain a signal compressible to a FTL pulse.

The pulse shape is measured by a frequency-resolved auto-correlation (FRAC) method. The pulse energy is appropriately reduced by adjusting the radius of open aperture of an iris. Figure 6-7 shows the FRAC trace of the signal after optimization of the parameters and alignment. The sech^2-fit pulse width is as short as 3.5 fs, which is shorter than the TL width. Because of the significant modulation of the spectral intensity, such an assumption cannot give an accurate pulse width.[2] In other words, an assumption of the spectral shape should not be used in the case of such a short pulse.

(a)

(b)

(c)
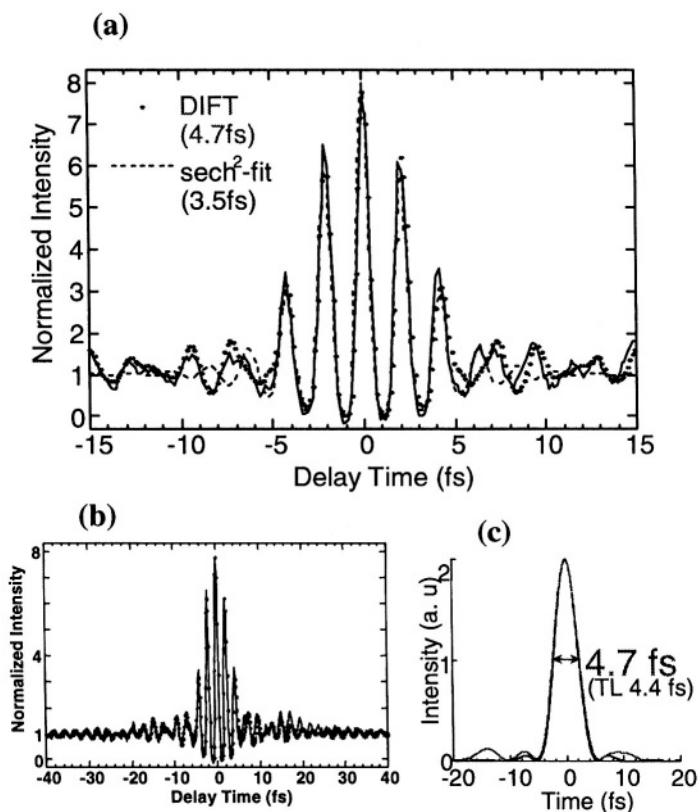
Figure 6-7. Frequency-resolved autocorrelation trace of the compressor output for: (a) $|\tau| <$ 15 fs and (b) $|\tau| < 40$ fs (τ: delay time). Measured trace (solid curve), calculated trace from Fourier transform of the measured spectrum (full circles) (where DIFT means decay including Fourier transform), and calculated trace using *sech²* with 3.5 fs width traces (dashed curve) are shown. The calculated pulse width using the measured FRAC trace is 4.7 fs, while that obtained by Fourier transformation of the measured spectrum (c) is 4.7 ± 0.1 fs.

The pulse duration is 4.7 fs but the FWHM of the cross-correlation trace is broadened to about 8 fs because of geometrical smearing due to the finite angle between the pump and probe beams to avoid an artificial signal caused by interference between them. The probe pulse light after the sample is spectrally dispersed by a 30 cm focal length monochromator (Ritsu, MC-30) equipped with a Si photodiode. The spectral resolution of the total spectroscopic system is about 3 nm. The broad spectrum of the probe pulse allows investigation over a broad probe-photon energy range extending from 1.6 to 2.3 eV corresponding to a wavelength range from 775 to 540 nm. The pump pulse energy and photon density are about 14 nJ and 5.9×10^{14} **photons/cm²**, respectively. The polarizations of both the pump and probe are

parallel to the aggregate axis (*x*-axis). Single-channel pump-probe spectroscopy was performed to observe the time trace of the change in normalized transmittance using a conventional lock-in amplifier. Details of the real-time spectroscopy system are described elsewhere [1, 11, 22].

Multi-channel pump-probe spectroscopy was also employed with the use of a CCD camera coupled to a polychromator. The reference and probe pulses were dispersed by the polychromator (Acton, model 320i; grating, 150 grooves/mm, blaze wavelength 500 nm) and detected simultaneously by a two-dimensional CCD camera (Roper Scientific, TE/CCD-1100-PB/UVAR; 1100×330 pixels) within 500 ms. The spectral resolution of the total system was about 4 nm. Two sets of 500 laser shots were accumulated under excitation and non-excitation conditions, one after the other, and this procedure was repeated 10 times for each set of delay times. All measurements were performed at room temperature (293 ± 1 K).

3.   RESULTS AND DISCUSSION

3.1   Real-Time Spectra

The time dependence of the transmittance change in porphyrin J-aggregates at six different probe photon energies is shown in Fig. 6-8 (a). The laser spectrum covers the whole width of the Q-band of the TPPS J-aggregates, while the B-band is outside of the laser spectrum. It can be safely assumed that the Q-exciton is generated by the one-photon resonant transition process and no B-exciton can be produced at the excitation photon flux of 1.2×10^{29} photons/s.cm^2.

The overall slow dynamics of the transmittance change originates from the dynamics of the excited states of J-aggregates by photo-excitation. The positive signal observed over the whole range of delay times for $E_{\text{probe}} < 1.77$ eV is attributed to bleaching of the Q-band absorption. At probe photon energies higher than 1.8 eV, the signal becomes negative due to an induced absorption. Additional complicated oscillation features are observed both for negative delay and around the time origin defined as the time when the probe pulse is maximally overlapping the pump pulse. They are due to the pump-perturbed free induction decay of the probe-induced polarization [37], and cross-phase modulation [30], and are also partly due to residual interference between the pump and probe pulses. Measured decay curves of the transmittance change are well-fitted by the sum of two exponential decay functions, which are convoluted with the cross-correlation function. Since nearly chirp-free pulses are used for both pump and probe, the same cross-

correlation function can be used for convolution with the response function over the whole range of probe-photon energy. At the peak transition energy of the Q-band ($E_{probe} = 1.75$ eV), the fast and slow decay components are determined to be 45 ± 4 fs and 1.5 ± 0.1 fs, respectively. The origin of these decay components are discussed in the following section.
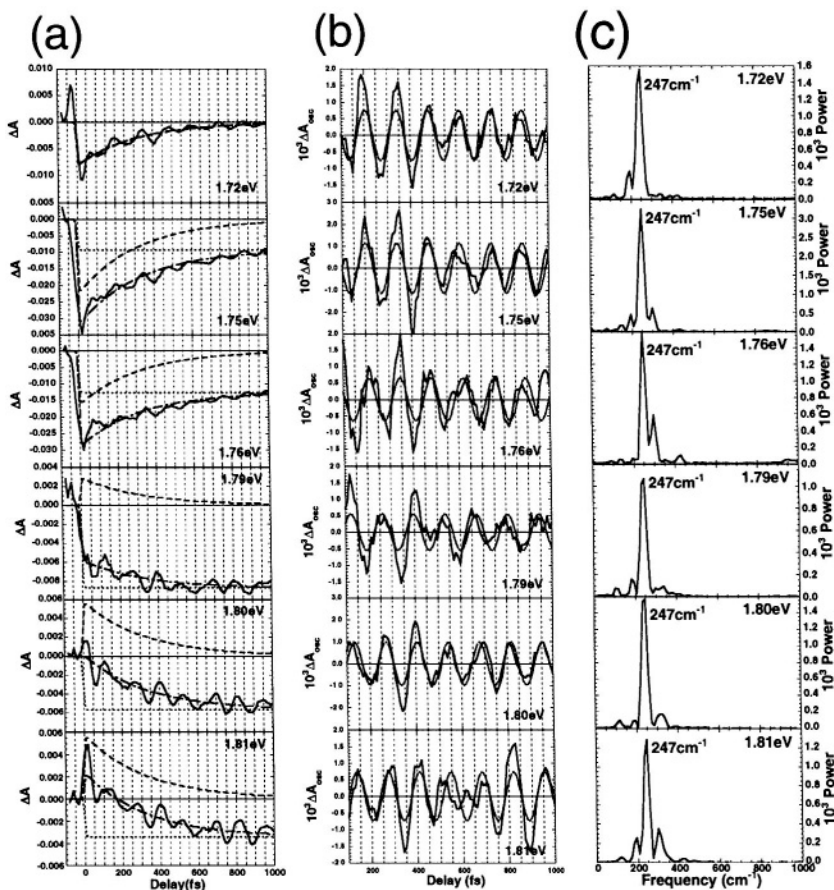
Figure 6-8. (a) Dependence on delay time of the induced absorption change of TPPS J-aggregates (solid line) and fitted results (dashed (A), dotted (B), and dot-dashed (ΔA) lines using Eq. 6.1) at six probe-photon energies marked on the right; (b) Dependence on delay time of the oscillating component in (a) (solid line) and fitted result (dotted line); (c) Fourier-power spectrum of the oscillating component (b) integrated from 100 fs to 1.2 ps.

3.2   **Dynamics of the Electronic States**

The time-dependent transmittance change is composed of the excitonic and molecular vibrational contributions. The former and the latter correspond to the slow dynamics component and the oscillating component, respectively. It is noteworthy that the oscillating component is observed only around the Q-band. In this section, we focus on the slow dynamics component. The signal is composed of three components. The first is bleaching due to $|1,S_1> \rightarrow |G>$ (where $|G>$ denotes the ground state and $|1,S_1>$ the first one-exciton state). The second is induced absorption (IA) due to a transition between two different n-exciton states ($|n+1,S_1> \leftarrow |n,S_1>$ (n = 1, 2,...)). Among the states, n-exciton states with n > 1 are called multi-exciton states (MES). The third is IA due to a transition to higher excited exciton states ($|1,S_n> \leftarrow |1,S_1>$ (n = 2, 3,...)). In the above notation, n in $|n,S_1>$ denotes the number of S_1-excitons (Q-excitons) in a single mesoaggregate [16, 17, 39], and $|1,S_n>$ indicates a one-exciton state of the S_n-exciton, namely, the excited state of a single exciton originating from an S_n excited state in a TPPS molecule. Although both induced emission ($|1,S_1> \rightarrow |G>$) and bleaching due to ground-state depopulation ($|1,S_1> \leftarrow |G>$) can contribute to the negative absorbance signal, the former is considered to be the dominant effect. This is because the oscillatory signal due to the latter, which corresponds to impulsive stimulated Raman scattering, must be described by a sine function when it is probed at a wavelength close to the pump centre wavelength.

The positive signal in the normalized difference transmittance $\Delta T/T(t)$ around the Q-band is associated with photo-induced bleaching and induced emission, while the negative signal originates from two sources.

First, the IA with the transient oscillation is observed only around the Q-band since the IA due to the transition from the 1-exciton state to MES is expected to be observed at higher probe-photon energy than the photon energy in the stationary absorption spectral peak. This is for the following reason. In order to create one more exciton in the aggregate, more energy is needed, since the first exciton occupies a finite phase space and the second exciton must occupy another phase space with higher energy than the first because the same phase space is not allowed to be occupied due to the Pauli exclusion principle. Even though excitons are a quasi-boson composed of fermions, namely electrons and holes, deviation from the bosonic properties appear in the optical nonlinearity. Therefore the IA with the transient oscillation is attributable to IA due to a transition among MESs. The existence of a transition among MESs is also confirmed by time-resolved pump-probe experiments using a 100 fs pump pulse [23].

Second, the IA without the transient oscillation has a broad spectrum far above the Q-band. This is ascribed to a transition to the higher excited exciton states. The absorption spectra of the S_n-exciton states (n >> 1) are expected to be broad and the oscillation is smeared out since the amplitude of the modulation of the normalized transmittance is partly proportional to the first derivative of the spectra of the ground-state absorption or the induced absorption. This is discussed later in this chapter.

Next, we focus on the origin of the slow and fast decay components. The lifetime of the Q-exciton is reported to be ~ 100 ps [14, 22, 23]. Hence, both the slow and fast decay components with lifetimes of 45 ± 4 fs and 1.5 ± 0.1 ps cannot be attributed to the Q-exciton. In our previous study, the decay time constant of the 1 ps component increases with excitation power, and the signal amplitude was found to increase faster than linearly with pump power. From these results, the 1 ps component was attributed to the lifetime of the S_2-exciton photo-generated by two-photon absorption. In our more recent report, however, it was found that the spectrum of the 1 ps component in the IA shifted to the blue side as the delay time increased in the pump-probe experiment using a 100 fs pump pulse [23]. Similar behavior is also observed in the IA ($|1,S_n> \leftarrow |1,S_1>$ (n = 2, 3,...) signal in the present experiment.
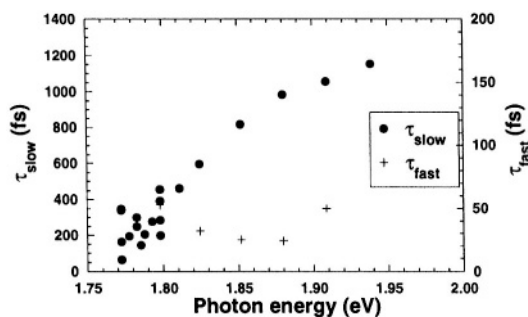
Figure 6-9. Probe-photon energy dependence of the slow (τ_{slow}) and fast (τ_{fast}) decay time constants in the transient signals.

Figure 6-9 shows the probe photon energy dependence of the decay times of the slow and fast decay components. The slow decay time constant of the IA increases up to 1.2 ps with probe photon energy, which means a blue-shifted IA. These results indicate that the slow decay component cannot be attributed to the two-photon generated S_2-exciton. This component is, therefore, ascribed to the non-thermal S_1-excitons (Q-excitons), which are thermalized with a decay time of about 1 ps. In fact, the slow decay time constant is shown to increase slightly with pump power, which also supports

this assignment. On the other hand, the decay time of the fast decay component is insensitive to the probe photon energy and is about 100 fs. This component is then attributed to the fast relaxation process from higher MESs, ($|n+1,S_1\rangle \leftarrow |n,S_1\rangle$ ($n = 1, 2,\ldots$)), which is expected to be faster than the recovery of the bleaching. In the following, the bleaching and IA ($|n+1,S_1\rangle \leftarrow |n,S_1\rangle$ ($n = 1, 2,\ldots$)) signal with transient oscillation is considered.

3.3   Two-Dimensional Real-Time Spectrum

As shown in Fig. 6-1, the laser spectrum covers the whole width of the S_1-exciton state of the TPPS J-aggregates, while the S_2-exciton state is completely outside of the laser spectrum. It is concluded that the S_2-exciton is not photo-excited for the excitation photon flux ($I = 1.2 \times 10^{29}$ photons/s.cm^2) by the two-photon absorption process, for the following reason. A typical value of the two-photon absorption cross-section for anthracene is of the order of 10^{-50} cm^4.s [32], which is known to be relatively large among aromatic molecules. Even if the two-photon absorption cross section for the porphyrin J-aggregate, $\sigma^{(2)}$, is assumed to have a similar large value, the magnitude of $\sigma^{(2)}I = 1.2 \times 10^{-21}$ cm^2 is still many orders of magnitude smaller than the one-photon absorption cross section for the porphyrin J-aggregate ($\sim 10^{-15}$ cm^2). Hence, no S_2-exciton can be created under the present experimental conditions.

The difference absorption spectrum is displayed as a function of the delay time in Fig. 6-8 (a). The dominant features commonly appearing in the traces are high-frequency oscillations in addition to the underlying slow-dynamics transient components. The size of the oscillatory signal is drastically reduced for probe energies around 1.78 eV. The overall slow dynamics of the induced change of absorbance (ΔA) by photo-excitation originates from excited states of the excitons. Following excitation of the J-aggregates, a negative ΔA is observed over the whole range of delay times for 1.71 eV $\leq E_{prob} \leq 1.78$ eV, where E_{prob} represents the probe-photon energy. This is attributed to bleaching and photo-induced emission (PIE) of the S_1-exciton state. At probe energies higher than 1.78 eV, the ΔA signal becomes positive due to photo-induced absorption (PIA). In fact, because of the bleaching around 1.85 eV, the ΔA signal overshoots to become negative around 1.80 eV as the delay time increases. The positive ΔA signal is more clearly observed if the red side of the Q-band is photo-excited. Note that the bleaching, PIE, and PIA spectra overlap with each other.

The measured decay traces are fitted to convoluted curves of the system response function with the following equation, and the results are presented in Fig. 6-8 (a) as dashed (A), dotted (B), and solid (ΔA) lines:

$$\Delta A(\hbar\omega) = A(\hbar\omega)\exp(-t/\tau) + B(\hbar\omega) \tag{6.1}$$

The decay time does not change significantly around the Q-band, and is determined to be about 320 fs. The spectral profile of each component ($A(\hbar\omega)$ solid and $B(\hbar\omega)$ dashed) is shown in Fig. 6-10. In the following, the exponential decay contribution, $A(\hbar\omega)$, is referred to as the 320 fs decay component.
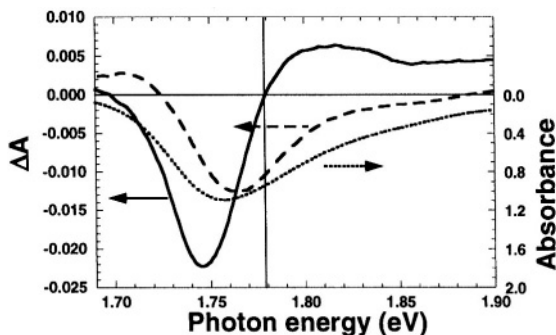

Figure 6-10. 320 fs decay component (solid line) and constant (dashed line) components in the transient signal and the stationary absorption spectrum (dotted line).

Next, the origin of the 320 fs decay and the constant components are discussed. The 320 fs decay component cannot be attributed to the Q-exciton (S_1-exciton), because the Q-exciton lifetime has been established to be in the range of 100 - 300 ps [33]. Since no B-exciton (S_2-exciton) is created under the present conditions, the 320 fs decay component cannot be ascribed to the B-exciton. The key is the blue-shifted PIA predominantly contributing to the 320 fs decay component, which is one of the characteristic features of the exciton system in J-aggregates. Because of the Pauli exclusion principle (in other words, phase-space-filling effect in the present system), the creation of an exciton in the aggregate requires higher photon energy as the number of the exciton is increased [24]. Hence, the blue-shifted PIA is attributed to a transition to the multi-exciton state ($|n+1,S_1\rangle \leftarrow |n,S_1\rangle$ ($n = 1, 2,...$)) and the 320 fs decay component to a fast relaxation process from higher MESs ($|n,S_1\rangle$ ($n = 2, 3...$)) to the one-exciton state, which is expected to be faster than the decay of the S_1 exciton. A similar decay time (200 fs) has also been observed for pseudoisocyanine (PIC) J-aggregates and is also ascribed to a relaxation process from the higher MESs [24, 33]. On the other hand, the constant component can be explained by several relaxation processes in the Q-band and the lifetime of the Q-exciton.

3.4   Dynamics of Excitonic States

The time-dependent ΔA signal consists of a slow relaxation component due to exciton decay and a highly oscillating component due to molecular vibration. It is noteworthy that the latter is observed only around the Q-band. In this section, the slow relaxation component is discussed in detail. The excitonic transitions are classified in terms of the following three components, namely, bleaching and PIE due to $|1,S_1> \leftarrow |G>$ and $|1,S_1> \rightarrow |G>$, respectively, and PIA due to a transition to the MES ($|n+1,S_1> \leftarrow |n,S_1>$ ($n = 1,2,...$)).   Here, n in $|n,S_1>$ denotes the number of S_1-excitons (Q-excitons) in a single aggregate. Because of the small Stokes shift, the bleaching is indistinguishable from PIE. Both the bleaching and PIE give a negative signal in the induced absorption spectrum. On the other hand, the positive signal at a probe-photon energy slightly higher than the peak of the Q-band originates from PIA due to a transition such as $|n+1,S_1> \leftarrow |n,S_1>$ ($n = 1,2,...$). This PIA becomes observable when the red side of the Q-band is excited. Since the transient oscillation is observed only around the Q-band, the signals due to PIA as well as bleaching/PIE are modulated. In addition, another PIA due to a transition to higher-excited exciton states ($|1,S_m> \leftarrow |1,S_1>$ ($m = 2, 3,...$)) is also observed far above the Q-band ($E_{prob} \gg 1.75$ eV) at about $E_{prob} < 1.71$ eV. Here, $|1,S_m>$ indicates a one-exciton state of the S_m-exciton, namely, the excited state of an exciton originating from an S_m-excited state in a TPPS molecule. This has been confirmed by 100 fs pump-probe spectroscopy [23, 33]. This PIA does not show a transient oscillation.

3.5   Analysis of Coherent Molecular Vibration

For the discussion of the molecular vibration, traces smoothened by averaging over a 200 fs period are subtracted from the experimentally observed transient traces. In order to avoid elimination of the fast decay dynamics of electronic origin in the process of smoothing and subtraction, we have carefully checked the dependence of the Fourier power spectrum on the time window (200 fs in the present report) and found that there was no prominent peak below 240 cm^{-1}. It has also been confirmed that the decay component is more dominant than the oscillating component below 240 cm^{-1} because a similar result to Fig. 6-8 (c) is obtained by Fourier transformation of the oscillating component shown in Fig 6-8 (b), calculated by subtraction of the fitted slow relaxation component from the trace (not shown). The two-dimensional contour plot of the Fourier-power spectrum of the oscillating components is displayed in Fig. 6-11 as functions of probe-photon energy and oscillation frequency. The resolution is determined to be

13 cm^{-1} (FWHM) from the width of the delay time window in the Fourier transformation analysis. The Fourier power spectrum clearly shows an intense peak at 247 ± 7 cm^{-1}. This frequency corresponds to an oscillation period of about 135 fs. Other higher frequency modes are much weaker than the 247 cm^{-1} peak in the Fourier power spectrum. A peak close to 247 cm^{-1} is observed in the resonance Raman spectrum shown in Fig. 6-2. This peak is enhanced by aggregation and is assigned to the ruffling mode [26]. As clearly shown in Fig. 6-11, the intensity at the 247 cm^{-1} peak is drastically reduced at a probe photon energy around 1.78 eV, where the sign of the oscillation amplitude is reversed (in other words, a **π-phase** difference).

Figure 6-2 shows another peak at 316 cm^{-1} under resonant excitation of the B-band. This is assigned to the doming mode [26] and is also enhanced by aggregation. The peak around 315 cm^{-1} in Fig. 6-8 (c) can be attributed to this mode; however, it is very weak in the real-time spectrum compared with the ruffling mode. It may be explained by the different coupling property of the B-exciton with the Q-exciton for the doming mode.
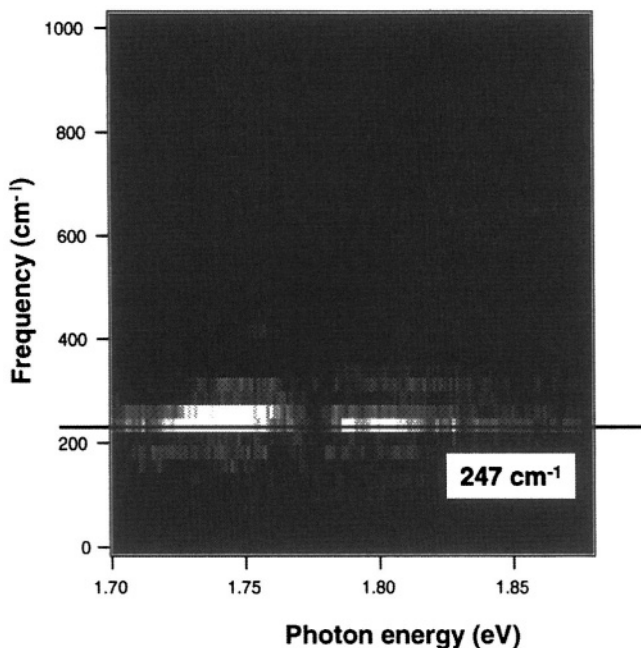

Figure 6-11. Two-dimensional contour plot of the Fourier power spectrum of the oscillating component of the induced absorption spectrum. The vertical and horizontal axes correspond to the oscillation frequency and probe photon energy, respectively. Brighter regions indicate greater signal intensities.

3.6   Analysis of Phase and Amplitude of the Oscillation

Owing to the extremely high time resolution, the phase and amplitude of the oscillation can be precisely evaluated.   The oscillating component in Fig. 6-8 (b) is fitted to a cosine function with a fixed oscillating frequency of 247 cm^{-1}, which is also shown in Fig. 6-8 (b). Figure 6-12 shows the probe photon energy dependence of the phase and amplitude of the oscillation. The continuous spectra of the phase and amplitude clearly show that the phase is constant throughout the Q-band $((1.1 \pm 3.8) \times 10^{-1}$ radian), and that the sign of the amplitude is reversed around 1.78 eV. This result is consistent with that calculated by complex Fourier transformation. The probe photon energy where the sign-reversal takes place is slightly higher than the peak of the Q-band and is located very close to the probe photon energy of the null absorbance change in the 320 fs decay component. Since the sign of the bleaching and/or PIE signal is opposite to that of the PIA signal, the spectral profile of the amplitude indicates that the oscillations are in-phase for bleaching/PIE and PIA. This can be rephrased in the following way: all the oscillations in the absolute value of the absorbance change over the whole spectral range are synchronous with each other with a constant phase.
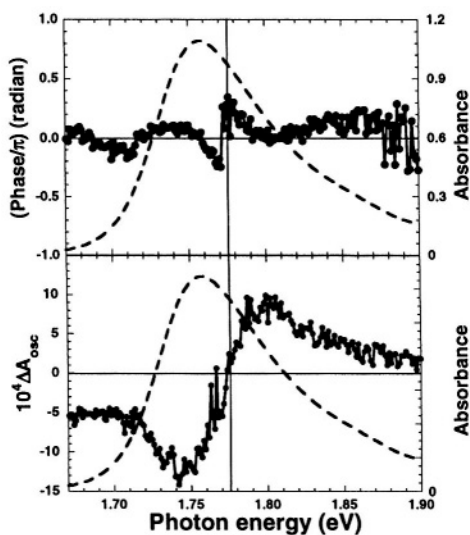

Figure 6-12. Probe photon energy dependence of the phase (upper) and amplitude (lower) of the oscillation in the transient signals (dots). The oscillating component is fitted by a cosine function with a period of 135 fs. Dashed curves are the absorption spectrum of the sample.

3.7   Exciton-Vibration Interaction

We are now in a position to investigate the exciton-vibration interaction in more detail. In comparison with the electron-vibration interaction in the monomer, the exciton-vibration interaction in the aggregate system is different in the following three aspects. First, the Stokes shift of the fluorescence is quite small (less than 20 meV).   Second, as shown in Fig. 6-2, the low-frequency Raman mode (244 and **316 cm^{-1}**) is strongly enhanced in the aggregate Raman spectrum. Finally, the transition from the one-exciton state to a two-exciton state is located at a probe photon energy slightly higher than the stationary absorption peak. Related to these three differences, the spectral and temporal profiles show characteristic properties inherent in the exciton system in the J-aggregates.

The experimental results show synchronous modulation in the transitions due to $|1,S_1> \leftarrow |G>$, $|1,S_1> \rightarrow |G>$, and $|n+1,S_1> \leftarrow |n,S_1>$ ($n=1,2,...$).   In order to interpret this intriguing experimental result, the following four models are discussed in the following sections:

(a)   Quantum beat between different n-exciton states.
(b)   Conventional wave-packet motion on the ground-state potential energy surface (PES), in other words, impulsive stimulated Raman scattering (ISRS).
(c)   Conventional wave-packet motion on the excited-state PES.
(d)   Dynamic intensity borrowing (DIB).

3.7.1   Quantum beat between different n exciton states

First, we discuss model (a). The transient oscillation could be ascribed to a beating between different n-exciton states (MESs; n = 1, 2,...), which are simultaneously photo-excited by the broad excitation pulse. However, the oscillation persists for periods longer than 1 ps. This means that the lifetime of the oscillation is much longer than the relaxation time of the MESs to the one-exciton state (~ 320 fs). Therefore, a quantum beat between the different n-exciton states is unlikely. A quantum beat between the one-exciton states with different momenta (k = 1, 3...) could also be one of the candidates. However, model (a) can be ruled out because the oscillator strength is concentrated in the k = 1 one-exciton state (~ 80%) and the other transition (k = 3, 5,...) is expected to take place only with a vanishingly small probability. In addition to the above-mentioned facts, the modulation frequency of **247 cm^{-1}** is in excellent agreement with the resonance Raman spectrum. This indicates that the oscillation originates not from the inherent electronic property of the exciton state but from the exciton-vibration interaction.

3.7.2   Wave-packet motion on ground-state potential energy surface

Second, we focus on model (b). The time dependence of the absorbance change due to the wave packet prepared on the ground state PES by induced stimulated Raman scattering process (ISRS; Fig. 6-13 (b)) is described by a sine function and the amplitude spectrum of the oscillation is approximately expressed by the first derivative of the stationary absorption spectrum. Under the present conditions, however, the contribution of the ground-state oscillation is negligible for the following two reasons. First, the oscillation is not described by a sine function but is much closer to a cosine function. Second, the phase of the oscillation in the bleaching and/or PIE signals is identical with that of the oscillation in the PIA, which must be ascribed to the wave-packet motion on the excited-state PES. If the ground-state oscillation is also contributing to the signal, this excellent agreement of the phase relationship will no longer be observed. Therefore, the wave-packet motion on the ground-state PES does not contribute much to the observed oscillatory signal. Similar conclusions have been drawn by Bradforth et al. [35] and Chachisvilis et al. [13] in biological systems.
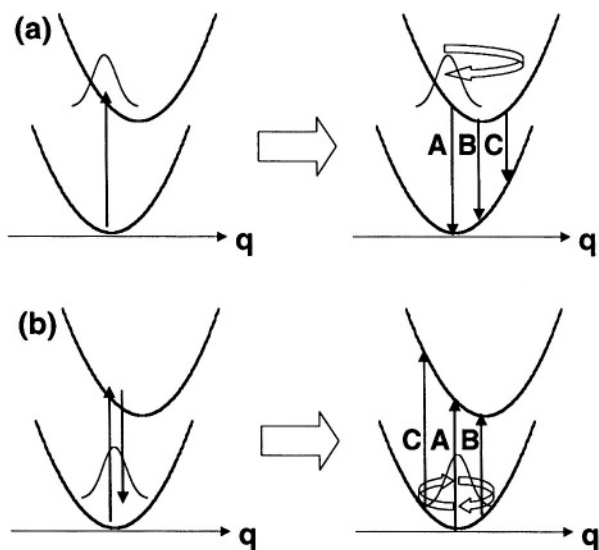
Figure 6-13. Wave-packet motions on the (a) excited- and (b) ground-state potential energy surfaces. In case (a), the phases of the oscillation are 0, $\pi/2$ and π for positions A, B and C, respectively. In case (b), the phases of the oscillation are 0, $\pi/2$ and $3\pi/2$ for positions A, B, and C, respectively.

3.7.3   **Wave-packet motion on excited-state potential energy surface**

Third, we consider model (c). In this scheme, the wave packet prepared by the excitation pulse moves on the excited-state PES as shown in Fig. 6-13 (a). Therefore the oscillation amplitude is given by a cosine function. If we assume the system is described by a simple two-level system which is composed of only the ground state and one excited state, the amplitude spectrum of the oscillation can be expressed approximately by the first derivative of the fluorescence spectrum. Strictly speaking, it must be corrected to be the induced emission spectrum and the dynamic property must be included. The phases of the oscillation are 0, $\pi/2$ and π for three probe photon energies at A, B and C, respectively labelled in Fig. 6-13 (a). In the present experiment, the Stokes shift of the fluorescence signal is measured to be less than 20 meV; therefore the whole probe photon energy dependence of the phase shown in Fig. 6-13 (a) can be detected with the use of our broadband laser pulse. Assuming a wave-packet motion on a harmonic PES, the oscillation must show a π–phase difference between $E_{\text{probe}} = E_{\text{abs}} = 1.76$ eV and $E_{\text{probe}} = 2E_{\text{fluo}} - E_{\text{abs}} = 1.72$ eV, where E_{abs} and E_{fluo} are the peak photon energies of the absorption and fluorescence spectra, respectively. The former and the latter correspond to the positions indicated by A and C, respectively, in Fig. 6-13 (a). Although a π–phase difference could be sufficiently resolved under the present conditions, such a phase shift is not observed between 1.72 and 1.76 eV but found around 1.78 eV, which is slightly higher than $E_{\text{abs}} \approx 1.76$ eV. Hence, the oscillation cannot be explained only by taking account of the PIE process from the excited-state wave packet. In the present case, in fact, the PIA due to the transition to the MES must also be considered. This PIA is located at a probe photon energy slightly higher than the peak of the Q-band absorption.

If the amplitude of the oscillation due to the PIA is more dominant than the one due to bleaching/PIE, the above-mentioned π–phase difference may be cancelled. However, this is not the case for the following reason. As discussed in our previous paper [22], the oscillator strength of the transition due to PIA corresponding to the transition from the $k = 1$ one-exciton state to the $(k_1, k_2) = (2, 1)$ two-exciton state is calculated to be $1.27(N + 1)^2 \mu_0^2$, where μ_0 is the transition dipole moment of the monomer. This is 1.57 times larger than the oscillator strength of the transition due to bleaching corresponding to the transition from the ground state to the $k = 1$ one-exciton state [33]. The latter oscillator strength is calculated to be $0.81(N + 1)^2 \mu_0^2$. On the other hand, in order to explain the phase spectrum of the oscillation component, the ratio of the PIA to PIE is calculated to be 1.95 ± 0.02 from our observed time-resolved data, which is substantially larger than the theoretical estimate (1.57). In addition, there are two remaining problems

regarding model (c). First, the conventional wave-packet model (c) is based on the simultaneous photo-excitation of the multi-vibrational quantum states depending on the Franck-Condon factor. However, the vibronic excitation of the Q-band is known to originate mainly from a Herzberg-Teller-type transition [22, 34]. This will be discussed later in more detail. Secondly, if the signal originates from model (c), the signal intensity integrated over the whole spectral region of the Q-band must not be modulated, because this model only produces a spectral shift. As will be shown later, however, the integrated signal intensity shows a non-negligible modulation, which cannot be explained by model (c). Concerning the phase of the oscillation, Champion et al. have discussed the effect of inhomogeneous broadening [38]. However, the phase spectrum was calculated based on a wavelength-selected pump pulse, and this does not correspond to our experimental conditions of broadband excitation.

3.7.4   Dynamic intensity borrowing

In this section, we propose the following new mechanism (model (d), which also induces a coherent oscillation: modulation of the transition dipole moment of the Q-band. This model is beyond the Condon approximation, because the transition dipole moment depends on the vibrational coordinate. The modulation frequency corresponds to the $247 \ \mathrm{cm^{-1}}$ ruffling-mode vibration.

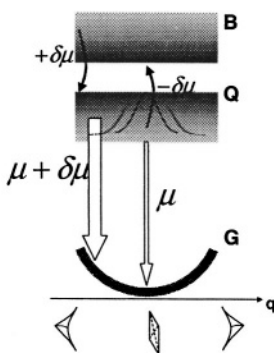*Figure 6-14.* Potential energy curves for the J-aggregates (model (d)). A simplified picture of the ruffling mode is also shown below. The larger and smaller oscillator strength is indicated as a thick line with partially dark and light parts of the PES of the Q- and B-band.

The key point of this model is the spectroscopic property of the Q-band. Although the Q-state is an originally forbidden state because of the

symmetry of the electronic structure, it becomes allowed because of mixing of the electronic property with the B-state by configuration interaction (electron-electron correlation) and vibronic coupling [37, 39]. Therefore, the modulation of the Q-transition can be explained by an additional intensity borrowing from the B-band. We call this new mechanism "dynamic intensity borrowing (DIB)". Figure 6-14 shows a schematic energy diagram for the DIB mechanism. Because of the small Stokes shift of the stationary fluorescence spectrum, it is assumed that the bottom of the excited-state PES is simply located just above the bottom of the ground state PES. A wave packet is created on the excited-state PES because of the vibronic coupling and the small anharmonicity. The wave packet on the excited-state PES becomes narrower or broader with time evolution and no probe photon energy dependence is expected, as shown in Fig. 6-8, unless DIB occurs. Dynamic intensity borrowing allows the oscillator strength to be modulated as a function of the normal coordinate, which results in a coherent oscillation in the induced absorption signal, as shown in Fig. 6-15.
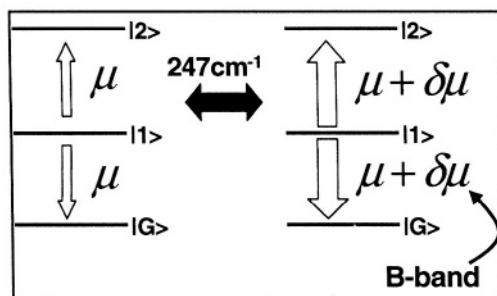
Figure 6-15. Modulated transition dipole moment due to a coherent molecular vibration (model (d)). |G>, |1>, and |2> denote the ground state, one- and two-exciton states, respectively.

The increase (or decrease) of the transition dipole moment is reflected by the increase (or decrease) of the signal intensity both for the bleaching and/or PIE and PIA. As a result, DIB can explain the synchronous oscillations for the bleaching and/or PIE and PIA in terms of the modulation of the transition dipole moment. If this model is valid, the total signal intensity associated with the Q-exciton must also be modulated. It can be evaluated by integrating the signal intensity over the whole spectral region of the Q-band, which is defined by $\int \Delta A(\hbar\omega)d\omega$. The integrated signal intensity over the probe photon energy region extending from 1.65 to 1.91 eV is shown in Fig. 6-16 as a function of the delay time. It clearly shows a non-

negligible amplitude of the coherent oscillation mainly with a frequency of $247 \, \text{cm}^{-1}$. Considering that the spectral range from 1.65 to 1.91 eV is wide enough to sum all non-negligible oscillating signals due to the Q-band, the oscillator strength of the Q-exciton is also modulated by the $247 \, \text{cm}^{-1}$ frequency component. This cannot be explained by model (c), because model (c) predicts only a spectral shift.
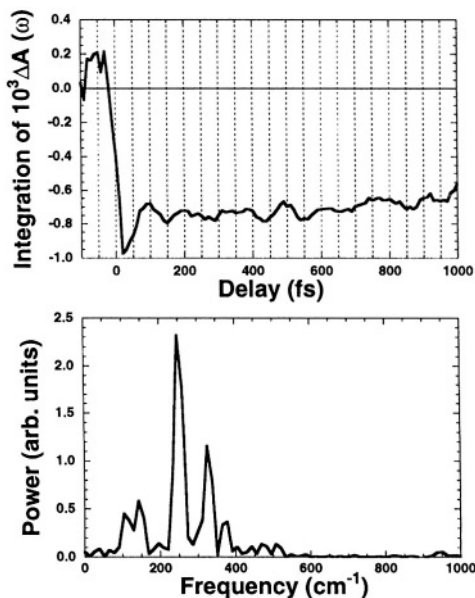
Figure 6-16. Integrated signal intensity of the induced absorption change from 1.65 to 1.91 eV (upper) and the Fourier power spectrum of the oscillating component (lower).

A similar intensity borrowing mechanism has also been discussed for the stationary resonance Raman spectrum of metalloporphyrins [39-42]. Intensity borrowing is a well-known and widely observed phenomenon in partially-allowed optical transitions of many molecular systems. The resonance Raman spectrum under B-band excitation shows a dominant contribution of the Albrecht A-term (Franck-Condon type) [43]. On the other hand, in the case of the Q-band, the scattering intensity from depolarized and anomalously polarized vibrations is often as intense as polarized mode scattering [22, 34, 43]. Concerning Q-band excitation, the Albrecht B-term (Herzberg-Teller type) scattering is dominant and is also explained by a vibronic intensity borrowing mechanism from the B-band to the Q-band [22, 34].

3.8   **Theoretical Analysis of Results**

3.8.1   **Herzberg-Teller type wave-packet motion**

According to model (d), the modulation of the transition dipole moment depends on the normal coordinate. Hence, this can also be called a "Herzberg-Teller-type" wave-packet model in contrast with the conventional "Franck-Condon-type" wave-packet model. In the following, we derive an analytical expression for the wave-packet motion based on a coordinate-dependent transition dipole moment. In general, the vibronic coupling effect is approximately expressed by the expansion of the transition dipole moment, $\hat{\mu}(\hat{q})$, using a Herzberg-Teller expansion of the ground- and excited-state wavefunctions. Here $\hat{q}$ denotes the vibrational normal coordinate. In the present system, vibronic coupling occurs predominantly between the Q- and B-bands; therefore the following three wavefunctions are taken into account:

$$\left| G(r,q) \right\rangle = \left| \psi_G(r) \chi_n^G(q) \right\rangle \tag{6.2}$$

$$\left| B(r,q) \right\rangle = \left(\left| \psi_B(r) \right\rangle - \frac{H_{\text{vib}}}{\Delta E_{BQ}} q \left| \psi_B(r) \right\rangle \right) \left| \chi_l^B(q) \right\rangle \tag{6.3}$$

$$\left| Q(r,q) \right\rangle = \left(\left| \psi_Q(r) \right\rangle + \frac{H_{\text{vib}}}{\Delta E_{BQ}} q \left| \psi_B(r) \right\rangle \right) \left| \chi_m^Q(q) \right\rangle. \tag{6.4}$$

Here, $\psi_X(r)$ and $\chi^X(q)$ represent wavefunctions of the electron and nucleus for the X (= G, B, and Q) -state, respectively, as a function of the electron and nuclear coordinates, r and q, respectively. For the nuclear wavefunctions, the vibrational quantum numbers are described by n, l, and m. The first term in $|Q(r,q)\rangle$, namely $|\psi_Q(r)\rangle$, consists of two terms:

$$\left| \psi_Q(r) \right\rangle = \left| \psi_Q^0(r) \right\rangle + \alpha \left| \psi_B(r) \right\rangle. \tag{6.5}$$

The first term, $\left| \psi_Q^0(r) \right\rangle$, is an optically forbidden state. On the hand, the second term is an optically allowed state, which originates from configuration interaction (CI) with the B-band. The coefficient α represents the degree of CI. The matrix element of the transition dipole moment from the ground state to the Q-band is calculated as follows:

$$\langle Q(r,q)|\hat{\mu}(\hat{q})|G(r,q)\rangle = \langle \chi_m^Q(q)| \left(\langle \psi_Q(r)| + \frac{H_{vib}}{\Delta E_{BQ}} \langle \psi_B(r)|\hat{q} \right) \mu |\psi_G(r)\chi_n^G(q)\rangle$$

$$= \mu_{QG} \langle \chi_m^Q | \chi_n^G \rangle \cong |\alpha|^2 \, \mu_{BG} \qquad \text{(if } n = m = 0) \qquad (6.6)$$

$$= \beta \mu_{BG} q_{mn}. \qquad \text{(if } n \neq m \text{ and } m \neq 0) \qquad (6.7)$$

Here, $q_{mn} = \langle \chi_m^Q |\mu| \chi_n^G \rangle$, $\mu_{QG} = \langle \psi_Q |\mu| \psi_G \rangle$, $\mu_{BG} = \langle \psi_B |\mu| \psi_G \rangle$, and $\beta = H_{vib}/\Delta E_{BQ}$. Although multimode effects should be taken into account [44], we roughly assume $\langle \chi_0^Q | \chi_0^G \rangle \cong 1$, which means that all vibronic excitation is not caused by the Franck-Condon component but by the term in Eq. 6.7 associated with the vibronic coupling [37]. Although the symmetry is important for the vibronic interaction and the coefficient, q_{mn}, the symmetry of the ruffling mode for the aggregate is not as well defined as for the monomer. Taking account of the time evolution, the wavefunction, $|\Psi(t)\rangle$, is expressed as follows assuming an impulsive limit:

$$|\Psi(t)\rangle \equiv \exp(-i\hat{H}t/\hbar)\hat{\mu}|G(r,q)\rangle$$

$$\propto |\alpha|^2 \, \mu_{BG} |\psi_B \chi_0^Q\rangle \qquad (6.8)$$

$$+ \beta \mu_{BG} \sum_{m \neq 0} q_{m0} \exp(-im\Omega t)|\psi_B \chi_m^Q\rangle.$$

Here, Ω corresponds to the 247 cm^{-1} vibrational frequency. The transition from the excited-state wave packet, $|\Psi(t)\rangle$, to the ground state, $|G(r,q)\rangle$, is calculated as follows using Eq. 6.8:

$$|\langle G(r,q)|\mu|\Psi(t)\rangle|^2 = |\alpha|^4 (\mu_{BG})^4$$

$$+ |\beta|^2 (\mu_{BG})^2 \sum_{m \neq 0} |q_{m0}|^2 \exp(-im\Omega t) \qquad (6.9)$$

From Eq. 6.9 it can be understood that a wave-packet can be created by the Q-transition through vibronic coupling with the B-transition. Therefore, DIB corresponds to a real-time observation of the vibronic coupling (vibronic intensity borrowing) between the Q- and B-bands, which is manifested by the coefficient q_{m0}. In a similar way, we can also calculate the oscillator strength of the transition from the n-exciton state to the (n+1)-exciton state |n+1,S$_1$> ← |n,S$_1$> (n = 1, 2,...). Therefore, both the bleaching/PIE and PIA signals are synchronously modulated, which agrees with the experimental result.

3.8.2 Evaluation of amount of modulated transition dipole moment

As discussed in Sect. 3.7.4, the Q- and B-transitions are mixed with each other by the DIB mechanism, which is induced by the sub-5-fs excitation pulse through the vibrational motion of the porphyrin molecules comprising a J-aggregate. Based on the DIB mechanism, the amount of modulation of the transition dipole moment can be evaluated. The normalized modulation of the transition dipole moment is simply expressed as $\delta\mu_{QG}/\mu_{QG}$, in which μ_{QG} and $\delta\mu_{QG}$ represent the Q-transition dipole moment of a TPPS molecule and the change of μ_{QG} induced by the molecular vibration, respectively. It is noted that the modulation of μ_{QG} also changes the inter-molecular dipole-dipole interaction, J, to $J + \delta J$ which is given by

$$J_{QG} = \mu_{QG}{}^2 \left(1 - 3\cos^2\theta\right)/\hbar a^3$$
$$\frac{\delta J_{QG}}{J_{QG}} = \frac{2\delta\mu_{QG}}{\mu_{QG}} + \frac{3\sin(2\theta)}{3\cos^2\theta - 1}\delta\theta - \frac{3}{a}\delta a. \tag{6.10}$$

Here, all transition dipole moments in the molecules are assumed to be parallel to each other and to be aligned making a common angle θ with the aggregate axis. The molecules are set at equidistance with a lattice constant a. Since the transition energy from the ground state to the lowest one-exciton state is originally red-shifted by $2J$ in comparison with that of the monomer, the modulation of J gives rise to a peak shift of the J-band with a bandwidth of $4J$ in the transient absorption spectrum. This is one of the characteristic features of the exciton system in comparison with the molecular system. In the following, the data are analyzed phenomenologically. The nonlinear spectrum, $S_{NL}(\omega)$, is assumed to be modulated as $S_{NL}(\omega)$ by $\delta\mu_{QG}$ and $\delta(2J)$, which is given by

$$S'_{NL}(\omega) = S_{NL}(\omega - \delta\omega(t))(1 + \delta\alpha(t)), \tag{6.11}$$

where

$$\delta\alpha(t) = \delta\alpha\cos(\Omega t) \equiv \delta(\mu_{QG}^2)/\mu_{QG}^2 \cos(\Omega t) \tag{6.12}$$

$$\delta\omega(t) = \delta\omega\cos(\Omega t) \equiv \delta(2J)\cos(\Omega t). \tag{6.13}$$

Here, $\delta\alpha$ and $\delta\omega$ correspond to the amplitude modulation and the spectral shift, respectively, of the nonlinear spectrum. The modulation frequency, Ω, corresponds to the $247\ \mathrm{cm}^{-1}$ ruffling mode. In the present model, it is assumed that both $\delta\alpha$ and $\delta\omega$ are independent of the probe photon energy, ω, and that all μ_{QG} and J are effectively modulated. Equation 6.11 can be

expressed approximately as

$$S'_{NL}(\omega) \approx S_{NL}(\omega) + \left(\delta\alpha \cdot S_{NL}(\omega) - \delta\omega \cdot \frac{dS_{NL}(\omega)}{d\omega} \right) \cos(\Omega t)$$

$$= S_{slow}(\omega) + S_{osc}(\omega) \cos(\Omega t). \tag{6.14}$$

The nonlinear spectrum, $S_{NL}(\omega)$, consists of a slow dynamical component ($S_{Nslow}(\omega)$) and an oscillating component ($S_{osc}(\omega)$). For the slow-dynamic component, the 320 fs decay component is employed. Figure 6-17 shows the best-fitted results ($\delta\alpha . S_{NL}(\omega)$ dashed, $\delta\omega[dS_{NL}(\omega)/d\omega]$ dotted, $S_{osc}(\omega)$ solid) for the oscillating component using Eq. 6.14.
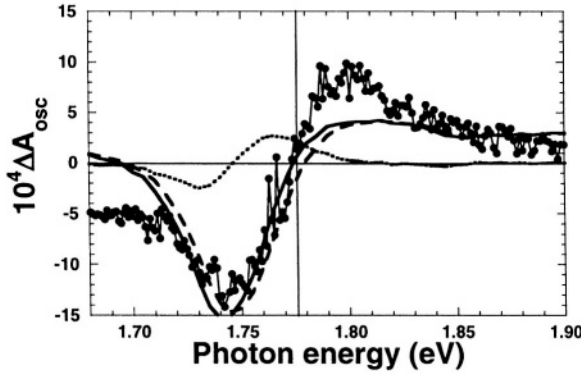

Figure 6-17. Fitted result based on model (d): dynamic intensity borrowing.

The experimental result is reproduced satisfactory by the fitted curve with $\delta\alpha = (6 \pm 1) \times 10^{-2}$ and $\delta\omega = (-8 \pm 4) \times 10^{-4}$ eV. From the value of $\delta\alpha$, $\delta\mu_{QG}/\mu_{QG}$ is estimated to be $(3 \pm 1) \times 10^{-2}$. Using $\delta\alpha$, $\delta\omega$, and Eq. 6.10, the amount of the dipole-dipole interaction of the Q-band can be estimated to be $2J_Q = \delta\omega/\delta\alpha = (13 \pm 9)$ meV assuming $\delta\theta = \delta a = 0$. This value is much smaller than that calculated by the energy shifts from the monomer to the J-aggregate in the stationary absorption spectrum (170 meV). This may mean that the energy shift in the stationary absorption spectrum is not only due to the dipole-dipole interaction. This is also supported by the fact that the magnitude of the energy shift for the B-band is only about twice that of the Q-band. Since the oscillator strengths of the Q- and B-bands differ by a factor of ten ($\mu_Q^2/\mu_B^2 = 0.1$), the ratio J_Q/J_B, must also be different by the same order [see Eq. (6.10)]. A Coulombic interaction between molecules caused by the aggregation could be one of the other mechanisms associated

with this energy shift. A third possible mechanism for the difference is the effect of $\delta\theta$ and δa. Another possibility is the effect of the ground-state stabilization, which is sometimes called the crystal shift in the J-aggregate with respect to the ground state in the monomer molecule. This is now being studied to clarify the difference. In the following section the value obtained for the normalized modulation of the dipole moment is used.

3.8.3 Evaluation of magnitude of the oscillator strength transfer

Based on vibronic coupling theory, we estimate the amount of transfer of the oscillator strength from the B-band to the Q-band. The perturbed transition dipole moment of the Q-band, μ'_{OG}, is expressed as follows:

$$
\begin{aligned}
\mu'_{QG} &= \mu_{QG} + \delta\mu_{QG} \\
&= \mu_{QG} + \frac{V_{\text{DIB}}}{\Delta E_{BQ}}\mu_{BG},
\end{aligned}
\tag{6.15}
$$

where V_{DIB} denotes the interaction Hamiltonian due to the DIB. Equation 6.15 is written as follows:

$$
\frac{\delta\mu_{QG}}{\mu_{QG}} = \frac{V_{\text{DIB}}}{\Delta E_{BQ}}\frac{\mu_{BG}}{\mu_{QG}}.
\tag{6.16}
$$

Here, $\Delta E_{BQ} \approx 0.94$ eV and $\mu_{QG}/\mu_{BG} \approx 0.32$ are estimated from the stationary absorption spectrum of the monomer. The magnitude of $\delta\mu_{QG}/\mu_{QG}$ has also been estimated to be 3.0%. Hence, $V_{\text{DIB}} = 9$ meV = 73 cm^{-1} is obtained using Eq. 6.16. This value of V_{DIB} is much less than the vibration frequency, 247 cm^{-1}, which is consistent with our model. The modulated transition dipole moment is expressed as follows:

$$
\mu'_{QG} = \mu_{QG} + \delta\mu_{QG} = (32 + 0.96)\times10^{-2}\,\mu_{BG}.
\tag{6.17}
$$

Consequently, the modulation of the Q-transition dipole moment in a real-time spectrum is estimated to be about 0.96% of the B-transition dipole moment, which is in good agreement with our previous result [22, 34].

4.   CONCLUSIONS

A coherent molecular vibration coupled to a Frenkel exciton is observed using sub-5-fs laser pulses and a multi-channel pump-probe experimental set-up. The oscillation originates from molecular vibration and is assigned to the $247 \ cm^{-1}$-ruffling mode. In comparison with the conventional model (c) regarded as a Franck-Condon-type wave-packet motion [Fig. 6-11 (a)], the dynamic intensity borrowing [Fig. 6-12, model (d)], which we propose for the first time, can be called a Herzberg-Teller-type wave-packet motion. In fact, the DIB corresponds to a real-time observation of the Herzberg-Teller-type wave-packet motion. The coherent oscillation is explained by the modulated transition dipole moment of the Q-transition, which is caused by the DIB mechanism from the intense B-band to the weak Q-band through the molecular vibration. The modulated transition dipole moment is estimated to be about 3%, which corresponds to about 0.96% borrowing of the B-transition dipole moment.

Acknowledgments

References

1. T. Kobayashi and A. Shirakawa, *Appl. Phys. B* **70,** S239 (2000).
2. G.M. Gale, M. Cavallari, T. J. Driscoll and F. Hasche, *Opt. Lett.* **20,**1562 (1995).
3. A. Shirakawa and T. Kobayashi, *Appl. Phys. Lett.* **72**, 147 (1998).
4. G. Cerullo, M. Nisoli and S. D. Silvestri, *Opt. Lett.* **23**, 1283 (1998).
5. A. Shirakawa, I. Sakane and T. Kobayashi, *Opt. Lett.* **23**, 1292 (1998).
6. A. Shirakawa, I. Sakane, M. Takasaka and T. Kobayashi, *Appl. Phys. Lett.* **74,** 2268 (1999).
7. M.J. Rosker, F.W. Wise and C.L. Tang, *Phys. Rev. Lett.* **57**, 321 (1986).
8. H.L. Fragnito, J.Y. Bigot, P.C. Becker and C.V. Shank, *Chem. Phys. Lett.* **160,** 101 (1989).
9. W.T. Pollard, S.L. Dexheimer, Q. Wang, L.A. Peteanu, C.V. Shank and R.A. Mathies, *J. Phys. Chem.* **96**, 6147 (1992).
10. G. Cerullo, G. Lanzani, M. Muccini, C. Taliani and S.D. Silvestri, *Phys. Rev. Lett.* **83,** 231 (1999).
11. T. Kobayashi and A. Shirakawa, *Chem. Phys. Lett.* **321,** 385 (2000).
12. M.H. Vos, F. Rappaport, J.C. Lambry, J. Breton and J.L. Martin, *Nature* **363,** 320 (1993).
13. M. Chachisvilis and V. Sundstrom, *Chem. Phys. Lett.* **261,** 165 (1996).
14. R. Monshouwer, A. Baltuska, F.V. Mourik and R.V. Grondelle, *J. Phys. Chem. A,* **102,** 4360 (1998).
15. A. Sugita, T. Saito, H. Kano, M. Yamashita and T. Kobayashi, *Phys. Rev. Lett.* **86,** 2158 (2001).

16. *J-aggregates* (World Scientific, Ed. T. Kobayashi, 1996).
17. S. Mukamel, *Principles of Nonlinear Optical Spectroscopy* (Oxford, 1995).
18. A.S. Davydov, *Theory of Molecular Excitons* (Plenum, 1971).
19. T. Kobayashi, *Mol. Cryst. Liq. Cryst.* **314,** 1 (1998).
20. E.B. Fleisher, J.M. Palmer, T.S. Srivastava and A.J. Chatterjee, *Am. Chem. Soc.* **93,** 3162(1971).
21. R.F. Pasternack, P.R. Huber, P. Boyd, G. Engasser, L. Francesconi, E. Gibbs, P. Fasella, G.C. Venturo and L. de C. Hinds, *Am. Chem. Soc.* **94,** 4511 (1972).
22. H. Kano, T. Saito and T. Kobayashi, *J. Phys. Chem. B* **105**, 413 (2001).
23. K. Misawa, H. Ono, L. Minoshima and T. Kobayashi, *Appl. Phys. Lett.* **63,** 577 (1993).
24. J. Knoester and F.C. Spano, *Phys. Rev. Lett.* **74,** 2780 (1995).
25. O. Ohno, Y. Kaizu and T. Kobayashi, *J. Chem. Phys.* **99**, 4128 (1993).
26. D.L. Akins, S. Ozcelik, H.R. Zhu and C. Guo, *J. Phys. Chem.* **100**, 14390 (1996).
27. B. Ren, Z.Q. Tian and D.L. Akins, *Chem. Phys. Lett.* **328,** 17 (2000).
28. H.L. Fragnito, J.Y. Bigot, P.C. Becker and C.V. Shank, *Chem. Phys. Lett.* **160,** 101 (1989).
29. W.T. Pollard, H.L. Fragnito, J.Y. Bigot, C.V. Shank and R.A. Mathies, *Chem. Phys. Lett.* **168**, 239 (1999).-
30. W.T. Pollard, S.L. Dexheimer, Q. Wang, L.A. Peteanu, C.V. Shank and R.A. Mathies, *J. Phys. Chem.* **96,** 6147 (1992).
31. G.A. Shick, M.R. O'Grady and R.K. Tiwari, *J. Chem. Phys.* **97,** 1339 (1993).
32. R. Pantell, F. Pradere, J. Hanus, M. Schott and H. Pathoff, *J. Chem. Phys.* **46,** 3507 (1967).
33. K. Minoshima, K., M. Taiji, K. Misawa and T. Kobayashi, *Chem. Phys. Lett.* **218,** 67 (1994).
34. H. Kano and T. Kobayashi, *J. Chem. Phys.* **116,** 184 (2002).
35. S.E. Bradforth, R. Jimenez, F.V. Mourik, R.V. Grondelle and G.R. Fleming, *J. Phys. Chem.* **99,** 16179 (1995).
36. M. Burgel, D.A. Wiersma and K. Duppen, *J. Chem. Phys.* **102,** 20 (1995).
37. M.H. Perrin, M. Gouterman and C.L. Perrin, *J. Chem. Phys.* **50,** 4137 (1969).
38. A.T.N. Kumer, F. Rosca, A. Widom and P.M. Champion, *J. Chem. Phys.* **114**, 701 (2001).
39. *The Porphyrins, Vol III, Physical Chemistry, Part A* (Ed. D. Dolphin, Academic Press, 1979).
40. J.A. Schelnutt, *J. Chem. Phys.* **72,** 3948 (1980).
41. X.-Y. Li, R.S. Czernuszewicz, J.R. Kincaid and T.G. Spiro, *J. Am. Chem. Soc.* **111**, 7012 (1989).
42. R.S. Czernuszewicz, X.-Y. Li and T.G. Spiro, *J. Am. Chem. Soc.* **111,** 7024 (1989).
43. A.C. Albrecht, *J. Chem. Phys.* **33,**156 (1960).
44. P.M. Champion, *Chem. Phys. Lett.* **86**, 231 (1982).

Chapter 7

VIBRATIONAL ECHO CORRELATION SPECTROSCOPY
A New Probe of Hydrogen Bond Dynamics in Water and Methanol

John B. Asbury, Tobias Steinel and M.D. Fayer
Department of Chemistry, Stanford University
Stanford, CA 94305, USA

Abstract   Multidimensional vibrational echo correlation spectroscopy with full phase resolution is used to measure hydrogen bond dynamics in water and methanol. The OD hydroxyl stretches of methanol-OD oligomers in CCl_4 and HOD in H_2O are studied using the shortest mid-IR pulses (< 45 fs, < 4 cycles of light) produced to date. The pulses have sufficient spectral bandwidth to span the very broad $(> 400 \text{ cm}^{-1})$ spectrum of the 0-1 and 1-2 vibrational transitions. Hydrogen bond population dynamics are extricated with exceptional detail in MeOD oligomers because the different hydrogen-bonded species are spectrally distinct. The experimental results along with detailed calculations indicate the strongest hydrogen bonds are selectively broken through a non-equilibrium relaxation pathway following vibrational relaxation of the hydroxyl stretch. Following hydrogen bond breaking, the broken MeOD oligomers retain a detailed structural memory of the prior intact hydrogen bond network. The correlation spectra are also a sensitive probe of the structural fluctuations in water and provide a stringent test of water models that are widely used in simulations of aqueous systems. The analysis of the 2D band shapes demonstrates that different hydrogen-bonded species are subject to distinct (wavelength-dependent) ultrafast (~ 100 fs) local fluctuations and essentially identical slower (0.4 ps and ~ 2 ps) structural rearrangements. Observation of wavelength-dependent dynamics demonstrates that standard theoretical approaches assuming Gaussian fluctuations cannot adequately describe water dynamics.

Key words: Infrared, water, methanol, hydrogen bond dynamics, vibrational echoes.

1.   INTRODUCTION

Hydrogen bonding liquids have generated a great deal of experimental [1-13] and theoretical [13-21] study because of their importance as solvents in chemical and biological systems.   The facile evolution of hydrogen-bonded networks [22] plays an important role in determining their properties. Examination of the hydroxyl stretch of hydrogen-bonding liquids provides information on hydrogen bonding because the stretch frequency is sensitive to the nature and extent of hydrogen bonding [16, 17, 22-25]. Strong evidence for the correlation between the hydroxyl stretch frequency and the hydrogen bond strength in solids is obtained from correlating crystallographic data and spectroscopic data [24]. From the crystallographic data, the length of the hydrogen bond can be determined. A shorter length corresponds to a stronger bond. The same relationship also applies to liquids [16, 17, 22, 23, 25].

Studying the dynamics of the hydroxyl stretch provides a gateway to understand the evolution of hydrogen bond networks. Hydrogen bonds are constantly being broken and formed [22]. Stronger hydrogen bonds become weaker and weaker hydrogen bonds become stronger because of the continual structural evolution of the hydrogen bond networks. Large global fluctuations in hydrogen bond networks, which result in the formation and breaking of hydrogen bonds and equilibration of the networks [16, 17, 21], can be accessed by studying hydrogen bond population dynamics reported by the hydroxyl stretch [3-5, 26, 27]. Smaller fluctuations in the strengths of hydrogen bonds causes hydroxyl stretch frequency spectral diffusion [16]. These motions can be accessed by studying the spectral diffusion dynamics of the hydroxyl stretch before or after hydrogen bonds have broken [27, 28].

Linear absorption spectroscopy can provide information on the influence of the number and types of hydrogen bonds on the hydroxyl stretch frequency. However, it cannot be used to examine the structural evolution of hydrogen bonds. The inhomogeneous broadening of the hydroxyl stretch [2-7, 11, 13, 15] prevents the spectral evolution from being observed in the absorption line. As a result, the linear absorption spectrum can only provide time-independent information.

It is in the context of hydrogen bond dynamics that ultrafast infrared experiments gain their importance [1-13]. Most ultrafast infrared experiments have utilized pump-probe spectroscopy [1, 2, 9-12], which can examine hydroxyl population dynamics.   Pump-probe experiments give vibrational lifetimes, hydrogen bond breaking and reformation rates, and some information on spectral diffusion [1, 2, 10, 11]. The dynamics of hydrogen bond evolution can be explicated with much greater detail using vibrational echo experiments [29, 30] because the inhomogeneous

contribution to the line shape can be eliminated and the underlying dynamical line shapes can be observed. Because of the complexity of hydrogen bonding systems, analysis of different contributions to dynamical vibrational spectra are enhanced by the use of ultrafast multidimensional methods. Such methods can separate and narrow the dynamic spectral features [29, 30], permitting the observation of various contributions to the dynamics. Multidimensional techniques are beginning to be applied to hydrogen bonding systems [3-5, 8]. Multidimensional vibrational echo methods are akin to multidimensional NMR experiments [31, 32]. However, vibrational stimulated echoes operate on a sufficiently fast time scale (tens of fs) to directly examine the time evolution of hydrogen bonding networks.
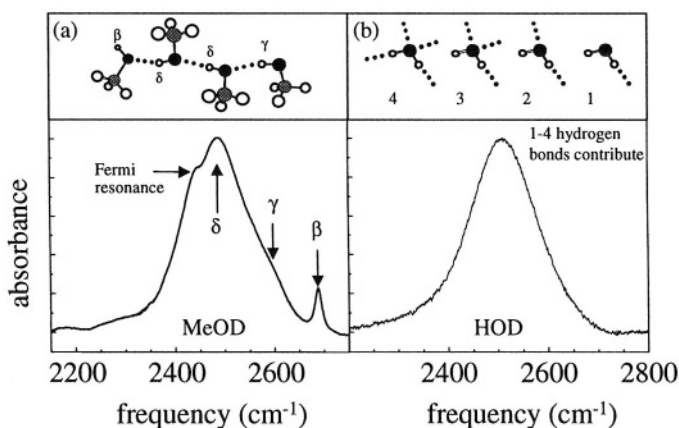

Figure 7-1. (a) The linear absorption spectrum of a 10% solution of methanol-OD in CC14. βs are hydroxyls that are acceptors but not donors. γs are donors but not acceptors. δs are both donors and acceptors. These are illustrated schematically at the top of the figure. The shoulder on the red side of the spectrum is a Fermi resonance with the overtone of the methyl rocking mode. This feature is absent in fully deuterated methanol. (b) The linear absorption spectrum of a 5% solution of HOD in H_2O. Water is capable of forming up to four hydrogen bonds, as illustrated at top of figure. However, they are not resolved in the linear spectrum.

The linear absorption spectra of the hydrogen-bonding liquids studied in this work, 10% methanol-OD oligomers in CCl_4 solution and 5% HOD in H_2O, are displayed in Fig. 7-1. Examples of the different hydrogen-bonded species formed by MeOD and H_2O are displayed at the top of the figure. A MeOD that is both a hydrogen bond donor and acceptor (called δ), has a very broad hydroxyl stretch band (~ 150 cm^{-1}) centered at ~ 2490 cm^{-1} [see Fig. 7-1(a)] [19, 23, 33]. (There is a shoulder on the red side of the δ band caused by a Fermi resonance with the overtone of the methyl rocking mode [34].) For a MeOD that is a hydrogen bond donor but not an acceptor (called γ), the frequency shifts to ~ 2600 cm^{-1} and the spectrum is

significantly narrower than the δ band ($\sim 80 \text{ cm}^{-1}$). A MeOD that is a hydrogen bond acceptor but not a donor (called β) absorbs still further to the blue at $\sim 2690 \text{ cm}^{-1}$, and the band is relatively narrow ($\sim 20 \text{ cm}^{-1}$) [19, 23, 33]. Water also displays spectral shifts to the blue when the extent of hydrogen bonding decreases [16, 17]. However, because water can have many more hydrogen bonds, there is not a simple one-to-one correspondence between the number of hydrogen bonds and the frequency [16, 17]. Consequently, methanol oligomers in CCl_4 are an important system for studying the dynamics of hydrogen bonded networks [3-5].

Below, multidimensional stimulated vibrational echoes with full phase information are applied to the study of hydrogen bond dynamics in MeOD oligomers in CCl_4 and HOD in H_2O. To perform the experiments, we use the shortest mid-IR pulses produced to date (< 45 fs or < 4 cycles of light) [3-5]. Because of the very large bandwidth associated with the ultrashort pulses, it is possible to perform experiments on the entire broad hydroxyl stretching 0-1 and 1-2 bands of water and MeOD even though the combined ground state and first excited state bands are $\sim 400 \text{ cm}^{-1}$ wide. The experiments yield time-dependent vibrational echo correlation spectra, which provide a fundamentally new probe of hydrogen bond dynamics. The correlation spectra display the hydrogen bond population dynamics and the spectral diffusion dynamics simultaneously in two frequency dimensions, which facilitates the determination of the complicated dynamics with exceptional detail.

2.   EXPERIMENTAL PROCEDURES

The ultrashort IR pulses are generated using a Ti:Sapphire regeneratively amplified laser/OPA system. The output of the regenerative amplifier is 26 fs transform-limited 2/3 mJ pulses at 1 kHz repetition rate. These are used to pump a substantially modified Spectra Physics short pulse IR OPA. The output of the OPA is compressed to produce < 50 fs virtually transform-limited IR pulses as measured by collinear autocorrelation. Figure 7-2 displays a collinear autocorrelation trace of the shortest IR pulses produced to date. The solid line displays the experimentally measured collinear autocorrelation trace and the dashed line displays a Gaussian fit with a 40 fs full width at half maximum (FWHM). The oscillations in the time trace result from the interference of the pulses with the period of the $\sim 2700 \text{ cm}^{-1}$ optical cycle. The spectrum of the pulse displayed in the inset (solid line) demonstrates that the IR pulse, which is centered at $\sim 2700 \text{ cm}^{-1}$, is transform-limited with a spectral FWHM of 368 cm^{-1}, determined by the Gaussian fit to the spectrum (dashed line). For the experiments, the pulses

were centered at ~ 2500 cm^{-1} and the compression was readjusted to give transform-limited pulses in the sample as measured by a sample that gave a purely non-resonant signal. The long-term stability is such that data were collected continuously for as long as 5 days.
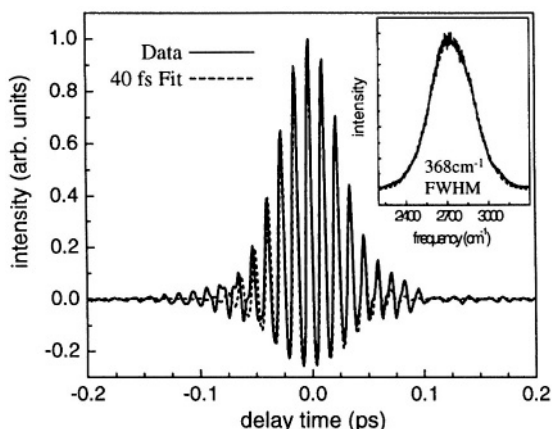

Figure 7-2. Collinear autocorrelation of shortest mid-IR pulse produced to date. The solid line is the experimental data and the dashed line represents a 40 fs FWHM Gaussian fit to the data. The oscillations result from the ~ 2700 cm^{-1} optical cycle of the mid-IR light. The inset displays the corresponding spectrum of the mid-IR pulse, which demonstrates the pulse is transform-limited.

For the heterodyne-detected multidimensional stimulated vibrational echoes, the IR beam is split into 5 beams. Three of the beams are the excitation beams for the stimulated vibrational echo. A fourth beam is the local oscillator (LO) used to heterodyne-detect the vibrational echo signal. The fifth beam is used as a probe in pump-probe experiments. All of the beams that pass through the sample are optically identical and are compensated for group velocity dispersion (GVD) simultaneously. The vibrational echo signal combined with the LO or the probe beam is passed through a monochromator. Depending on the experiment, the heterodyne detected echo or the probe beam is detected by a 32 element Mercury Cadmium Telluride (MCT) array. At each monochromator setting, the array detects 32 individual wavelengths. The data were processed using a computer that acted as a digital lock-in amplifier that was synchronized to an optical chopper.

Difference intensity measurements were made for both the vibrational echo and pump-probe experiments. For the first laser pulse, the array measured the local oscillator or probe beam and the corresponding signal field. For the next laser shot, the optical chopper blocked one of the beams to prevent the signal field from being generated and only the local oscillator or probe beam was measured. The difference between these two

measurements was then normalized by the spectrum of the local oscillator or probe detected in the second shot to remove the effect of pixel-to-pixel variations in the array. Both the heterodyne-detected vibrational echo and the pump-probe signal are quadratic in the intensity of the laser. A single-element detector measured the overall intensity of the laser, and was used to do a second normalization of the signals to provide the proper quadratic normalization.

The samples, 10% MeOD in CCl_4 or 5% HOD in H_2O, were held in a sample cell of CaF_2 flats with a spacing of $50 \ \mu m$ and $6 \ \mu m$, respectively. The peak absorbance of the samples was < 0.2. Such low absorbance is necessary to prevent serious distortions of the pulses as they propagate through the sample.

For the spectrally resolved pump-probe experiments, the change in transmission spectrum was collected as a function of the delay between the pump and probe pulses. The monochromator was stepped across the spectrum so that the arrays of wavelengths measured by the different array blocks matched up to form a continuous spectrum across the entire hydroxyl stretch band. The pump pulse was delayed in variable steps. The spectrum of the pump and probe pulses were identical. The spectrum of the probe was removed from the data as the data were collected. The data were not corrected for the spectrum of the pump; it is sufficiently broad to span the desired spectral region.

The phase-resolved, heterodyne-detected, stimulated vibrational echo was spectrally resolved in a monochromator and measured as a function of the frequency variable, ω_m, and two time variables, τ and T_w, which are defined as the time between the first and second radiation field-matter interactions and the second and third interactions, respectively. The measured signal is the absolute value squared of the sum of the vibrational echo electric field, S, and the local oscillator electric field, L: $|L+S|^2 = L^2 + 2LS + S^2$. The L^2 term is time-independent and the S^2 is negligibly small; hence, neither contributes to the time dependence of the signal. The spectrum of the $2LS$ term is the ω_m frequency axis. As the τ variable is scanned in 2 fs steps, the phase of the echo electric field is scanned relative to the fixed local oscillator electric field, resulting in an interferogram measured as a function of the τ variable for each frequency, ω_m, that is detected through the monochromator. The interferogram contains the amplitude, sign, frequency, and phase of the echo electric field as it varies with τ. By numerical Fourier transformation, this interferogram is converted into the frequency variable ω_τ. For each ω_m frequency measured, a spectrum as a function of ω_τ is calculated. In NMR, the ω_τ and the ω_m axes are generally referred to as the ω_1 and the ω_3 axes, respectively [31].

The interferogram contains both the absorptive and dispersive components of the vibrational echo signal. To obtain purely absorptive features, two sets of quantum pathways are measured independently by appropriate time-ordering of the pulses in the experiment [32]. With pulses 1 and 2 at the time origin, pathway 1 or 2 is obtained by scanning pulse 1 or 2 to negative time, respectively. In principle, by adding the Fourier transforms of the interferograms from the two pathways, the dispersive component cancels leaving only the absorptive component [3, 32]. The 2D vibrational echo correlation spectra are constructed by plotting the amplitude of the absorptive part of the stimulated vibrational echo as a function of both ω_m and ω_τ.

Lack of perfect knowledge of the timing of the pulses and consideration of chirp on the vibrational echo pulse requires a "phasing" procedure to be used [3]. The projection slice theorem [3, 31, 32] is employed to generate the absorptive 2D correlation spectrum. The projection of the absorptive 2D correlation spectrum onto the ω_m axis is equivalent to the IR pump-probe spectrum recorded at the same T_w, as long as all the contributions to the stimulated vibrational echo are absorptive. Consequently, comparison of the projected 2D stimulated vibrational echo spectrum with the pump-probe spectrum permits the correct isolation of the absorptive vibrational echo correlation spectrum from the 2D spectrum obtained from the addition of the two quantum pathways.

It is possible to come relatively close to the correct correlation spectrum prior to the "phasing" procedure because the very short pulses permit their time origins to be known within a few fs. The frequency-dependent phasing factor used to correct the 2D spectra has the form

$$S_C(\omega_m, \omega_\tau) = S_1(\omega_m, \omega_\tau)\Phi_1(\omega_m, \omega_\tau) + S_2(\omega_m, \omega_\tau)\Phi_2(\omega_m, \omega_\tau)$$

$$\Phi_1(\omega_m, \omega_\tau) = \exp\left[i(\omega_m \Delta\tau_{LO,E} + \omega_\tau \Delta\tau_{1,2} + Q\omega_m\omega_m + C\omega_m\omega_\tau)\right] \quad (7.1)$$

$$\Phi_2(\omega_m, \omega_\tau) = \exp\left[i(\omega_m \Delta\tau_{LO,E} - \omega_\tau \Delta\tau_{1,2} + Q\omega_m\omega_m + C\omega_m\omega_\tau)\right]$$

Each term in Eq. 7.1 has a well-defined physical origin. S_C is the correlation spectrum. S_1 and S_2 are the spectra recorded for pathways 1 and 2, respectively. $\Delta\tau_{LO,E}$ accounts for the lack of perfect knowledge of the time separation of the LO pulse and the vibrational echo pulse; the term involving Q accounts for linear chirp introduced into the echo pulse by the rear window of the sample cell; $\Delta\tau_{1,2}$ accounts for the lack of perfect knowledge of the time origins of excitation pulses 1 and 2; and the term involving C accounts for the linear chirp caused by propagation of the echo pulse through the sample. The methods employed to minimize the uncertainty in the

phasing parameters have been described elsewhere [27]. Following phasing, the errors in the time origins are $< 100 \times 10^{-18}$ s and the chirp across the entire spectrum is $< 100 \times 10^{-18}$ s.

3.   RESULTS AND DISCUSSION

The following discussion of multidimensional vibrational echo correlation spectroscopy as a fundamentally new probe of hydrogen bond dynamics is broken into two sections. In the first section, we report on hydrogen bond population dynamics in MeOD oligomers in CCl_4 and the subsequent influence of those dynamics on the oligomers that are perturbed by hydrogen bond breaking. In the second section, we focus on the structural evolution of hydrogen bond networks in water observed through spectral diffusion of the OD stretch of HOD in H_2O. The timescales and assignments of structural evolution are discussed, including the transition from fluctuations that are dominated by the local hydrogen-bonded structure to fluctuations that are more global in nature and lead to equilibration of the hydrogen bond network.

3.1.   Hydrogen Bond Population Dynamics in MeOD

Figure 7-3 displays some of the 2D correlation spectra for MeOD, four contour plots at $T_w = 125$ fs, 1.2 ps, 1.8 ps, and 5.0 ps. The maximum positive signal has been normalized to unity in each plot for a clear presentation. The contours represent equal 10% graduations. Although the amplitudes of the data have been obscured by the normalization, the relative amplitudes between data sets are well defined and will be used in the analysis described below. The ω_τ axis is the axis of the first radiation field interaction. The ω_m axis is the axis of the emission of the echo pulse. If the frequency of the first interaction and the emission are the same, a peak will appear on the diagonal. If the frequency of the emission is different from the frequency of the first interaction, a peak will appear off diagonal. The positive going band on the diagonal in the 125 fs spectrum corresponds to the 0-1 transition of the δ band with some contribution from the 0-1 γ band on the blue end. The center frequencies of the δ and γ 0-1 transitions are indicated by horizontal and vertical lines. The negative going band below the main diagonal band arises from the 1-2 transition of the δ band. The 1-2 band is off-diagonal because the emission is shifted to lower frequency by the vibrational anharmonicity ($\sim 150 \text{ cm}^{-1}$).

As the T_w delay increases, the correlation spectra displayed in Fig. 7-3 exhibit changes that provide insight into the mechanism of hydrogen bond evolution. By $T_w = 1.2$ ps, the correlation spectrum has changed dramatically due to vibrational relaxation and hydrogen bond breaking. A good fraction of the initially produced excited-state population has decayed to the ground state because the vibrational lifetime of the δOD stretch is ~ 0.5 ps [1]. The magnitude of the δ 1-2 off diagonal peak reflects the δ excited state decay. By $T_w = 1.8$ ps, the δ excited state has completely decayed. Because the lifetime of the γ band (~ 1 ps) is longer than that of the δ band, the diagonal γ 0-1 band is uncovered as the δ band decays. By $T_w = 1.8$ ps, the diagonal γ peak is almost gone.
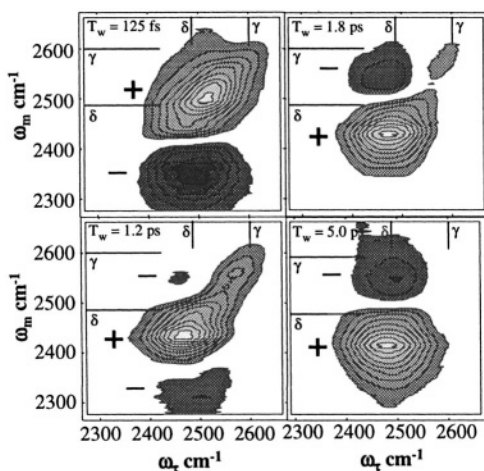

Figure 7-3. Correlation spectra for $T_w = 125$ fs, 1.2 ps, 1.8 ps, and 5 ps. The contours represent 10% steps. The vertical and horizontal lines mark the center frequencies of the δ and γ 0-1 transitions. The positive going band are the δ and γ 0-1 transitions. The negative going off-diagonal band is from the δ and γ 1-2 transitions. As T_w increases, the δ and γ 1-2 bands (bottom) decay, the δ 0-1 band changes shape, and photoproduct γ peak appears (top).

As will be demonstrated below, when the δ OD excited state relaxes, hydrogen bonds break [1, 9, 35], producing photoproduct γ ODs. The resulting photoproduct γ peak, located above the δ band, is visible by $T_w = 1.2$ ps. The diagonal δ band progressively contracts to the red as T_w increases. The off- diagonal photoproduct γ peak located above the δ 0-1 band grows with increasing T_w delay. By $T_w = 5.0$ ps, the only remaining features are the preserved δ and the photoproduct γ bands. Comparison of the center of the preserved δ band at $T_w = 5.0$ ps and the center of the initially excited δ band (indicated by the horizontal line at $2490 \ cm^{-1}$)

demonstrates that the preserved δ band is contracted to the red and shifted off-diagonal along the ω_m axis. For times longer than ~ 5 ps, the peaks do not change shape significantly, but slowly decay in magnitude on a time scale of tens of ps because of hydrogen bond recombination [1, 9, 35]. An important aspect of the 2D correlation spectrum is that the photoproduct γ is spectrally separated in the plane from the equilibrium γ band (see Fig. 7-3, $T_w = 1.2$ ps and 1.8 ps), in contrast to 1D spectroscopies.

The $T_w = 5.0$ ps correlation spectrum displays signal at the δ 0-1 band even though the vibrational excited-state lifetime is only ~ 0.5 ps. Normally, the decay of the excited state into the ground state causes the vibrational echo signal to decay. However, there is both an excited-state and ground-state contribution to the signal [36]. Following vibrational relaxation, a few tens of percent of the initially excited δ s break a hydrogen bond in ~ 200 fs, removing them as δ absorbers [1]. The broken bond eliminates two δ s and creates a γ and a β. Thus, the ground state is not completely filled following complete relaxation of the excited state. This leaves some amplitude in the ground state pathway, although the excited-state pathway has decayed completely. The ground-state signal remains for the hydrogen bond recombination time, which is tens of ps [1, 9, 35].

The correlation spectra displayed in Fig. 7-3 demonstrate that the δ 0-1 band shifts to the red and moves off-diagonal as T_w becomes longer than the vibrational lifetime. Understanding the origin of this shift provides insight into the mechanism of hydrogen bond evolution and the coupling between the vibrational modes involved in the hydrogen-bonded network. The δ 0-1 band may shift because vibrational relaxation simply "heats" the hydrogen bond network, producing changes that would be the same as raising the equilibrium temperature. Or, the shift may result from selectively breaking a subset of hydrogen bonds associated with the low frequency side of the δ band following vibrational relaxation. To discriminate between these two mechanisms, we have performed detailed calculations to model the correlation spectra. Four models of hydrogen bond population dynamics were considered and have been described in detail elsewhere [5]. We give here a very brief overview of the modeling procedure and discuss only the two models which gave the best results. The correlation spectra are fitted using the sum of 2-dimensional Gaussian band shapes for the δ and γ, 0-1 and 1-2 bands. For the $T_w = 125$ fs correlation spectrum, the widths and positions of the bands are set equal to the equilibrium δ and γ widths and positions as determined from linear spectroscopy of the sample and by determination of the anharmonicity of the hydroxyl stretch (150 cm^{-1}, see Fig. 7-3, 125 fs panel). The $T_w = 125$ fs correlation spectrum is very well described by this model. The calculations use results of the fits to the 125 fs

data and factors that are unique to each model to calculate the 5 ps data. The 1-2 bands do not contribute because 5 ps is much longer than the lifetime.

The experiments also give the ratios of the amplitudes of the 0-1 bands at 125 fs to those at 5 ps. From comparison of the fit to the $T_w = 125$ fs correlation spectrum with the fit to the 5 ps correlation spectrum using each model, the ratios of the amplitudes are determined for each model.
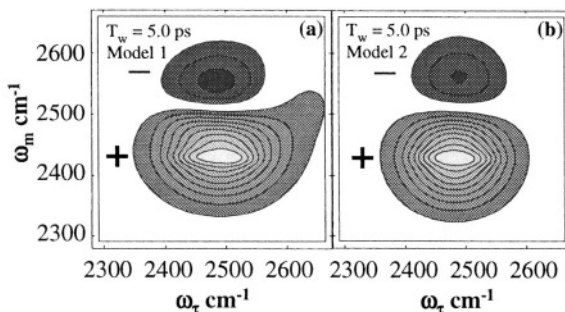

Figure 7-4. Simulated correlation spectra calculated from two models of hydrogen bond breaking. Model 2 provides a more quantitative and meaningful description of the data. See text for details.

Model 1: Following vibrational relaxation of the initially excited OD stretch, the deposited energy causes hydrogen bond weakening. Weakening of hydrogen bonds shifts their absorption to the blue (higher energy) [16, 17, 22-25]. The δ and γ bleach responsible for the long-lived vibrational echo signal is not filled in by the vibrational relaxation because the population is shifted to the blue. The center positions and widths of the preserved δ and γ bleach bands are described by their equilibrium spectra. The weakened δ and γ photoproducts have spectra that are shifted to the blue along the ω_m axis. In the calculations, the magnitude of the blue shift is allowed to vary to give the best fit to the 5 ps data (5 ps panel, Fig. 7-3). The sum of the residuals squared, $R^2 = 1.1$. The correlation spectrum calculated from Model 1 is displayed in panel (a) of Fig. 7-4. The model does a reasonable job of reproducing aspects of the data (compare to 5 ps panel of Fig. 7-3). However, it does not have the correct shape. The preserved band (positive going) is elongated to the upper right because of the preserved γ portion of the spectrum. Even more significant, to obtain this best fit, the amplitudes of the bands are unphysical. To get the features in the correct positions along the ω_m axis requires a very small shift (5 cm^{-1}) of the weakened band produced by vibrational relaxation. Because of the small shift, the preserved δ bleach band strongly overlaps and nearly cancels the weakened photoproduct band. To obtain the correct ratio of the amplitude of the

$T_w = 5.0$ ps data relative to the 125 fs data, Model 1 requires the magnitude of the preserved bleach δ band to be ~ 9 times larger than the magnitude of the initial δ bleach, which would require the concentration of initially excited MeODs *increasing* by a factor of ~ 9 between $T_w = 125$ fs and 5.0 ps. Obviously this result is not possible. Model 1 cannot describe the data. Model 1 is essentially a thermal equilibration model. Detailed measurements of the pump-probe spectrum show that it takes ≥ 30 ps for the system to reach thermal equilibrium (at which time the pump-probe spectrum is the same as the temperature difference spectrum), again demonstrating that the mechanism that gives rise to the 5 ps data is not thermal equilibration.

Model 2: Vibrational relaxation of initially excited OD stretches selectively breaks hydrogen bonds on the red side of the δ band and produces red-shifted γ photoproducts. In the calculations, the spectral region of hydrogen bond breaking is allowed to vary to give the best fit to the 5 ps data (5 ps panel, Fig. 7-3). The sum of the residuals squared, $R^2 = 0.13$. The simulated correlation spectrum calculated from Model 2 is displayed in panel (b) of Fig. 7-4. This model provides an excellent description of the $T_w = 5.0$ ps experimental data. The shape of the spectrum is correct, and the R^2 value is a factor of ~ 8 smaller for Model 2 compared to Model 1. Note also the differences in the fine details of the centers of the positive going calculated peaks in Figs. 7-4 a and b. The center of Fig. 7-4 b is strikingly close to that of the data in the 5 ps panel of Fig. 7-3. In addition to having the correct shape and a better R^2, Model 2 predicts a physically reasonable magnitude for the amplitudes of the bands at 5 ps relative to 125 fs. Model 2 gives the preserved δ bleach to ~ 60% of the initial δ bleach, that is, 60% of the initially excited δ MeODs break a hydrogen bond, which is within a few tens of percent of the value determined by independent measurements of the quantum yield of hydrogen bond breaking in MeOD oligomers, not an unphysical 900% too large.

The results presented above demonstrate that the δ band is contracted to the red and the photoproduct γ band is generated, also to the red, because vibrational relaxation selectively breaks the stronger hydrogen bonds (the red side of the line). Breaking of the strongest hydrogen bonds is at first surprising. However, this non-equilibrium mechanism can occur if vibrational relaxation on the low energy side of the line populates different modes from vibrational relaxation on the high energy side of the line, and the modes populated through the lower energy relaxation pathway are more effective at breaking hydrogen bonds. Significant support for the proposed origins of the non-equilibrium mechanism comes from the IR pump/Raman probe experiments of Iwaki and Dlott, who observed that the pathway for vibrational relaxation was different on the red and blue sides of the hydroxyl

stretching band in OH methanol [37]. Excitation on the red side led to vibrational relaxation that produced substantially more relative population of hydroxyl bends compared to excitation on the blue side that put much more population in the CH bends and other modes [37]. The hydroxyl bends would be expected to be strongly coupled to the hydrogen bond in contrast to CH stretches. This necessary feature of the proposed mechanism is indeed observed experimentally.

3.2. Photoproduct γ Band Spectral Diffusion in MeOD

In the above discussion, we did not discuss the spectral diffusion dynamics observed along the ω_τ axis because the hydrogen bond population dynamics under study could be modeled without considering spectral diffusion. We now discuss the evolution of hydrogen-bonded networks through the observation of spectral diffusion following the breaking of hydrogen bonds.
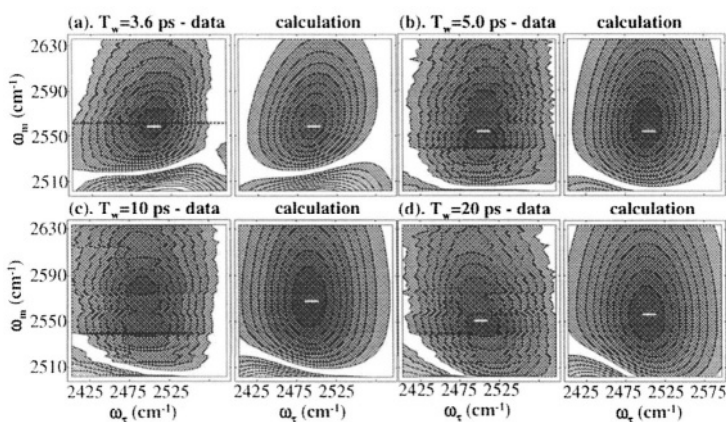

Figure 7-5. Contour plots of portions of correlation spectra showing the region around the photoproduct γ peak for $T_w =$ (a) 3.6 ps, (b) 5.0 ps, (c) 10.0 ps and (d) 20.0 ps, and calculations of the same spectra. As T_w increases, the ω_τ axis reports the dephasing dynamics of the photoproduct γ peak band-shape changes along both the ω_m and ω_τ axes. The broadening along the ω_m axis results from the evolution toward the equilibrium spectrum of the initially prepared photoproduct γ distribution. Spectral diffusion along the ω_τ axis reports the dephasing dynamics of the photoproduct γ peak.

Correlation spectra were measured focusing on the photoproduct γ peak for T_w delays long compared to the excited-state lifetime. Four close-up views of the off-diagonal photoproduct γ peak measured at 3.6, 5.0, 10, and

20 ps T_w delays are displayed in Fig. 7-5. The out-of-plane axes, shown as contours in each panel of Fig. 7-5, have been normalized to the absolute value magnitude of the photoproduct γ peak. The contours display equal 10% graduations. For reference, the photoproduct γ peak at the $T_w = 5.0$ ps (Fig. 7-5) is the same as the photoproduct γ peak displayed in the $T_w = 5.0$ ps correlation spectrum shown in Fig. 7-3, except that the scale has been normalized. The amplitude of the photoproduct γ peak decays by a factor of 4 between 3.6 and 20 ps. The decay in the signal is indicated in Fig. 7-5 by the decreased signal-to-noise ratio at longer T_w delay. The photoproduct γ band decays as hydrogen bonds recombine on the ~ 10 ps time scale [1, 5].

   The dynamics of the photoproduct γ peak displayed in Fig. 7-5 reflect only the dynamics of the ground-state hydrogen-bonded network because the excited-state dynamics are complete (δ and γ vibrational lifetimes 0.5 ps and 1 ps, respectively). At $T_w = 3.6$ ps the photoproduct γ peak is narrowest along both ω_m and ω_τ axes. As T_w increases, the peak shows the influence of equilibration of the perturbed hydrogen bond network and spectral diffusion dynamics. As T_w increases, the initially created photoproduct γ spectral distribution, which is narrowed and red-shifted along the ω_m axis, equilibrates to its steady-state distribution, which increases the width of the peak along the ω_m axis. Spectral diffusion results in the increase of the dynamical linewidth along the ω_τ axis as T_w increases.

   From the model previously used to simulate the $T_w = 5.0$ ps experimental data (see Fig. 7-4, panel (b)) we assigned a center frequency of 2560 cm^{-1} to the photoproduct γ peak [5]. The apparent center of the photoproduct γ peak displayed in Figs. 7-3 to 7-5 confirms this assignment (note the displacement along the ω_m axis of the photoproduct γ peak from the horizontal line that marks the center frequency of the equilibrium γ peak in Fig. 7-3). The photoproduct γ band is red-shifted by about 40 cm^{-1} relative to the initially excited γ distribution. This frequency shift indicates the photoproduct γs are not randomly distributed throughout the inhomogeneous γ band but are created with at least some frequency correlation with their origin on the low frequency side of the δ band.

   The correlation spectra displayed in Figs. 7-3 to 7-5 contain the dynamical line shape along the ω_τ axis as a function of frequency and waiting time, T_w. Changes in the dynamical line shape as a function of T_w give the spectral diffusion dynamics occurring within the hydroxyl stretch peak [2, 16, 38, 39].

   The qualitative changes in the dynamical line shape can be seen in the data by looking at a cross sectional cut of the photoproduct γ peak at a particular ω_m value and projecting it onto the ω_τ axis. The horizontal dashed line shown in the $T_w = 3.6$ ps panel of Fig. 7-5 illustrates such a cut at the apparent center of the photoproduct γ hydroxyl stretch peak at ~ 2560 cm^{-1}.

As T_w increases, the photoproduct γ band changes shape and the ~ 2560 cm^{-1} cut becomes broader. The dynamical line measured in the correlation spectra is narrow when spectral diffusion has not randomized the distribution of hydroxyl stretch frequencies. As spectral diffusion occurs, the dynamical linewidth broadens. Because the hydroxyl stretch frequency is correlated with the strength of hydrogen bonds [15, 16, 22-25, 40] the time evolution of the vibrational echo correlation spectra reflects the structural evolution of the hydrogen bonding network.

To quantify the spectral diffusion dynamics observed in the photoproduct γ peak as a function of T_w delay, we calculated the correlation spectra displayed in Fig. 7-5 using the model described above. One 2-dimensional Gaussian peak was used to describe the photoproduct γ band and another was used for the preserved δ band, which appears as the positive going feature barely visible at the bottom of the correlation spectra in Fig. 7-5 and can be seen in Figs. 7-3 and 7-4. Although the δ band is not shown in detail in Fig. 7-5, its inclusion in the calculations is necessary to obtain a correct description of the γ band. The Fermi resonance peak and its two cross peaks with the δ band were included as well. Their positions and amplitudes relative to the preserved δ bleach were determined from the fit to the $T_w =$ 125 fs correlation spectrum [5].
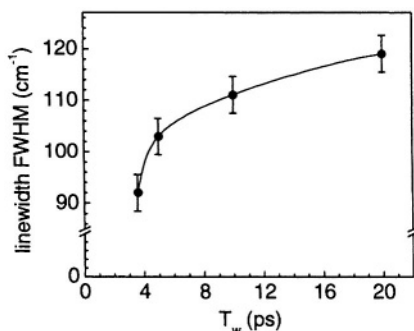

Figure 7-6. Plot of the linewidth (FWHM) of photoproduct γ peak along the ω_τ axis versus T_w. Changes in the dynamical linewidth are direct evidence of spectral diffusion. Spectral diffusion along the ω_τ axis demonstrates the existence of fine frequency correlation in the photoproduct γ band. The line through the data is a guide to the eye.

Figure 7-5 also displays the corresponding 2-dimensional Gaussian fit to each correlation spectrum at $T_w = 3.6$, 5.0, 10, and 20 ps. The 2-dimensional Gaussian fitting procedure enables us to quantitatively measure the dynamical linewidth of the photoproduct γ peak without interference from the preserved δ peak or the three peaks associated with the Fermi resonance.

After fitting the correlation spectra, the amplitudes of every peak except the photoproduct γ peak are nulled. A cross-sectional cut of the photoproduct γ peak at $\omega_m = 2560 \text{ cm}^{-1}$ is fit with a Gaussian. The resulting FWHM is a measure of the dynamical linewidth. Figure 7-6 displays the dynamical line widths extracted from the vibrational echo correlation spectra displayed in Fig. 7-5 plotted versus the corresponding T_w delay. The error bars indicate the upper and lower bounds of the fit to the dynamical linewidth at which the R^2 values are twice their optimal value. The line through the data is a guide to the eye. At the shortest T_w delay following the completion of vibrational relaxation ($T_w = 3.6 \text{ ps}$), the dynamical linewidth is ~ 90 cm^{-1}. This width grows to ~ 120 cm^{-1} by $T_w = 20 \text{ ps}$.

The changing dynamical linewidth with increasing T_w delay demonstrates spectral diffusion in the photoproduct γ band. Furthermore, the photoproduct γ band is initially created shifted to the red relative to the equilibrium γ band. The shift of the photoproduct γ band to the red shows that there is at least some frequency correlation between the parent δ s and the photoproduct γ s, which we call *coarse frequency correlation.* By coarse correlation, we mean that a δ having two stronger than average hydrogen bonds produces a photoproduct γ having one stronger than average hydrogen bond. The data also demonstrate that there is a more subtle type of correlation that we call *fine frequency correlation.* The fine correlation shows that a direct correlation exists between a δ absorber at frequency ω_0 and a narrow distribution of photoproduct γ s centered at frequency $\omega_0 + \Delta$, where $\Delta = \sim 130 \text{ cm}^{-1}$ [5] is the shift in the hydroxyl stretch frequency that results from breaking a hydrogen bond. Fine frequency correlation will occur if the photoproducts have a detailed "memory" of the structure of the prior intact hydrogen bond networks, which is slowly erased as the broken networks evolve in time away from their structures immediately following hydrogen bond breaking.

The observation of fine frequency correlation means that the photoproduct γ s have memory of the frequency of the original unbroken oligomer. A γ is the end of the oligomer piece that was created by breaking a hydrogen bond in the original oligomer. Because the hydroxyl stretch frequency is correlated with structure, memory of the frequency implies memory of the original structure that gave rise to the new oligomer fragment. Here, we will consider two likely mechanisms that could give rise to the frequency memory.

The first mechanism involves the correlation of the strengths of adjacent hydrogen bonds. The strength of a hydrogen bond is correlated to its length [15, 16, 22-25, 40], although the angle and donating hydroxyl bond length can have significant influence as well [16, 20, 41]. Therefore, the first mechanism involves correlation in the microscopic density variations across

the hydrogen-bonded network that extend over one or more MeODs. When a stronger than average hydrogen bond in a high microscopic density region of the network is excited and subsequently breaks, the remaining adjacent hydrogen bond, that produces the γ, is also a stronger than average hydrogen bond. If the hydrogen bond strength is the overwhelming factor that determines the frequency, then the frequency of the photoproduct γ will be correlated with the reactant δ, consistent with the observations.

The second mechanism recognizes that other structural degrees of freedom besides the donated and accepted hydrogen bonds may contribute to the δ and γ hydroxyl stretch transition frequencies. In MeOD, there are the positions and orientations of the methyl groups, as well as the configuration of other MeODs that are not directly hydrogen-bonded to the MeOD of interest. For the oligomers studied here in CCl_4, there is also the local solvent configuration. In pure MeOD, the surrounding liquid that is not directly hydrogen bonded to an initially excited δ could be considered the solvent. When the reactant δ is broken and the photoproduct γ is formed, the other degrees of freedom of the oligomer and the solvent will not necessarily be affected immediately. Preservation of these other structural degrees of freedom could produce the observed frequency correlation.

The photoproduct γ peak appears red-shifted $40 \ cm^{-1}$ relative to the γ band in the linear absorption spectrum. This red shift is a significant fraction of the total shift caused by the second hydrogen bond ($\sim 100 \ cm^{-1}$). Therefore, the gross memory of the broken hydrogen bond must be comparatively strong relative to the hydrogen bond that was initially present. It is questionable whether the local environment can play a strong enough role in determining the hydroxyl stretch frequency to produce this type of coarse frequency correlation. However, the demonstrated existence of a frequency grating in the red contracted photoproduct γ band requires a fine as well as coarse frequency memory.

The existence of both coarse and fine frequency correlation may be consistent with both mechanisms contributing to the frequency correlation exhibited by the γ photoproduct, which suggests the following physical picture. For a given hydrogen bond oligomer of MeODs the strengths of adjacent hydrogen bonds are correlated and the microscopic density of the network is higher in places due to the shorter hydrogen bonds that connect two or more MeODs. When a hydrogen bond breaks and a δ becomes a γ, the microscopic density in the network cannot immediately respond to the perturbation, which produces the coarse frequency correlation observed along the ω_m axis. In addition, other structural degrees of freedom of the network are not immediately randomized, which produces the fine frequency correlation. As the T_w delay increases, the perturbed network evolves away from its initial structure. The microscopic density changes around the

photoproduct γ, which causes the spectral evolution observed along the ω_m axis as T_w increases. The other degrees of freedom of the network and the solvent also randomize, which erases the fine frequency correlation and causes the dynamical line width to increase along the ω_τ axis.

The fine and coarse frequency correlation described here further supports the model of hydrogen bond dynamics presented above [5] in which it was shown that the strongest hydrogen bonds are selectively broken giving rise to the photoproduct γ band (see Fig. 7-4 and the discussion surrounding it). Another mechanism, in which energy is deposited into the networks by vibrational relaxation causing all of the hydrogen bonds to weaken, is inconsistent with fine frequency correlation. The fine frequency correlation in particular as well as the coarse frequency correlation demonstrates that the hydrogen bond network around the photoproduct γ retains significant memory of the prior unbroken network.

3.3.   Structural Evolution in Water, an Overview

By understanding the detailed hydrogen bond population dynamics in MeOD, we are able to extend the conclusions to our study of the structural evolution of hydrogen bond networks in water. Water and other hydrogen bonding liquids are known to break hydrogen bonds following excitation of the hydroxyl stretch [1, 3, 9, 35, 42]. We have performed detailed spectrally resolved IR pump-probe experiments and find that broken hydrogen bond photoproducts do not make a measurable contribution to the spectrum for pump-probe delays < 2 ps. Consequently, we only consider correlation spectra measured at T_w delays < 2 ps. Studying the OD stretch in water not only provides dynamical information on water itself, but with a vibrational lifetime of ~ 1.8 ps rather than the ~ 0.7 ps lifetime of the OH stretch in D_2O [43], the time window is doubled in which we can extract the dynamics of the hydrogen-bonded network unperturbed by photoproducts.

Vibrational echo correlation spectra were taken for T_w delays between 100 fs and 1.6 ps. Figure 7-7 displays correlation spectra for four of the T_w delays, 100 fs, 400 fs, 800 fs, and 1.6 ps. Two peaks are observed along the ω_m axis corresponding to the 0-1 and the 1-2 transitions. The positive going peak, corresponding to the vibrational echo emitted at the 0-1 transition frequency, appears on the diagonal. The negative going peak, corresponding to the vibrational echo emitted at the 1-2 transition frequency, appears red-shifted along the ω_m axis by the anharmonicity. From a fit we find the anharmonicity of the OD stretch vibration to be $140 \pm 20 \text{ cm}^{-1}$.

Looking in particular at the 0-1 band, it is obvious that the correlation spectra undergo a dramatic change in shape from $T_w = 100 \text{ fs}$ to 1.6 ps. Its

width along the ω_{τ} axis (horizontal axis) is the dynamical linewidth of the 0-1 transition. The width is caused by the very fast fluctuations of the hydrogen-bonded network. As T_w is increased, additional fluctuations come into play that cause the dynamical linewidth to broaden further. Changes in the dynamical linewidth report the spectral diffusion dynamics [16, 39]. Therefore, the change in the shape of the correlation spectrum provides information on the hydrogen bond dynamics on different time scales.
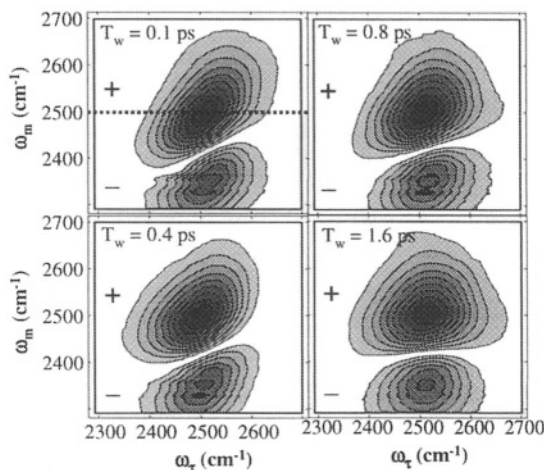
Figure 7-7. The experimental vibrational echo correlation spectra of the OD stretch of HOD in H_2O as a function of time T_w. The positive going peak arises from the 0-1 transition. The negative going peak arises from the 1-2 transition. As time progresses the elongation of the peaks decreases because of fluctuation in the hydrogen-bonded network.

Molecular Dynamics (MD) Simulations and Comparison to Data. The key quantity that connects the vibrational echo correlation spectra and simulations of water dynamics is the frequency-frequency correlation function (FFCF) of the hydroxyl stretch frequency. The FFCF is defined as $C(t) = \langle \delta\omega(t)\delta\omega(0) \rangle$, where $\delta\omega$ is the change in the hydroxyl stretch frequency from its average value. The FFCF describes the loss of correlation of the frequency of the ensemble of OD stretch oscillators as time progresses. As the structure of the hydrogen-bonding network evolves, the frequency of a given OD oscillator changes. At sufficiently long time, a given oscillator samples all frequencies in the absorption spectrum, and the FFCF decays to zero. The time dependence of the vibrational echo correlation spectra provides a good test for the FFCF, while the linear absorption spectrum does not.

The methods we use to compare the dynamics predicted from MD simulation with the experimentally observed dynamics are (i) a particular

water model simulation is implemented, (ii) the FFCF for a given model of water is generated from a method that involves electronic structure calculations and classical MD simulations [44], and (iii), we calculate the vibrational echo correlation spectra from the FFCF using time-dependent diagrammatic perturbation theory to obtain the full third-order non-linear material response [30, 36]. In addition to the FFCFs obtained from the water models, we construct a phenomenological tri-exponential FFCF and vary its parameters until the calculations resulting from (iii) reproduce the experimental correlation spectra.

The calculations from the two water models and the phenomenological FFCF are compared to the data by comparing the dynamical line widths of the corresponding correlation spectra at the center of the 0-1 band ($\omega_m = 2500$ cm^{-1}). The dynamical linewidth is the projection of a line through the spectrum at a particular ω_m onto the ω_τ axis. This method makes it possible to construct a simple plot to compare the data and calculations and, more importantly, look for an ω_m dependence of the hydrogen bond network dynamics, as will be discussed below.

FFCFs for the OH stretch of HOD in D_2O have been calculated previously [16] for the TIP4P [45] model of water. Here, calculations for TIP4P [45] and SPC/E [46] water models were performed using a new method [44]. The method is based on *ab initio* electronic structure calculations of clusters of molecules. First, configurations of molecules are generated from a classical molecular dynamics simulation of the HOD/H_2O system. Then a representative set of $HOD(H_2O)_n$ clusters are extracted from the simulation. For each cluster *ab initio* calculations (using density functional theory) are performed for different values of the OD stretch coordinate, and in doing so, an anharmonic potential curve that leads to the 0-1 OD transition frequency for the HOD molecule in that cluster is generated. From looking at a hundred or so clusters, it was determined that there is a linear correlation between the OD frequency and the component of the electric field from the H_2O molecules on the D atom in the direction of the OD bond vector. Assuming this same linear correlation holds for the full liquid, the normalized FFCF becomes the normalized electric field time correlation function. The latter can be generated from a completely classical molecular dynamics simulation.

The FFCFs obtained from MD simulation are exceedingly well described by a sum of three exponential functions, although a small oscillatory feature at early times, which does not change the observables, is not captured. We will henceforth refer to the tri-exponential analytical representation as the FFCF. It has the form

$$C(t) = \Delta_0^2 \exp(-t/\tau_0) + \Delta_1^2 \exp(-t/\tau_1) + \Delta_2^2 \exp(-t/\tau_2). \quad (7.2)$$

The overall amplitude of Eq. 7.2 was adjusted so that the calculation of the linear absorption line shape was able to reproduce the full width at half maximum of the experimentally measured absorption spectrum [28]. Parameters for the two water model FFCFs are summarized in Table 7-1 along with a phenomenological FFCF we obtained by fitting the data as discussed below. All FFCFs reproduce the linear line shape with equal accuracy, showing that the linear line shape is not a good test of water dynamics [28].

Table 7-1. **FFCF Parameters**

FFCF	Δ_0 (rad/ps), (%)	τ_0 (ps)	Δ_1 (rad/ps), (%)	τ_1 (ps)	Δ_2 (rad/ps), (%)	τ_2 (ps)
Tri-Exp.	11.5, (43)	0.032	4.2, (16)	0.4	10.8, (41)	1.8
SPC/E [46]	12.1, (52)	0.031	9.0, (29)	0.28	7.4, (19)	0.98
TIP4P [45]	13.0, (58)	0.032	10.2, (36)	0.34	4.4, (6)	0.90

Using the above procedures, we calculated the theoretical vibrational echo correlation spectra with the appropriately scaled FFCFs taking into account both the 0-1 and 1-2 transitions of the hydroxyl stretch. Figure 7-8 shows the results for four T_ws, 100 fs, 400 fs, 800 fs, and 1.6 ps for the SPC/E [46] water model. Comparison of the experimental and MD correlation spectra in Fig. 7-7 and Fig. 7-8 demonstrate a qualitative, but not a quantitative agreement. The 0-1 peak appears on the diagonal and the 1-2 peak appears shifted off-diagonal by the anharmonicity. The 0-1 peak in the T_w = 100 fs correlation spectrum displays the characteristic elongation along the diagonal that demonstrates the presence of inhomogeneity in the hydroxyl stretch peak. As T_w increases to 1.6 ps, the shape of the 0-1 peak changes, reflecting the substantial increase in the dynamical linewidth.
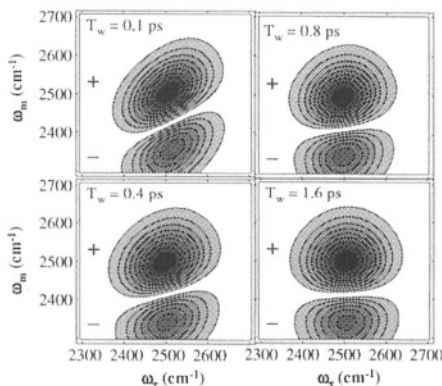
Figure 7-8 Simulated vibrational echo correlation spectra calculated from the FFCF that are derived from the SPC/E model of water.

   A quantitative comparison of the data and the results of the water model
FFCF calculations and the phenomenological FFCF calculations are shown
in Fig. 7-9.   The main figure plots the dynamical linewidths for ω_m =
2500 cm^{-1} extracted from the data and from the calculations.   The
experimental data appear as diamonds with error bars.   The horizontal line at
147 cm^{-1} is the long time asymptotic linewidth.   This width is narrower than
the absorption spectrum (FWHM is 162 cm^{-1}) because the measured
dynamical linewidth is the product of the absorption spectrum and the laser
intensity spectrum raised to the power of 1.5.   The pulses used in the
experiment, which were ~ 45 fs duration, had a very broad spectrum, but
their spectral width did reduce the measured dynamical linewidth.
Calculations demonstrate that 6 fs pulses are required for the asymptotic
value of the measured dynamical linewidth to be indistinguishable from the
absorption spectrum.   The top curve (dots) is from the TIP4P [45] model and
the next lowest curve (dashes) is from the SPC/E [46] model. The solid line
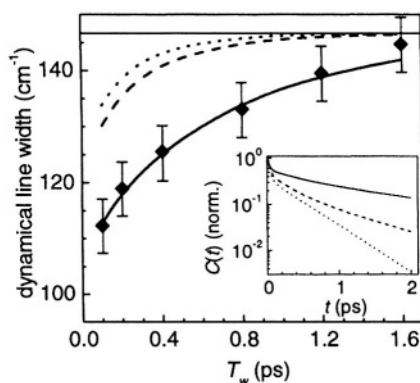comes from calculations using the fitted phenomenological FFCF.

Figure 7-9.   Dynamical linewidths for ω_m = 2500 cm^{-1} from the experimental correlation
spectra (diamonds with error bars), the TIP4P (dots) and SPC/E (dashes) water models, and
the FFCF obtained from fitting the data (solid line through the data).   See Table 7-1 for
parameters.   The horizontal line at 147 cm^{-1} is the long time asymptotic linewidth.   Inset:
FFCFs derived from the experimental data (solid line) and calculations using the water
models SPC/E(dashes) and TIP4P (dots).

   In this fit the parameters for a tri-exponential FFCF were constrained to
be consistent with other complementary experiments and calculations.   The
magnitude of the FFCF is determined by the linear absorption spectrum. The
time constant of the fast component was set at 32 fs to be consistent with the
fast components of the FFCFs obtained by MD simulation.   This time scale
is also consistent with recent work by Elsaesser and co-workers who found
that a 30 fs component to the FFCF provided the best fit to their 2 pulse

vibrational echo measurement of water [7]. The time constant for the intermediate component was set equal to the intermediate decay component (400 fs) in a vibrational echo peak shift measurement we performed in the course of these experiments. This can be done since the vibrational echo peak shift has been demonstrated to reproduce the FFCF [47, 48] given a sufficient waiting time, T_w, so that the value of the normalized FFCF << 1 [48]. Therefore, in the fitting procedure, three parameters were allowed to vary independently, the pre-exponential factors of two of the components and the time constant of the slowest component.

We find that the dynamical linewidths derived from the water models do not reproduce the data within experimental error. The linewidth from the TIP4P [45] model reaches its asymptotic value already by $T_w = 1.6$ ps and the SPC/E [46] linewidth is close to that asymptotic value at that time. However, the data and the linewidths obtained from the fit to the data are still removed from the asymptotic value approaching it relatively slowly.

The time dependence of the model line shapes is correlated to the time dependence of the model FFCFs. The inset in Fig. 7-9 compares model and phenomenological FFCFs directly. It is evident that both model FFCFs have too much amplitude at short time and the long time components are too fast (see also Table 7-1).

Of particular interest here is the long time component of the FFCF because the time constant and amplitude of this component are in substantial error when calculated from the water models. The SPC/E [46] and TIP4P [45] model give a time constant of the slow component of the FFCF of 0.98 ps and 0.9 ps, respectively, and both have too little amplitude in the slow component. The best least squares fit through the experimental data gives a 1.8 ps time constant. We estimate upper and lower bounds of ± 0.5 ps based on a factor of two increase in the sum of the squares of the residuals.

Comparison of the phenomenological FFCF with those derived from MD simulation demonstrates the TIP4P [45] and SPC/E [46] models of water describe well the fast fluctuations in water but not the slower fluctuations. The TIP4P model essentially misses the slow component. The SPC/E model does better, but over-estimates the magnitude of the intermediate and under-estimates the magnitude of the slow components. In addition, the SPC/E model under-estimates the time scale of the slow component by a factor of ~ 2. Two very different methods were used to calculate the FFCF for TIP4P, the one described here [44] and the one used previously [16], but the results are virtually identical. This demonstrates that the failure of the MD simulations to reproduce the data is in the water models themselves, rather than the method used to calculate the OD oscillator frequency fluctuations.

Analysis of the TIP4P [45] model for the OH stretch of the HOD/D_2O system indicates that the fast component of the FFCF arises from hindered

translational motion of the hydrogen bond (stretching of the hydrogen bond length coordinate) [16]. The slower component of the FFCF calculated for the HOD/D_2O system has been assigned to the influence of hydrogen bond formation and breaking (hydrogen bond equilibration) [16, 17, 21]. Our analysis demonstrates this time scale (~ 0.5 ps) is too fast to describe the slow dynamics that we observe in water. Some MD simulations report hydrogen bond breaking times of ~ 2 ps [20, 49]. This time scale corresponds with the slow component of the phenomenological FFCF we obtained from the data. Nonetheless, it still is plausible that the slow time scale evolution found in our experiments is due to hydrogen bond equilibration, that is, the breaking and formation of hydrogen bonds.

3.4.   Local Structure Dependent Evolution in Water

Inherent in the FFCF analysis presented above was the underlying assumption that the dynamics of water molecules (as interrogated by the OD stretch) are the same at all frequencies within the broad hydroxyl stretching band. A water molecule can make zero to four hydrogen bonds. These species have different transition frequencies, although they are not resolvable within the broad hydroxyl stretch absorption band [14, 16]. Furthermore, the strength of a hydrogen bond determines the hydroxyl stretch transition frequency to a great extent [24]. On long time scales, hydrogen bonds will break and form, and strong hydrogen bonds will weaken and weak hydrogen bonds will strengthen. Therefore, it is expected that the dynamics will be independent of frequency as water molecules sample all conformations on long time scales. However, the different hydrogen-bonded conformations persist on short time scales. As we show below, hydrogen bond dynamics are frequency-dependent, which demonstrates the different hydrogen-bonded conformations of water have different dynamics.

The dynamical linewidths were determined from the full correlation spectrum at a number of frequencies, ω_m, and T_w delays [50]. A procedure [28] was used to determine if the 1-2 band was interfering with the determination of the dynamic linewidths of the 0-1 band. It was found that for frequencies ≥ 2500 cm^{-1}, the 1-2 band causes no significant perturbation. Some of the results are shown in Fig. 7-10 [50]. The 100 fs data and the line fit to it demonstrate very clearly that the dynamical linewidths, and therefore the hydrogen bond dynamics, vary as a function of frequency. As the frequency increases, the dynamical linewidth increases. The increase in width can be seen in the 100 fs correlation spectrum shown in Fig. 7-7. The spectrum is clearly broader for higher ω_m. However, the 400 fs data and line

fit in Fig. 7-10 show that by 400 fs, within experimental error, there is no longer frequency dependence to the dynamical linewidth. The inset in Fig. 7-10 displays the change in the dynamical linewidth with ω_m as a function of T_w. The points are the slopes of lines like the 100 fs line in the body of Fig. 7-10. The line through the data yields the time scale for the decay of the inhomogeneity in the dynamics as ~ 100 fs.
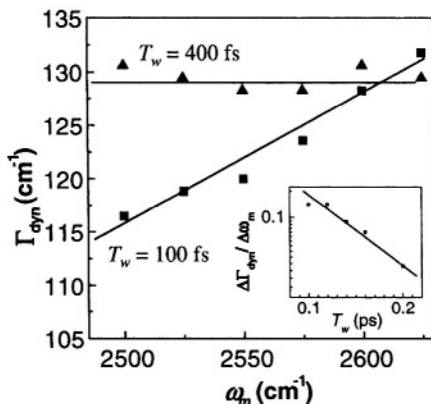

Figure 7-10. Dependence of the dynamical linewidth Γ_{dyn} on ω_m for two T_ws, 100 fs and 400 fs. For 100 fs there is a distinct dependence of width on ω_m. By 400 fs there is no dependence of width on ω_m. Inset: the decay of the inhomogeneity in dynamical linewidth with T_w. The inhomogeneity decays on a time scale of ~ 100 fs.

The results show that hydrogen bond dynamics observed through their effect on the hydroxyl stretch frequency depend on the hydroxyl stretch frequency examined. The amount of spectral diffusion is smaller at lower frequencies at short times. Recent MD simulations demonstrate that the hydroxyl stretch band is composed of differently hydrogen-bonded species [17, 21]. The red side of the line is composed primarily of water molecules with more hydrogen bonds than the blue side of the line. In addition, stronger hydrogen bonds red-shift the frequency relative to weaker hydrogen bonds for a given number of hydrogen bonds. However, the bands for different numbers of hydrogen bonds, inhomogeneously broadened by the strengths of the hydrogen bonds, overlap substantially, and are not spectroscopically resolvable. Nonetheless, it is safe to say that the blue side of the line corresponds to fewer and weaker hydrogen bonds relative to the red side of the line.

Analysis of simulations indicates that the short time spectral diffusion (structural evolution) arises mainly from hindered translational motion of the hydrogen bond under observation (stretching of the hydrogen bond length

coordinate) although angular variations play some role [14, 16, 17, 21]. The slower spectral diffusion is assigned to the influence of hydrogen bond equilibration (formation and breaking) [16, 17, 21, 50]. Any given water molecule, over time, will experience all hydrogen bonding configurations. There is an average number of hydrogen bonds for water molecules. A particular water molecule at $t = 0$ will have a certain number of hydrogen bonds. Over time it will regress toward the average. For some molecules the regression will require a net formation of hydrogen bonds, while for others it will require a net breaking of hydrogen bonds. This equilibration process will result in hydroxyl stretch frequency shifts and is less local than the very fast fluctuations.

The wavelength dependence of the dynamic linewidths displayed in Fig. 7-3 provides qualitative insight into the different nature of spectral diffusion due to fast local fluctuations and slower hydrogen bond equilibration [50]. With fewer hydrogen bonds, the blue side local networks will not be as constrained, and fluctuations about the local structure that give rise to spectral diffusion will be greater. This is born out by the simulations when wavelength-dependent conditional probabilities are examined [51]. The second moment of these conditional probability distributions (see Ref. 51, Fig. 8.2), which is closely related to the dynamical linewidth, shows that spectral diffusion at 100 fs is greater on the blue side of the line than in the center. For times longer than ~ 400 fs, the lack of a wavelength dependence in the data suggests that the dynamics and associated spectral diffusion are dominated by more substantial network structural evolution (hydrogen bond equilibration) that does not depend on the details of the local structure [50]. Thus, 400 fs may be a rough boundary between very local fast fluctuations about relatively fixed structures and the randomization of the local structures. While the fast fluctuations make important contributions to the vibrational echo correlation spectra, it is the equilibration time scale that may be of greater importance in chemical and biological processes that require significant local structural changes in the water solvent.

The calculations presented in Figs. 7-8 and 7-9, and the detailed comparisons between the data and simulations presented previously [28], were performed with the diagrammatic perturbation theory treatment of non-linear optical experiments [36]. Because of the Gaussian approximation that is at the core of the treatment, a single FFCF describes an entire absorption line. The data presented here show that an advance in theory is required to describe complex systems such as water on all time scales. A new theory needs to be able to describe wavelength-dependent differences at short times in a natural manner and then go over to the current calculated results at longer time.

The fundamentally important observations on the differences in dynamics for different water structures at short times [50] do not change the basic conclusions drawn from comparisons of data and simulations (see Fig. 7-9) about the efficacy of the water simulation models [28]. The major deviations between FFCFs obtained from the simulations and from the data mainly occur for times > 400 fs, times for which there is no wavelength dependence. Independent of the wavelength selected for comparison, the simulated results do not agree with the data. The ability of a new theory to relate different wavelength-dependent dynamics displayed in Fig. 7-10 to different local network structures will be significant.

4. CONCLUDING REMARKS

The results of ultrafast heterodyne-detected multidimensional stimulated vibrational echo correlation spectroscopy *with full phase information* were employed to study the dynamics of hydrogen bond networks in MeOD and water (H_2O). By using extremely short pulses (< 50 fs), it is possible to excite the entire very broad hydroxyl-stretching band including the 1-2 transition. The multidimensional correlation spectroscopy makes it possible to extract the hydrogen bond population dynamics with exceptional detail. Spectral diffusion dynamics of the hydroxyl stretch 0-1 transition of water were elucidated with great sensitivity in a comprehensive manner.

The vibrational echo correlation spectra of MeOD display the hydrogen bond population dynamics in two dimensions, which allows the mechanism of hydrogen bond evolution to be determined with great detail. At short time, the correlation spectrum (see Fig. 7-3) is dominated by the hydrogen bonded OD stretch 0-1 transition (positive going peak) and the 1-2 transition (negative going peak). As T_w is increased the broad diagonal δ band contracts to the red side of the line and shifts off the diagonal. Detailed calculations used to model the experimental correlation spectra demonstrate that the hydroxyls with absorption on the red side of the δ band (strong hydrogen bonds) selectively break hydrogen bonds following vibrational energy relaxation. It is proposed that the strong hydrogen bonds (red side of the hydroxyl stretch band) are selectively broken because the low frequency modes that are excited by vibrational energy relaxation of the hydroxyl stretch differ from those that are excited by vibrational energy relaxation of the higher frequency hydroxyl stretches (weaker hydrogen bonds).

The correlation spectra of MeOD also demonstrate that the hydroxyls with absorption on the red side of the δ band (strong hydrogen bonds) create a photoproduct γ band that is frequency-correlated with the initially excited δ band. The photoproduct γ band is created on the red side of the equilibrium

γ inhomogeneous distribution. The red-shifted spectrum of the photoproduct γ shows that there is coarse frequency correlation between the reactant δ s and the photoproduct γ s. As time progresses, the photoproduct γ band broadens along the ω_m axis. The time-dependent correlation spectra also provide a second frequency axis, the ω_τ axis. Spectral diffusion is observed along the ω_τ axis (see Figs. 7-5 and 7-6). The observation of spectral diffusion shows that the frequency grating created in the δ excited state by the application of the first two excitation pulses is transferred, at least to some extent, to the photoproduct γ band by hydrogen bond breaking. Therefore, there is fine frequency correlation in the photoproduct γ band. The frequencies are not randomized by hydrogen bond breaking. Therefore, there is structural memory of the parent hydrogen bonded oligomer by the oligomer fragment formed by hydrogen bond breaking

Understanding the hydrogen bond population dynamics in MeOD enables us to experimentally access the structural evolution of the hydrogen bond network in water without complication from hydrogen bond breaking. The vibrational echo correlation spectra of water (see Fig. 7-5) display clear broadening along the ω_τ (horizontal) axis as T_w is increased. Once the contribution from the 1-2 transition is removed, a cut across the correlation spectrum through the center of the 0-1 peak (2500 cm^{-1}) reports the dynamical linewidth for each value of T_w. The dynamical linewidth of the 0-1 peak is a sensitive spectroscopic probe of the frequency fluctuations in water. From the analysis of the dynamical linewidths, it was found that the frequency fluctuations in water occur on multiple time scales out to at least 2 ps. This result is in contrast with dynamics of water recently calculated using molecular dynamics simulations of two water models, TIP4P and SPC/E. While the SPC/E model is somewhat better, both water models produce dynamical lines that broaden too rapidly. The spectral diffusion dynamics in water were shown to be frequency-dependent and are more complex than previously assumed. New theoretical approaches that go beyond the Gaussian approximation/cumulant truncation [15, 52] will be necessary to fully understand water.

Acknowledgments

References

1. K. J. Gaffney, P. H. Davis, I. R. Piletic, N. E. Levinger and M. D. Fayer, *J. Phys. Chem. A* **106**, 12012 (2002).

2. I. R. Piletic, K. J. Gaffney and M. D. Fayer, *J. Chem. Phys,* **119,**423 (2003).

3. J. B. Asbury, T. Steinel, C. Stromberg, K. J. Gaffney, I. R. Piletic, A. Goun and M. D. Fayer, *Chem. Phys. Lett.* **374**, 362 (2003).

4. J. B. Asbury, T. Steinel, C. Stromberg, K. J. Gaffney, I. R. Piletic, A. Goun and M. D. Fayer, *Phys. Rev. Lett.* **91,** 237402 (2003).

5. J. B. Asbury, T. Steinel, C. Stromberg, K. J. Gaffney, I. R. Piletic and M. D. Fayer, *J. Chem. Phys.* **119,** 12981 (2003).

6. J. Stenger, D. Madsen, P. Hamm, E. T. J. Nibbering and T. Elsaesser, *J. Phys. Chem. A.* **106,** 2341 (2002).

7. J. Stenger, D. Madsen, P. Hamm, E. T. J. Nibbering and T. Elsaesser, *Phys. Rev. Lett.* **87,**027401(2001).

8. S. Yeremenko, M. S. Pshenichnikov and D. A. Wiersma, *Chem. Phys. Lett.* **369**,107 (2003).

9. H. Graener, T. Q. Ye and A. Laubereau, *J. Chem. Phys.* **90**, 3413 (1989).

10. R. Laenen, C. Rausch and A. Laubereau, *Phys. Rev. Lett.* **80**, 2622 (1998); S. Bratos, G. M. Gale, G. Gallot, F. Hache, N. Lascoux and J. C. Leicknam, *Phys. Rev. E* **61**, 5211 (2000).

11. G. M. Gale, G. Gallot, F. Hache, N. Lascoux, S. Bratos and J. C. Leicknam, *Phys. Rev. Lett.* **82**, 1068 (1999).

12. H. J. Bakker, H. K. Neinhuys, G. Gallot, N. Lascoux, G. M. Gale, J. C. Leicknam and S. Bratos, *J. Chem. Phys.* **116,** 2592 (2002); M. F. Kropman, H.-K. Nienhuys, S. Woutersen and H. J. Bakker, *J. Phys. Chem. A* **105,** 4622 (2001).

13. C. J. Fecko, J. D. Eaves, J. J. Loparo, A. Tokmakoff and P. L. Geissler, *Science* **301,** 1698(2003).

14. C. P. Lawrence and J. L. Skinner, *J. Chem. Phys.* **117**, 5827 (2002).

15. C. P. Lawrence and J. L. Skinner, *J. Chem. Phys.* **117**, 8847 (2002).

16. C. P. Lawrence and J. L. Skinner, *J. Chem. Phys.* **118**, 264 (2003).

17. C. P. Lawrence and J. L. Skinner, *Chem. Phys. Lett.* **369,** 472 (2003).

18. M. Haughney, M. Ferrario and I. R. McDonald, *J. Phys. Chem.* **91**,4934 (1987); M. Matsumoto and K. E. Gubbins, *J. Chem. Phys.* **93**,1981 (1990); D. M. zum Buschenfelde and A. Staib, *Chem. Phys.* **236,** 253 (1998).

19. A. Staib, *J. Chem. Phys.* **108**,4554 (1998).

20. A. Luzar, *J. Chem. Phys.* **113,** 10663 (2000).

21. R. Rey, K. B. Møller and J. T. Hynes, *J. Phys. Chem. A* **106**, 11993 (2002).

22. G. C. Pimentel and A. L. McClellan, *The Hydrogen Bond.* (W. H. Freeman and Co., San Francisco, 1960).

23. U. Liddel and E. D. Becker, *Spectrochima Acta* **10,** 70 (1957).

24. A. Novak, in *Structure and Bonding* (Ed. J. D. Dunitz, Springer-Verlag, Berlin, 1974), Vol. 18, pp. 177.

25. M. Falk and T. A. Ford, *Canadian J. Chem.* **44,** 1699 (1966).

26. J. B. Asbury, T. Steinel and M. D. Fayer, *J. Phys. Chem. B.* **108**, in press (2004).

27. J. B. Asbury, T. Steinel and M. D. Fayer, *J. Luminescence* **107**, 271 (2004).

28. J. B. Asbury, T. Steinel, C. Stromberg, S. A. Corcelli, C. P. Lawrence, J. L. Skinner and M. D. Fayer, *J. Phys.Chem. A* **108**, 1107 (2004).

29. D. Zimdars, A. Tokmakoff, S. Chen, S. R. Greenfield, M. D. Fayer, T. I. Smith and H. A. Schwettman, *Phys. Rev. Lett.* **70**, 2718 (1993); A. Tokmakoff and M. D. Fayer, *J. Chem. Phys.* **102**, 2810 (1995); K. D. Rector, J. R. Engholm, C. W. Rella, J. R. Hill, D. D. Dlott and M. D. Fayer, *J. Phys. Chem. A* **103**, 2381 (1999); P. Hamm, M. Lim and R. M. Hochstrasser, *Phys. Rev. Lett.* **81,** 5326 (1998); M. T. Zanni, M. C. Asplund and R. M. Hochstrasser, *J. Chem. Phys.* **114**,4579 (2001); K. A. Merchant, D. E. Thompson and M. D. Fayer, *Phys. Rev. Lett.* **86**, 3899 (2001); O. Golonzka, M. Khalil, N. Demirdoven and A. Tokmakoff, *Phys. Rev. Lett.* **86**, 2154 (2001); R. Venkatramani and S. Mukamel, *J. Chem. Phys.* **117**, 11089 (2002).

30. S. Mukamel, *Ann. Rev. Phys. Chem.* **51,** 691 (2000).

31. R. R. Ernst, G. Bodenhausen and A. Wokaun, *Nuclear Magnetic Resonance in One and Two Dimensions.* (Oxford University Press, Oxford, 1987).

32. M. Khalil, N. Demirdöven and A. Tokmakoff, *Phys. Rev. Lett.* **90**, 047401 (2003); M. Khalil, N. Demirdöven and A. Tokmakoff, *J. Phys. Chem. A* **107**, 5258 (2003).

33. M. C. R. Symons and V. K. Thomas, *J. Chem. Soc., Faraday Trans.* 1 **77**, 1883 (1981); O. Kristiansson, *J. Mol. Struct.* **477**, 105 (1999).

34. J. E. Bertie and S. L. Zhang, *J. Mol. Struct.* **413-414,** 333 (1997).

35. R. Laenen and C. Rausch, *J. Chem. Phys.* **106**, 8974 (1997).

36. S. Mukamel, *Principles of Nonlinear Optical Spectroscopy.* (Oxford University Press, New York, 1995).

37. L. K. Iwaki and D. D. Dlott, *J. Phys. Chem. A* **104**, 9101 (2000).

38. M. Berg, C. A. Walsh, L. R. Narasimhan, K. A. Littau and M. D. Fayer, *J. Chem. Phys.* **88**, 1564 (1988); K. A. Littau, Y. S. Bai and M. D. Fayer, *Chem. Phys. Lett.* **159**, 1 (1989); A. Tokmakoff, R. S. Urdahl, D. Zimdars, A. S. Kwok, R. S. Francis and M. D. Fayer, *J. Chem. Phys.* **102**, 3919 (1995); A. Tokmakoff, *J. Phys. Chem. A* **104**, 4247 (2000); J. D. Hybl, Y. Christophe and D. M. Jonas, *Chem. Phys.* **266**, 295 (2001).

39. M. A. Berg, K. D. Rector and M. D. Fayer, *J. Chem. Phys.* **113**, 3233 (2000).

40. W. Mikenda, *J. Mol. Struct.* **147**, 1 (1986).

41. D. Bertolini, M. Cassettari, M. Ferrario, P. Grigolini and G. Salvetti, *Adv. Chem. Phys.* **62**, 277 (1985).

42. A. J. Lock, S. Woutersen and H. J. Bakker, *J. Phys. Chem. A* **105**, 1238 (2001).

43. S. Woutersen, U. Emmerichs and H. J. Bakker, *Science* **278**, 658 (1997).

44. S. A. Corcelli, C. P. Lawrence and J. L. Skinner, *J. Chem. Phys.* **120**, 8107 (2004).

45. W. L. Jorgensen, J. Chandrasekhar and J. D. Nadura, *J. Chem. Phys.* **79**, 926 (1983).

46. H. J. C. Berendsen, J. R. Grigera and T. P. Straatsma, *J. Phys. Chem.* **91,** 6269 (1987).

47. T. H. Joo, Y. W. Jia, J. Y. Yu, D. M. Jonas and G. R. Fleming, *J. Chem. Phys.* **104**, 6089 (1996); W. de Boeij, M. S. Pshenichnikov and D. A. Wiersma, *Chem. Phys. Lett.* **253**, 53 (1996).

48. A. Piryatinski and J. L. Skinner, *J. Phys. Chem. B* **106**, 8055 (2002).

49. J. Marti, J. A. Padro and E. Guardia, *J. Chem. Phys.* **105**, 639 (1996).

50. T. Steinel, J. B. Asbury, S. A. Corcelli, C. P. Lawrence, J. L. Skinner and M. D. Fayer, *Chem. Phys. Lett.* **386**, 295 (2004).

51. C. P. Lawrence, University of Wisconsin at Madison, 2003.

52. A. Piryatinski, C. P. Lawrence and J. L. Skinner, *J. Chem. Phys.* **118**, 9672 (2003).

Chapter 8

SPECTRALLY RESOLVED TWO-COLOUR FEMTOSECOND PHOTON ECHOES

Lap Van Dao, Craig Lincoln, Martin Lowe and Peter Hannaford
Centre for Atom Optics and Ultrafast Spectroscopy
Swinburne University of Technology, Hawthorn, Australia 3122 dvlap@swin.edu.au,
phannaford@swin.edu.au

Abstract   We describe a potentially powerful multidimensional technique based on spectrally resolved 2-colour 3-pulse photon echoes in the visible region for probing vibrational and electronic dynamics in complex molecular systems on a femtosecond time scale. Recording of the spectrum of the photon echo signals yields detailed information about the temporal evolution of the amplitude of the nonlinear polarization induced in the sample by the three temporally separated femtosecond laser pulses. Suitable selection of the wavelengths of the three laser pulses allows different sets of energy levels to be selected and the dynamics of the ground and excited states to be separated and investigated. The technique is applied to studies of dynamical processes in a wide range of molecular systems, including the dye molecules Rhodamine 101, Rhodamine B and cresyl violet; the blue emitting semiconductor gallium nitride; semiconductor CdTe/ZnSe quantum dots; and the biomolecules myoglobin and carbonmonoxy myoglobin.

1.   INTRODUCTION

Following the pioneering of "femtochemistry" by Ahmed Zewail in the 1980s [1], attention has focussed on developing multidimensional femtosecond techniques, similar to those employed in pulsed NMR [2], to study ultrafast dynamical processes in complex molecular systems in real

time [3-14]. These techniques include nonlinear coherent spectroscopies such as stimulated photon echoes [15], based on sequences of femtosecond laser pulses, and Raman echoes, involving pairs of femtosecond pulses followed by a probe pulse [4]. Multiple-pulse nonlinear coherent techniques probe correlations between the electric fields generated by the femtosecond pulses in the phase-matching directions and allow detailed dynamical and spectroscopic information to be extracted in the presence of strong inhomogeneous broadening. Spreading the information over more than one dimension, for example, by employing several femtosecond pulses with independently controllable time delays, helps to unravel and extract complex dynamical and spectroscopic information, such as population relaxation times, dephasing times (or homogeneous broadening), inhomogeneous broadening, and vibrational structure of transient species. Although significant progress has been made in recent years towards developing such multidimensional femtosecond techniques, the field is "still in its infancy, and considerable experimental and theoretical effort will be required in order to develop it into a routine structural and dynamical tool" [4].

In this chapter we review a potentially powerful multidimensional technique based on *spectrally resolved* 2-colour 3-pulse photon echoes in the visible region for probing vibrational and electronic dynamics in ground and excited states of complex molecular systems [13, 14]. Two femtosecond pulses with wave vectors $\mathbf{k_1}$, $\mathbf{k_2}$, wavelength $\lambda_1 = \lambda_2$ and separated by t_{12}, and a third pulse, with wave vector $\mathbf{k_3}$ and wavelength λ_3, illuminate the sample and generate photon echo signals at times near t_{12} after the third pulse in the phase-matching directions $\mathbf{k_4} = -\mathbf{k_1} + \mathbf{k_2} + \mathbf{k_3}$, $\mathbf{k_5} = -\mathbf{k_2} + \mathbf{k_1} + \mathbf{k_3}$ or $\mathbf{k_6} = -\mathbf{k_3} + \mathbf{k_1} + \mathbf{k_2}$. The photon echo signals, which are spatially separated from the exciting beams, are analysed simultaneously in two or more spectrometers equipped with CCD detectors, and the spectra of the photon echo signals are recorded for various values of the pulse delays t_{12}, t_{23} and the wavelengths λ_1, λ_3. Spectral analysis of the photon echo signals yields detailed information about the temporal evolution of the amplitude of the nonlinear polarization induced in the sample by the three femtosecond pulses. Suitable selection of the wavelengths of the three laser pulses allows different sets of energy levels to be selected and the dynamics of the ground and excited electronic states to be separated and investigated.

We apply spectrally resolved 2-colour 3-pulse photon echoes to studies of ultrafast dynamical processes in a wide range of molecular systems, including the dye molecules Rhodamine 101, Rhodamine B and cresyl violet; the blue-emitting semiconductor gallium nitride; semiconductor CdTe/ZnSe quantum dots; and the biomolecules myoglobin and carbonmonoxy myoglobin. Two-colour 3-pulse photon echo spectra with $\lambda_1 = \lambda_2 \neq \lambda_3$ are presented for the phase-matching directions $\mathbf{k_4} = -\mathbf{k_1} + \mathbf{k_2} + \mathbf{k_3}$ and $\mathbf{k_6} = -\mathbf{k_3} + \mathbf{k_1} + \mathbf{k_2}$.

2.   PHYSICAL PRINCIPLES

2.1   Bloch Equation Description

The key features of photon echoes may be readily seen using a simple optical Bloch equation treatment for a *two-level* system based on that described by Zinth and Kaiser [15]. Optical pulses with electric field $E = E_0 \cos(\omega t + \mathbf{k}.\mathbf{r})$, angular frequency ω, and wave vector $\mathbf{k}$ interact with an inhomogeneously broadened ensemble of two-level molecules (ground state $|g\rangle$ and excited state $|e\rangle$) to generate a polarization, which for an isotropic medium may be expanded as $\mathbf{P} = \mathbf{P}^{(1)} + \mathbf{P}^{(3)} + \mathbf{P}^{(5)} + \ldots$

The equations of motion for the four components of the density matrix $\boldsymbol{\rho}$ of the ensemble of two-level molecules are [15]

$$\partial\rho_{ee}/\partial t = \tfrac{1}{2}i\Omega\,(\tilde{\rho}_{ge}\mathrm{e}^{-i\mathbf{k}r} - \tilde{\rho}_{eg}\,\mathrm{e}^{i\mathbf{k}r}) - \rho_{ee}/T_1 \qquad (8.1a)$$

$$\partial\tilde{\rho}_{ge}/\partial t = \tfrac{1}{2}i\Omega\,(\rho_{ee} - \rho_{gg})\,\mathrm{e}^{-\mathbf{k}r} - (i\Delta - 1/T_2)\,\rho_{ge} \qquad (8.1b)$$

$$\rho_{gg} = 1 - \rho_{ee}. \qquad (8.1c)$$

The components ρ_{ee}, ρ_{gg} represent the populations of the states $|g\rangle$, $|e\rangle$, the ρ_{eg}, ρ_{ge} are optical coherences (superposition states) between $|g\rangle$ and $|e\rangle$, $\tilde{\rho}_{ge} = \rho_{ge}\exp(i\omega t)$, and we have applied the rotating wave approximation. In Eq. 8.1, $\Omega = \mu_{ge}E_0/\hbar$ is the Rabi frequency, μ_{ge} is the dipole matrix element, $\Delta = (\omega_{ge} - \omega)$ is the detuning from the molecular resonance frequency ω_{ge}, $T_1 = \gamma_e^{-1}$ is the population relaxation time of $|e\rangle$, and $T_2 = \gamma_{ge}^{-1}$ is the dephasing time of the optical transition $|g\rangle \to |e\rangle$.

For a sequence of *three* excitation pulses separated by times t_{12} and t_{23} (see Fig. 8-1) and for pulse durations short compared with the relaxation times T_1 and T_2, the density matrix at time t after the third pulse may be determined from a product of interaction and evolution matrices [15]:

$$\boldsymbol{\rho}(t) = Y(t)X(A_3)Y(t_{23})X(A_2)Y(t_{12})X(A_1)\,\boldsymbol{\rho}(0), \qquad (8.2)$$

where the $X(A)$ represent the time evolution during interaction with the optical pulses of area $A = \int\Omega dt$, and the $Y(t)$ represent the free evolution during the time intervals between the interactions. In Eq. 8.2 allowance is made for the pulse durations through the pulse areas A. The polarization induced in the sample is determined by solving Eq. 8.2 for ρ_{eg} and ρ_{ge} [15]:

$$P(t) = \mu_{ge}N\,[\rho_{eg}(t) + \rho_{ge}(t)] \tag{8.3a}$$
$$\propto\ P_1^{(1)}(t) + P_2^{(3)}(t,\,t_{12}) + P_3^{(3)}(t,\,t_{12},\,t_{23}), \tag{8.3b}$$

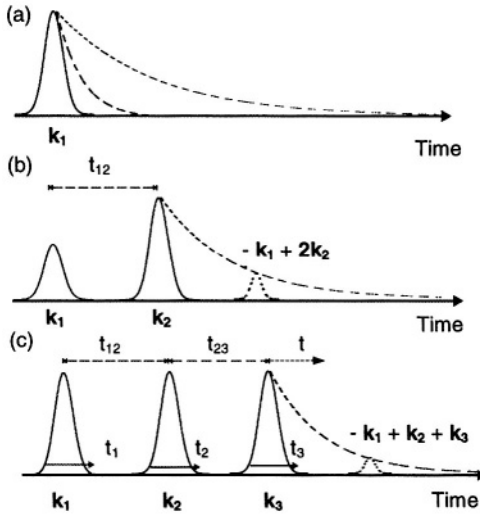where N is the number of molecules per unit volume.

Figure 8-1. Schematic diagram of (a) 1-pulse, (b) 2-pulse, and (c) 3-pulse excitation. The generated coherent signals are shown for a homogeneously broadened transition (long decay curves) and an inhomogeneously broadened transition [(a) short-decay curve; (b, c) small dashed echo signals near time $t = t_{12}$ after the final pulse]. Adapted from Ref. 15.

The first-order polarization in Eq. 8.3b, which corresponds to *single-pulse* excitation (Fig. 8-1 a), is given by

$$P_1^{(1)}(t)\ \propto\ \int d\omega\,G(\omega)\exp(-i\omega t)\exp(-\gamma_{ge}t)\sin A_1 \exp(-i\mathbf{k_1}.\mathbf{r}) \tag{8.4a}$$

in the direction $\mathbf{k_1}$ for pulse 1, with corresponding terms for pulses 2 and 3. For pure homogeneous broadening $[G(\omega) = \delta(\omega - \omega_{ge})]$ the polarization decays at the dephasing time $\gamma_{ge}^{-1} = T_2$. In the presence of inhomogeneous broadening, $G(\omega)$, the range of molecular environments in the ensemble can lead to rapid dephasing of the polarization due to interference between 1the different resonance frequencies, and information about T_2 is essentially lost.

The third-order polarization in Eq. 8-3b for the case of *two-pulse* excitation (Fig. 8.1 b) is given by

$$P_2^{(3)}(t,\,t_{12})\ \propto\ \int d\omega\,G(\omega)\exp[-i\omega(t - t_{12}) - \gamma_{ge}(t + t_{12})]\sin A_1 \sin^2 A_2/2$$
$$\times \exp[-i(-\mathbf{k_1} + 2\mathbf{k_2}).\mathbf{r}] \tag{8.4b}$$

in the direction $-\mathbf{k_1} + 2\mathbf{k_2}$ for the pulse sequence (1, 2), with corresponding terms for the sequences (2, 1), (2, 3), (3, 2), etc. With inhomogeneous broadening the interference term $G(\omega)\exp[-i\omega(t - t_{12})]$ in Eq. 8.4b vanishes at time $t = t_{12}$, and a "photon echo" appears at times near $t = t_{12}$. The amplitude of the 2-pulse echo is proportional to $\exp(-\gamma_{ge}t_{12})$, allowing a determination of T_2. The 2-pulse echo signal is strongest for pulse areas $A_1 = \pi/2$ (generation of optical coherence) and $A_2 = \pi$ (reversal of phase).

The third-order polarization in Eq. 8-3b for the case of *three-pulse* excitation (Fig. 8-1 c) is given by

$$P_3^{(3)}(t, t_{12}, t_{23}) \propto \int d\omega \, G(\omega) \exp[-i\omega(t - t_{12}) - \gamma_{ge}(t + t_{12})] \exp(-\gamma_e t_{23})$$
$$\times \sin A_1 \sin A_2 \sin A_2 \exp[-i(-\mathbf{k_1} + \mathbf{k_2} + \mathbf{k_3}).r] \quad (8.4c)$$

in the phase-matching direction $\mathbf{k_4} = -\mathbf{k_1} + \mathbf{k_2} + \mathbf{k_3}$ for the pulse sequence (1, 2, 3), with corresponding terms for the other phase-matching directions $\mathbf{k_5}$ and $\mathbf{k_6}$ for the pulse sequences (2, 1, 3) and (3, 1, 2). In the presence of inhomogeneous broadening the interference term $G(\omega)\exp[-i\omega(t - t_{12})]$ in Eq. 8.4c vanishes at time $t = t_{12}$, and a 3-pulse photon echo signal appears at delay times near $t = t_{12}$. The amplitude of the 3-pulse photon echo is proportional to $\exp(-2\gamma_{ge}t_{12})\exp(-\gamma_e t_{23})$, enabling the determination of both $\gamma_{ge}^{-1} = T_2$ (by varying t_{12}) and $\gamma_e^{-1} = T_1$ (by varying t_{23}). The 3-pulse photon echo signal is strongest for pulse areas $A_1 = \pi/2 = A_2 = A_3$.

The above treatment allows a simple physical description of 3-pulse photon echoes [16]. The first $\pi/2$ pulse with wave vector $\mathbf{k_1}$ prepares the inhomogeneously broadened ensemble in a superposition of $|g\rangle$ and $|e\rangle$ to create optical coherences ρ_{eg} and ρ_{ge}. After the system has evolved for time t_{12} the second $\pi/2$ pulse with wave vector $\mathbf{k_2}$ creates population in the excited state ρ_{ee} or a second-order population change in the ground state ρ_{gg}. The populations ρ_{ee} and ρ_{gg}, which are coupled to the optical coherences ρ_{ge} and ρ_{eg} via the coupled equations (8.1), "store" the optical coherences and phase information in the excited or ground states. After a further evolution time t_{23} the third $\pi/2$ pulse with wave vector $\mathbf{k_3}$ converts the populations back into optical coherences, in which the phases of the frequency components are now opposite to those of the initial optical coherence contributions. For an inhomogeneously broadened ensemble this *rephasing* of the polarization leads to the generation of a *photon echo* signal at times near $t = t_{12}$ after the third pulse in the phase-matching direction $\mathbf{k_4} = -\mathbf{k_1} + \mathbf{k_2} + \mathbf{k_3}$. For times $t < 0$ the third $\pi/2$ pulse creates a contribution to the optical coherences in which the phases of the frequency components are the same as those of the initial optical coherences, leading to a *free induction decay* (FID) starting at $t = 0$, which carries information about the dephasing of the transition.

The above treatment for an ensemble of *two-level* molecules is instructive in describing the key features of photon echoes, and is justified when the pulses are separated in time and short compared with the relaxation times T_1 and T_2. However, when additional molecular levels are involved in the relaxation processes, a more general treatment is required.

2.2   Nonlinear Optical Response Theory

We present here a standard treatment [3], based on nonlinear optical response theory, which is applicable to multi-level systems, though it is a weak-field treatment and does not yield some features such as the sinusoidal dependence on pulse areas (and the optimum pulse areas $A_1 = \pi/2 = A_2 = A_2$).

In terms of nonlinear optical response theory, the third-order polarization induced by the three pulses, with electric fields E_1, E_2, E_3 and angular frequencies ω_1, ω_2, ω_3, is given by [3, 17]

$$P^{(3)}(t, t_{12}, t_{23}) \approx N(i/\hbar)^3 \int_0^\infty dt_3 \int_0^\infty dt_2 \int_0^\infty dt_1 \, [R_A(t_3, t_2, t_1) + R_B(t_3, t_2, t_1)], \quad (8.5)$$

where t_1, t_2, t_3 are time variables for pulses 1, 2, 3 which allow for integration over the temporal profiles of the pulses $E_3(t - t_{23} - t_3)$, etc. R_A and R_B are third-order optical response functions:

$$R_A(t_3, t_2, t_1) = [R_{II}(t_3, t_2, t_1) + R_{III}(t_3, t_2, t_1)]$$
$$\times E_3(t - t_{23} - t_3) \exp[- i\omega_3(t - t_{23} - t_3)]$$
$$\times E_2(t - t_3 - t_2) \exp[- i\omega_2(t - t_3 - t_2)]$$
$$\times E_1^*(t + t_{12} - t_3 - t_2 - t_1) \exp[i\omega_1(t + t_{12} - t_3 - t_2 - t_1)] \quad (8.6a)$$

$$R_B(t_3, t_2, t_1) = [R_I(t_3, t_2, t_1) + R_{IV}(t_3, t_2, t_1)]$$
$$\times E_3(t - t_{23} - t_3) \exp[- i\omega_3(t - t_{23} - t_3)]$$
$$\times E_2(t - t_3 - t_2 - t_1) \exp[- i\omega_2(t - t_3 - t_2 - t_1)]$$
$$\times E_1^*(t - t_{12} - t_3 - t_2) \exp[i\omega_1(t - t_{12} - t_3 - t_2)]. \quad (8.6b)$$

R_I to R_{IV} and their complex conjugates are nonlinear response functions. For a simple two-level system with inhomogeneous broadening given by a Gaussian distribution $G(\omega) = \exp[- (\omega - \omega_{ge})^2/\Gamma^2]$ (where Γ is the $1/e$ half-width), the nonlinear response functions are given by [3, 18-20]

$$R_I(t_3, t_2, t_1) = \exp\{- [(i\omega_{ge} + \gamma_{ge})(t_3 + t_1)] + \gamma_e t_2 + \Gamma^2(t_3 + t_1)^2/4\} \quad (8.7a)$$
$$= R_{IV}(t_3, t_2, t_1)$$
$$R_{II}(t_3, t_2, t_1) = \exp\{- [(i\omega_{ge} + \gamma_{ge})(t_3 - t_1)] + \gamma_e t_2 + 2\gamma_{ge} t_1 + \Gamma^2(t_3 - t_1)^2/4\},$$
$$= R_{III}(t_3, t_2, t_1) \quad (8.7b)$$

The nonlinear response functions, R_I to R_{IV}, may be illustrated by double-sided Feynman diagrams (Fig. 8-2 (i)), which represent the time evolution of the density matrix upon sequential interaction with the three optical pulses and the free evolution during the time intervals between the interactions [3, 17].
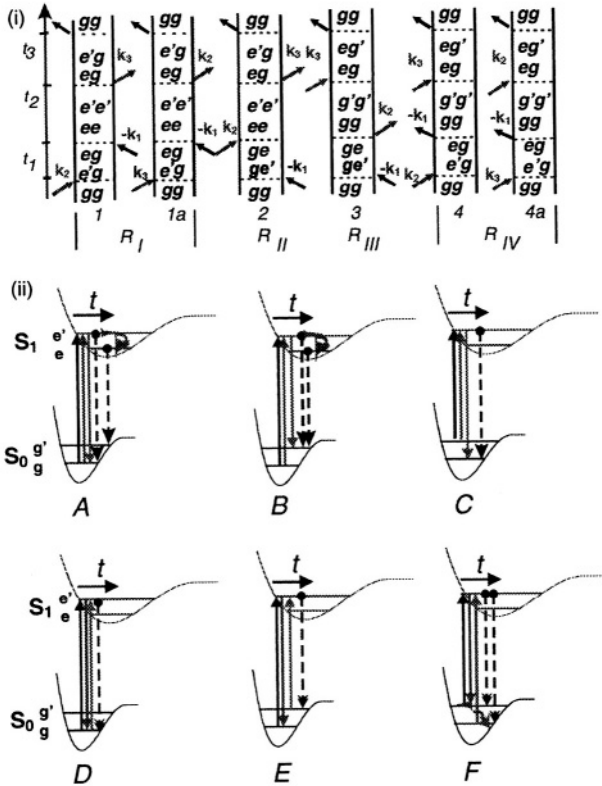

Figure 8-2. (i) Feynman diagrams (1 - 4a) illustrating the interaction of three optical pulses with a two electronic state system with ground state S_0 comprising two vibrational levels $|g\rangle$, $|g'\rangle$ and excited state S_1 with two vibrational levels $|e\rangle$, $|e'\rangle$. The gg, $e'g$, etc in (i) represent the density matrices ρ_{gg}, $\rho_{e'g}$, etc. (ii) Schematic illustration of 1-colour (A, D) and 2-colour (B, C, E, F) 3-pulse excitation for generation of population in the excited (A, B, C) or ground (D, E, F) states. The solid vertical arrows represent interactions by pulses $\mathbf{k_1}$, $\mathbf{k_2}$, $\mathbf{k_3}$ and the dashed vertical arrows represent photon echo transitions. Reproduced from [14].

We first consider the case of a *one-colour* three-pulse experiment. We assume a two electronic state system with ground state S_0 comprising two vibrational levels $|g\rangle$, $|g'\rangle$ and an excited state S_1 with two vibrational levels $|e\rangle$, $|e'\rangle$, as illustrated in Fig. 8-2 (ii). Figure 8-2 (i) (diagrams 1 - 4a) shows the Feynman diagrams representing the possible 3-pulse interactions for the

phase-matching direction $\mathbf{k_4} = -\mathbf{k_1} + \mathbf{k_2} + \mathbf{k_3}$. When the time ordering of the pulses is $\mathbf{k_1}$, $\mathbf{k_2}$, $\mathbf{k_3}$ (diagrams 2, 3) and the three laser pulses are tuned to $|g\rangle \rightarrow |e'\rangle$, the first pulse $\mathbf{k_1}$ creates optical coherences ρ_{eg} and ρ_{ge} and the second pulse $\mathbf{k_2}$ generates population in the excited state $\rho_{e'e'}$ (diagram 2) or a second-order population in the ground state ρ_{gg} (diagram 3), which are both coupled to $\rho_{ge'}$ and $\rho_{e'g}$. The third pulse $\mathbf{k_3}$ converts the populations back into optical coherences $\rho_{ge'}$ and $\rho_{e'g}$, in which the phases of the frequency components are opposite to those of the initial optical coherence contributions. For an inhomogeneously broadened ensemble this *rephasing* of the polarization leads to the generation of a *photon echo* signal at times near $t = t_{12}$ after the third pulse in the phase-matching direction $\mathbf{k_4} = -\mathbf{k_1} + \mathbf{k_2} + \mathbf{k_3}$. The relevant nonlinear response functions for these pathways are R_{II} and R_{III}. R_{I} and R_{II} describe the evolution of the *excited state* population during t_{23} while R_{III} and R_{IV} describe the evolution of the *ground state* population.

When the first interaction is $\mathbf{k_2}$ (diagrams 1, 4) or $\mathbf{k_3}$ (diagrams 1a, 4a) the third pulse creates a contribution to the optical coherences ($\rho_{e'g}$ and $\rho_{ge'}$) in which the phases of the frequency components are the same as those of the initial optical coherence contributions, resulting in a *free induction decay* signal. The nonlinear response functions in this case are R_{I} and R_{IV}. For an inhomogeneously broadened system the FID signal would have peaked at negative delay times (see Eq. 8.7a); however, as a result of causality only the tail of the FID contribution is actually observed in an experiment.

When the nonlinear signals are detected in the other phase-matching directions, $\mathbf{k_5} = -\mathbf{k_2} + \mathbf{k_1} + \mathbf{k_3}$ or $\mathbf{k_6} = -\mathbf{k_3} + \mathbf{k_1} + \mathbf{k_2}$, the Feynman diagrams are similar to those in Fig. 8-2 (i), but with $-\mathbf{k_1}$ replaced by $-\mathbf{k_2}$ or $-\mathbf{k_3}$, respectively. Thus, in the case of our 2-colour experiments in which $\omega_1 = \omega_2 \neq \omega_3$, the signal for $\mathbf{k_5}$ is the same as for $\mathbf{k_4}$ but with the sign of the coherence time t_{12} reversed, while the signal for $\mathbf{k_6}$ has frequency centred at $\omega_6 = 2\omega_1 - \omega_3 \pm \delta\omega_6$ (where the $\delta\omega_6$ allows for frequency shifts associated with the transfer of optical coherence to other transitions) and can yield additional information to that of $\mathbf{k_4}$ or $\mathbf{k_5}$ (see Sects. 4.3.2 and 5.1).

When the signal is recorded with a slow detector, i.e., in a time-integrated measurement, the photon echo signal is given by

$$S(t_{12}, t_{23}) \propto \int_0^\infty |P^{(3)}(t, t_{12}, t_{23})|^2 \, dt, \qquad\qquad (8.8)$$

where $P^{(3)}$ is given by Eqs. 8.5, 8.6, 8.7. In such a time-integrated measurement information about the temporal evolution of the nonlinear polarization is lost.

2.3   **Spectrally Resolved Photon Echoes**

A convenient way to obtain information about the temporal evolution of the nonlinear polarization is to record the *spectrum* of the photon echo signal using a spectrometer [13, 14]. The frequency-domain third-order polarization is determined by Fourier transformation of the time-domain third-order polarization (Eq. 8.5) with respect to *t:*

$$\widetilde{P}^{(3)}(\omega, t_{12}, t_{23}) = \int_{-\infty}^{\infty} P^{(3)}(t, t_{12}, t_{23}) \exp(i\omega t) \, dt. \qquad (8.9)$$

Inclusion of the response functions (8.6), (8.7) for a 2-level system with Gaussian inhomogeneous broadening, and assuming δ-function pulses, then gives [20]:

$$
\begin{aligned}
\widetilde{P}^{(3)}(\omega, t_{12}, t_{23}) \propto\ & N\mu_{ge}^{4} \exp[(i\omega_3 - \gamma_e)t_{23}] \exp[(i(\omega_{ge} - \omega) + \gamma_{ge})^2/\Gamma^2] \\
& \times \{\exp[-i\omega_{ge}(t_{23} - t_{12})] \operatorname{erfc}[i(\omega_{ge} - \omega)/\Gamma + \gamma_{ge}/\Gamma + t_{12}/2]\, \Theta(t_{12})\, \Theta(t_{23}) \\
& + \exp\{-[i\omega_{ge}(t_{23} + t_{12}) + 2\gamma_{ge}t_{12}]\operatorname{erfc}[i(\omega_{ge} - \omega)\Gamma + \gamma_{ge}/\Gamma - t_{12}\Gamma/2] \\
& \times \Theta(-t_{12})\, \Theta(t_{23})\},
\end{aligned}
\qquad (8.10)
$$

where Θ is the Heaviside step function. The error function erfc leads to a frequency shift of $\widetilde{P}^{(3)}(\omega, t_{12}, t_{23})$, characterised by the inhomogeneous broadening parameter Γ, and hence to a wavelength shift of the echo signal.

The (time-integrated) frequency-domain signal field radiated by the polarization $P^{(3)}$ is given by [21]

$$E_S(\omega, t_{12}, t_{23}) \propto [2\pi i \ell \omega / n(\omega)c]\, \widetilde{P}^{(3)}(\omega, t_{12}, t_{23}), \qquad (8.11)$$

where $n(\omega)$ is the real part of the linear refractive index of the sample at frequency ω and ℓ is the length of the sample. The spectrally resolved photon echo signal intensity is then

$$S_{SPE}(\lambda_D, t_{12}, t_{23}) \propto |E_S(\omega, t_{12}, t_{23})|^2 \propto |\widetilde{P}^{(3)}(\lambda_D, t_{12}, t_{23})|^2, \qquad (8.12)$$

where λ_D is the wavelength detected by the spectrometer.

The spectrally resolved photon echo signal, given by Eq. 8.12, yields detailed information about the time evolution of the *amplitude* of $P^{(3)}(t, t_{12}, t_{23})$, via Fourier transformation. Complete information about the evolution of the system, including both amplitude and phase, could be obtained, for example, by mixing the generated signal field with a local oscillator as a function of time (heterodyne detection) [22]. However, for the purposes of investigating the dynamics of many molecular processes, the

absolute phase of the generated signal is not needed and it is sufficient to record the spectrum of the generated signal.

When the first and second pulses temporally overlap in the sample, they may interfere to create a periodic standing wave pattern, which can induce a *population grating* by absorption in the sample [23]. The third pulse can then be diffracted by the population grating in the phase-matching direction $\mathbf{k_4} = -\mathbf{k_1} + \mathbf{k_2} + \mathbf{k_3}$. In this case the spectrum of the population grating signal is determined by the spectral profile of the probe pulse $I_{\text{probe}}(\lambda_D)$. The efficiency of the (transient) population grating, $\eta(\lambda_D, t_{12}, t_{23})$, is proportional to $[\exp(-t_{23}/\tau_{\text{life}}) - \exp(-t_{23}/\tau_{\text{rise}})]$, where τ_{rise} and τ_{life} are the lifetime and build-up time of the population grating. The *total* nonlinear signal spectrum, including the contribution of the population grating, may then be written as

$$S_D(\lambda_D, t_{12}, t_{23}) = S_{\text{SPE}}(\lambda_D, t_{12}, t_{23}) + \eta(\lambda_D, t_{12}, t_{23}) \, I_{\text{probe}}(\lambda_D). \qquad (8.13)$$

We now consider the case of a *two-colour* three-pulse photon echo experiment. We assume a 3-level system with ground state $|g\rangle$ and two excited vibrational levels $|e\rangle$, $|e'\rangle$ (where $\omega_{ge'} > \omega_{ge}$). The first two pulses are tuned to $|g\rangle \rightarrow |e'\rangle$ and the third pulse to $|g\rangle \rightarrow |e\rangle$. The first pulse $\mathbf{k_1}$ creates optical coherences $\rho_{ge'}$ and $\rho_{e'g}$ and the second pulse $\mathbf{k_2}$ generates populations in the excited state ($\rho_{e'e'}$) or ground state (ρ_{gg}) which are coupled to $\rho_{ge'}$ and $\rho_{e'g}$. If the spectral bandwidth of the short laser pulses ($200-300$ cm^{-1} in our experiments) spans the vibrational splitting $\Delta\omega_{ee'} = \omega_{ge'} - \omega_{ge}$ the pulses can create vibrational coherence $\rho_{ee'}$ between $|e\rangle$ and $|e'\rangle$ which is coupled to both $\rho_{ge'}$, $\rho_{e'g}$ and the ρ_{ge}, ρ_{eg} created by the third pulse $\mathbf{k_3}$, thus allowing the optical coherences $\rho_{ge'}$, $\rho_{e'g}$ to be transferred to the transition $|e\rangle \rightarrow |g\rangle$ that is resonant with the third pulse and a photon echo to be created at times near $\omega_1 t_{23}/\omega_3$ after the third pulse. Furthermore, the optical coherence ensemble "stored" in the populations of the excited-state or ground-state vibrational levels may relax to other vibrational levels, leading to the transfer of optical coherence and the appearance of photon echo signals at wavelengths different from the probe pulse (e.g., $|e\rangle \rightarrow |g'\rangle$ in Fig. 8-2 (ii) B).

In our simulations for a *multi-level* system the induced polarization is represented by a sum over n independent two-level systems having different transition frequencies [24]:

$$\widetilde{P}_{\text{SUM}}^{(3)}(\omega, t_{12}, t_{23}) = \Sigma \, \widetilde{P}_n^{(3)}(\omega, t_{12}, t_{23}), \qquad (8.14)$$

where $\widetilde{P}_n^{(3)}(\omega, t_{12}, t_{23})$ is given by Eq. 8.10, but with the term $N\mu_{ge}^4$ replaced by $f_T N\mu_{ge}^4$, and f_T is the efficiency for transfer of optical coherence from the pump transition to the photon echo transition.

3. EXPERIMENTAL

Our femtosecond laser system consists of a Spectra Physics Tsunami mode-locked Ti:sapphire oscillator and a Spitfire regenerative amplifier, which delivers 80 fs, 1 mJ pulses at 800 nm and repetition rate 1 kHz. The laser pulses from the regenerative amplifier are split into two beams, which pump two independently tunable optical parametric amplifiers (OPAs), thus providing a 2-colour source of femtosecond laser pulses. The observation of strong 2-colour photon echo signals (Sect. 4.3) indicates that the pulses from the two OPAs are effectively phase-locked with a minimal amount of phase jitter. This is consistent with the results of Bellini [25] on the phase coherence properties of chirped-pulse amplifiers. Frequency resolved optical gating (FROG) measurements [26] show that the pulses from the OPAs, after optimisation, have a minimal amount of linear chirp.

The OPAs have several options for frequency generation – second harmonic generation (SHG), fourth harmonic generation (FHG) or sum frequency generation (SFG) – allowing coverage of a broad range of wavelengths (250 – 2000 nm) with a pulse duration of about 100 fs. The FWHM of the spectral profile of the pulses from the OPAs in the SFG option is $200 - 300 \text{ cm}^{-1}$, or 7 – 10 nm near 570 nm.

The output of the first OPA is split into two beams, which provide the first and second pulses with wave vectors $\mathbf{k_1}$ and $\mathbf{k_2}$, and the output of the second OPA provides the third pulse with wave vector $\mathbf{k_3}$. The three pulsed beams with time delays t_{12} and t_{23} are aligned in a triangular configuration and focussed by a 15 cm focal length lens into the sample (Fig. 8-3). The energy density of each pulse at the sample spot is typically $1 - 10 \text{ }\mu\text{J/cm}^2$. The three pulses are normally linearly polarized with parallel polarisations. The signal is measured in the phase-matching directions $\mathbf{k_4} = -\mathbf{k_1} + \mathbf{k_2} + \mathbf{k_3}$, $\mathbf{k_5} = -\mathbf{k_2} + \mathbf{k_1} + \mathbf{k_3}$ or $\mathbf{k_6} = -\mathbf{k_3} + \mathbf{k_1} + \mathbf{k_2}$ and detected by one or more spectrometers equipped with CCD detectors and having a spectral resolution of about 1 nm. The spectra of the photon echo signals are recorded over a range of t_{12} or t_{23} by scanning the other time delay. In more recent experiments the $\mathbf{k_4}, \mathbf{k_5}, \mathbf{k_6}$ signals, together with a FROG signal, are detected simultaneously in a rapid multi-channel detection system consisting of a pair of spectrometers fitted with four Ames Photonics GARRY 3000 linear CCD detectors with simultaneous acquisition [27].

The test sample for most of the investigations is the laser dye Rhodamine 101 (Rh101) in methanol (10^{-4} M) at room temperature. The linear absorption and fluorescence spectra for Rh101 are shown in Fig. 8-4. The maxima of the absorption and fluorescence bands occur at 570 nm and 600 nm, respectively.
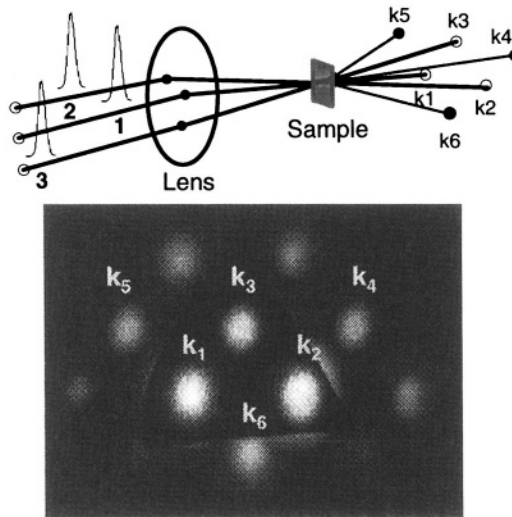
Figure 8-3. Upper: Schematic diagram of the 3-pulse photon echo experiment. Lower: Three-pulse photon echo signals in the phase matching directions $\mathbf{k_4} = -\mathbf{k_1} + \mathbf{k_2} + \mathbf{k_3}$, $\mathbf{k_5} = -\mathbf{k_2} + \mathbf{k_1} + \mathbf{k_3}$ and $\mathbf{k_6} = -\mathbf{k_3} + \mathbf{k_1} + \mathbf{k_2}$ for Rhodamine 101 in methanol (10^{-4} M). Also present are some weak 2-pulse photon echoes in the directions $\mathbf{k_a} = -\mathbf{k_1} + 2\mathbf{k_2}$, $\mathbf{k_b} = -\mathbf{k_2} + 2\mathbf{k_3}$, etc.

Figure 8-3 shows 3-pulse photon echo signals emitted in the (triangular) phase-matching directions $\mathbf{k_4}$, $\mathbf{k_5}$ and $\mathbf{k_6}$ for Rh101. Also present are some weak 2-pulse photon echo signals corresponding to the phase-matching directions $\mathbf{k_a} = -\mathbf{k_1} + 2\mathbf{k_2}$, $\mathbf{k_b} = -\mathbf{k_2} + 2\mathbf{k_3}$, etc. The photon echo signals are spatially separated from the three excitation beams $\mathbf{k_1}$, $\mathbf{k_2}$, $\mathbf{k_3}$ and thus can be detected free from background light.

4.   SPECTRALLY RESOLVED PHOTON ECHOES

4.1   One-Colour Two-Pulse Photon Echoes

We consider first the simple case of 2-pulse excitation. Here, the 'third' pulse can be considered to temporally coincide with the second pulse and the Feynman diagrams for this interaction are diagrams 2 and 3 in Fig. 8-2 (i) in the limit of zero population time ($t_{23} = 0$).

Figure 8-4 shows 1-colour 2-pulse photon echo spectra versus time delay t_{12} recorded for Rh101 in methanol (10^{-4} M) in the direction $\mathbf{k_a} = -\mathbf{k_1} + 2\mathbf{k_2}$ as the laser is tuned to different wavelengths across the absorption spectrum. The *spectrally integrated* photon echo signals (closed circles in Fig. 8-4) contain information mainly about the optical dephasing, which decays

rapidly at T_2. The *spectrally resolved* photon echo signals (contour plots in Fig. 8-4) contain, in addition, detailed information about the inhomogeneous broadening, which is reflected in the shape and width of the spectra. The photon echo spectra exhibit increased broadening and a red wavelength shift at excitation wavelengths close to maximum absorption (570 nm) and also a peak shift in time, which is associated with the inhomogeneous broadening (Eq. 8.7b).
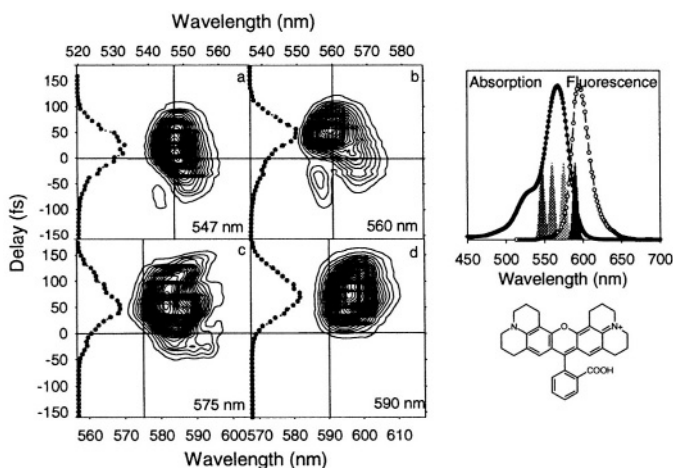
Figure 8-4. Left: Contour plots of 1-colour 2-pulse photon echo spectra for Rh101 in methanol (10^{-4} M) detected in the direction $\mathbf{k_a} = -\mathbf{k_1} + 2\mathbf{k_2}$ versus time delay between the pulses for the centre laser wavelengths: (a) 547 nm, (b) 560 nm, (c) 575 nm, and (d) 590 nm. The closed circles represent the spectrally integrated echo signals. The vertical lines indicate the centre wavelength of the pulses and the horizontal lines indicate zero delay time. Right: Linear absorption and fluorescence spectra for 10^{-4} M Rh101 in methanol and chemical structure for Rh101. Also shown are the four laser wavelengths. Reproduced from [14].

4.2 One-Colour Three-Pulse Photon Echoes

For 3-pulse excitation, terms corresponding to all six Feynman diagrams in Fig. 8-2 (i) can contribute to the signal. Diagrams A and D illustrate the possible interactions for 1-colour 3-pulse excitation.

As in the 2-pulse case, the 3-pulse spectra contain information about the optical dephasing, which decays rapidly at T_2 with increasing coherence time t_{12}, and the line broadening including inhomogeneous broadening, but in addition they contain information about the population relaxation, which decays at T_1 with increasing population time t_{23}, and dynamical processes associated with the relaxation of the population.

Figure 8-5 shows 1-colour 3-pulse spectra for Rh101 plotted against population time t_{23} for coherence times $t_{12} = -40$ fs and $+40$ fs (which are

shorter than the pulse duration ~ 100 fs). For $t_{12} < 0$, the spectra exhibit a FID component for $t_{23} < 0$, and also weak photon echo and population grating components for $t_{23} > 0$ which arise from the temporal overlap of the first two pulses. For $t_{12} > 0$ the spectra show strong photon echo and population grating components, which exhibit a red wavelength shift and increased broadening for excitation wavelengths close to maximum absorption (570 nm). The red shift increases with increasing t_{23}, reflecting the dynamics of the population. In addition, quantum beat oscillations resulting from vibrational coherences generated by the short laser pulses are observed for the excitation wavelengths 575 nm and 590 nm (Fig. 8-5, b3, b4). Figures 8-4 and 8-5 illustrate the increasing information available when the photon echo data are spread over 1D (spectrally integrated 2-pulse), 2D (spectrally resolved 2-pulse) and 3D (spectrally resolved 3-pulse).
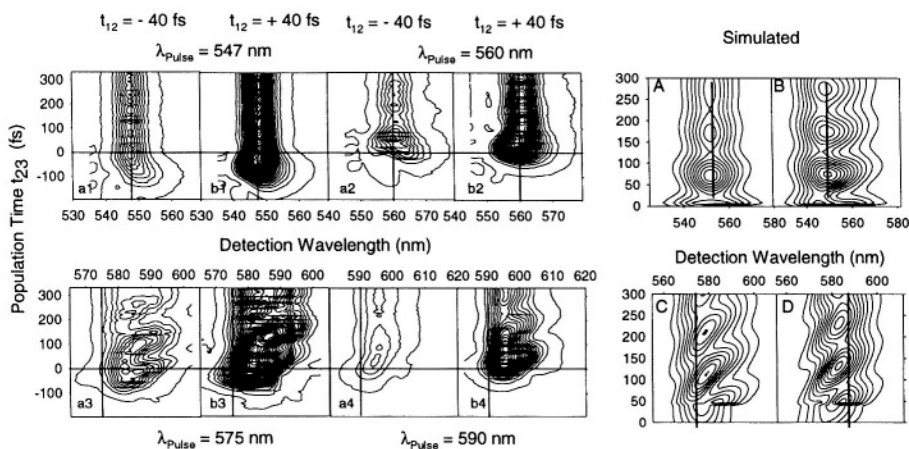
Figure 8-5. Left: One-colour three-pulse photon echo spectra for Rh101 in the direction $\mathbf{k_4} = -\mathbf{k_1} + \mathbf{k_2} + \mathbf{k_3}$ versus population time t_{23} for $t_{12} = \pm 40$ fs and centre laser wavelengths: (a) 547 nm, (b) 560 nm, (c) 575 nm, and (d) 590 nm. Right: Simulated photon echo spectra for a pair of 2-level systems with $\omega_{ge'} = 17{,}390$ cm^{-1} (575 nm), splitting $\Delta\omega = \omega_{ge'} - \omega_{ge} = 300$ cm^{-1} (10 nm), $\Gamma = 0.75\Delta\omega$, $\gamma_{e'}^{-1} = 200$ fs, $\gamma_{ge}^{-1} = 6$ ps, and with: (A) $\gamma_e^{-1} = 200$ fs, $\omega = (\omega_{ge'} + \omega_{ge})/2$, delay between transitions $\Delta\tau = 0$; (B) $\gamma_e^{-1} = 6$ ps, $\omega = (\omega_{ge'} + \omega_{ge})/2$, $\Delta\tau = 0$; (C) $\gamma_e^{-1} = 6$ ps, $\omega = \omega_{ge'}$, $\Delta\tau = 50$ fs; (D) $\gamma_e^{-1} = 6$ ps, $\omega = (\omega_{ge'} + \omega_{ge})/2$, $\Delta\tau = 50$ fs. Reproduced from [14].

Figure 8-5 A-D shows *simulated* spectra calculated from Eqs. 8.10, 8.13, 8.14 for a pair of two-level systems with a common ground level $|g\rangle$ and two excited vibrational levels $|e'\rangle$ and $|e\rangle$, and with transition frequency $\omega_{ge'} = 17{,}390$ cm^{-1} (575 nm) and splitting $\Delta\omega = \omega_{ge'} - \omega_{ge} = 300$ cm^{-1} (10 nm). The lifetime of the population grating is taken to be the recovery time of the ground state, which is typically very long (> 100 ps) in dye systems. When the lifetime of both excited levels is short a broadening on both sides of the photon echo spectrum is observed at short t_{23}, where the photon echo makes

a large contribution to the signal (Fig. 8-5 A). The simulation with short lifetimes for both excited levels ($\gamma_{e'}^{-1} = \gamma_e^{-1} = 200$ fs) corresponds to the case of short excitation wavelength involving high excited-state vibrational levels (547 nm or 560 nm – Fig. 8-5, a1, a2, b1, b2). When the lifetime of the lower excited level $|e\rangle$ is long ($\gamma_e^{-1} = 6$ ps) a broadening of the photon echo spectrum on the long wavelength side can be seen at short t_{23} (Fig. 8-5 B). Figures 8-5 C and 8-5 D show the cases when the transition $|e\rangle \rightarrow |g\rangle$ is delayed relative to $|g\rangle \rightarrow |e'\rangle$ by $\Delta\tau = 50$ fs, which represents the time for transfer of optical coherence from transition $|g\rangle \rightarrow |e'\rangle$ to $|g\rangle \rightarrow |e\rangle$, and when the laser frequency is tuned to $\omega_{ge'}$ and $(\omega_{ge'} + \omega_{ge})/2$, respectively. These two simulations, with a long lifetime for the lower excited level ($\gamma_e^{-1} = 6$ ps), correspond to the case of long excitation wavelengths involving low excited-state vibrational levels (575 nm or 590 nm – Fig. 8-5, a3, b3, a4, b4).

4.3   Two-Colour Three-Pulse Photon Echoes

Two-colour 3-pulse echo experiments, in which the wavelength of one of the pulses is varied relative to that of the other two pulses, provide an additional degree of freedom which allows different sets of energy levels to be excited and the dynamics of the ground and excited states to be separated.

4.3.1   Detection of $k_4 = -k_1 + k_2 + k_3$

In our two-colour experiments in which $\omega_1 = \omega_2 \neq \omega_3$, the signal detected in the direction $\mathbf{k}_4 = -\mathbf{k}_1 + \mathbf{k}_2 + \mathbf{k}_3$ has frequency centred at $\omega_4 = \omega_3 \pm \delta\omega_4$, where the $\pm \delta\omega_4$ allows for frequency shifts associated with the transfer of optical coherence to other transitions. When $\omega_1 > \omega_3$ ($\lambda_1 < \lambda_3$) relaxation in the *excited state* vibrational manifold and transfer of optical coherence to other transitions can lead to photon echoes with wavelengths longer than λ_3 (Fig. 8-2 (ii) B). When $\omega_1 < \omega_3$ ($\lambda_1 > \lambda_3$) relaxation in the *ground state* vibrational manifold and transfer of optical coherence to other transitions can lead to photon echoes with wavelengths shorter than λ_3 (Fig. 8-2 (ii) F).

Figure 8-6 shows 2-colour 3-pulse echo spectra recorded for Rh101 versus population time t_{23} for $t_{12} = -40$ fs (i.e., for partially overlapping 100 fs pulses), $\lambda_1 = 560$ nm, and $\lambda_3 =$ (a) 570 nm and (b) 580 nm.

We consider first the spectrum in Fig. 8-6 (a).

(i) For detection wavelengths $\lambda_{det} \approx \lambda_1 = 560$ nm and for negative population times t_{23}, there is a weak *free induction decay* component which decays rapidly at the optical dephasing time T_2. This component, which is enhanced for negative coherence times t_{12}, is observable only for negative population times t_{23} and when the two pulses overlap temporally.
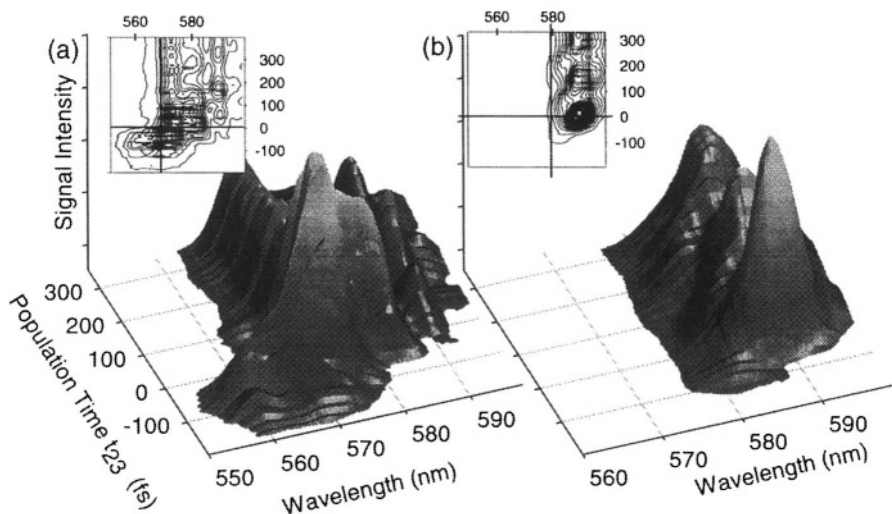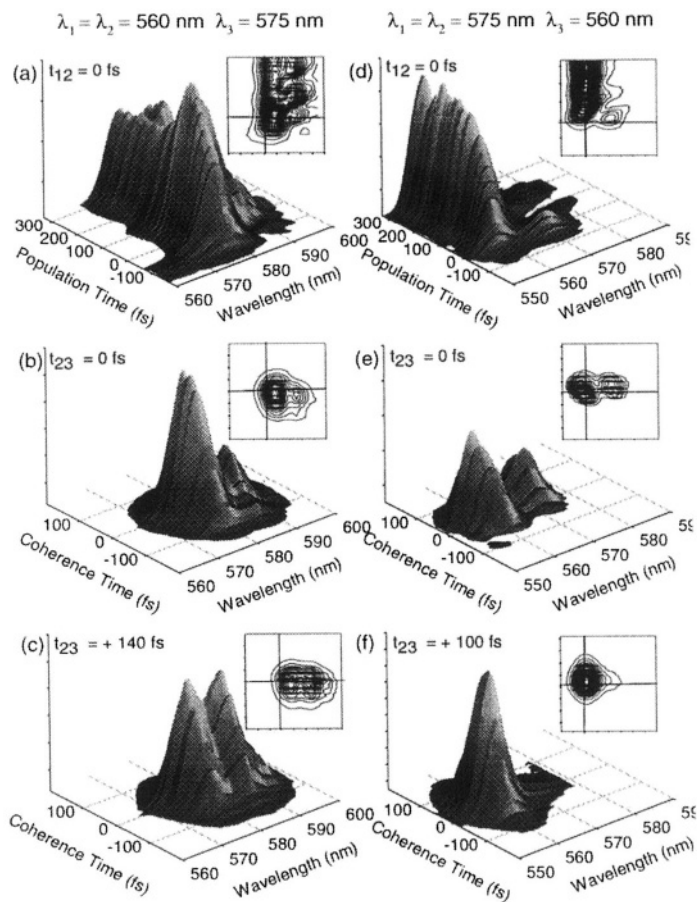
Figure 8-6. Two-colour three-pulse photon echo spectra for Rh101 detected in the direction $\mathbf{k_4} = -\mathbf{k_1} + \mathbf{k_2} + \mathbf{k_3}$ versus population time t_{23} for $t_{12} = -40$ fs, $\lambda_1 = 560$ nm, and (a) $\lambda_3 = 570$ nm, (b) 580 nm. Insets: Contour plots of the spectra. Straight lines indicate the centre wavelength of the third pulse (vertical lines) and zero population time (horizontal lines).

(ii) For $\lambda_{det} \approx \lambda_3 = 570$ nm, there is a narrow *population grating* component, which decays slowly at the population relaxation time T_1 for positive t_{23}. This component arises when the spectral profile of the third pulse overlaps the spectral profile of the first two pulses (centred at 560 nm), thus allowing transitions to be induced from the same ground vibrational level as the first two pulses and the third pulse to be diffracted by the population grating created by the first two partially overlapping pulses.

(iii) For $\lambda_{det} > \lambda_3$, there is a *photon echo* signal, which exhibits quantum beat oscillations.

We now consider the spectrum in Fig. 8-6 (b), in which the wavelength of the third pulse is raised by just 10 nm, i.e., by about the spectral bandwidth of the laser pulses. In this case both the population grating component (centred at $\lambda_3 = 580$ nm) and the FID component (centred at $\lambda_1 = 560$ nm) are suppressed, and we are left with a pure photon echo signal. The spectral profile of the third pulse (centred at 580 nm) is now shifted too much to overlap with the spectral profile of the first two pulses (centred at 560 nm) and thus to be diffracted by the population grating, or to allow formation of a FID signal. Figures 8-6 (a) and (b) illustrate how, by suitable

selection of the experimental parameters in multi-dimensional space, it is possible to select specific quantum pathways for the molecules.

Figure 8-7. Two-colour three-pulse photon echo spectra for Rh101 detected in the direction $k_4 = -k_1 + k_2 + k_3$ versus population time (a, d) or coherence time (b, c, e, f) at fixed values of the other time delay for λ_1 or λ_3 close to the absorption maximum (575 nm) and on the *blue* side (560 nm) of the absorption maximum. Insets: Contour plots of the photon echo spectra. Reproduced from [14].

Figure 8-7 shows photon echo spectra for two combinations of pulse wavelength, at 560 nm and 575 nm, and versus population time t_{23} for $t_{12} = 0$ and versus coherence time t_{12} for various $t_{23} > 0$. These two wavelengths differ by more than the spectral bandwidth of the pulses, and correspond approximately to the maximum of the absorption band (575 nm) and to the *blue* side of the absorption maximum (560 nm). The shorter wavelength involves transitions from near the lowest vibrational level in the ground state to near the highest vibrational level in the excited state (see Fig. 8-2 (ii) B).

The change in the photon echo spectrum for different pulse wavelengths reflects the energy relaxation in the relevant vibrational ladders. When $\lambda_1 < \lambda_3$ (Figs. 8-7 (b), (c)) the echo spectrum is enhanced on the *red* wavelength side, especially at longer population times t_{23}. This enhancement reflects the dynamics of vibrational relaxation in the *excited state*, as illustrated in Fig. 8-2 (ii) B. By contrast, when $\lambda_1 > \lambda_3$ (Figs. 8-7 (e), (f)) the echo spectrum is enhanced on the *blue* wavelength side, reflecting the dynamics of vibrational relaxation in the *ground state*, as illustrated in Fig. 8-2 (ii) F.

In scans of t_{12} (Fig. 8-7 (b), (c), (e), (f)) the photon echo spectra exhibit a splitting, amounting to $270\ \mathrm{cm}^{-1}$ in the case of Fig. 8.7 (c). The occurrence of the splitting is attributed to overlap of the spectral bandwidth of the laser pulses with the frequencies of strong vibrational transitions.
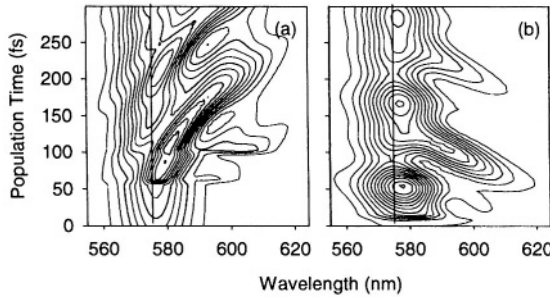
Figure 8-8. Simulated photon echo spectra for three two-level systems with transition frequency $\omega_{ge''} = 17{,}390\ \mathrm{cm}^{-1}$ (575 nm), splitting $\Delta\omega = 260\ \mathrm{cm}^{-1}$ (8.6 nm), $\Gamma = 0.5\Delta\omega$, $\gamma_{ge}^{-1} = 6$ ps, and with: (a) $\gamma_{e''}^{-1} = 200$ fs, $\gamma_{e'}^{-1} = 400$ fs, $\gamma_e^{-1} = 6$ ps, $\omega_3 = \omega_{ge''}$, $\Delta\tau = 80$ fs; (b) $\gamma_g^{-1} = 6$ ps, $\gamma_{g'}^{-1} = \gamma_{g''}^{-1} = 200$ fs, $\omega_3 = \omega_{ge}$, $\Delta\tau = 25$ fs.

Figure 8-8 shows simulated spectra calculated from Eqs. 8.10, 8.13, 8.14 for *three* two-level systems with a common ground state $|g\rangle$ [Fig. 8-8 (a)] or a common excited state $|e\rangle$ (Fig. 8-8 (b)), and for time delays $\Delta\tau$ between the three transitions of (a) 80 fs or (b) 25 fs. We note that in these 2-colour experiments the pulses span a wider range of wavelengths than in the 1-colour experiments and the number of transition frequencies involved in the generation of the photon echo signal can be larger. Figure 8-8 (a), with $\Delta\tau = 80$ fs, represents a simulation for vibrational relaxation in the *excited state* $(\lambda_1 < \lambda_3)$, which results in the transfer of optical coherence from the initially excited transition to other lower frequency transitions (Fig. 8-7 (a)). Figure 8-8 (b), with $\Delta\tau = 25$ fs, represents a simulation for vibrational relaxation in the *ground state* $(\lambda_1 > \lambda_3)$, which results in the transfer of optical coherence from the initially excited transition to other higher frequency transitions (Fig. 8-7 (d)).
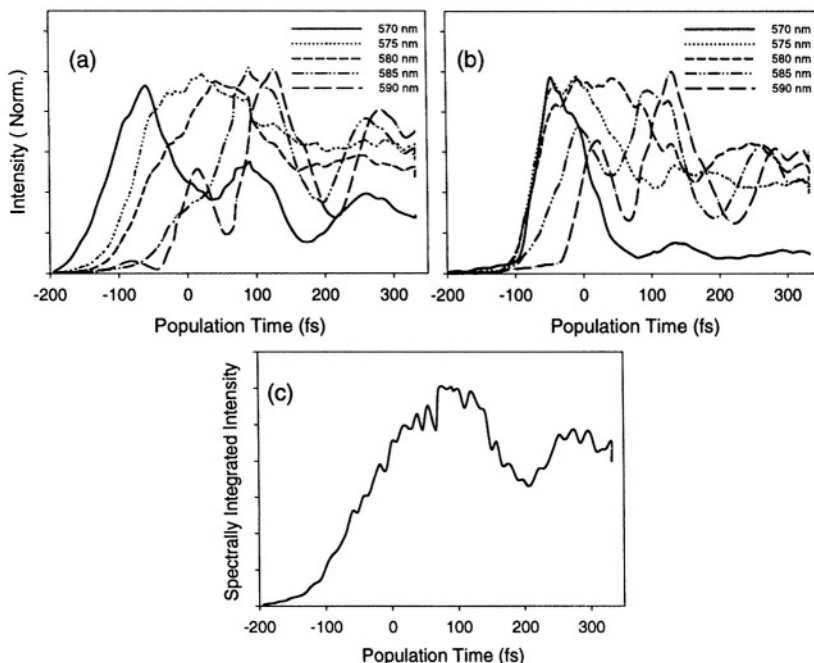
Figure 8-9. Intensity of the three-pulse photon echo signals taken with a spectral window of 1 nm for detection wavelengths of 570, 575, 580, 585, and 590 nm as a function of population time t_{23}, and with: (a) $\lambda_1 = 560$ nm, $\lambda_3 = 575$ nm, and (b) $\lambda_1 = \lambda_3 = 575$ nm (one-colour). (c) is the spectrally integrated signal with $\lambda_1 = 560$ nm, $\lambda_3 = 575$ nm. Reproduced from [14].

In Fig. 8-7 (a), the photon echo spectra exhibit quantum beats, due to vibrational coherences, having frequencies of about 160, 210, 320, 440 and 580 cm^{-1}. The oscillations are clearly visible in separate echo intensity versus t_{23} plots taken with a narrow detection wavelength window (Fig. 8-9 (a)), in which the beat frequency is strongly dependent on the selected detection wavelength. In spectrally resolved measurements the detection wavelength is sharply defined and the high visibility arises from the small number of contributing beat frequencies. In the spectrally integrated signal versus t_{23} plot (Fig. 8-9 (c)) only one oscillation mode, with frequency ~ 260 cm^{-1} (i.e., close to the splitting in Fig. 8.7 (c)), is observed and with low visibility. In the 2-colour spectrally resolved experiment (Fig. 8-9 (a)) the time for the signal to reach a maximum increases with detection wavelength whereas in the 1-colour experiment (Fig. 8-9 (b)) such a dependence is not observed in the region covered by the laser pulse. The observed time delay reflects the vibrational relaxation time in real time, which for Rh101 in methanol increases with detection wavelength at the rate of about 80 fs/5 nm.

4.3.2   Detection of $k_6 = - k_3 + k_1 + k_2$

In our 2-colour experiments in which $\omega_1 = \omega_2 \neq \omega_3$, the signal detected in the phase-matching direction $k_6 = - k_3 + k_2 + k_1$ has frequency centred at $\omega_6 = 2\omega_1 - \omega_3 \pm \delta\omega_6$, and this can yield additional information to k_4 or k_5. In this case the pulse k_3 precedes k_2 and k_1, and the "coherence time" is given by $- t_{23}$ and the "population time" by $- t_{12}$.
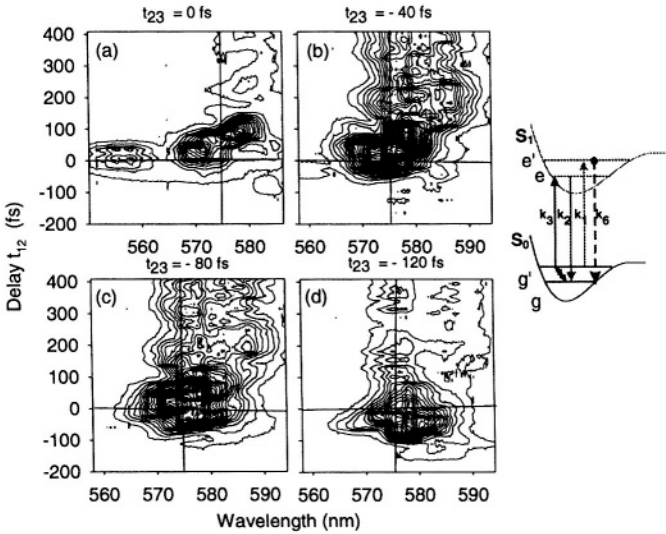
Figure 8-10. Contour plots of 2-colour 3-pulse photon echo spectra for Rh101 detected in the phase-matching direction $k_6 = - k_3 + k_1 + k_2$ versus time delay t_{12} (population time) for coherence times $t_{23} = 0, - 40$ fs, $- 80$ fs, $- 120$ fs and $\lambda_3 = 590$ nm, $\lambda_1 = 575$ nm. Right: Molecular energy level diagram illustrating the generation of the k_6 signal (for $\omega_3 < \omega_2$).

We consider a two electronic state system $S_0 - S_1$ consisting of two excited vibrational levels $|e\rangle$, $|e'\rangle$ and two ground vibrational levels $|g\rangle$, $|g'\rangle$ (Fig. 8-10, right). When $\omega_3 < \omega_2$, the first pulse k_3 with frequency ω_3 creates optical coherences $\rho_{g'e}$ and $\rho_{eg'}$ between the higher ground level $|g'\rangle$ and the lower excited level $|e\rangle$. The second pulse k_2 with frequency $\omega_2 > \omega_3$ takes the system down to level $|g\rangle$, creating coherences ρ_{eg} and ρ_{ge}. The third pulse k_1 with frequency $\omega_1 = \omega_2$ can then create coherences $\rho_{g'e'}$ and $\rho_{e'g'}$, allowing generation of a "pure" *four-wave mixing* signal for the transition $|e'\rangle \rightarrow |g\rangle$ at frequency $\omega_6 = 2\omega_1 - \omega_3$ in the direction k_6. The "pure" four-wave mixing signal is expected to be observed when the three pulses are present at the same time ($t_{12} \approx t_{23} \approx 0$) and to decay rapidly at the optical dephasing time T_2. The interaction of the first two pulses with the system cannot create population in the ground ($\rho_{g'g'}$, ρ_{gg}) or excited (ρ_{ee}, $\rho_{e'e'}$) levels directly

because the two pulses have different frequencies. However, when the optical coherences $\rho_{g'e}$ and $\rho_{eg'}$ can be transferred from the transition $|g'\rangle \to |e\rangle$ to $|g\rangle \to |e\rangle$ due to vibrational relaxation in the ground state, population can be created in the ground and excited states which can then lead to generation of a *photon echo* at frequency $\omega_6 = 2\omega_1 - \omega_3 \pm \delta\omega_6$ with a time delay characteristic of the ground-state vibrational relaxation time. In addition, when the first two (phase-locked) pulses $\mathbf{k_3}$ and $\mathbf{k_2}$ with frequencies ω_3 and ω_2 temporally overlap in the sample they can interfere to form a moving wave which can induce a moving population grating in the sample. The third pulse $\mathbf{k_1}$ can then be diffracted in the phase-matching direction $\mathbf{k_6}$ to give a *population grating* signal at frequency ω_1.

Figure 8-10 shows contour plots of photon echo spectra detected in the $\mathbf{k_6}$ direction for Rh101 when scanning the time delay t_{12} (population time) for various values of t_{23} (coherence time). The wavelengths of pulses $\mathbf{k_3}$ and $\mathbf{k_2}$ are centred at $\lambda_3 = 590$ nm and $\lambda_2 = 575$ nm and pulse $\mathbf{k_1}$ at $\lambda_1 = 575$ nm. For $t_{23} = 0$ and $t_{12} \approx 0$ a "pure" four-wave mixing signal with wavelength near 561 nm, corresponding to $\omega_6 = 2\omega_1 - \omega_3$ (Fig. 8-10a), is observed. For $t_{23} < 0$, photon echo signals centred at wavelengths longer than $\lambda_6 \approx 561$ nm and a population grating signal centred at $\lambda_1 = 575$ nm with long population decay time are the main contributors to the signal. These results reflect the transfer of optical coherence during vibrational relaxation and provide information about the vibrational dynamics of the system.

5.   MOLECULAR SYSTEMS

5.1   Dye Molecules

It is of interest to compare the photon echo spectra for Rh101 with spectra of other dye molecules such as Rhodamine B and cresyl violet.

Rhodamine B (RhB) has linear absorption and fluorescence bands with maxima near 550 and 580 nm, respectively. Figure 8-11 shows 2-colour 3-pulse photon echo spectra detected in the direction $\mathbf{k_4}$ for RhB in methanol (10^{-4} M) [28]. The echo spectra for RhB are narrower than for Rh101 and show less structure. In addition, for $\lambda_1 < \lambda_3$, RhB does not show the strong red-enhancement of the photon echo exhibited by Rh101. These differences reflect the differing structure of the molecules. Rh101 is a fairly rigid, planar molecule with a stable excited state comprising a range of vibrational levels. RhB contains side-chain amino groups, and elongation or rotation of the C-N bonds can reduce the stability of the ground and excited states.
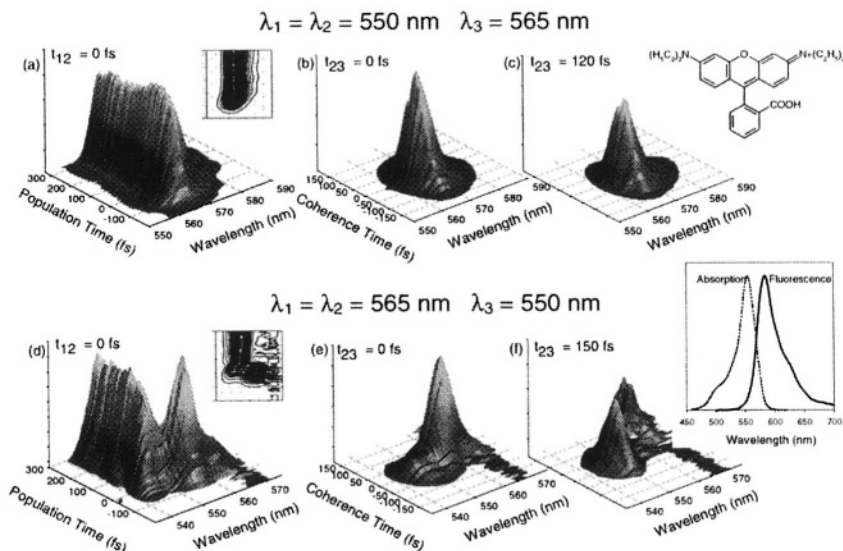
Figure 8-11. Two-colour three-pulse photon echo spectra for RhB detected in the direction k_4 $= - k_1 + k_2 + k_3$ versus population time t_{23} or coherence time t_{12} for λ_1 or λ_3 at the absorption maximum (550 nm) and on the *red* side (565 nm) of the absorption maximum. Insets: Contour plots of the photon echo spectra. Right: Chemical structure for RhB, and linear absorption and fluorescence spectra for 10^{-4} M RhB. Reproduced from [14].

Cresyl violet has vibrational structure which is well characterized [29] and represents a convenient test molecule. The maximum of the absorption band occurs at 600 nm. Figure 8-12 shows the two-colour 3-pulse photon echo spectra for cresyl violet in methanol (10^{-4} M) detected in the direction $k_6 = - k_3 + k_2 + k_1$ for pulse wavelengths $\lambda_1 = 600$ nm, and $\lambda_3 = 585$ nm (a, c) and 615 nm (b, d). For $\lambda_3 = 615$ nm (red side of absorption maximum) a component with detection wavelength near 586 nm, corresponding to $\omega_6 = 2\omega_1 - \omega_3$, appears at $t_{12} \approx 0$ and exhibits an increasing red shift with evolving coherence time t_{23} (Fig. 8-12d). For $\lambda_3 = 585$ nm (blue side of absorption maximum) there is no component near 616 nm at $t_{12} \approx 0$ (corresponding to $\omega_6 = 2\omega_1 - \omega_3$) (Fig. 8-11a), which may be a result of a very short dephasing time expected for transitions involving high-lying excited vibrational levels. For scans of the population time t_{12} (Figs. 8-12a, b), there is a long-lived population grating component at detection wavelengths near 600 nm which exhibits quantum beat oscillations. The oscillations, and also the observed splitting in the spectra (Figs. 8-12c, d), provide information about the vibrational splitting in the ground and excited states. The spectral splitting in Fig. 8-11d is ~ 340 cm^{-1} (~ 12 nm), which is in agreement with the lowest vibrational frequency in the cresyl violet spectrum, 335 – 343 cm^{-1} [29].

$\lambda_1 = \lambda_2 = 600$ nm **k_6** Direction

$\lambda_3 = 585$ nm $\lambda_3 = 615$ nm
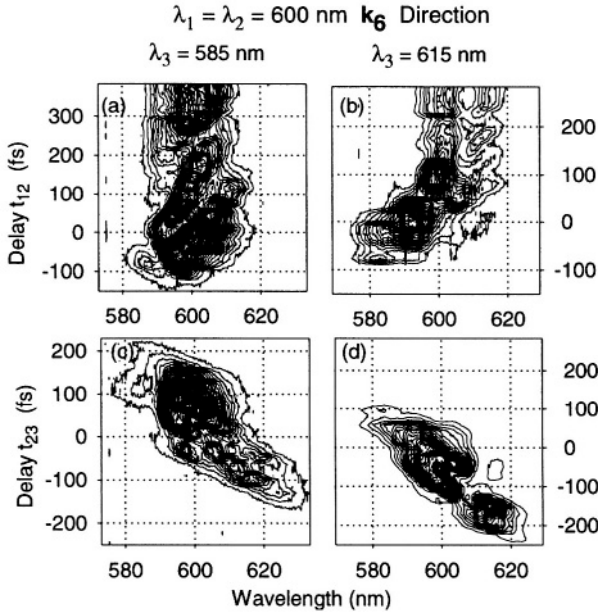
Figure 8-12. Two-colour three-pulse photon echo spectra for cresyl violet in methanol $(10^{-4}\,\text{M})$ detected in the phase-matching direction $\mathbf{k_6} = -\,\mathbf{k_3} + \mathbf{k_2} + \mathbf{k_1}$ versus time delay t_{12} (population time) with $t_{23} = -\,30\,\text{fs}$ (a, b) and versus time delay t_{23} (coherence time) with $t_{12} = 0$ (c, d), for $\lambda_1 = \lambda_2 = 600\,\text{nm}$ (absorption maximum) and λ_3 on the *blue* (585 nm) and *red* (625 nm) side of the absorption maximum.

5.2   Semiconductor Materials

5.2.1   Gallium nitride

Gallium nitride has become an important semiconductor for fabricating blue diode lasers, light emitting diodes and other optoelectronic devices [30]. In addition to emission in the blue, GaN exhibits a broad "yellow band" near 510 - 560 nm (2.3 eV), the origin of which is not well understood.

Figure 8-13 shows 2-colour 3-pulse photon echo spectra recorded in the direction $\mathbf{k_4} = -\,\mathbf{k_1} + \mathbf{k_2} + \mathbf{k_3}$ for an undoped GaN epitaxial layer in the region of the yellow band for two combinations of laser wavelengths near 530 nm [31]. For $\Delta\lambda = \lambda_3 - \lambda_1 = +\,5\,\text{nm}$ ($\omega_3 < \omega_1$) some broadening and initial shifting of the photon echo spectra at short population time can be seen (Fig. 8-13 (a), (b)), while for $\Delta\lambda = -\,5\,\text{nm}$ ($\omega_3 > \omega_1$) only broadening of the photon echo spectrum is observed (Fig. 8-13 (c), (d)).
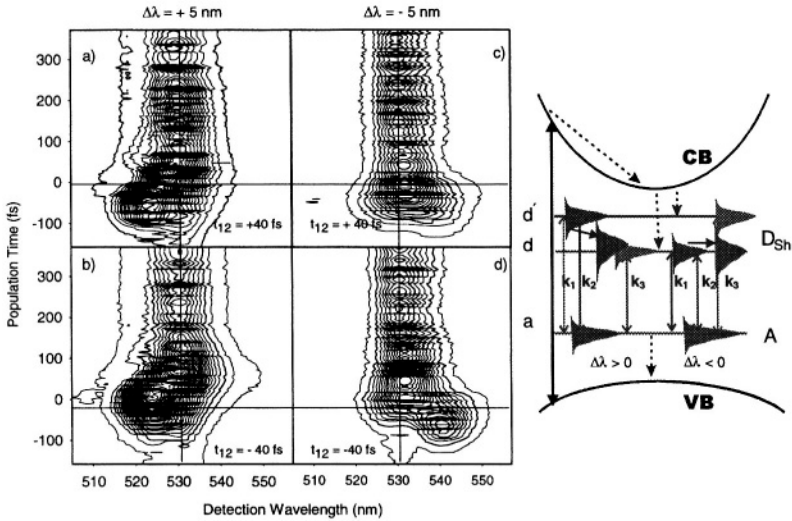
Figure 8-13. Two-colour 3-pulse photon echo spectra for GaN detected in the direction $\mathbf{k_4}$ versus t_{23} for $t_{12} = \pm 40$ fs and $\Delta\lambda = \lambda_3 - \lambda_1 = \pm 5$ nm near 530 nm. Right: Three-level system illustrating dynamics for pulse wavelengths with: $\Delta\lambda > 0$ and $\Delta\lambda < 0$. CB: conduction band; VB: valence band; $\mathbf{D_{sh}}$: shallow donor levels; A: acceptor levels. Reproduced from [31].

The first pulse $\mathbf{k_1}$ creates optical coherences $\rho_{ad'}$ and $\rho_{d'a}$ between an acceptor level a and a high donor level d' and the second pulse $\mathbf{k_2}$ generates population (in the donor or acceptor levels) which is coupled to $\rho_{ad'}$ and $\rho_{d'a}$. Transfer of the optical coherences $\rho_{ad'}$ and $\rho_{d'a}$ to the transition $a \rightarrow d$, which is resonant with the third pulse $\mathbf{k_3}$, allows the generation of a photon echo at $\omega_4 = \omega_3 \pm \delta\omega_4$ with a delay time characteristic of the carrier relaxation time.

The occurrence of coherence transfer from $a \rightarrow d'$ to $a \rightarrow d$ for the case $\Delta\lambda = \lambda_3 - \lambda_1 < 0$ is consistent with a "V-shape" level structure, with strong coupling of the donor levels, rather than a "Λ-shape" structure. This suggests that the yellow band of GaN originates from a transition involving recombination of a shallow donor and a deep acceptor [32], rather than between a neutrally charged deep donor and shallow acceptor levels [33].

5.2.2   Semiconductor quantum dots

Spectrally resolved 2-colour 3-pulse photon echoes have been used to characterise CdTe quantum dots grown on ZnSe by molecular beam epitaxy [34, 35]. These samples, in which the dot size is comparable to the exciton radii, have unique electronic properties due to the effect of 3-D confinement. The photoluminescence spectrum at low temperature (10 – 200 K) has a peak wavelength of 542 nm (2.3 eV) with FWHM = 150 meV. The population grating signal shows a fast decay component (2 – 3 ps),

corresponding to migration and tunnelling of the exciton to neighbouring quantum dots, followed by a slower decay component (20 ps to > 100 ps) which is related to the lifetime of the exciton. The migration and tunnelling processes occur with high probability because of the high density of dots.
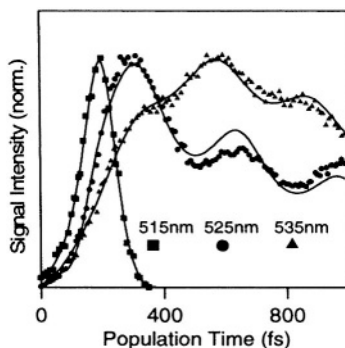
Figure 8-14. Spectrally resolved 2-colour (515, 530 nm) 3-pulse photon echo signals for CdTe quantum dots grown on ZnSe, recorded at detection wavelengths of 515 nm (■), 525 nm (●), and 535 nm (▲) at room temperature. The solid lines are theoretical fits to the data, as described in Ref. 34. Reproduced from [34].

Figure 8-14 shows plots of the peak intensity of the spectrally resolved 2-colour 3-pulse photon echo spectra versus population time t_{23} recorded at detection wavelengths of 515, 525, and 535 nm. The photon echo signals for detection wavelengths of 525 and 535 nm exhibit a slowly decaying quantum beat component, in which the period of the beats corresponds to an exciton binding energy of about 13 meV and the dephasing times correspond to homogeneous linewidths of 0.8 – 1.2 meV. These quantities show a weak dependence on detection wavelength which is associated with a distribution of dot sizes. For the detection wavelength 515 nm, the decay time of the photon echo signal is very short since this wavelength is very close to the excitation wavelength, where the density of excited carriers is high and there is strong carrier-carrier scattering and excitation-induced dephasing.

5.3   Biological Molecules

Spectrally resolved 2-colour 3-pulse photon echoes is currently being applied to study ultrafast transient processes that occur during the photodissociation of carbonmonoxy myoglobin (MbCO) into myoglobin (Mb) and CO [28, 36]. Myoglobin is the single heme analogue of the more complex haemoglobin and is responsible for the storage of oxygen in animals and plants. Myoglobin has broad absorption bands centred near 560 nm (Q-band) and 420 nm (Soret-band).
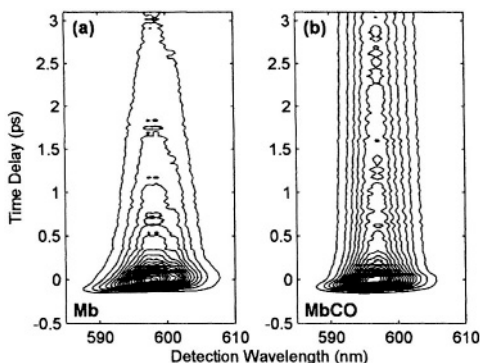
Figure 8-15. Contour plots of 2-colour 3-pulse photon echo spectra detected in the direction $k_4 = - k_1 + k_2 + k_3$ versus population time t_{23} for (a) myoglobin and (b) carbonmonoxy myoglobin, and $\lambda_1 = 580$ nm, $\lambda_3 = 600$ nm and $t_{12} = 0$.

Figure 8-15 shows the 2-colour 3-pulse photon echo spectra for Mb and MbCO detected in the $k_4 = - k_1 + k_2 + k_3$ direction versus population time t_{23} for $\lambda_1 = 580$ nm, $\lambda_3 = 600$ nm and $t_{12} = 0$. The spectrum for MbCO is narrower than for Mb and the population lifetimes are comparable when allowance is made for the slowly decaying background of photo-product states. MbCO also exhibits a sustained blue shift of about $42\ cm^{-1}$, relative to Mb, which is close to the frequency assigned to the heme doming mode [37]. This shift, in addition to the narrower spectral shape of MbCO, may be due to the partially dissociated photo-product [Mb*···CO] [38], which still contains the carbon monoxide molecule prior to complete dissociation into Mb and CO. The photon echo spectra also exhibit weak quantum beat oscillations, which have frequencies and decay times in reasonable agreement with the Raman ground-state vibrational data reported for myoblobin [37]. Fourier transform spectra of the quantum beat patterns show significant differences between the amplitudes of given vibrational modes for the MbCO photo-product and Mb [36].

6.   SUMMARY AND FUTURE DIRECTIONS

Spectrally resolved 2-colour 3-pulse photon echoes in the visible region provide a potentially powerful multidimensional technique for studying vibrational and electronic dynamics in excited and ground electronic states of a wide range of molecular systems. Recording the spectrum of the photon echo signal allows one to probe the time evolution of the amplitude of the third-order polarization induced in the sample by the femtosecond laser pulses. The large number of degrees of freedom available allows the

separation and extraction of certain specific types of dynamical and spectroscopic information, such as the population relaxation times of the levels, the optical dephasing time, inhomogeneous broadening, and the vibrational structure of transient species. Suitable selection of the wavelengths of the pulses together with spectral analysis of the photon echo signals allows specific quantum pathways to be selected and the dynamics of the ground and excited states to be separated. Simultaneous detection of the two-colour photon echo spectra in different phase-matching directions ($\mathbf{k_4} = -\mathbf{k_1} + \mathbf{k_2} + \mathbf{k_3}$ and $\mathbf{k_6} = -\mathbf{k_3} + \mathbf{k_1} + \mathbf{k_2}$) can provide additional information about the dynamics. The use of spectrally resolved photon echoes also allows the resolution of specific quantum beat frequencies corresponding to different selected pairs of transitions.

To allow a full quantitative interpretation of the photon echo spectra in multi-dimensional space (i.e., versus t_{12}, t_{23}, λ_1, λ_3, λ_{det} in both the $\mathbf{k_4}$ and $\mathbf{k_6}$ directions), it is necessary to have a full theoretical model for a multi-level system including the effects of the finite duration of the pulses. Such a model is currently being developed.

We plan to apply spectrally resolved 2-colour 3-pulse photon echoes to study molecular and electronic dynamics in a wide range of complex molecular systems including biological protein molecules [36]; light-harvesting molecules [39]; semiconductor materials [31]; semiconductor nanostructures [33]; and synthetic complex polymers [40, 41]. This will include investigations using blue femtosecond pulses and femtosecond pulses with various polarisations.

Acknowledgments

References

1. See, e.g., A.H. Zewail, *Femtochemistry – Ultrafast Dynamics of the Chemical Bond,* Vols. I, II (World Scientific, Singapore, 1994).
2. See, e.g., R.R. Ernst, G. Bodenhausen and A. Wokaun, *Principles of Nuclear Magnetic Resonance in One and Two Dimensions* (Oxford University Press, Oxford, 1987).
3. S. Mukamel, *Principles of Nonlinear Optical Spectroscopy* (Oxford University Press, New York, 1995).
4. S. Mukamel, A. Piryatinski and V. Chernyak, *Acc. Chem. Res.* **32,** 145 (1999).

5.   S. Mukamel, *Ann. Rev. Phys. Chem.* **51**, 691 (2000).
6.   R. Agarwal, B.S. Prall, A.H. Rizvi, M. Yang and G.R. Fleming, *J. Chem. Phys.* **116**, 6243 (2002), and references therein.
7.   W.P. de Boeij, M.S. Pshenichnikov and D.A. Wiersma, *Chem. Phys.* **233**, 287 (1998).
8.   J.D. Hybl, A.A. Ferro and D.M. Jonas, *J. Chem. Phys.* **115**, 6606 (2001).
9.   M.C. Asplund, M. Lim and R.M. Hochstrasser, *Chem. Phys. Lett.* **323**, 269 (2000).
10. D.E. Thompson, K.A. Merchant and M.D. Fayer, *J. Chem. Phys.* **115**, 317 (2001).
11. C. Scheurer and S. Mukamel, *J. Chem. Phys.* **115**, 4989 (2001).
12. L.D. Book, A.E. Ostafin, N. Ponomarenko, J.R. Norris and N.F. Scherer, *J. Phys. Chem. B* **104**, 8295 (2000).
13. L.V. Dao, C. Lincoln, M. Lowe and P. Hannaford, *Physica B* **327**, 123 (2003).
14. L.V. Dao, C. Lincoln, M. Lowe and P. Hannaford, *J. Chem. Phys.* **120**, 8434 (2004).
15. W. Zinth and W. Kaiser, In *Topics in Applied Physics,* Vol. 60 (Springer-Verlag, Heidelberg, 1988), p 235.
16. See, e.g., J.. Fourkas, *Ann. Rev. Phys. Chem.* **53**, 17 (2002).
17. A.W. Albrecht, J.D. Hybl, S.M. Sarah, S.M.G. Feader and D.M. Jonas, *J. Chem. Phys.* **111**, 10934(1999).
18. Y.R. Shen, *The Principles of Nonlinear Optics* (Wiley-Interscience, New York, 1984).
19. S.M.G. Feader and D.M. Jonas, *J. Phys. Chem.* A **103**, 10489 (1999).
20. J. Erland, V.G. Lyssenko and J.M. Hvam, *Phys. Rev. B* **63**, 155317 (2001).
21. C. Crepin, *Phys. Rev. A* **67**, 013401 (2003).
22. See, e.g., J.B. Asbury, T. Steinel and M.D. Fayer, Chapter 7 of this volume.
23. J.D. Hybl, A.W. Albrecht, S.M.G. Feader and D.M. Jonas, *Chem. Phys. Lett.* **297**, 307 (1998).
24. J.M. Shacklette and S.T. Cundiff, *Phys. Rev. B* **66**, 045309 (2002).
25. M. Bellini, Chapter 2 of this volume.
26. X. Gu, S. Akturk, A. Shreenath, Q. Cao and R. Trebino, Chapter 3 of this volume.
27. M. Aizengendler and A. Stanco, Lastek Laboratories, Thebarton, Australia, personal communication.
28. L.V. Dao, C.N. Lincoln, R.M. Lowe and P. Hannaford, In *Laser Spectroscopy* (Eds. P. Hannaford, A. Sidorov, H. Bachor and K. Baldwin, World Scientific, 2004), p 96.
29. E. Vogel, A. Gbureck and W. Kiefer, *J. Molecular Structure* **550-551**, 177 (2000).
30. S. Nakamura and G. Fasol, *The Blue Laser Diode* (Springer, New`York, 1997).
31. L.V. Dao, M. Lowe and P. Hannaford, *J. Phys. B* **36**, 1719 (2003).
32. T. Ogino and M. Aoki, *Jpn. J. Appl. Phys.* **19**, 2395 (1980).
33. E.R. Glaser et al., *Phys. Rev. B* **51**, 13326 (1995).
34. L.V. Dao, M. Lowe, P. Hannaford, H. Makino, T. Takai and T. Yao, *Appl. Phys. Lett.* **81**, 1806 (2002).
35. L.V. Dao, M. Lowe, P. Hannaford, H. Makino, T. Takai and T. Yao, *Int. J. Nanoscience* (in press).
36. C.N. Lincoln, *PhD Thesis,* Swinburne University of Technology (in preparation).
37. F. Rosca, A.T.N. Kumar, X. Ye, T. Sjodin, A.A. Demitov and P.M. Champion, *J. Phys. Chem. A* **104**, 4280 (2000).
38. S. Franzen, L. Kiger, C. Poyard and J-L. Martin, *Biophys. J.* **80**, 2372 (2001).
39. T. Ritz, A. Damjanovic, K. Schulten, J-P. Zhang and Y. Koyama, *Photosynthesis Research* **66**, 125 (2000).
40. N. Lokan, M.N. Paddon-Row, T.A. Smith, M.L. Rosa and K.P. Ghiggino, *J. Am. Chem. Soc.* **121**, 2917 (1999).
41. G.D. Scholes, D.S. Larson, G.R. Fleming, G. Rumbles and P.L. Burn, *Phys. Rev. B* **61**, 13670 (2000).

Chapter 9

OPTIMAL CONTROL OF ATOMIC, MOLECULAR AND ELECTRON DYNAMICS WITH TAILORED FEMTOSECOND LASER PULSES

Tobias Brixner, Thomas Pfeifer and Gustav Gerber
Physics Department, University of Würzburg
Am Hubland, 97074 Würzburg, Germany

Matthias Wollenhaupt and Thomas Baumert
Institute of Physics, University of Kassel
Heinrich-Plett-Str. 40, 34132 Kassel, Germany

Abstract   With the invention of the laser, the dream was realized to actively exert control over quantum systems. Active control over the dynamics of quantum mechanical systems is a fascinating perspective in modern physics. Cleavage and creation of predetermined chemical bonds, selective population transfer in atoms and molecules, and steering the dynamics of bound and free electrons have been important milestones along this way. A promising tool for this purpose is available with femtosecond laser technologies. In this chapter we review some of our work on adaptive femtosecond quantum control where a learning algorithm and direct experimental feedback signals are employed to optimize user-defined objectives. Femtosecond laser pulses are modified in frequency-domain pulse shapers, which apart from phase- and intensity-modulation can also modify the polarization state as a function of time. We will highlight the major advances in the field of optimal control by presenting our own illustrative experimental examples such as gas-phase and liquid-phase femtochemistry, control in weak and strong laser fields, and control of electron dynamics.

Key words: Optimal control, coherent control, femtosecond laser-pulse shaping, femtochemistry, gas-phase/liquid phase photochemistry, electron dynamics, high-order harmonic generation, intense ultrashort laser-matter interaction.

1.   INTRODUCTION

Since the early days of quantum mechanics there has been a desire to "understand" in detail the general behavior of quantum systems. This quest has been accompanied by the implicit dream not only to be able to observe in a passive way, but in fact also to actively control quantum mechanical processes. The key question in quantum control is: Can one find external control parameters which guide the temporal evolution of quantum-mechanical systems in a desired way, even if this evolution is very complex? The theoretical and experimental development of suitable control schemes is a fascinating prospect of modern physics.

Immediate applications are found in many different branches of scientific and engineering research. A selected but by no means comprehensive list of examples includes applications in photochemistry (microscopic control of chemical reactions), quantum optics (optimized generation of high-harmonic soft X-rays), atomic and molecular physics (wavepacket shaping and selective photo-excitation), biophysics (optimization of nonlinear imaging techniques), solid-state physics (coherent current control), tele-communications (optical signal encoding), or applications in related quantum technologies (such as quantum computing or quantum cryptography). But, in addition to these direct benefits, the successful implementation of quantum control concepts is also likely to provide new insights into the intricacies of the underlying quantum mechanical dynamics.

The required temporal structure of the control fields is tied to the timescale of quantum mechanical motion. Focusing on chemical reaction dynamics, this timescale is determined by the atomic motions within their molecular frameworks and has been made accessible to experiment by the development during the last 20 years of femtosecond laser technology. Ultrashort light pulses can now be used to follow in real-time the primary events of many chemical – and also physical or biological – processes. The emerging field in the area of chemistry has been accordingly termed "femtochemistry", and Ahmed Zewail has received the Nobel Prize in Chemistry in 1999 "for his studies of the transition states of chemical reactions using femtosecond spectroscopy" [1].

The combination of quantum control with femtosecond laser spectroscopy – femtosecond quantum control – is a new research field which goes beyond "simple" observation, seeking to *control* chemical reactions by suitably "shaped" femtosecond light fields. In this way, it is possible to influence product distributions in such a way that the generation of desired products is enhanced while the formation of unwanted by-products is simultaneously reduced. In contrast to the methods used in "conventional" chemistry, this is done on a "microscopic" level – directly in the investigated

molecule – by forcing the dynamical evolution of quantum wavefunctions into the desired direction. A number of recent review articles and books have treated the subject of quantum control from different perspectives [2-10].

In this chapter, we illustrate fundamental concepts and mechanisms of quantum control on prototypal small systems and then discuss the principles and applications of adaptive control on large systems with many degrees of freedom. And although we take the experimental examples from our own research, we point out that other groups have also contributed significantly to the rapidly evolving field of coherent control. Applications of the closed-loop learning scheme to molecular systems were first demonstrated in a population-transfer experiment by Bardeen et al. [11] and our group was then the first to realize automated quantum control of photodissociation reactions in complex molecules [12]. Other early examples of the adaptive scheme include the excitation of different vibrational modes in a molecular liquid [13] and the control of vibrational dynamics in a four-wave mixing experiment [14].

But optimal quantum control is not limited to molecular systems. Femtosecond laser pulse shapers and learning loops have been used for automated pulse compression [15-17] and optimized generation of arbitrary laser pulse shapes [18, 19], control of two-photon transitions in atoms [20, 21], shaping of Rydberg wavepackets [22], optimization of high-harmonic generation [23, 24], and control of ultrafast semiconductor nonlinearities [25]. Shaped electric fields have also been suggested to be of use in the context of laser cooling [26]. Furthermore, recent developments include the transfer of adaptive control methods to achieve selective photoexcitation in the liquid phase [27, 28], control over energy transfer even in a biological system [29], and the optimization of Raman-type nonlinear spectroscopy and microscopy [30].

This chapter is structured as follows: In Sect. 2 we introduce and demonstrate simple one-parameter control schemes. Simple atomic and molecular systems are the subject of the investigations presented, since they can be almost fully understood by theoretical approaches. Section 3 deals with more complex molecules in the gas phase, which are harder to understand through modeling. Therefore, many-parameter control schemes have to be introduced in order to steer those systems into the desired target states. Increasing the density of the particles in the experiment leads us into the liquid phase in Sect. 4, where control is partially impaired through loss of coherence due to solute-solvent interactions. We show that this problem can be addressed by using adaptive laser-pulse shaping. Finally, Sect. 5 shows that we are not limited to controlling atomic and molecular excitation. We show that transfer of coherence to electrons and electronic motion can be controlled, paving the way for a new era of optimal control.

2.   ONE-PARAMETER CONTROL ON PROTOTYPES: ATOMS AND DIMERS IN THE GAS PHASE

Currently, much attention is focused on the utilization of adaptive feedback-controlled femtosecond pulse shaping making available a most versatile instrument for multi-parameter control schemes [12, 23, 28, 29, 31-34]. These techniques (see also Sects. 3-5) have proven to be universal in the sense that they enable the optimization of virtually any conceivable quantity and are capable of delivering the optimal electric field without knowledge of the underlying potential energy surface. However, the individual control mechanisms may be inferred, if only for very simple systems. In order to obtain a better physical insight into such a multi-parameter control scenario it is essential to investigate one-parameter control schemes in detail on pertinent model systems.

The choice of a suitable model system is governed by several requirements: in order to support the validity of the physical pictures of the control process full quantum-mechanical simulations of the experiment should be feasible. Therefore, "computable" systems such as diatomic molecules (or atoms) are most workable. Moreover, a detailed knowledge of all electronic states involved is a prerequisite. Insight into the dynamics of the control can be accomplished if the experiment allows structural and electronic changes in the configuration to be monitored with high spatial and temporal resolution. Measurements of kinetic photo-electrons using time-of-flight (TOF) spectrometry combined with a femtosecond multiphoton ionization pump-probe technique on Na_2 in a molecular beam allows molecular motion to be mapped with sub-Ångström spatial and femtosecond temporal resolution [35]. Therefore, such an approach is ideally suited for detailed studies of how quantum control can be achieved. In general, ionization techniques in combination with femtosecond pump-probe techniques have the advantage that the limitation of the probe transition to a localized Franck-Condon window is overcome and that due to the mass sensitivity a detailed product analysis can be performed. In addition, kinetic energy time-of-flight (KETOF) spectroscopy on the product species [36, 37] as well as zero electron kinetic energy (ZEKE) techniques [38] have been employed in that context.

Published examples from our own work for such one-parameter control schemes elucidating the mechanism of quantum control are presented. The general topic has been detailed in recent textbooks [4, 39].

2.1 Control in the Perturbative Limit

In the range where the Rabi frequency Ω_R is smaller than $2\pi/T$, where T is the interaction time, the light-matter interaction is usually described with help of perturbation theory. In a one-photon process this regime does not allow control over a final-state population [40] although during the interaction an interesting population dynamics is observed [41]. Here, we discuss multi-photon ionization of the Na_2 molecule with respect to control. We start with a description of the excitation scheme before we discuss the so-called Tannor-Kosloff-Rice scheme and the influence of simple shaped laser pulses.

2.1.1 Excitation scheme
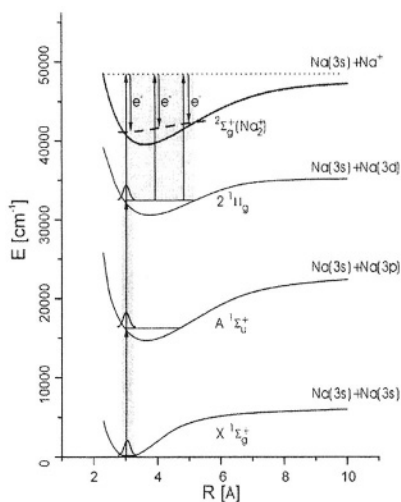
Figure 9-1. Excitation scheme for the Na_2 molecule. The pump laser in the range of 620 nm creates wave packets in the A $^1\Sigma_u^+$ and the 2 $^1\Pi_g$ at the inner turning points. The time-delayed probe laser ionizes the sodium dimer. As indicated, the kinetic energy of the photo-electrons depends on the internuclear coordinate because of the monotonic increasing difference potential (dashed line, see text).

The excitation scheme of the experiment is depicted in Fig. 9-1. At 620 nm three photons are needed to ionize the Na_2 molecule from its neutral ground state X $^1\Sigma_g^+$ into its ionic ground state $^2\Sigma_g^+$. The dynamical aspect of this multi-photon excitation has been investigated in this wavelength regime in detail with ion detection [42]. Due to the spectral width of the laser pulse and due to the Franck-Condon principle one-photon excitation prepares a wave- packet at the inner turning point of the A $^1\Sigma_u^+$ state potential by

coherent superposition of vibrational levels. The round-trip time of this wave-packet is about 310 fs ($\approx 110 \text{ cm}^{-1}$). Two-photon excitation leads to preparation of a wave packet at the inner turning point of the $2\ ^1\Pi_g$ state potential with a roundtrip time of about 370 fs ($\approx 90 \text{ cm}^{-1}$). In Ref. 42, it was found that the $A\ ^1\Sigma_u^+$ state wave-packet motion is reflected in the total Na_2^+ ion yield due to a resonance-enhanced "direct" photo-ionization process via the $2\ ^1\Pi_g$ state into the Na_2^+ ($^2\Sigma_g^+$) state at the inner turning point of the molecular potential curves involved. In those experiments the $2\ ^1\Pi_g$ state wave-packet motion could only be detected in the Na_2^+ and Na^+ fragment signal due to the excitation of a doubly excited neutral state of the Na_2 molecule near the outer turning point of the $2\ ^1\Pi_g$ state potential (not shown in Fig. 9-1) and its subsequent decay channels as auto-ionization (indirect photo-ionization) and auto-ionization-induced fragmentation [42]. Note that "direct" photo-ionization out of the $2\ ^1\Pi_g$ state into the $Na_2^+\ ^2\Sigma_g^+$ state cannot provide the dynamical information on the wave-packet prepared in this state when detected by the total Na_2^+ ion yield, since a large part of the internuclear distances is sampled in a pump-probe experiment [43, 44]. However, by the detection of kinetic energy resolved photo-electrons this dynamical information is obtained, because electrons of different kinetic energies are formed at different internuclear distances. In such a direct photo-ionization process the released kinetic energy of the photo-electrons can be determined by a classical difference potential analysis [45]. Let E_1 and E_2 denote the total energy of the nuclei in molecular potentials $V_1(R)$ and $V_2(R)$ before and after the absorption of a photon with energy $h\nu$. Due to the Franck-Condon principle the nuclei will not noticeably change either their relative position or their velocities during an electronic transition. This means the transition occurs at a fixed internuclear distance and will conserve the kinetic energy $E_{kin}(R)$. For a transition between neutral states the energy net result can be written:

$$V_1(R) + E_{kin}(R) + h\nu = V_2(R) + E_{kin}(R) \Leftrightarrow V_2(R) - V_1(R) = h\nu.$$

The classical transition is graphically simply given by the intersection of a horizontal line with height $h\nu$ with the difference potential $V_2(R) - V_1(R)$. Considering transitions between a neutral and an ionic state we have to modify this analysis slightly, as the ejected electron carries away the excess kinetic energy $E_{electron}$ and we obtain $V_2(R) - V_1(R) = h\nu - E_{electron} \leq h\nu$. It is convenient to shift the difference potential with respect to E_1, so that we can analyse the excitation within the potential energy diagram. The dashed line in Fig. 9-1 displays the difference potential $^2\Sigma_g^+$ (Na_2^+) $- 2\ ^1\Pi_g + 2\ h\nu$ relevant for this experiment. Within this concept, the expected photo-electron energy in this photo-ionization process out of the $2\ ^1\Pi_g$ state

is decreasing with increasing internuclear distance. At the inner turning point of the potential curve photo-electrons of about 0.94 eV are formed where at the outer turning point photo-electrons of about 0.78 eV are released. By recording transient photo-electron spectra the molecular wave-packet motion on neutral electronic states along all energetically allowed internuclear distances is probed simultaneously. Note that the autoionization processes of the doubly excited state lead to photo-electrons with less than 0.5 eV kinetic energy [36], which can be separated from the electrons released in the "direct" photo-ionization process.
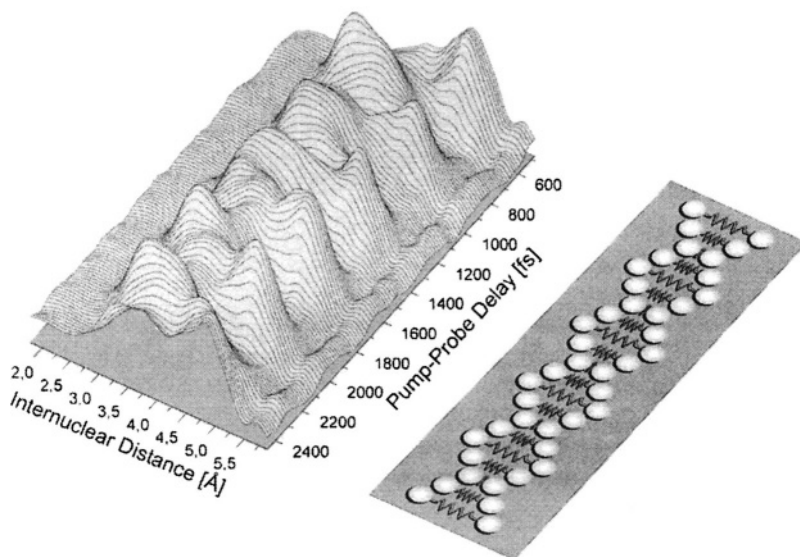
Figure 9-2. After calibration of the spectrometer with the help of atomic resonances, the measured TOF axis is converted into an energy axis. Taking the difference potential into account the mapped wave-packet dynamics as a function of the internuclear distance is obtained with sub-Å spatial resolution. The corresponding harmonic oscillation of a classical diatomic is shown for comparison.

In Fig. 9-2 the measured photo-electron distribution is shown as a function of the pump-probe delay for the same intensity ($I_0 \approx 10^{11}$ W/cm^2, 70 fs, 620 nm) of pump and probe laser. By the variation of the pump-probe delay the dynamics of the molecule in the two neutral states $2\ ^1\Pi_g$ and $A\ ^1\Sigma_u^+$ (via the $2\ ^1\Pi_g$) is monitored. In particular, the propagation of the $2\ ^1\Pi_g$ wave-packet between the turning points is resolved. In order to obtain the mapped wave-packet dynamics as a function of the internuclear distance R we have transformed the TOF axis to the corresponding kinetic energy axis and used the difference potential $^2\Sigma_g^+$ (Na$_2^+$) $-\ 2\ ^1\Pi_g$. Taking the slope of the

difference potential, the energy resolution of our spectrometer and the spectral width of our fs laser pulses into account, we obtain a spatial resolution of about 0.5 Å.

2.1.2   Control via the Tannor-Kosloff-Rice scheme
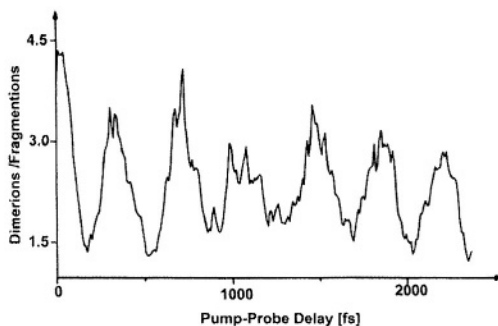
Figure 9-3. Ratio of Na^+ and Na_2^+ ion signals as a function of pump-probe delay. At the outer turning point of the $2\ ^1\Pi_g$ state the wave-packet is excited to a doubly excited neutral state that decays *inter alia* via fragmentation. Data are taken from Ref. 42.

In the time domain the so-called Tannor-Kosloff-Rice scheme [46] is a very illustrative way of how to obtain control over different products via photo-excitation of a molecule. They have proposed that controlling the time duration of a wave-packet on an excited electronic potential energy surface can be used to achieve different products. In practice, this means that a pump laser will prepare a vibrational wave-packet on an electronic excited potential and with the help of a time-delayed probe laser the product state will be populated either by dumping the wave-packet down again or by further excitation. In the case studied here we obtain a higher kinetic energy of photo-electrons at the inner turning point and a lower kinetic energy of the photo-electrons at the outer turning point from the ionization of a vibrational wave-packet propagating in the $2\ ^1\Pi_g$ state (see Fig. 9-1). If we consider electrons with different energy as different photo-products it is evident from Fig. 9-2 that by controlling the duration of the wave-packet in the $2\ ^1\Pi_g$ state we have access to different product states. Note that at the outer turning point we have access to a doubly excited neutral state that decays *inter alia* via fragmentation . By this means we were able to control the photo-product ratio Na^+/Na_2^+ in a pump-probe experiment (see Fig. 9-3) [47, 48].   Further early experimental examples employing this scheme can be found, for example, in the NaI molecule [49] and in the XeI [50] system. Indications that control of wave-packet propagation is an important parameter in adaptive feedback experiments have been reported [34, 51].
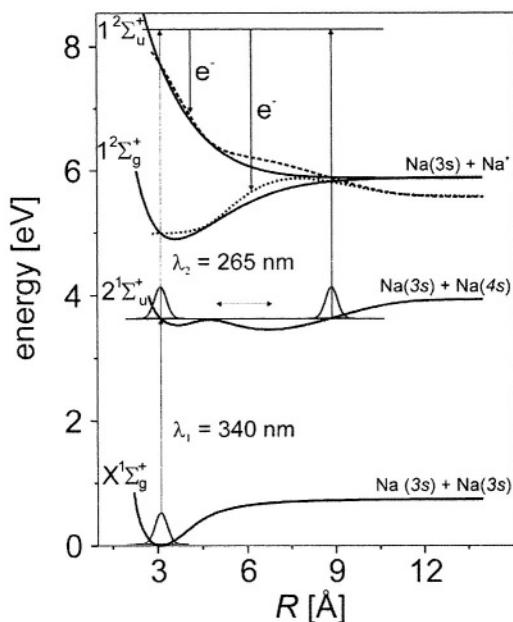
Figure 9-4. Potential energy curves for $\lambda_1 = 340$ nm excitation of the $2\,^1\Sigma_u^+$ double-minimum state (pump) in Na_2 and subsequent $\lambda_2 = 265$ nm ionization to the bound $1\,^2\Sigma_g^+$ and repulsive $1\,^2\Sigma_u^+$ ionic states (probe). The corresponding difference potentials for the bound (dotted) and the repulsive (dashed) ionic states are displayed. Energy resolved photo-electron spectra from both ionic states are measured.

Another aspect in quantum control is introduced by non-adiabatic coupling of the potential curves involved in the time evolution of a quantum system [52]. The coupling of the covalent and ionic potentials in NaI is a prominent example (Ref. 53, and references therein). Electronic changes along the internuclear coordinate (R) are also predicted for the $2\,^1\Sigma_u^+$ double-minimum potential well in the Na_2 molecule (Fig. 9-4). According to theory [54] the change of electronic structure near the avoided crossing at 4.7 Å leads to photo-ionization probabilities rapidly changing with geometry. Our approach to measuring the R-dependent photo-ionization probabilities is based on the comparison of simulated photo-electron spectra assuming an R-independent ionization probability and measured data. We performed a two-color ($\lambda_1 = 340$ nm pump and $\lambda_2 = 265$ nm probe) pump-probe experiment (see Fig. 9-4). At an excitation wavelength of 340 nm, the generated wave-packet oscillates between 3 and 9 Å and thus samples the inner Rydberg region and the outer well which has ionic character at large internuclear distances [55]. The ionization probe wavelength of 265 nm was chosen (i) to map the complete energetically allowed range of internuclear distances, and

(ii) to simultaneously project the wave-packet motion onto the $1\ ^2\Sigma_g^+$ bound and the $1\ ^2\Sigma_u^+$ repulsive ionic state. Since the photo-electron spectra directly reveal the ionization pathway, competing ionization processes can be identified or ruled out [56]. More sophisticated information about the time evolution of the molecular electronic structure could be obtained with the use of angle-resolved photo-electron spectroscopy, in principle, as was studied theoretically [54, 57] and also demonstrated experimentally [58, 59].
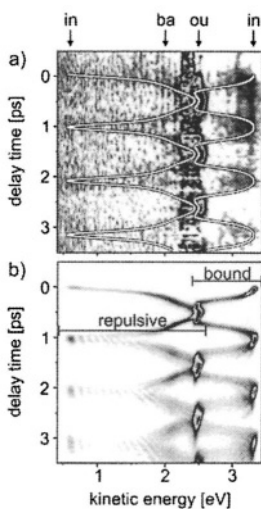
Figure 9-5. (a) Measured and (b) calculated time evolution of photo-electron spectra for $\lambda_1 =$ 340 nm excitation and $\lambda_2 = 265$ nm ionization. The kinetic energy for inner (in) and outer (ou) turning point and the barrier (ba) is indicated with arrows. Photo-electrons from the repulsive and bound ionic state are observed at 0.4 - 2.6 eV and 2.4 - 3.5 eV, respectively (indicated by horizontal bars). Electrons from both ionic states formed at the outer turning point overlap at 2.5 eV. To guide the eye the measured signal is superimposed by the electron energies obtained by classical trajectory calculation and difference potential analysis (white line in (a)).

Figure 9-5a shows a grey-scale representation of the measured photo-electron spectra obtained within the first 3.5 ps time delay between pump and probe pulses. To enhance the visibility of the measured signal the kinetic energy for "classical electrons" is superimposed as a white line in Fig. 9-5a. For this purpose, classical trajectory calculations were performed to model the wave-packet motion and the corresponding photo-electron energies were obtained from difference potential analysis. For comparison the quantum-mechanically calculated photo-electron distributions from both the bound $1\ ^2\Sigma_g^+$ and repulsive $1\ ^2\Sigma_u^+$ ionic states are depicted in Fig. 9-5b.

The variation of $\mu(R)$ is observed such that (i) ionization to the bound ionic state is favored at all internuclear distances, and (ii) for the bound ionic state the ionization probability at the outer turning point is 4.0 ± 0.4 times larger than at the inner turning point. Our results demonstrate the utilization of wave-packets as a local probe for an R-dependent ionization probability and in particular the usefulness of energy-resolved photo-electron detection to unambiguously identify the ionization pathway. A detailed discussion of the results is given in Ref. 56.

2.1.3 Control via simple shaped pulses

In the following we report on a strong chirp dependence of the three-photon ionization probability of Na_2 using simple phase-shaped femtosecond laser pulses in the excitation scheme of Fig. 9-1. We will see that both pulse duration and phase modulation of an ultrashort pulse are active control parameters. We show that for a certain chirp a higher ionization yield in the multi-photon process is observed when simultaneously the population in the intermediate states is minimal. As this experiment is performed in the perturbative regime the physical mechanisms of rapid adiabatic passage [60], by which 100 % population transfer can be achieved with chirped laser pulses, is not operative. For a detailed discussion of our experiment see Ref. 61.

Figure 9-6 shows photo-electron spectra obtained from ionizing Na_2 with up-chirped (increasing laser frequency with time) and down-chirped (decreasing laser frequency with time) laser pulses at 620 nm. The chirped pulses were produced by increasing or decreasing the optical pathway in a prism sequence (SF10) that is used to compress the pulses coming out of an optical parametric generator (OPG) down to their transform limit of 40 fs. The upper and lower spectra in Fig. 9-6a were obtained with linearly chirped pulses $(3500 \pm 500 \text{ fs}^2)$, which corresponds to a pulse duration of approximately 240 fs.

The ionization yield is seen to double when the frequency order is switched from blue first to red first within the exciting laser pulse. Note that the up- and down-chirped pulses are identical in all their pulse parameters, except for being reversed in time. This indicates that the change in the electron spectra is indeed due to the phase modulation and not to other effects such as different pulse durations or different intensity distributions. In order to better understand the experimental results, we performed quantum mechanical calculations following the method employed in Refs. 62 and 63. We included the electric field of a linearly chirped Gaussian laser pulse in analytical form (see, e.g., Ref. 64). In accordance with the experimental conditions (the laser beam was attenuated appropriately) calculations were

performed in the weak-field limit taking into account the $X\,^1\Sigma_g^+$, $A\,^1\Sigma_u^+$ and $2\,^1\Pi_g$ neutral electronic states and coupling the $2\,^1\Pi_g$ state to the continuum of the ionic ground state $^2\Sigma_g^+$ (Na_2^+). R-independent dipole matrix elements were assumed for all transitions. The calculated electron spectra depicted in Fig. 9-6b qualitatively reproduce the measured results. In addition, the population in the $2\,^1\Pi_g$ state as a function of time was calculated for both chirp directions, which is shown in Fig. 9-6c.
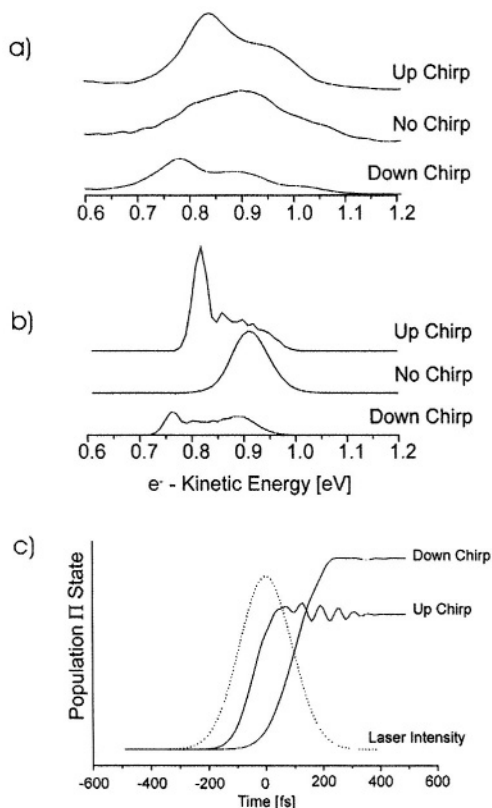
Figure 9-6. a) Electron spectra measured with single up-chirped (+3500 fs^2), down-chirped (− 3500 fs^2) and unchirped laser pulses. The transform-limited pulses of 40 fs duration are centered at a wavelength of 618 nm. The chirped pulses are of 240 fs duration. b) Calculated spectra using the same parameters as above. c) Calculated temporal development of the population in the $2\,^1\Pi_g$ state during interaction with up- and down-chirped laser pulses (± 3500 fs^2). The chirped pulse profile is shown as a dotted line.

Since the Franck-Condon maximum for both the $A\,^1\Sigma_u^+ \leftarrow X\,^1\Sigma_g^+$ state transition as well as for the $2\,^1\Pi_g \leftarrow A\,^1\Sigma_u^+$ state transition is shifted towards

the red of the central laser wavelength, the up-chirped laser pulse transfers population to the excited states earlier, while a down-chirped laser pulse can efficiently excite the intermediate states only with its trailing edge. For the subsequent ionization process this temporal behavior is essential. In order to achieve a high ionization yield the population in the $2\ {}^1\Pi_g$ state must be high at the maximum laser intensity, which is achieved with up-chirped but not with down-chirped laser pulses.

However, Fig. 9-6c also yields a very surprising result. The total population transferred to the $2\ {}^1\Pi_g$ state after the end of the pulse is much larger for a down-chirped laser although the ionization yield with this pulse is smaller. This is not due to population transfer to the ionic ground state since in the weak-field limit ionization does not (significantly) decrease the neutral state population. Rather, a mechanism very similar to that in the experiments described in Ref. 65 is responsible for this effect. To understand this a semiclassical argument based on the difference potential analysis is very illuminating. When a chirped laser pulse is used, the photon energy h*v* is changing in time. For a down-chirped pulse the decreasing laser frequency follows the decrease in the difference potential $2\ {}^1\Pi_g$ - A ${}^1\Sigma_u^+$ (not shown in Fig. 9-1) as the excited-state wave-packet propagates to larger internuclear distances. Excitation is "synchronized" to the wave-packet motion over a wider range of the nuclear coordinate for a down-chirped laser pulse and the corresponding final population in the $2\ {}^1\Pi_g$ state is higher. With the opposite chirp direction (up chirp), on the other hand, one observes a higher ionization yield while the intermediate state population is kept low. This kind of optimization is desired in coherent control schemes, because this is a prototype of simultaneous maximization versus minimization of photo-products. Besides the strong chirp dependence of the ionization yield observable in the electron spectra of Fig. 9-6a and 9-6b, a very different electron signal is observed for unchirped 40 fs laser pulses compared to the chirped laser pulses of 240 fs duration ($3500\ fs^2$). The short laser pulse predominantly yields electrons with kinetic energy of about 0.9 eV, while the electron spectra obtained with the longer (chirped) pulses are dominated by electrons around 0.8 eV. This behavior can again be understood by a difference potential analysis, this time for the transition from the $2\ {}^1\Pi_g$ state to the ionic ground state (see Fig. 9-1).

Since the difference potential is increasing with internuclear distance, the electrons released have less kinetic energy when formed at the outer turning point of a wave-packet propagating in the $2\ {}^1\Pi_g$ potential than those formed at the inner turning point (see Fig. 9-1). The duration of the transform-limited 40 fs pulse is much shorter than the oscillation period (approx. 370 fs) of the wave-packet for the excited $2\ {}^1\Pi_g$ state, and the wave-packet has no time to move to large internuclear distances during the laser

interaction. The up- and down-chirped laser pulses, however, are of much longer duration, which allows the wave-packets to sweep the whole range of allowed internuclear distances while ionization takes place. The resulting electron spectra therefore extend to lower kinetic energies, which correspond to the outer turning point where the wave-packets spend more time.

Taking the pulse duration as an active control parameter is also operative in larger molecules as demonstrated in the fragmentation of $Fe(CO)_5$ [66].

2.2   Control in Strong Laser Fields

We now turn to the topic of strong-field interaction characterized by the Rabi frequency Ω_R being larger than $2\pi/T$, where T is the interaction time.

2.2.1   Coherent coupling of molecular electronic states

In general, the wavelength range needed for the excitation of an intermediate state will differ from the wavelength range to reach the product state at a certain bond configuration. If the two wavelength regimes are not contained within the spectral width of the laser pulse a weak-field approach may not be efficient. A solution can be found by utilizing intensity-dependent effects as was demonstrated for Na_2 [67, 68]. Such effects are also expected to be operative in the adaptive feedback approach for larger molecules [12, 32, 69]. In our prototype measurements, according to the excitation scheme in Fig. 9-1, the pump laser intensity is kept fixed at $I_0 \approx 10^{11}$ W/cm^2 whereas the probe laser intensity is increased from I_0 to $10\,I_0$. The propagation of the vibrational wave-packets over all allowed internuclear distances is monitored with a probe laser of variable intensity to detect the influence of high laser intensities on the molecular potential sensitive to the internuclear distance. In Fig. 9-7a and 9-7b the power spectrum densities of Fast Fourier Transformations at electron energies corresponding to the outer turning point of the wave-packets are shown. For a probe intensity of I_0 only the frequency components of the $2\,^1\Pi_g$ state are seen as expected in the weak-field regime according to the excitation scheme in Fig. 9-1. However, with increasing probe laser intensity a contribution of the A $^1\Sigma_u^+$ state is seen at the outer turning point as displayed in Fig. 9-7b for a probe laser intensity of $6\,I_0$. An explanation of this resonant behavior is possible in terms of light-induced potentials [67, 70]. The high probe laser intensity also affects the location for the observation of a ground-state wave-packet. As seen from the excitation scheme in Fig. 9-1 one would expect the frequency contributions of the ground-state wave-packet to be at the inner turning point.
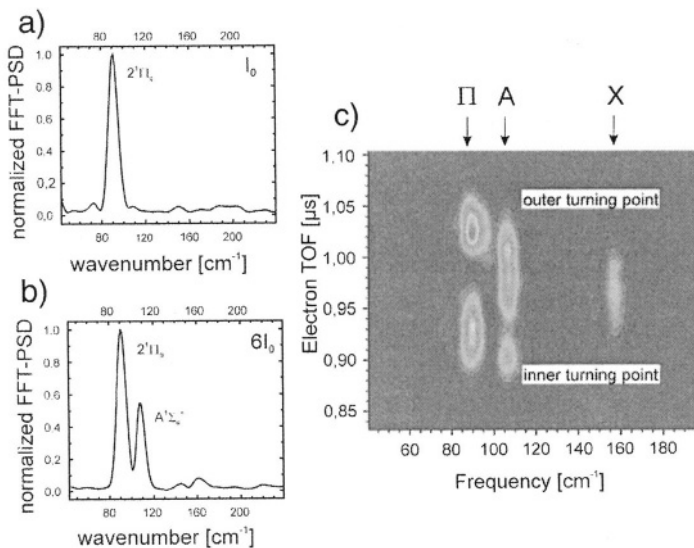
Figure 9-7. Fast Fourier Transformation Power Spectrum Density (FFT-PSD) performed at the outer turning point of the wave-packet motion for the $2\ ^1\Pi_g$ state for a pump laser intensity I_0 of approximately 10^{11} W/cm^2. (a) Probe laser intensity is I_0. (b) Probe laser intensity is $6\ I_0$. Note the additional frequency components due to wave-packet motion in the $A\ ^1\Sigma_u^+$ state. As the FFT is taken on electrons coming from the outer turning point of the $2\ ^1\Pi_g$ state, this is a resonance-enhanced contribution and not due to direct non-resonant two-photon ionization out of the $A\ ^1\Sigma_u^+$ state. (c) Spectrogram for same excitation conditions as in (b). In addition to the appearance of the $A\ ^1\Sigma_u^+$ state frequency at the outer turning point, a shift of the ground-state frequency to larger internuclear distances is observed.

Figure 9-7c displays the spectrogram for a pump intensity of 10^{11} W/cm^2 and the 6 times higher probe intensity as depicted in Fig. 9-7b. Obviously, the frequency contributions of the $X\ ^1\Sigma_g^+$ state are shifted to larger internuclear distances. This observation can partly also be interpreted in the frame of light-induced potentials. However, for a full comparison of the experiment with theory the vectorial character of the transition moment for this multi-photon process has to be taken into account as well as additional electronic states in the energetic range of the $2\ ^1\Pi_g$ state. Corresponding calculations are currently being performed [71].

Alternatively, the effect of varying the pump laser intensity while keeping the probe laser intensity fixed was also investigated. Figure 9-8a shows the calculated temporal evolution of the population in the $X\ ^1\Sigma_g^+$, $A\ ^1\Sigma_u^+$ and $2\ ^1\Pi_g$ states during the pump pulse according to Ref. 63. For low intensities (I_1) the population of the excited states rises monotonicly with time. With increasing intensity (I_2) the onset of Rabi oscillations is observed. Population is transferred efficiently within the electronic states during the

pump pulse. The highest intensity (I_3) was chosen so that the $2\ ^1\Pi_g$ state is completely depopulated at the end of the pump pulse thereby performing a "2π" excitation in the terminology of a two state system. Figure 9-8b shows the population of the $2\ ^1\Pi_g$ state at the end of the pump pulse as a function of the pump intensity. The experimental realization of such a molecular "2π" excitation is accomplished by increasing the pump laser from I_0 to $2\ I_0$ and keeping the probe laser intensity at $10\ I_0$. Figure 9-8c shows sections through the FFT of the photo-electron distribution at the inner turning point for both intensities. At I_0 the contribution at $90\ cm^{-1}$ indicates the presence of population in the $2\ ^1\Pi_g$ state. When the pump intensity is doubled, the frequency component at $90\ cm^{-1}$ vanishes thus demonstrating control of the population in the $2\ ^1\Pi_g$ state.
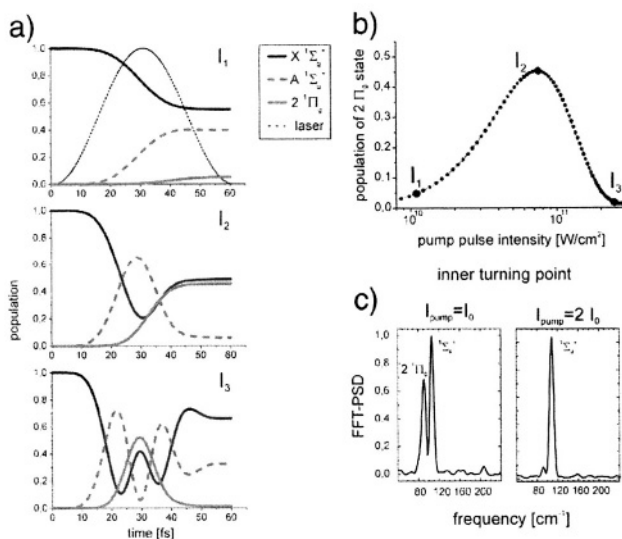
Figure 9-8. a) Temporal evolution of the population in the $X\ ^1\Sigma_g^+$, $A\ ^1\Sigma_u^+$ and $2\ ^1\Pi_g$ states during the pump pulse for laser intensities ranging from ~ 10^{10} to 10^{11} W/cm^2. The laser intensity is drawn as a dotted line in the upper figure. b) Population of the $2\ ^1\Pi_g$ state at the end of the pump pulse as a function of the laser intensity. c) Experimental verification of the "2π" excitation; pulse width is 70 fs, probe intensity = $10\ I_0$. Left: $I_{pump} = I_0 = 10^{11}$ W/cm^2. Right: $I_{pump} = 2\ I_0$.

Coherent coupling of electronic states was also investigated in the Na_3 molecule [72]. In the Na_2 prototype further strong-field effects like molecular above threshold ionization [73] and the transition from dissociation along light-induced potentials to field ionization as a function of

laser intensity [74] were investigated in our group with the help of photo-electron spectroscopy and KETOF spectroscopy, respectively.

2.2.2   Coherent coupling of atomic electronic states – control beyond population transfer and spectral interferences

In this section we discuss the control of the quantum mechanical phase in intense laser fields. In order to obtain a clear physical picture, the experiments are performed on an atomic state using a sequence of two intense femtosecond phase-locked laser pulses. The Autler-Townes effect [75, 76] in the photo-ionization of the excited $4p$ state of the K atom is used to follow the temporal evolution of the complex amplitude c_{4p} of the excited state. Coherent control in strong fields beyond (i) population control (as discussed up to now in this chapter), and (ii) spectral interference [20, 77, 78] is demonstrated, since (i) control is achieved without altering the population during the second intense laser pulse, i.e., the population during the second laser pulse is frozen, and (ii) the quantum mechanical phase is controlled without changing the spectrum of the pulse sequence [79]. The control mechanism relies on the interplay of the quantum mechanical phase imparted by the intensity of the first pulse and the optical phase of the second pulse determined by the time delay. Moreover, an uncommon symmetry of the control parameters, *delay* time and *laser intensity,* is observed: with respect to the interferences in the photo-electron spectra the role of time delay and laser intensity is interchangeable for suitable excitation conditions.

In the experiment a sequence of two intense laser pulses is used to excite K atoms in an atomic beam from the $4s$ to the $4p$ state. Simultaneously, the pulses ionize the excited-state atoms to the continuum via two-photon ionization (Fig. 9-9). Photo-electron spectra were taken at various delay times between the two laser pulses and at different laser intensities at a fixed delay time.

The experiments were carried out in a high-vacuum chamber where a beam of atomic potassium K ($4s$) intersects perpendicularly with the femtosecond laser pulses leading to photo-ionization. The released photo-electrons are detected employing a magnetic bottle time-of-flight electron spectrometer. The 785 nm, 30 fs FWHM laser pulses provided by an amplified 1 kHz Ti:sapphire laser system are split into two beams using a Mach-Zehnder interferometer. In the first experiment the time delay τ between the pulses is varied in the range 80 to 100 fs with 0.2 fs resolution at a fixed laser intensity I_0 (0.54×10^{12} W/cm^2). In the second experiment the time delay is kept fixed at 98.6 fs, whereas the energy of both beams is varied from $0.7\,I_0$ to $3\,I_0$.
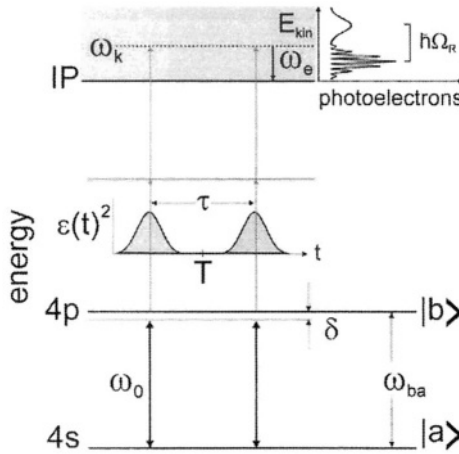
Figure 9-9. Energy level diagram for the excitation of K atoms. A sequence of two intense laser pulses coherently couples the K 4s and 4p states. The photo-electron spectra from simultaneous two-photon ionization provide information on the quantum mechanical phase.

At first, we discuss the results of the experiment using a variable time delay at a fixed laser intensity I_0. Figure 9-10b (left) shows the measured photo-electron spectra as a function of the delay time. Oscillations in the photo-electron signal around the period of the transition frequency are observed. The oscillations of slow and fast photo-electrons are out-of-phase. Sections through the photo-electron distribution were taken along the time delay axis for the fast and the slow photo-electrons [Fig. 9-10a (left)]. In the second experiment the laser intensity was varied but the time delay was fixed [Fig. 9-10b (right)] in order to demonstrate that the control of the interferences is determined by the quantum mechanical phase. The optical spectrum of the pulse sequence remains unchanged for all intensities. A monotonic increase of the splitting of both Autler-Townes components with increasing laser intensity (I_0 to I_2) is observed. The slow electron signal exhibits pronounced oscillations as the intensity is increased.

The observations are discussed in terms of the excited-state amplitudes $c_{4p}(t)$ and the dressed-state picture [60, 80]. The intensity of the first laser is high enough to cause Rabi cycling and, therefore, Autler-Townes splitting of $\hbar \Omega_R$ in the photo-electron spectrum. The observed control of interference in the Autler-Townes doublet arises if the intensity of the first pulse is chosen to yield a population of $|c_{4p}(T)|^2 = 0.5$, i.e., a pulse area of $\Theta = (n+0.5)\pi$. The subsequent time evolution ($t > T$) of c_{4p} depends on the optical phase $\omega_0 \tau$ of the second laser pulse. If the phase $\omega_0 \tau$ takes half integer multiples of π, $|c_{4p}(t)|^2$ is unchanged during the second laser pulse but the quantum mechanical phase is controlled by the second pulse. With regard to photo-

ionization the observations are interpreted in terms of the population of the dressed states. For suitable excitation only one of the dressed states is selectively populated during the second laser pulse and hence interference is only seen in one Autler-Townes component.
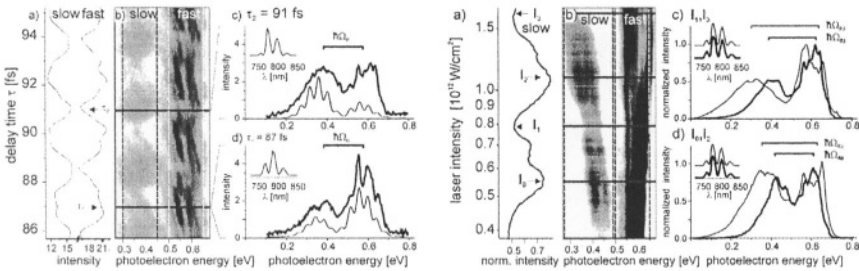
Figure 9-10. Left: (b) Experimental photo-electron spectra as a function of the delay time τ. (a) Sections through the photo-electron distribution along the time delay axis. (c) and (d) Photo- electron spectra at 87 and 91 fs. Right: (b) Measured photo-electron spectra as a function of the laser intensity (normalized) at a fixed delay time. (a) Sections through the photo-electron distribution along the laser intensity axis. (c) and (d) Photo-electron spectra at different laser intensities. The insets show the corresponding optical spectra.

The control mechanism combines phase control and high-intensity effects through the use of phase-locked pulses and intensities that are large enough to cause Rabi cycling. We believe that such mechanisms are at play in many other circumstances as well and that they open the door to a deeper understanding of quantum control in intense laser fields. Especially, the combination of phase modulation of intense laser pulses with well defined model systems will provide insights into the physical mechanisms driving the strong-field control in "open-loop" and "closed-loop" experiments.

3. MANY-PARAMETER CONTROL IN THE GAS PHASE

After the above discussion of one-parameter control schemes on prototypal small systems, we now turn to more complex molecules. Since a large number of degrees of freedom needs to be considered, the external control fields necessarily also have to exhibit more complexity. In general, it will not be sufficient to vary a single control parameter such as a pump-probe delay time. Instead, multi-parameter spectral phase shaping of femtosecond laser pulses is employed, using an automated learning loop and experimental feedback.

3.1   **Closed-Loop Femtosecond Pulse Shaping**
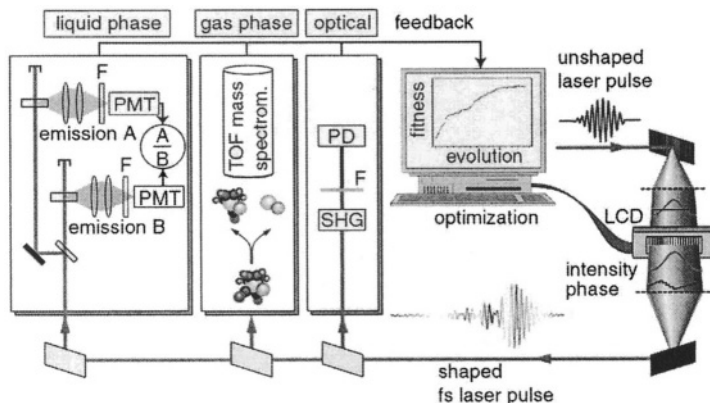
Figure 9-11. Experimental set-up. A femtosecond pulse shaper (right side) is used to generate phase-modulated laser pulses for closed-loop adaptive quantum control. Depending on the type of experiment, experimental feedback signals may be collected from purely optical signal processing (second-harmonic generation, SHG, detected in a photodiode, PD), from gas-phase time-of-flight (TOF) mass spectrometry, or from liquid-phase emission spectroscopy (where the signals are detected after filtering with photomultiplier tubes, PMT). These signals are processed in a computer learning algorithm (based on an evolution strategy approach) which iteratively improves the applied laser pulse shape until an optimum is reached.

The experimental set-up of adaptive femtosecond quantum control is shown in Fig. 9-11. A femtosecond laser pulse shaper (right side of the figure) is used to impose specific spectral phase modulations [16, 17, 81]. The device consists of a zero-dispersion compressor in a 4f-geometry, which is used to spatially disperse and recollimate the femtosecond laser pulse spectrum. Insertion of a liquid-crystal display (LCD) in the Fourier plane of the compressor provides a mechanism for convenient manipulation of the individual wavelength components. By applying voltages, the refractive indices at 128 separate pixels across the laser spectrum can be changed, and upon transmission of the laser beam through the LCD, a frequency-dependent phase is acquired. In this way, an immensely large number of different spectrally phase-modulated femtosecond laser pulses can be produced. In all experiments described below, the spectral amplitudes have not been changed, and therefore the integrated pulse energy remains constant for different pulse shapes. On the other hand, by virtue of the Fourier transformation, spectral phase changes result in phase- and amplitude-modulated laser pulse profiles as a function of time.

The laser pulses can then be used in a number of different experimental schemes. We have implemented purely optical experiments as well as control methods in gas-phase and liquid-phase environments. The resulting experimental signals are recorded and processed within a learning algorithm based on the evolution strategy approach [16, 82, 83], which in turn controls and improves the pulse-shaper settings ("closing the loop"). Evolutionary algorithms use concepts from biological evolution to solve complex optimization problems for which simple models do not exist. In short, a particular laser electric field is represented by the array of voltages applied to the LCD in the pulse shaper. This configuration is called the genetic code of one individual. After applying this laser pulse in the experiment and recording the feedback signals, a user-defined "fitness function" delivers a number which describes how well the optimization objective is fulfilled. Individuals out of a randomly initialized population pool are then selected according to their fitness ("survival of the fittest") and allowed to produce offspring by cross-over, mutation, and cloning operators. The new generation of individuals thus inherit good genetic properties and improve their adaptation to the "environment" so that after cycling through the evolutionary loop for many generations, an optimized laser pulse shape results. This method does not require any model for the system's response, and it is capable of working within large optimization parameter sets.

In the case of an optical control experiment, second-harmonic generation (SHG) in a thin nonlinear crystal can be used as the feedback signal. The temporally integrated SHG yield is a measure for pulse intensity and thus (at constant pulse energies) for pulse duration. The shorter the pulse, the more SHG light is detected. Maximization of SHG hence automatically leads to bandwidth-limited (i.e., the shortest possible) laser pulses at a given spectral bandwidth, improving the output from commercial femtosecond laser systems [15-17]. In connection with quantum control experiments, SHG is also used as a "reference signal" measuring pulse duration, as explained in Sect. 3.3.

Control of photodissociation reactions in the gas phase can be carried out by monitoring the photo-fragment yields in a time-of-flight (TOF) mass spectrometer. For this purpose, the shaped laser pulses are focused into a molecular beam of the reactant substance, initiating different fragmentation and ionization processes. Quantitative product analysis at single-mass-unit resolution is possible even for large molecules by employing a reflectron geometry of the spectrometer [84]. Selected mass peaks are then recorded by boxcar averagers, and ratios as well as absolute yields can be optimized within the evolutionary algorithm. The implementation of liquid-phase control is described in Sect. 4.
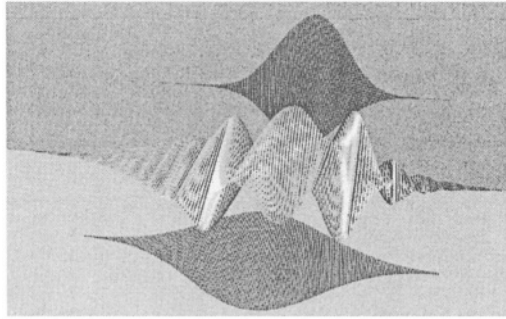
Figure 9-12. Electric field representation for a polarization-shaped femtosecond laser pulse. Time evolves from left to right in this simulation, and electric field amplitudes are indicated by the sizes of the corresponding ellipses. The momentary frequency is indicated by grey shading (or by colours on the front cover), and the shadows represent the amplitude envelopes of component $E(x)$ (bottom) and component $E(y)$ (top) separately.

Further technological development in our group also allows the control of vectorial light polarization on an ultrafast timescale [85-88]. The electric-field polarization (ellipticity and orientation angle), intensity, and oscillation frequency can be varied within a single femtosecond laser pulse with this pulse-shaping device. Without discussing the details of the experimental set-up, it can be said that the basic scheme is similar to the phase-only pulse shaper discussed in this section. However, here a two-layer LCD is used to spectrally manipulate two orthogonal polarization components, and their interference leads to complex polarization profiles in the time domain. An example for such a pulse is shown in Fig. 9-12 (also shown on the front cover of this volume). In this figure, the sizes of the ellipses represent the amplitudes of the electric field at specific times, and the grey shading (or colours on the front cover) indicate the momentary oscillation frequency. It can be seen that the polarization state evolves in a complicated fashion, reaching different transient, linear elliptical and circular polarization regions. Care must be taken in the accurate characterization of these pulse shapers since each optical element between pulse shaper and experiment (such as mirrors or beam splitters) can modify the polarization profile in a non-trivial way [86]. Polarization femtosecond pulse shaping can be considered to be a novel spectroscopic technique, because the temporal as well as three-dimensional spatial properties of quantum-wave functions can potentially be addressed and controlled. Recently, the first adaptive polarization control experiments have been performed on the multiphoton ionization of the potassium dimer prototype [89].

3.2 Control of Product Ratios

One of the initial motivations of molecular quantum control was the desire to be able to "steer" the outcome of chemical reactions such that a certain end-product is produced efficiently while undesired by-products are simultaneously suppressed. This desire can be formulated as the control of photo-product "branching ratios", i.e., the maximization of product yield ratios where the desired substance is placed in the numerator and the undesired molecule in the denominator of the fitness function.

In the first experiments of this kind [12], we have controlled a product branching ratio in the complex organometallic molecule $CpFe(CO)_2Cl$ (where $Cp = C_5H_5$). The two selected separate product channels lead either to the loss of one carbonyl ligand or to almost complete fragmentation, where only the Fe–Cl bond remains. As can be seen in Fig. 9-13, it is then possible to both maximize (5:1) and minimize (1:1) the ratio $CpFeCOCl^+/FeCl^+$ between these two channels compared to unshaped laser pulses (2.5:1). This first example already demonstrates the prospects of this adaptive control technique. Indeed, chemical reaction control (here photodissociation) can be carried out on large molecules. It should be emphasized that control is possible without information about the reaction mechanism or potential energy surfaces. The evolutionary algorithm rather finds the optimal control laser field automatically by means of the experimental feedback signal.
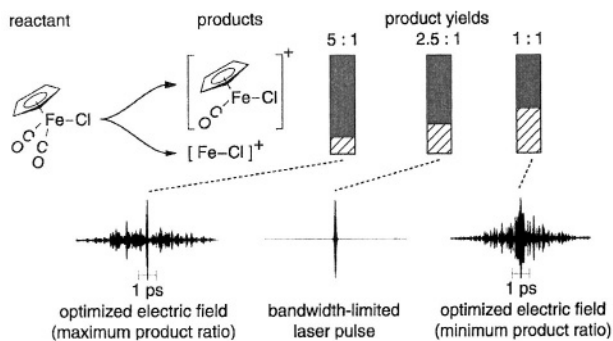
Figure 9-13. Quantum control of the $CpFeCOCl^+/FeCl^+$ product ratio. The top part displays relative yields of the two investigated product channels leading to $CpFeCOCl^+$ (black blocks) and $FeCl^+$ (shaded blocks). The bottom part shows the temporal electric fields leading to a maximum (left) and minimum (right) $CpFeCOCl^+/FeCl^+$ ratio, as well as the electric field of a bandwidth-limited laser pulse (middle) leading to an intermediate branching ratio. The electric fields are calculated by Fourier-transforming the measured laser spectrum and the spectral phase applied by the pulse shaper.

It is also seen that the optimized electric fields after optimization show considerable complexity. A separate analysis [90] revealed that it is not possible to obtain the same or similar results by trivial intensity variation effects; rather the detailed structure is relevant. In further experiments, we have also shown that the optimal electric fields are sensitive with respect to ligand variation [91].

3.3   Bond-Selective Photochemistry

While in the example just shown, the $CpFeCOCl^+/FeCl^+$ photodissociation reaction branching ratio was controlled, the question of explicit selective bond breakage was not addressed. In the next example, however, the goal was to control competing reactions in which the bond cleaved in one channel is preserved in the other channel. This would correspond to "real" bond-selective photochemistry (i.e., to break either one or the other bond). The molecule of choice here was CH_2BrCl, and we attempted to break preferentially the stronger C–Cl bond while keeping the weaker C–Br bond intact [92], While in some polyhaloalkanes such as CH_2BrI, bond selectivity has been achieved with simple one-parameter wavelength tuning of the excitation laser [93], the situation is different in CH_2BrCl, where strong non-adiabatic coupling among competing dissociation channels [94] leads to a loss of photo-product specificity. The question is therefore if in such a situation adaptive control (using complex many-parameter shaped fields at one given central wavelength) could be used to break selectively one of the carbon–halogen bonds.

During evolutionary optimization, it was indeed possible to increase the CH_2Br^+/CH_2Cl^+ ratio by 100% from 0.083 for bandwidth-limited laser pulses to 0.167 for the optimized pulse shape. In order to analyze the effect of different laser pulse shapes on a certain control objective, and especially to investigate the influence of pulse duration, correlation-type diagrams are useful: for each pulse shape during optimization, we simultaneously record several experimental observables and plot their values against each other (Fig. 9-14). In this way it is possible to see if the respective quantities are correlated (i.e., directly related) or independent. Specifically, we use SHG as a "test" quantity, because it represents a simple way to characterize laser pulse intensity. The presence or absence of correlations of SHG with the optimization objective then tells us whether the control mechanism is intensity dependent in a simple fashion or not.

In the present example of CH_2Br^+/CH_2Cl^+ maximization, the distribution of scatter points evolves along the increasing CH_2Br^+/CH_2Cl^+ axis as a function of generation (Fig. 9-14a). And, even though only a relatively narrow range of SHG yields (i.e., intensities) is explored, significant control

over bond selectivity is achieved (large values along the vertical axis). On the other hand, if SHG is maximized in a comparative but independent optimization (leading to the shortest possible laser pulses with the highest pulse intensities), the scatter distribution evolves mainly along the horizontally increasing SHG axis (Fig. 9-14b). A large number of pulse intensities is sampled (also within the SHG region of Fig. 9-14a), but in this case the CH_2Br^+/CH_2Cl^+ ratio changes only slightly during this variation. This result shows that the quantum control experiment of selective bond breakage cannot be solved with simple intensity variation as in the SHG experiment. Rather the detailed structure of the electric laser field is relevant.
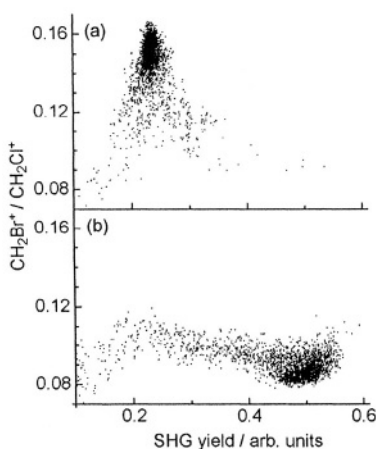
Figure 9-14. Correlation diagrams for selective bond breakage in CH_2BrCl. The value of the CH_2Br^+/CH_2Cl^+ branching ratio is plotted versus second-harmonic generation (SHG) yield for all laser pulses explored in the two optimizations of (a) CH_2Br^+/CH_2Cl^+ maximization and (b) SHG maximization.

Generalized concepts of correlation diagrams can shed further light on the fundamental processes involved in quantum control. For example, one could explore correlations between different molecular fragments, SHG, other nonlinear signals, and also the structure of the electric field itself (using suitable parameterizations).

3.4   Organic Chemical Conversion

Bond-selective photochemistry, as just illustrated, has an important potential use in chemical synthesis for the production of reactive intermediates or the formation of specific products. Due to the generality of

the adaptive approach, this is not limited to any particular class of chemical reactions. With this technique, specific functional groups could be separated from a reactant molecule while leaving the rest of the molecule intact. Such selective reactive steps would be especially helpful in organic chemical synthesis. As an example, we worked with lactic acid ($CH_3CHOHCOOH$). Here, the objective was to efficiently generate ethanol by carboxylic abstraction [95]. This is a prototype example for chemical conversion, where one often desires to remove an acid group, say, without destroying the remainder of the molecule that was just carefully synthesized. We therefore maximized the branching ratio for the removal of COOH versus the removal of CH_3, where the methyl group corresponds to an unwanted side-product arising after cleavage of the "wrong" bond.
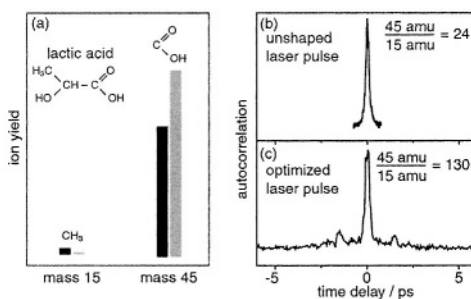
Figure 9-15. Selective bond breaking in lactic acid. The desired product is COOH, the undesired fragment is CH_3. (a) Absolute product yields are shown before (left columns) and after (right columns) optimization. The corresponding branching ratio is increased by a factor of five from the case of (b) unmodulated laser pulses toward (c) optimized laser pulses. The respective pulse shapes are characterized here by intensity autocorrelations.

In Fig. 9-15 it is seen that the $COOH^+/CH_3^+$ ratio can be increased by a factor of five compared to unshaped laser pulses. Thus, bond-selective photodissociation is also achieved in this complex organic molecule. It was possible to break a desired bond without further fragmentation of the remaining molecule. It should also be pointed out that not only the branching ratio (i.e., the purity) has been maximized, but also the absolute yield of the desired fragment was increased compared to the unoptimized situation. In the example shown here, this behavior came "free" with the ratio optimization, but in the general case this need not be true. In other words, optimizing a branching ratio does not necessarily mean that the product yield in the numerator increases while the product yield in the denominator decreases. For practical reasons, however, one often also wants to have explicit control over these absolute yields, i.e., to achieve high efficiency

along with high selectivity. The next section shows how to deal with this situation.

3.5   Multiple Optimization Goals

The philosophy of adaptive control is such that what ever objective we want to achieve with a control experiment one needs to incorporate it into the fitness function. Thus, a higher fitness yield has to represent all of the simultaneous optimization objectives at once. We investigated this in the example of the photofragmentation/photoionization of $Fe(CO)_5$, where we explicitly dealt with the relation between the control of relative product yields (i.e., ratios) versus absolute yields [51]. For this purpose, we defined a generalized fitness function of the form $f(x,y) = ax/\max\{y,y_n\} + bx + cy$, where x and y are the signal heights of wanted and unwanted photo-product, respectively, y_0 is a threshold value which prevents very low signals from below the noise level entering into the fitness calculation (and thus generating physically meaningless high values for the product ratio), and the parameters a, b, c determine the importance of ratio optimization with respect to optimization of the absolute signals.
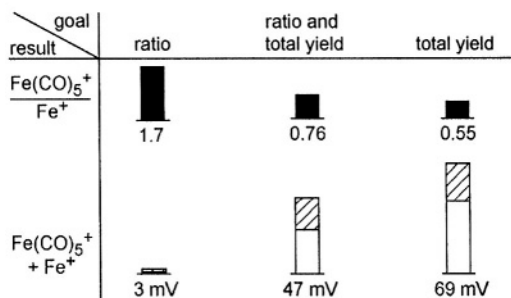
Figure 9-16. Simultaneous control of relative and absolute product yields. This experiment was carried out with 400 nm laser pulses which have been frequency-doubled after the phase shaper. Both the optimized branching ratio (upper row of blocks) and the individual yields (lower row) are shown if the emphasis is put on maximization of the ratio alone (left column), both the ratio and the total yield (middle column), or mainly the total yield (right column). In all cases, the product ratio is higher than that achieved with unmodulated laser pulses.

Our objective here was to maximize the $Fe(CO)_5^+/Fe^+$ yield while simultaneously controlling the individual contributions. Setting $x = Fe(CO)_5^+$ and $y = Fe^+$, the parameters a, b, and c were varied in a systematic fashion, and for each setting an evolutionary optimization was conducted. The results are summarized in Fig. 9-16. If most of the weight is put on the optimization

of $Fe(CO)_5^+/Fe^+$ (left column), the highest value of this ratio within the series is reached. The absolute signal heights, however, are rather small. With increasing weight on those absolute yields (higher values for *b* and *c* with respect to *a*), the total signal increases more and more as desired (albeit at cost to the branching ratio). These results show that it is indeed possible to actively control absolute and relative product yields at the same time. Similarly, if other optimization objectives are desired (e.g., suppression of more than one side-product), the corresponding experimental observables simply have to be included into the fitness function as additional terms. A suitable selection of weighting parameters then determines the relative importance of these goals.In addition to these investigations, we have used $Fe(CO)_5$ to illustrate that, in some simple cases, optimized pulse shapes can be interpreted by comparison with pump-probe mass spectra, yielding insight into the fragmentation dynamics [51].

4.   MANY-PARAMETER CONTROL IN THE LIQUID PHASE

Probably the most intriguing initial motivation for quantum control was selective photochemistry in the liquid phase by which macroscopic amounts of chemical substances could be synthesized. While this dream has still not been realized experimentally, a number of breakthroughs toward achieving this goal have been achieved. For example, the possibility of cleaving specifically selected bonds within large molecules has been demonstrated in the gas phase (see Sect. 3). Our first approach to liquid-phase quantum control dealt with selective photo-excitation, monitoring a photo-physical (rather than photo-chemical) observable. We have shown how light pulses can be optimized such that they selectively transfer electronic population within one specific complex dye molecule in solution [96]. This scheme could potentially be used for selective photo-excitation within mixtures of molecules.

Liquid-phase control poses additional difficulties compared to gas-phase experiments. The additional interaction of the reactant molecule with the surrounding solvent is likely to increase the complexity of the quantum dynamical light-induced photo-processes. However, because of the experimental implementation of a closed-loop learning algorithm, optimal laser pulse shapes can always be found under the given experimental conditions, and no detailed information about the dynamics is needed. The experimenter simply has to define a suitable feedback signal which monitors the evolution of the system in that system parameter which is desired to be controlled. For example, with the objective to control excited-state

population, we have used emission spectroscopy to assign the amount of population which was transferred to the emissive state (see Fig. 9-11).

4.1 Control of Metal-Ligand Charge-Transfer Excitation

We have investigated the dye molecule DCM and the organometallic complex [Ru(dpb)$_3$](PF$_6$)$_2$, where dpb=4,4'-diphenyl-2,2'-bipyridin, both dissolved in methanol. After excitation with at least two photons at 800 nm and the possibility for additional interaction of the excited species with the electric field of the shaped femtosecond laser pulse, the amount of excited-state population was recorded by monitoring the spontaneous emission signal from each of the two molecules. The objective here was to excite DCM while not exciting (or at least reducing the excitation of) [Ru(dpb)$_3$]$^{2+}$ [28]. This cannot be done by simple wavelength tuning because the absorption profiles of the two molecules in the relevant energy range show the same wavelength dependence, so that their linear absorption ratio is constant (Fig. 9-17a). Varying the laser intensity is also not a useful control parameter, because the same response is found for both molecules, and the observed emission ratio does not change as a function of pulse energy (Fig. 9-17b). Not even different linear chirps (i.e., laser pulses in which the momentary photon frequency increases or decreases linearly with time) have an effect on the ratio of the excitation probabilities (Fig. 9-17c). Also, the two-photon absorption cross sections have the same wavelength dependence within the laser spectrum, so that scanning the fundamental wavelength does not give selectivity (Fig. 9-17d).
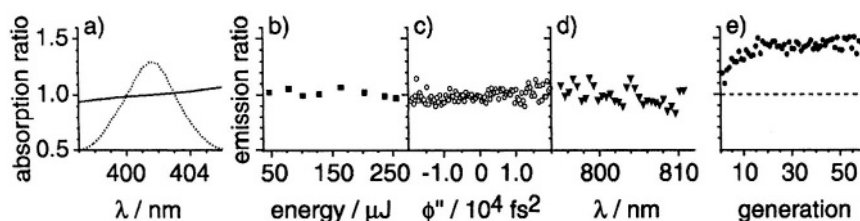
Figure 9-17. Control of liquid-phase molecular excitation. a) The relative DCM/[Ru(dpb)$_3$]$^{2+}$ linear absorption ratio (solid line) is shown as a function of wavelength. The second-order power spectrum (dotted line) of a bandwidth-limited laser pulse is shown to illustrate possible two-photon transition frequencies. The DCM/[Ru(dpb)$_3$]$^{2+}$ emission ratio is plotted b) for varying pulse energies of unshaped laser pulses, c) for varying second-order spectral phase (i.e., linear chirp), d) for scanning a symmetric and rectangular window of 5 nm width over the laser spectrum, and e) for many-parameter phase-shaping as a function of generation number within the evolutionary algorithm.

   However, selective excitation can be achieved with many-parameter adaptive quantum control in which all 128 LCD pixels are optimized independently. It is shown in Fig. 9-17e how the emission ratio evolves as a function of generation number within the evolutionary algorithm so that finally a 50% increase is observed. Thus it is possible to selectively excite one specific molecular species even within mixtures of molecules with identical absorption profiles. It should be emphasized that control is possible in the presence of complex solute-solvent interactions. The feedback signal rises significantly above the level given by the (unsuccessful) single-parameter schemes (indicated by the dashed line). The failure of the single-parameter schemes indicates that the control mechanism cannot be based on the initial excitation step (which is identical for the two molecules), but exploits the differences in the dynamical wave-packet evolutions on excited-state potential energy surfaces.

4.2   Control of Photo-Isomerization
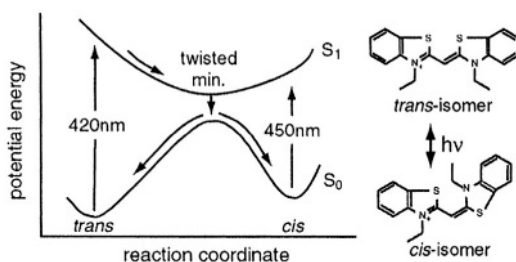
Figure 9-18. Molecular structure of the two isomer configurations and simplified potential energy surface of the cyanine dye NK88.

   The next step of the liquid-phase control experiments would be to control a chemical reaction, rather than a photo-physical process. A field of chemistry that has attracted much attention from the coherent control theory community is stereochemistry and in particular the controlled conversion of one enantiomer into the other. A first step towards reaching this goal would be the ability to control geometrical rearrangements of a molecule after the interaction with light. In the context of photo-isomerisation, *cis-trans* isomerisation has attracted much attention because of its importance in chemistry and biology (e.g., primary step of vision) [97]. An intensely

investigated class of molecules that exhibit *cis-trans* isomerization are symmetrical cyanines (see Ref. 98 for a summary). Our molecule 3,3'-diethyl-2,2'-thiacyanine iodide (NK88) also belongs to this class and its thermodynamically stable form is the *trans*-isomer. Irradiated by light around 420 nm the NK88 molecule can undergo the *cis-trans* isomerization process with a certain probability (see Fig. 9-18). Enhancement as well as reduction of the relative yield of *cis*- to *trans*-isomers after photo-excitation can be achieved with optimized femtosecond laser pulses [99]. In order to monitor the amount of achieved control we measured the ratio of generated *cis*-isomers to excited *trans*-isomers by transient absorption spectroscopy in the visible.

5. COHERENT CONTROL OF ELECTRON MOTION

5.1 Coherence Transfer to Free Electrons

After the pioneering electron diffraction experiments of Davisson and Germer [100] which demonstrated the wave properties of matter, interferences of matter waves have been among the most successful confirmation of the wave-particle duality [101]. The interferences of free electron wave-packets generated by a pair of identical, time-delayed, femtosecond laser pulses which ionize excited atomic potassium is reviewed in this section. The experimental results show that the temporal coherence of light pulses is transferred to free electron wave-packets.

The idea of the experiment is shown in Fig. 9-19. A pair of two time-delayed (τ) femtosecond laser pulses generates free electron wave-packets in the ionic continuum (Fig. 9-19a). The time evolution of the electron wave-packet is depicted in Fig. 9-19c for two 30 fs FWHM, 790 nm Gaussian laser pulses with a delay τ of 120 fs. At the end of the laser interaction (350 fs) the outward moving electron wave-packet exhibits a double-peaked structure similar to the exciting laser pulse pair but slightly distorted due to the dispersion of matter waves. Progressing dispersion spreads the partial wave-packets leading to transient interference structures (900 fs). The shape of the wave-packet eventually converges to the photo-electron spectrum taken on a spatial scale (5000 fs). Accordingly, the different arrival times at the detector translate into the spectrum measured in a time-of-flight photo-electron spectrometer.
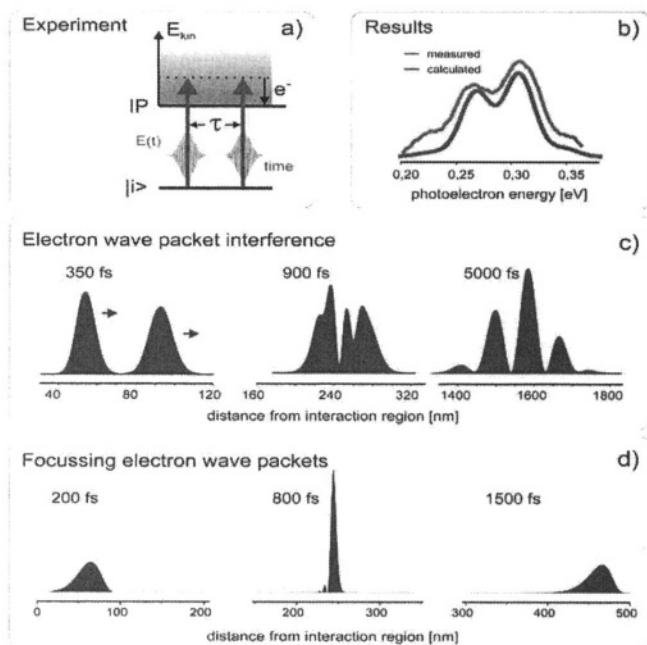
Figure 9-19. Principle of the experiment. (a) A sequence of two time delayed (τ) femtosecond laser pulses creates a double-peaked electron wave-packet. (b) Comparison of experimental and calculated photo-electron spectra with a delay of τ = 96 fs. (c) Time evolution of the double-peaked wave-packet. (d) Spatial focussing of an electron wave-packet: time evolution of a single chirped electron wave-packet.

In Fig. 9-19d calculations of the time evolution of the electron wave-packet created by a single chirped laser pulse (25 fs, -1000 fs^2) demonstrate that electron wave-packets can be spatially focussed. The physical mechanism is based on the generation of chirped electrons, i.e., electrons with low frequency components (slow) first and high frequency components (fast) later. Since the fast components eventually overtake the slow ones (at 800 fs), spatial focussing (at 250 nm) can be achieved. Using stronger chirps, the point of minimal spatial uncertainty can be shifted to much longer distances.

To quantitatively interpret the results a theoretical description of the experiment was given in Ref. 102. The laser electric field $E(t)$ couples the initially prepared 5p state ($|i\rangle$) to the the continuum. In the weak-field regime the spectrum of photo-electrons $P_e(\omega)$ with a kinetic energy of $\hbar\omega_e$ generated by the pulse pair is described by

$$P_e(\omega_e) \propto \left(1 + \cos(\omega_{ph}\tau)\right)\text{PSD}(\omega),$$

where $PSD(\omega)$ describes the power spectral density of the driving electric field. From this equation we expect the photo-electron signal at a given photo-electron energy to oscillate sinusoidally as a function of the pulse delay time τ with the respective photon frequency ω_{nh}. Likewise, at fixed delay time τ, fringes in the photo-electron spectrum with an energy separation of h/τ should be visible (see Fig. 9-19b).

The spatio-temporal evolution of the electron wave-packet is described by quasi-free electron wave functions which are approximated by plane waves with a frequency of ω_e

$$\psi(x,t) = \int_0^\infty c(\omega_e, t) e^{i(k_e x - \omega_e t)} d\omega_e$$

and the corresponding wave number $k_e = \sqrt{2m\omega_e}/\hbar$.

The experiments were carried out in a high-vacuum chamber where a beam of atomic potassium K (4s) intersects perpendicularly with the femtosecond laser pulses leading to photo-ionization. The released photo-electrons are detected employing a magnetic-bottle-type electron spectrometer with an energy resolution of 25 meV for electrons with a kinetic energy of 1 eV. The laser beam at the fundamental wavelength – provided by an amplified 1 kHz Ti:Sapphire laser system – is split into two beams. One beam (810 nm) is frequency-doubled to provide $0.2\ \mu J$ of 100 fs, 405 nm photons perpendicularly polarized with respect to the TOF-axis. This beam is used to prepare the K (5p) state as the initial state in our experiment. The other beam is delayed by 3 ns (T) and then coupled into a Mach-Zehnder type interferometer to generate a pair of two identical laser pulses ($1\ \mu J$, $< 10^{12}\ W/cm^2$, 30 fs at 790 nm) with a well-defined temporal spacing τ. The laser intensity was kept low in order to avoid 790 nm multi-photon ionization from the K (4s) ground state. The pair of 790 nm laser pulses has parallel polarization and the electrons are formed in a one-photon ionization process from the K (5p) state. The energy spectrum of the released photo-electrons is recorded as a function of the delay time τ between the two 790 nm laser pulses.

To quantify the experimental results, the fringes in the photo-electron spectrum are directly compared to simulated spectra as demonstrated in Fig. 9-18b. In this comparison, the resolution of the spectrometer (25 meV) was taken into account.

This experiment demonstrates the coherence transfer from light pulses to free electron wave-packets, thus opening the door to a whole variety of exciting new experiments. Our experiments prove that the coherence is preserved on a time scale much longer than the laser interaction. Shaped femtosecond laser pulses have been reported to create optimal wave-packets in order to achieve evolution towards a pre-selected target [12, 22, 61, 103].

Our results show that shaped free electron wave-packets with a predetermined evolution – such as focussed electron wave-packets – can be generated [104]. This may significantly stimulate, for example, experiments on time-resolved electron diffraction [105, 106] and the striking experiments on electron recollision [107]. If the free electron wave-packet is generated by a bandwidth-limited laser pulse and a time delayed shaped laser pulse, one can characterize the shaped laser pulse from the resulting interference pattern in the electron spectrum in analogy to spectral interferometry. This approach has the advantage that it also works in the XUV spectral region and beyond, where pulse characterization methods of complex formed laser pulses are in demand.

5.2   Selective Optimization of High-Order Harmonic Generation

When a highly-intense short laser pulse interacts with a dielectric medium, it is partially converted into the extended ultraviolet (XUV) frequency range, a process termed high-harmonic generation (HHG). It owes its name to the fact that the XUV light generated is emitted coherently into a spectrum consisting of (odd) integer multiples of the fundamental laser frequency.

The origin of this spectral shape lies in the temporal electronic response of the atomic or molecular medium. Every half-cycle of the oscillating laser field, when the field strength is close to the maximum, an electron is tunnel-ionized and driven away from its parent ion. As the sign of the electric field of the laser reverses, the electron starts to accelerate again towards the ion, to which it can possibly return and with which it can recombine [108]. A high-energy photon is then released to carry the excess energy, consisting of the kinetic energy of the returned electron and the ionization potential. The periodic repetition of this ultrashort process (attosecond time scale) leads to the characteristic harmonic line spectrum.

Under standard experimental conditions the XUV harmonic spectrum exhibits another property: starting at lowest orders and moving to higher orders, the high-harmonic intensity drops for a few harmonic orders, then stays roughly constant in the so called plateau region (up to orders ~ 300 [109]) and finally vanishes abruptly at a particular photon energy (cut-off). This large bandwidth of coherent radiation can be used to generate XUV light pulses of a few hundreds of attoseconds duration. These in turn provide a tool to study the electronic dynamics of all kinds of atomic [110] and molecular systems.

To the same extent as this large bandwidth might be beneficial to attosecond pulse generation and observation of electronic dynamics, it is

unfavorable for monitoring and controlling molecular dynamics. For this purpose, a small-bandwidth XUV source would clearly be advantageous. In particular for applications in ultrafast photo-electron spectroscopy a high degree of monochromaticity of the XUV light is a very desirable property. Beyond spectroscopy, also zone-plate nanoscale microscopy using high-harmonic radiation could be improved by exploiting the same property [111].

Thus, it seems reasonable to investigate whether it is possible to control the process of HHG in such a manner that just *one* particular harmonic order is generated while all the others are suppressed. Even beyond this, there is the question of whether it is feasible to *control the overall shape* of the harmonic spectrum. This could open the door to a new era of quantum control, since we could directly steer electrons on their natural time scale [112].

We have been able to show that it is indeed possible not only to enhance specific harmonic orders while suppressing neighboring ones but also to engineer the harmonic XUV spectral shape in more general ways [24]. Selective generation and suppression of single and groups of harmonics is feasible. Our work can be regarded as the first significant step towards quantum control in the XUV spectral region.

Additionally, our experiments represent a direct example for coherent control of electronic motion, since we are able to control the harmonic spectrum emitted by the extended and nonlinear motion of the electron in the vicinity of its parent ion.

In our set-up [113], we use a deformable membrane mirror to shape our laser pulses. This mirror replaces the commonly used retro-reflecting mirror in the prism compressor installed after a hollow-fiber compression stage. By applying control voltages to each of its nineteen electrodes, we are able to create different surface shapes that translate into different spectral phase functions of the laser pulse. A hollow-fiber set-up [114] is used for HHG. Aluminum filters are employed to separate the harmonic light from the intense fundamental laser pulse. For spectral analysis, we use a grazing incidence spectrometer equipped with a backside-illuminated charge-coupled-device camera. A computer is used to read out the spectrometer and to control the deformable mirror. An evolutionary algorithm (Sect. 3.1) [16] iteratively optimizes the harmonic spectrum towards a given shape criterion. This is done by maximizing the fitness function which is a map of the spectrum onto a scalar number. It increases when the spectrum comes closer to the desired shape.

Results of a typical shape optimization experiment are presented in Figs. 9-19a-c. Our goal was to selectively enhance the 25th harmonic order (integrated spectral signal in region A indicated in Fig. 9-20) while at the

same time suppressing the generation of neighbouring orders (region B). The intensity of the 25th harmonic increased by a factor of four while neighboring orders are a factor of three less intense. It is thus possible to generate single harmonic orders with high brightness. We show the fitness of the fittest individual along with the average fitness for each population. To monitor the stability, we plot the fitness of the pulse shape obtained with our reference mirror shape in Fig. 9-20c. The reference mirror shape is obtained when all actuators are set to the same voltage level. We need to define this as a reference since only then the mirror does allow for introduction of both positive and negative surface curvature. The set-up was manually optimized for maximum harmonic output (spectrum shown in Fig. 9-20a) for the reference mirror shape prior to running the optimization algorithm.
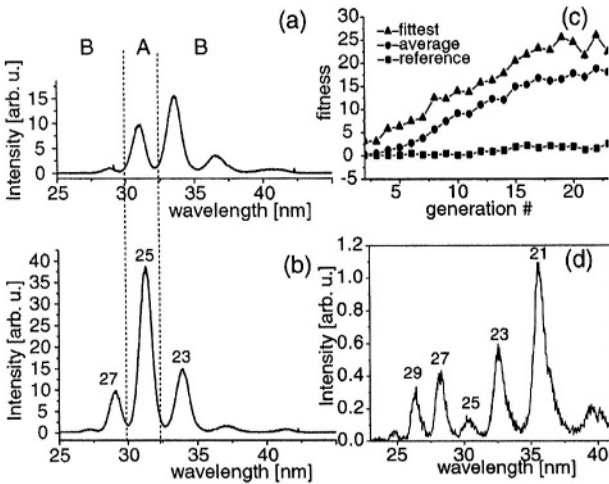
Figure 9-20. Engineering of coherent XUV spectra by controlling electron motion. Optimization experiments were carried out to maximize (a-c) and to minimize (d) single selected harmonics. The fitness of the fittest laser pulse shape increases during the run of the evolutionary algorithm. The reference pulse shape stays at a constant value, indicating stable experimental conditions.

However, a much larger degree of control is possible. Not only can we enhance a particular harmonic, but we already demonstrated isolated harmonic emission at different orders as well as selective generation of groups of harmonics. Another example is the selective minimization of a harmonic, which is depicted in Fig. 9-20d.

We performed simulations based on the solution of the Schrödinger equation for a one-dimensional model atom to elucidate structural changes

of the produced XUV pulses in the time domain. The same evolutionary optimization strategy as employed in the experiments was used for the simulation both for enhancement (Fig. 9-21a) and suppression (Fig. 9-21b) of a single harmonic order (in this case the 23rd). The corresponding trains of attosecond pulses are shown in Fig. 9-21 beside the optimized spectra. Although the changes in the infrared driver pulses are miniscule, the temporal XUV structure changes dramatically, demonstrating comprehensive control over XUV-pulse shape. Remarkably, the ratio of suppressed harmonic orders versus enhanced ones is much less than in the experiments. This agrees with common theoretical knowledge about the single-atom response and proves that controlling spatial propagation effects is important to generate arbitrarily shaped XUV-spectra and attosecond pulses.

We are confident that these findings about control over coherent XUV spectra represent a key to open up a new field of quantum control. The controllable frequency ranges and bandwidths match typical values associated with electronic inner shell processes and electron dynamics in general. Not only can basic molecular vibration and rotation be addressed using femtosecond infrared laser pulses but we can now directly engineer electronic states for further applications.
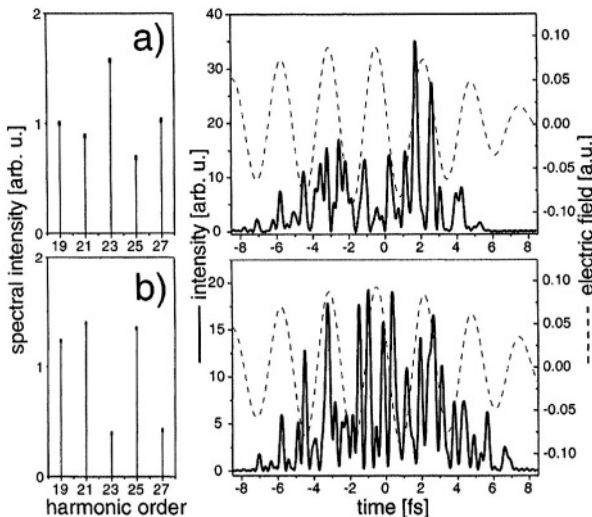
Figure 9-21. Simulation results of coherent XUV engineering. Selective optimization of the 23rd harmonic order with respect to its neighbouring orders. Both relative maximization (a) and minimization (b) were achieved. The corresponding XUV pulse shapes are plotted to the right. The temporal structure of the XUV pulses changes dramatically even though the infrared driving laser pulses are only slightly modified.

6.   CONCLUSIONS

In this chapter, we have described femtosecond coherent control techniques and their experimental applications to a variety of quantum systems. Several research routes are pursued in this field. One of the objectives is to provide a basic understanding of mechanisms and control scenarios by investigating suitable model systems. The variation of a limited and small number of control parameters such as pulse intensities, pump-probe delay times, or linear chirp provides new insight into the nature of light-induced dynamics. In most cases, the analysis can be carried out in a wave-packet picture because the spectrally broad femtosecond pulses excite a coherent superposition of energy eigenstates. For multi-photon excitation, higher-order spectral interferences also have to be taken into account. For strong-field interactions, additional effects such as light-induced potentials or the control of quantum phase beyond population transfer and spectral interferences have to be considered. The control "elements" discussed separately in these small-scale model systems can be employed in an optimally combined fashion by using adaptive femtosecond pulse shaping.

The ability to control the spectral-temporal characteristics of light fields in a sophisticated manner has led to a number of experimental breakthroughs. Here the main objective is to reach a specific "target state" of quantum systems. For example, the target can be a certain product distribution after photochemical reactions. Using an automated learning algorithm with experimental feedback, it is indeed possible to control the photodissociation of complex molecules in the gas phase. In the liquid phase additional complications arise due to solute-solvent interactions, but nevertheless selective photo-excitation was achieved, paving the way toward bimolecular reaction control with macroscopic yields.

Apart from their application in atomic or molecular dynamics, femtosecond coherent phase properties can also be transferred onto the motion of free electrons, allowing shaped electron wave-packets to be created. In the case of high-harmonic generation, excitation with adaptively shaped femtosecond pulses leads to tailored XUV spectra, thus making the tools of shaped electric fields also available for the control of inner-shell processes on an attosecond timescale.

Quantum control tells us a lot about the investigated systems and fundamental light-matter interactions. In this sense, it can be considered a sophisticated spectroscopic tool. After the initial suggestions in the late 1980s and many more theoretical investigations, we now witness a huge increase in experimental results. The ability to "make" certain photo-chemical or photo-physical states has been demonstrated in many systems, as more and more groups world-wide join this exciting research field. One

challenge for the future is certainly the realization of reaction control in liquids where specific bonds are broken and others are formed. This could lead to applications in the pharmaceutical industry. But also in "understanding" the underlying processes advances have been made, although there are still many questions to be addressed.

In general, the coherent control of quantum dynamics with tailored femtosecond light fields opens many perspectives in fundamental and applied sciences. Wherever femtosecond light-matter interaction plays a role in physical, chemical, or biological processes, or even in material sciences, specifically shaped laser pulses can be used to increase contrast and efficiency, and to introduce selectivity in a very general sense.

Acknowledgments

References

1. *Nobel Prize in Chemistry* 1999. Ref. Type: Internet Communication.
2. W. S. Warren, H. Rabitz and M. Dahleh, *Science* **259**, 1581 (1993).
3. R. J. Gordon and S. A. Rice, *Ann. Rev. Phys. Chem.* **48,** 601 (1997).
4. S. A. Rice and M. Zhao, *Optical Control of Molecular Dynamics* (Wiley, New York, 2000), pp. 496-497.
5. H. Rabitz, R. de Vivie-Riedle, M. Motzkus and K. Kompa, *Science* **288,** 824 (2000).
6. M. Shapiro and P. Brumer, in *Advances in Atomic, Molecular, and Optical Physics,* B. Bederson and H. Walther, Eds. (Academic Press, London, 1999), vol. 42.
7. T. Brixner, N. H. Damrauer, G. Gerber, in *Advances in Atomic, Molecular, and Optical Physics,* B. Bederson and H. Walther, Eds. (Academic Press, London, 2001), vol. 46.
8. D. J. Tannor, *Introduction to Quantum Mechanics: A Time-Dependent Perspective* (University Science Press, Sausalito, 2004).
9. M. Shapiro, I. Khavkine, M. Spanner and M. Y. Ivanov, *Phys. Rev. A* **67,** 13406 (2003).
10. T. Brixner and G. Gerber, *Chem. Phys. Chem.* **4,** 418 (2003).
11. C. J. Bardeen et al., *Chem. Phys. Lett.* **280**, 151 (1997).
12. A. Assion et al., *Science* **282,** 919 (1998).
13. T. C. Weinacht, J. L. White and P. H. Bucksbaum, *J. Phys. Chem. A* **103,** 10166 (1999).

14. T. Hornung, R. Meier and M. Motzkus, *Chem. Phys. Lett.* **326,** 445 (2000).
15. D. Yelin, D. Meshulach and Y. Silberberg, *Opt. Lett.* **22**, 1793 (1997).
16. T. Baumert, T. Brixner, V. Seyfried, M. Strehle and G. Gerber, *Appl. Phys. B* **65**, 779 (1997).
17. T. Brixner, M. Strehle and G. Gerber, *Appl. Phys. B* **68**, 281 (1999).
18. D. Meshulach, D. Yelin and Y. Silberberg, *J. Opt. Soc. Am. B* **15,** 1615 (1998).
19. T. Brixner, A. Oehrlein, M. Strehle and G. Gerber, *Appl. Phys. B* **70,** S119 (2000).
20. D. Meshulach and Y. Silberberg, *Nature* **396,** 239 (1998).
21. T. Hornung et al., *Appl. Phys. B* **71,** 277 (2000).
22. T. C. Weinacht, J. Ahn and P. H. Bucksbaum, *Nature* **397**, 233 (1999).
23. R. Bartels et al., *Nature* **406,** 164 (2000).
24. T. Pfeifer, D. Walter, C. Winterfeldt and C. Spielmann, submitted (2004).
25. J. Kunde et al., *Appl. Phys. Lett.* **77,** 924 (2000).
26. D. J. Tannor and A. Bartana, *J. Phys. Chem. A* **103,** 10359 (1999).
27. N. Dudovich, D. Oron and Y. Silberberg, *Nature* **418,** 512 (2002).
28. T. Brixner, N. H. Damrauer, P. Niklaus and G. Gerber, *Nature* **414,** 57 (2001).
29. J. L. Herek, W. Wohlleben, R. J. Cogdell, D. Zeidler and M. Motzkus, *Nature* **417,** 533 (2002).
30. D. Oron, N. Dudovich, D. Yelin and Y. Silberberg, *Phys. Rev. Lett.* **88,** 063004 (2002).
31. R. S. Judson and H. Rabitz, *Phys. Rev. Lett.* **68,** 1500 (1992).
32. R. J. Levis, G. M. Menkir and H. Rabitz, *Science* **292,** 709 (2001).
33. T. C. Weinacht et al., *Chem. Phys. Lett.* **344,** 333 (2001).
34. C. Daniel et al., *Science* **299,** 536 (2003).
35. A. Assion, M. Geisler, J. Helbing, V. Seyfried and T. Baumert, *Phys. Rev. A* **54,** R4605 (1996).
36. T. Baumert, B. Buehler, R. Thalweiser and G. Gerber, *Phys. Rev. Lett.* **64,** 733 (1990).
37. T. Baumert, S. Pedersen and A. H. Zewail, *J. Phys. Chem.* **97,** 12447 (1993).
38. T. Baumert, R. Thalweiser and G. Gerber, *Chem. Phys. Lett.* **209,** 29 (1993).
39. M. Shapiro and P. Brumer, *Principles of the Quantum Control of Molecular Processes* (John Wiley & Sons, Hoboken, New Jersey, Ed. 1, 2003).
40. P. Brumer and M. Shapiro, *Chem. Phys.* **139,** 221 (1989).
41. S. Zamith et al., *Phys. Rev. Lett.* **87,** 033001 (2001).
42. T. Baumert, M. Grosser, R. Thalweiser and G. Gerber, *Phys. Rev. Lett.* **67,** 3753 (1991).
43. T. Baumert et al., *J. Phys. Chem.* **95,** 8103 (1991).
44. V. Engel, *Chem. Phys. Lett.* **178,** 130 (1991).
45. R. S. Mulliken, *J. Chem. Phys.* **55,** 309 (1971).
46. D. J. Tannor, R. Kosloff and S. A. Rice, *J. Chem. Phys.* **85,** 5805 (1986).
47. T. Baumert and G. Gerber, *Israel J.* Chem. **34,** 103 (1994).
48. T. Baumert and G. Gerber, *Advances in Atomic, Molecular, and Optical Physics* **35,** 163 (1995).
49. J. L. Herek, A. Materny and A. H. Zewail, *Chem. Phys. Lett.* **228,** 15 (1994).
50. E. D. Potter, J. L. Herek, S. Pedersen, Q. Liu and A. H. Zewail, *Nature* **355,** 66 (1992).
51. M. Bergt, T. Brixner, B. Kiefer, M. Strehle and G. Gerber, *J. Phys. Chem. A* **103,** 10381 (1999).
52. V. Blanchet and A. Stolow, *J. Chem. Phys.* **108,** 4371 (1998).
53. P. Cong, G. Roberts, J. L. Herek, A. Mohktari and A. H. Zewail, *J. Phys. Chem.* **100,** 7832 (1996).
54. K. Takatsuka, Y. Arasaki, K. Wang and V. McKoy, *Faraday Discuss.* **115,** 1 (2000).
55. Y. Arasaki, K. Takatsuka, K. Wang and V. McKoy, *Chem. Phys. Lett.* **302,** 363 (1999).
56. M. Wollenhaupt et al., *Chem. Phys. Lett.* **376,** 457 (2003).

57. T. Seideman, *Ann. Rev. Phys. Chem.* **53,** 41 (2002).

58. L. Wang, H. Kohguchi and T. Suzuki, *Faraday Discuss.* **113,** 37 (1999).

59. J. A. Davies, R. E. Continetti, D. W. Chandler and C. C. Hayden, *Phys. Rev. Lett.* **84,** 5983 (2000).

60. N. V. Vitanov, T. Halfmann, B. W. Shore and K. Bergmann, *Ann. Rev. Phys. Chem.* **52,** 763 (2001).

61. A. Assion, T. Baumert, J. Helbing, V. Seyfried and G. Gerber, *Chem. Phys. Lett.* **259,** 488 (1996).

62. V. Engel, *Comp. Phys. Comm.* **63,** 228 (1991).

63. Ch. Meier and V. Engel, in *Femtosecond Chemistry,* J. Manz and L. Woeste, Eds. (VCH, Weinheim, 1995), Chap. 11.

64. S. De Silvestri, P. Laporta and O. Svelto, *IEEE J. Quantum Electron.* **QE-20**, 533 (1984).

65. C. J. Bardeen, Q. Wang and C. V. Shank, *Phys. Rev. Lett.* **75,** 3410 (1995).

66. L. Banares, T. Baumert, M. Bergt, B. Kiefer and G. Gerber, *J. Chem. Phys.* **108,** 5799 (1998).

67. T. Frohnmeyer, M. Hofmann, M. Strehle and T. Baumert, *Chem. Phys. Lett.* **312,** 447 (1999).

68. T. Frohnmeyer, M. Strehle and T. Baumert, *Appl. Phys. B* **71**, 259 (2000).

69. R. J. Levis, G. M. Menkir and H. Rabitz, *Science* **292,** 709 (2001).

70. M. Machholm and A. Suzor-Weiner, *J. Chem. Phys.* **105,** 971 (1996).

71. C. Meier, *Toulouse University, Private Communication* (2004).

72. T. Baumert, J. Helbing and G. Gerber, in *Advances in Chemical Physics – Photochemistry: Chemical Reactions and their Control on the Femtosecond Time Scale,* I. Prigogine and S. A. Rice, Eds. (John Wiley & Sons, Inc., New York, 1997).

73. A. Assion, T. Baumert, J. Helbing, V. Seyfried and G. Gerber, *Phys. Rev. A* **55,** 1899 (1997).

74. A. Assion, T. Baumert, U. Weichmann and G. Gerber, *Phys. Rev. Lett.* **86,** 5695 (2001).

75. S. H. Autler and C. H. Townes, *Phys. Rev.* **100**, 703 (1955).

76. U. Lambrecht, M. Nurhuda and F.H.M. Faisal, *Phys. Rev. A* **57,** R3176 (1997).

77. V. V. Lozovoy, I. Pastirk, K. A. Walowicz and M. Dantus, *J. Chem. Phys.* **118,** 3187 (2003).

78. R. Netz, A. Nazarkin and R. Sauerbrey, *Phys. Rev. Lett.* **90**, 063001 (2003).

79. M. Wollenhaupt et al., *Phys. Rev. A* **68,** 015401-1 (2003).

80. B. W. Shore, *The Theory of Coherent Atomic Excitation,* Volume 1 (Wiley, New York, 1990).

81. A. M. Weiner, *Rev. Sci. Instrum.* **71,** 1929 (2000).

82. D. E. Goldberg, *Genetic Algorithms in Search, Optimization, and Machine Learning* (Addison-Wesley, Reading, 1993).

83. H.-P. Schwefel, *Evolution and Optimum Seeking* (Wiley, New York, 1995).

84. B. A. Mamyrin, *Int. J. Mass Spectrom. Ion Processes* **131,** 1 (1993).

85. T. Brixner and G. Gerber, *Opt. Lett.* **26,** 557 (2001).

86. T. Brixner, G. Krampert, P. Niklaus and G. Gerber, *Appl. Phys. B* **74,** S133 (2002).

87. T. Brixner, *Appl. Phys. B* **76,** 531 (2003).

88. T. Brixner, N. H. Damrauer, G. Krampert, P. Niklaus and G. Gerber, *J. Opt. Soc. Am. B* **20,** 878 (2003).

89. T. Brixner et al. *Phys. Rev. Lett.* **92**, 208301 (2004).

90. T. Brixner, B. Kiefer and G. Gerber, *Chem. Phys.* **267,** 241 (2001).

91. M. Bergt, T. Brixner, C. Dietl, B. Kiefer and G. Gerber, *J. Organomet. Chem.* **661,** 199 (2002).

92. N. H. Damrauer et al., *Eur. Phys. J. D* **20,** 71 (2002).

93. L. J. Butler, E. J. Hintsa, S. F. Shane and Y. T. Lee, *J. Chem. Phys.* **86,** 2051 (1987).

94. D. G. Abrashkevich, M. Shapiro and P. Brumer, *J. Chem. Phys.* **116,** 5584 (2002).

95. T. Brixner, N. H. Damrauer, G. Krampert, P. Niklaus and G. Gerber, *J. Mod. Optics* **50,** 539 (2003).

96. T. Brixner, N. H. Damrauer, B. Kiefer and G. Gerber, *J. Chem. Phys.* **118,** 3692 (2003).

97. Q. Wang, R. W. Schoenlein, L. A. Peteanu, R. A. Mathies and C. V. Shank, *Science* **266,** 422 (1994).

98. Y. H. Meyer, M. Pittman and P. Plaza, *J. Photochem. Photobiol. A* **114,** 1 (1998).

99. G. Krampert, G. Vogt, P. Niklaus and G. Gerber, *submitted to Nature* (2004).

100. C. Davisson and L. H. Germer, *Phys. Rev.* **30,** 705 (1927).

101. L. de Broglie, Thesis, Masson & Cie, Paris (1924).

102. M. Wollenhaupt, A. Assion, D. Liese, C. Sarpe-Tudoran and T. Baumert, *Phys. Rev. Lett.* **89,** 173001-1 (2002).

103. C. J. Bardeen et al., *J. Phys. Chem. A* **101,** 3815 (1997).

104. J. C. Delagnes and M. A. Bouchene, *J. Phys. B* **35,** 1819 (2002).

105. J. C. Williamson, M. Dantus, S. B. Kim and A. H. Zewail, *Chem. Phys. Lett.* **196,** 529 (1992).

106. H. Ihee et al., *Science* **291**, 458 (2001).

107. V. R. Bhardwaj, D. M. Rayner, D. M. Villeneuve and P. B. Corkum, *Phys. Rev. Lett.* **87,** 253003-1 (2001).

108. P. B. Corkum, *Phys. Rev. Lett.* **71**, 1994 (1993).

109. C. Spielmann et al., *Science* **278,** 661 (1997).

110. M. Drescher et al., *Nature* **419,** 803 (2002).

111. M. Wieland et al., *Appl. Phys. Lett.* **81,** 2520 (2002).

112. R. Kienberger et al., *Science* **297,** 1144 (2002).

113. T. Pfeifer, U. Weichmann, S. Zipfel and G. Gerber, *J. Mod. Optics* **50,** 705 (2003).

114. A. Rundquist, C. G. Durfee III, Z. Chang, C. Herne and S. Backus, *Science* **280,** 1412 (1998).

Chapter 10

COHERENT CONTROL OF ATOMIC DYNAMICS WITH CHIRPED AND SHAPED PULSES

Béatrice Chatel and Bertrand Girard

Laboratoire de Collisions, Agrégats et Réactivité (CNRS UMR 5589), IRSAMC
Université Paul Sabatier, 31062 Toulouse CEDEX, France
beatrice@irsamc.ups-tlse.fr, bertrand.girard@irsamc.ups-tlse.fr

Abstract   We review in this chapter the "open-loop" approach to coherent control. A particular laser shape is designed to achieve the specific goal chosen by the experimentalist. This approach is particularly suitable for simple systems (atoms here). It provides a fruitful basis which can be used to understand the effect of shaped pulses in more complex systems. Several simple spectral or temporal shapes are used in the examples described: chirped pulses, simple spectral phase shaping (phase steps), simple temporal shaping (holes synthesized with amplitude and phase shaping). These shapes are applied either to simple one-photon transitions where the transient excited population is recorded, or to multiphoton transitions (with resonant or non-resonant intermediate states). Ladder climbing is a particularly important application of this approach.

Keywords: Ultrafast pulses, coherent control, optimal control, pulse shaping, chirped pulses, ladder climbing.

1.   INTRODUCTION

Use of optimally shaped pulses to guide and control the temporal evolution of a system has been an active field [1] of research in the last decade after the initial proposal by Rabitz et al. in 1992 [2, 3]. Recent experimental advances have led to successful control of molecular ionization and dissociation [4–6], atomic and molecular fluorescence [7–10], the reactivity of clusters [11, 12], the shape of Rydberg wave functions [13], excitations in semiconductors [14, 15] and also the energy flow in a biological system [16]. These works were spurred by the technological breakthrough [17] for generating arbitrarily tailored pulses.

The effect of laser pulse shapes on the quantum system is related to the nature of the interaction. For a linear response of the system (one-photon transition in the weak field regime), the final outcome depends only on the spectral component at the resonance frequency and is therefore independent of the general pulse shape, and particularly the spectral phases [18]. This explains, for instance, why signals equivalent to wave-packet interferences could be observed with incoherent light as well as with ultrashort pulses [19–21]. However, the temporal evolution towards the final state may depend strongly on the pulse shape. A straight-forward illustration of this statement is the non-resonant interaction which leads to transient excitation of the system, but to no final excitation. Many other examples will be presented throughout Sect. 3 of this chapter where chirped, simply shaped, or chirped and shaped pulses are used to excite a two-level atom while coherent transients are observed. Fascinating behaviors will be described.

For a non-linear interaction such as a multiphoton process or a one-photon transition in the saturation regime (see Sect. 3.6), the situation is drastically different. Many frequency components (if not all) contribute to the final state which is therefore strongly sensitive to shaping effects. Applications of pulse shaping to Two-Photon Absorption is described in detail in Sect. 4. Sequential excitation such as in pump-probe experiments are also sensitive to shaping effects even if the pulses do not overlap. Effectively, when several excited states are involved (which is required in order to create a wave packet), the final state depends on the relative phases imprinted in the excited states by the pump pulse.

In the absence of predesigned control mechanisms only a closed loop scheme [2, 3] may be employed to find efficient pulse shapes [5]: The outcome of many different shapes is fed back into an algorithm that iteratively optimizes the excitation shape without insight into the physical mechanism that is triggered by a particular shape. By contrast the effect of pulse shape on small systems can be systematically studied within an open-loop scheme [8, 9, 22–29]. This open-loop approach is well adapted to small systems for which theoretical predictions are reliable. It consists of reaching a specific goal (manipulation of the temporal response of a system excited by a light pulse) without any experimental feed-back. Physical analysis of the process allows one to predetermine the theoretical pulse shape which leads to the desired result. It is then implemented experimentally.

This chapter presents several examples demonstrated in alkali atoms by the groups of Noordam, Silberberg and our group. It is organized as follows. Sect. 2 describes briefly the main features of chirped pulses and pulse shapers which are used throughout the chapter. The examples of the approach of open-loop

control are given in Sect. 3 for Coherent Transients observed during one-photon excitation and in Sect. 4 for final population control in two-photon absorption.

2. CHIRPED PULSES AND PULSE SHAPERS

We describe in this section the basic tools used to modify the laser pulse shapes. The simplest way to shape ultrashort pulses consists of using passive dispersive devices. Using a pair of gratings is an efficient way to generate pulses with strong chirps. Changing the distance between the gratings allows one to vary the chirp of the pulse. Several experiments presented in this chapter have been performed with chirped pulses. Glass rods of strongly dispersive materials (SF10, SF58 ...) can also be used to generate strong fixed chirps. The spectral electric field is given by

$$\tilde{E}(\omega) = \sqrt{\pi}\mathcal{E}_0 T_0 \, e^{-(\omega-\omega_0)^2 T_0^2/4} \, e^{i\phi''(\omega-\omega_0)^2/2}, \tag{10.1}$$

where $2T_0$ is the field transform-limited temporal width (at $1/e$), $\delta\omega_L = 4/T_0$ the field spectral width, and $\phi'' = \frac{d^2\phi}{d\omega^2}$ the quadratic phase dispersion responsible for the Group Velocity Dispersion (GVD) induced in the pulse by the chirping process. Expression 10.1 corresponds to the temporal electric field

$$E(t) = \mathcal{E}_0 \sqrt{\frac{T_0}{T_p}} e^{-\Gamma t^2} \, e^{-i(\omega_0 t + \varphi_0/2)}, \quad \tan\varphi_0 = -\alpha T_p^2, \tag{10.2}$$

where only the resonant component (within the rotating wave approximation) has been written. Here $\Gamma = 1/T_p^2 + i\alpha$ and T_p (respectively T_0) is the half-width at $1/e$ of the chirped pulse (respectively Fourier-transform limited pulse). T_p and α are related to the chirp rate ϕ'' by

$$T_p = T_0\sqrt{1 + \left(\frac{2\phi''}{T_0^2}\right)^2}, \quad \alpha = \frac{2\phi''}{T_0^4 + (2\phi'')^2}. \tag{10.3}$$

In the case of strongly chirped pulses ($|\phi''| \gg T_0^2$), we have $T_p \simeq 2|\phi''|/T_0$ and $\alpha \simeq 1/2\phi''$ so that the laser frequency is linearly swept during the pulse:

$$\omega(t) = \omega_0 + 2\alpha(t - t_0). \tag{10.4}$$

This property as well as the pulse lengthening are the two main features of chirped pulses which are used.

The last decade has seen the development of active devices which offer many pulse shaping capabilities (see also Chapter 9: "Optimal Control of Atomic,

Molecular and Electronic Dynamics with Tailored Femtosecond Laser Pulses"). These pulse shaping techniques have been recently reviewed in detail [17]. Due to their ultrashort duration femtosecond pulses are not easily shaped in the time domain. Thanks to the Fourier transform, the common way is to synthesize them in the spectral domain. The most usual device for both high fidelity and wide flexibility of shapes involves a pair of diffraction gratings and lenses arranged in a zero-dispersion 4-f line with a pulse shaping mask at the Fourier plane. This mask, which can be a liquid crystal spatial light modulator (LC-SLM) [17], acousto-optic modulator [30]or deformable mirror [31], modulates the spectral phase and/or amplitude. Shaping without Fourier transform optics is also possible by using an actively controlled acousto-optic programmable filter [32]. In the following experiments, the pulse shaper devices are principally based on a 4-f line using cylindrical mirrors instead of lenses to limit aberrations (see Fig. 10.1).
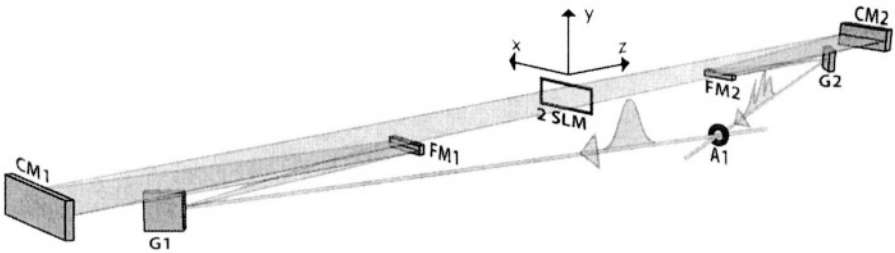
Figure 10.1. Scheme of a liquid crystal-spatial light modulator (LC-SLM) based pulse shaper. G1,G2: gratings; FM1, FM2: folding mirrors; CM1, CM2: cylindrical mirrors; A1: centering aperture [33].

Liquid crystal modulators are placed in the Fourier plane. Depending on the experiment, 128 pixels phase-only, 128 pixels phase and amplitude, or 640 pixels phase and amplitude are used. The latter (two LC-SLM from Jenoptik company) is inserted in a highly dispersive zero-dispersion line, which provides a phase and amplitude pulse shaper with high spectral resolution corresponding to a wide temporal range [33]. The effect of the pulse shaper is to multiply the input electric field $E_{in}(\omega)$ by a filter function $A(\omega) e^{i\phi(\omega)}$:

$$E_{out}(\omega) = E_{in}(\omega) \times A(\omega) e^{i\phi(\omega)} \tag{10.5}$$

3. OBSERVATION AND CONTROL OF COHERENT TRANSIENTS IN ONE-PHOTON TRANSITIONS

3.1 Introduction

When the interaction between the electromagnetic field and the matter is in the linear regime, the final state populations can be entirely deduced from the power spectrum. This is, for instance, the case for a one-photon transition in the weak field regime. However, the phase of the wave function is sensitive to the various phases of the electric field. This can have important consequences for applications where a subsequent excitation is performed, in particular when coherent superpositions are involved. The transient evolution of the excited-state population is also strongly dependent on the detailed laser shape. As an intuitive illustration of this statement, the transient response to a non-resonant excitation follows the electric field pulse envelope, independently of its spectrum. For instance, simply changing the pulse duration will change this transient response.

A resonant interaction leads to radically different behaviors. Fourier Transform (FT) limited pulses produce a step-wise excitation in the weak-field and Rabi oscillations in the intermediate and strong field regime. Chirped pulses produce a total population inversion in the strong field with a final state robust with respect to small variations of laser parameters [34, 35]. Chirped pulses in the weak field lead to a less intuitive behavior which illustrates the relative importance of the various stages of the interaction. Most of the population transfer occurs at resonance. The small fraction of excited state amplitude transferred after resonance leads to strong interferences, whereas interaction before resonance results in negligible effects [24].

In this Sect. 3, we describe several experiments in which the spectral phase of an ultrashort pulse (femtosecond to picosecond scale) is modified in simple ways, namely by chirping (adding a quadratic spectral phase), or by applying a phase step, or by combining these two techniques. In a next example, we show how pulse shapers can also be used to mimic a temporal filter. The last two subsections are devoted to the particular study of saturation effects for intermediate intensities and to the reconstruction of the pulse shape from the measurement of a set of several coherent transients.

All the cases studied in Sect. 3 are illustrated with textbook examples where the transient excitation of a two-level atom ($|g\rangle$ and $|e\rangle$), of increasing energies $\hbar\omega_g$ and $\hbar\omega_e$, respectively, is studied. The real-time evolution of the excited-state population is monitored with an ultrashort probe pulse overlapping partially (in time) with the excitation ("pump") pulse which excites the atom towards a third level $|f\rangle$ (energy $\hbar\omega_f$) (see Fig. 10.2). The state $|e\rangle$ is excited from

the ground state $|g\rangle$ with a resonant shaped or chirped ultrashort pulse $E_1(t)$ of carrier frequency ω_1 close to resonance ($\omega_1 \simeq \omega_{eg} = \omega_e - \omega_g$). The transient excited population is probed in real time by a second ultrashort pulse $E_2(t)$ (frequency ω_2), which is Fourier transform limited, of duration $\tau_2 = T_2\sqrt{2\ln 2}$ (T_2 is the half-width at $1/e$ of the field), which is short compared to the characteristic features of $E_1(t)$. $E_2(t)$ transfers the excited population from $|e\rangle$ to the final state $|f\rangle$ ($\omega_2 \simeq \omega_{fe} = \omega_f - \omega_e$). Moreover, these transitions are spectrally separated compared to the laser linewidths ($|\omega_{fe} - \omega_{eg}| \gg \Delta\omega_1, \Delta\omega_2$); so that each laser is assumed to interact with one atomic transition only. Measurement of the $|f\rangle$ population as a function of the pump-probe delay can thus be considered as equivalent to a real-time measurement of the population in $|e\rangle$.
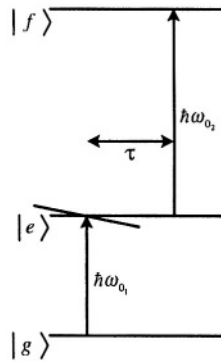
Figure 10.2. General principle of transient studies. The transient population in $|e\rangle$ excited by the shaped or chirped pulse $E_1(t)$ is probed in real time by excitation towards $|f\rangle$ induced by $E_2(t)$. Population decay (fluorescence) from $|f\rangle$ is recorded as a function of pump-probe delay τ.

The various experiments described below have been performed with a weak laser field so that first-order perturbation theory can be used to describe the result of the interaction and to calculate the excited-state population:

$$a_e(t) = \frac{\mu_{eg}}{i\hbar} \int_{-\infty}^{t} E_1(t') \exp\left(i\omega_{eg}t'\right) dt'. \tag{10.6}$$

Since pulse shaping affects directly the laser pulse spectrum, it is often better suited to rewrite Eq. 10.6 with the spectral field $\tilde{E}_1(\omega)$:

$$a_e(t) = \frac{-\mu_{eg}}{\hbar} \int_{-\infty}^{+\infty} \frac{\tilde{E}_1(\omega)}{\omega_{eg} - \omega} \exp\left[i\left(\omega_{eg} - \omega\right)t\right] d\omega. \tag{10.7}$$

The Rb ($5S_{1/2} \rightarrow 5P_{1/2}$) transition at 795 nm is used for the experiments. The final state $|f\rangle$ depends on the experiment. Cascading fluorescence from $|f\rangle$ is detected as a function of the pump-probe delay.

3.2   Control of Transient Dynamics with Shaped Pulses

In time-resolved experiments, shaped pulses can be used either to maximize the population transfer at a given time (within the laser pulse) or to change the temporal behavior. The first example takes advantage of the fact that contributions above and below resonance have opposite signs (see Eq. 10.7) and thus they contribute destructively. At $t = 0$ (maximum of the pump pulse), the excited state amplitude can be rewritten as [27]

$$a_e\,(t = 0) \;=\; \frac{-\mu_{eg}}{\hbar}\left[i\pi\tilde{E}_1(\omega_{eg}) + \wp\int_{-\infty}^{+\infty}\frac{\tilde{E}_1(\omega)}{\omega_{eg}-\omega}d\omega\right], \qquad (10.8)$$

where $\wp$ is the Cauchy principal part. Therefore, for a symmetric electric field (with respect to the resonance frequency ω_{eg}), above and below resonance contributions add destructively and only the resonant part remains. Applying a π-step on the spectral phase at ω_{eg} will change the symmetric part of the electric field to antisymmetric so that the destructive interferences are changed to constructive.

The experiment was performed on the Rb atom. The excited state $5P_{1/2}$ is probed through the $5P_{1/2} \rightarrow 4D_{3/2}$ transition followed by the radiative cascade $4D_{3/2} \rightarrow 5P_{3/2} \rightarrow 5S_{1/2}$, which is monitored as a function of pump-probe delay. Figure 10.3 compares the result of the shaped pulse with a transform limited pulse [27]. As can be seen, the transient population is increased by a factor of about 1.8 at time zero. The population decreases then to a value lower than the asymptotic population reached with transform limited pulses. This is due to the hole in the amplitude associated with the phase step [29]. A third plot displays the result of an "optimised" pulse (step height and position) where a step of 0.7π is applied slightly after resonance. For this optimized pulse, the hole in the amplitude has reduced effects.

3.3   Chirped Pulses in the Weak Field Regime: Observation of Coherent Transients

The resonant interaction of a chirped pulse with a two-level atom leads to phenomena which may appear unexpected at first sight. In the strong field regime, adiabatic transfer is the dominant process. In the weak field regime, the resonant and non-resonant parts both have significant contributions. Moreover,
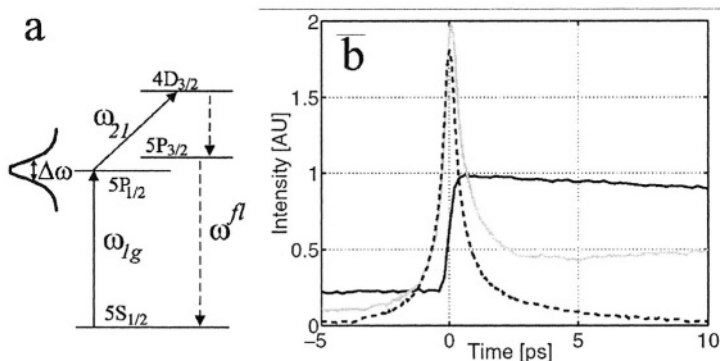
Figure 10.3. Control of transient dynamics with simple shapes. (a) Excitation and detection scheme in Rb; (b) Transient population measurement (through $5P_{3/2} \rightarrow 5S_{1/2}$ fluorescence) as a function of the probe delay for the following pulse shapes: transform limited pump pulse (solid black line), resonant π-step shaped pulse (dashed line), shifted 0.7π step (solid grey line) (reproduced from [27]).

contributions before the laser frequency reached resonance have totally different effects from after resonance contributions on the excited-state population.

The first laser pulse is obtained by frequency chirping a Fourier transform limited laser pulse as described in Sect. 2. Its expression is given by Eqs. 10.1– 10.2. The second pulse is kept as short as possible compared to the chirped pump pulse duration ($\tau_2 \ll \tau_{1c}$) in order to probe the transient population. This ensures that the final-state population (in state $|f\rangle$) recorded at a delay τ reproduces the $|e\rangle$ state population at time τ, $a_e(\tau)$.

With the expression for the electric field (Eq. 10.2), the probability amplitude of state $|e\rangle$ (Eq. 10.6) can be written as

$$a_e(t) \propto \int_{-\infty}^{t} \exp\left(-\frac{t'^2}{T_{1c}^2}\right) \exp\left(-i\frac{(t'-t_0)^2 + t_0^2}{2\phi_1''}\right) dt', \qquad (10.9)$$

where $t_0 = (\omega_{eg} - \omega_1)\phi_1''$ is the time when the laser sweeping frequency goes through the atomic resonance.

In the stationary phase approximation, the main contribution to $a_e(t)$ arises from delays within the interval $\left[t_0 - \sqrt{\phi_1''}; t_0 + \sqrt{\phi_1''}\right]$. This corresponds to the interval during which the laser frequency is resonant with the atomic transition. Non-resonant transitions can also contribute to the excited-state amplitude, but with a smaller efficiency. As time increases from t_0, new contributions are added to the amplitude $a_e(t)$. These contributions have a phase which increases more and more rapidly, leading alternatively to an increase and a decrease of the

excited-state amplitude. Similar transients were observed on much longer time scales in NMR [36]and in infrared excitation [37, 38].

The transient excited state population is probed on the (5p - ns, n'd) transitions with an ultrashort pulse (at 607 nm). The excitation scheme is depicted in Fig. 10.4, together with the experimental set-up [24].
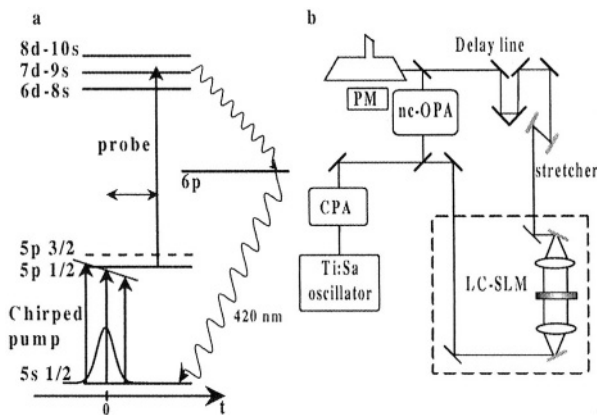
Figure 10.4. (a) Simplified energy-level diagram of rubidium, with excitation and detection schemes. The pump pulse is chirped (and drawn here slightly off-resonance). The $6p \rightarrow 5s$ fluorescence is monitored as a function of the pump-probe delay. (b) Experimental set-up. The pulse shaper is shown with lenses for clarity. CPA: regenerative amplifier; PM: photomultiplier; nc-OPA: non-collinear optical parametric amplifier. The liquid crystal spatial light modulator (LC-SLM) can be optionally added for the experiments described in Sects. 3.4 and 3.5.

The pump pulse is negatively chirped with a pair of gratings (here $\phi_1'' = -8.10^5 \text{ fs}^2$). The pump-probe signal is detected by monitoring the fluorescence at 420 nm due to the radiative cascade (ns, n'd) $\rightarrow 6p \rightarrow 5s$ collected by a photomultiplier.

The experimental result for resonant excitation at 795 nm is presented in Fig. 10.5, together with numerical solutions of the Schödinger equation (projected on the 5s, 5p, 6d up to 10s states).

The agreement is excellent. When the instantaneous laser frequency passes through resonance, a large increase of the fluorescence signal is observed. After resonance, the large amplitude oscillations are the signature of the coherent transients (CT). They correspond to beats between the excited atomic dipole and the exciting field. Thus, according to the linear frequency sweep (see Eq. 10.4), the oscillation frequency of the interferences increases linearly with time: $\omega_1(t) - \omega_{eg} = t/\phi_1''$.

Another way to explain the CT phenomenon is to examine the behavior of $a_e(t)$ in the complex plane as displayed in the inset of Fig. 10.5. The probability
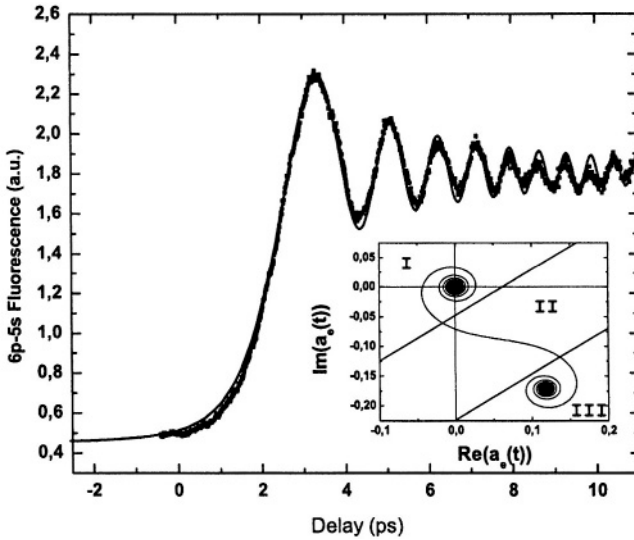
Figure 10.5. Experimental coherent transients in Rb ($\lambda_{probe} = 795\,\text{nm}$), for a chirp of $-8.\,10^5\,\text{fs}^2$ (dots) and the corresponding simulation obtained by numerical resolution of the Schrödinger equation (solid line) [24]. Inset: Theoretical excited-state amplitude drawn in the complex plane.

amplitude follows a double spiral starting from the origin. Three regions can be distinguished. The two spirals result from contributions before (I) and after (III) resonance. The intermediate region (II: time interval $\left[t_0 - \sqrt{\phi_1''}; t_0 + \sqrt{\phi_1''}\right]$) corresponds to the passage through resonance. It provides the main contribution to the population. This contribution is characterized by a sharp increase of $|a_e(t)|$, in an almost "straight" direction as expected from the stationary phase approximation applied to Eq. 10.9. The two spirals, although similar, have totally different consequences. The first one (I) winds round the origin with an increasing radius. The resulting probability thus increases slowly and regularly. After resonance (III), a second spiral winds round the asymptotic value leading to strong oscillations of the population.

The general expression of the excited-state amplitude (Eq. 10.9) presents strong similarities with Fresnel diffraction of a Gaussian beam by a sharp edge [39]. Effectively, the spirals displayed in the inset of Fig. 10.5 are similar to the well-known Cornu spirals. In Eq. 10.9 the variable t' corresponds to the position of the sharp edge in the Gaussian beam. This analogy was first introduced by Rothenberg et al. when studying the propagation of a chirped

pulse through a resonant medium where self-induced heterodyne was observed [39, 40].

By moving slightly the central laser frequency away from resonance, one can change the relative weight of the before- and after-resonance contributions. This changes the relative weight of the Cornu spirals [24]. For instance, increasing the after-resonance contribution will increase strongly the amplitude and number of oscillations.

Other analogies between time and space Fresnel diffraction have been reported by several groups [41, 42]. One example deals with two-photon absorption (or frequency doubling) from a chirped pulse [41]. The spatial coordinate was associated with the laser frequency instead of the pump-probe delay in our present case. By inserting masks in the laser spectrum, the equivalent of a Fresnel zone lens was reproduced in the spectral domain. The frequency-doubled pulse was thus spectrally focused. In our case, pulse shaping of the laser pump pulse should provide similar effects as a Fresnel lens. For instance, by slicing the temporal profile of the pump pulse, it is possible to suppress the destructive interference contributions to $a_e(t)$ and increase significantly its asymptotic value. We describe in Sect. 3.5 this approach, which is the temporal equivalent of Fresnel lenses.

3.4 Control of Coherent Transients with Simple Spectral Shapes

The coherent transients described in the previous subsection result directly from interferences between resonant and non-resonant excitation paths. They are thus strongly sensitive to small modifications of the electric field driving these paths. In this section, we demonstrate how a spectral phase shift of π applied at a frequency ω_{step} reached after resonance has a striking effect on the CT.

The time to frequency correspondence holds for strongly chirped pulses ($|\phi_1''| \gg \tau_1^2$). It can be used to understand the effect of the spectral phase step as depicted in Fig. 10.6. The corresponding arrival time of this frequency is $t_{step} = (\omega_{step} - \omega_0) \phi''$. On an interval of width $\mp 0.9\sqrt{|\phi''|}$ centered on t_{step}, the temporal electric field is a combination of shifted and unshifted initial field. Before $t_1 = t_{step} - 0.9\sqrt{|\phi''|}$, the electric field is unchanged, whereas after $t_2 = t_{step} + 0.9\sqrt{|\phi''|}$, the electric field is totally affected by the phase step. The effect on the CT is thus the following: they remain unaffected before t_1 and are phase shifted (by π) after t_2. A smooth transition is expected between t_1 and t_2.

The experimental demonstration has been performed on the Rb ($5S_{1/2} \rightarrow 5P_{1/2}$) transition using both a low resolution (128 pixels SLM) [28]and a high
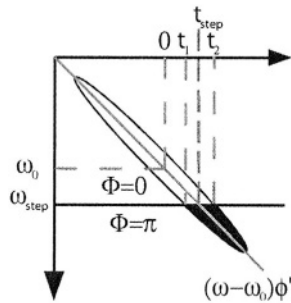
Figure 10.6. Effect of a π-step on a strongly chirped pulse displayed in the time-frequency representation (Wigner plot). Passage through resonance (ω_0) defines $t = 0$. The steep transition in the frequency domain (of the order of the inter-pixel gap width) induces a broad transition in the time domain, on an interval $[t_1, t_2]$ of width $|t_2 - t_1| \simeq 1.8 \times \sqrt{|\phi''|} = 1.7$ ps.

resolution (640 pixels SLM [43, 33]) pulse shaper [29]. Figure 10.7 presents the comparison between initial CT and inverted CT with a π-step applied 1 pixel after resonance with the low resolution pulse shaper.
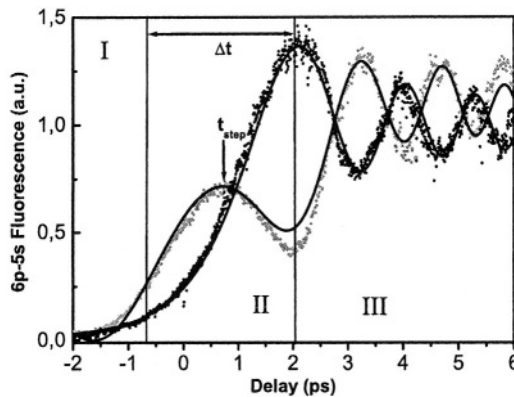
Figure 10.7. Shaped coherent transients with a low resolution pulse shaper [28, 29]. Experimental (dotted) and numerical (solid) results: chirped pump pulse (black), and π-step shaped chirped pulse (grey). Here $\phi'' = -9.4.\,10^5\,\text{fs}^2$ corresponding to $\tau_c \simeq 21$ ps; $\lambda_{step} = 2\pi c/\omega_{step} = 795.23$ nm.

The scattered data are the experimental points and the solid line shows the corresponding theoretical result obtained by first-order perturbation theory. The agreement is excellent. The inverted CT behave as expected and the three intervals described above are clearly seen.

The sensitivity of shaped CT to the position of the step is huge. Figure 10.8 gives an example of several inverted CT obtained with the high resolution
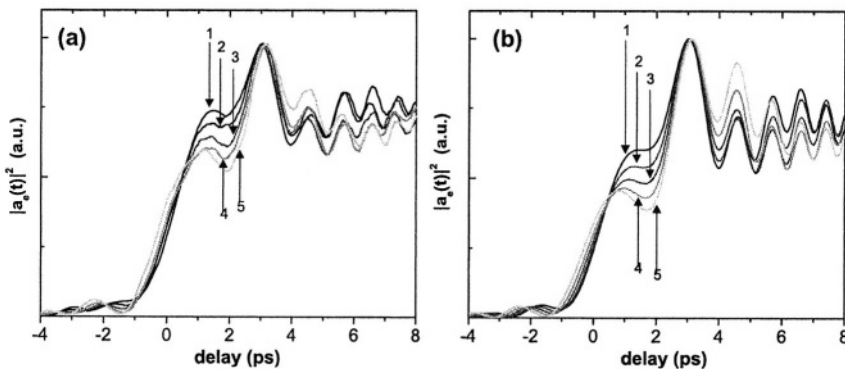
Figure 10.8. Shaped coherent transients with a high resolution pulse shaper. (a) experimental scans with phase π-step shifted by one pixel between each scan, with detunings from resonance ranging from 0.30nm (curve 5) to 0.54nm(curve 1). (b) Corresponding simulations [29].

pulse shaper where the position of the phase step is shifted 1 pixel by 1 pixel (corresponding here to 0.06nm). The sensitivity is clear and the agreement with theory is again excellent.

These simple spectral shapes demonstrate the high sensitivity of CT to the applied shape. It is thus well suited as a test of the sensitivity of high resolution pulse shapers. To apply the CT shaper testing method, an atomic resonance lying within the pulse spectrum is required. Up or down chirp is chosen such that the resonance is crossed early, leading to long oscillations [24]. The population scales down linearly, but the CT oscillation inversion point could be demonstrated over the entire spectrum while maintaining the same signal-to-noise ratio. Then, the sharpness of the atomic transition makes shifts of the phase step by single pixels visible. The CT method provides a simple, yet rich, test system for high resolution femtosecond pulse shaping, such as needed for new shapers [43, 33]. Moreover, since atomic transitions can be found over a very broad spectral range, this method provides a tool to observe shaping effects in spectral domains where usual methods cannot be used.

3.5 Control of Coherent Transients with Simple Temporal Shapes: Temporal Fresnel Lenses

The second set of experiments reported in this work is based on the strong similarity between the expression of the excited-state amplitude [24]and Fresnel diffraction of a Gaussian beam by a sharp edge. Fresnel lenses are based on the

control of constructive versus destructive interferences. The latter interferences are either suppressed or switched to constructive by changing selectively their sign [44]. The same principle is used for quasi-phase matching in fibers or nonlinear devices [45]. Thus, by slicing out temporal sections in the pump pulse, the equivalent of a Fresnel zone lens can be reproduced in the time domain. So it should be possible to suppress the destructive (or constructive) contributions to $a_e(t)$ and increase (or decrease) significantly its asymptotic value by converting the oscillations into staircase patterns. Figure 10.9 shows a theoretical simulation of the climbing staircase pattern when a single cut is made in the time domain (inset of Fig. 10.9) during the first decreasing part of the CT. As expected the predicted final population is enhanced.
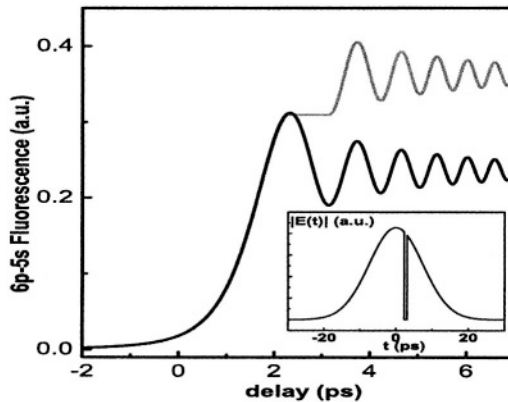
Figure 10.9. Fresnel zone lens analogy: excited transient population with unshaped chirped pump pulse (black line) and with calculated shaped pulse (solid grey line). Inset: corresponding shaped temporal envelope of the pump pulse.

Slicing the pulse on a time scale of ~ 100 fs is not directly possible in the time domain. As usual in fs pulse shaping, the required shape can be obtained by filtering the spectral profile. While decreasing the excitation energy (the area under spectra in Fig. 10.10a), the shaped temporal profile produces a redistribution of frequencies. In particular as shown on Fig. 10.10a, the intensity (black line) at resonance (λ_{eg}) is increased compared to the initial spectrum (black dashed line). Thus the passive temporal filter of the inset of Fig. 10.9 corresponds to an active spectral filter.

This active spectral filter was simulated using a passive spectral filter, and applying an appropriate normalization factor by comparison of the shaped and unshaped pulse area. The required spectrum is obtained by Fourier transforming the shaped temporal profile (inset of Fig. 10.9). Its amplitude, represented
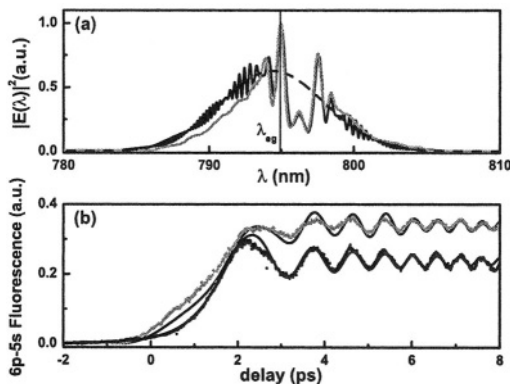
Figure 10.10.   Realization of a temporal Fresnel lens with a low resolution pulse shaper. (a) Calculated (black) and realized (grey) spectra. Original spectrum (dashed line). $\lambda_{eg} = 794.95\,\text{nm}$. (b) Transient population measurements (dots) and numerical solution (line) obtained with the experimental spectrum (grey), together with the normal CT (black). Here, $\phi'' = -4.9.\,10^5\,\text{fs}^2$ corresponding to $\tau_c \simeq 12.4\,\text{ps}$ [28].

in Fig. 10.10a (black line), is highly structured. It was implemented experimentally by using the low resolution pulse shaper as a pure amplitude modulator. This leads to the spectrum (grey line) observed on Fig. 10.10a. It has been smoothed by the finite resolution of the pulse shaper [28]. However, the fastest oscillations are associated with the sharpness of the cutting, whereas the main features of physical interest (position and width of the temporal hole) are contained in the large peaks which are preserved even in the smoothed spectrum as our experiments have demonstrated. The corresponding phase is mainly quadratic (introduced by the stretcher as for unshaped CT) with some residual terms which have been neglected. Qualitatively, the agreement between the experimental result shown Fig. 10.10b and the ideal result displayed Fig. 10.9 is excellent. That includes the in-phase revival of oscillations after the suppressed interference, precisely as intended by the control goal.

Some small quantitative discrepancies remain. They have been attributed to various factors which can be improved: the low resolution of the pulse shaper, the neglect of the residual, non-quadratic phase. Similar experiments have been performed to suppress the first increasing part in the oscillations leading again to a good agreement with theoretical simulations.

These results demonstrate that if the system is well-known it is possible to predetermine the control mechanism and the exact corresponding shape and to apply it directly without feedback in open-loop coherent control.

3.6   **Strong Field: Saturation of Coherent Transients**

All the previous treatments have been performed in the weak field regime for which the response of the system is proportional to the excitation. Increasing the laser intensity brings the interaction closer towards adiabatic transfer for which total transfer is achieved with a continuous growth of the population [46]. However, there is a full range of intermediate laser intensities for which oscillations remain, although they are no more symmetric with respect to the asymptotic value. Looking in the complex plane at the probability amplitude $a_e(t)$ (calculated through exact resolution of the Schrödinger equation), one observes a spiral which is progressively distorted and then bounces on the circle of unity radius (which is the absolute population limit) as can be observed in Fig. 10.11 [47].
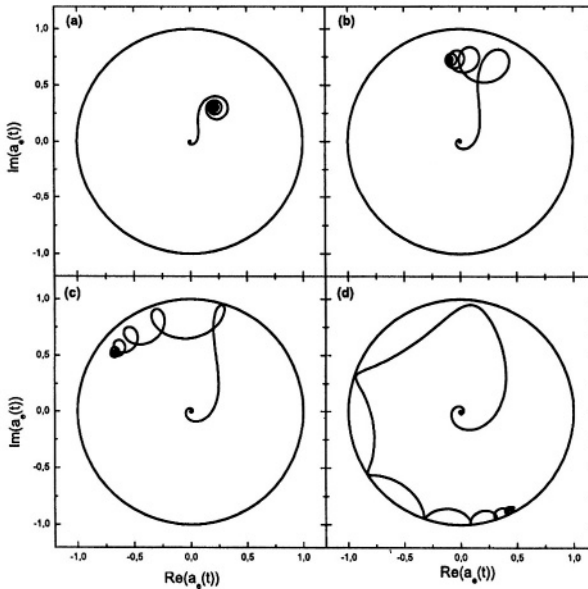
Figure 10.11. Theoretical simulation of coherent transients in the intermediate field regime. Probability amplitude represented in the complex plane (the unity circle is the absolute limit) [47].

Experiments have been performed with pump and probe laser pulses having the same diameter. Therefore, the response corresponding to different intensities (from weak field to intermediate field regime) associated with various positions in the transverse profiles must be averaged. Figure 10.12 shows simulations corresponding to a range of laser intensities (from the weak field to the

intermediate field regime) together with an experimental result and the theoretical fit averaged over these various intensities. The agreement is excellent.
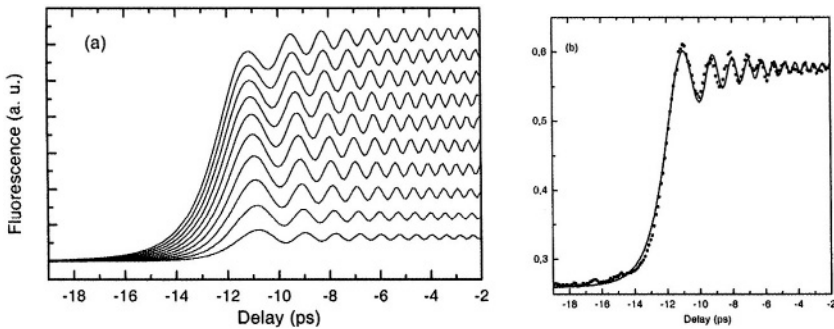
Figure 10.12. (a) Theoretical simulation of coherent transients in the intermediate field regime for various intensities. (b) Experimental result together with averaged simulation [47].

3.7 Reconstruction of Wave Function and Laser Pulse from Coherent Transients

The high sensitivity of coherent transients to slight modifications of the laser pulse opens possibilities to use CT measurements as a characterization of the laser pulse. In a simple approach, if the general shape of the laser pulse is known and only few parameters need to be determined (such as the step position or height as in Sect. 3.4) one can use a simple adjustment of these parameters to fit the experimental curve with the predicted one. However, one would like to establish a general method able to determine any pulse shape. Using the CT needs to have a dominant quadratic spectral phase. It can be added to the pulse if necessary. One difficulty resides in the fact that only the part of the pulse after resonance leads to oscillations which can be used to determine the shape. Another difficulty is that the measured quantity is related to the probability whereas the relevant quantity proportional to the integral of the laser electric field is the probability amplitude which is not directly measured.

These difficulties can be overcome by combining several measurements. In order to observe oscillations over the whole pulse duration, the excited state must be initially populated so that interferences are present from the beginning until the end. This is achieved with a sequence of two pulses with a well defined phase relationship. These can be obtained either with a Michelson-type interferometer [18]or with a pulse shaper. The first pulse is short (this constraint is in fact not necessary, provided that the pulse splitting is larger than their total duration) and the second pulse is strongly chirped in order to exhibit the CT. The first part of the second pulse (before resonance) produces interferences with the

population excited by the first pulse as can be observed on Fig. 10.13. This scheme provides interferences over the whole duration of the second pulse. If $a_e^{(k)}(t)$ is the population amplitude excited by pulse k, the total population at time t during the second pulse is given by

$$P_e(t) = \left| a_e^{(1)}(+\infty) + a_e^{(2)}(t) \right|^2$$

$$= \left| a_e^{(1)}(+\infty) \right|^2 + 2\text{Re}\left(a_e^{(1)}(+\infty) a_e^{(2)}(t)^* \right) + \left| a_e^{(2)}(t) \right|^2. \qquad (10.10)$$

The last two contributions in $P_e(t)$ depend on t and on the second pulse. For a second pulse smaller than the first one, the cross term is dominant in Eq. 10.10 so that the response is linear with respect to the second pulse. However, this measurement is incomplete since it provides only $\text{Re}\left(a_e^{(1)}(+\infty) a_e^{(2)}(t)^* \right)$. This can be supplemented with a second measurement in which the second pulse is in quadrature (phase-shifted by $\theta = \pi/2$ with respect to the first measurement). This provides therefore the complementary part $\text{Im}\left(a_e^{(1)}(+\infty) a_e^{(2)}(t)^* \right)$ [48]. Combining the results from these two scans allows one to extract the contribution from the second pulse $a_e^{(2)}(t)$ even when the intensities are of comparable magnitude (through the solution of a nonlinear equation).
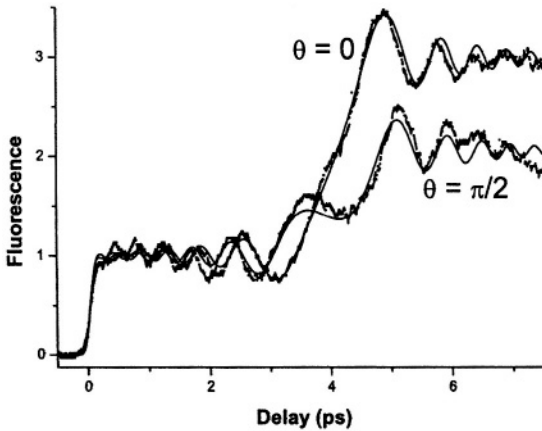
Figure 10.13. Coherent transients produced by a set of two pulses [48]. The first pulse is FT limited and the second is strongly chirped ($\phi'' = 2.\,10^5\,\text{fs}^2$). The two data sets correspond to a relative phase of 0 and $\pi/2$, respectively, as indicated. Solid lines are theoretical fits.

The experiment is based on the same scheme as depicted in Fig. 10.4, but without the grating pairs. The high resolution pulse shaper is used to generate the two pulses: the first pulse is FT limited and the second is chirped with
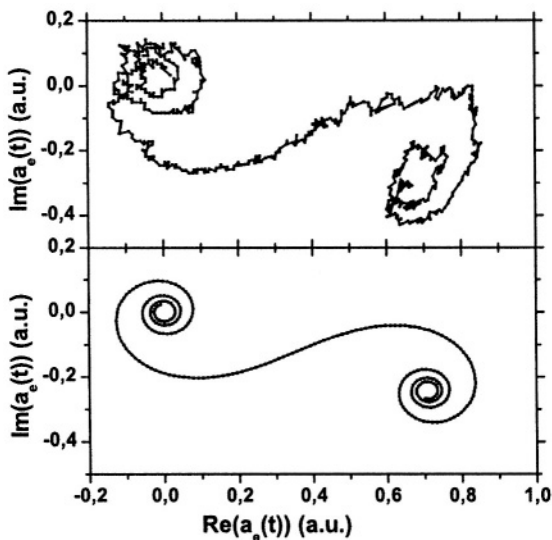
Figure 10.14. Reconstructed probability amplitude $a_e^{(2)}(t)$ deduced from the combination of the two measurements presented in Fig. 10.13 [48]. The Cornu spiral appears clearly. Top: experiment; bottom: theory.

$\phi'' = 2.10^5 \, \text{fs}^2$ and delayed by $\phi' = 4 \, \text{ps}$. The complex transmission $H_\theta(\omega)$ applied to the pulse shaper is therefore

$$H_\theta(\omega) = 1 + \exp\left[i\left(\theta + \phi'(\omega - \omega_l) + \phi''(\omega - \omega_l)^2/2,\right)\right] \qquad (10.11)$$

with $\theta = 0$. A second recording is performed with a phase shift $\theta = \pi/2$ applied to the second pulse. Figure 10.13 shows a preliminary experimental example of an application of this scheme. The reconstructed excited state probability amplitude $a_e(t)$ resulting from the second pulse is plotted in the complex plane in Fig. 10.14 (top). The agreement with the theoretical expectation (Fig. 10.14 bottom) is very good for a preliminary experiment.

4. CONTROL OF TWO-PHOTON TRANSITIONS - QUANTUM LADDER CLIMBING

Two-photon transitions represent the lowest-order nonlinear interaction and they are thus chosen as an illustration of some control schemes. In particular quantum interferences between the various paths leading to the same final state are allowed [49, 50]. These schemes have been well studied in atoms to understand several possibilities of controlling these interferences [51–53].

Generally, high optical intensity is required for efficient multiphoton excitation of the quantum systems to the excited states [54]. In some situations, however, lower-intensity, chirped or shaped pulses can provide efficient transfer of population in atoms [51–53]or molecules [55, 34].

For two-photon transitions two cases are easily distinguishable depending on whether intermediate states are close to resonance [9]or not [8, 22]. These two cases will be considered in the next two subsections. Let us note that in the case of non-resonant intermediate states, two-photon transitions and *a fortiori* multiphoton transitions can be reached by many routes through a continuum of virtual levels. Consider the resonant interaction of a weak ultrashort pulse with a two-level atom. Let $|g\rangle$ and $|e\rangle$ (with energies E_g and E_e) be the ground and excited states, respectively (see Fig. 10.15).
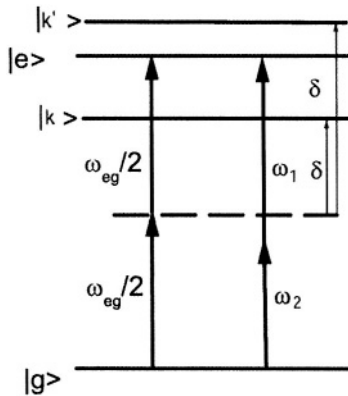
Figure 10.15.   Energy-level diagram of a two-photon absorption with non-resonant intermediate state(s).

The duration of the excitation pulse is assumed to be much shorter than the lifetime of the excited states involved. Assuming the atom is initially in the ground state, and that the pulse is not resonant with any one-photon transition, it may still induce two-photon transitions. Second-order time-dependent perturbation theory leads to the general expression

$$a_e(+\infty) = -\frac{1}{\hbar^2} \sum_k \mu_{ek}\mu_{kg} \int_{-\infty}^{+\infty} dt\, E(t)e^{i\omega_{ek}t} \int_{-\infty}^{t} dt'\, E(t')e^{i\omega_{kg}t'} \quad (10.12)$$

where μ_{kg} (respectively μ_{ek}) is the dipole moment matrix element $|g\rangle \longrightarrow |k\rangle$ (respectively $|k\rangle \longrightarrow |e\rangle$), and $\omega_{ij} = \omega_i - \omega_j$. The summation is performed over all possible intermediate states of the unperturbed atom. Most standard treatments of two-photon transitions assume continuous excitations, and the

integration is performed explicitly. In the case of short-pulse excitation, it is instructive to examine first the summation over the intermediate levels. At that point, one has to distinguish the case where these are close (see Sect. 4.1) or far from resonance (see Sect. 4.2). The excitation pulse $E(t)$ is produced by a short pulse containing a band of frequencies around a central frequency ω_0. The Fourier transform of $E(t)$ is $\tilde{E}(\omega) = \mathcal{E}(\omega)exp[i\phi(\omega)]$, where $\mathcal{E}(\omega)$ and $\phi(\omega)$ are the spectral amplitude and spectral phase, respectively.

4.1   Weak-Field Two-Photon Transition with a Non-Resonant Intermediate State

In this section we assume that all the intermediate states are far from resonance (Fig. 10.15). Then the contributions of all intermediate levels add coherently only for a short duration and therefore the integral over t' in Eq. (10.12) reduces only to the contribution $t = t'$ so that the probability of exciting level $|e\rangle$ is simply

$$P_e^{(2)} \propto \left| \int_{-\infty}^{+\infty} dt E^2(t) e^{i\omega_{eg}t} \right|^2 . \tag{10.13}$$

$E^2(t)$ can be decomposed into three bands of frequencies. Two frequencies around $\pm 2\omega_0$, with $2\omega_0 \simeq \omega_{eg}$, correspond to two-photon absorption (TPA) and two-photon emission (TPE). The last frequency band near $\omega \doteq 0$ corresponds to Raman transitions. Then one can rewrite the expression of the two-photon absorption in the case of intermediate levels far from resonance and in the frequency domain:

$$P_e^{(2)} \propto \left| \int_{-\infty}^{+\infty} d\omega \tilde{E}(\frac{\omega_{eg}}{2} + \omega) \tilde{E}(\frac{\omega_{eg}}{2} - \omega) \right|^2 \tag{10.14a}$$

$$= \left| \int_{-\infty}^{+\infty} d\omega \mathcal{E}(\frac{\omega_{eg}}{2} + \omega) \mathcal{E}(\frac{\omega_{eg}}{2} - \omega) \times e^{[i\{\phi(\frac{\omega_{eg}}{2}+\omega)+\phi(\frac{\omega_{eg}}{2}-\omega)\}]} \right|^2 \tag{10.14b}$$

Note that, in contrast to a single-photon transition, all frequency components of the pulse contribute to the transition. More precisely, each pair of photons of frequencies (ω_i, ω_j) contained in the pulse spectrum which satisfy $\omega_{eg} = \omega_i + \omega_j$ contribute to the TPA. The two-photon transition probability can therefore be controlled by tailoring the spectral phase of a single pulse. Examining Eq. 10.14b, it is easy to verify that the flat phase $(\phi(\omega) = 0)$ maximizes the TPA. One well-known example concerns the second harmonic generation in a nonlinear crystal: the pulse which maximizes such a signal is the transform-limited pulse [56]. Since pulse shaping cannot help improve the TPA efficiency, it can be

used to reduce it by introducing destructive interferences between the various paths involved. This approach, besides its fundamental interest, can in practice be a better alternative than simply reducing the laser intensity, since it can allow a particular transition to be controlled selectively.

Silberberg et al. have demonstrated such a control by tailoring the pulse spectral phase [8]. A phase-only 128 pixels SLM pulse shaper was used. This does not affect the power spectrum. The experiment was performed on the $6S_{1/2} - 8S_{1/2}$ two-photon transition of atomic cesium at a wavelength of 411 nm induced by femtosecond pulses centered at 822 nm. Each of the excited atoms decays spontaneously to the ground level through the 7P level. So the TPA is directly proportional to the 7P-6S fluorescence which is monitored. Two analytic waveforms are applied to demonstrate this coherent control, as described below. Concentrating on Eq. 10.14b, one can note that for any antisymmetric spectral phase distribution around the two-photon transition frequency $\omega_{eg}/2$ such that $\phi(\omega_{eg}/2 + \omega) = -\phi(\omega_{eg}/2 - \omega)$ the phase terms vanishes. Then the TPA is independent of the spectral phase and the transition probability in this case is equal to the one obtained with a transform limited pulse, despite this antisymmetric phase significantly affecting the temporal pulse shape. In fact, the pulse can be spread in time into a very small amplitude without affecting the TPA.

Although antisymmetric phase distributions do not affect the two-photon transition probability, other phase distributions can be tailored to cancel the two-photon transition probability. Such so-called dark pulses, which could come in various temporal shapes, induce no net two-photon transitions, and are the appropriate coherent superposition of optical frequencies that cancels TPA. They are analogous to dark states, which are coherent superpositions of quantum states that do not absorb resonant light [57, 18, 58]. It is also clear from the expression $\phi(\omega_{eg}/2 + \omega) + \phi(\omega_{eg}/2 - \omega)$ in Eq. 10.14b that only the symmetric part of the phase function $\phi(\omega)$ has an effect on TPA.

In one example, a spectral phase-only filter $H(\omega) = \exp(i[\alpha \cos(\beta\omega + \theta)])$ is applied. α, β and θ are the modulation depth, frequency and phase, respectively. For $\theta = 0$, the function is symmetric and should give the better shaping sensitivity. Indeed, as displayed on Fig. 10.16a, varying the modulation depth provides several values for which TPA vanishes completely. Thus, a carefully chosen modulation depth ($\alpha \approx 1.2$ for the first minimum) can lead to the appropriate coherent superposition of optical frequencies which cancels TPA. Varying the value of θ over the interval of π allows one to change continuously from a symmetric to an antisymmetric phase function. Figure 10.16b shows clearly the modulation corresponding to maximizing or cancelling the TPA. Note that by simply shifting the phase modulation filter across the spectrum, affecting
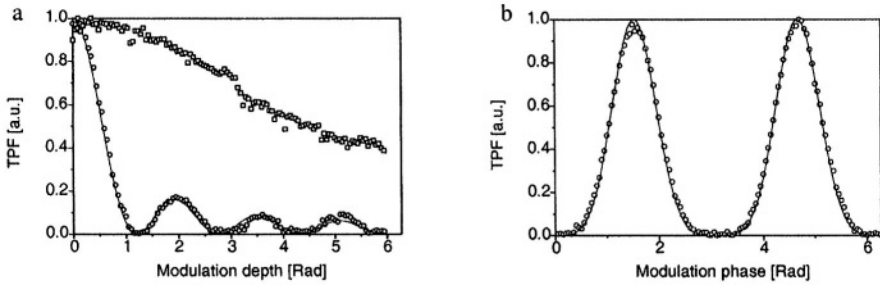
Figure 10.16. (a) Two-photon absorption for a totally symmetric $\phi(\omega) = \alpha \cos(\beta\omega)$ (circles) and totally antisymmetric $\phi(\omega) = \alpha \sin(\beta\omega)$ (squares) phase function. (b) Experimental (circles) and calculated (line) fluorescence signal for phase distribution equal to $\alpha \cos(\beta\omega + \theta)$ as a function of the modulation phase θ for $\alpha = 1.2$ (first zero of the function, see (a)) and $\beta = 220$ fs (reproduced from [8]).

neither the total power nor the power spectrum of the pulse, the fluorescence yield was controlled to better than 1 part in 200. Similar results were obtained for the Na $(3s \rightarrow 5s)$ transition [10]. The advantage of using such a modulated phase function is to provide the capability of achieving maximum efficiency for certain transitions together with a negligible efficiency for others [59].

A phase-modulated spectrum corresponds in the time domain to a sequence of pulses with intensities given by a Bessel function. This situation has some relationship with experiments based on a sequence of two identical pulses produced by a Michelson interferometer [60–68]. In this case, varying the delay between the pulses over a small interval (comparable to the optical period) is equivalent to shifting the modulated spectrum (note however that here the intensity is modulated). This changes the interferences from constructive to destructive [18]. TPA control was indeed achieved with this technique [49, 50].

A spectral π-step applied at resonance provides another simple antisymmetric shape for which the TPA rate is unchanged. Shifting the position of this π-step changes progressively the balance between negative and positive contributions in Eq. 10.14b [22]. For a particular position, they counteract each other exactly and the TPA rate vanishes. Figure 10.17 shows the TPA as a function of the position δ of the π-step. A dark pulse is created for two particular positions, $\delta = \pm 0.31 \, \Delta\omega$.

These general principles hold for multiphoton absorption including other multiphoton processes with application to gas-phase molecules [59]or solid state systems [69], to multiphoton microscopy [70]and Coherent Anti-Stokes Raman Scattering [71].
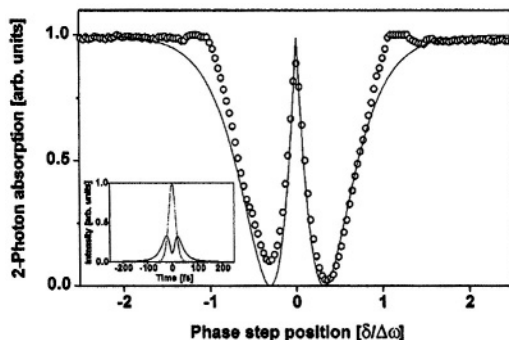
Figure 10.17. Experimental (circles) and calculated results (solid) for two-photon transitions in Cs excited by a π spectral phase step, as a function of the normalized step position $\delta/\Delta\omega$, with $\Delta\omega$ corresponding to $\Delta\lambda = 23$ nm. Calculated results were obtained assuming transform limited 31 fs $sech^2$ intensity input pulses. Inset: calculated temporal intensity distribution of the dark pulse corresponding to $\delta/\Delta\omega = 0.31$ (solid) and the transform-limited input pulse having the same power spectrum (dashed) (reproduced from [22]).

4.2   Weak-Field Two-Photon Transition with a Resonant Intermediate State

The efficiency of a multiphoton process is greatly enhanced when the intermediate state is nearly resonant [72, 73]. This is in fact easier to achieve with ultrashort pulses, thanks to their broad spectrum [74]. This can be the case with some atomic or molecular excited electronic states. This is indeed intrinsically the case for vibrational levels in a molecule since they are nearly equidistant. For instance, exciting molecules towards a specific highly excited vibrational state can be efficiently achieved with a multiphoton transition using photons tuned close to the vibrational frequency [55], whereas direct single-photon excitation is highly unfavored by poor Franck-Condon factors. Therefore, stepwise excitation up the vibrational ladder is required. Several experiments have been performed using far-infrared lasers ([75–78]). However, due to the complexity of molecular systems combined with the experimental difficulties inherent in the excitation and characterization of infrared transitions, it is instructive to study extensively a theoretically and experimentally simpler system, an anharmonic quantum ladder (with two steps) in an alkali atom (Rb or Na) [52, 35, 74, 79, 80].

In the presence of a resonant intermediate state $|i\rangle$ the sequential paths opened by the presence of the intermediate levels have a crucial role. Figure 10.18 presents the level scheme. The sequential transition frequencies are ω_{ig} and ω_{ei}.
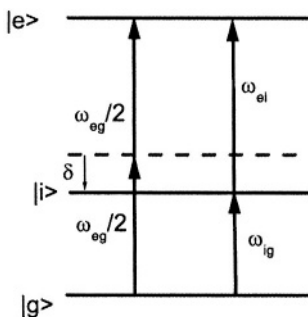
Figure 10.18. Energy-level diagram of a two-photon absorption with near-resonant intermediate state.

The carrier frequency ω_0 of the weak ultrashort excitation pulse is assumed to be on two-photon resonance ($\omega_0 = \omega_{eg}/2$). The one-photon detuning $\delta = \omega_{ig} - \omega_0$ is smaller than or comparable to the spectral bandwidth of the laser. The general expression (Eq. 10.12) of the excited-state amplitude due to a two-photon transition can be written, in the case of an intermediate resonant level $|i\rangle$, as [9]

$$a_e = -\frac{\mu_{ei}\mu_{ig}}{\hbar^2}\left[\frac{1}{2}\tilde{E}(\omega_{ig})\tilde{E}(\omega_{ei})\right.$$
$$\left. + \frac{i}{2\pi}\wp\int_{-\infty}^{+\infty}d\omega\frac{\tilde{E}(\omega)\tilde{E}(\omega_{eg}-\omega)}{\omega-\omega_{ig}}\right], \qquad (10.15)$$

where μ_{ei} and μ_{ig} are the dipole moment matrix elements and $\wp$ is the principal Cauchy value. Silberberg et al. [9] assigned the first term in Eq. 10.15 to the resonant contribution through the intermediate state and the second term to the off-resonance contributions. However, this second term includes contributions from the whole spectrum, including also the one-photon resonance ($\omega = \omega_{ig}$) with a significant weight. In this case it is possible to enhance the transition probability by shaping the excitation pulse. Two approaches have been demonstrated experimentally as well as theoretically and are described in the next sections.

Simply shaped laser pulses.   The first term in Eq. 10.15 is phase-shifted by $\pi/2$ with respect to the second term. Also the spectral components below and above the resonance excite the system in-phase and π out-of-phase, respectively. So a transform-limited pulse induces destructive quantum interferences between the frequency pairs in which the first exciting photon is red detuned and those in which it is blue detuned. Silberberg *et* al. utilize these phase relations to

enhance the nonlinear response [9]. The experiments have been performed on the $(5S_{1/2} \rightarrow 5P_{1/2} \rightarrow 5D_{3/2})$ ladder in Rb.

In a first spectacular example, a highly counter-intuitive result is obtained: blocking parts of the spectrum of the exciting pulse (corresponding to destructive interferences), which reduces the power by 71%, leads to an enhancement of the TPA rate by a factor two. In a second example, applying a phase shift of $\pi/2$ to a spectral window inverts the sign of $\tilde{E}(\omega)\tilde{E}(\omega_{eg} - \omega)$ in order to compensate for the sign change at resonance. This maximizes the enhancement of the TPA rate.
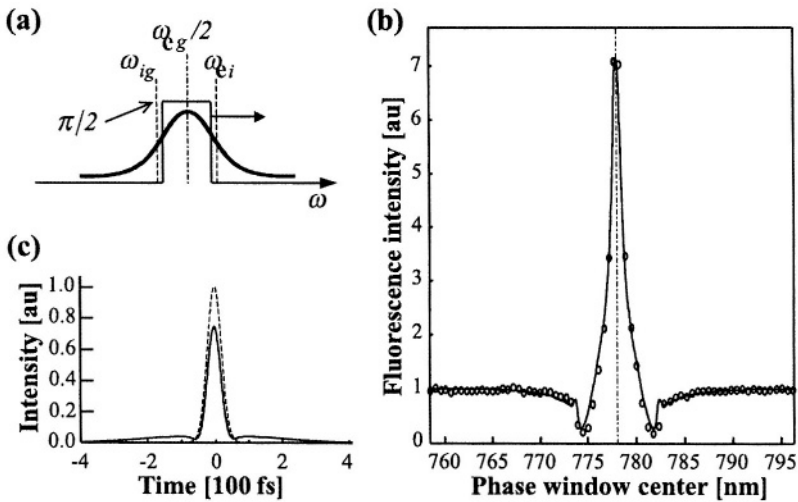
Figure 10.19. Experimental and calculated results for enhancement of resonant TPA in Rb by scanning a 4 nm $\pi/2$ phase window over the spectrum of the pulse. (a) The applied phase mask at its optimal position, centered on $\omega_{eg}/2$, with its leading and trailing edges close to the resonance frequencies. (b) Experimental (circles) and calculated (line) normalized fluorescence intensity as a function of the spectral position of the phase window. A maximum enhancement factor of seven occurred when the window was centered on $\omega_{eg}/2$, (778.1 nm, dashed line), as shown in (a), performing the desired sign inversion about ω_{ig}. (c) Calculated temporal intensities of the optimal shaped pulse (solid curve) and the initial transform limited pulse (dashed curve), showing a 26% reduction of the peak intensity due to the broadening of the pulse (reproduced from [9]).

Figure 10.19 shows the spectacular enhancement of the TPA. Also, in this experiment, the fluorescence rate from the 6P state is directly proportional to the TPA and is monitored as a function of the position of the time window. Maximum enhancement by a factor of seven is achieved when the phase window is centered on ω_{eg} and has a width of δ. These results confirm that in this case all photon pairs interfere constructively, and thus the transition probability is maximized.

Chirped excitation of a three-level quantum ladder. Another simple pulse shape is obtained by simply chirping the pulse with a quadratic spectral phase. This provides a symmetric phase function which is expected to induce significant control capabilities. This approach offers several advantages due to the simplicity of the theoretical treatment and of the experimental set-up. It has therefore been widely studied, particularly in the case of quantum ladder systems.

In the particular case of a chirped Gaussian field given by Eq. 10.1, expression 10.15 can be written using the complex error function:

$$a_e = -\frac{\mu_{ek}\mu_{kg}}{2\hbar^2}\tilde{E}(\omega_{kg})\tilde{E}(\omega_{ek})[1 - \text{erf}(i\frac{\delta}{\sqrt{2\gamma}})], \qquad (10.16)$$

where $1/\gamma = T_0^2 - 2i\phi''$. The error function oscillates as a function of its argument. However, this exact expression does not provide any direct physical interpretation.

It has been shown that for large chirps ($|\phi''| \gg 1/T_0^2$), Eq. 10.15 can be split into two distinct contributions [74, 80]: one is due to the direct two-photon excitation while the second is due to the sequential process. Two frequency ranges provide major contributions to the second term in Eq. 10.15, around ω_0 and ω_{ig}, respectively. The first results from the stationary phase approximation, and gives the direct two-photon transition amplitude. It corresponds to a small range of frequencies (width $\simeq 1/\sqrt{|\phi''|}$) centered on ω_0 that can fulfil the two-photon resonance condition. The second is due to the pole in the principal Cauchy value, and provides a second significant contribution, identical to the sequential contribution already present in Eq.10.15. Finally, one obtains the probability amplitude $a_e = a_s + a_d$, with

$$a_s = -\frac{\mu_{ei}\mu_{ig}}{\hbar^2}\tilde{E}(\omega_{ei})\tilde{E}(\omega_{ig})\frac{1 - \sin(\phi''\delta)}{2}, \qquad (10.17a)$$

$$a_d = -\frac{\mu_{ei}\mu_{ig}}{\hbar^2}\frac{\tilde{E}^2(\omega_0)}{\delta\sqrt{2\pi T_0 T_p}}e^{-i(\theta+\pi)/2}, \qquad (10.17b)$$

where a_s and a_d are the sequential and direct contributions, respectively, and $\tan\theta = -2\phi''/T_0^2$.

Note that a_d corresponds exactly to the non-resonant excited state amplitude [9] with a far off-resonance intermediate state. $|a_d|^2$ is plotted in Fig. 10.20 (dash-dotted). It decreases as $\simeq 1/T_p$ or $1/\sqrt{1 + (2\phi''/T_0^2)^2}$ and has a FWHM of $T_0^2\sqrt{3}$. The sequential contribution probability $|a_s|^2$ (Eq. 10.17a) is a step-like function (dashed line in Fig. 10.20) depending only on the power spectrum
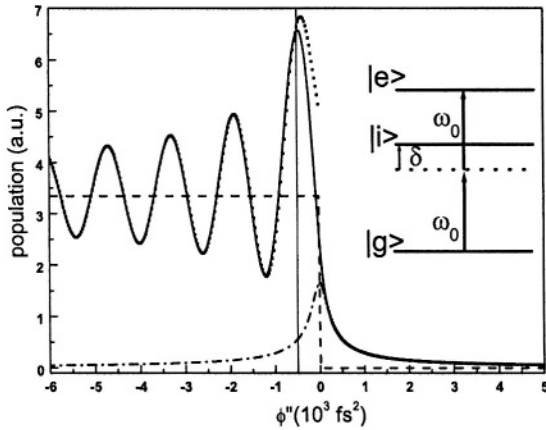
Figure 10.20. Population of the excited state as a function of chirp for $\delta > 0$. Dashed line: sequential contribution $|a_s|^2$; dash-dotted line: direct contribution $|a_d|^2$. Total two-photon contribution $|a_e|^2$: exact expression using Eq. 10.15 (solid line) and approximate expression using Eqs. 10.17a–10.17b (squares). Inset: three-level system. ω_0 is the carrier frequency of the laser and δ the detuning. The vertical line corresponds to $\phi'' = -3\pi/4\delta^2$ [74, 80].

at each one-photon transition. The sharp transition around zero chirp corresponds to a change in the frequency order. Indeed, the sequential transition is only possible if excitation of the intermediate state $|i\rangle$ precedes excitation from $|i\rangle$ to $|e\rangle$ (ω_{ig} before ω_{ei}). A chirp-dependent phase factor $e^{i\phi''\delta^2}$, arising from the electric field (see Eq. 10.1) is contained in the sequential term (Eq. 10.17a). This phase difference accumulated between both paths leads to strong interferences for the total population $|a_e|^2$ as a function of the quadratic phase dispersion ϕ'' as shown in Fig. 10.20 (solid line). Depending on the sign of the one-photon detuning δ, the interferences occur for positive or negative chirp. The period of the corresponding oscillations is thus equal to $\phi''_{2\pi} = 2\pi/\delta^2$. In Fig. 10.20 the analytic approximation of $|a_e|^2 = |a_s + a_d|^2$ (Eqs. 10.17a–10.17b) is plotted with squares (for $\delta > 0$ and $\delta/\delta\omega_L \simeq 0.5$). For $\phi'' > 0$, $|a_e|^2$ has the same behavior as $|a_d|^2$. It corresponds to the population transferred by two photons with the same energy $\hbar\omega_{eg}/2$. On the other hand, for $\phi'' < 0$ the population oscillates strongly around $|a_s|^2$. The first maximum is reached when both amplitudes have nearly the same phase factors, i.e., for $\phi'' \simeq -3\pi/4\delta^2$ (this value is only approximate since the variation of the magnitude of a_d is not taken into account and since this is at the limit of validity of the approximation made to derive Eqs. 10.17a–10.17b).
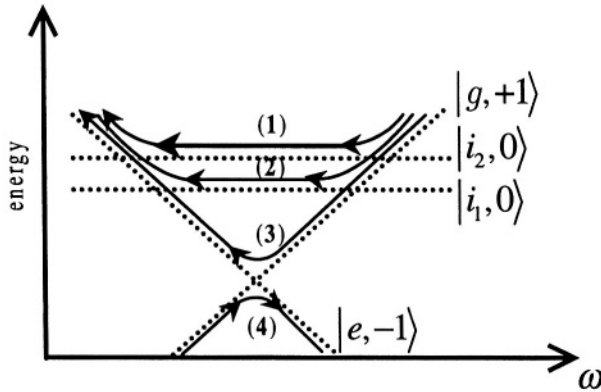
Figure 10.21. Dressed-state picture of a ladder system with two intermediate states. The arrows indicate the different paths.

These interferences were first observed experimentally by Noordam et al. in Rb on the $(5S_{1/2} \rightarrow 5P_{3/2} \rightarrow 5D_{3/2,5/2})$ ladder at 780 nm [52, 79]. A pair of gratings is used to chirp the pulse. The frequency-doubled output of a Q-switched Nd:YAG pulse is used to post-ionize the population from the 5d state. The measured total photoelectron yield is detected and monitored as a function of the chirp rate for several fluences of the excitation laser pulse. The effect of high fluence will be explained below in Sect. 4.3. Only Fig. 10.23(c) corresponds to the low fluence studied here. The step around zero chirp as well as the oscillations for positive chirp are clearly visible, as predicted by theory. The small contrast as compared to the prediction in Fig. 10.20 is due to a smaller value of $\delta/\delta\omega_L$ ($\simeq 0.25$).

Chirped excitation of a quantum ladder with two intermediate states.
   Adding new sequential paths leads to multiple interferences and increases the possibilities of improving the interference contrast and the final excitation probability. For instance, this is obtained when the different detunings $\delta_k = \omega_{i_k g} - \omega_0$ are kept close together. The direct path is not qualitatively changed, only $\mu_{ei}\mu_{ig}/\delta$ should be replaced by $\sum_k \mu_{ei_k}\mu_{i_kg}/\delta_k$.
   In the simplest case of two intermediate states, interferences occur between three paths as can easily be seen from the dressed-state picture. The dressed atomic states are $|a, n\rangle$, where $|a\rangle$ is an atomic state and $|n\rangle$ the photon number state, as shown on Fig. 10.21. A given manifold of neighboring energy levels consists of $|g, n+1\rangle$, $|i_k, n\rangle$, and $|e, n-1\rangle$. The dotted lines represent the diabatic states, and the solid lines the quantum paths (taking into account the atom-field coupling).

For a positively (respectively negatively) chirped pulse, the temporal evolution of the system corresponds to a traversal of the diagram from left to right (respectively from right to left). At each crossing, the wave-packet splits into two components of relative magnitude depending on the coupling strength. Here, in the weak field regime, the major component remains on the diabatic curve. The two sequential paths (1) and (2) correspond to two successive one-photon transitions. They can be followed only for negative chirp (for $\delta > 0$). Paths (3) and (4) are the direct two-photon transitions for negative and positive chirp, respectively. Note that for small enough chirps ($|\phi''| \leq T_0^2$), all the frequencies can be considered to be present simultaneously, and the dressed-state picture is not appropriate to explain the observations. Then the distinction between the sequential and direct two-photon processes is not relevant.

As qualitatively explained by Noordam et al. [79], the relative phase between the paths is given by the product of the chirp rate by the enclosed area defined by these paths in the dressed-state diagram. This leads to oscillations of the final population as a function of the chirp. Here, in the case of two intermediate states, the oscillations result from the beats of three interference periods: two rapid oscillations due to the interferences of sequential paths (1) and (2) with the direct path (3), and one slow oscillation corresponding to interferences between path (1) and (2) (in the case of a splitting small compared to the one-photon detunings δ_k). The probability of each path depends on the strength of the coupling at the crossing which is proportional to the laser electric field amplitude and the respective dipole moments. Since these paths have similar strengths, the interferences between the two sequential paths are highly contrasted. Moreover, the amplitude of these interferences do not depend on the chirp whereas the amplitude of the sequential-direct interference decreases with $|\phi''|$. Finally, the sequential-sequential interferences depend critically on the value of $\delta_k/\delta\omega_L$ as shown in Noordam's experiment.

In order to illustrate this scheme involving two sequential paths, an experiment has been performed on the ($3S_{1/2} \rightarrow 3P_{1/2,3/2} \rightarrow 5S_{1/2}$) and ($3S_{1/2} \rightarrow 3P_{1/2,3/2} \rightarrow 4D_{3/2,5/2}$) ladders in Na [74].

The output of a home-made non-collinear optical parametric amplifier (NcOPA) [81], stretched by the combination of a glass rod and a pair of gratings, is used to excite a vapor of sodium atoms. The 4p-3s fluorescence being proportional to the TPA rate is monitored as a function of the chirp. The signal obtained is plotted in Fig. 10.22. Strong oscillations with two periods are clearly visible and in perfect agreement with theory. In this case, $\delta/\delta\omega_L \simeq 0.5$ which leads to a high contrast of 80% as shown in Fig. 10.22. A FT limited pulse ($\phi'' = 0$) has an efficiency about 1/3 of the maximum reached for $\phi'' \simeq -3\pi/4\delta^2$. Other
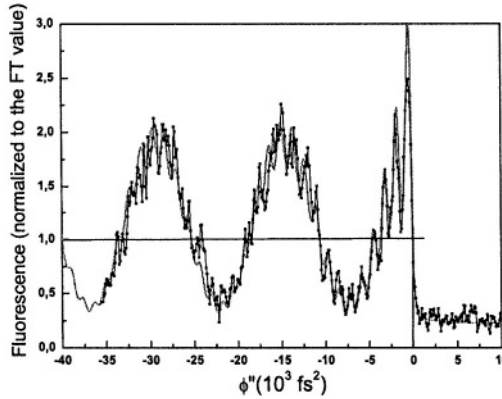
Figure 10.22. Excited 5s population (measured by the 4p-3s fluorescence) as a function of chirp in the 3s - 3p - 5s ladder. Black line and squares: experiment; grey line: theory. The large slow oscillation is due to sequential - sequential interference whereas the rapid oscillations of decreasing amplitude are due to direct path - sequential path interferences [74, 80].

experiments have been performed with more than one final state. The role of the spectral cubic phase has also been studied in detail [80].

Finally, the slow oscillations can also be regarded as resulting from a wave-packet oscillating between a bright and a dark state. This wave-packet, which is a coherent superposition of the two intermediate states, is created by the first sequential transition at $t_i = (\delta_1 + \delta_2)\phi''/2$ and detected when the laser frequency reaches the second sequential transition at $t_f = -(\delta_1 + \delta_2)\phi''/2$. The accumulated relative phase between the two levels is $(t_f - t_i)\Delta E/\hbar = (t_f - t_i)(\delta_2 - \delta_1) = (\delta_2^2 - \delta_1^2)\phi''$, as calculated above. The dark state $|L = 1, M_L = \pm 1\rangle$ cannot be excited towards the final state without any change of the laser polarization during the pulse. This explains the much higher contrast observed here compared to previous spin precession studies [58, 82].

4.3 Adiabatic Excitation of a Quantum Ladder

The previous sections described the weak field regime interaction in which strongly contrasted interferences were observed. The total rate is proportional to the square of the laser fluence, as expected from a second-order process. Increasing the laser intensity results therefore in an increase of the TPA rate. However, one reaches rapidly the intermediate or strong field regime where new phenomena can be observed. In particular, adiabatic passage can result
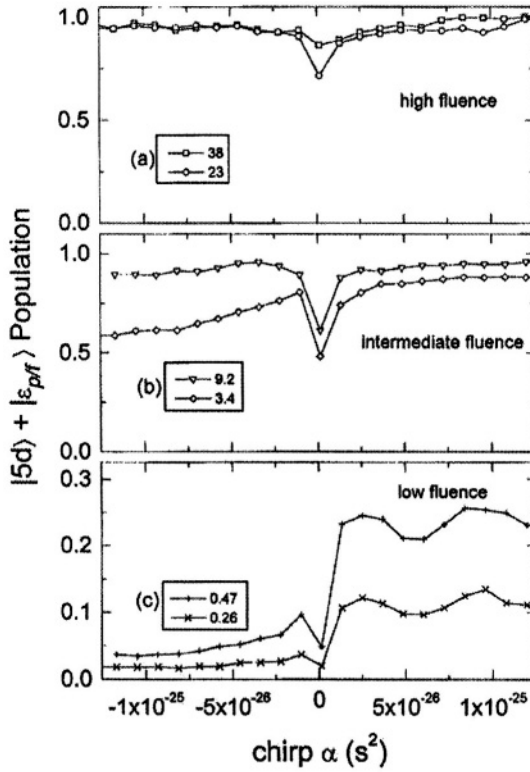
Figure 10.23. Measured total photo-electron yield as a function of chirp at several different fluences: (a) 38 and $23mJ/cm^2$, (b) 9.2 and $3.4mJ/cm^2$, and (c) 0.47 and $0.26mJ/cm^2$. All the data sets have been scaled vertically by a single parameter such that the largest signal corresponds to 100% population transfer to the upper state. For intermediate fluence, a FT limited pulse ($\phi'' = 0$) has the weakest efficiency. Rabi oscillations are then less efficient than sequential adiabatic transfer (positive chirp) and even less than two-photon adiabatic transfer (negative chirp) (reproduced from [35]).

in an almost total transfer, with a good robustness with respect to variation of parameters such as the laser intensity compared to the Rabi oscillations [51,83].

Using the same anharmonic quantum ladder in Rb (see above), Noordam et al. obtained the signature of the adiabatic passage by increasing the fluence as shown in Fig. 10.23 [35]. In the low-intensity limit efficient transfers occurs only for intuitively chirped pulses, as shown previously. At intermediate fluence, population is efficiently transferred for both the intuitive and the counter-intuitive chirp. The quantum interferences disappear progressively. For the intuitive red-to-blue chirp the adiabaticity condition is independent of chirp. At very high fluences, essentially full population transfer is achieved with

either direction of chirped pulses. Note that, in all cases, the efficiency of transfer is significantly higher for chirped pulses than for Fourier-transform-limited pulses. In this last case, because of Rabi oscillations with different pulse areas for different transverse positions in the laser beam and for different pulses, the average population is 0.5.

5.   CONCLUSION

Many fascinating issues have been addressed in this chapter. Some of the processes analyzed in detail here are likely to be involved in excitation of complex systems with shaped pulses in a closed-loop scheme [5]. These mechanisms may therefore be useful in analyzing the way the optimal shapes act on the system.

Many other examples of simple systems excited with predefined shaped laser pulses have been demonstrated recently. A sequence of two chirped pulses was used to combine the advantage of wave-packet interferences and chirped pulses allowing a precise determination of the excitation time [84]. In this case, constructive or destructive interferences allow one to select the desired state to be excited. Moreover, the rate of chirp can be used to choose the excitation time. Rovibrational wave-packets in Li_2 have been, for instance, time-shifted [85] or tailored to use interferences in order to maximize their ionization efficiency at a chosen time [26]. Pulse shaping has also been used to store quantum phases in atomic Rydberg states [13, 86] or in molecules [87]. The realization of an AND gate in Li_2 has also been demonstrated [88].

Chirp effects in ladder climbing of molecular electronic states were demonstrated in Na_2 [89]. In the strong field, spectacular schemes based on adiabatic transfer would lead to an apparent violation of the Franck-Condon principle [90].

Strong field effects can also lead to highly nonlinear processes such as in the molecular centrifuge [91] in which a succession of hundreds of rotational Raman transitions are followed adiabatically with chirped pulses [92] until reaching dissociation of the molecule.

Finally, an unexpected application of two-photon ladder climbing is the possibility of creating a polychromatic artificial star with mesospheric sodium [93]. Several approaches based on sequences of π-pulses have been proposed [94], but schemes such as chirped pulse excitation described in Sect. 4.2 could be easier to realize.

Acknowledgments

participation in parts of the experiments performed in our group and described here; Prof. Y. Silberberg and B. Noordam for letting us reproduce part of their results; and C. Meier for critical reading of the manuscript. Part of the work reviewed here has been financially supported through the European Union Marie Curie networks (contract HPRN-CT-1999-00129, COCOMO).

References

1. H. Rabitz, R. de Vivie-Riedle, M. Motzkus and K. Kompa, *Science* **288**, 824 (2000).

2. R. S. Judson and H. Rabitz, *Phys. Rev. Lett.* **68,** 1500 (1992).

3. W. S. Warren, H. Rabitz and M. Dahleh, *Science* **259**, 1581 (1993).

4. L. Zhu, V. D. Kleiman, X. Li, S. P. Lu, K. Trentelman and R. J. Gordon, *Science* **270**, 77 (1995).

5. A. Assion,T. Baumert, M. Bergt,T. Brixner, B. Kiefer, V. Seyfried, M. Strehle andG. Gerber, *Science* **282**, 919(1998).

6. R. J. Levis, G. M. Menkir and H. Rabitz, *Science* **292**, 709 (2001).

7. C. J. Bardeen, V. V. Yakovlev, K. R. Wilson, S. D. Carpenter, P. M. Weber and W. S. Warren, *Chem. Phys. Lett.* **280**,151 (1997).

8. D. Meshulach and Y. Silberberg, *Nature* **396**, 239 (1998).

9. N. Dudovich, B. Dayan, S. H. G. Faeder and Y. Silberberg, *Phys. Rev. Lett.* **86,** 47 (2001).

10. T. Hornung, R. Meier, D. Zeidler, K.-L. Kompa, D. Proch and M. Motzkus, *Appl. Phys. B* **71,** 277 (2000).

11. S. Vajda, A. Bartelt, E-C. Kaposta, T. Leisner, C. Lupulescu, S. Minemoto, P. Rosendo-Francisco and L. Wöste, *Chem. Phys.* **267**, 231 (2001).

12. C. Daniel, J. Full, L. Gonzalez, C. Lupulescu, J. Manz, A. Merli, S. Vajda and L. Wöste, *Science* **299,** 536 (2003).

13. T. C. Weinacht, J. Ahn and P. H. Bucksbaum, *Nature* **397**, 233 (1999).

14. A. P. Heberle, J. J. Baumberg and K. Köhler, *Phys. Rev. Lett.* **75,** 2598 (1995).

15. J. Kunde, B. Baumann, S. Arlt, F. Morier-Genoud, U. Siegner and U. Keller, *J. Opt. Soc. Am. B* **18,** 872(2001).

16. J. L. Herek, W. Wohlleben, R. J. Cogdell, D. Zeidler and M. Motzkus, *Nature* **417**, 533 (2002).

17. A. M. Weiner, *Rev. Sci. Instr.* **71**, 1929 (2000).

18. M. A. Bouchene, V. Blanchet, C. Nicole, N. Melikechi, B. Girard, H. Ruppe, S. Rutz, E. Schreiber and L. Wöste, *Eur. Phys. J. D* **2**, 131 (1998).

19. R. R. Jones, D. W. Schumacher, T. F. Gallagher and P. H. Bucksbaum, *J. Phys. B* **28**, L405 (1995).

20. L. C. Snoek, S. G. Clement, F. J. M. Harren and W. J. van der Zande, *Chem. Phys. Lett.* **258,** 460 (1996).

21. S. Cavalieri, M. Materazzi, R. Eramo, L. Fini and A. Giugni, *Opt. Commun.* **182**,161 (2000).

22. D. Meshulach and Y. Silberberg, *Phys. Rev. A* **60**,1287 (1999).

23. T. Hornung, R. Meier, R. de Vivie-Riedle and M. Motzkus, *Chem. Phys.* **267**, 261 (2001).

24. S. Zamith, J. Degert, S. Stock, B. De Beauvoir, V. Blanchet, M. A. Bouchene and B. Girard, *Phys. Rev. Lett.* **87**, 033001 (2001).

25. H. U. Stauffer, J. B. Ballard, Z. Amitay and S. R. Leone, *J. Chem. Phys.* **116**, 946 (2002); J. B. Ballard, H. U. Stauffer, Z. Amitay and S. R. Leone, *J. Chem. Phys.* **116,** 1350 (2002).

26. J. B. Ballard, H. U. Stauffer, E. Mirowski and S. R. Leone, *Phys. Rev. A* **66,** 043402 (2002).

27. N. Dudovich, D. Oron and Y. Silberberg, *Phys. Rev. Lett.* **88**, 123004 (2002).

28. J. Degert, W. Wohlleben, B. Chatel, M. Motzkus and B. Girard, *Phys. Rev. Lett.* **89**, 203003 (2002).

29. W. Wohlleben, J. Degert, A. Monmayrant, B. Chatel, M. Motzkus and B. Girard, *Appl. Phys. B* (in press).

30. M. A. Dugan, J. X. Tull and W. S. Warren, *J. Opt. Soc. Am. B* **14**, 2348 (1997).

31. E. Zeek, K. Maginnis, S. Backus, U. Russek, M. Murnane, G. Mourou, H. Kapteyn and G. Vdovin, *Opt. Lett.* **24**, 493 (1999).

32. F. Verluise, V. Laude, Z. Cheng, C. Spielmann and P. Tournois, *Opt. Lett.* **25**, 575 (2000).

33. A. Monmayrant and B. Chatel, *Rev. Sci. Instr.* (in press).

34. J. S. Melinger, A. Hariharan, S. R. Gandhi and W. S. Warren, *J. Chem. Phys.* **95**,2210 (1991).

35. D. J. Maas, C. W. Rella, P. Antoine, E. S. Toma and L. D. Noordam, *Phys. Rev. A* **59,** 1374 (1999).

36. A. Abragam, *Principles of Nuclear Magnetism* (Clarendon Press, Oxford, 1961).

37. R. L. Shoemaker and R. G. Brewer, *Phys. Rev. Lett.* **28,** 1430 (1972).

38. B. Macke and P. Glorieux, *Chem. Phys. Lett.* **14,** 85 (1972).

39. J. E. Rothenberg, *IEEE J. Quant. Electronics* **QE-22,** 174 (1986).

40. J. E. Rothenberg and D. Grischkowsky, *J. Opt. Soc. Am. B* **3**, 1235 (1986).

41. B. Broers, L. D. Noordam and H. B. van Linden van den Heuvell, *Phys. Rev. A* **46***,* 2749 (1992).

42. L. Ménager, I. Lorgeré and J. L. Legouet, *Opt. Lett.* **25,** 1316 (2000).

43. G. Stobrawa, M. Hacker, T. Feurer, D. Zeidler, M. Motzkus and F. Reichel, *Appl. Phys. B* **72,** 627 (2001).

44. M. Born and E. Wolf, *Principles of Optics* (Pergamon, Oxford, UK, 1980).

45. G. A. Magel, M. M. Fejer and R. L. Byer, *Appl. Phys. Lett.* **56**, 108 (1990).

46. N. V. Vitanov, *Phys. Rev. A* **59***, 988 (1999).

47. S. Zamith, Thesis, Univ. P. Sabatier (Toulouse), 2001.

48. A. Monmayrant, B. Chatel and B. Girard, *Opt. Commun.,* in preparation (2004).

49. V. Blanchet, C. Nicole, M. A. Bouchene and B. Girard, *Phys. Rev. Lett.* **78,** 2716 (1997).

50. M. Bellini, A. Bartoli and T. W. Hänsch, *Opt. Lett.* **22**, 540 (1997).

51. J. Oreg, G. Kazak and J. H. Eberly, *Phys. Rev. A* **32,** 2776 (1985).

52. B. Broers, H. B. van Linden van den Heuvell and L. D. Noordam, *Phys. Rev. Lett.* **69**, 2062 (1992).

53. Y. B. Band, *Phys. Rev. A* **50**, 5046 (1994); N. V. Vitanov, *J. Phys. B* **31**,709 (1998); R. Marani and E. J. Robinson, *J. Phys. B* **32**, 711 (1999).

54. R. R. Jones, *Phys. Rev. Lett.* **74**, 1091 (1995).

55. S. Chelkowski, A. D. Bandrauk and P. B. Corkum, *Phys. Rev. Lett.* **65**, 2355 (1990); S. Guérin,*Phys. Rev. A* **56**, 1458 (1997).

56. T. Baumert, T. Brixner, V. Seyfried, M. Strehle and G. Gerber,*Appl. Phys. B* **65,** 779 (1997).

57. E. Arimondo, *Coherent Population Trapping in Laser Spectroscopy, E.* Wolf (Elsevier, Amsterdam, 1996), Vol. 35.

58. C. Nicole, M. A. Bouchene, S. Zamith, N. Melikechi and B. Girard, *Phys. Rev. A* **60,** R1755 (1999).

59. V. V. Lozovoy, I. Pastirk, K. A. Walowicz and M. Dantus, *J. Chem. Phys.* **118,** 3187 (2003).

60. J. T. Fourkas, W. L. Wilson, G. Wäckerle, A. E. Frost and M. D. Fayer, *J. Opt. Soc. Am. B* **6**,1905 (1989).

61. N. F. Scherer, A. J. Ruggiero, M. Du and G. R. Fleming, *J. Chem. Phys.* **93**, 856 (1990).

62. N. F. Scherer, R. J. Carlson, A. Matro, M. Du, A. J. Ruggiero, V. Romerorochin, J. A. Cina, G. R. Fleming and S. A. Rice, *J. Chem. Phys.* **95**, 1487 (1991).

63. N. F. Scherer, A. Matro, L. D. Ziegler, M. Du, R. J. Carlson, J. A. Cina and G. R. Fleming, *J. Chem. Phys.* **96,** 4180 (1992).

64. R. R. Jones, C. S. Raman, D. W. Schumacher and P. H. Bucksbaum, *Phys. Rev. Lett.* **71**, 2575 (1993).

65. V Blanchet, M. A. Bouchene, O. Cabrol and B. Girard, *Chem. Phys. Lett.* **233**, 491 (1995).

66. V. Blanchet, M. A. Bouchene and B. Girard, *J. Chem. Phys.* **108**, 4862 (1998).

67. J. A. Cina, *J. Chem. Phys.* **113**, 9488 (2000).

68. V. V. Lozovoy, B. I. Grimberg, I. Pastirk and M. Dantus, *Chem. Phys.* **267**, 99 (2001).

69. K. A. Walowicz, I. Pastirk, V. V. Lozovoy and M. Dantus, *J. Phys. Chem. A* **106,** 9369 (2002).

70. I. Pastirk, J. M. Dela-Cruz, K. A. Walowicz, V. V. Lozovoy and M. Dantus, *Optics Express* **11**, 14 (2003).

71. N. Dudovich, D. Oron and Y. Silberberg, *Nature* **418,** 512 (2002); D. Oron, N. Dudovich, D. Yelin and Y. Silberberg, *Phys. Rev. Lett.* **88,** 063004 (2002); D. Oron, N. Dudovich, D. Yelin and Y. Silberberg, *Phys. Rev. A* **65**, 043408 (2002); D. Oron, N. Dudovich and Y. Silberberg, *Phys. Rev. Lett.* **89,** 273001 (2002).

72. F. Biraben, B. Cagnac and G. Grynberg, *Phys. Rev. Lett.* **32**, 643 (1974).

73. J. E. Bjorkholm and P. F. Liao, *Phys. Rev. Lett.* **33**, 128 (1974).

74. B. Chatel, J. Degert, S. Stock and B. Girard, *Phys. Rev. A* **68,** 041402R (2003).

75. D. J. Maas, D. I. Duncan, A. F. G. van der Meer, W. J. van der Zande and L. D. Noordam, *Chem. Phys. Lett.* **270**,45 (1997); R. B. Vrijen, D. I. Duncan and L. D. Noordam, *Phys. Rev. A* **56**, 2205 (1997); D. J. Maas, D. I. Duncan, R. B. Vrijen, W. J. van der Zande and L. D. Noordam, *Chem. Phys. Lett.* **290,** 75 (1998).

76. G. von Helden, I. Holleman, G. Meijer and B. Sartakov, *Optics Express* **4**, 2 (1999).

77. T. Witte, T. Hornung, L. Windhorn, D. Proch, R. de Vivie-Riedle, M. Motzkus and K. L. Kompa, *J. Chem. Phys.* **118**, 2021 (2003).

78. C. Ventalon, J. M. Fraser, M. H. Vos, A. Alexandrou, J.-L. Martin and M. Joffre, in preparation (2004).

79. P. Balling, D. J. Maas and L. D. Noordam, *Phys. Rev. A* **50,**4276 (1994).

80. B. Chatel, J. Degert and B. Girard, *Phys. Rev. A,* submitted.

81. E. Riedle, M. Beutter, S. Lochbrunner, J. Piel, S. Schenkl, S. Spörlein and W. Zinth, *Appl. Phys. B* **71**, 457 (2000).

82. E. Sokell, S. Zamith, M. A. Bouchene and B. Girard, *J. Phys. B* **33,** 2005 (2000); S. Zamith, M. A. Bouchene, E. Sokell, C. Nicole, V. Blanchet and B. Girard, *Eur. Phys. J. D* **12**, 255 (2000).

83. U. Gaubatz, P. Rudecki, S. Schiemann and K. Bergmann, *J. Chem. Phys.* **92,** 5363 (1990); K. Bergmann, H. Theuer and B. W. Shore, *Rev. Mod. Phys.* **70,** 1003 (1998).

84. R. Netz, T. Feurer, G. Roberts and R. Sauerbrey, *Phys. Rev. A* **65,** 043406 (2002); R. Netz, A. Nazarkin and R. Sauerbrey, *Phys. Rev. Lett.* **90,** 063001 (2003).

85. Z. Amitay, J. B. Ballard, H. U. Stauffer and S. R. Leone, *Chem. Phys.* **267**, 141 (2001).

86. J. Ahn, T. C. Weinacht and P. H. Bucksbaum, *Science* **287**, 463 (2000).

87. V. V. Lozovoy and M. Dantus, *Chem. Phys. Lett.* **351,** 213 (2002).

88. Z. Amitay, R. Kosloff and S. R. Leone, *Chem. Phys. Lett.* **359,** 8 (2002).

89. A. Assion, T. Baumert, J. Helbing, V. Seyfried and G. Gerber, *Chem. Phys. Lett.* **259**, 488 (1996).

90. B. Garraway and K.-A. Suominen, *Phys. Rev. Lett.* **80**, 932 (1998); S. Kallush and Y. B. Band, *Phys. Rev. A* **61,** 041401 (2000); B. Y. Chang, I. R. Sola, V. S. Malinovsky and J. Santamaria, *J. Chem. Phys.* **113**, 4901 (2000).

91. D. M. Villeneuve, S. A. Aseyev, P. Dietrich, M. Spanner, M. Y. Ivanov and P. B. Corkum, *Phys. Rev. Lett.* **85**, 542 (2000).

92. N. Vitanov and B. Girard, *Phys. Rev. A* **69,** 033409 (2004).

93. R. Foy, A. Migus, F. Biraben, G. Grynberg, P. R. McCullough and M. Tallon, *Astron. Astrophys. Suppl. Series* **111**, 569 (1995).

94. J. Biegert, J. C. Diels and P. W. Milonni, *Opt. Lett.* **25**, 683 (2000); J. Biegert and J.-C. Diels, *Phys. Rev. A* **67**, 043403 (2003).

Chapter 11

ULTRAFAST PROCESSES IN HIGHLY EXCITED WIDE-GAP DIELECTRIC THIN FILMS

M. Mero, J. Zeller and W. Rudolph
Department of Physics and Astronomy
University of New Mexico, Albuquerque, NM 87131, USA
wrudolph@unm.edu

Abstract   The response of wide-gap dielectric oxide materials to high-intensity femtosecond laser pulses is studied. The scaling of the threshold for dielectric breakdown with pulse duration and bandgap in the sub-picosecond regime was investigated using thin oxide films. A phenomenological model can explain the observations as the interplay of multiphoton ionization, impact ionization, and carrier relaxation. Transient reflection and transmission measurements were performed to monitor the temporal evolution of the dielectric constant that reflect processes in the excited electron gas and the lattice dynamics at excitation densities close to breakdown. The time-dependent dielectric constant is retrieved from the reflection and transmission data using an algorithm that takes into account standing waves formed by pump and probe in the film. A theoretical description based on the solution of the Boltzmann equation for the electron and phonon system after excitation including the formation of self-trapped excitons is presented. The contribution of individual scattering processes to the material response is studied and compared to the experimental data.

1.   INTRODUCTION

When a femtosecond (fs) laser pulse strikes the surface of a dielectric material various processes are triggered depending on the pulse intensity (see Fig. 11.1). At low fluences the material is brought out of equilibrium temporarily and relaxes back to its initial state with some characteristic time constant. At a certain intensity the solid damages which is often visible as a crater left behind by the ablated material. This regime of fs pulse-matter interaction has gained a
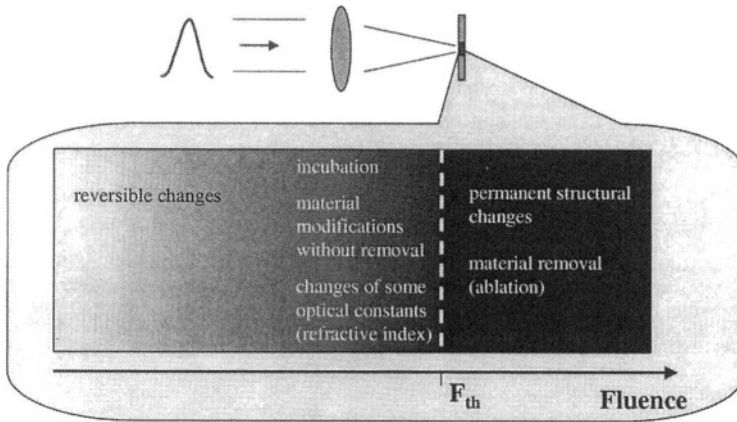
Figure 11.1. Schematic diagram of processes following femtosecond pulse excitation of solid-state materials as a function of fluence.

great deal of interest recently because of its importance for laser micromachining. It turned out that microstructuring of dielectric materials with fs pulses is superior with respect to structure, size and reproducibility as compared to picosecond and longer pulses [1–4]. On the other hand, laser damage is undesirable in optical components and its study will lead to materials with higher damage resistance. In many materials there is an intermediate regime where the light-matter interaction does not lead to ablation or to clearly visible material modification, although the material does not return to the initial state. A variety of processes have been identified, among them color center formation and laser-induced chemical material modifications [5, 6]. While undesirable in some cases, permanent refractive index changes have been explored to write waveguides and three-dimensional structures in dielectrics with fs pulses [5, 7–9]. The latter is possible because the wide-gap materials are transparent and the aforementioned processes are mediated by nonlinear optical processes that occur only at the high intensities in the laser focus.

Prior to breakdown the material is in a state far from thermal equilibrium. The study of the evolution of this state with fs spectroscopy allows one to gain insight into elementary processes that occur on a fast time scale [10]. Current models of fs pulse induced damage of dielectric materials are based on the excitation of electrons from the valence band (VB) to the conduction band (CB) until a critical density is reached [11–13]. At this point the lattice becomes unstable. The high electron density results in a strong (linear) absorption in a thin surface layer (skin depth on the order of the wavelength), which can result in heating and evaporation. Also, the photo-emission of electrons produces a region where

neutrality is not maintained within a short time window. This can lead to what is called "Coulomb explosion" [14].

One of the fundamental questions is how this critical electron density is produced. Being transparent to near-IR radiation, dielectric materials have to be excited by a nonlinear optical process, which is possible owing to the high intensity of the fs pulse. The initial excitation steps occur during the pulse and involve an interplay of multiphoton absorption (MPA) and tunnelling as described by Keldysh's theory [15]. Once in the conduction band, the electrons can gain further energy from the radiation field (free electron absorption, inverse Bremsstrahlung) until their energy is large enough for impact ionization. Impact ionization refers to a collision between an energetic CB electron and an electron in the VB as a result of which two electrons are produced at the bottom of the CB. Impact ionization can result in an exponential increase of the CB electron density, also known as avalanche ionization.

The elementary processes in the conduction band following the excitation involve electron-electron (e-e), electron-phonon (e-ph), and electron-phonon-photon (e-ph-pht) scattering (see Fig. 11.2). While typical in all solid materials their study with fs resolution at high carrier densities is particularly straightforward in dielectrics. Due to the large bandgap, processes such as bandgap shrinkage and state filling that can mask the measurable signals [16]have only minor effects when probed with pulses in the near-IR spectral region. Dielectric thin films are therefore good candidates for studying electron plasmas far from equilibrium. The aim of this chapter is to present experimental and theoretical results describing the response of oxide films to near-IR femtosecond laser pulse excitation below and above the threshold for dielectric breakdown. In Section 2 we discuss fundamental processes in wide-gap dielectrics induced by fs laser pulses. We introduce a computer model based on the Boltzmann equation to monitor the transient behavior of the electron and phonon gas after laser excitation and a simple phenomenological model of damage. Section 3 presents results of breakdown measurements with pulses from 25 fs to 1 ps and a comparison to the phenomenological model. In Section 4 we present transient absorption and reflection measurements to determine the time-dependent dielectric constant. In Section 5 we compare theory and experiment and conclude in Section 6.

2. MODELLING OF PROCESSES FOLLOWING FS PULSE EXCITATION

2.1 Microscopic Model Based on the Boltzmann Equation

Different theoretical approaches to calculate the temporal evolution of a solid material after laser excitation exist, such as the Fokker-Planck equation [17, 13]and the Boltzmann transport equations [18]. We chose the Boltzmann-
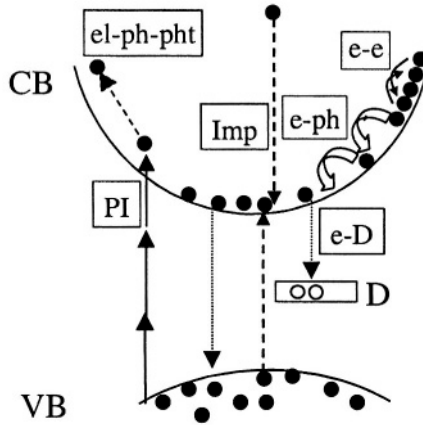
Figure 11.2. Schematic diagram of energy deposition and dissipation in wide-gap dielectric materials through excitation of electrons from the valence band (VB) to the conduction band (CB) in the presence of defect states (D). Contributing processes are photoionization (PI), impact ionization (Imp), electron-phonon-photon scattering (e-ph-pht), electron-phonon scattering (e-ph), electron-electron scattering (e-e) and electron-defect interaction (e-D).

equation approach since it allows one to model processes in the solid at a microscopic level based on first principles. The solid is described in terms of electrons and lattice ions. The electron system is represented by an energy-dependent distribution function $f(E)$ for the conduction band electrons, and the lattice by the wavevector (q) dependent phonon occupation numbers $s_\beta(q)$ of a phonon mode β. Defect levels inside the forbidden bandgap with a density N_D can be included [19]. If the distribution functions $f(E,t)$, $s_\beta(q,t)$ and $N_D(t)$ are known, the time-dependent optical response of the excited dielectric can be calculated and compared to the experiment. The coupled Boltzmann equations for electrons and phonons can be written symbolically as a sum of collision terms for the different interaction processes j:

$$\frac{\partial f(E)}{\partial t} = \sum_j \left(\frac{\partial f(E)}{\partial t} \right)_j \tag{11.1}$$

$$\frac{\partial s_\beta(q)}{\partial t} = \sum_j \left(\frac{\partial s_\beta(q)}{\partial t} \right)_j . \tag{11.2}$$

Note that the energy E of the electrons is measured with respect to the bottom of the CB band.

While this approach allows one to consider an arbitrary number of processes, only the most important ones are usually included; so that an accurate description of the observations within experimental accuracy becomes possible. The

processes included in our simulations are explained in detail below (see also the paper by Kaiser et al. [18]). The carrier excitation processes are photo-ionization (PI) and impact ionization (Imp). Carrier-scattering processes that we include are e-e, e-ph-pht interaction as well as decay of electrons from the CB into a defect level D inside the forbidden bandgap (e-D). The phonon evolution is described by e-ph-pht interaction and defect-phonon interaction (ph-D).

Several approximations and simplifications were made to speed up the simulations and to use effective parameters of materials whose specifics are not well known. The simulation traces the CB electrons only while the VB was assumed fully occupied. This approximation is justified when the CB electron density is still small compared to the total valence band electron density ($N_V \approx 10^{23}$ cm^{-3}), which is valid even under our high-excitation conditions ($N_e \leq 10^{21}$ cm^{-3}). The CB was assumed to be parabolic and isotropic. Three phonon modes, one acoustic and two optical, were taken into account.

2.1.1 Photoionization (PI).

Being transparent to near-IR radiation the initial excitation of CB electrons from the VB can only be through a nonlinear optical process. At the high intensities encountered close to the optical damage threshold, ordinary quantum-mechanical perturbation theory fails, requiring a non-perturbative calculation of CB carrier generation rates. The most common approach is that by Keldysh [15]. This approach allows one to calculate analytically the ionization rate in solids for arbitrarily strong laser intensities. Using the approach in Ref. [18], one can use the Keldysh-rate to find an expression for the PI collision term:

$$\left. \frac{\partial f(E)}{\partial t} \right|_{PI} =$$

$$\frac{\sqrt{2}\pi^2 \hbar^3 \dot{W}}{\sqrt{m_r^3(m\hbar\Omega - \Delta)}} f_v \left(E_0 \frac{m_c}{m_r} - E \right) [1 - f(E)] \, \delta \left(\frac{m_c}{m_r}(E_0 - E) \right), (11.3)$$

where $\dot{W}$ is the photoionization rate given by the Keldysh-theory, f_v is the occupation number in the valence band, $E_0 = (m_r/m_c)(m\hbar\Omega - \Delta)$ is the energy of the final state in the conduction band that is derived from momentum and energy conservation assuming m photons are involved in the excitation, m_r is the reduced mass, and m_c (m_v) is the effective mass in the CB (VB).

The low ($\gamma_K \gg 1$) and high ($\gamma_K \ll 1$) intensity limit of the general Keldysh theory ($\gamma_K = \Omega\sqrt{m_r E_g}/e\mathcal{E}_0$, where $\mathcal{E}_0$ is the electric field amplitude) are multiphoton ionization (MPI) and tunnelling, respectively, for which separate analytical formulae exist. Keldysh theory assumes that the generated CB electron oscillates in the AC electric field $\mathcal{E}(t)$ of the laser with an average kinetic energy $E_p = e^2\mathcal{E}_0^2/(4m_r\Omega^2)$, called the ponderomotive potential. This energy
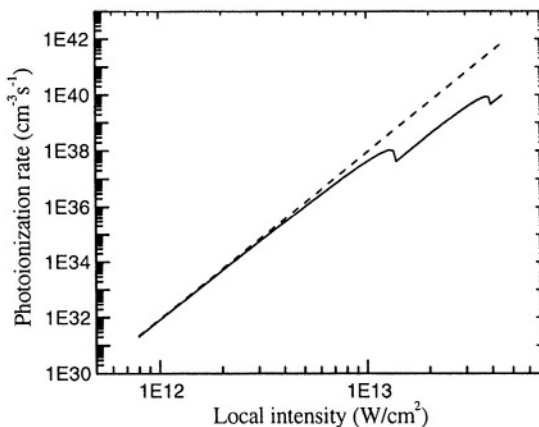
Figure 11.3. Photoionization rate as a function of the local laser intensity in SiO_2 ($n_0 = 1.5$) calculated with the general Keldysh formalism (solid line) for a bandgap of $E_g = 8.3$ eV, an excitation wavelength of $\lambda = 800$ nm, and a reduced mass $m_r = 0.5m_0$, where m_0 is the free electron mass. The multiphoton ionization (MPI) limit is shown for comparison (dashed line).

has to be added to the bandgap energy E_g to obtain the effective ionization potential $\Delta = E_g + E_p$.

Figure 11.3 shows the photoionization rate as a function of intensity for SiO_2, the material with the largest bandgap in our studies. The solid curve was obtained by using the general Keldysh formula. The steps in the curve are related to the increase of the effective ionization potential leading to higher-order transitions. The dashed curve was calculated with the Keldsyh MPI formula that has the form of $\beta_m I^m$, where β_m is the multiphoton absorption (MPA) coefficient of order m. Strictly speaking, the MPI formula is only applicable at low intensities, but we extrapolated the rate to high intensities for reasons that will become clear in Section 3. The slope of these curves give the power exponent of the intensity in a $\beta_m I^m$-like scaling law for a constant β_m. The slope of the MPI curve is six, corresponding to a 6-photon process. The slope of the general curve starts at a value of six but decreases with intensity when tunneling becomes important.

2.1.2   Electron-electron interaction (e-e).   Electron-electron interaction is described as a two-body collision mediated by a screened Coulomb interaction between two electrons that conserves momentum and energy. Two electrons with initial wave vectors $\vec{k}$ and $\vec{k_2}$ collide and scatter into the final states of wave vectors $\vec{k_1}$ and $\vec{k_3}$. Owing to energy conservation in the electron system, the result of this scattering mechanism is to relax a non-equilibrium elec-

tron distribution towards an equilibrium Fermi-Dirac distribution $f_{FD}(E, T_e)$ of electron temperature T_e.

The total electron density N_e affects the strength of the e-e interaction in different ways. First, the rate of e-e scattering increases with N_e. Second, the screening of the Coulomb interaction increases with N_e, which has the effect of slowing down the interaction process. Third, the Pauli exclusion principle limits the number of empty final scattering states when $f(E)$ approaches unity, which also decreases the scattering rate at high carrier densities.

The e-e collision term can be written as

$$\frac{\partial f(E)}{\partial t}\bigg|_{e-e} = \frac{1}{\hbar^4}\left(\frac{m_c}{2\pi\hbar}\right)^3\left(\frac{e^2}{\varepsilon_0}\right)^2\frac{1}{k(E)}\int dE_1\int dE_2\int_{\kappa_i}^{\kappa_e}d\kappa\frac{1}{(\kappa^2+q_0^2)^2}$$
$$\times\ \{[1-f(E)]\,[1-f(E_2)]\,f(E_1)f(E_3)$$
$$-\ [1-f(E_1)]\,[1-f(E_3)]\,f(E)f(E_2)\}, \tag{11.4}$$

where $E_2 = E_1 + E_3 - E$, q_0 is the Debye screening length, and $k_i = \sqrt{2m_cE_i/\hbar^2}$. The integration over the energies E_2 and E_1 is performed in the limits $(0, \infty)$ for E_2 and $(0, E')$ for E_1, where $E' = E + E_2$. The maximum energy E' describes the limit where one electron carries the total energy after collision. The limits of the κ integration are determined by the minimum and maximum of k values from an interval defined as the intersection of the interval $(|k_2 - k_3|, k_2 + k_3)$ with the interval $(|k - k_1|, k + k_1)$. Note that all energies are defined positive and with respect to the CB edge.

2.1.3 Impact ionization (Imp). This is another example of e-e scattering but, unlike the previous case, the electrons involved are from two different bands. Electrons that are excited by free-carrier absorption beyond a critical energy E_{cr} above the CB edge interact with valence band electrons via Coulomb interaction. As a result, the CB electron loses most of its kinetic energy, while secondary electrons are elevated from the VB into the CB. The requirement of energy and momentum conservation results in a critical energy $E_{cr} \approx 1.5\Delta$, where Δ is the effective ionization potential. The latter is the sum of the bandgap energy E_g and the ponderomotive potential. Only CB electrons with $E > E_{cr}$ can undergo impact ionization. The corresponding collision term can be written as

$$\frac{\partial f(E)}{\partial t}\bigg|_{imp} = \frac{1}{(2\pi\hbar)^3}\left(\frac{e^2}{\varepsilon_0}\right)^2\frac{\hbar^2}{2\Delta}\left(\frac{m_c}{\hbar^2}\right)^2\left(1+\frac{m_v}{m_0}\right)\frac{1}{k(E)}(A-B), \tag{11.5}$$

where

$$A = \int \int_{\mathcal{E}_A} dE_1 dE_2 f(E_1) f(E_2) \left[1 - f(E)\right] \left[1 - f(E_3^a)\right] \left[I(\mathcal{K}_A) + I(\mathcal{K}_B)\right]$$
(11.6)

and

$$B = \int \int_{\mathcal{E}_C} dE_1 dE_2 f(E) f(E_2) \left[1 - f(E_1)\right] \left[1 - f(E_3^c)\right] I(\mathcal{K}_C), \quad (11.7)$$

where f_v is the valence band electron distribution function and the integral $I(\mathcal{K}) = \int_{\kappa_i}^{\kappa_e} \kappa^2 \left(\kappa^2 + q_0^2\right)^{-2} d\kappa$. The integration limit κ_i (κ_e) is the minimum (maximum) of the κ-interval defined as

$$\left[|k_i - k_j^\gamma| \le \kappa \le (k_i + k_j^\gamma)\right] \cap \left[|k - k_\ell| \le \kappa \le (k + k_\ell)\right], \quad (11.8)$$

where $\cap$ means intersection. The indices (i, j, ℓ, γ) are $(2,3,1,a)$ for $\mathcal{K}_A$, $(1,3,2,a)$ for $\mathcal{K}_B$, and $(2,3,1,c)$ for $\mathcal{K}_C$. Here, $k_3^{a,c} = [\pm(k_1^2 - k^2) - \mu k_2^2 - k_4^2]^{1/2}$ where the plus (minus) sign refers to k_3^a (k_3^c), and $\mu = m_c/m_v$. $E_3^{a,c} = \pm(E_1 - E - E_2) - E_4$, where the plus (minus) refers to E_3^a (E_3^c), $E_4 = \Delta$, and $E_i = \hbar^2 k_i^2/(2m_c)$ for $i = 1, 3, 4$, or no index, and $E_i = \hbar^2 k_i^2/(2m_v)$ for $i = 2$.

2.1.4   Electron-phonon-photon interaction (e-ph-pht).   Electron-phonon-photon interaction is the quantum mechanical analogue of free-carrier absorption. The CB electrons absorb or emit ℓ photons of energy $\hbar\Omega$ and either absorb ("+") or emit ("-") a phonon of energy $\hbar\omega(q)$. As photons carry virtually no momentum, a phonon is needed for both energy conservation, $E_f = E_i \pm \ell\hbar\Omega \pm \hbar\omega(q)$, and momentum conservation, $\vec{k}_f = \vec{k}_i \pm \vec{q}$. Here the subscripts i and f denote the initial and final state, respectively.

Unlike in strongly polar materials like the halides, electron-phonon interaction in dielectrics is described by deformation potential theory, in which only longitudinal phonons interact with the electrons. Depending on the electric field strengths, only a small number M of multiphoton processes needs to be included in the interaction. For simplicity, we chose $M = 0, \pm 1$. After the pulse, $M = 0$ and "e-ph-pht" describes electron-phonon scattering without the involvement of photons. The associated energy exchange results in a relaxation of an energetic electron distribution towards the band edge and a simultaneous increase of the total phonon energy, which will eventually increase the lattice temperature. The collision term can be written as

$$\frac{\partial f(E)}{\partial t}\bigg|_{e-ph-pht} = \frac{1}{2\pi\hbar^3} \frac{m_c}{k(E)} \sum_{\beta=0}^{2} \sum_{\ell=-\infty}^{+\infty} \left\langle J_\ell^2 \left(\frac{e\vec{\mathcal{E}}\vec{q}}{m_c\Omega^2}\right) \right\rangle (M + N),$$
(11.9)
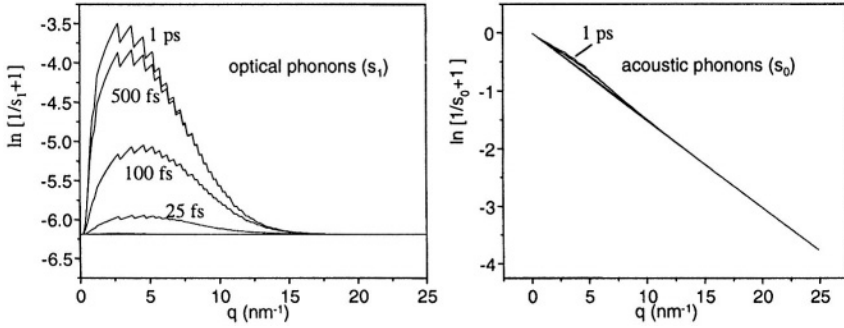
Figure 11.4. Optical and acoustic phonon distribution as a result of e-ph-pht interaction at different times as a function of the wave number of the respective phonon mode. The ripples are numerical artifacts. The simulation was done for a 25 fs square pulse of $\mathcal{E}_0 = 45$ MV/cm at $\lambda = 800$ nm exciting Ta_2O_5 with $n_0 = 2.17$, $E_g = 3.8$ eV, $m_c = 0.75m_0$, $m_v = m_0$, $C_D = 20$ eV, $\rho = 8200$ kg/m^3 and no defects. The optical phonon energies are 80 and 160 meV, and the sound velocity is 5935 m/s. Impact ionization has only a negligible effect on the electron density, and therefore it was not included.

where

$$M = \int_+ dq\, qV(\beta, q)\left[(1-f(E))\,f(E^+)\,(s_\beta(q)+1) - f(E)\,(1-f(E^+))\,s_\beta(q)\right]$$
(11.10)

and

$$N = \int_- dq\, qV(\beta, q)\left[(1-f(E))\,f(E^-)s_\beta(q) - f(E)\,(1-f(E^-))\,(s_\beta(q)+1)\right].$$
(11.11)

Here, C_D is the deformation potential constant, $V(\beta, q) = \frac{\hbar}{2\rho\omega_\beta(q)}C_D^2$, $E^\pm = E + [\ell\hbar\Omega \pm \hbar\omega_\beta(q)]$, J_ℓ is the Bessel function of order ℓ, $\langle\rangle$ means averaging over the angle between the electric field vector $\vec{\mathcal{E}}$ and the phonon wave vector $\vec{q}$, and ρ is the mass density. The integrations run over all values of q for which

$$\left|\frac{1}{2kq}\left[\frac{2m_c}{\hbar^2}[\ell\hbar\Omega \pm \hbar\omega(q)] - q^2\right]\right| \leq 1$$

holds, where the "+" ("-") sign refers to $\int_+$ ($\int_-$) in Eq. 11.10 (Eq. 11.11).

Owing to different dispersion relations for optical ($E_{LO} \approx$const.) and acoustic phonons ($E_{LA} \propto q$), the time evolution of electron and phonon distributions due to e-ph scattering and the associated energy exchange depend on the phonon mode. This can be seen in Fig. 11.4, where the time evolution of optical and acoustic phonons under otherwise identical conditions is shown. As optical phonons have a generally higher energy than acoustic phonons in polar materials like dielectrics, energy transfer is more effective in electron-optical-phonon
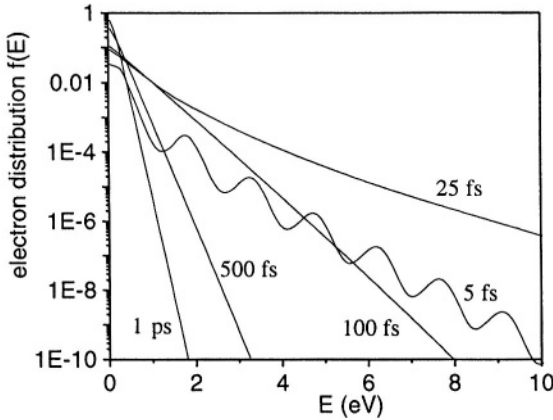
Figure 11.5.   Electron distribution at different times after excitation calculated with the Boltzmann equation and Keldysh theory. The simulation was done for the same material and laser parameters as in Fig. 11.4.

than in electron-acoustic-phonon interaction and therefore proceeds faster. The distribution of acoustic phonons is hardly affected by the electron system.

Figure 11.5 summarizes the effect of the processes discussed so far on the electron distribution function $f(E)$. For the duration of the laser pulse ($\tau_p = 25$ fs), the main effect of e-ph-pht interaction is to heat up the CB electrons to states far above the band edge, while the effect on the phonon population is negligible. At early times the multiphoton excitation and carrier heating leads to a modulated electron distribution with the period determined by the photon energy $\hbar\Omega$. Fast e-e scattering washes out these modulations and produces a thermalized electron distribution. Electron-phonon scattering dissipates energy to the phonon system resulting in a relaxation of the electron distribution towards the edge of the conduction band.

2.1.5   Carrier decay into defects (e-D).   All interaction mechanisms described so far are typical for processes in the conduction band and have to be considered for all solids. In addition, the electron-hole gas excited in wide bandgap materials tends to form self-trapped excitons (STEs) in the forbidden bandgap [20]. Time-resolved studies indicate that STEs have a binding energy E_D on the order of eV and can form on a sub-ps timescale [21–23](see also Sect. 5). STEs have been observed in dielectric and ionic materials, e.g., NaCl, SiO_2 [21, 24]and TiO_2 [25].

STEs are electron-hole pairs in polar compounds that strongly interact with the lattice. Following the continuum model of STEs [26, 20, 27], the formation process illustrated in Fig. 11.6a can be summarized as follows. Initially
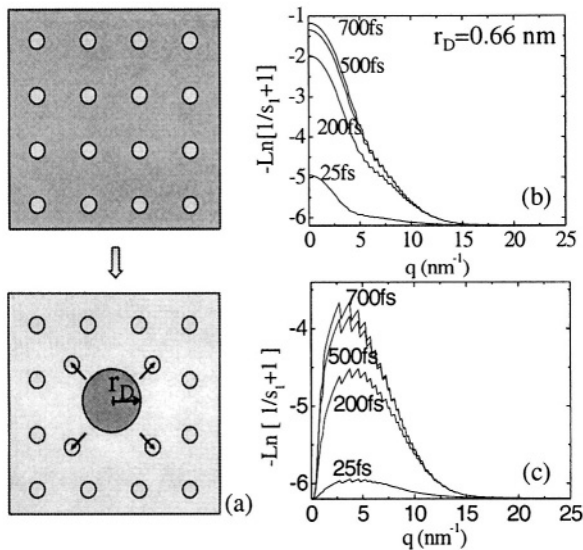
Figure 11.6. (a) Diagram of STE formation. The small circles indicate lattice ions within a delocalized electron-hole gas (background). The small arrows show ion (lattice) displacement near an STE of radius r_D. (b) Calculated phonon occupation number (ln scale) of an optical phonon mode caused by conduction-band electron-phonon interaction including STE-formation at different times after excitation. (c) as in (b), but without STE-formation (no defects). The ripples are numerical artifacts. The simulation was done for the same material and laser parameters as in Fig. 11.4.

delocalized excited electrons and holes couple to acoustic phonons via deformation potential interaction and to optical phonons via Coulomb interaction. The state of minimum energy for the system of charge carriers and lattice involves a localized electron-hole pair. This electron-hole pair resides within a characteristic radius r_D and can be described by a Gaussian wave function $\Psi_{STE}(r) \propto \exp(-(4\ln 2)r^2/r_D^2)$. The lattice ions around the charge carriers are displaced by $\Delta(r) \propto |\Psi_{STE}(r)|^2$ with respect to their equilibrium positions, leading to elastic strain in the lattice. The strength of the deformation potential, the elastic constant and the strength of the Coulomb interaction determine the degree of localization of the STE.

The process of STE formation can proceed through intermediary steps, depending on material parameters like the electron and hole effective masses and the phonon-coupling strength of the electron and the hole [28]. In one scenario, an exciton will form before self-trapping, leading to a trapping rate independent of carrier density, which has been observed in SiO_2 [21]. In another possible scenario, the electron or hole differ in their ability to couple to the lattice. One of the carriers will be trapped first and then recombine with the other charge

carrier to form an STE. The resulting bi-molecular decay law can be observed as an increase of the trapping rate with carrier density, as was observed in NaCl, for example [21].

To include the formation of STEs in the Boltzmann-equation based simulation, collision terms for the electron-defect and the phonon-defect interaction were derived based on the continuum model. The actual structure of the term $\partial f/\partial t|_{e-D}$ needs to be specified depending on the scenario chosen for the STE formation. For case one, it can be written as

$$\left.\frac{\partial f}{\partial t}\right|_{e-D} = -\frac{f(E)\,\sigma_{el}(E)}{T_D}. \tag{11.12}$$

Here, we assumed a cross section σ_{el} that depends on the electron energy and a decay time T_D that is energy-independent.

For the bi-molecular decay, case two, we can write

$$\left.\frac{\partial f(E,t)}{\partial t}\right|_{e-D} = -K_S f(E,t)\left[\overline{N}_D + (N_e(t) - \overline{N}_e)\right], \tag{11.13}$$

where $\overline{N}_e$ is the CB electron density that would be generated in the absence of defect formation and K_S is an effective decay constant. Here, we also allowed for the fact that the maximum number of STE is limited to a certain value, $\overline{N}_D < \overline{N}_e$ [21].

To derive the collision integral for phonon-defect interaction, the lattice displacement resulting from STE-formation was interpreted as a source for phonon excitation. Within this framework we can express the rate of phonon production as

$$\left.\frac{\partial s_\beta(q)}{\partial t}\right|_{ph-D} = \eta_\beta(q)\,\sigma_{ph}(q)\frac{dN_D}{dt}, \tag{11.14}$$

where $\sigma_{ph}(q) = \exp\left[-(q\cdot r_D)^2/(4\ln 2)\right]$ is the wavenumber-dependent phonon excitation cross section. The functional dependence of this cross section was derived from an expansion of the lattice displacement into phonon modes with wave number q. The pre-factor $\eta_\beta(q)$ is determined by the requirement of energy conservation for the system of electrons, STEs and phonons (see Ref. [19]for details). The effect of STE formation on the phonon dynamics is shown in Fig. 11.6b for the case of a weakly-localized STE. STE formation leads to a stronger phonon excitation than in the absence of STE formation (cf. Fig. 11.6c). Phonon modes with a small wave number q are disproportionally excited by the lattice displacement.

2.2   Phenomenological Model of Dielectric Breakdown

For many practical applications it is desirable to describe the damage behavior of optical materials with a simple theory that requires only a few material

parameters (figures of merit). In the modelling of fs laser breakdown it is generally assumed that a certain critical energy deposition into the material is necessary, which for the case of dielectrics translates into the creation of a critical electron density in the CB. Therefore, even though damage is a very complex phenomenon, the main processes leading to dielectric breakdown can formally be expressed in a rate equation for the electron density in the conduction band [13, 29, 30]:

$$\frac{dN_e(t)}{dt} = \alpha N_e(t)\xi I(t) + \beta_m [\xi I(t)]^m - \frac{N_e(t)}{T}. \qquad (11.15)$$

Here, N_e is the electron density, $I(t)$ is the pulse intensity, α is the impact ionization parameter, β_m is the multiphoton absorption (MPA) coefficient of order m, T is an effective relaxation time, and ξ takes into account the local intensity modification in the film. The breakdown threshold is reached when

$$N_e(t_{\max}) = N_{e,\max} = N_{e,cr}, \qquad (11.16)$$

which can happen during or immediately after the pulse. This critical density is chosen to be 10^{21} cm^{-3}. At this carrier density, the plasma frequency is close to the laser frequency resulting in strong absorption. In the framework of this model the damage behavior of the material is characterized by the parameters α, β_m, and T.

Equation 11.15 without the decay term was derived from a more complete theory based on a Fokker-Planck equation to describe electron dynamics in the conduction band [13]. It is applicable when the rate of Joule heating in the conduction band is much larger than the cooling rate due to electron-phonon scattering, and when the so called flux-doubling approximation is valid. The latter means that every electron that reaches the critical energy of impact ionization will immediately excite a new valence electron, resulting in two electrons, both at the bottom of the conduction band. For the experimental breakdown fluence versus pulse duration data published so far, this model predicts a dominant avalanche contribution in the electron excitation for pulse durations as short as of a few tens of fs. The dominant avalanche also makes the predicted threshold fluences only logarithmically sensitive to the choice of the critical electron density. The linear scaling of avalanche ionization with intensity is established only after a few tens of fs. Therefore, below this duration the applicability of Eq. 11.15 is somewhat questionable (for more information see Ref. [13]).

An additional complication in the modelling of fs breakdown is the sub-ps dynamics of electrons excited to the conduction band observed in bulk materials [21, 30] and the formation of STEs. We included those processes by an effective relaxation time *T*. The associated decay term in Eq. 11.15 is to represent both the electrons leaving the conduction band and the possible ionization of STEs (re-excitation).

3. DIELECTRIC BREAKDOWN BEHAVIOR OF OXIDE THIN FILMS

Numerous experimental studies have been conducted on the pulse duration scaling of ultrashort laser induced damage of dielectric materials [13, 29, 31]. We investigated five oxides (TiO_2, Ta_2O_5, HfO_2, Al_2O_3, and SiO_2) with bandgaps ranging from 3.3 to 8.3 eV (see Table 11.1). The films were deposited by ion-beam sputtering (IBS) on fused silica substrates with a thickness of $6\lambda/4n_0$ where $\lambda = 790$ nm and n_0 is the refractive index of the material at this wavelength. Single pulses from a femtosecond Ti:sapphire oscillator-amplifier system were used to excite the samples [29]. The pulse fluence was varied with neutral glass filters and a pair of Brewster plates. The pulse duration was tuned from 25 fs to 1.3 ps by adjusting a prism compressor at the amplifier output and inserting glass slabs of various lengths into the beam path. The occurrence of damage was monitored with a CCD camera-microscope detector. A distinct change of the scattered intensity (pattern) of the weak amplified spontaneous emission was visible at the point of damage.

Table 11.1. Parameters of investigated oxide films, thickness $d = 6\lambda/4n_0$ with $\lambda = 790$ nm.

Material	Refractive index n_0	Thickness (nm)	Bandgap energy (eV)
TiO_2	2.39	496	3.3
Ta_2O_5	2.17	546	3.8
HfO_2	2.09	568	5.1
Al_2O_3	1.65	716	6.5
SiO_2	1.50	790	8.3

The measured damage fluences as a function of the pulse duration, $F_{th}(\tau_p)$, for the five different oxides are shown in Fig. 11.7. The thresholds are very well defined. Except for the shortest (bandwidth-limited) pulses, the measurements were performed with up-chirped pulses. Tests with down-chirped pulses did not result in different threshold fluences. A fit of the measurements to Eq. 11.15 yields the material parameters (figures of merit) α, β_m, and T (see Table 11.2).

The values obtained for the avalanche coefficient agree with the results of the numerical simulations in Ref. [13] within an order of magnitude. Depending on the material and excitation wavelength, MPA coefficients known from the literature can vary by several orders of magnitude (for β_3 values see, for example, Refs. [32, 33]). The coefficients determined by us through this indirect method are within these accepted ranges. The MPA coefficients calculated with the Keldysh formula were a few orders of magnitude higher than our fit values, depending on the unknown reduced masses (cf. Table 11.2). The larger the bandgap, the larger is the deviation.
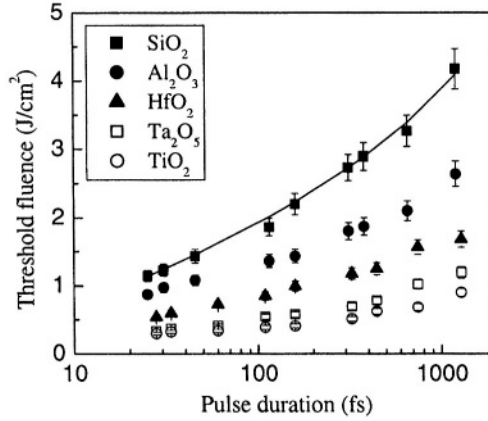
Figure 11.7. Measured pulse fluence for breakdown as a function of pulse duration for five oxide thin films (cf. Table 11.1). The fluence values shown represent the actual peak fluence in the film taking into account local field effects.

Table 11.2. Material parameters obtained from a fit of Eq. 11.15 to the experiment (columns 3 – 5). Avalanche coefficient α (cm²/J), m-th order multiphoton ionization coefficient β_m (cm^{2m-3}fs^{m-1}/J^m), and effective decay constant T (fs). The quantity m is the order of the multiphoton process needed to excite the material with photons at $\lambda = 800$ nm. The last two columns show the MPA coefficients obtained from Keldysh theory for two different effective masses.

Material	m	α	β_m	T	$\beta_m^K(0.1m_0)$	$\beta_m^K(1.0m_0)$
TiO$_2$	3	34.1	1.5×10^{23}	120	6.3×10^{26}	2.0×10^{25}
Ta$_2$O$_5$	3	11.2	6.7×10^{24}	490	6.2×10^{26}	1.9×10^{25}
HfO$_2$	4	9.9	2.9×10^{25}	1050	2.8×10^{28}	8.9×10^{25}
Al$_2$O$_3$	5	12.4	2.3×10^{24}	220	2.7×10^{30}	8.6×10^{26}
SiO$_2$	6	7.9	9.9×10^{25}	220	1.2×10^{32}	3.8×10^{27}

As was discussed in Sect. 2.1.1, according to the predictions of the Keldysh theory, using constant β_m and m in the rate equation is only approximately justified when approaching breakdown field strengths. Figure 11.3 shows that the MPI rates extrapolated to high intensities are larger than the actual rates. Therefore, if we take the low field value of the intensity power exponent in the rate equation model, the fitting always underestimates the MPA coefficients. For SiO$_2$, for example, the intensity amplitude at threshold is above 10^{13} W/cm^2 for a pulse duration of up to 240 fs. Therefore, overestimation of the multiphoton coefficient is largest for this material.

The relaxation times extracted from the fit to the model range from 120 fs to 1ps (Table 11.2). Similarly short carrier lifetimes were observed in Refs. [21,
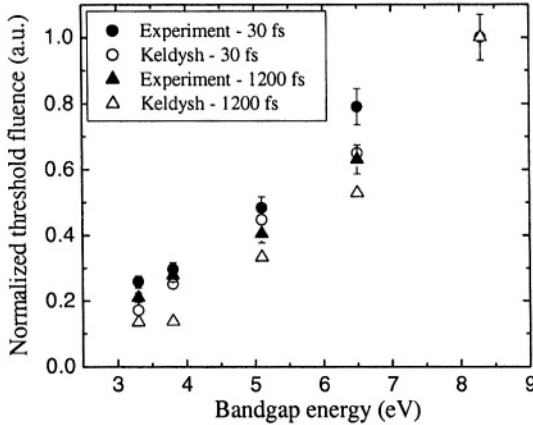
Figure 11.8. Calculated and observed normalized (to the fluence at the largest bandgap) fluence for breakdown as a function of bandgap for two different pulse durations. ($N_{e,cr} = 10^{21}$ cm^{-3}, $m_r = 0.2m_0$)

30]and were associated with the formation of self-trapped excitons. Our pump-probe measurements (see next section) also suggest that formation of trap states in the bandgap occurs on an ultrafast timescale (~ 1 ps).

Figure 11.8 shows the fluence necessary to generate a certain electron density (10^{21} cm^{-3}) through high-field ionization as a function of the bandgap energy (open symbols). The calculations are based on the general Keldysh formula in its representation in Eq. (4) of Ref. [34][1]. If we approximate $F_{th}(E_g)$ by a linear function, the slope turns out to be rather insensitive to the actual choice of the somewhat arbitrarily chosen reduced mass and critical electron density within the reasonable limits of $m_0 > m_r > 0.1m_0$ and 10^{19} cm$^{-3} < N_e < 10^{21}$ cm^{-3}, respectively.

It is interesting to note that for short pulse durations one can even get approximate absolute agreement between the predictions of the Keldysh theory and the experiment for $N_{e,cr} = 10^{21}$ cm^{-3} and $m_r = 0.2m_0$. For longer pulses the Keldysh theory overestimates the thresholds but still gives the right bandgap scaling, which suggests that there is an increasing avalanche contribution to the electron generation that is roughly independent of the bandgap energy.

The scaling of F_{th} with bandgap energy is nearly independent of pulse duration as the data for 30 fs and 1.2 ps shown in Fig. 11.8 suggest. To explain this behavior, let us discuss the bandgap dependence of the two electron-generating mechanisms, impact ionization and photoionization, separately. We will see

---

[1]The definitions of the complete elliptic integrals in Ref. [34]use an argument that is the square of the argument used in the Keldysh paper [15].

that at a constant fluence both rates tend to scale as E_g^{-1} under certain conditions.

The critical energy for impact ionization increases with the bandgap (see Sect. 2.1.3). To lowest order, the Joule heating rate is proportional to the laser intensity (or fluence at a given pulse duration) independent of E_g. The impact ionization itself is also bandgap-independent within the flux-doubling approximation [13, 35], which assumes that every electron reaching the critical energy for impact ionization excites another valence electron. Therefore, at a given pulse duration and constant fluence the avalanche rate is expected to scale as E_g^{-1}.

In spite of the strong nonlinear dependence of the photoionization rates on intensity, the threshold fluences still depend only weakly on bandgap energy. One can derive an explicit approximate analytical expression of the bandgap dependence in the following way. The seed conduction band electron density is taken to be a bandgap-independent constant and proportional to the mth power of the threshold fluence as a result of multiphoton absorption:

$$N_{\text{seed}} = \int_{-\infty}^{\infty} \beta_m (\xi I_{th}(t))^m dt = \beta_m \left(\frac{2\sqrt{\ln(2)}}{\tau_p \sqrt{\pi}} \right)^{m-1} \frac{1}{\sqrt{m}} (\xi F_{th})^m,$$

(11.17)

where we assumed a Gaussian excitation pulse. In the MPA limit ($\gamma_K \gg 1$), the Keldysh formula [15] yields

$$\beta_m = \zeta \left(\frac{e^2}{8 \Omega^2 m_r c \varepsilon_0} \right)^m \frac{\exp(2m)}{(n_0 E_g)^m}.$$

(11.18)

Since the optical thickness of the investigated films is constant, ξ is approximately material (bandgap) independent as is the case for ζ which is approximately given by $0.036\Omega(m_r \Omega/\hbar)^{3/2}$. Thus

$$F_{th} \propto Q(m) n_0 E_g,$$

(11.19)

where

$$Q(m) = \left[N_{\text{seed}} \frac{\sqrt{m}}{\zeta} \left(\frac{\tau_p \sqrt{\pi}}{2\sqrt{\ln(2)}} \right)^{m-1} \right]^{1/m}.$$

(11.20)

It can be shown that for our case, where $3 \leq m \leq 6$, $N_{\text{seed}} > 10^{19} \text{cm}^{-3}$ and $0.1 m_0 < m_r < m_0$, the Taylor series of $Q(m)$ with respect to m can be terminated after the zeroth-order term. To zeroth order, n_0 is also independent of m. Equation 11.19 then yields the scaling law $F_{th} \propto E_g$ observed in the experiments.
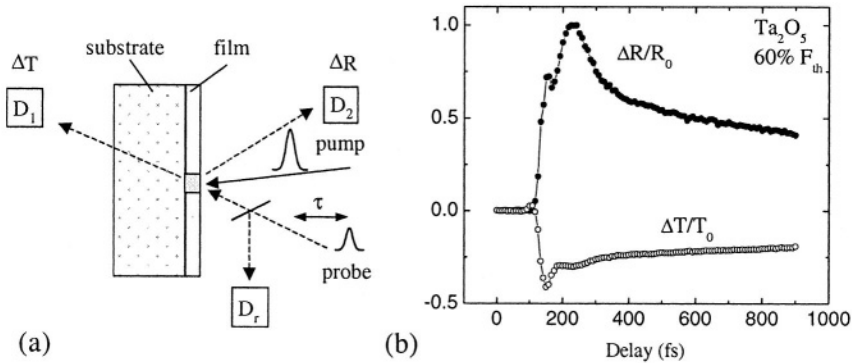
Figure 11.9. (a) Experimental set-up for transient reflection and transmission measurements. (b) Results for Ta_2O_5 for delays < 1 ps. The actual zero delay is at the first peak of the ΔR curve (coherent artifact).

4. TIME-RESOLVED REFLECTION AND TRANSMISSION STUDIES

4.1 Experiments

Transient processes following excitation close to the threshold for dielectric breakdown were studied with pump-probe experiments [10]. The experimental lay-out is sketched in Fig. 11.9a. Pulses from a Ti:sapphire oscillator-amplifier system (25 fs, 800 nm, 10 Hz) were split into a pump and a probe pulse with adjustable delay. The pump-induced change in transmission ΔT and reflection ΔR were measured as a function of delay τ. The repetition rate of the laser was reduced to 10 Hz to avoid accumulation effects (incubation) in the dielectric films. Figure 11.9b shows representative data for one of the materials, Ta_2O_5. For more details we refer to Ref. [36]. The peaks at zero delay represent artifacts originating from the overlap of pump and probe in the film and substrate and associated processes such as cross-phase modulation and transient gratings. To avoid these ambiguities the data evaluation started 60 fs after the coherence spike. The reflection and transmission data contain the material response convoluted with Fabry-Perot effects in the film. The next section describes the procedure used to retrieve the time-dependent dielectric constant from these measurements [37].

4.2 Retrieval of the Dielectric Constant

A summary of the retrieval procedure is shown in Fig. 11.10. The excitation of the film by the pump is controlled by the local intensity, which in turn is the result of interference effects. Hence the change in the complex dielectric
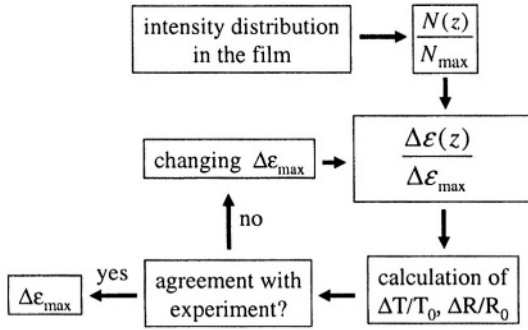
Figure 11.10. Flow chart of the $\Delta\varepsilon$-retrieval from reflection (ΔR) and transmission (ΔT) data.

function $\Delta\varepsilon(z)$ is spatially modulated leading to an amplitude and phase grating. Here, z is the position inside the film measured from the air-film interface. Since the overall absorption of the pump in the film is small, the action of the film on the pump pulse can be neglected. As the geometrical length of the pump pulse is much greater than the film thickness, the spatial and temporal dependence can be factorized. Thus, the intensity distribution in the film is

$$I(t, z) = I_p(t) \times \left| t_{12} \frac{1 + r_{23} \exp[i2k_0(z - d)]}{1 + r_{12}r_{23} \exp(-i2k_0d)} \right|^2 . \tag{11.21}$$

Here, $k_0 = 2\pi n_0 \cos(\theta_p)/\lambda_p$, where λ_p is the center wavelength of the pump, θ_p is the propagation angle of the pump in the film, and r_{ij} (t_{ij}) are the amplitude reflection (transmission) coefficients for the interface from medium i to medium j. The subscripts 1, 2, and 3 refer to air, film and substrate, respectively. $I_p(t)$ is the incident pump intensity. Note that the second factor on the right hand side of Eq. 11.21 is the ξ-factor in Eq. 11.15. Based on the Drude theory of electron-hole plasmas, we make the ansatz that the change in the dielectric function is proportional to the conduction band electron density. In other words, $\Delta\varepsilon(z) = \Delta\varepsilon_{\max} \times N(z)/N_{\max}$, where $\Delta\varepsilon_{\max}$ is the unknown. The spatially modulated electron density can be calculated using Eq. 11.15 with the coefficients determined from the fit to the $F_{th}(\tau_p)$ data (cf. Table 11.2). The film is divided into slices. The optical matrix formalism can be applied to the air-slices-substrate system to calculate R and T for a certain $\Delta\varepsilon_{\max}$. A computer search algorithm is used to find the value of $\Delta\varepsilon_{\max}$ that fits the experimental reflection and transmission best at given delay (cf. Fig. 11.10). Care has to be taken to exclude unphysical solutions, for example, by requiring that $\Delta R, \Delta T \to 0$ if $\Delta\varepsilon_{\max} \to 0$. The number of slices has to be chosen sufficiently large to make the retrieval results independent of its actual choice.
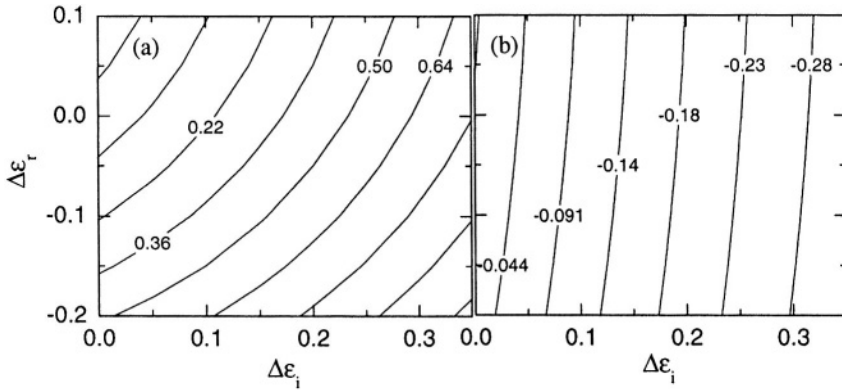
Figure 11.11. $\Delta R/R_0$ (a) and $\Delta T/T_0$ (b) contours in the complex $(\Delta\varepsilon_r, \Delta\varepsilon_i)$-space for the Ta$_2O_5$ film and the experimental conditions of Fig. 11.9.

The optimal angles of incidence of pump and probe were determined from the requirement of unique data retrieval and the least sensitivity of the results to experimental fluctuations. Figure 11.11 illustrates the problem. The plots show reflection and transmission changes in the complex $(\Delta\varepsilon_r, \Delta\varepsilon_i)$ space, where $\Delta\varepsilon_r$ and $\Delta\varepsilon_i$ represent the real and imaginary components of the complex dielectric function, respectively. As their intersection determines $\Delta\varepsilon_{\max}$, the signal contours for reflection and transmission must not be parallel to ensure a unique retrieval. This can be accomplished by a proper choice of pump and probe angle.

4.3   Interpretation of the Experiments

Figure 11.12 displays the time-dependent dielectric constant retrieved from the pump-probe measurements shown in Fig. 11.9 within the first 2.5 ps after excitation. The insets show the behavior on a 100 ps time scale. The sign of both the real and imaginary part of the dielectric constant at early times is consistent with what one can expect from an electron plasma according to Drude theory. The fast initial decay is due to electron-phonon scattering transferring excitation energy from the electron system to the lattice. The observed time constant of about 100 fs is consistent with simulations based on the Boltzmann equation (see below). This first decay is followed by processes on time scales of ps to tens of ps. One of the key features is that the real part of the dielectric constant $\Delta\varepsilon_r$ changes sign.

The sign reversal cannot be explained by the response of a free carrier gas only. It is, however, consistent with the formation of a deep defect state with a time constant T_D. Let us assume that the defect state at an energy E_D below the conduction band edge forms the lower level and the conduction band the
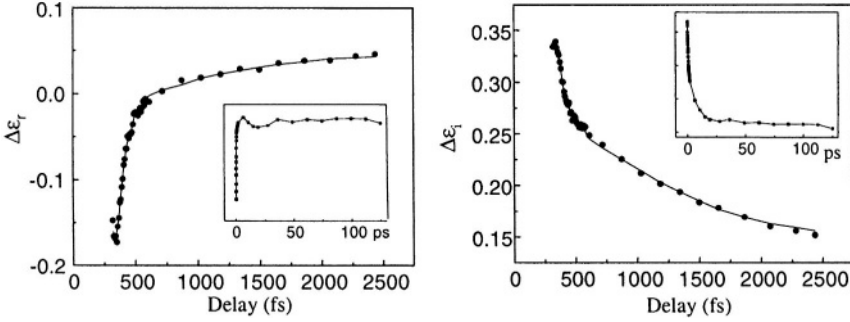
Figure 11.12. Real and imaginary part of the dielectric constant of Ta_2O_5 retrieved from transient reflection and transmission measurements. The insets show the behavior on a 100 ps time scale. Note the sign change for the real part.

upper level of a two-level system. When the photon energy $\hbar\Omega$ of the probe beam is smaller than $\hbar\Omega_D = E_D$, a positive contribution to $\Delta\varepsilon_r$ is expected from the Lorentz oscillator model:

$$\Delta\tilde{\epsilon}_D = \frac{e^2 f_D}{\varepsilon_0 m_D} N_D(t) \left[\frac{\Omega_D^2 - \Omega^2}{(\Omega_D^2 - \Omega^2)^2 + \Omega^2\Gamma_D^2} - \frac{i\Omega\Gamma_D}{(\Omega_D^2 - \Omega^2)^2 + \Omega^2\Gamma_D^2} \right].$$

$$(11.22)$$

Here, m_D is the effective mass of the defect, f_D, Γ_D and $\Omega_D = E_D/\hbar$ are the oscillator strength, the scattering rate, and the resonance frequency of the transition, respectively. Consistent with the sign change of $\Delta\varepsilon_r$ is the observed decay of $\Delta\varepsilon_i$, which can be interpreted as a transition of carriers from the conduction band into state D. The ps decay rate is dependent on the pump fluence, decreasing with increasing excitation fluence. This behavior is typical of a bi-molecular decay, where the decay rate is proportional to the product of excited electron and hole densities $N_e(t)N_h(t)$. A simple estimation of $\Delta\varepsilon_r$ based on the Drude model for the CB electrons and a two-level system for the STEs suggests $N_D \leq 10^{20}$ cm^{-3} at excitation levels close to breakdown [36].

5. COMPARISON OF EXPERIMENT AND THEORY

The electron and phonon population numbers $f(E,t)$, $s_\beta(q,t)$ and $N_D(t)$ from the solution of the Boltzmann transport equation can be used to predict the dielectric function $\varepsilon(t) = \varepsilon_r(t) - i\varepsilon_i(t)$ probed by a laser pulse at a frequency Ω_{pr}. For a weak probe pulse only the e-ph-pht interaction needs to be considered. By integrating the e-ph-pht interaction matrix element over all electron and phonon states allowed by energy and momentum conservation, the absorption change $\Delta\alpha(\Omega_{pr})$ can be calculated at each time step as a function of probe frequency Ω_{pr}. The imaginary part of the induced change of the di-
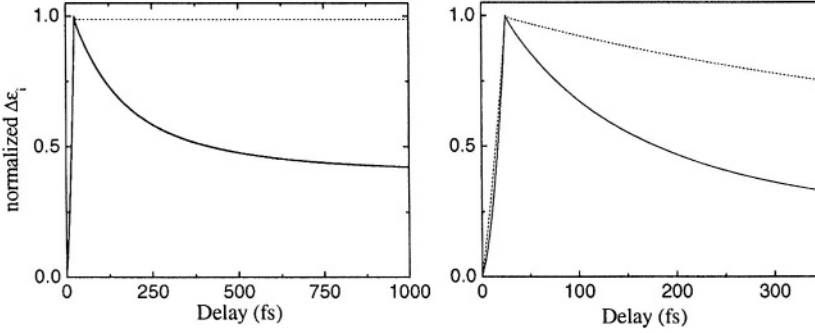
Figure 11.13. Left: Time-dependent imaginary part of the dielectric constant $\Delta\varepsilon_i(t)$ as a result of e-ph and e-e scattering (solid line) and e-e scattering only (dashed line) for $m_c = 0.75m_0$ and $C_D = 20$ eV. Right: Behavior of $\Delta\varepsilon_i(t)$ as a result of e-ph and e-e scattering for strong ($C_D = 35$ eV) and moderate ($C_D = 20$ eV) e-ph coupling and $m_c = 0.5m_0$.

electric constant is $\Delta\varepsilon_i(t) = (n_0\lambda_0/2\pi)\Delta\alpha(t)$, from which the real part can be obtained using a Kramers-Kronig transformation:

$$\Delta\varepsilon_r(\Omega_{pr}) = 1 + \frac{2}{\pi}\mathcal{P}\int_0^\infty \frac{\Omega'\Delta\varepsilon_i(\Omega')}{\Omega'^2 - \Omega_{pr}^2}d\Omega', \qquad (11.23)$$

where $\mathcal{P}$ refers to the principal value of the integral. By carefully adjusting the material parameters used in the Boltzmann equations, the agreement between theory and experiment can be optimized and the physical processes at play in highly-excited dielectrics identified.

It is instructive to compare the effect of different scattering mechanisms on the change of $\Delta\varepsilon_i$. In Fig. 11.13, the normalized $\Delta\varepsilon_i$ as a result of the numerical solution of the Boltzmann equations is plotted for different relaxation scenarios. Figure 11.13 (left) compares the effect of e-e scattering and the combined action of e-e and e-ph scattering on the relaxation of $\Delta\varepsilon_i$. Obviously, the decay of $\Delta\varepsilon_i$ on a 100 fs time scale is controlled by the interaction of the electrons with phonons. The redistribution of energy within the electron system due to e-e scattering does not lead to a significant change in $\Delta\varepsilon_i$ and measurable reflection and transmission signals.

Figure 11.13 (right) shows the relaxation behavior of two different e-ph coupling constants, that is, two different deformation potentials C_D. The stronger (weaker) the electron-phonon coupling, the faster (slower) $\Delta\varepsilon_i$ decays, and the larger (smaller) a value of $\Delta\varepsilon_{\max}$ (not shown) can be expected. The reason is that the e-ph interaction is responsible for both carrier heating during the excitation pulse and carrier relaxation. More efficient carrier heating increases the proportion of high-energy electrons. These carriers contribute more efficiently
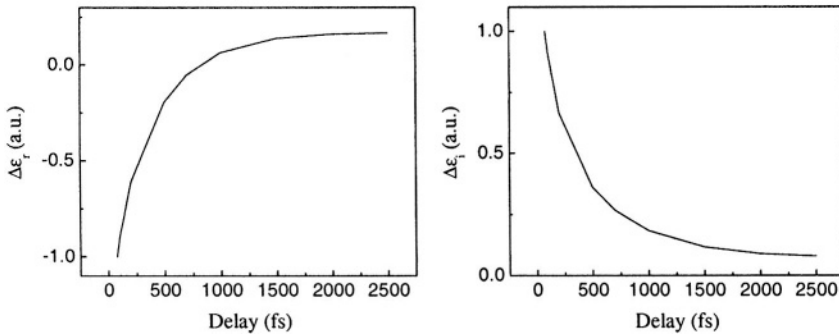
Figure 11.14. Left: Real part of the induced change of the dielectric constant as a function of time. Right: Imaginary part of the the induced change of the dielectric constant as a function of time. The data were obtained from the computer simulation of Boltzmann equations for the electrons, phonons, and STEs following the procedure outlined in the text.

to the absorption change and $\Delta\varepsilon_i$, respectively, and have faster scattering times. This explains the larger $\Delta\varepsilon_{max}$ for larger C_D and the faster recovery.

Figure 11.14 shows the results of a simulation where all the significant processes were turned on. The essential experimental observations – the initial recovery on a 100 fs time scale followed by a slower (ps) component and the sign change of $\Delta\varepsilon_r$ – can be reproduced for a certain choice of material parameters. There are a number of input quantities (material parameters), such as the deformation potential C_D, the number of phonon modes, and the parameters associated with the formation of the defect state, that are not well known for the oxide films used in the experiments (this was also the reason for including only three phonon modes into the simulation of materials with many atoms per unit cell). For this reason we did not attempt at this point a detailed fit of the experimental results shown in Fig. 11.12. This can be done after assuming certain values for some of these parameters and leaving some open to be retrieved from a fit. It should also be mentioned that the induced reflection change does not relax completely even after a few ns. This may indicate that the STEs are relatively long-lived.

6.   SUMMARY

Dielectric breakdown produced by femtosecond laser pulses in oxide films shows very deterministic features depending on the properties of the materials used. The scaling of the damage threshold with pulse duration in the sub-picosecond range can be explained with a phenomenological model that includes multiphoton absorption, impact ionization, and carrier relaxation. Subsequently, three figures of merit – the multiphoton absorption coefficient, the impact ionization coefficient, and an effective decay time – can predict the

damage behavior. The damage fluence scales linearly with the bandgap of the material rather independently of the pulse duration. This experimental observation is consistent with scaling laws that can be derived from Keldysh theory and impact ionization within the framework of the flux-doubling model.

The dynamics of the excited electron plasma at excitation levels close to but below the damage threshold can be studied with femtosecond pump-probe experiments in reflection and transmission. A retrieval algorithm that takes into account standing-wave effects of both pump and probe in the film allows one to obtain the time-dependent dielectric constant. To interpret these experiments we performed theoretical simulations that were based on the Boltzmann equation for the electron and phonon system supplemented with a term that describes the formation of defects (self-trapped excitons). This model can reproduce the experimental observations. In particular, the observed sign change of the real part of the dielectric constant within 1 ps after excitation can be attributed to the formation of STEs. These defect states are likely contributors to incubation effects observed in damage studies with multiple pulses [29].

Acknowledgements

References

1. P. Pronko et al., *Opt. Commun.* **114,** 106 (1995).

2. M. Lenzner, J. Krüger, W. Kautek and F. Krausz, *Applied Physics A* **68**, 369 (1999).

3. M. Perry et al., *J. Appl. Phys.* **85**, 6803 (1999).

4. A. Joglekar et al., *Appl. Phys. B* **77**, 25 (2003).

5. K. Davis, K. Miura, N. Sugimoto and K. Hirao, *Opt. Lett.* **21**, 1729 (1996).

6. Y. Cheng et al., *Opt. Exp.* **11,** 1809 (2003).

7. E. Glezer et al., *Opt. Lett.* **21**, 2023 (1996).

8. D. Homoelle, S. Wielandy, A. Gaeta, N. Borrelli and C. Smith, *Opt. Lett.* **24**, 1311 (1999).

9. M. Will, S. Nolte, B. Chichkov and A. Tunnermann, *Appl. Opt.* **41,** 4360 (2002).

10. J.-C. Diels and W. Rudolph, *Ultrashort Laser Pulse Phenomena,* Academic Press, New York, 1996.

11. W. Smith, *Opt. Eng.* **17**, 489 (1978).

12. A. Vaidyanathan, T. Walker and A. Guenther, *J. Quant. Electron.* **16**, 89 (1980).

13. B. Stuart et al., *Phys. Rev. B* **53,** 1749 (1996).

14. R. Stoian, D. Ashkenasi, A. Rosenfeld and E. Campbell, *Phys. Rev. B* **62,** 13167 (2000).

15. L. Keldysh, *Soviet Physics JETP* **20**, 1307 (1965).

16. J. P. Callan, A.-T. Kim, L. Huang and E. Mazur, *Chem. Phys.* **251**, 167 (2000).

17. L. Holway and D. Fradin, *J. Appl. Phys.* **46**, 279 (1975).

18. A. Kaiser, B. Rethfeld, M. Vicanek and G. Simon, *Phys. Rev. B* **61**, 11437 (2000).

19. J. Zeller, M. Mero, P. Alsing, J. McIver and W. Rudolph, in preparation (2004); see also *SPIE Proceedings.* vol. 5273 (2003).

20. M. Ueta, H. Kanzaki, K. Kobayashi, Y. Toyozawa and E. Hanamura, volume 60 of *Springer Series in Solid-State Science,* chapter 4, Springer-Verlag, Heidelberg, 1986.

21. P. Martin et al., *Phys. Rev. B* **55**, 5799 (1997).

22. P. Audebert et al., *Phys. Rev. Lett.* **73,** 1990 (1994).

23. S. Guizard et al., *Europhys. Lett.* **29**,401 (1995).

24. M. Georgiev and N. Itoh, *J. Phys. C* **2,** 10021 (1990).

25. H. Tang, K. Prasad, R. Sanjinbs, P. Schmid and F. Lévy, *J. Appl. Phys.* **75,** 2042 (1994).

26. K. Song and R. Williams, *Self-Trapped Excitons,* volume 105 of *Springer Series in Solid-State Science,* chapter 1, p. 15, Springer-Verlag, Heidelberg, 2 edition, 1996.

27. I. Fugol, *Advances in Physics* **27**, 1 (1978).

28. A. Sumi, *J. Phys. Soc. Jpn.* **43**, 1286 (1977).

29. J. Jasapara, A. Nampoothiri, W. Rudolph, D. Ristau and K. Starke, *Phys. Rev. B* **63**,045117 (2001).

30. M. Li, S. Menon, J. Nibarger and G. Gibson, *Phys. Rev. Lett.* **82,** 2394 (1999).

31. A.-C. Tien, S. Backus, H. Kapteyn, M. Murnane and G. Mourou, *Phys. Rev. Lett.* **82**, 3883 (1999).

32. M. Demchuk et al., *Opt. Commun.* **83,** 273 (1991).

33. A. Streltsov et al., *Appl. Phys. Lett.* **75**, 3778 (1999).

34. L. Sudrie et al., *Phys. Rev. Lett.* **89**, 186601 (2002).

35. M. Sparks et al., *Phys. Rev. B* **24**, 3519 (1981).

36. A. J. Sabbah, M. Mero, J. Zeller and W. Rudolph, in preparation (2004); see also *SPIE Proceedings* vol. 5273 (2003).

37. J. Jasapara, M. Mero and W. Rudolph, *Appl. Phys. Lett.* **80,** 2637 (2002).

Index